NASA/CP-1999-209704/VOL2/PT2

1999 NASA High-Speed Research Program Aerodynamic Performance Workshop

Volume II—High Lift

Edited by
David E. Hahne
Langley Research Center, Hampton, Virginia

Proceedings of a workshop sponsored by
the National Aeronautics and Space
Administration, Washington D.C., and
held in Anaheim, California
February 8–12, 1999

National Aeronautics and
Space Administration

Langley Research Center
Hampton, Virginia 23681-2199

December 1999

The use of trademarks or names of manufacturers in this report is for accurate reporting and does not constitute an official endorsement, either expressed or implied, of such products or manufacturers by the National Aeronautics and Space Administration.

Available from:

NASA Center for AeroSpace Information (CASI)
7121 Standard Drive
Hanover, MD 21076-1320
(301) 621-0390

National Technical Information Service (NTIS)
5285 Port Royal Road
Springfield, VA 22161-2171
(703) 605-6000

PREFACE

The High-Speed Research Program sponsored the NASA High-Speed Research Program Aerodynamic Performance Review on February 8-12, 1999 in Anaheim, California. The review was designed to bring together NASA and industry High-Speed Civil Transport (HSCT) Aerodynamic Performance technology development participants in areas of: Configuration Aerodynamics (transonic and supersonic cruise drag prediction and minimization) and High-Lift. The review objectives were to: (1) report the progress and status of HSCT aerodynamic performance technology development; (2) disseminate this technology within the appropriate technical communities; and (3) promote synergy among the scientist and engineers working HSCT aerodynamics. The HSR AP Technical Review was held simultaneously with the annual review of the following airframe technology areas: Materials and Structures, Environmental Impact, Flight Deck, and Technology Integration. Thus, a fourth objective of the Review was to promote synergy between the Aerodynamic Performance technology area and the other technology areas within the airframe element of the HSR Program.

The work performed in the Configuration Aerodynamics (CA) element of the High-Speed Research Program during 1998 was presented in the following sessions:

Propulsion Integration
Analysis Methods
Design Optimization
Testing

The work performed in the High Lift (HL) element of the High-Speed Research Program during 1998 was presented in the following sessions:

High-Lift Configuration Development
Tools and Methods Development

The proceedings for the Aerodynamic Performance Annual Review are published in three volumes:

Volume I, Parts 1 and 2	Configuration Aerodynamics
Volume II, Parts 1 and 2	High Lift

AP Review Chairperson: David Hahne
NASA Langley Research Center

CONTENTS

Preface iii

VOLUME II – HIGH LIFT

Part 1*

High-Lift Configuration Development Session

Data Corrections and Wind-Tunnel Data Comparisons of a 5% TCA Model in the NASA Ames 12-Ft Pressure Tunnel 1
Fanny A. Zuniga (NASA Ames)

Wind Tunnel Test of a 5% HSCT (TCA) Model in the NASA Ames 12-Ft Pressure Tunnel 57
Robin Edwards, Roger Clark, David Yeh, and Ryan Polito (The Boeing Company, Phantom Works)

Wind Tunnel Test of a 5% HSCT TCA Model in the NASA Ames 12-Ft Pressure Tunnel (Stability and Control Summary) 159
Paul T. Glessner and Paul Kubiatko (The Boeing Company, Phantom Works)

TCA-4/NASA473 Test Results: A High-Lift and Stability and Control Test of the HSR 5% Model Including Planform Variations, Canard, and 3-Surface Configurations 191
Michael B. Elzey and Robert C. Griffiths (Boeing Commercial Airplane Group)

TCA Final Assessment and Test/Theory Comparisons for Sealed Slats 377
Allen W. Chen (Boeing Commercial Airplane Group)

HSR Leading Edge Trade Study 441
Warren Burggraf (Boeing Commercial Airplane Group)

TCA 2.8-38 Outboard LE Flap Chord Study 477
Art Powell (The Boeing Company, Phantom Works)

Impact of Wing Planform, Canard, and Leading Edge Flap Type on High Lift Performance and Technology Projection 515
Paul Meredith (Boeing Commercial Airplane Group)

Part 2

Tools and Methods Development Session

Numerical Analysis of a 5% HSCT TCA Model in the NASA Ames 12-Ft Pressure Tunnel 551
Chung-Jin Woan (The Boeing Company, Phantom Works)

*Part 1 is presented under separate cover.

CFD Assessment of TCA High-Lift Configurations 647
David T. Yeh and Roger W. Clark (The Boeing Company, Phantom Works)

A Comparison of CFL3D and TLNS CFD Results on TCA and REF-H High Lift Configurations 727
Tim Siebersma (Boeing Commercial Airplane Group)

Comparison of CFD Solutions with Test Data for TCA High Lift Configurations 803
Xuetong Fan (ASE Technologies, Inc.)

Numerical Analysis of Lateral Control Characteristics of HSCT Forebody Control Surfaces 857
David T. Yeh and Roger W. Clark (The Boeing Company, Phantom Works)

High-Lift CFD Validation 913
Wendy B. Lessard (NASA Langley)

Panel Method Analysis of Wind Tunnel Model Support Effects in the Langley 14 x 22-Ft and Ames 12-Ft Wind Tunnels 949
Ryan Polito (The Boeing Company, Phantom Works)

Evaluation of the Linear Prediction of the Effects of Planform Variation and Flap Deflection 993
Roger Clark and Ryan Polito (The Boeing Company, Phantom Works)

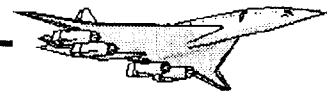

Numerical Analysis of a 5% HSCT TCA Model in the NASA Ames 12-ft Pressure Tunnel

By
Chung-Jin Woan
Boeing, Long Beach

HSR Airframe Technical Review

Aerodynamics High Lift

Anaheim, California
February 9-11, 1999

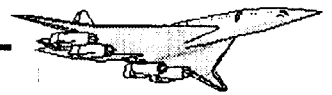

High Lift Technology Development (Task 33)

This slide shows an outline of the High-Lift Technology program.

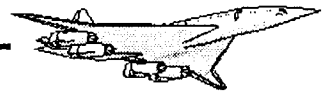

High Lift Technology Development (Task 33)

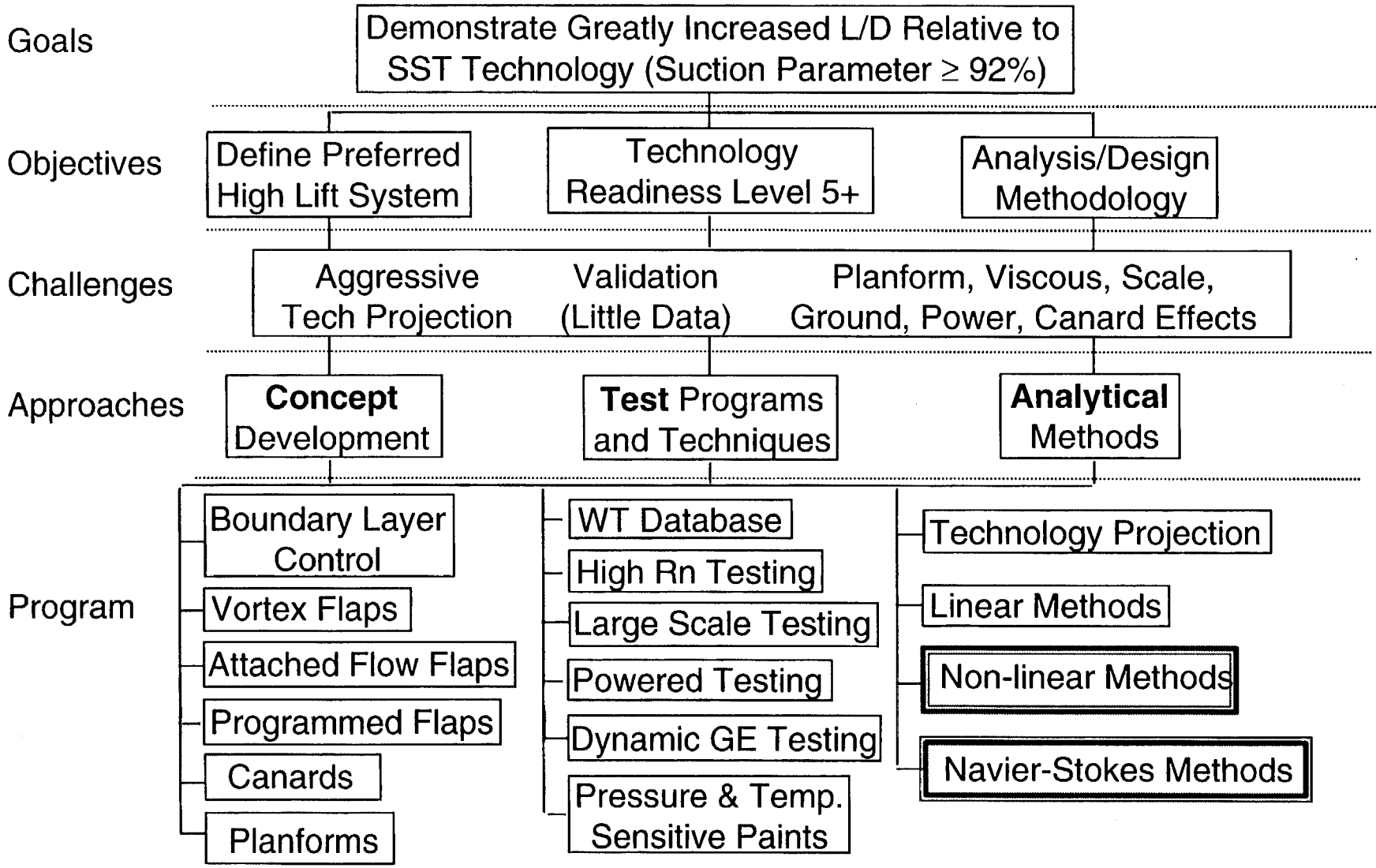

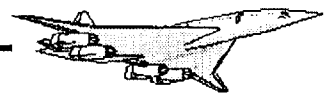

Outline

The presentation of this paper starts with a statement of objectives followed by the definitions of problems, gridding strategy, enhancements of CFL3D/MAGGIE, Baldwin-Lomax/Degani-Schiff turbulence model, and results. A few concluding remarks and recommendations will be made at the end of the presentation.

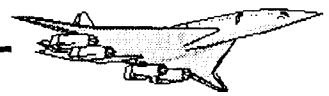

Outlines

- Objectives
- Definitions of problems and 5% TCA model
- Gridding strategy
- Enhancements of CFL3D/MAGGIE
- Baldwin-Lomax model with Degani-Schiff modification
- Results
  - Comparisons of CFD C_p, C_L, C_D, and C_M with test data
  - Tunnel wall and post effects
  - Boundary-layer profiles and Baldwin-Lomax's F(y) function
- Concluding remarks

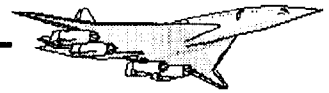

Objectives

The overall objective of this task is to develop an integrated wind-tunnel/free-air CFD process to speed up CFD turnaround time in HSCT high-lift configuration development.

The specific objective of this paper is to investigate the effects of the NASA/Ames 12-ft wind tunnel wall and model supports on the model aerodynamic characteristics using CFD, to evaluate the CFD results by comparison with experimental data, and to share our experience in obtaining the Navier-Stokes solutions of the wind tunnel flow simulations for the 5% TCA model.

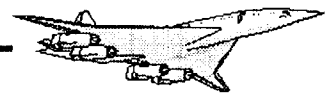

Objectives

- **Overall Objective**
  - Develop an integrated wind-tunnel/free-air CFD process to speed up CFD turnaround time in HSCT high-lift configuration development
- **Objectives of the Present Paper**
  - Investigate the effects of the NASA/Ames 12-ft wind tunnel wall and model supports on the model aerodynamic characteristics using CFD
  - Evaluate the CFD results by comparison with experimental data

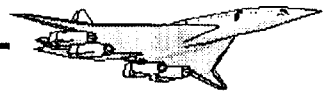

Definitions of Three CFD Problems

Shown here are the three CFD configurations considered: the full-scale free-air configuration, the 5% TCA model/wind-tunnel configuration, and the 5% TCA model/wind-tunnel/posts configuration. The TCA configuration considered has an outboard part-span deflected LE (leading edge) flap of 30 degrees and three deflected TE (trailing edge) flaps of 10 degrees. The test of this 5% TCA model is designated as TCA 3.

All the CFD flow simulations were made at Mach = 0.3, α = 10 degrees, and Re = 8 million.

The free-air CFD simulation has been done elsewhere by Dr. Yeh of Boeing Long Beach and its solution presented in this paper was provided by Dr. Yeh.

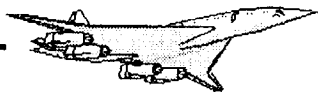

Definitions of Three CFD Problems

Part-Span LE deflected Flap

$\alpha = 10^{o}$
Mach = 0.3
Re = 8 Million

1. TCA Free-Air CFD

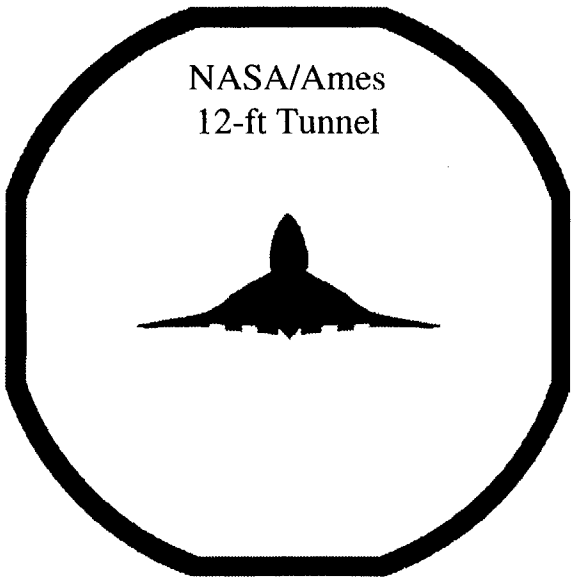

2. 5% TCA Model/Tunnel

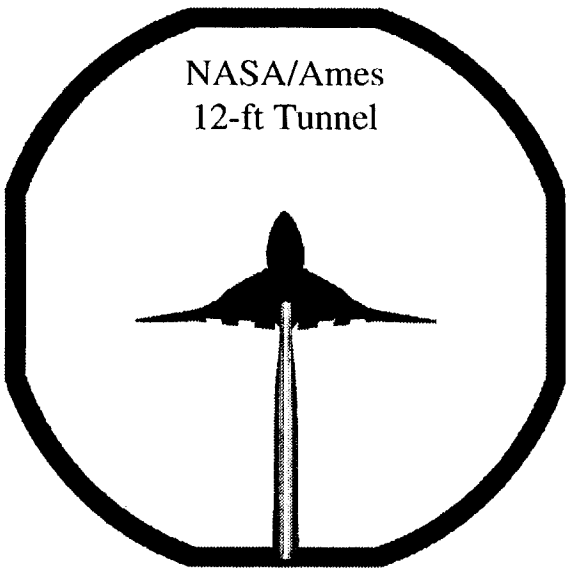

3. 5% TCA Model/Tunnel/Posts

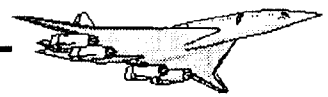

Relative Locations of 5% TCA and Posts

The dimensions of the CFD model of the NASA/Ames 12-ft wind tunnel and model supporting posts are shown here together with some key locations including the origin of the CFD coordinate system, the aircraft pivot point, the center of moment, the tunnel floor, and the post pivot point. The fuselage cross section in the plane of symmetry is shown at $\alpha = 0$ degree.

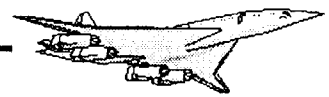

Relative Locations of 5% TCA and Posts

Inside NASA/Ames 12-ft Pressure Tunnel

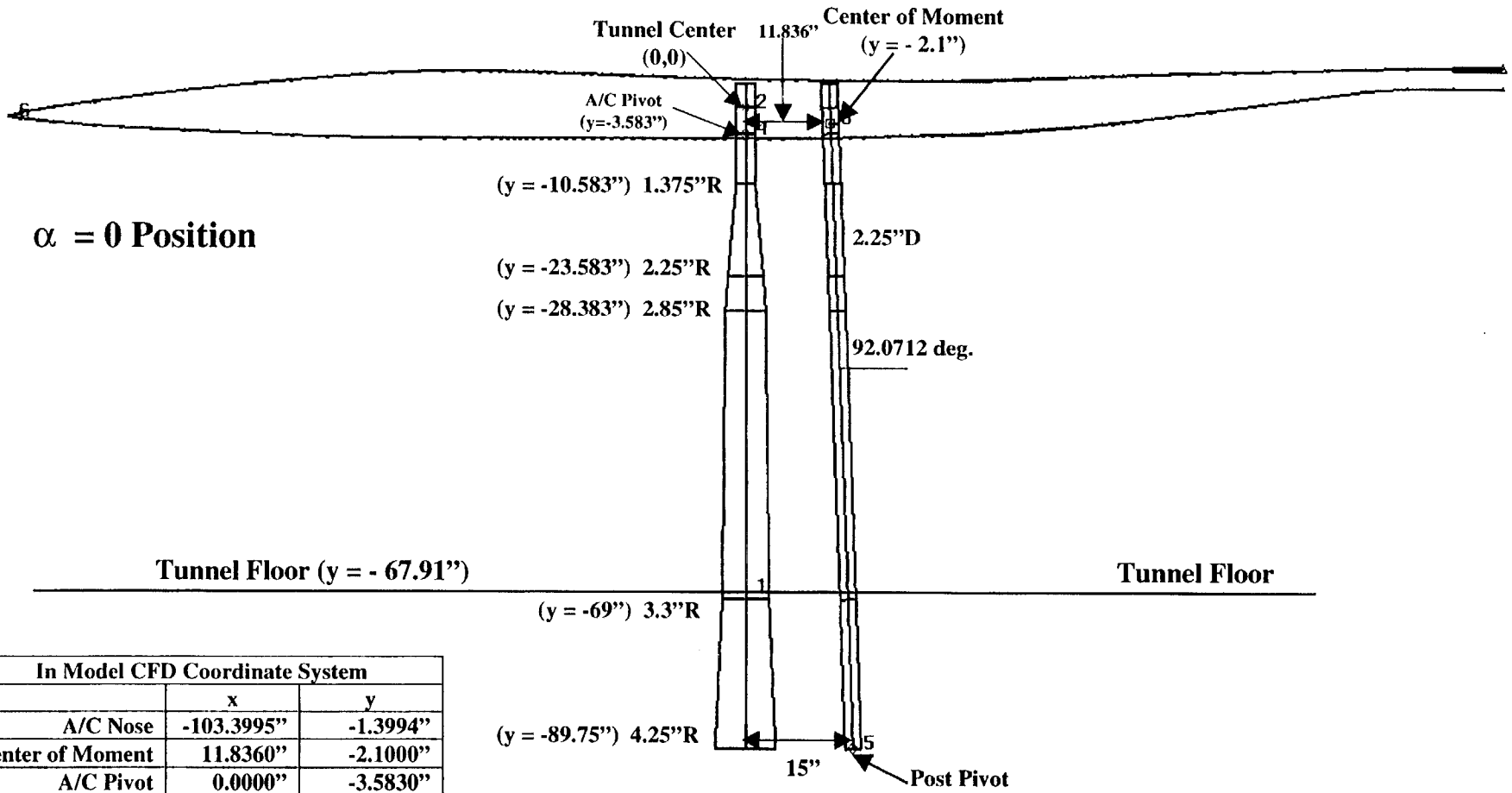

α = 0 Position

In Model CFD Coordinate System		
	x	y
A/C Nose	-103.3995"	-1.3994"
Center of Moment	11.8360"	-2.1000"
A/C Pivot	0.0000"	-3.5830"
Tunnel Floor		-67.9100"
Post Pivot	15.0000"	-89.6449"

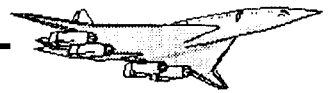

5% TCA Model Inside NASA/Ames 12-ft Pressure Tunnel

This is a 3-D view of our CFD model of the 5% TCA model inside the NASA/Ames 12-ft pressure tunnel. The model is shown at α = 10 degrees. Both model supporting posts were model in our CFD simulations.

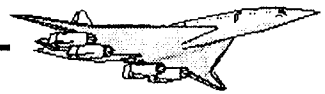

5% TCA Model Inside NASA/Ames 12-ft Pressure Tunnel

$\alpha = 10^{o}$ Position

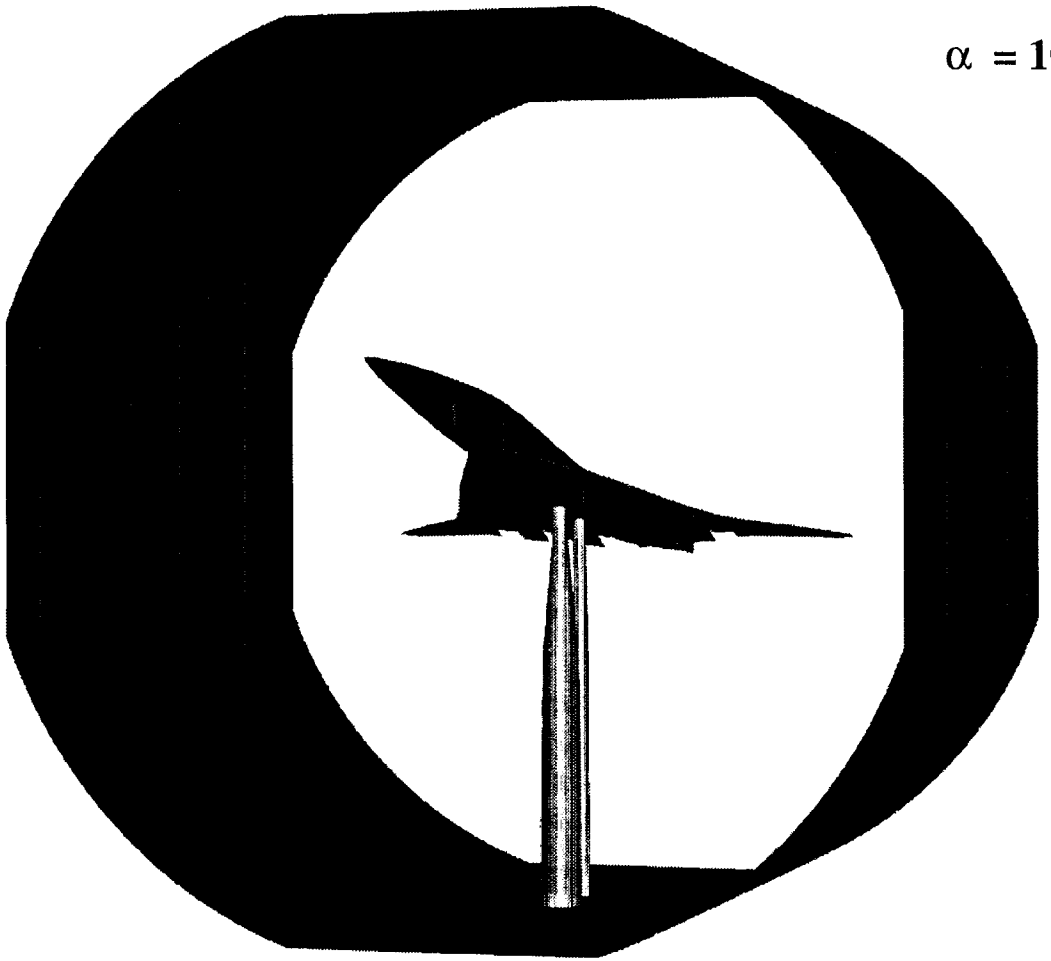

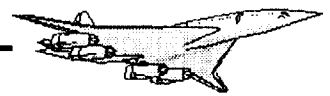

Gridding Strategy

Our gridding strategy employed the chimera (overset grid) technique as illustrated in this figure. The starting point is the given full-scale free-air airplane grid as shown in the left figure. The full-scale airplane grid was scaled down to 5% and the grid downstream of the back end of the fuselage was trimmed off and replaced by a mushroom grid. A tunnel grid was generated independently of the model grid and combined with the model grid to obtain a CFD model/tunnel grid. The middle figure shows a 3-D view of the constructed overset grid of the model/tunnel configuration. The resulting CFD model/tunnel grid is a 3-block overset grid.

To construct a model/tunnel/posts grid, six additional grids were generated: one fore post grid, one aft post grid, and four collar grids. The collar grids were used to join the two posts with the model and the wind-tunnel wall. The right figure shows a 3-D view of the constructed 9-block overset grid of the model/tunnel/posts configuration.

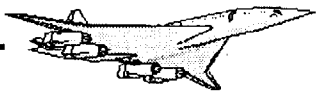

Gridding Strategy

Overset Grid

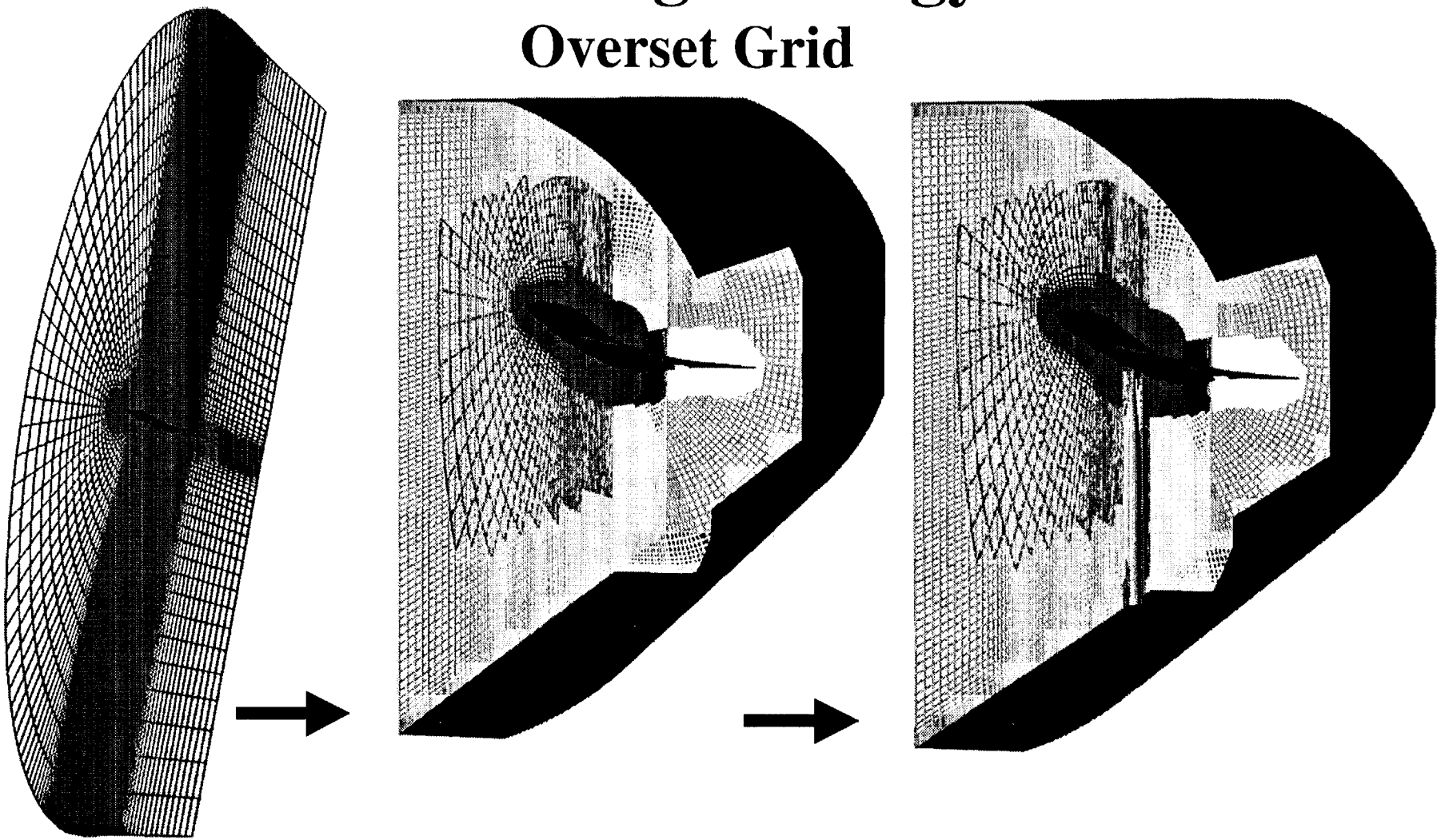

Free-Air

5% TCA Model/Tunnel

5% TCA Model/Tunnel/Posts

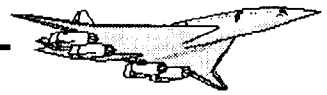

MAGGIE Calculated Overset Grid

This figure shows the overlapping grids in the plane of symmetry for the 9-block overset grid of the model/tunnel/posts case.

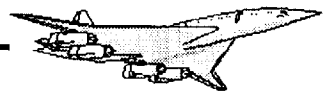

MAGGIE Calculated Overset Grid

5% TCA Model/Tunnel/Posts

Plane of Symmetry

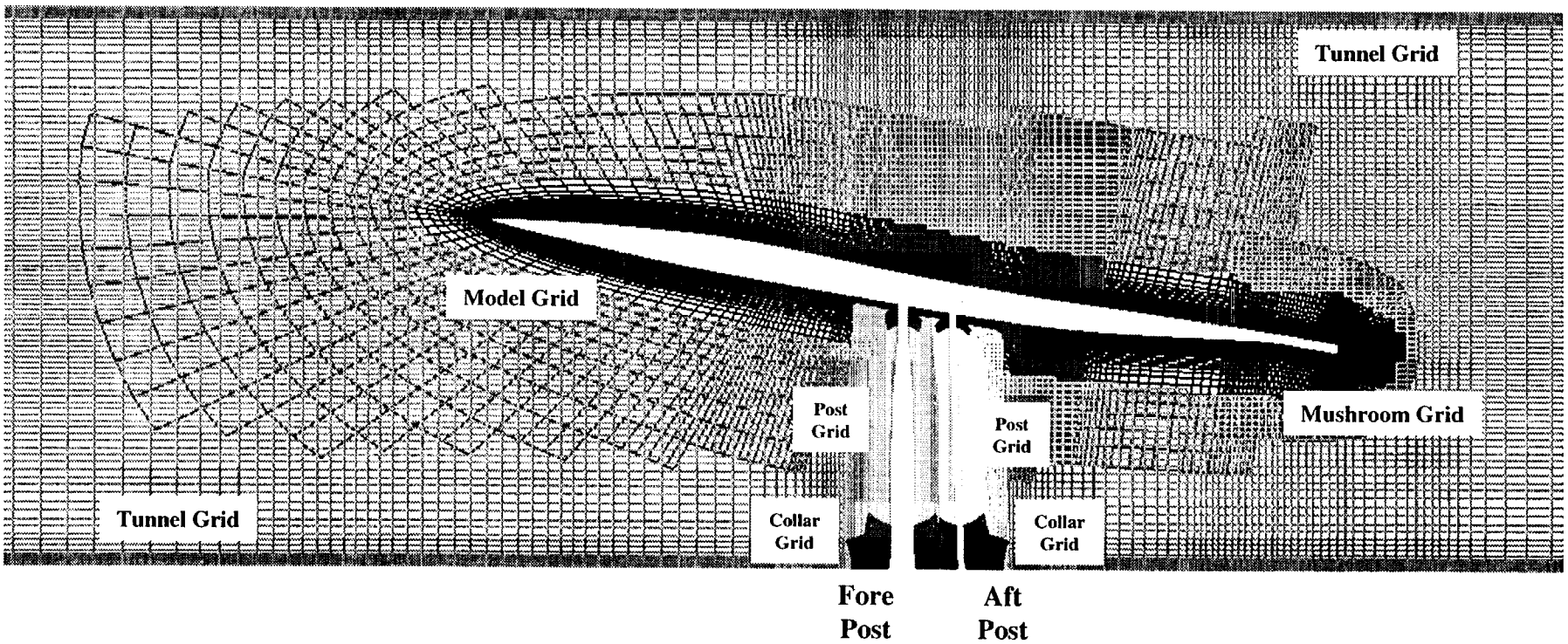

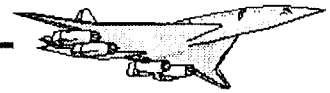

MAGGIE Calculated Overset Grid (Continued)

This figure shows an axial view of a few cross-sectional grids of the 9-block model/tunnel/posts overset grid.

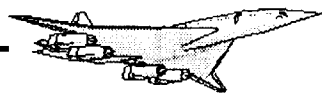

MAGGIE Calculated Overset Grid

5% TCA Model/Tunnel/Posts

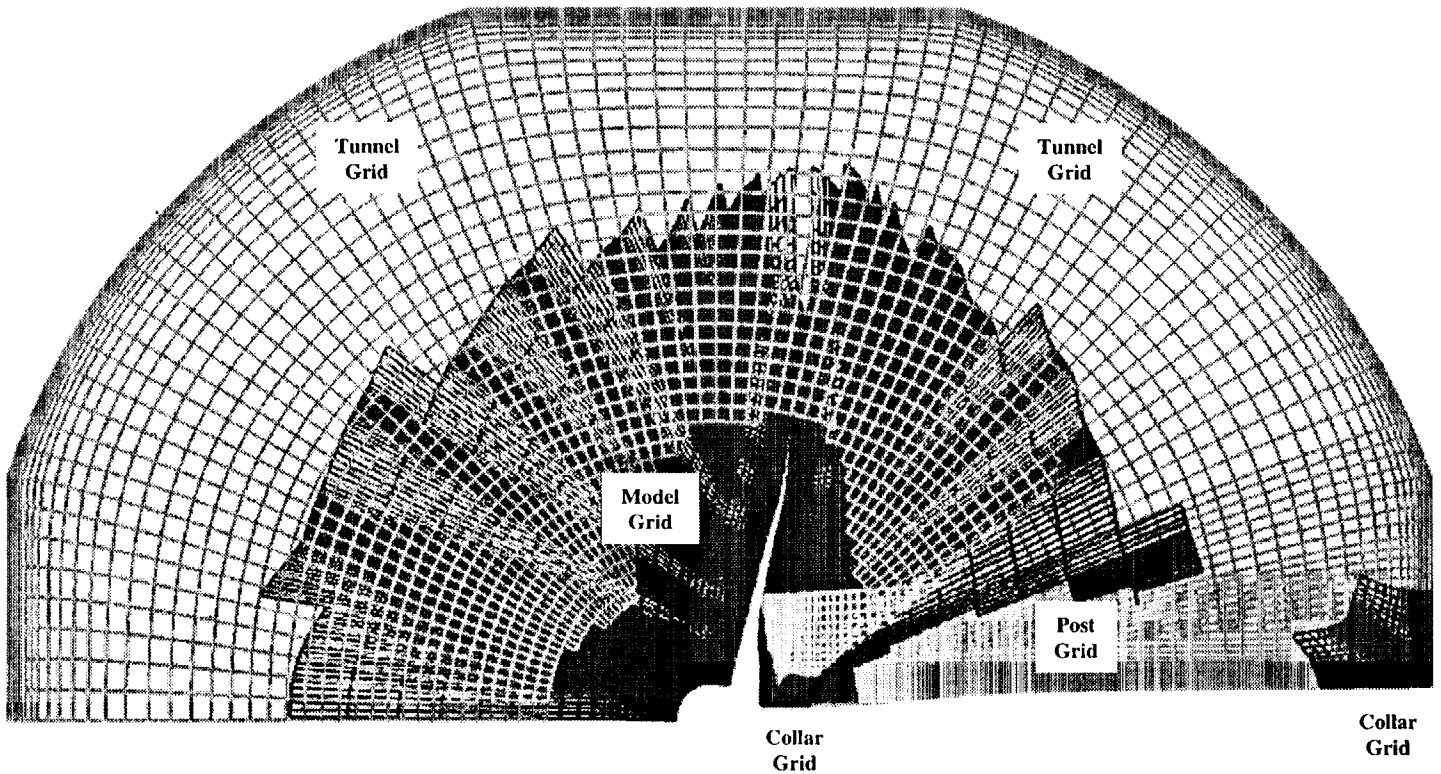

Cross-sectional Grids

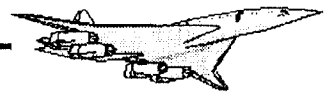

MAGGIE Calculated Overset Grid (Concluded)

The blowups of the collar grids shown here are used to show how the four collar grids join the post grids to the model and tunnel grids to form a complete overset grid for our model/tunnel/posts CFD simulation.

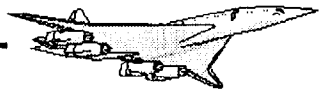

MAGGIE Calculated Overset Grid

5% TCA Model/Tunnel/Posts

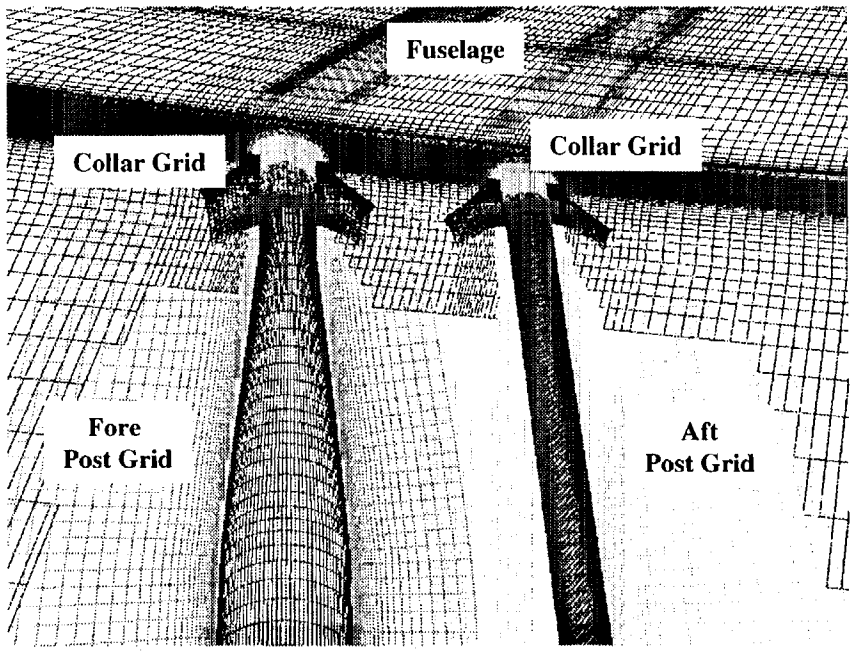

For Model and Posts

Collar Grids

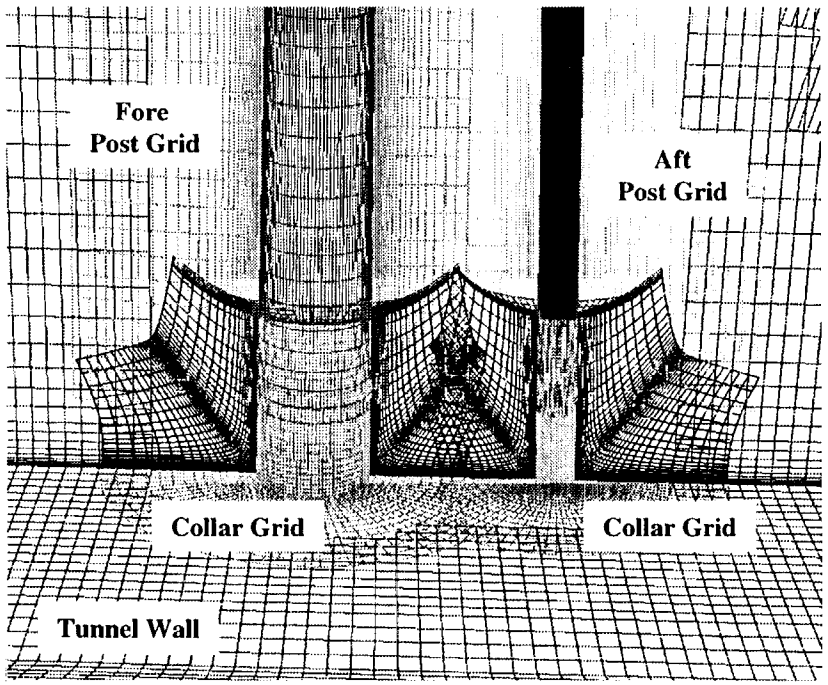

For Tunnel Wall and Posts

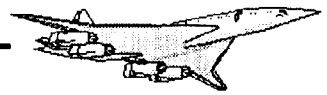

Region of Grid Refinement and Pressure Tap Location

It was found necessary to increase the density of the model grid in the streamwise direction around the posts in order to provide proper overlapping regions for the various grids. The region of the grid refinement is the area surrounded by the blue lines shown in this figure. Ninety eight grid points were added in the streamwise direction in this region. To maintain the structured grid topology, the grid refinement must be made to both upper and lower surfaces.

Also shown in this figure are the chordwise and spanwise pressure tap locations and the part-span deflected LE flap marked in red. This figure will be helpful as we examine the configuration surface pressure distributions in out later discussion.

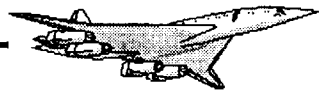

Region of Grid Refinement and Pressure Tap Locations for 5% TCA Model

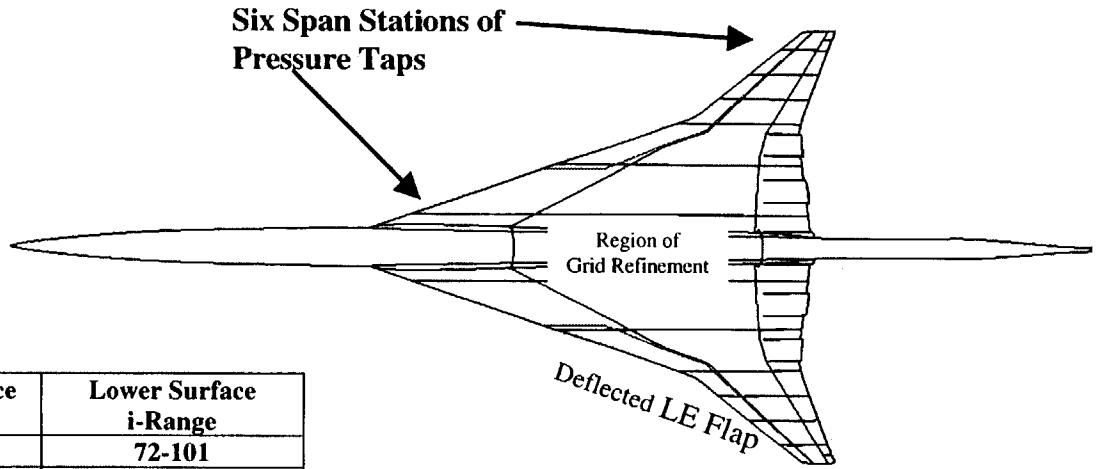

	Upper Surface i-Range	Lower Surface i-Range
Free Air	177-206	72-101
5% TCA Model	275-402	72-199
Added	98	98

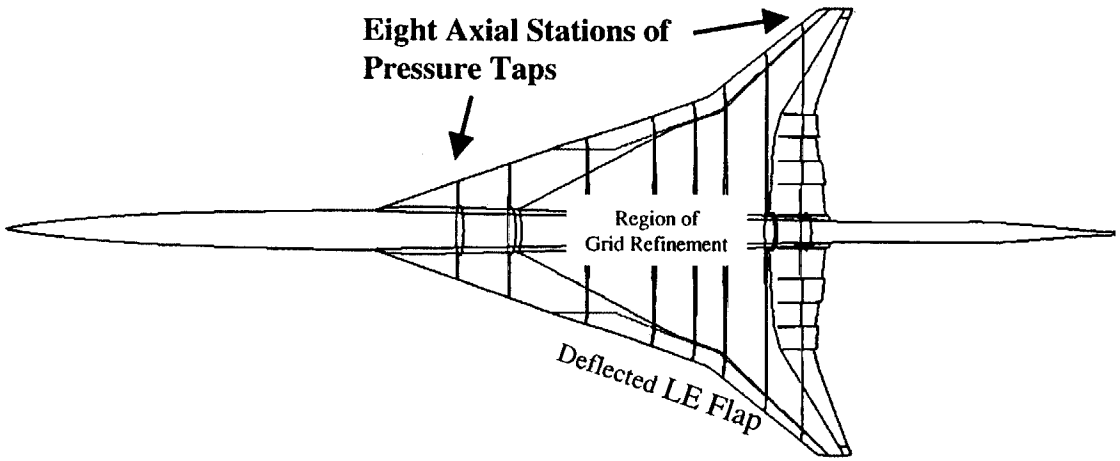

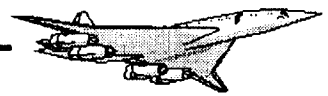

Dimensions of Computational Grids

Here we summarize the total number of grid points of each of the three CFD computational grids.

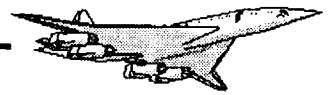

Dimensions of Computational Grids for 5% TCA Model

Case	Number of Blocks	Number of Grid Points
Free-Air	1	3,400,085
Model/Tunnel	3	7,009,795
Model/Tunnel/Posts	9	7,819,177

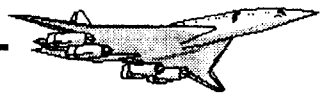

Enhancements of CFL3D/MAGGIE

During the course of our CFD wind-tunnel flow simulations, both the flow solver CFL3D and the overset grid preprocessor MAGGIE have been enhanced and streamlined:

CFL3D - CFL3D has been coupled with PRECFL3D into a single module with Fortran 90 run-time memory allocation capability. This has been done for both versions 4 and 5. With run-time memory allocation, a single executable can be used for all the problems with any required run-time memory sizes. The input to the coupled module is the same as the original CFL3D input. This totally eliminates the need of user's effort to compile and recompile CFL3D for flow simulations.

MAGGIE - MAGGIE has been greatly enhanced and sped up for dealing with complex configurations. Some of the major enhancements and their benefits are summarized in this view graph.

Overset Grid Force and Moment Integration - The NASA/Ames FOMOCO code has been (externally) coupled with CFL3D's PLOT3D grid and Q files and MAGGIE's overset grid connectivity file for force and moment integrations. FOMOCO uses a zipper grid to replace the overlapping grid region to avoid duplicative contribution from the overlapping grids. The following view graph shows the constructed zipper grids on the fuselage lower surface and around the fore and aft supporting posts for the model/tunnel/posts case.

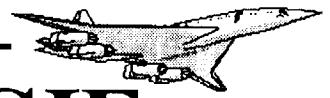

Enhancements of CFL3D/MAGGIE

CFL3D: Flow Solver

- **Run-time memory allocation**

FORTRAN 77 with	Fortran 90 with
Compile-Time Memory Allocation	**Run-Time** Memory Allocation

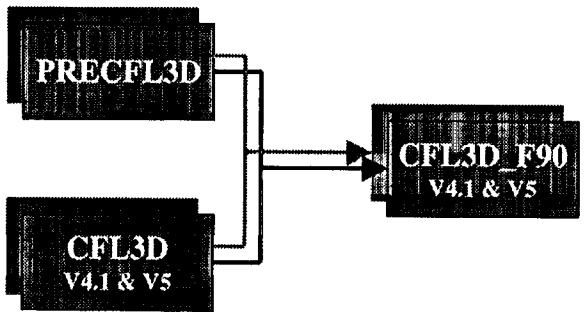

- **Integration of CFL3D/MAGGIE and FOMOCO**

Benefits:

- **Easy to compile**
- **One executable for all problems**
- **Force and moment integration over overlapping regions**

MAGGIE: Overset Grid Processor

- **Direct hole creation**
- **Direct fringe point specification**
- **Phantom grid capability**
- **Direct control over the ranges of the target and donor grids**

Benefits:

- **Increase capability for handling complex geometries**
- **Greatly speeds up computing process**

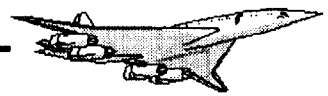

Zipper Grids

This figure shows a process of constructing zipper grids starting from a blocked grid (the top figure), through the overlapping grid (the middle figure), to the zipper grid (the bottom figure).

As shown in the bottom figure, a layer of triangular elements is used to join the post and fuselage grids and replace the grid overlapping regions as shown in the middle figure. This hybrid composite surface grid can be used for force and moment integration to avoid duplication of the contribution from the overlapping grids.

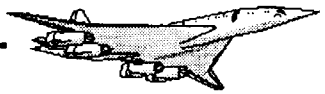

Zipper Grids

Used for Force and Moment Integration

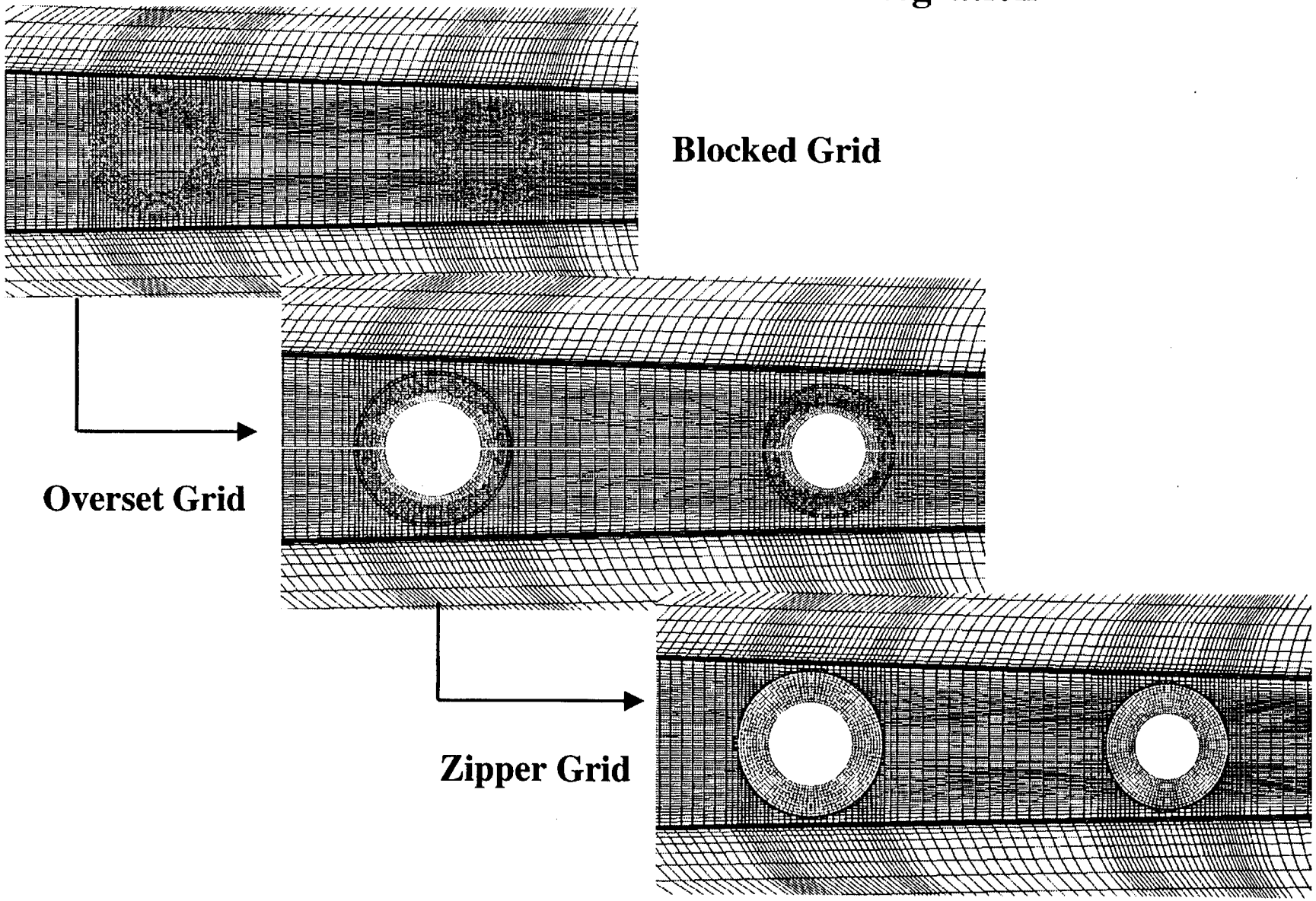

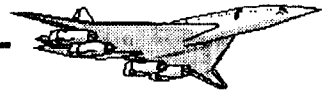

IVISC=3: Baldwin-Lomax Model with Degani-Schiff Modification

The equations for the Baldwin-Lomax Model with Degani-Schiff Modification presented here are intended to define the two types of the wind-tunnel flow simulations we performed for the 5% TCA model.

In CFL3D implementation, the search index range for finding the maximum value of the *F(y)* function is defined as follows:

$$0.2\eta_{max}+1<\eta<0.8\eta_{max}+1$$

Here η is the index normal to the surface considered. By default, CFL3D takes 80% of the maximum index value as η_{max}.

With the j-index as the model's off-body index, the two type flows we calculated are as follows:

Type 1: J0.8 (CFL3D Built-In) Method

$$\eta_{max}=0.8JDIM$$

Type 2: J0.25/0.5 Modified Method

$$\eta_{max}=\begin{cases}0.25JDIM & \text{In wing LE region}\\ 0.50JDIM & \text{Otherwise}\end{cases}$$

Here, *JDIM* is the maximum number of cells in the j-direction.

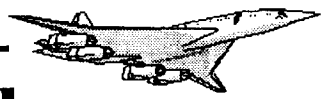

IVISC=3: Baldwin-LomaxModel

with Degani-Schiff Modification

Inner layer: $y \le y_{crossover}$

$$\mu_T = \mu_{T,inner} = \rho \ell^2 \Omega \frac{R_e}{M_\infty}$$

$$\ell = y\left[1-\exp(-y^+/26)\right]$$

Outer layer: $y \ge y_{crossover}$

$$\mu_T = \mu_{T,outer} = 0.0168(1.6)\rho F_{wake} F_{kleb} \frac{R_e}{M_\infty}$$

$$F_{wake} = \min\left[y_{\max} F_{\max}, 1.0 y_{\max} u_{dif}^2 / F_{\max}\right]$$

$$F(y) = y\Omega\left[1-\exp\left(-y^+/26\right)\right]$$

$$F_{kleb} = \left[1+5.5\left(\frac{0.3y}{y_{\max}}\right)^6\right]^{-1}$$

$$u_{dif} = \left(\sqrt{u^2+v^2+w^2}\right)_{\max} - \left(\sqrt{u^2+v^2+w^2}\right)_{\min}$$

Search Index Range for $F_{\max}$

$$0.2\eta_{\max} + 1 < \eta < 0.8\eta_{\max} + 1$$

J0.8 (CFL3D Built-In) Method

$$\eta_{\max} = 0.8 JDIM$$

J0.25/0.5 Modified Method

$$\eta_{\max} = \begin{cases} 0.25 JDIM & \text{In wing LE region} \\ 0.50 JDIM & \text{Otherwise} \end{cases}$$

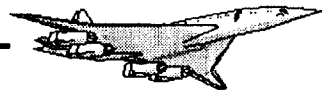

Effects of Searching Distance on Chordwise Cp

This figure shows chordwise Cp of three span stations for the J0.8 (the red chaindot lines) and J0.25/0.5 (the blue dash lines) solutions for the CFL3D solutions with the model and tunnel. Also shown are the free-air solution (the solid lines, a j0.25/0.5 type solution) and the TCA-3 test data (the up and down triangles).

It is very obvious from the comparison between the red chaindot lines and the red dash lines that leading edge vortex suction peaks are missing in the J0.8 solution. The J0.8 solution also shows a trailing edge flow separation.

This observation had motivated us to look into the boundary-layer flow characteristics. The following three view graphs show the boundary-layer profiles of the J0.8 and J0.25/0.5 solutions in terms of the local *F(y)* and velocity profiles at the 2nd outboard span station

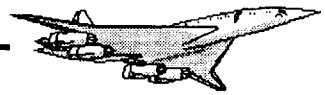

Effects of Searching Distance on Chordwise Cp in Baldwin-Lomax/Degani-Schiff Model

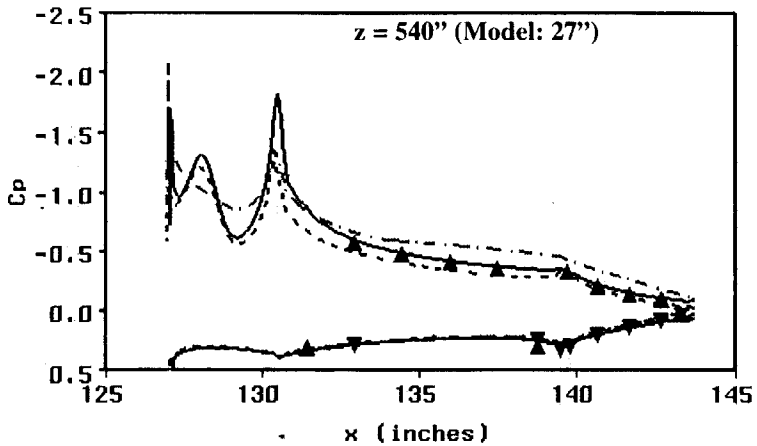

Test

Geometric $\alpha = 8.9922^{\circ}$

Corrected $\alpha = 9.772^{\circ}$

CFD

$\alpha = 10^{\circ}$

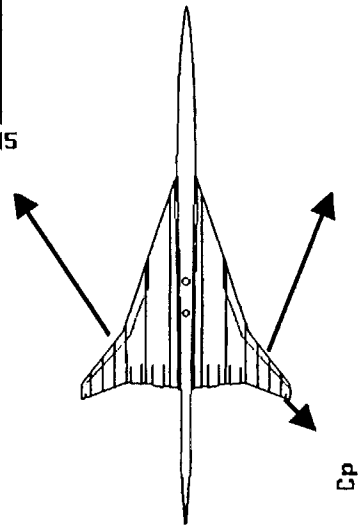

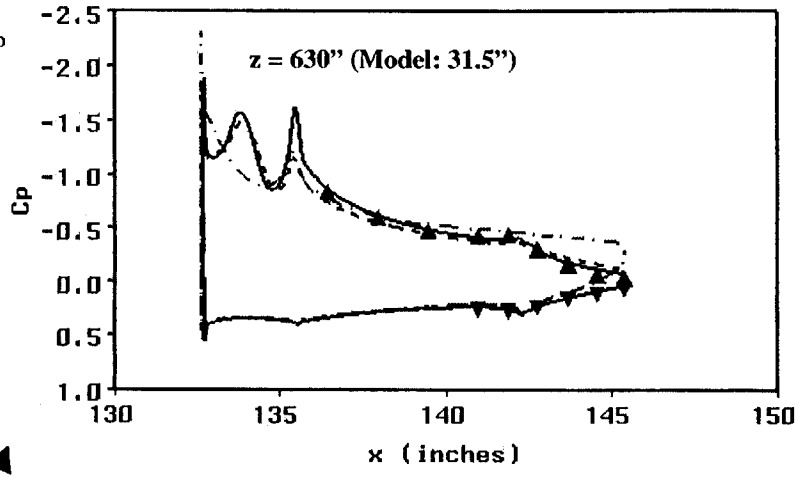

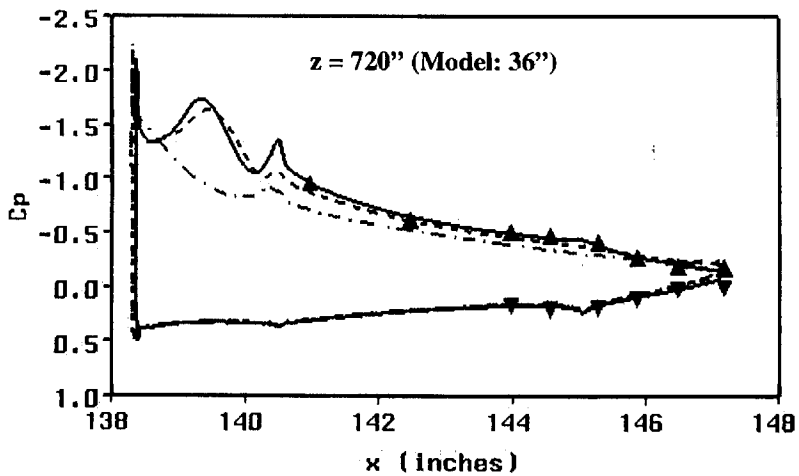

▲ US NASA/Ames 12-ft
▼ LS NASA/Ames 12-ft
—— US Free-Air
—— LS Free-Air
-·-·- US Tunnel J0.8
-·-·- LS Tunnel J0.8
···· US Tunnel J0.25/0.5
···· LS Tunnel J0.25/0.5

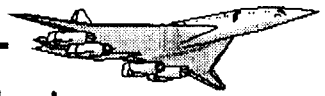

Comparison of Boundary-Layer Profiles of J0.8 and J0.25/J0.5 Solutions

Comparison of F-Function at Span Station z = 31.5" - The three upper figures of this view graph show the calculated local F(y) profiles for the J0.8 solution at three locations as indicated in the wing section. The red circles are the CFL3D computed Fmax locations. The blue squares are the calculated *Fmax* locations when J0.25/0.5 method is used for the same profiles. Shown in the three lower figures are the the calculated local F(y) profiles for the J0.25/0.5 solution at three locations as indicated in the wing section. The blue squares are the CFL3D computed Fmax locations. The red circles are the calculated *Fmax* locations when J0.8 method is used for the same profiles.

Blowup of *F*-Function - Shown in the next view graph are the blowups of the calculated *F*-function near the calculated *Fmax* locations for the J0.25/0.5 solution.

Comparison of velocity profiles - The velocity profiles at the three corresponding locations are shown in the view graph which follows the next view graph. Here, the red solid lines are the calculated velocity profiles for the J0.8 solution and the blue dots are the calculated velocity profiles for the J0.25/0.5 solution.

As shown in these figures, J0.8 method evaluated the *Fmax* at the core of the outer vortex flow resulting a large local length scale. This large length scale causes a thick boundary layer which in turn weakens and smears the leading edge vortex flow. The calculated flow eventually becomes separated at the wing trailing edge as indicated by the surface pressure shown in the previous view graph. A large wake flow is indicated by the velocity profile at the wing trailing edge.

J0.25/0.5 method evaluated higher suction peaks of the leading edge vortex flow and thinner boundary-layer corresponding to the smaller values of the calculated *Fmax* at both the leading and trailing edges.

As shown in the blowups of *F*-function, the *Fmax* values used in the J0.25/0.5 solution are simply those at the cutoff locations ($j = 0.25\ Jmax$ at LE *and* $0.5Jmax$ at TE).

It is obvious from the velocity profiles that there is a difficulty in numerical implementation in searching for proper *Fmax* locations for the Baldwin-Lomax/Degani-Schiff model in a complex leading edge vortex flows coupled with separated and wake flows. A more field-based turbulence model is warranted to be explored and studied for this type of flow simulation.

Note - In the rest of presentation, all the CFD solutions presented were calculated using the J0.25/0.5 method.

Comparison of F-Function at Span Station z = 31.5”

J0.8 Method

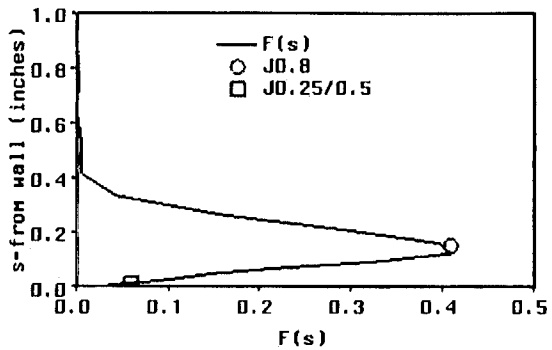

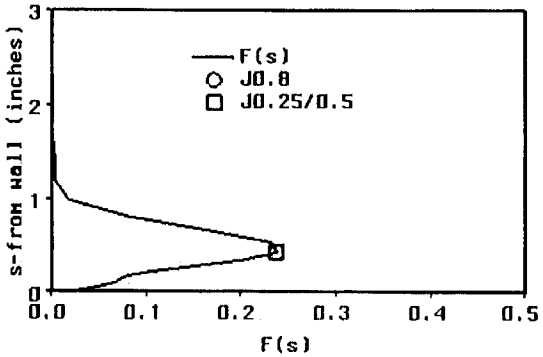

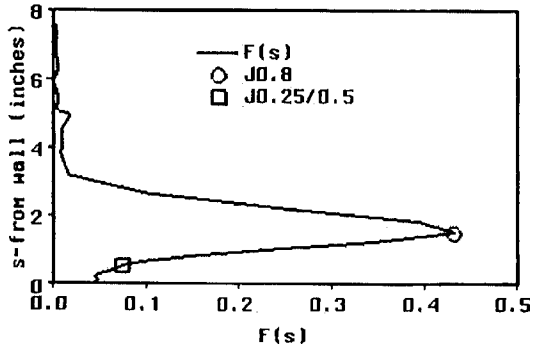

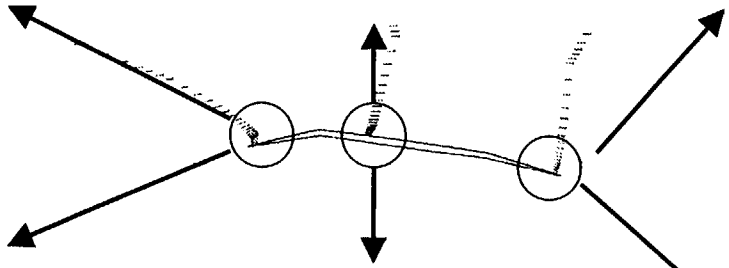

J0.25/0.5 Method

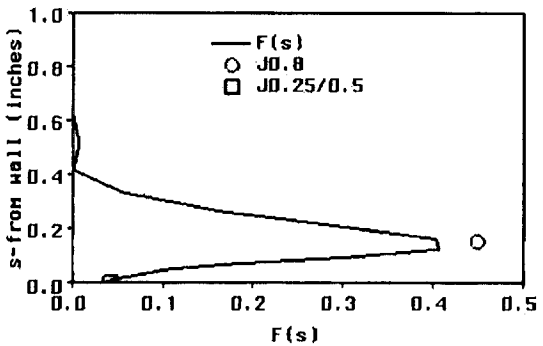

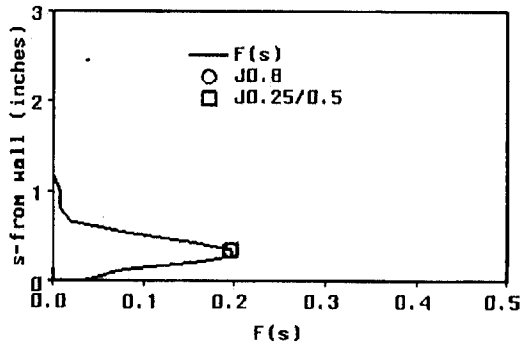

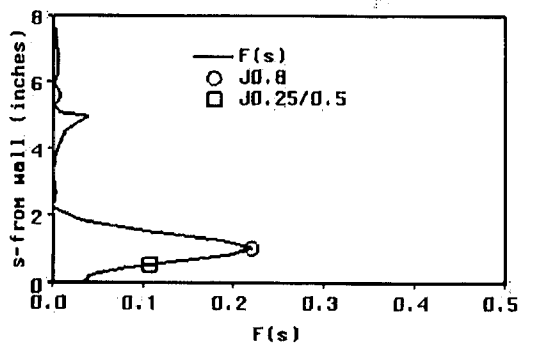

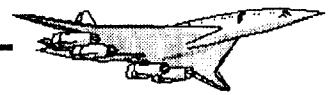

Blowup of F-Function

See the previous view graph for discussion.

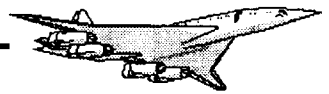

Blowup of F-Function
at Span Station z = 31.5" for J0.25/0.5 method

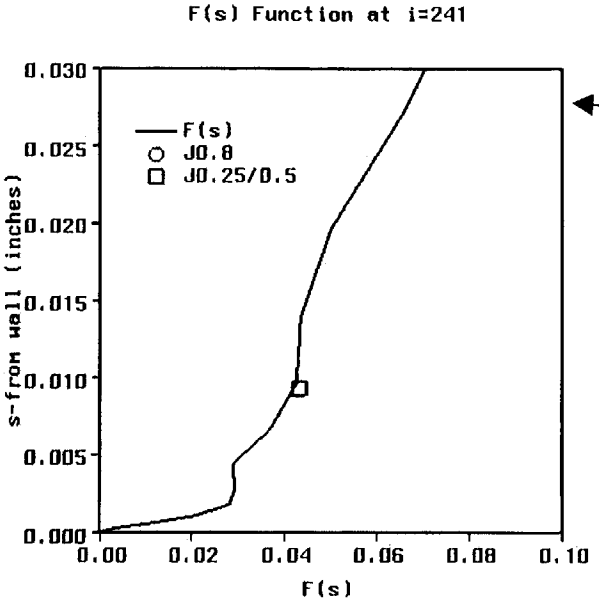

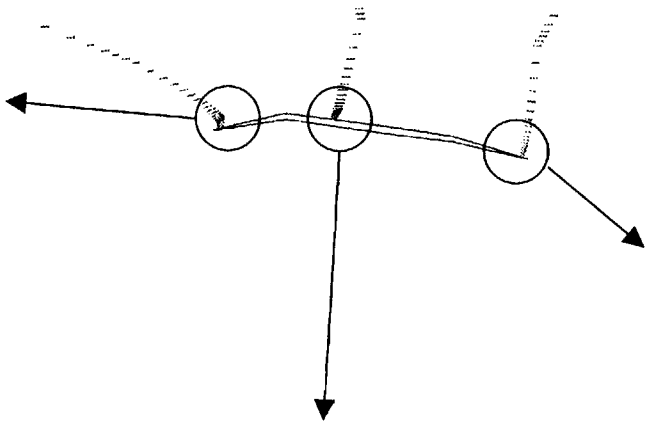

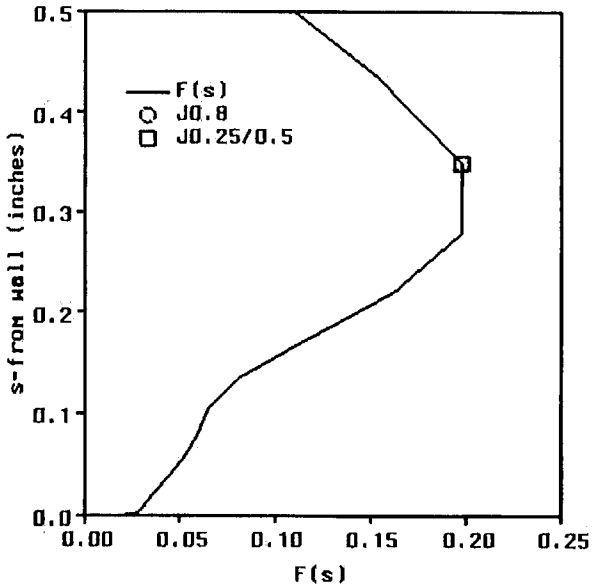

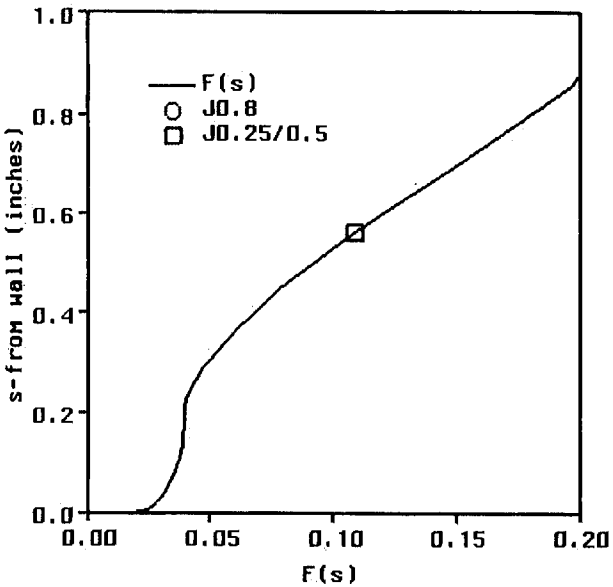

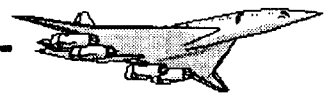

Comparison of Velocity Profiles

See the previous view graph for discussion.

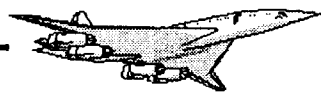

Comparison of Velocity Profiles
at Span Station z = 31.5”

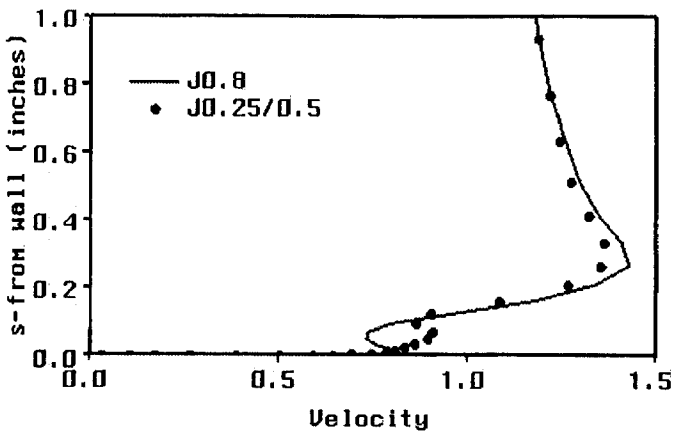

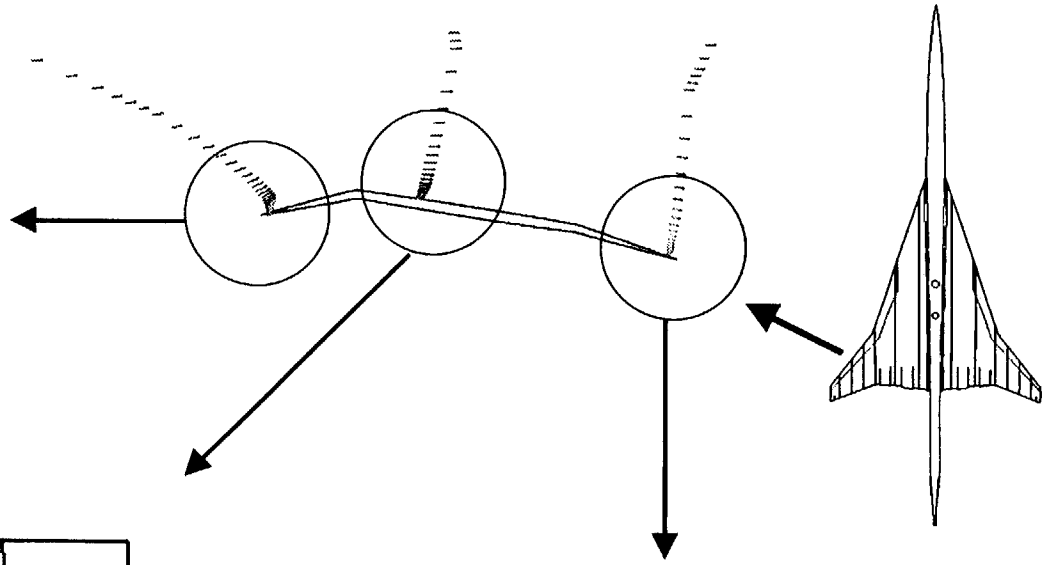

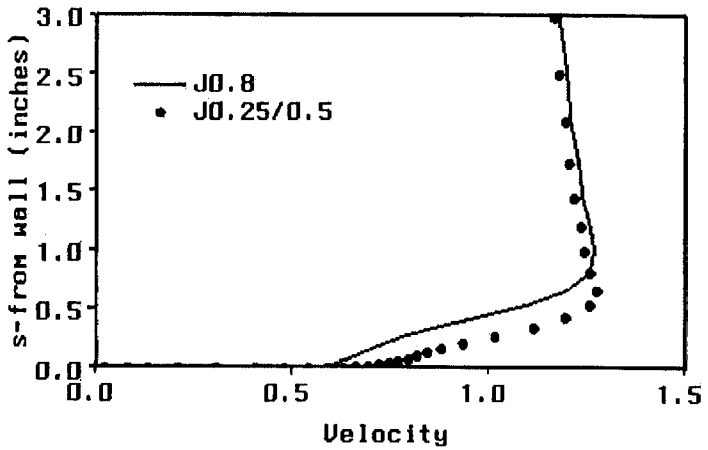

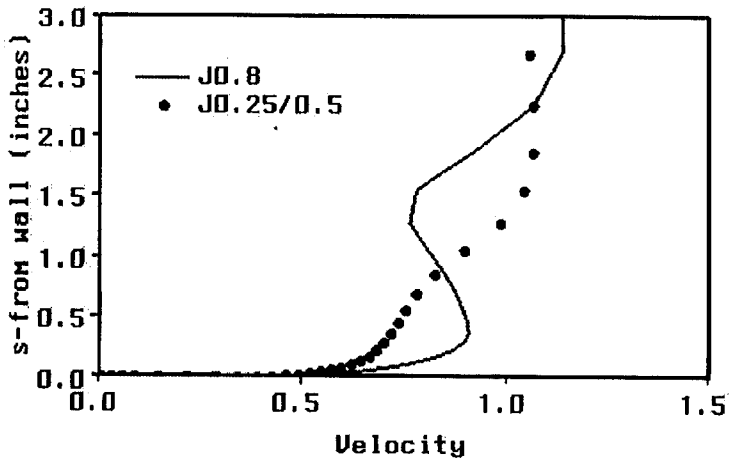

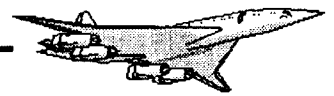

The Six Span Stations

This figure shows the six span stations where the measured pressure data from the NASA/Ames 12-ft pressure tunnel are available. The span locations are given in terms of both the full-scale and 5%-scale coordinate systems.

Also shown are the fore and aft post locations as indicated by the two circles.

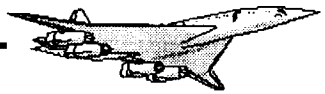

The Six Span Stations
Where CFD Results are Compared with Test Data

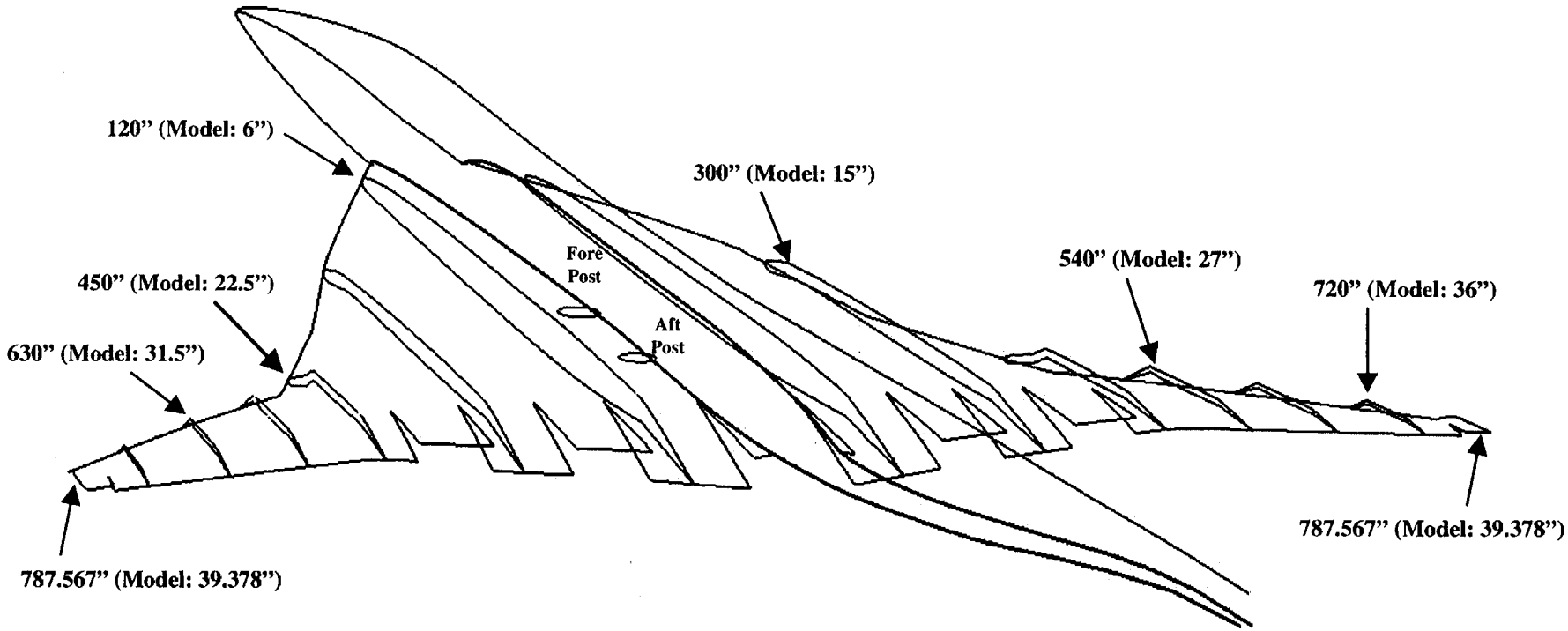

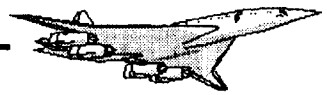

The Eight Axial Stations

This figure shows the eight axial stations where the measured pressure data from the NASA/Ames 12-ft pressure tunnel are available. The axial locations are given in terms of both the full-scale and 5%-scale coordinate systems.

Also shown are the fore and aft post locations as indicated by the circles.

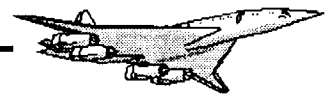

The Eight Axial Stations
where CFD Results are Compared with Test Data

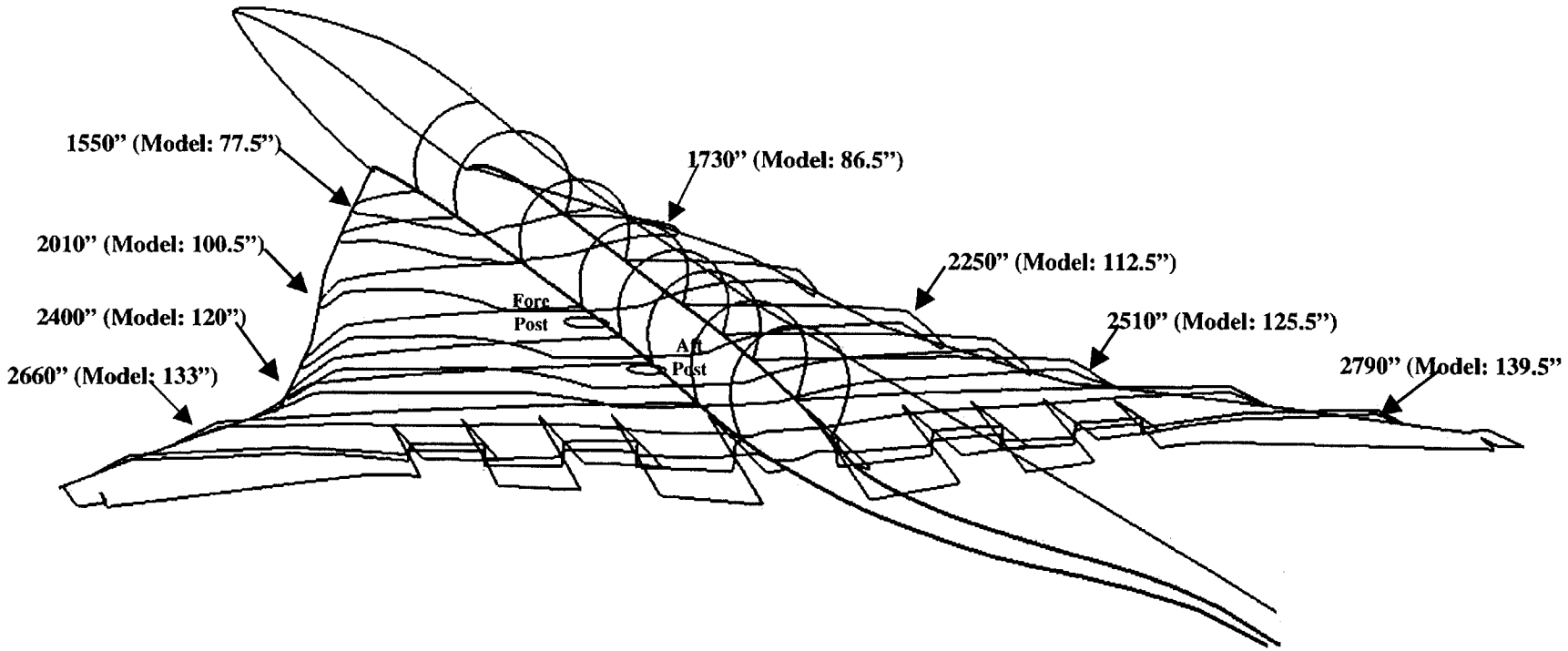

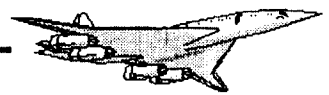

Comparison of Chordwise Cp

This figure is intended to be used in conjunction with the Cp plots that follow. It uses pressure contour bands to indicate the span and axial stations where the CFD calculated pressures are compared with the wind tunnel test data. It also shows how the section locations are related to the LE and TE flaps and the flap hinge lines so that the pressure suction peaks can easily be associated with either the LE vortex or the hinge lines.

To provide a comprehensive correlation between CFD results and the test data and to better understand the complex LE vortex flows, the CFD solutions at $\alpha = 10^{o}$ are compared with the test data at three angles of attack as follows:

Geometric α	Corrected α
8.9922^{o}	9.7720^{o}
10.9092^{o}	11.8271^{o}
12.8472^{o}	13.9281^{o}

Three sets of Cp are presented, each set corresponding to each of the three angles of attack mentioned above. Each set will include both the chordwise and spanwise Cp distributions.

Both the CFD and test data strongly suggest that the flow condition considered here is near the critical vortex flow range. That is, the existence of over-wing vortex flow is sensitive to small changes in the angle of attach.

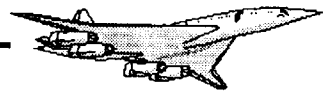

Comparison of Chordwise Cp between Model/tunnel and Model/Tunnel/posts Cases

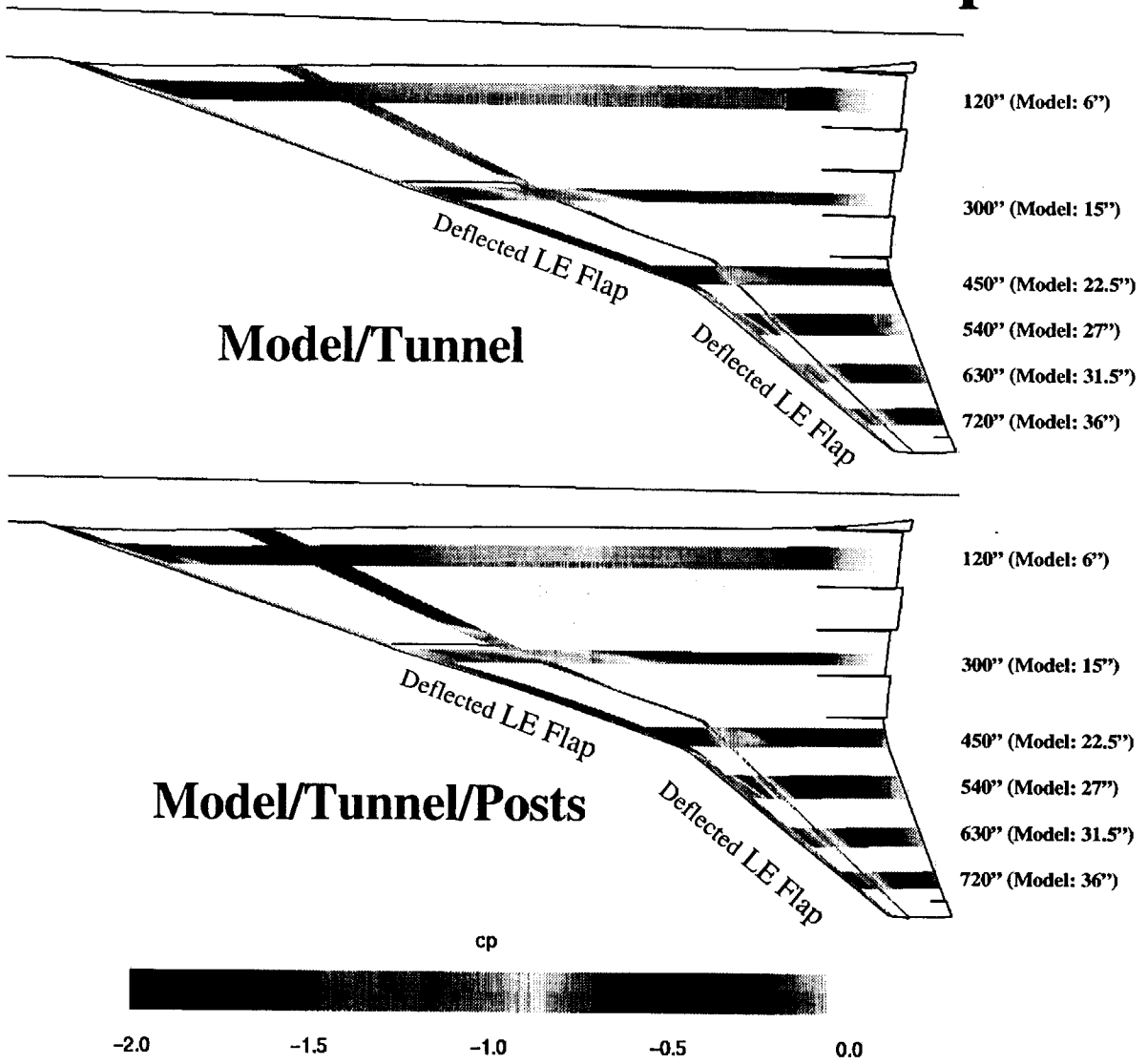

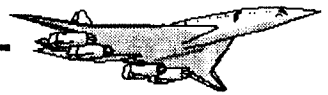

Set 1: Post Effects and Comparison of Chordwise Cp

This figure shows the chordwise pressure comparison at the three inboard span stations: z = 120" (Model: 6"), 300" (Model: 15"), and 450" (Model: 22.5"). The up and down triangles are the TCA-3 test data from the NASA/Ames 12-ft pressure tunnel . The black solid lines are the full-scale free-air CFD solution. The red chaindot lines are the model/tunnel CFD solution. The blue dash lines are the model/tunnel/posts CFD solution.

The geometric (uncorrected) α for the test data is **8.9922 degrees** (or 9.772 degrees after correction). All the CFD solutions were calculated at **α = 10 degrees.**

The upper surface pressures of the CFD wind-tunnel solutions at z = 6" and 15" indicate an over-wing vortex flow but it does not show in the free-air solution . The over-wing vortex flow can easily be visualized in the color contours of the upper wing surface pressures shown in the next view graph.

The effect of the two supporting posts on the wing lower surface pressures is clearly shown by the blue dash lines and accurate calculated by the CFD as compared to the test data at the fist two inboard sections: z = 6" and 15".

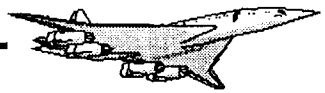

Set 1: Post Effects and Comparison of Chordwise Cp between CFD and Test Data

Test

Geometric $\alpha = 8.9922^{\circ}$

Corrected $\alpha = 9.772^{\circ}$

CFD

$\alpha = 10^{\circ}$

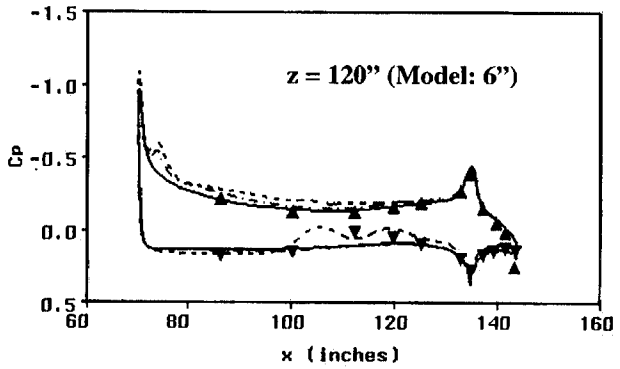

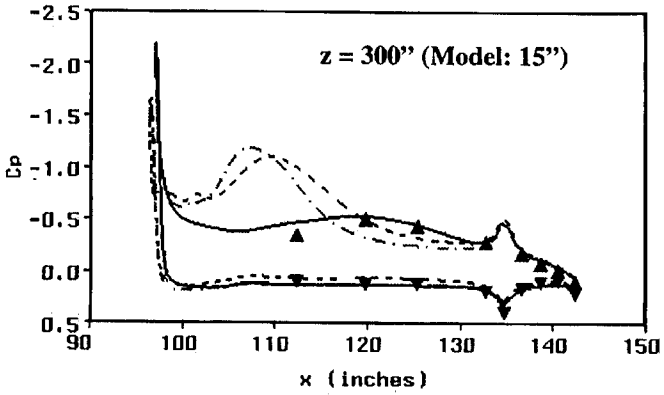

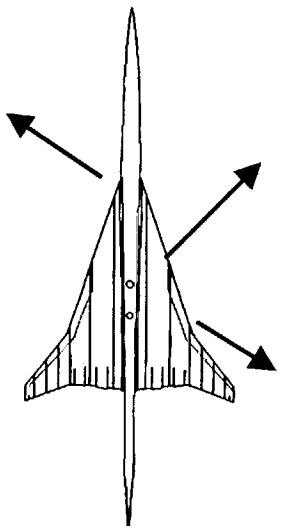

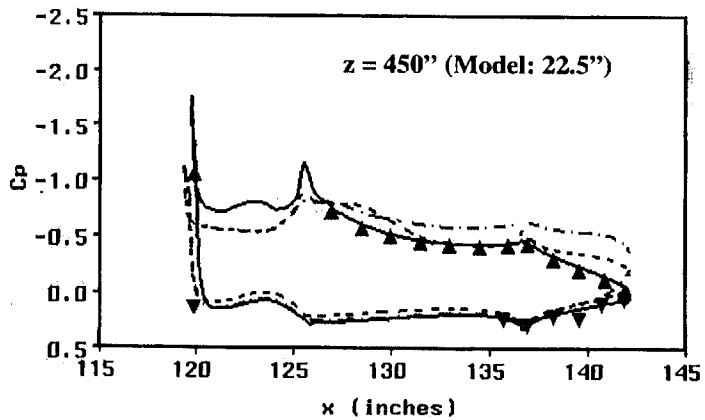

▲ US TCA-3 Run476
▼ LS TCA-3 Run476
US CFD Free-Air
LS CFD Free-Air
US CFD Model/TW
LS CFD Model/TW
US CFD Model/TW/Post
LS CFD Model/TW/Post

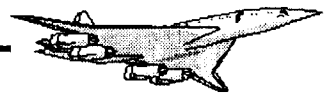

Set 1: Comparison of Surface Cp Contours (Continued)

The characteristics of the CFD calculated pressures at z = 22.5" can be visualized in the color pressure contours shown in this view graph. As shown in the middle figure of the next view graph, the higher negative pressures appearing in the model/tunnel is due to the interaction of the over-wing vortex flow and the side edge of the TE flap.

Also, see the previous view graph for discussion.

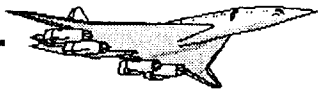

Comparison of Surface Cp Contours

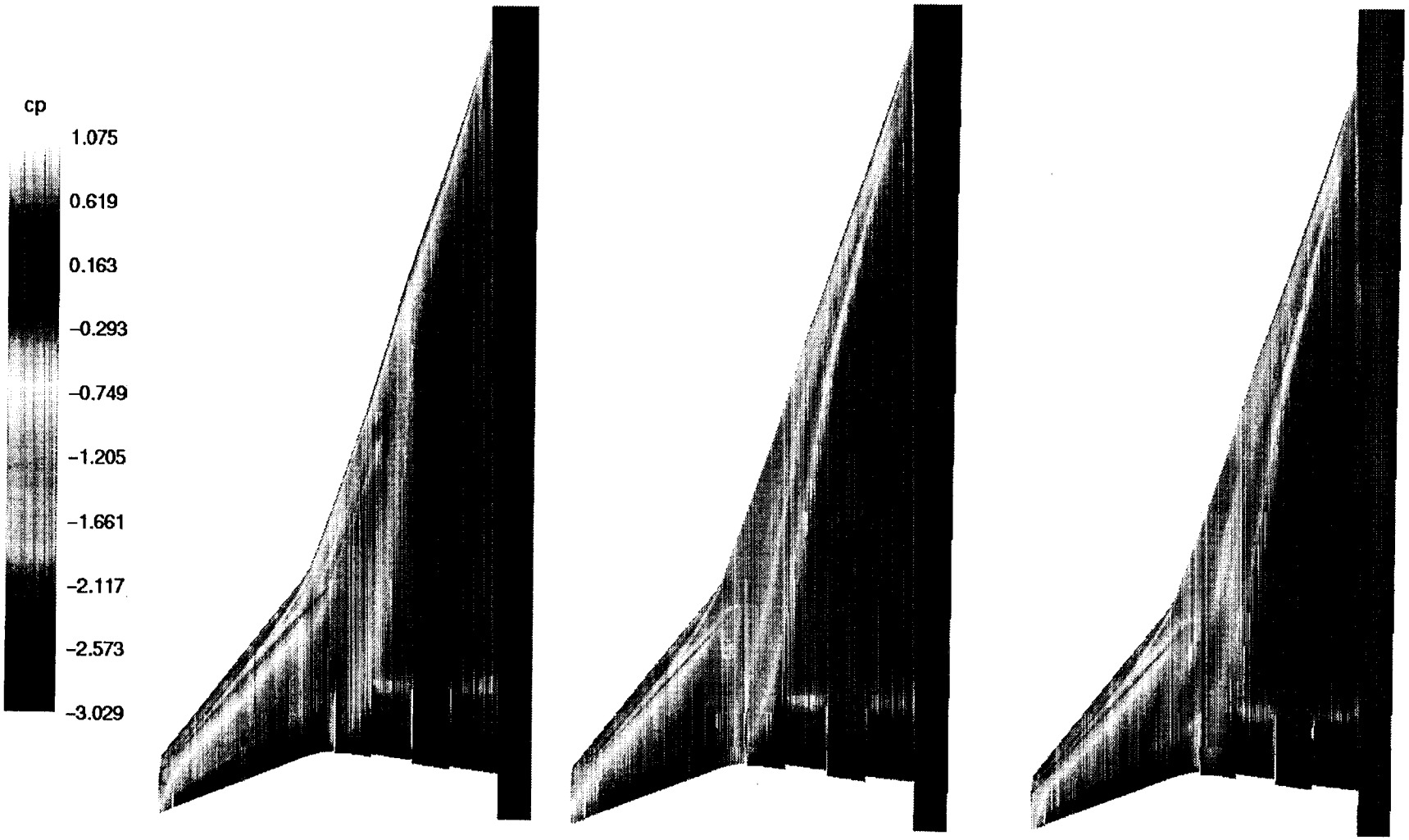

Free-Air **5% TCA Model/Tunnel** **5% TCA Model/Tunnel/Posts**

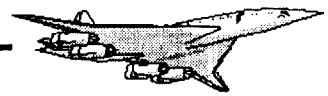

Set 1: Post Effects and Comparison of Chordwise Cp (Concluded)

This figure shows the chordwise pressure comparison at the three outboard span stations: z = 540" (Model: 27"), 630" (Model: 31.5"), and 720" (Model: 36"). The up and down triangles are the TCA-3 test data from the NASA/Ames 12-ft pressure tunnel . Again, the black solid lines are the full-scale free-air CFD solution. The red chaindot lines are the model/tunnel CFD solution. The blue dash lines are the model/tunnel/posts CFD solution.

As shown in the figures, all the three CFD solutions agree well with the test data. An outboard LE vortex flow is indicated by the vortex suction peaks and may be visualized in the color pressure contours shown in the previous view graph.

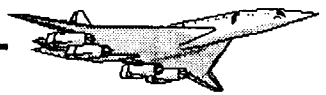

Set 1: Post Effects and Comparison of Chordwise Cp between CFD and Test Data

Test

Geometric $\alpha = 8.9922^{o}$

Corrected $\alpha = 9.772^{o}$

CFD

$\alpha = 10^{o}$

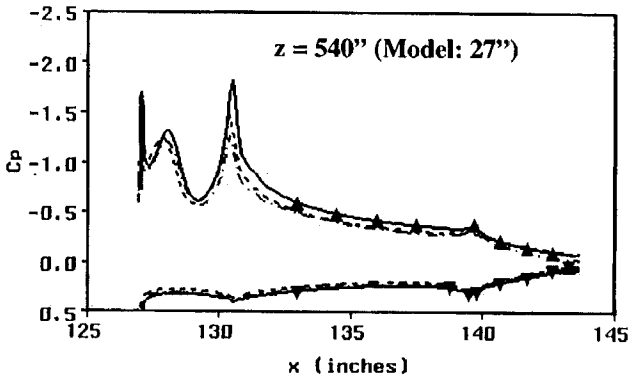

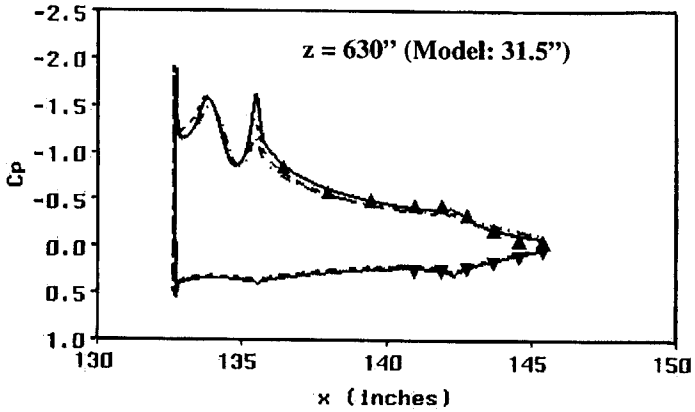

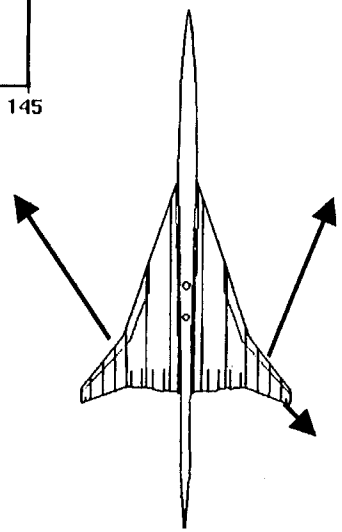

▲ US TCA-3 Run476
▼ LS TCA-3 Run476
—— US CFD Free-Air
—— LS CFD Free-Air
-·-·- US CFD Model/TW
-·-·- LS CFD Model/TW
---- US CFD Model/TW/Post
---- LS CFD Model/TW/Post

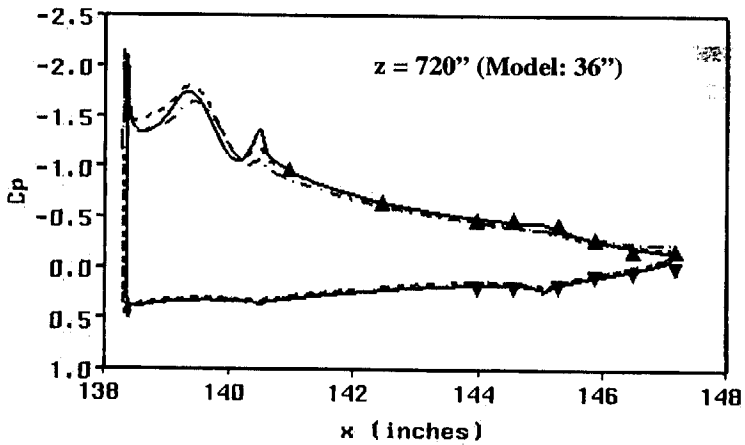

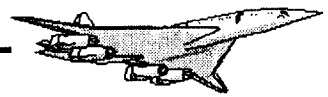

Set 1: Post Effects and Comparison of Spanwise Cp

This and the next view graphs show the spawise pressure comparison at the eight axial stations: x = 1550" (Model: 77.5"), 1730" (Model: 86.5"), 2010" (Model: 100.5"), 2250" (Model: 112.5"), 2400" (Model: 120"), 2510" (Model: 125.5"), 2660" (Model: 133"), and 2790" (Model: 139.5"). The up and down triangles are the TCA 3 test data from the NASA/Ames 12-ft pressure tunnel. The black solid lines are the full-scale free-air CFD solution. The red chaindot lines are the model/tunnel CFD solution. The blue dash lines are the model/tunnel/posts CFD solution.

As shown in the figures, all the three CFD solutions agree very favorably with the test data. The over-wing vortex flows for the CFD model/tunnel and model/tunnel/posts cases are clearly shown by the vortex suction peaks in the spanwise surface pressures represented by the red chaindot lines and the blue dash lines.

Again, the post effect is somewhat limited to the root and around the two post regions as shown by the lower surface pressures at stations: x = 100.5", 112.5", 120", and 125.5".

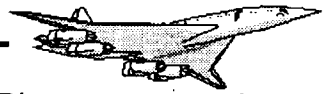

Set 1: Post Effects and Comparison of Spanwise Cp between CFD and Test Data

Test

Geometric $\alpha = 8.9922^{\circ}$

Corrected $\alpha = 9.772^{\circ}$

CFD

$\alpha = 10^{\circ}$

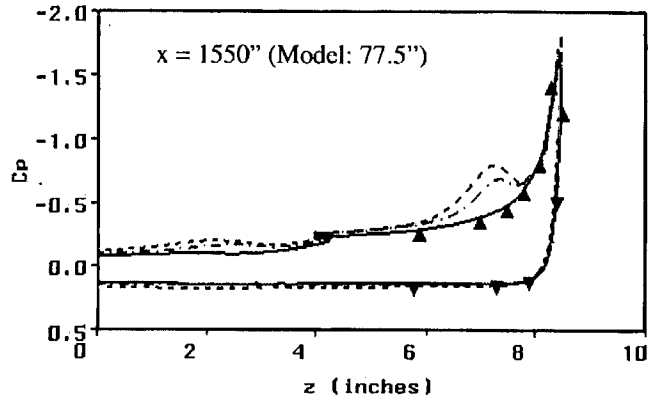

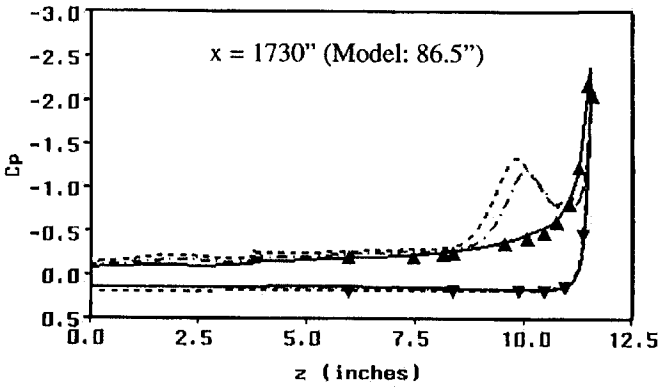

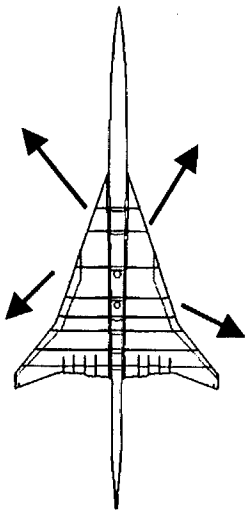

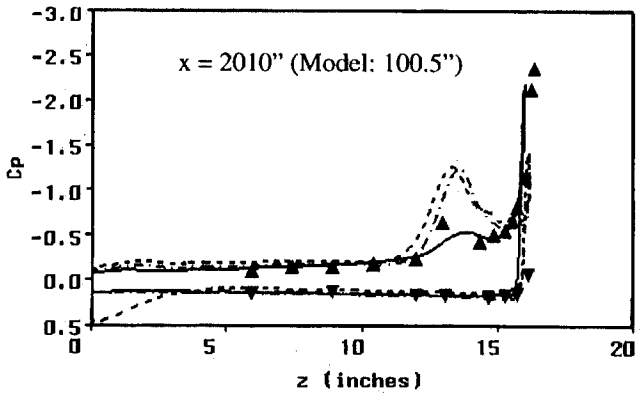

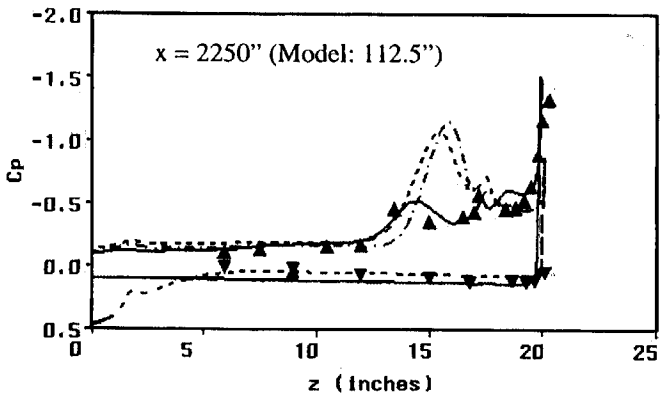

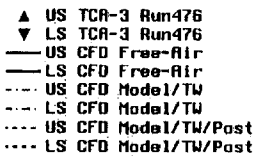

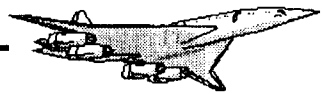

Set 1: Post Effects and Comparison of Spanwise Cp (Concluded)

See the previous view graph for discussion.

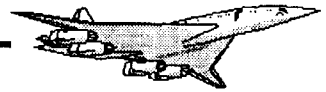

Set 1: Post Effects Comparison of Spanwise Cp between CFD and Test Data

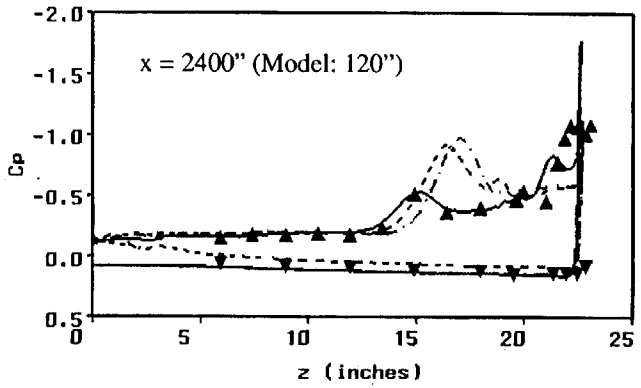

Test

Geometric $\alpha = 8.9922^{\circ}$

Corrected $\alpha = 9.772^{\circ}$

CFD

$\alpha = 10^{\circ}$

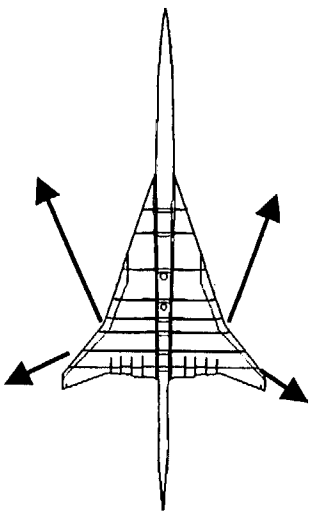

▲ US TCR-3 Run476
▼ LS TCR-3 Run476
US CFD Free-Air
LS CFD Free-Air
US CFD Model/TW
LS CFD Model/TW
US CFD Model/TW/Post
LS CFD Model/TW/Post

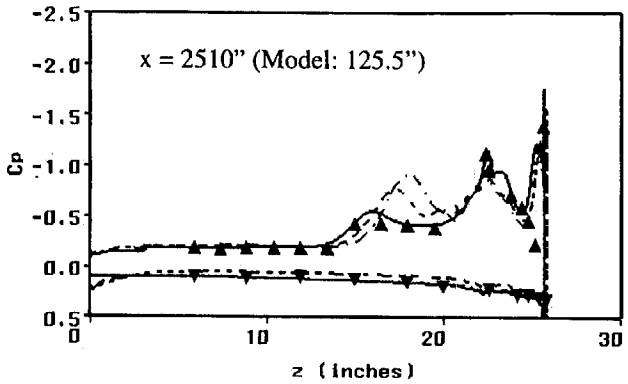

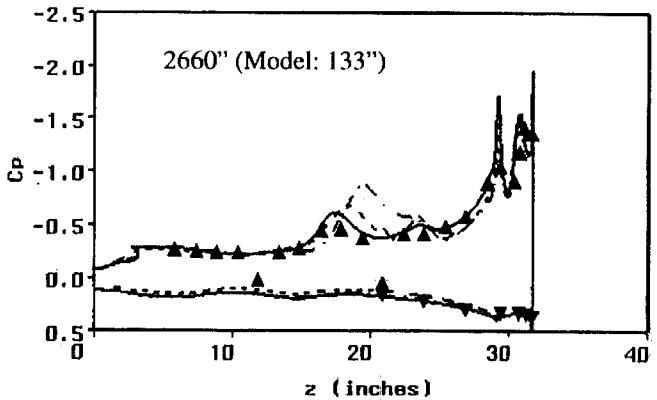

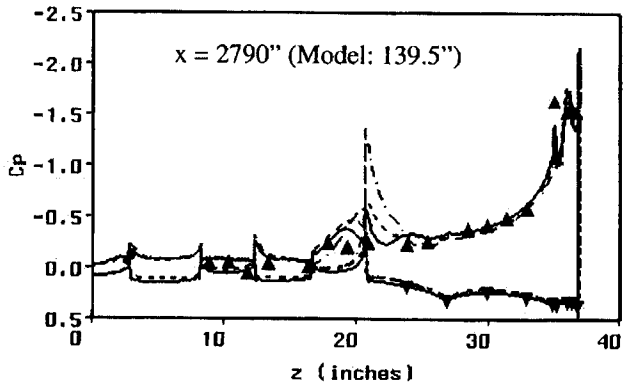

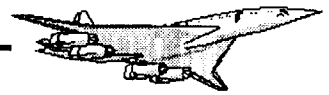

Set 2: Post Effects and Comparison of Chordwise Cp

This and the following three view graphs constitute the second set of Cp data. The $\alpha = 10^{o}$ CFD solutions are compared with the test data at **geometric $\alpha = 10.9092^{o}$** (corrected $\alpha = 11.8271^{o}$).

As shown in these view graphs, the pressure levels of the test data are very much similar to those in the fist set of data, i.e., at **geometric $\alpha = 8.9922^{o}$** except that at the wing tip span station at z = 720" (model: 36") which indicates a vortex flow right behind the LE flap hinge line.

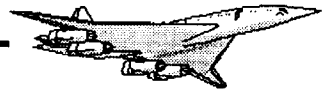

Set 2: Post Effects and Comparison of Chordwise Cp between CFD and Test Data

Test

Geometric $\alpha = 10.9092^{\circ}$

Corrected $\alpha = 11.8271^{\circ}$

CFD

$\alpha = 10^{\circ}$

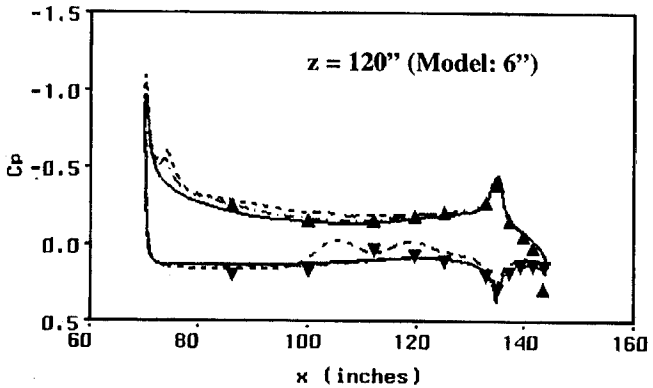

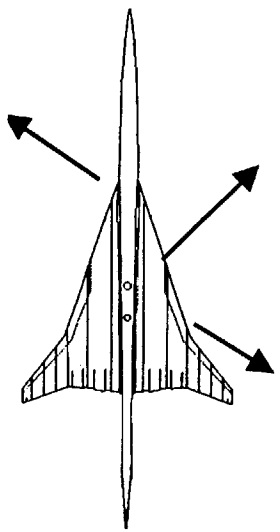

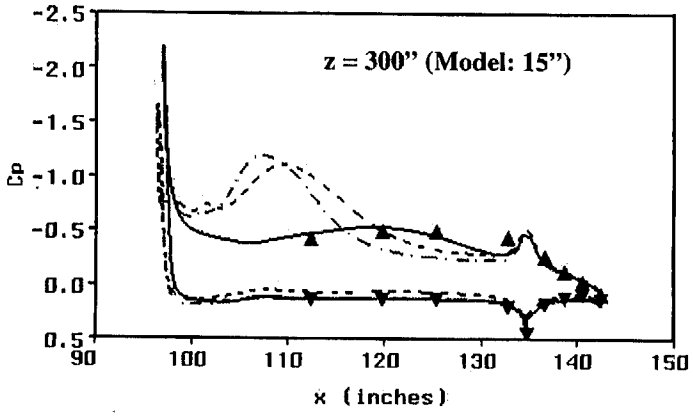

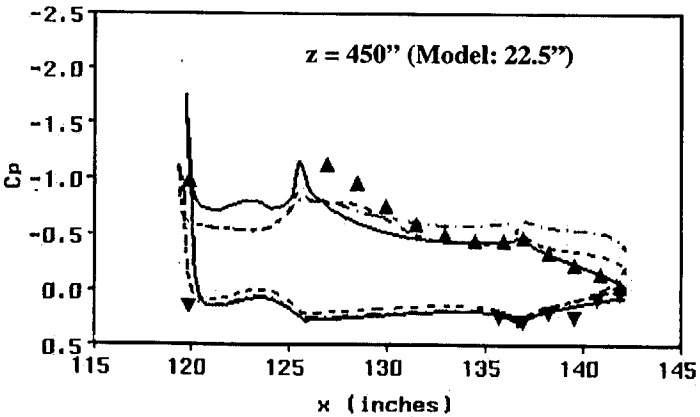

▲ US TCA-3 Run476
▼ LS TCA-3 Run476
—— US CFD Free-Air
—— LS CFD Free-Air
-·-·- US CFD Model/TW
-·-·- LS CFD Model/TW
···· US CFD Model/TW/Post
···· LS CFD Model/TW/Post

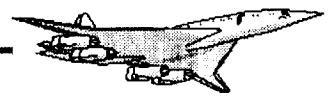

Set 2: Post Effects and Comparison of Chordwise Cp (Concluded)

See the previous view graph for discussion.

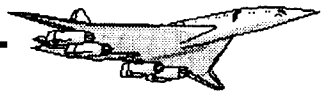

Set 2: Post Effects and Comparison of Chordwise Cp between CFD and Test Data

Test

Geometric $\alpha = 10.9092$

Corrected $\alpha = 11.8271^{c}$

CFD

$\alpha = 10^{o}$

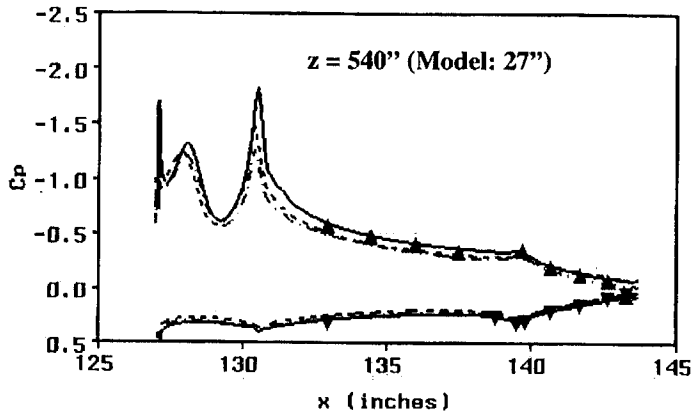

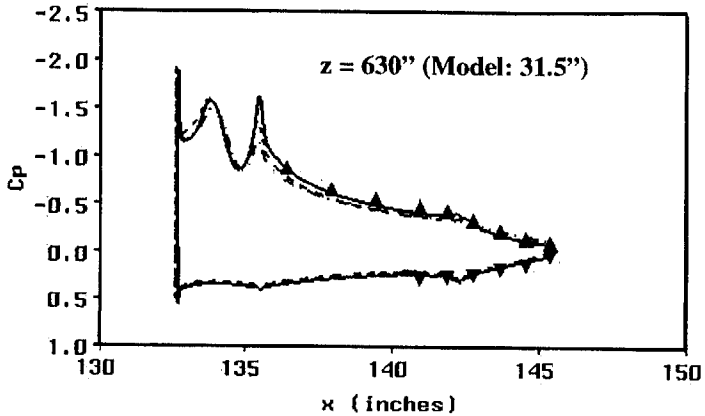

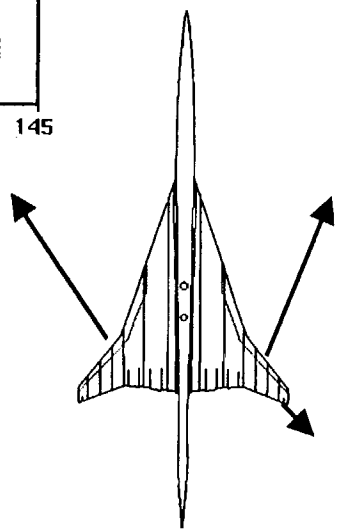

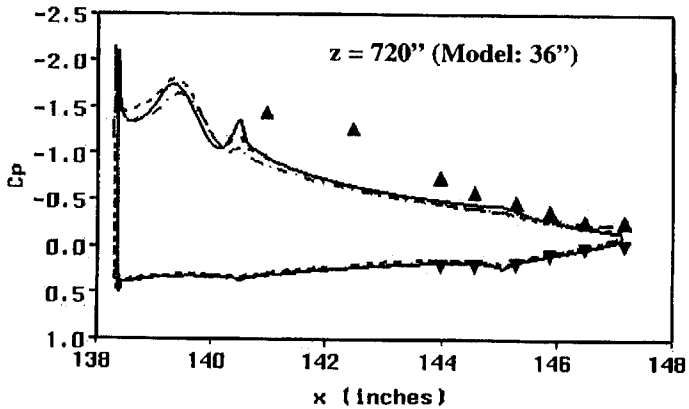

▲ US TCA-3 Run476
▼ LS TCA-3 Run476
—— US CFD Free-Air
—— LS CFD Free-Air
-·-·- US CFD Model/TW
-·-·- LS CFD Model/TW
···· US CFD Model/TW/Post
···· LS CFD Model/TW/Post

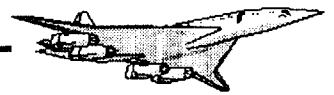

Set 2: Post Effects and Comparison of Spanwise Cp

See the previous view graph for discussion.

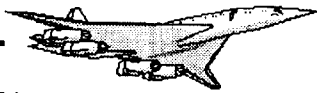

Set 2: Post Effects and Comparison of Spanwise Cp between CFD and Test Data

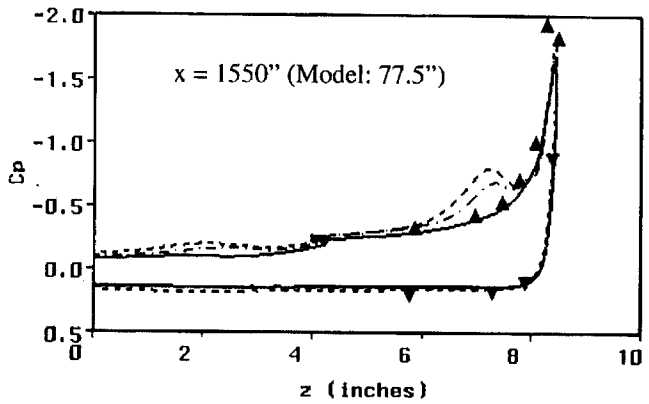

Test

Geometric $\alpha = 10.9092^{\circ}$

Corrected $\alpha = 11.8271^{\circ}$

CFD

$\alpha = 10^{\circ}$

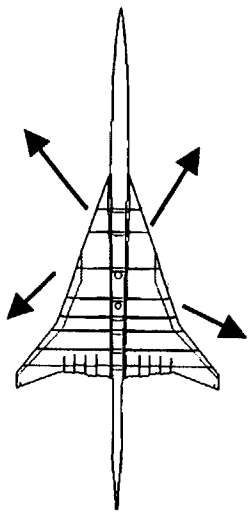

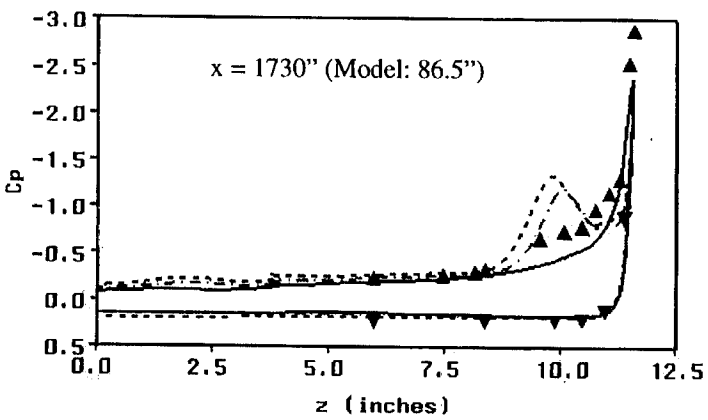

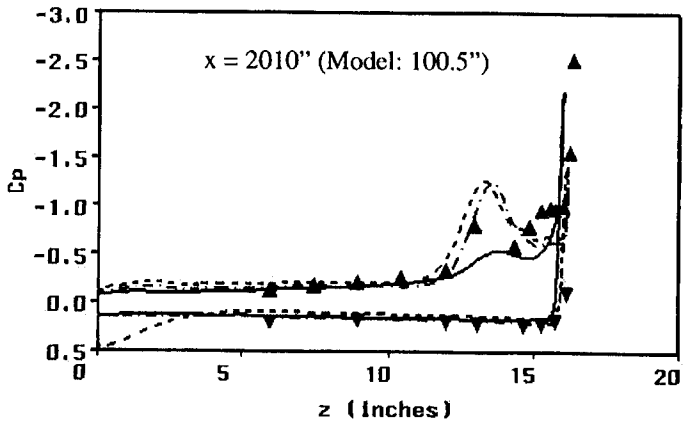

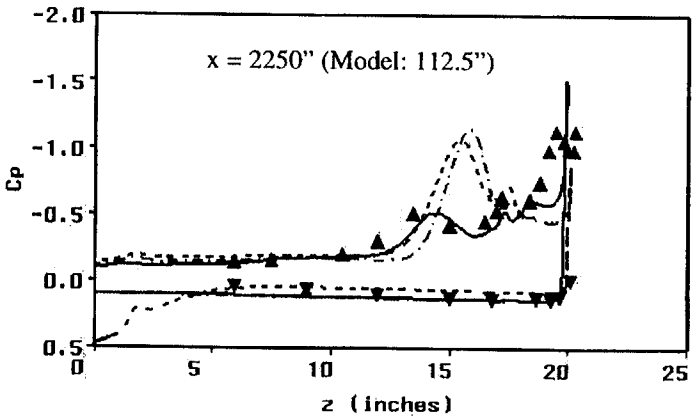

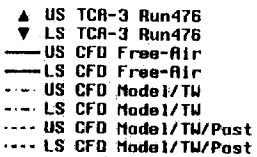

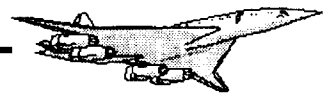

Set 2: Post Effects and Comparison of Spanwise Cp (Concluded)

See the previous view graph for discussion.

Set 2: Post Effects Comparison of Spanwise Cp between CFD and Test Data

Test

Geometric $\alpha = 10.9092^{\circ}$

Corrected $\alpha = 11.8271^{\circ}$

CFD

$\alpha = 10^{\circ}$

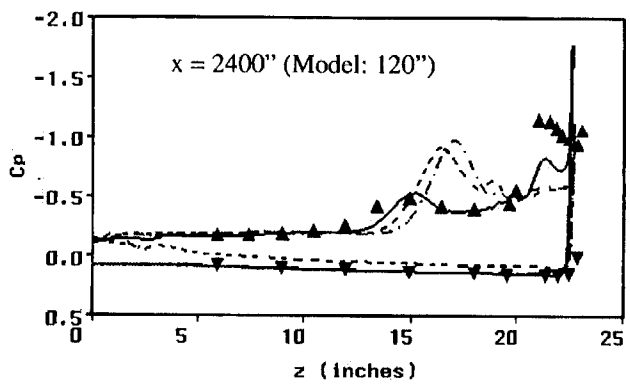

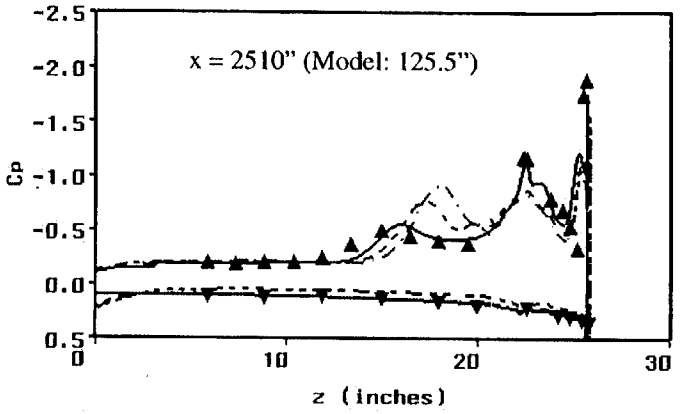

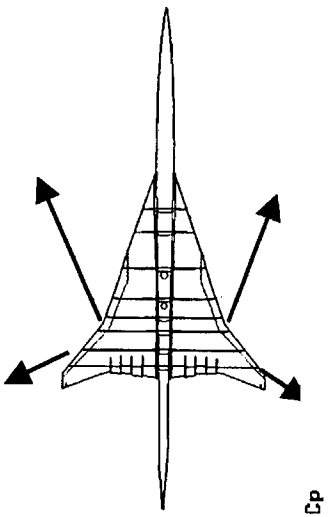

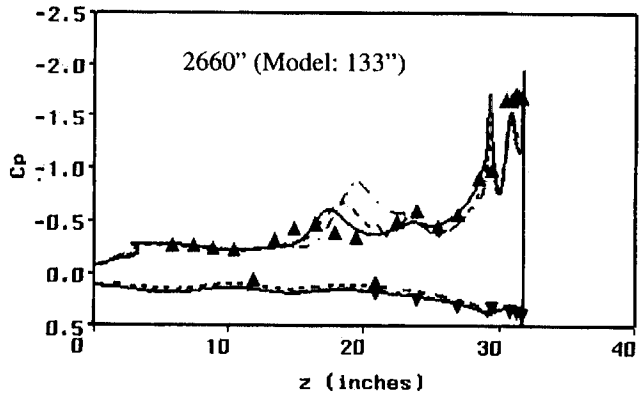

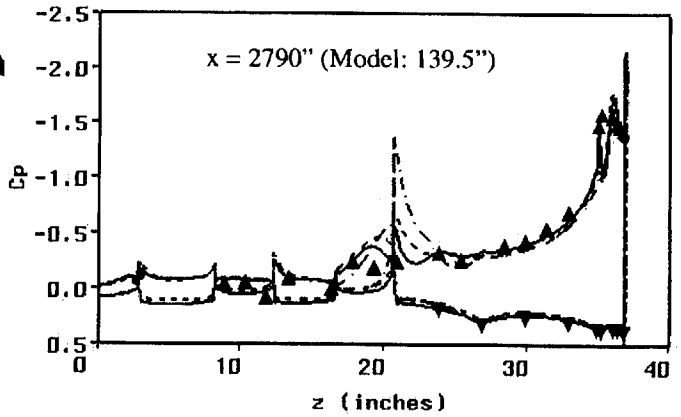

▲ US TCA-3 Run476
▼ LS TCA-3 Run476
US CFD Free-Air
LS CFD Free-Air
US CFD Model/TW
LS CFD Model/TW
US CFD Model/TW/Post
LS CFD Model/TW/Post

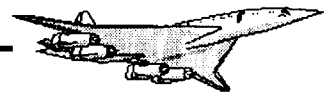

Set 3: Post Effects and Comparison of Chordwise Cp

This and the following three view graphs constitute the third set of Cp data. The $\alpha = 10^{\circ}$ CFD solutions are compared with the test data at **geometric $\alpha = 12.8472^{\circ}$** (corrected $\alpha = 13.9281^{\circ}$).

The spanwise pressures of the test data clearly indicate an over-wing vortex flow. Comparison between the second and third data sets shows that the experimental over-wing vortex flow starts set in at a geometric angle of attack in between 10 and 13 degrees.

Comparison of the surface pressures between the model/tunnel/posts solution and the test data shows that the CFD calculated vortex strength and location agree well with the experiment. However, it should be noted that the CFD angle of attack is at $\alpha = \mathbf{10^{\circ}}$ as compared to $\alpha = \mathbf{12.8472^{\circ}}$ for the test data. Hence, CFD calculated attack of attack of the LE vortex flow separation is smaller than that of the experiment.

The chordwise Cp distribution at the wing tip section indicates the merge of the inboard and outboard vortex flows.

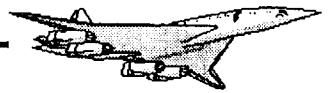

Set 3: Post Effects and Comparison of Chordwise Cp between CFD and Test Data

Test

Geometric $\alpha = 12.8472^{o}$

Corrected $\alpha = 13.9281^{o}$

CFD

$\alpha = 10^{o}$

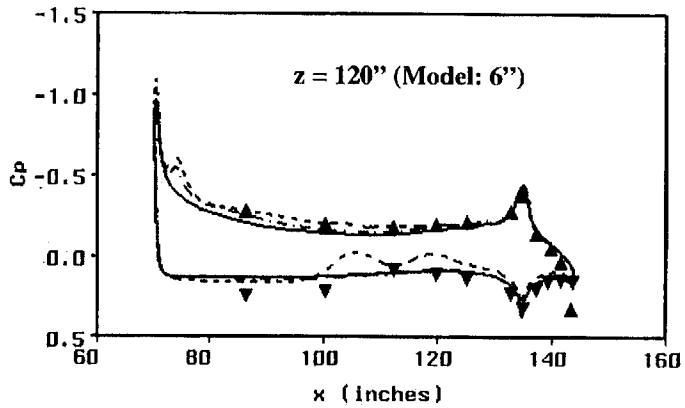

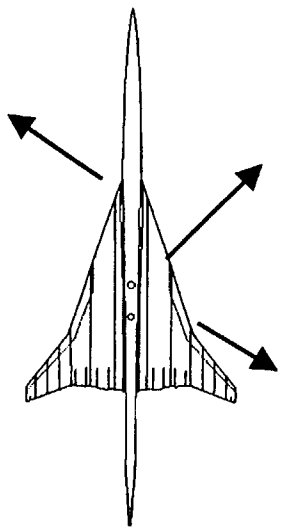

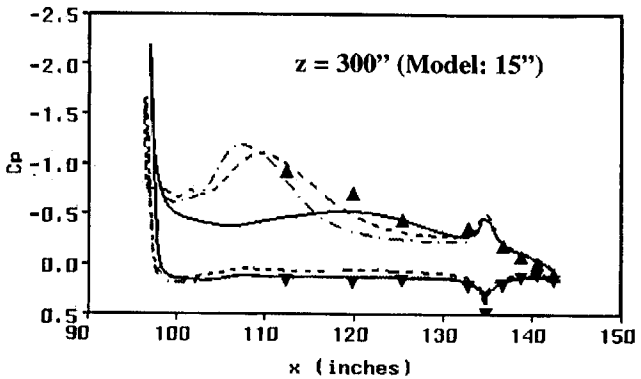

▲ US TCA-3 Run476
▼ LS TCA-3 Run476
—— US CFD Free-Air
—— LS CFD Free-Air
-·-·- US CFD Model/TW
-·-·- LS CFD Model/TW
---- US CFD Model/TW/Post
---- LS CFD Model/TW/Post

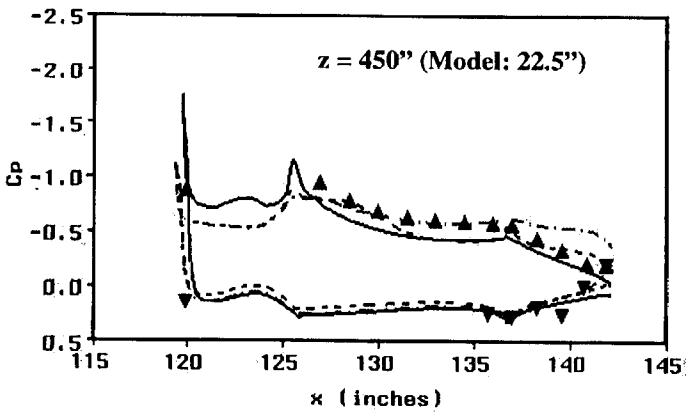

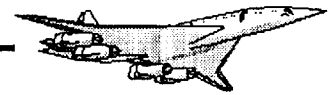

Set 3: Post Effects and Comparison of Chordwise Cp (Concluded)

See the previous view graph for discussion.

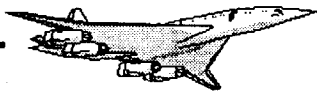

Set 3: Post Effects and Comparison of Chordwise Cp between CFD and Test Data

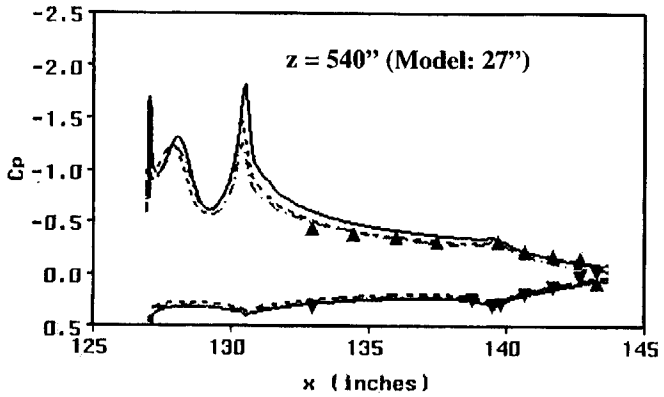

Test

Geometric $\alpha = 12.8472^{\circ}$

Corrected $\alpha = 13.9281^{\circ}$

CFD

$\alpha = 10^{\circ}$

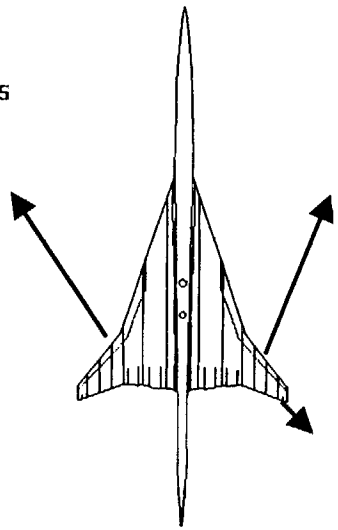

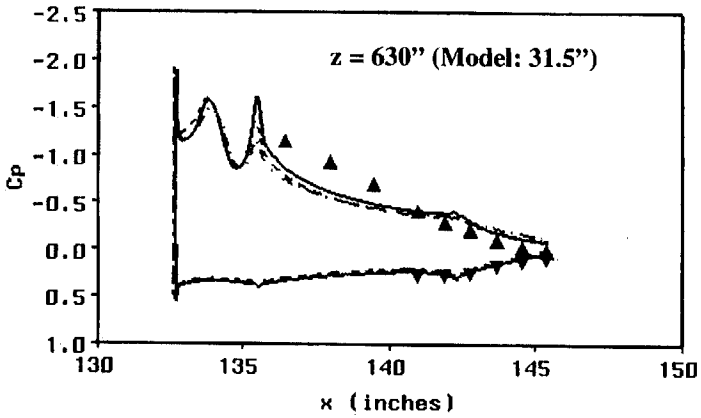

▲ US TCA-3 Run476
▼ LS TCA-3 Run476
—— US CFD Free-Air
—— LS CFD Free-Air
-·-·- US CFD Model/TW
-·-·- LS CFD Model/TW
···· US CFD Model/TW/Post
···· LS CFD Model/TW/Post

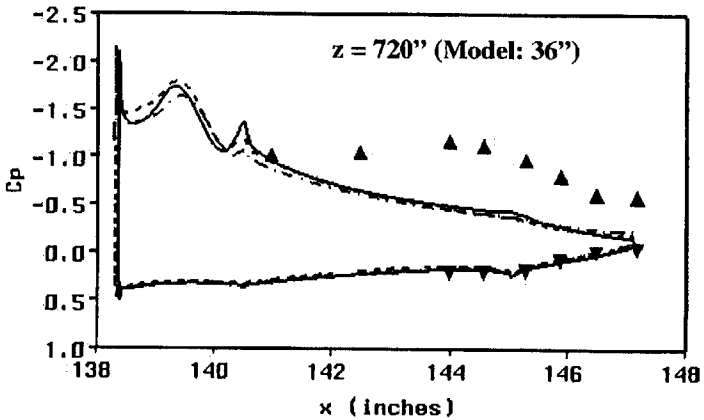

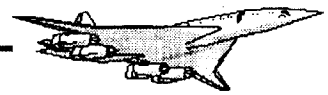

Set 3: Post Effects and Comparison of Spanwise Cp

See the previous view graph for discussion.

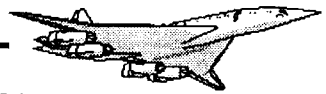

Set 3: Post Effects and Comparison of Spanwise Cp between CFD and Test Data

Test

Geometric $\alpha = 12.8472^{o}$

Corrected $\alpha = 13.9281^{o}$

CFD

$\alpha = 10^{o}$

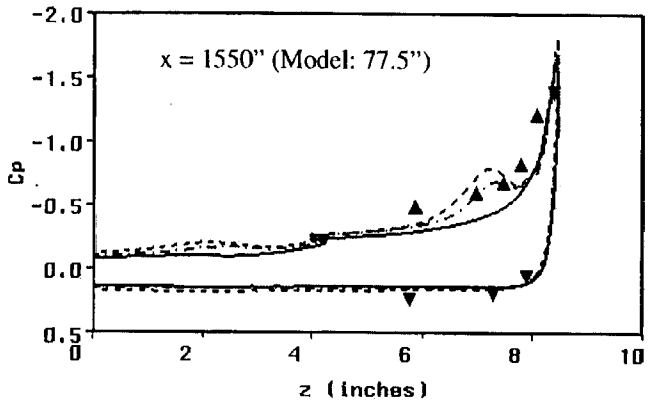

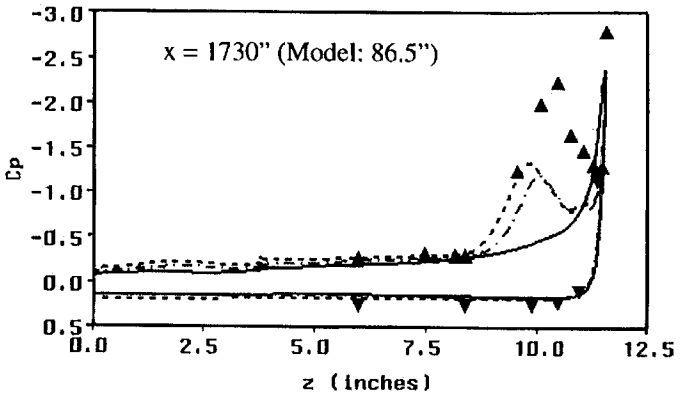

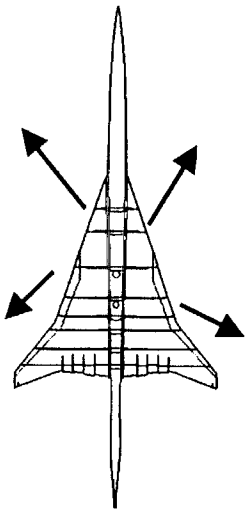

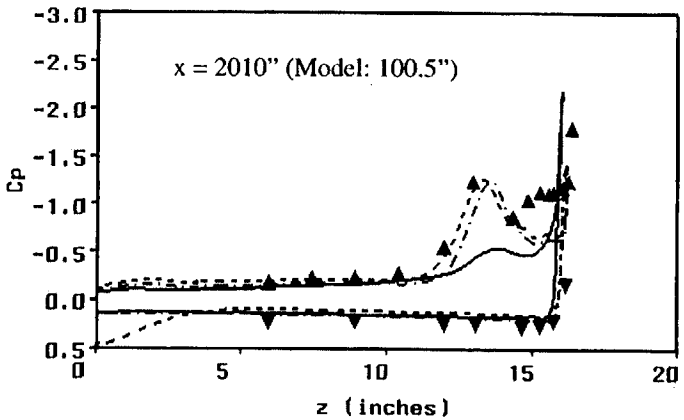

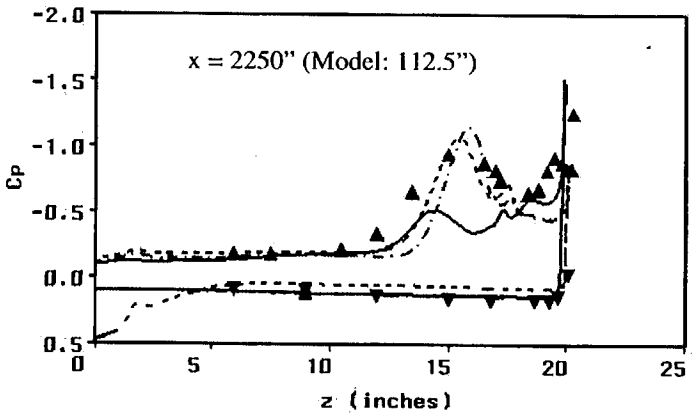

▲ US TCR-3 Run476
▼ LS TCR-3 Run476
US CFD Free-Air
LS CFD Free-Air
US CFD Model/TW
LS CFD Model/TW
US CFD Model/TW/Post
LS CFD Model/TW/Post

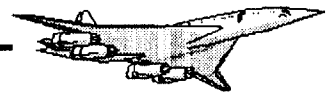

Set 3: Post Effects and Comparison of Spanwise Cp (Concluded)

See the previous view graph for discussion.

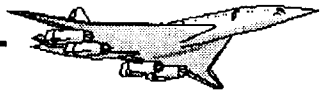

Set 3: Post Effects Comparison of Spanwise Cp between CFD and Test Data

Test

Geometric $\alpha = 12.8472^{\circ}$

Corrected $\alpha = 13.9281^{\circ}$

CFD

$\alpha = 10^{\circ}$

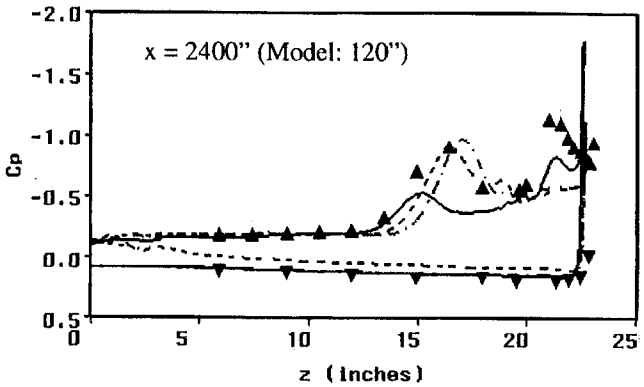

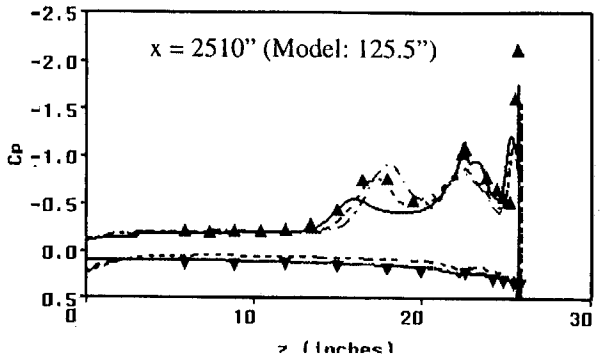

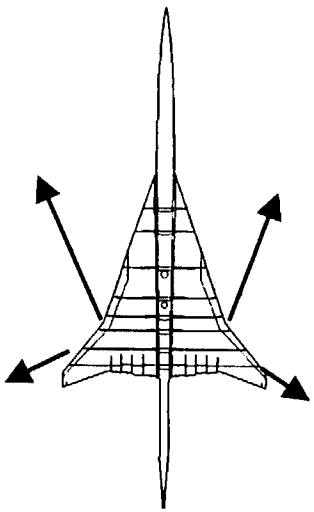

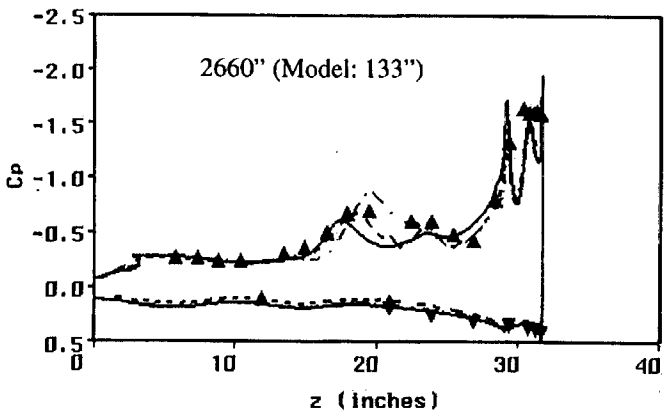

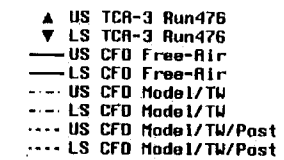

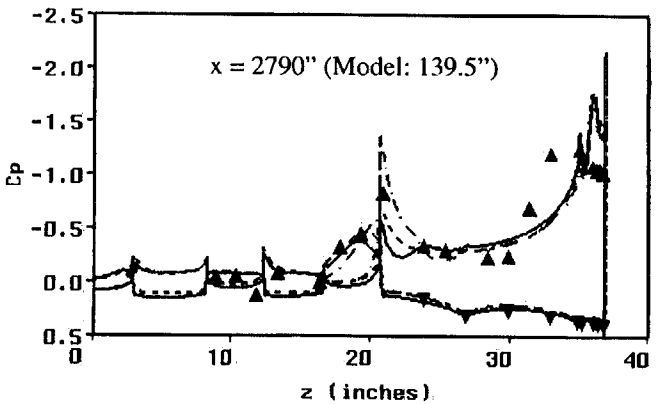

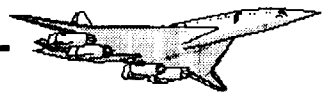

Comparison of the Lower Wing Surface Pressures

This figure compares the wing lower surface pressures between the model/tunnel and model/tunnel/posts cases.

As shown in the lower figure and the blowup in the next view graph, the major effect of posts on the surface pressure distribution is limited to the root and around the post regions.

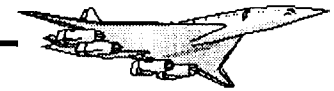

Comparison of the Lower Wing Surface Pressures
between the Model/Tunnel and Model/Tunnel/Posts Cases

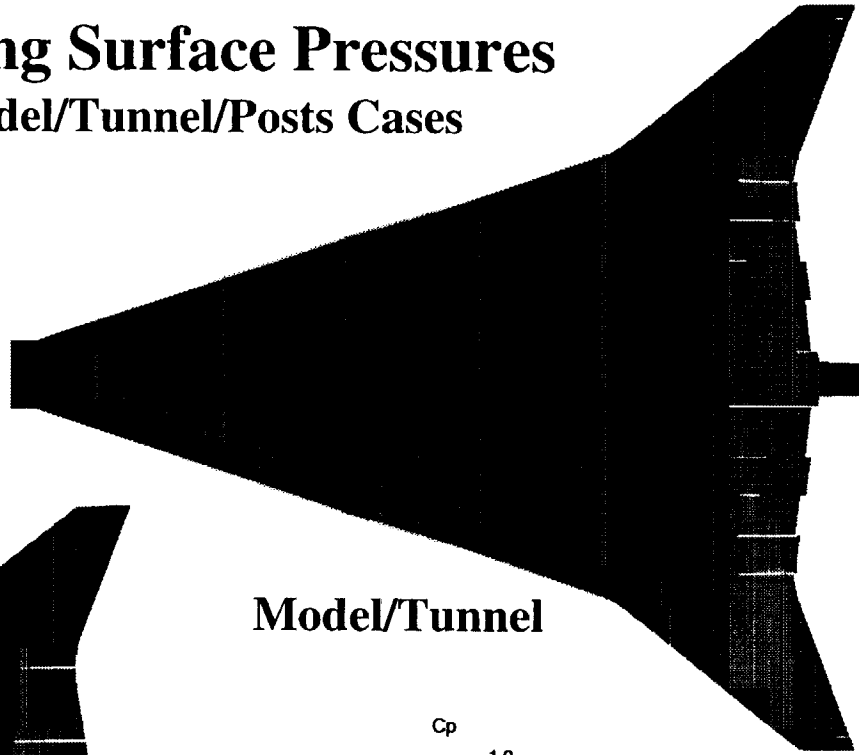

Model/Tunnel

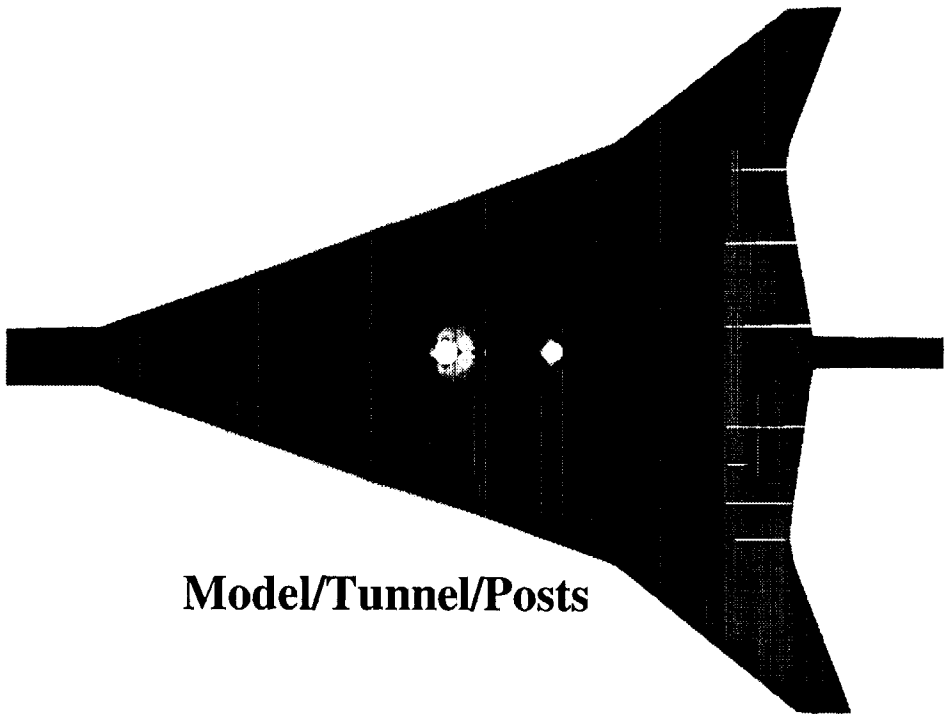

Model/Tunnel/Posts

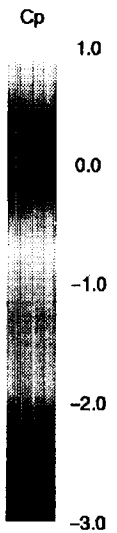

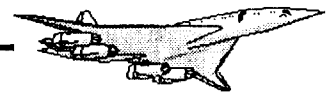

TCA Lower Surface Pressure Contour around the Posts

This figure shows a blowup of the wing lower surface pressure contour around the posts. As shown in the figure, the vortex shedding from the fore post has caused oscillation in numerical solution.

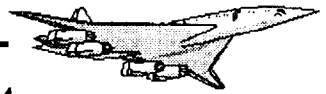

TCA Lower Surface Pressure Contour around the Posts

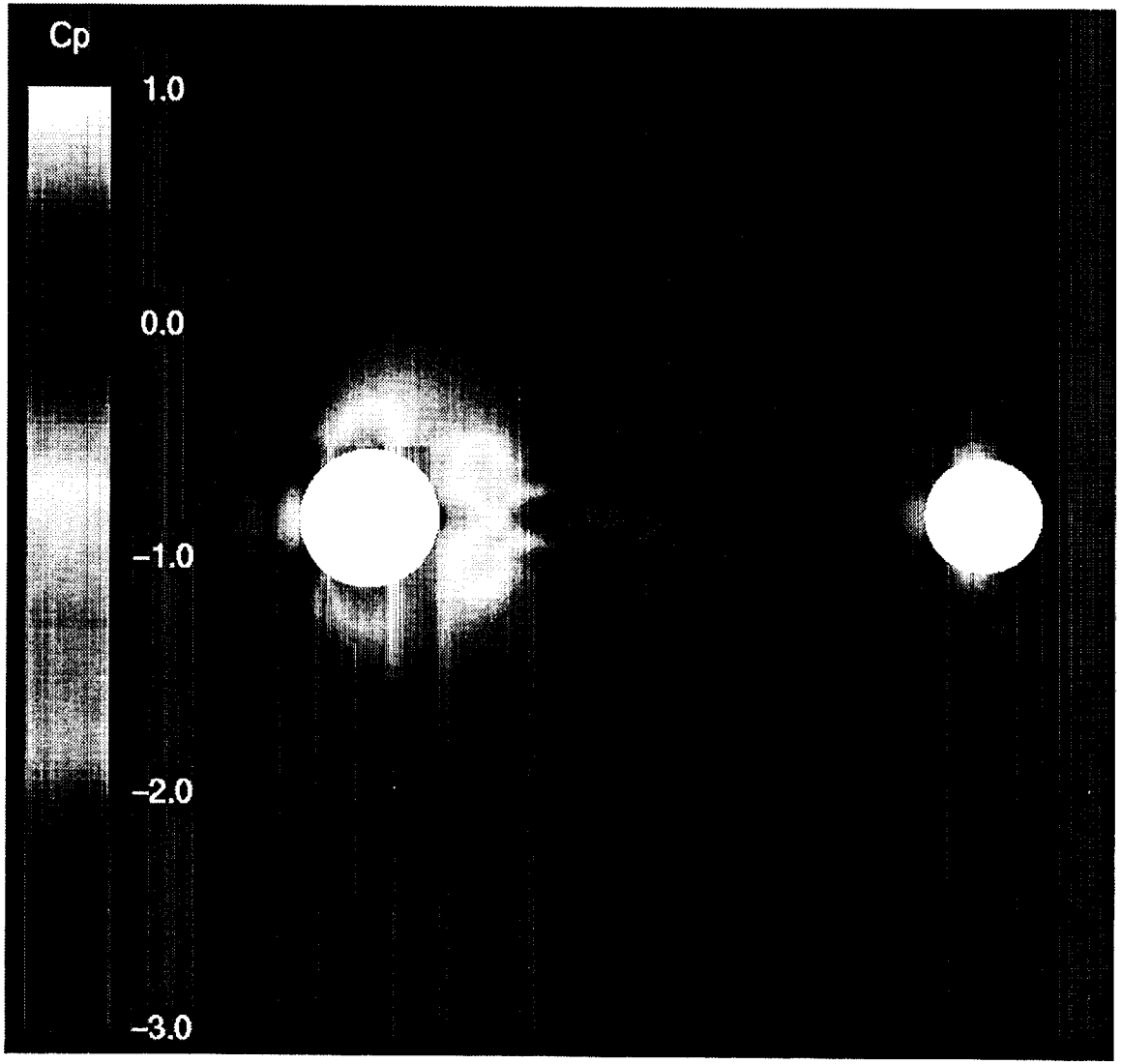

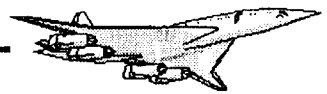

CFD Wind-Tunnel Flow Simulation for a 5% TCA Model

This figure shows three views of the CFD wind-tunnel flow simulation for the 5% TCA model inside the NASA/Ames 12-ft tunnel showing an over-wing vortex flow at Mach = 0.3, $\alpha = 10^{o}$, and Re = 8 million. The sectional color contours on the top of the wing surface are the total pressure contours.

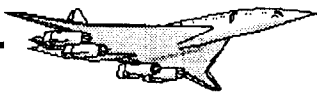

CFD Wind-Tunnel Simulation

for a 5% HSCT TCA Model

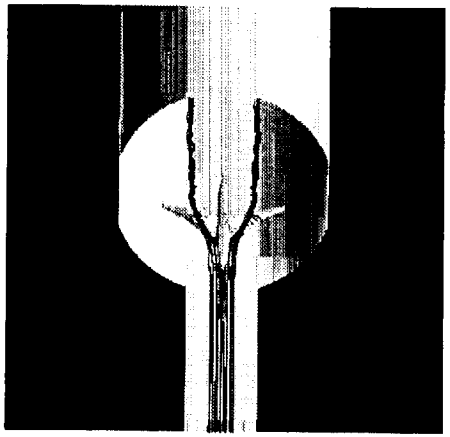

Top View

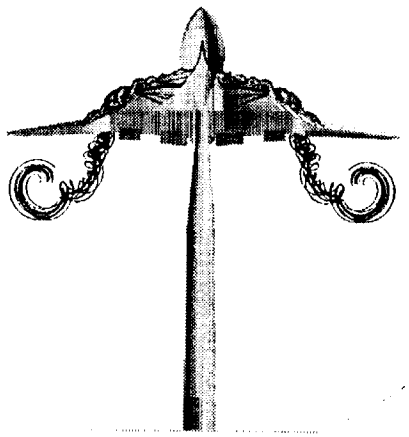

Tunnel Floor

Front View

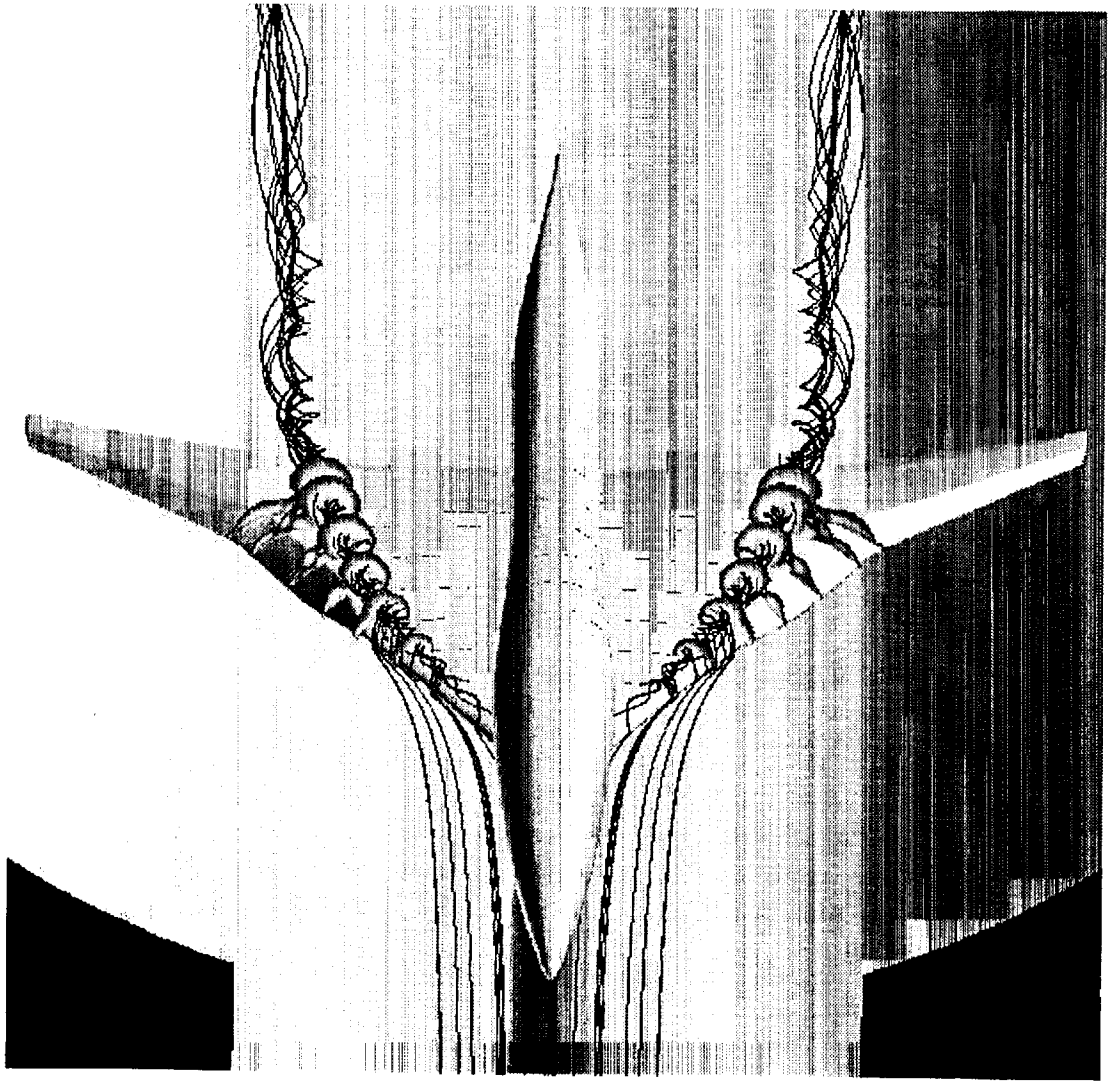

Blowup Showing the Over-Wing Vortex Flow

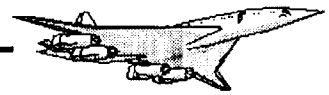

CFL3D Solution Convergence History

This figure shows the CFL3D solution convergence history in terms of C_L, C_D, and C_M for the three cases considered: free-air, model/tunnel, and model/tunnel/posts. The black solid lines represent the free-air case, the blue solid lines the model/tunnel case, and the red solid lines the model/tunnel/posts case. Also shown in the view graph are the uncorrected (the green dash lines) and corrected (the blue chaindot lines) data interpolated at $\alpha = 10$ degrees. As shown in the left figure the CFD calculated C_L's agree well with data. However, the CFD somewhat over predicts C_D.

The oscillation of C_L, C_D, and C_M in the model/tunnel/posts case is due to the shedding of vortices from the fore post as shown in the next view graph.

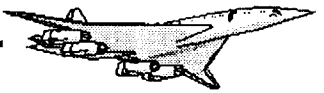

CFL3D Solution Convergence History

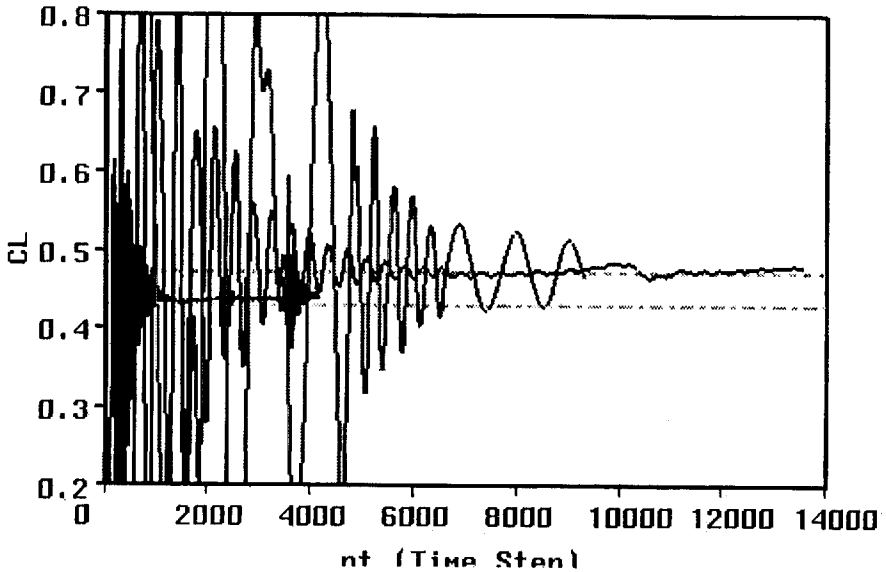

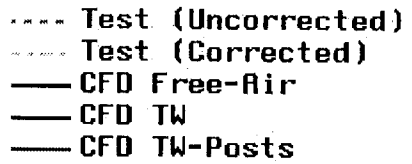

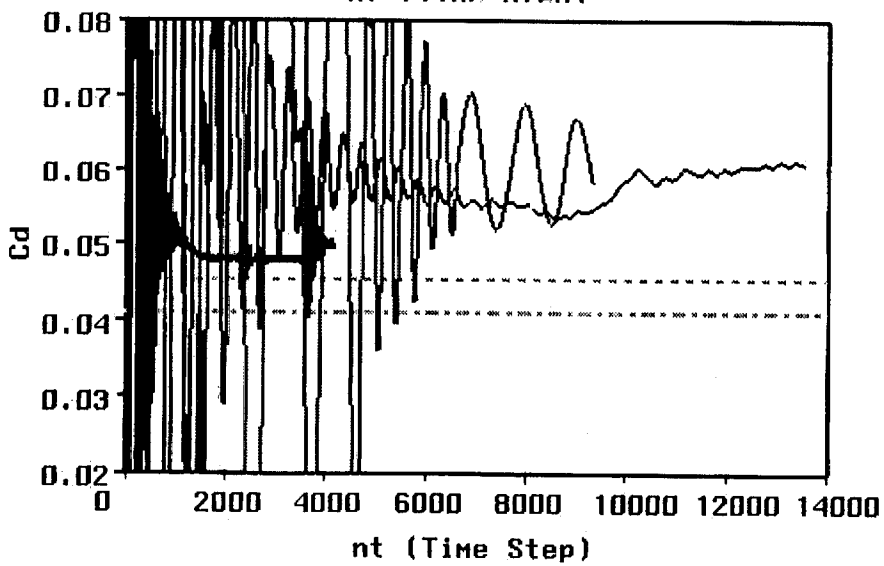

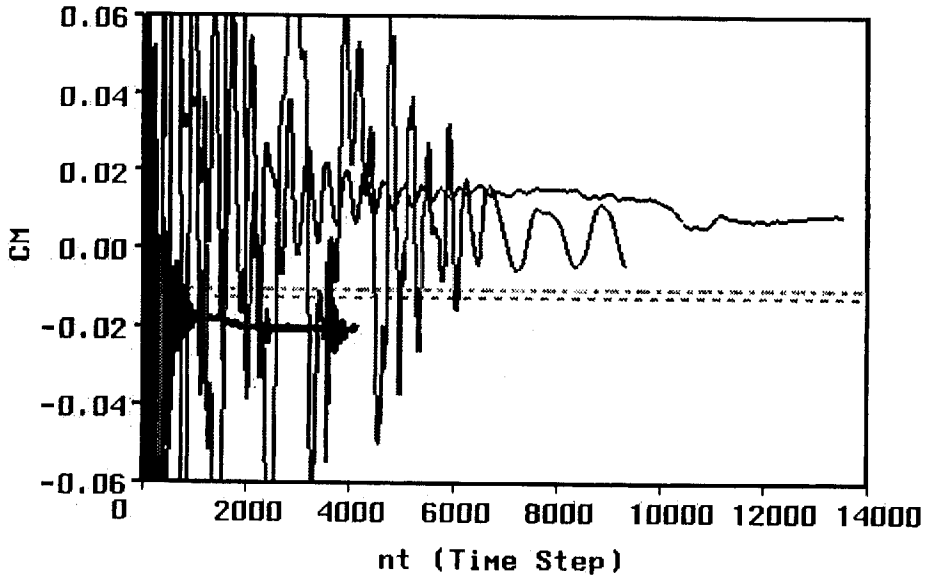

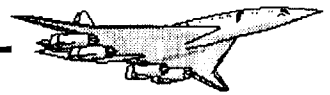

Pressure Contours around the Posts

This figure shows the surface pressure contours of the two model supporting posts. Also shown are a few cross-sectional pressure contour lines indicating trailing vortices of the fore post. It is noted that only half of the model/tunnel/posts configuration was used in our CFD simulation. By design, the trailing vortices become symmetric with respect to the symmetry plane. In reality, the trailing vortex pattern should be an asymmetric one with respect to the symmetry plane.

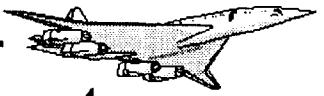

Pressure Contours around the Posts

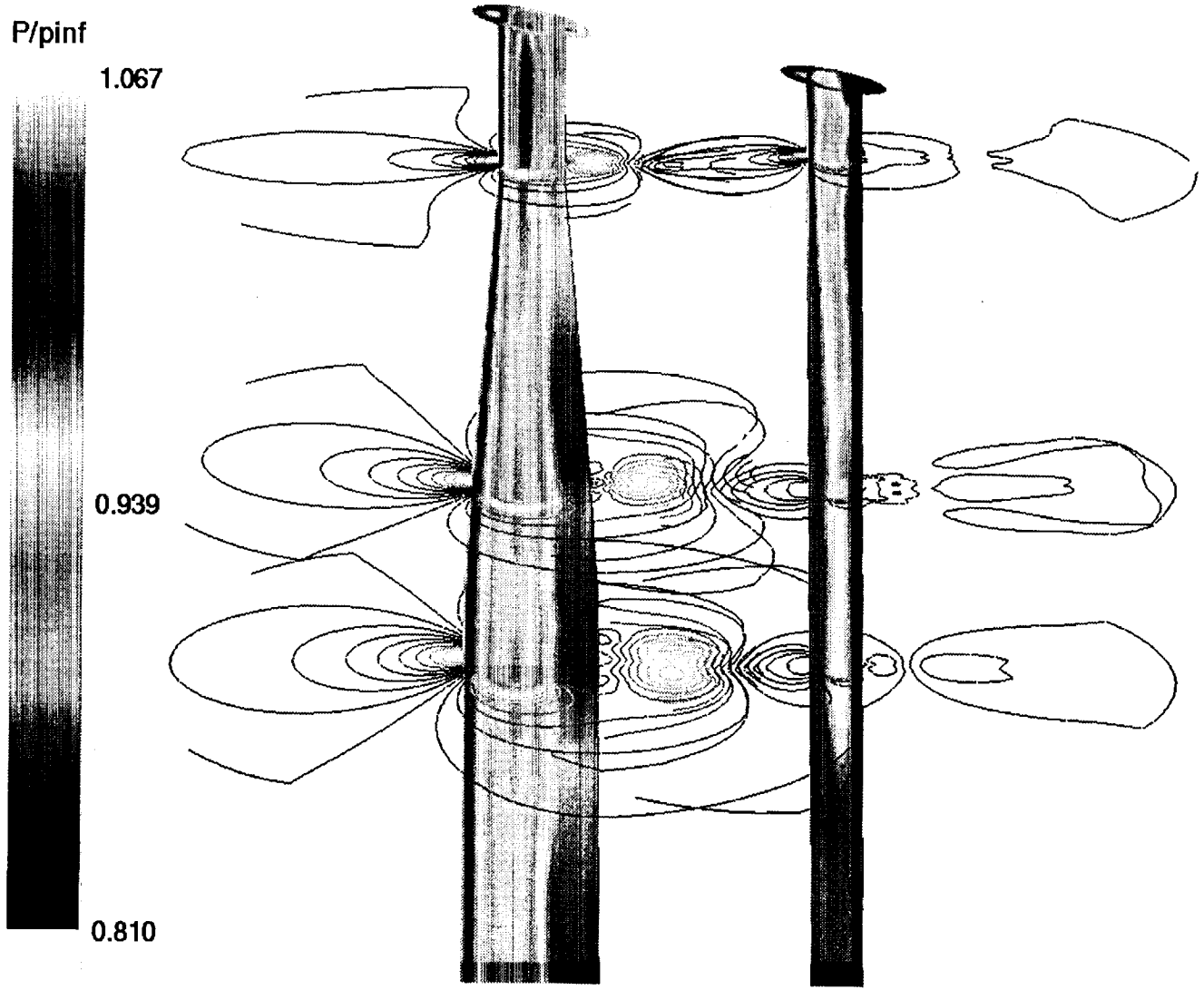

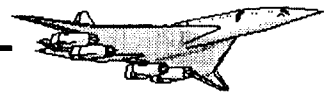

Comparison of CFL3D and FOMOCO Calculated C_L, C_D, and C_M

This table compares the CFL3D and FOMOCO calculated C_L, C_D, and C_M.

As shown in the table, the calculated results of the two methods agree well with each other for both cases.

It is noted that in the case of model/tunnel/posts, FOMOCO employed zipper grids in force and moment integration while CFL3D used directly the overlapping grids. It is apparent from the comparison of the two results that the effect of the small overlapping regions as show in the view graph entitled "Zipper Grids" on the overall integrated quantities is small in this case.

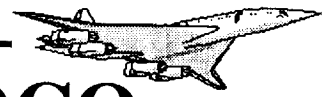

Comparison of CFL3D and FOMOCO Calculated C_L, C_D, and C_M

	C_L		C_D		C_M	
	CFL3D	FOMOCO	CFL3D	FOMOCO	CFL3D	FOMOCO
Model/Tunnel	0.47993	0.47936	0.060954	0.061163	0.008539	0.006315
Model/Tunnel/Posts	0.46527	0.46474	0.058349	0.058596	-0.004552	-0.006828

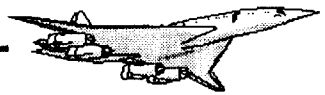

Comparisons of Forces and Moment

This view graph compares the CFD calculated C_L, C_D, and C_M with the wind-tunnel test data.

As shown in the figure, the CFD calculated C_L agrees well with the test data. C_D is over predicted by CFD. C_M is under predicted by free-air CFD and over predicted by both model/tunnel and model/tunnel/posts CFD.

Comparison between the model/tunnel and model/tunnel/posts results shows that the effect of posts is to reduce the values of C_L, C_D, and C_M.

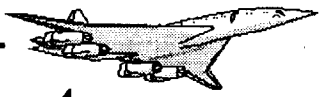

Comparisons of Forces and Moment

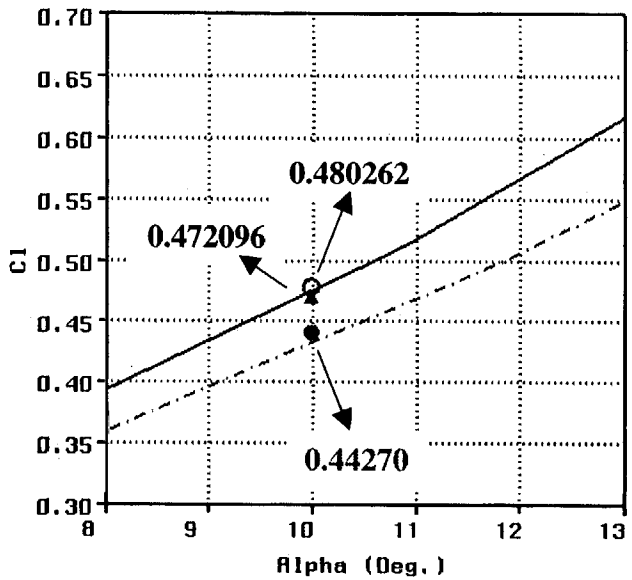

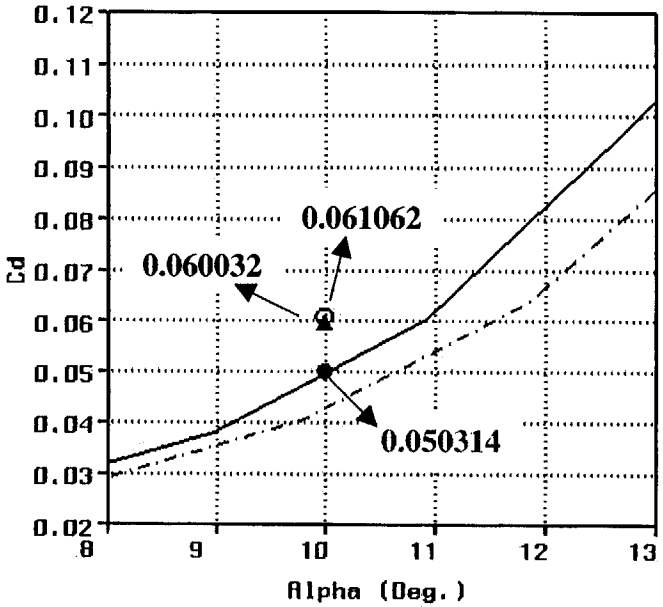

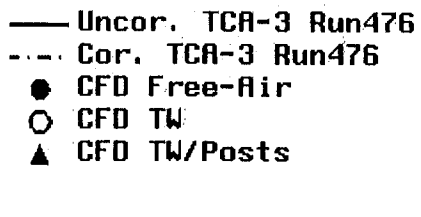

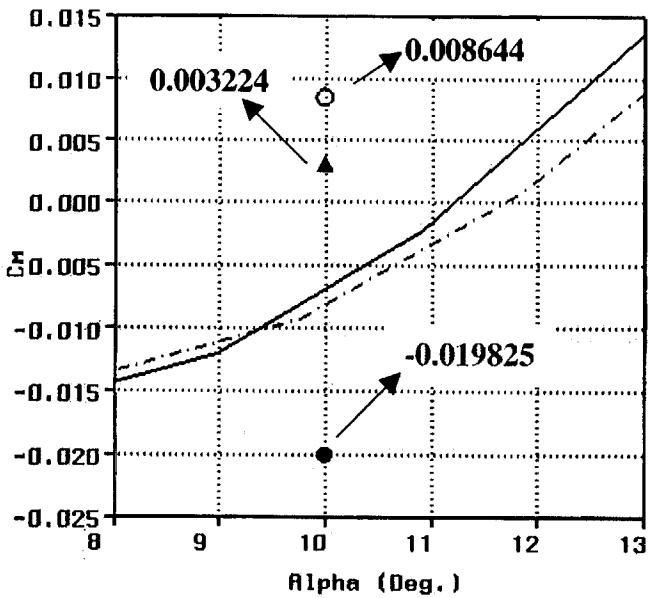

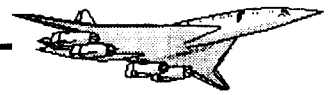

Comparisons of Force and Moment Increments between CFD and Test data

The increments of C_L, C_D, and C_M calculated by CFD are compared with those computed from the test data in this figure.

The CFD results are computed as the difference between the values of the CFD tunnel and free-air solutions.

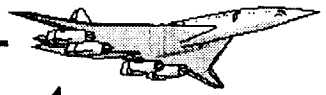

Comparisons of Force and Moment Increments between CFD and Test Data

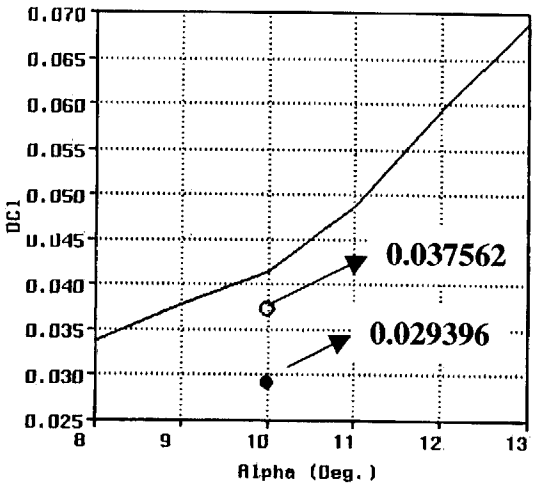

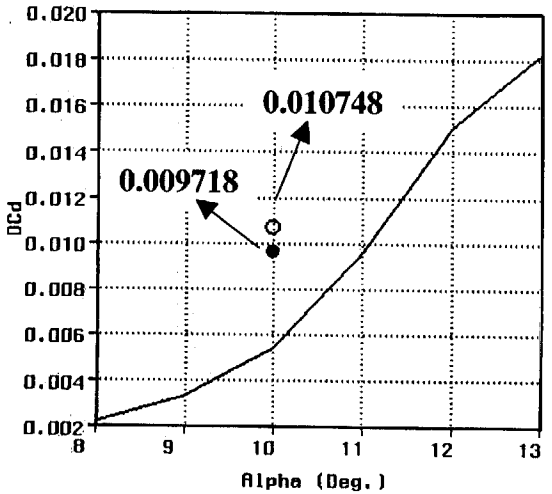

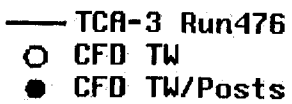

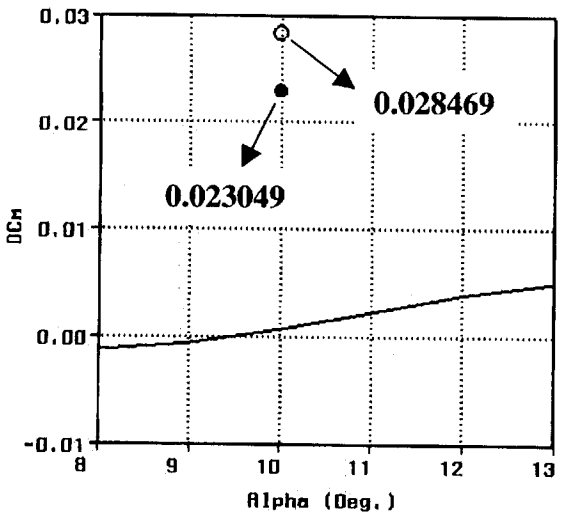

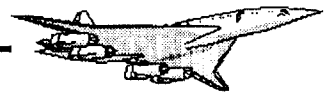

Table of Forces and Moment

This view graph summarizes the CFD calculated and the wind-tunnel measured C_L, C_D, and C_M at $\alpha = 10^o$.

Also shown are the force and moment increments.

For CFD, the increments are computed as the difference between the values of the CFD tunnel and free-air solutions.

It is noted that the numbers for the test data are interpolated from the test data at $\alpha = 10^o$.

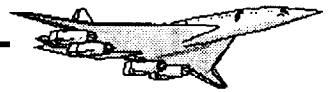

Table of Forces and Moment

C_L, L_D, and C_M

	α	C_L	C_D	C_M	L/D
Free-Air	10°	0.44270	0.050319	-0.01982	8.79786
Model/Tunnel	10°	0.480262	0.061062	0.00864	7.86515
Model/Tunnel/Posts	10°	0.472096	0.060032	0.00322	7.86407
TCA-3 Run476 (Uncorrected)	10°	0.475000	0.047730	-0.00762	9.95181
TCA-3 Run476 Corrected	10°	0.433480	0.042280	-0.00838	10.25260

Increments of C_L, L_D, and C_M

	dC_L	dC_D	dC_M
CFD Model/Tunnel	0.037562	0.010748	0.028469
CFD Model/Tunnel/Posts	0.029396	0.009718	0.023049
TCA-3 Run476	0.041520	0.005450	0.000760

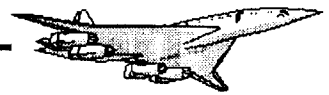

Concluding Remarks

MAGGIE has been greatly enhanced in speed and capability for handling complex geometries.

NASA/Ames FOMOCO has been coupled (externally) with CFL3D/MAGGIE for force and moment integration for configurations with overlapping surface grids.

CFL3D has been enhanced with Fortran 90 run-time memory allocation capability, allowing one executable for all the problems and eliminating the need of user's effort to compile and recompile programs for problems of varying memory sizes. This can increases user's productivity in an application environment.

Navier-Stokes solutions for the 5% TCA model in the NASA/Ames 12-ft pressure tunnel have been presented and compared with the free-air CFD solution and test data in terms of C_p, C_L, C_D, and C_M.

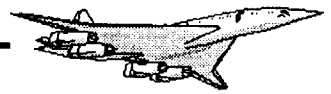

Concluding Remarks

- MAGGIE has been greatly enhanced in speed and capability for handling complex geometries
- NASA/Ames FOMOCO has been coupled with CFL3D/MAGGIE for force and moment integration for configurations with overlapping surface grids
- CFL3D has been enhanced with Fortran 90 run-time memory allocation capability, allowing one executable for all the problems
- Navier-Stokes solutions for the 5% TCA model in the NASA Ames 12-ft pressure tunnel have been presented and compared to the free-air CFD solution and test data in terms of C_p, C_L, C_D, and C_M

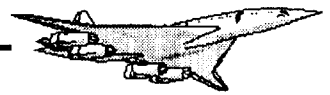

Concluding Remarks (Concluded)

Numerical results indicated that based on the CFL3D default implementation of the Baldwin-Lomax/Degani-Schiff model, the turbulence length scale was computed as the distance from the solid wall to the core of the primary vortex, resulting reduced vortex suction peak. Using reduced cutoff of searching distance, the CFD solutions were greatly improved in the regions of both leading and trailing edge flaps.

It is numerically difficult to implement the Degani-Schiff modification in the region where off-body vortex flow exists and or flow is separated.

In general, the CFD calculated surface pressures, lift and drag coefficients are compared very favorably with the wind-tunnel test data.

CFD calculated vortex strength and location agree well with the experiment. However, the CFD calculated attack of attack of the LE vortex flow separation is smaller than that of the experiment.

In general, the CFD calculated surface pressures, lift and drag coefficients are compared very favorably with the wind-tunnel test data.

The CFD calculated post effects on the lower wing surface pressures agree well with the test data.

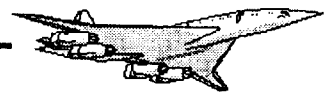

Concluding Remarks (Concluded)

- Numerical results indicated that based on the CFL3D default searching index range, the length scale was computed as the distance from the solid wall to the core of the primary vortex, resulting reduced vortex suction peak. With reduced cutoff of searching distance, the CFD solutions were greatly improved in the regions of both leading and trailing edge flaps
- It is numerically difficult to implement the Degani-Schiff modification in the region where off body vortex flow exist and or flow is separated
- CFD calculated vortex strength and location agree well with the experiment. However, the CFD calculated attack of attack of the LE vortex flow separation is smaller than that of the experiment
- In general, the CFD calculated surface pressures, lift and drag coefficients are compared very favorably with the wind-tunnel test data
- The CFD calculated post effects on the lower wing surface pressures agree well with the test data

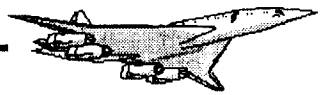

Recommendations

To minimize possible grid-topology effects, a single model grid should be used for all the flow simulations of free-air, model/tunnel, and model/tunnel/posts.

A field based turbulence model is desired to provide a robust CFD simulation of the LE vortex flows associated with HSCT high-lift devices

Good quality wind tunnel data is needed to evaluate, validate, and, calibrate turbulence model for LE vortex flow applications.

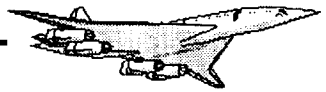

Recommendations

- To minimize possible grid-topology effects, a single model grid should be used for all the flow simulations of free-air, model/tunnel, and model/tunnel/posts

- A field based turbulence model is desired to provide a robust CFD simulation of the LE vortex flows associated with HSCT high-lift devices

- Good quality wind tunnel data is needed to evaluate, validate, and, calibrate turbulence model for LE vortex flow applications

CFD Assessment of TCA High–Lift Configurations

David T. Yeh and Roger W. Clark

Boeing, Long Beach

HSR Airframe Technical Review
High Lift Aerodynamics
at
Anaheim, CA
February 9–11, 1999

BOEING

This slide shows an outline of the High-Lift Technology program.

High Lift Technology Development (Task 33)

Increase L/D, Develop Analysis/Design Methodology

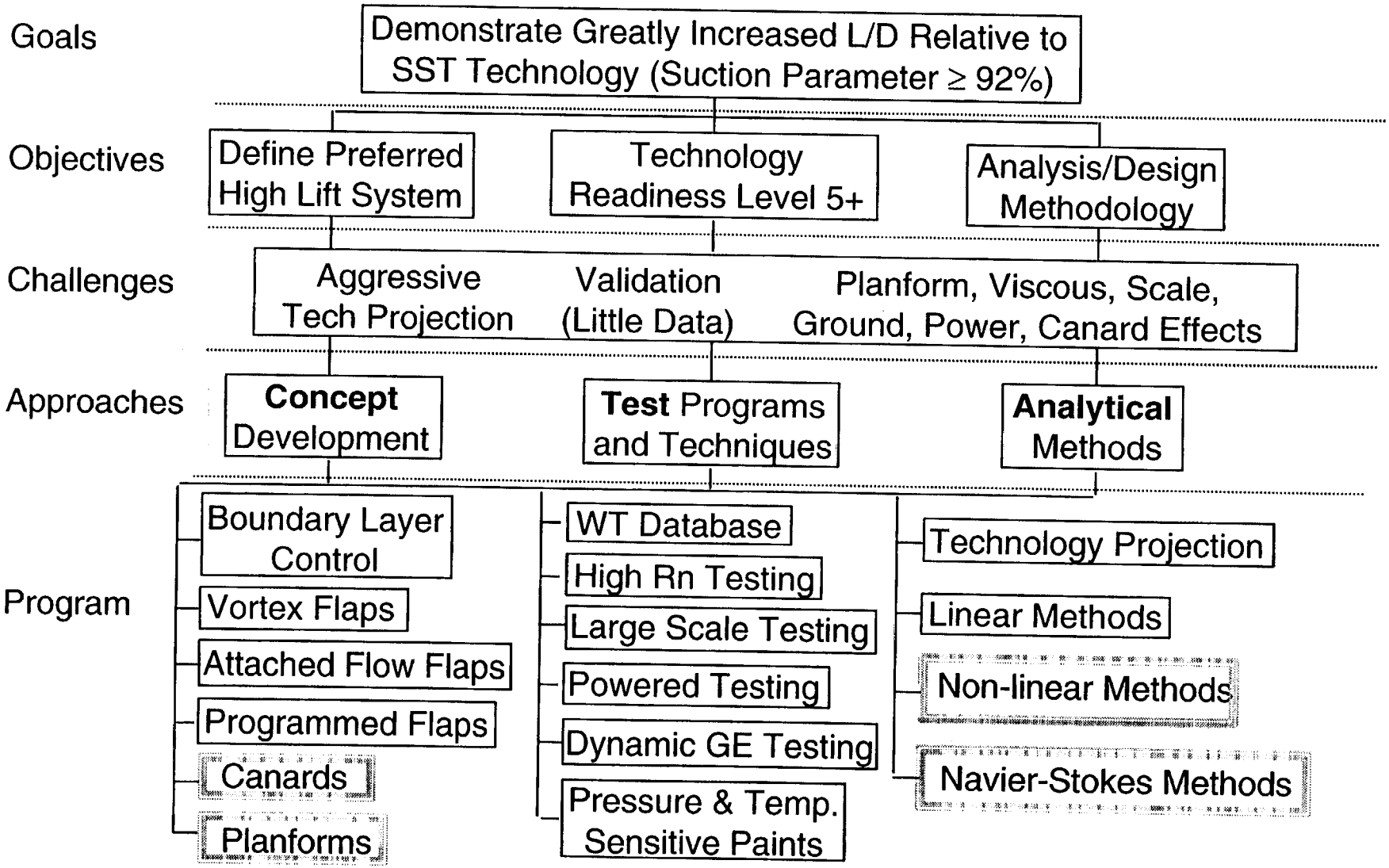

Outline

This report starts with the description of the objective for the HSCT high-lift CFD analysis, and the focus of current study, followed by the numerical approach. Numerical results will be presented on the effects of the wing planforms, inboard LE flap extent and the forebody chine effects at high-lift conditions. For the Wing/Body/Canard configurations, the influence of the canard on the high-lift configuration will be discussed. Code validation will be presented through the direct correlation with available tunnel test data. This report concludes with a summary and a description of the on-going high-lift CFD effort.

Outline

- Objective & Current Study Focus
- Approach
- Numerical Results and Code Validation
  - W/B Configurations – Planform Variation
    Inboard LE Flap Extent
    Forebody Chine Effect
  - W/B/C Configurations – Canard Effect
- Summary and Future Plans

BOEING

Objective - HSCT High Lift CFD Analysis

The objective of the high-lift CFD analysis is to provide the numerical tools for the design and optimization of the high-lift system including wind-tunnel support and the evaluation of the aerodynamic performance as the configuration evolves. To accomplish this objective, it is necessary to develop and enhance the numerical modeling capability for the high-lift devices such as various types of LE & TE flaps and forebody control surfaces. It is also necessary to assess the numerical capability to accurately model the flow phenomena under the high-lift conditions, near design as well as off-design conditions. The numerical solutions are also utilized to provide a better physical understanding of the flow physics.

Objective – HSCT High Lift CFD Analysis

HSCT Aerodynamics, Long Beach

- Develop/Enhance Modeling Capability
- Apply/Validate Numerical Methods

→ Analysis/ Design Tools →

- Wind Tunnel Support
- Configuration Evaluation
- High Lift System Design

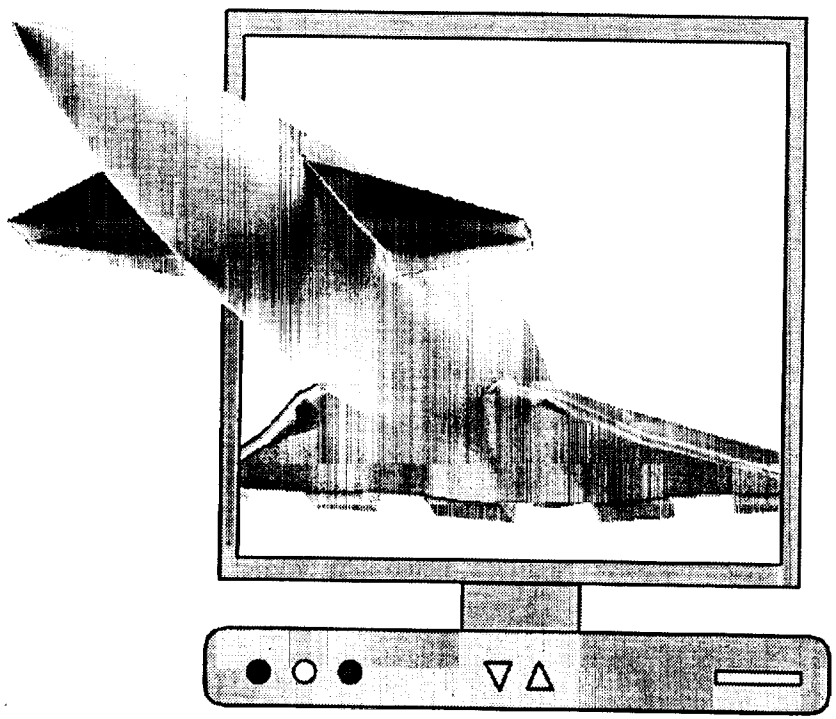

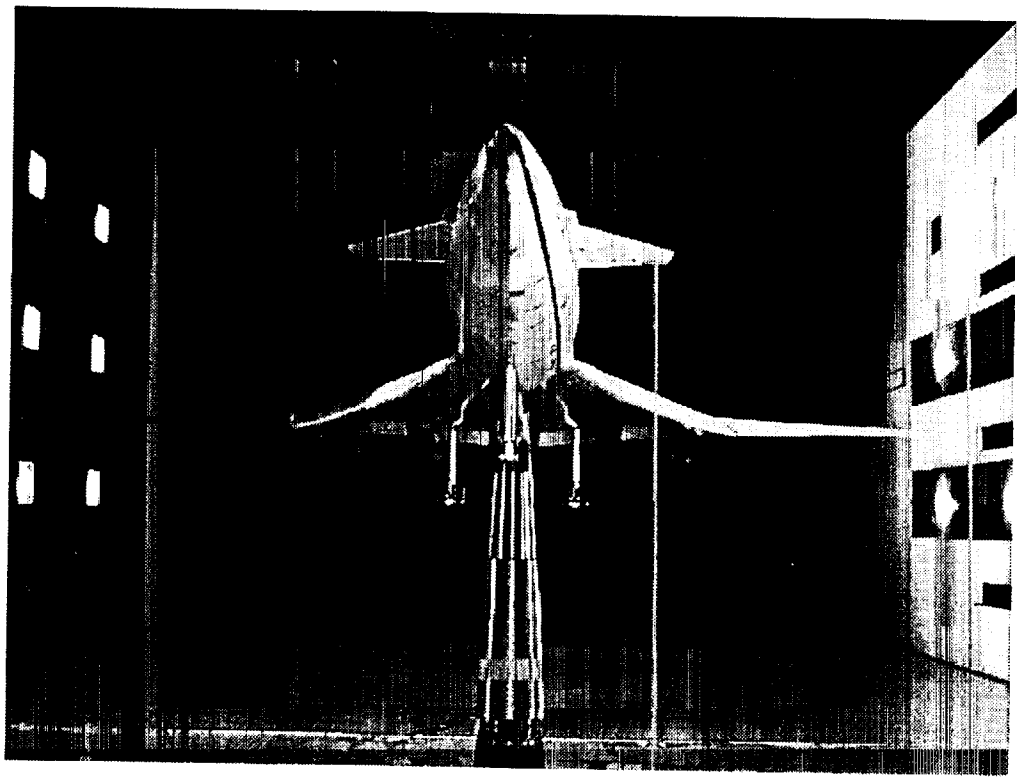

BOEING

Current Study Focus

The current study is focused primarily on the TCA-4 High-Lift Wind-Tunnel Test to assess the effects of planform variation as well the canard influence on the high-lift configurations. The planform study consists of 3 wings: W1, W2 and W3. These 3 wings have an identical geometry inboard of the wing break. The outboard sweep variation range from 52 degrees for the W1 (baseline TCA configuration) to 28 degrees for the W2, and the W3 has 38 degrees of outboard LE sweep. The W1 has an aspect ratio of 2.0 while the aspect ratio for both W2 and W3 is 2.8. The canard effect will be focused on its influence on the wing at high-lift conditions with both LE and TE flaps deflected.

Current Study Focus (TCA–4 Test)

- Planform Variation

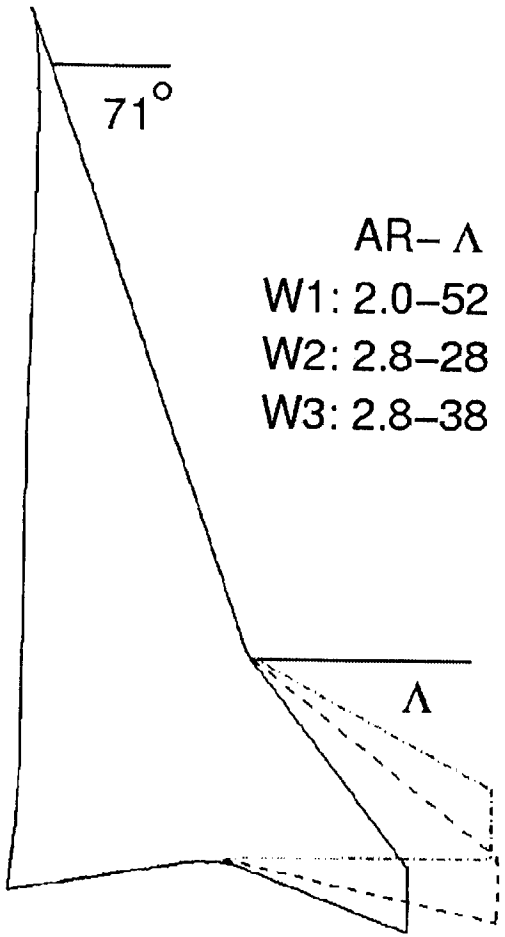

- Canard Effect

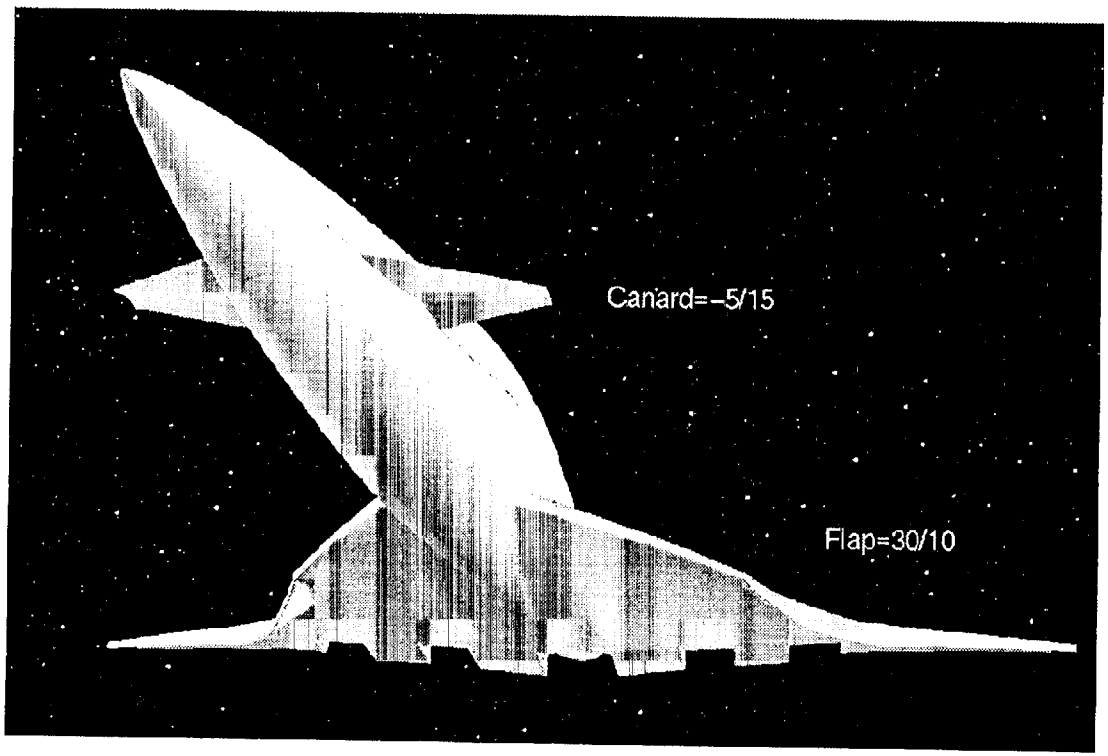

BOEING

Approach

The approach is to utilize the automated flap deflection and canard modeling procedures that have been developed under the HSR program to efficiently generate the computational models with multiple LE and TE flaps and forebody control surfaces. Once the the grid has been generated, the CFL3D code developed at NASA LaRC is used for high-lift flow simulations. Since the flow is dominated with viscous and vortical flow phenomena, the Navier-Stokes option of the code is used for all the simulations. The numerical results are compared with available test data for code validation as well as test support. The effects of planform variation and the canard interaction are analyzed through detailed graphical visualization and their impact on the high-lift performance will be evaluated.

Approach

- Utilize Automated Procedures for
  - Flap Deflections
  - Canard Modeling

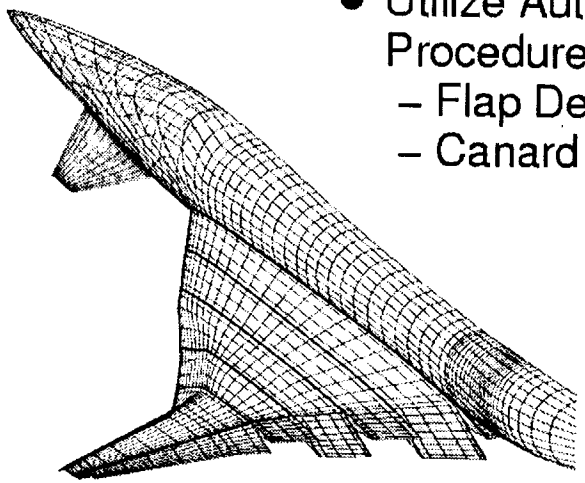

- Numerical Wind Tunnel

GRID →

CFL3D →

N–S Simulations

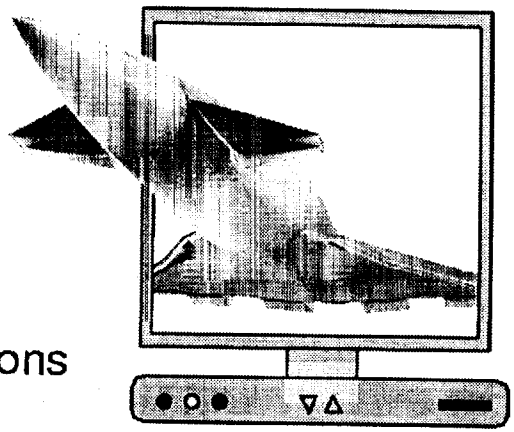

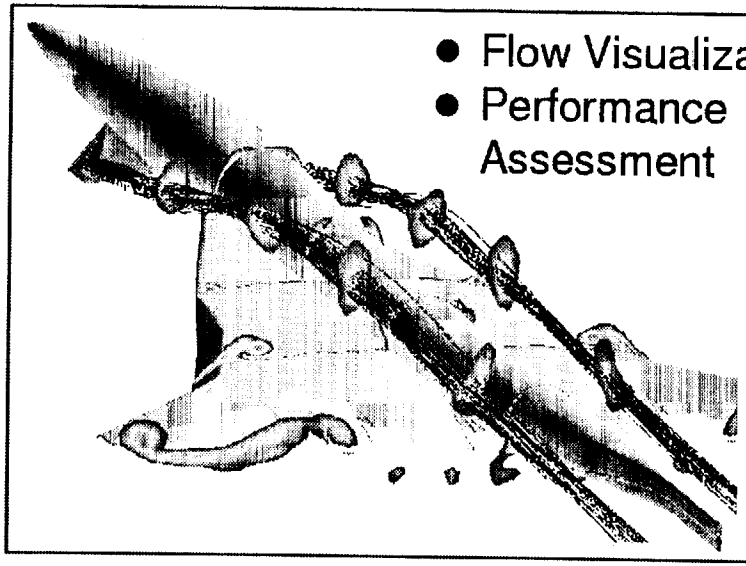

- Flow Visualization
- Performance Assessment

- Code Validation & Test Support

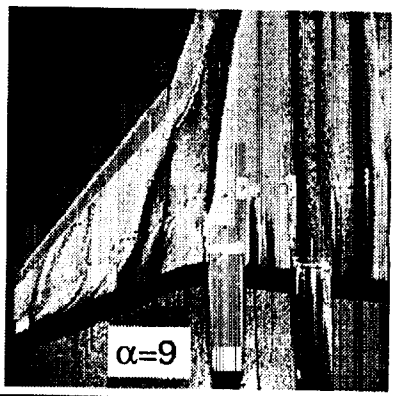

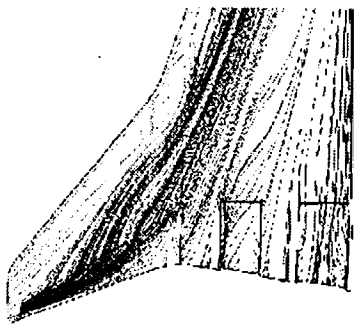

BOEING

Automated Flap Deflection Modeling Capability

Design and analysis of HSCT high-lift configurations require the modeling of the leading-edge (LE) and trailing-edge (TE) flaps with a wide range of planforms, spanwise and chordwise extent and angular deflections. In order to make the numerical modeling process feasible and efficient for the design and optimization of high-lift systems, an automated flap deflection process has been developed. This process can be used to modify the flaps-up CFD grid to account for multiple LE and TE flap deflections with minimal user interface. Since the modeling process has been described in detail in the 1997 HSR Workshop, the numerical capability of the process including recent enhancement is briefly described in this chart.

With the built-in flap modeling capability, additional features have been implemented for parametric studies of the high-lift performance. Some of the features include: (1) the scaling of the baseline LE flaps for flap chord study; (2) the improvement of the upper surface curvature on the LE flaps or around the hingeline using cubic spline with continuous slopes at the both ends; (3) the modeling of the LE flap extent through the input the flap geometries for part-span, full-span, or an intermediate LE flap geometry. This process has been successfully applied to a variety of HSCT planforms including, the Arrow Wing, TCA2.0-52, TCA2.8-38, TCA2.8-28, PTC, NCV configurations, as well as Reference H.

The following several charts summarize some of the numerical results with the focus on the TCA-4 test configurations and code validation. The numerical results on the effects of flap deflection and LE camber are referred to the 1998 HSR Workshop Proceedings under the High-Lift Aerodynamics.

Automated Flap Deflection Modeling Capability

HSCT Aerodynamics, Long Beach

– Modifies Flaps–Up CFD Grids for HSCT High–Lift Configurations

- Variable Flap Deflection
- Flap Chord Variation

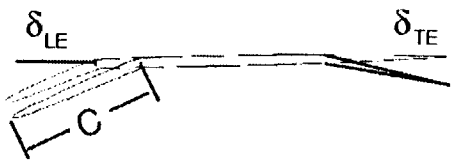

- LE Flap Extent

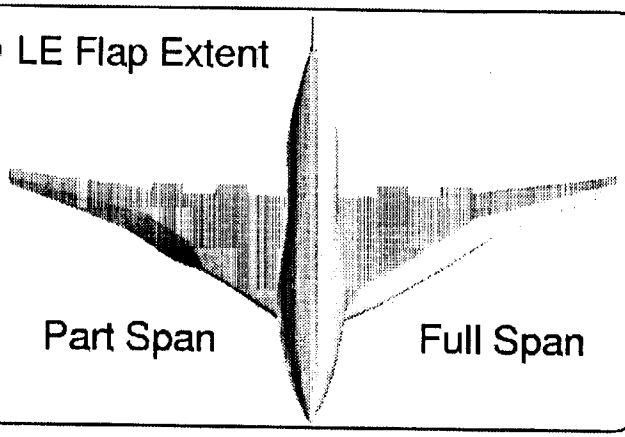

- LE Radius / Camber
- Hingeline Curvature

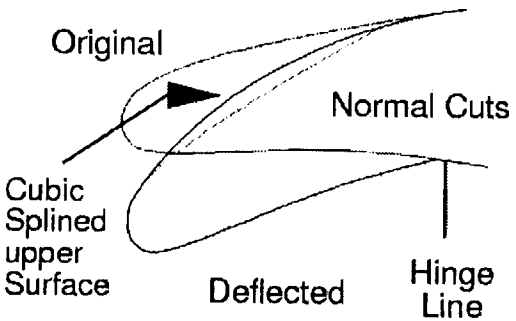

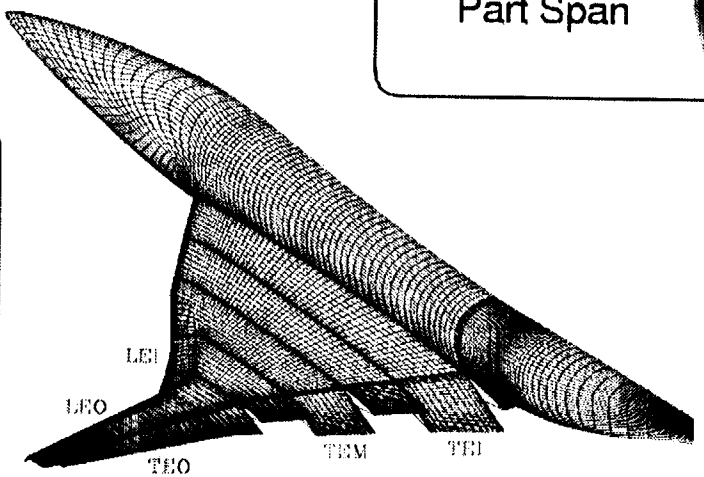

- Multiple LE & TE Flaps

- Planform Change

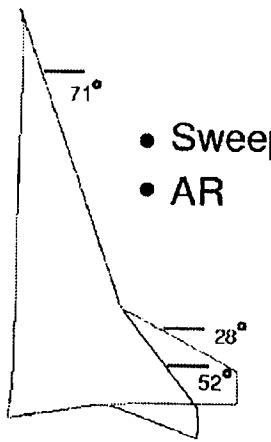

- Sweep
- AR

BOEING

Effect of Inboard LE Flaps on Flow Separation

The effect of inboard leading-edge(LE) flaps on the flow separation is illustrated through the releasing of the limiting streamlines near the leading-edge. At 10 degrees angle-of-attack with a 30-degree leading-edge flap deflection, the separation appears just inboard of the part-span LE flap. On the other hand, attached flow is attained on the deflected inboard leading-edge flaps for the full-span flap configuration. As a result, the full-span flap promotes the attached flow inboard and delays a premature leading-edge separation. The similar flow phenomena for the part-span and full-span flap configurations are also illustrated in the experimental oil-flow patterns obtained in the TCA-4 wind tunnel test.

Effect of Inboard LE Flaps on Flow Separation

δ (LE/TE) = 30°/10° , α=10°

- Separation starts inboard of LE flaps
- Attached flow achieved on the deflected inboard LE flaps

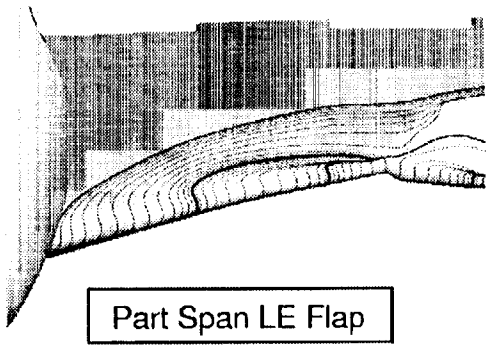

Limiting Streamlines

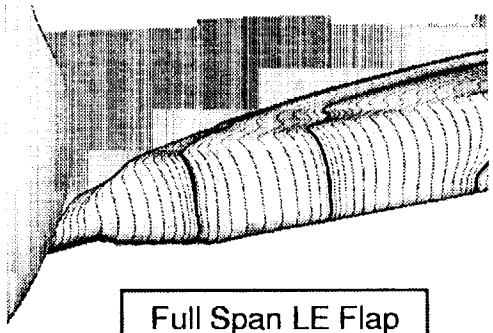

Part Span LE Flap

Full Span LE Flap

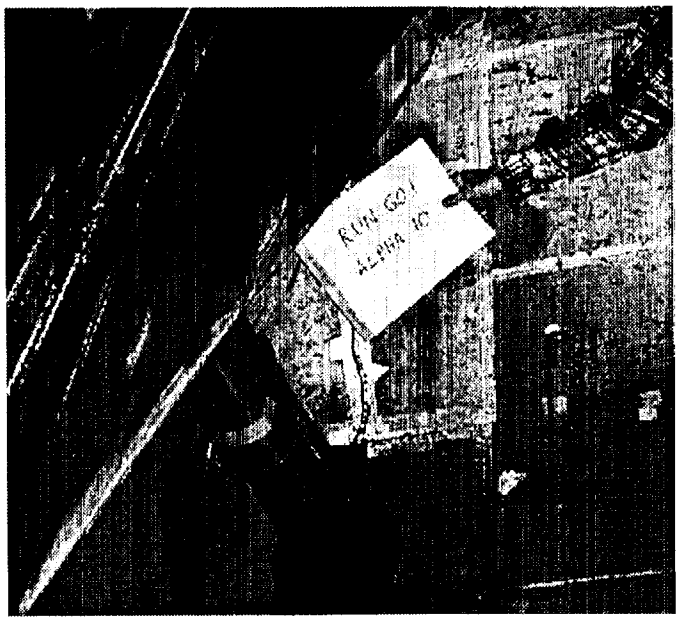

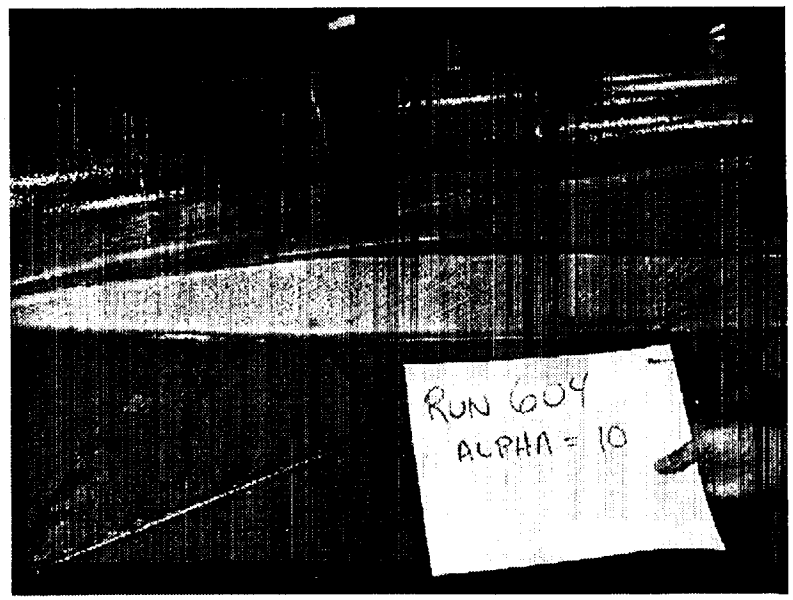

Effect of Inboard LE Flaps on W2 Upper Surface Flow

This chart shows the computed effect of inboard LE flaps on the upper surface pressure and the limiting streamlines for the W2 30/10 configuration at alpha 10. For the part-span LE flap case, it clearly shows the formation of the inboard LE vortex as indicated by the inboard spanwise flow and the vortex induced low pressure region. On the other hand, only a weak apex vortex flow pattern is visible for the full-span LE flap case. The predicted inboard flow appears to be attached, and the hingeline suction due to the flow acceleration is clearly seen in the full-span LE flap configuration.

Effect of Inboard LE Flaps on W2 Upper Surface Flow

HSCT Aerodynamics, Long Beach

Flaps(LE/TE)=30/10, M=0.3, α=10 deg

- Part Span LE Flaps

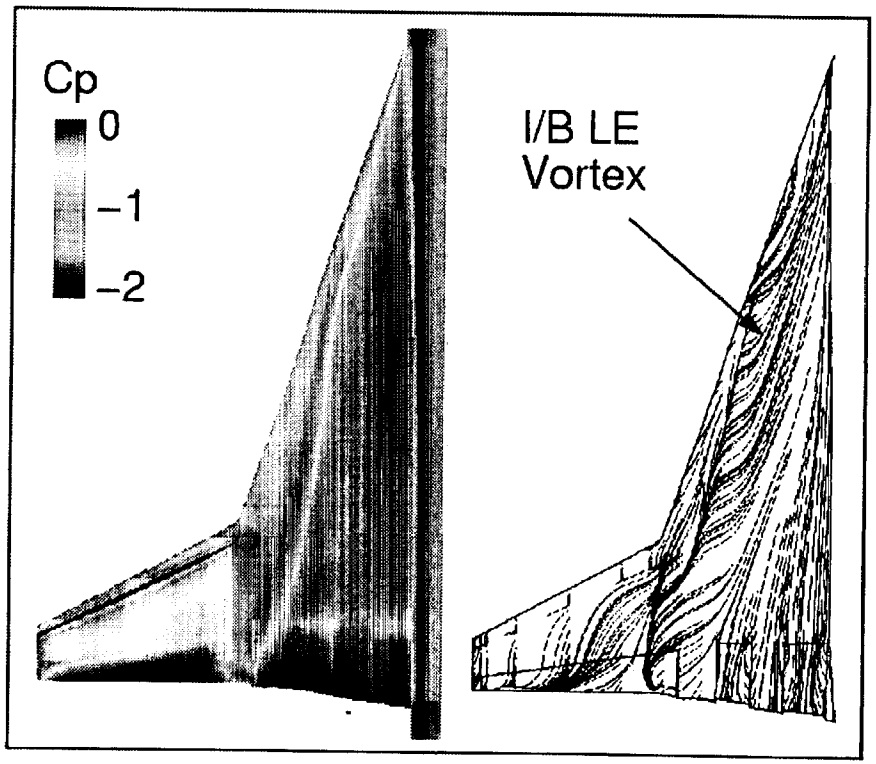

- Full Span LE Flaps

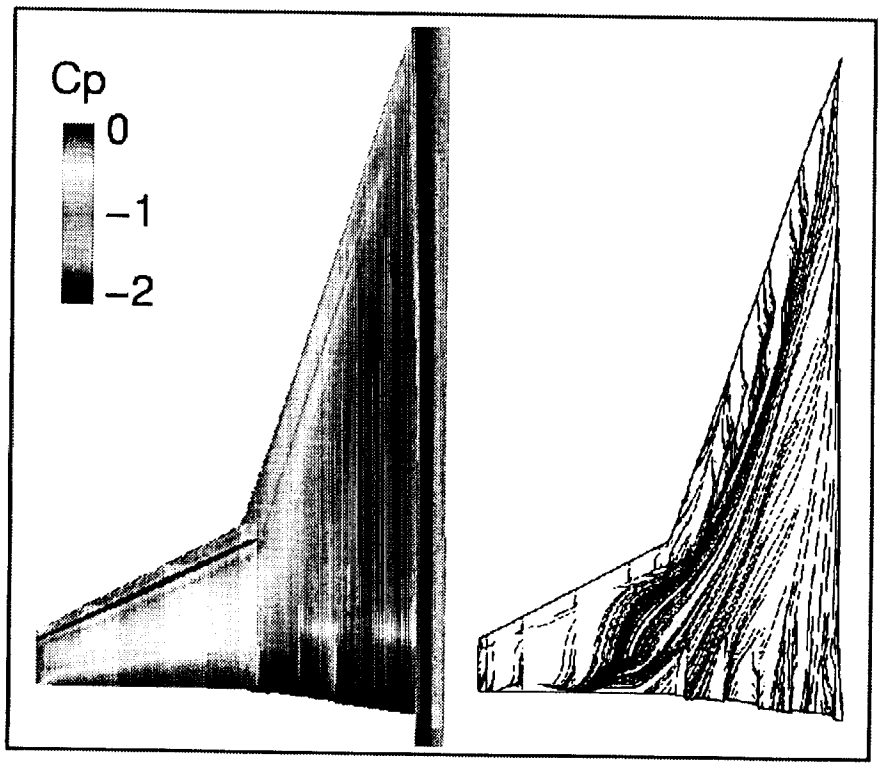

BOEING

Effect of Inboard LE Flaps on the Lift and Moment for W1

The force and moment comparison with the TCA-1 test are illustrated in this figure. Although the magnitudes are slightly different, the overall trend of the part-span versus full-span leading-edge flaps is clearly captured.

The results for the part-span leading-edge flap show a higher lift than that of a full-span flap configuration which indicates the presence of premature leading-edge separation resulting a stronger leading edge vortex. As a result, a significantly higher nose-up (positive) pitching moment is generated for the part-span than the full-span flap configuration.

Effect of Inboard LE Flaps on the Lift and Moment for W1

Flaps (LE/TE) = 30/10

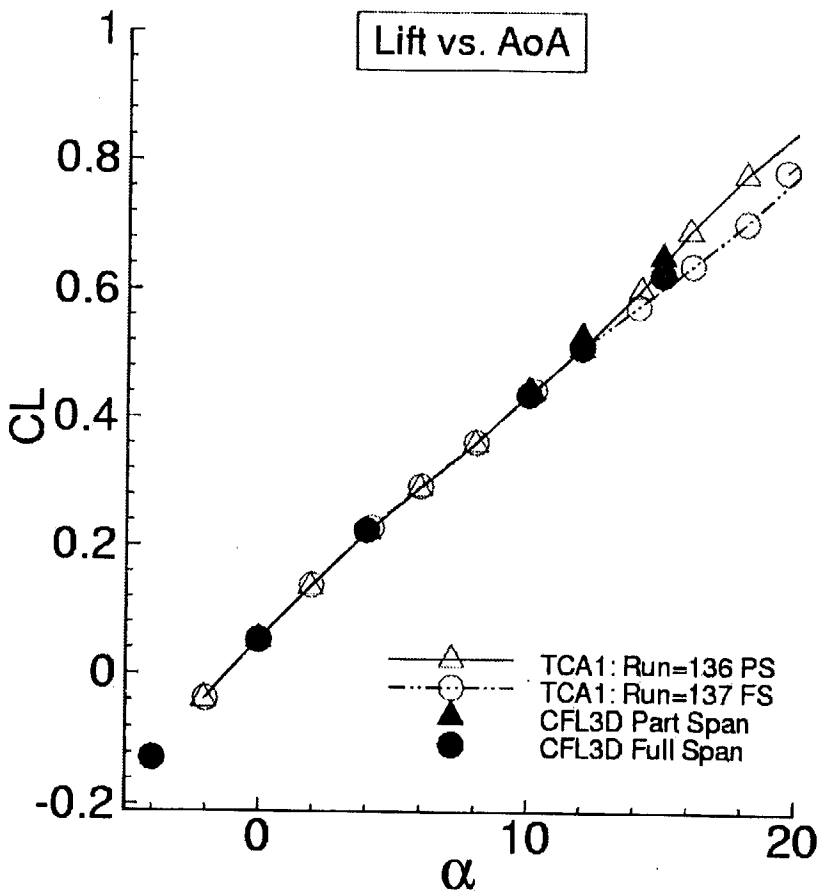

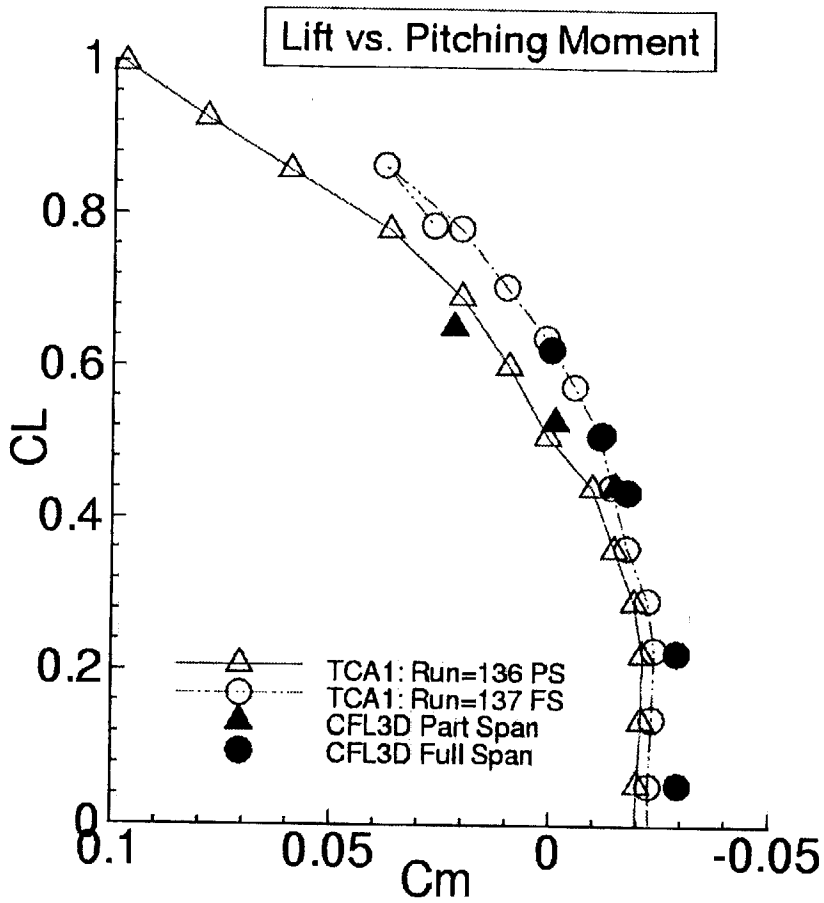

BOEING

Effect of Inboard LE Flaps on the drag and L/D for W1

The drag and lift-to-drag ratio comparison with the TCA-1 test are illustrated in this figure. The overall trend of the effect of part-span versus full-span leading-edge flaps is clearly captured.

Since the part-span flap configuration generates a stronger leading-edge vortex than the full-span flap configuration at the same flow condition, the results show a higher drag for the part-span configuration which translates into a lower lift-to-drag ratio.

Effect of Inboard LE Flaps on the Drag and L/D for W1

Flaps (LE/TE) = 30/10

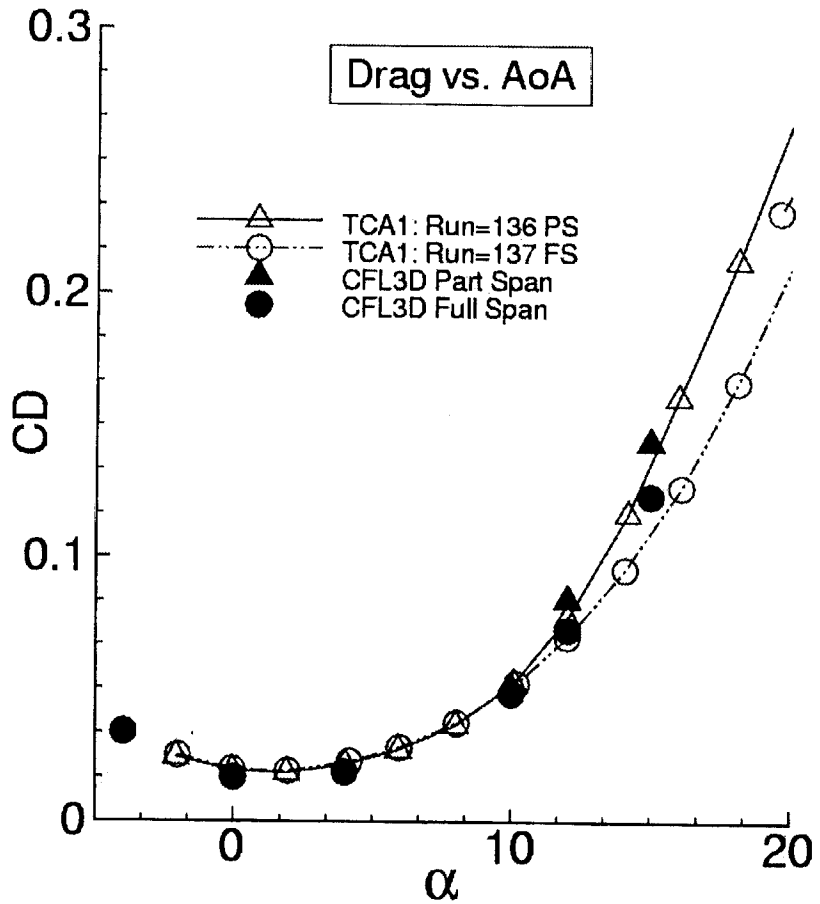

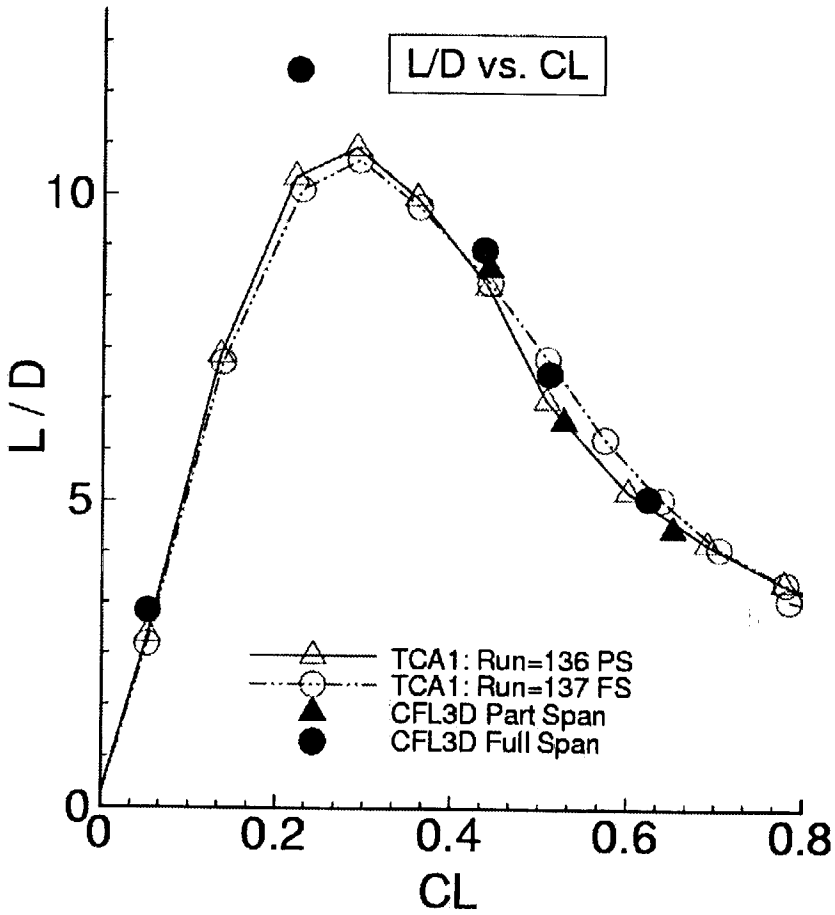

BOEING

Planform Effect on the Flow Features

Some of the flow features due to the planform variation are illustrated in this figure through the releasing of the particle traces. Since the particle traces for the W2 and W3 have similar patterns, only the W3 is shown to compare with the baseline TCA(W1). Both of the cases were simulated at M=0.3, alpha of 10 with the flaps (LE/TE) of 30/10 degrees. The formation of the forebody vortex, a weak apex vortex and the tip vortex are clearly seen for both W1 and W3 configurations. The noticable difference between these two wings is the flow phenomena in the outboard region. For the W3, attached flow is seen in the outboard region. On the other hand, an outboard flap vortex is formed for the higher outboard sweep wing (W1) at the same angle of attack.

Planform Effect on the Flow Features

M=0.3, α=10°, Re=8 million

Flaps(LE/TE)=30°/10°

W3(2.8–38)

- O/B Attached Flow

W1(2.0–52)

- O/B Flap Vortex

BOEING

Upper Surface Pressure Contours for Various TCA Planforms

This figure shows the upper surface pressure for these 3 wings (W1, W2 and W3) at alpha of 10 with flap settings (LE/TE) of 30/10. Similar pressure patterns can be seen for all 3 wings, where a weak apex vortex trails toward the TE in the inboard region as indicated by the vortex induced low pressure region. The flow acceleration around the inboard hingelines of the TE flap surfaces resulting a low pressure region can also be seen. The magnitude of the low pressure near the outboard LE hingeline is shown to increase as the hingeline sweep angle decreases. This is a result of higher streamwise deflection angles which result from the decrease in the outboard LE sweep angle. The lower pressure around the outboard TE hingelines for both W2 and W3 as compared to W1 is another indication of outboard attached flow and lower hingeline sweep.

Upper Surface Pressure Contours for Various TCA Planforms

HSCT Aerodynamics, Long Beach

δ(LE/TE)=30/10, Full Span LE Flaps, α=10

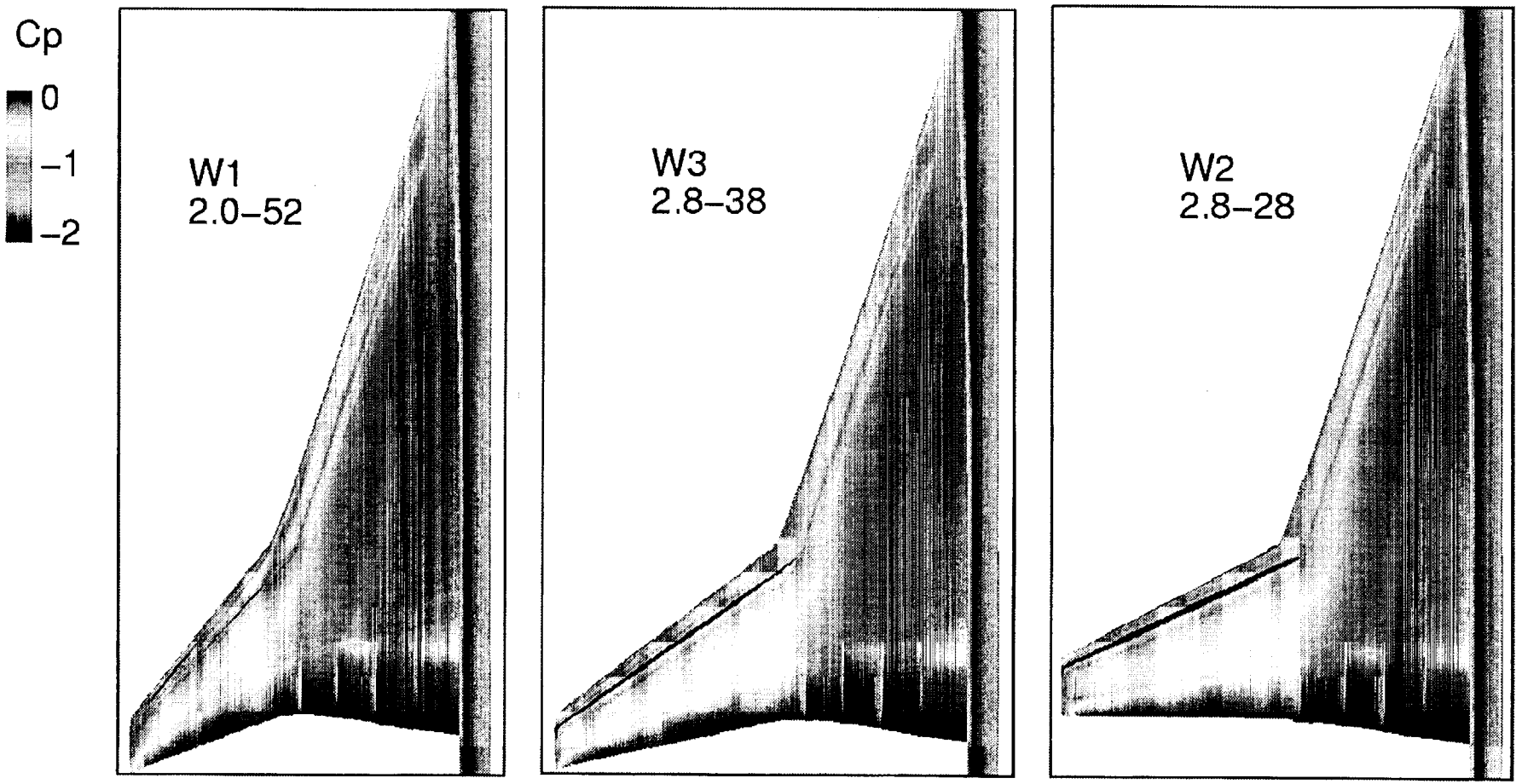

BOEING

"Oil" Flow Comparison for W3 30/10 at α=10

The upper surface oil flow comparison for the W3 30/10 configuration at alpha=10 degrees is illustrated in this figure. The overall flow pattern comparison between the predicted solution and the test results is similar in terms of the spanwise flow in the inboard region and an attached flow on the outboard wing panel and around the trailing edge flap hingeline. However, there appears to be an apex vortex that induces a spanwise flow which is not captured by the CFL3D code.

Grid sensitivity study has been conducted and the CFL3D solutions based on two different grids have shown very similar results (to be discussed later). Since the CFL3D solution is not grid sensitive, this discrepancy may be caused by the inadequacy of the Baldwin-Lomax turbulence model, and possibility the geometric differences between the CFD models and the wind-tunnel model.

"Oil" Flow Comparison for W3 30/10 at $\alpha=10^{\circ}$

HSCT Aerodynamics, Long Beach

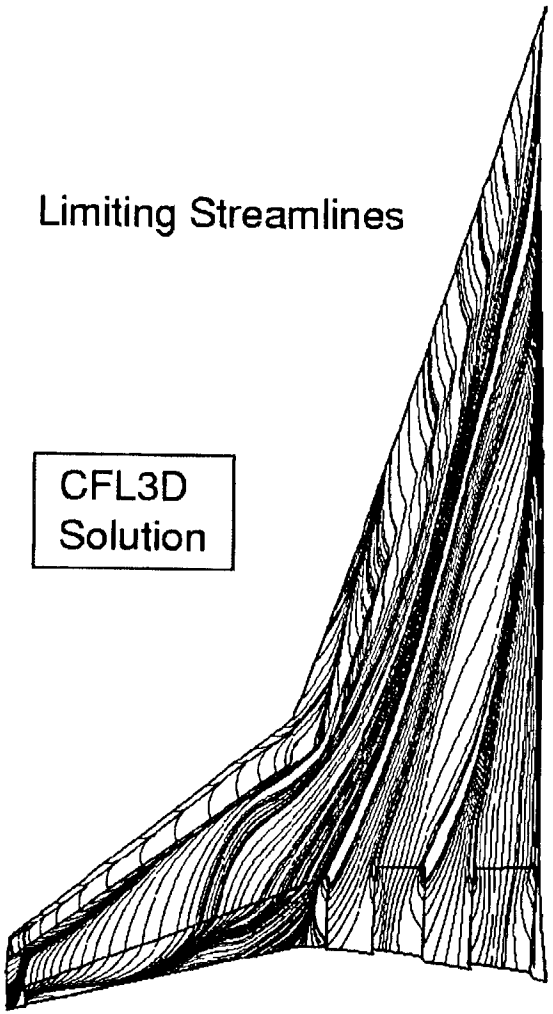

BOEING

Flow Pattern Comparison Near the Wing Break (W3 30/10)

A detailed "oil" flow comparison of the LE flap region at the wing break is illustrated in this figure along with predicted surface pressure. Similar flow patterns are observed between the test image and the numerical solution. The LE separation is observed to start from the upstream of the wing break. Flow reattachment is also seen on both the inboard and outboard LE flap surfaces. The outboard hingeline separation is also shown in the numerical solution. Unfortunately, the test image is not very clear in this region for verification.

Flow Pattern Comparison Near the Wing Break (W3 30/10)

HSCT Aerodynamics, Long Beach

Test 473
Run 298
α~10

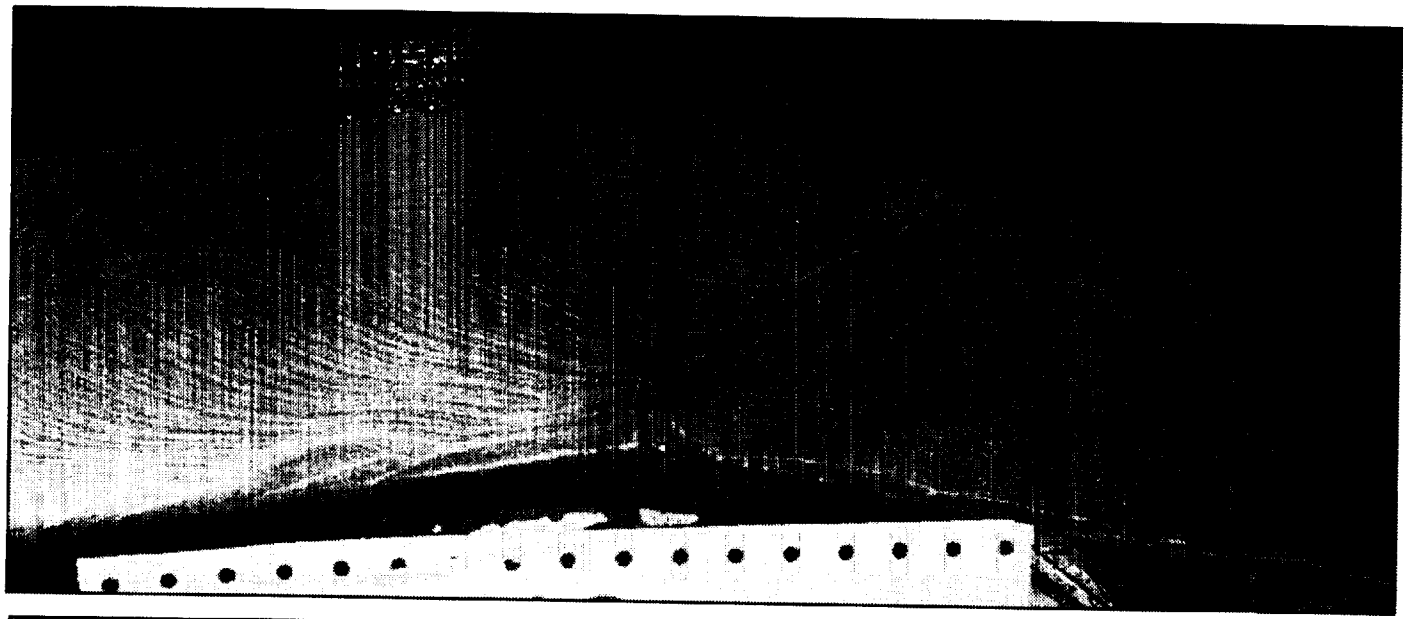

CFL3D
α=10

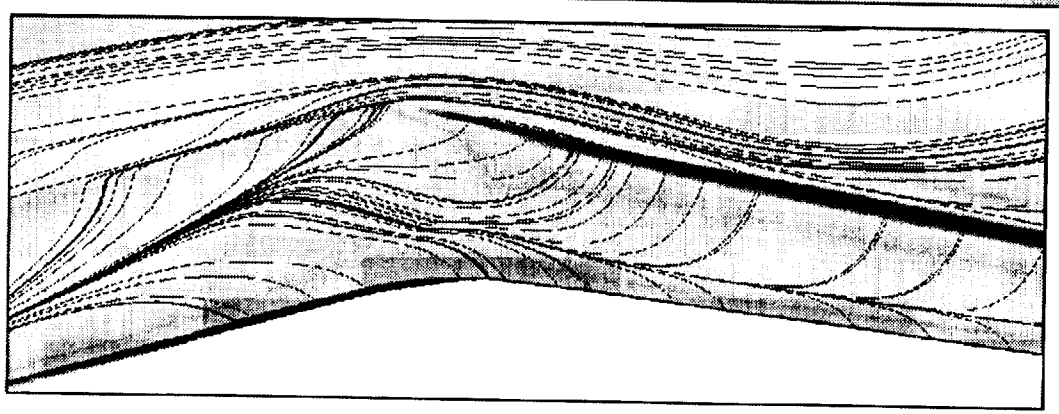

Limiting Streamlines
+
Computational Simulated Pressure(CSP)

BOEING

Flow Pattern Comparison at O/B LE Flaps (W3 30/10)

This figure shows the flow pattern in the outboard region for the W3 with 30/10 flap deflections. Similar flow patterns can be seen as the flow separates along the sharp LE and reattaches on the LE flaps. The flow accelerates around the LE hingeline resulting in a low pressure region and separates again due the pressure gradient. The flow then reattaches again on the main wing.

Flow Pattern Comparison at O/B LE Flaps (W3 30/10)

Test 473
Run 298
α~10

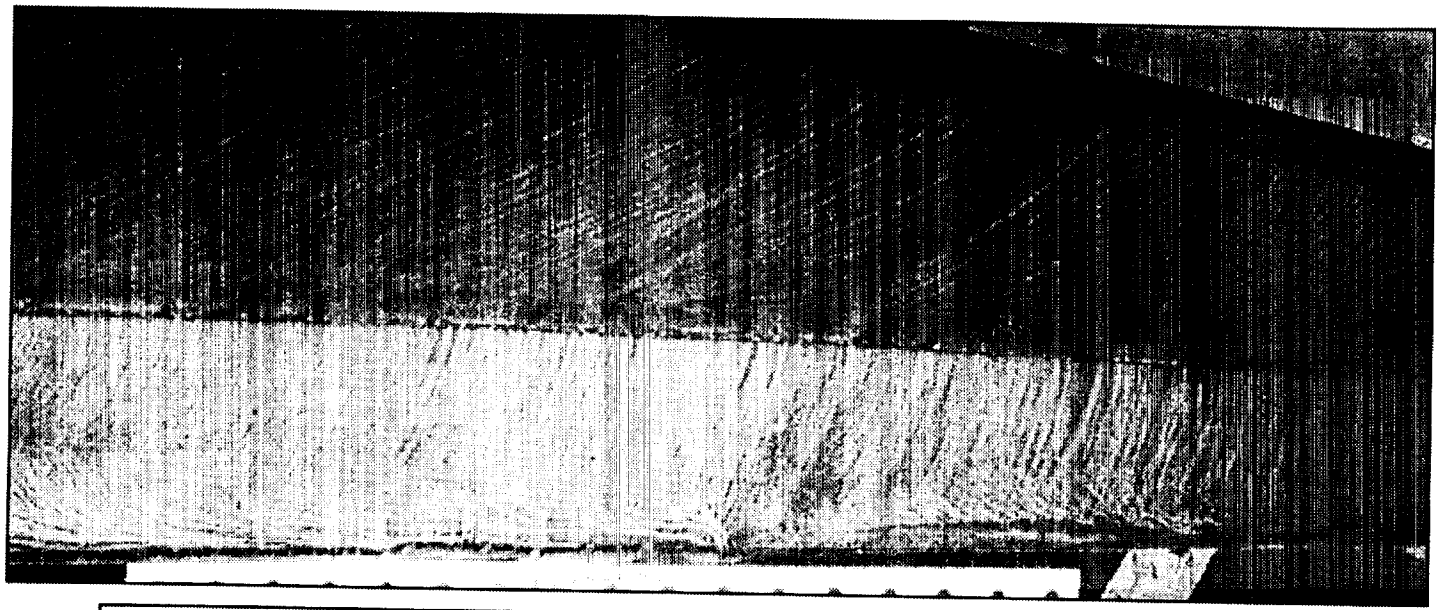

CFL3D
α=10

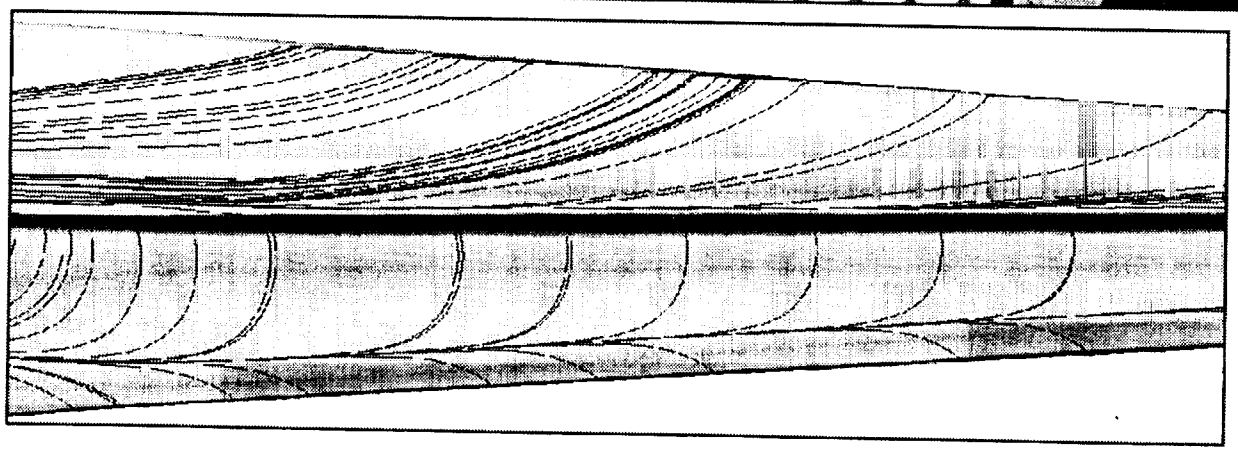

BOEING

Comparison of Computed and Measured Planform Effects

The lift and lift-to-drag ratio comparisons with test data for all 3 wings are illustrated in this figure.

The numerical capability to capture the effects of planform and leading edge sweep near the design condition (CL~.5) is illustrated in this figure. Favorable comparisons are observed between the numerical prediction and the test data for all 3 wings (W1, W2 and W3).

Comparison of Computed and Measured Planform Effects

Flaps (FS LE/TE)=30/10

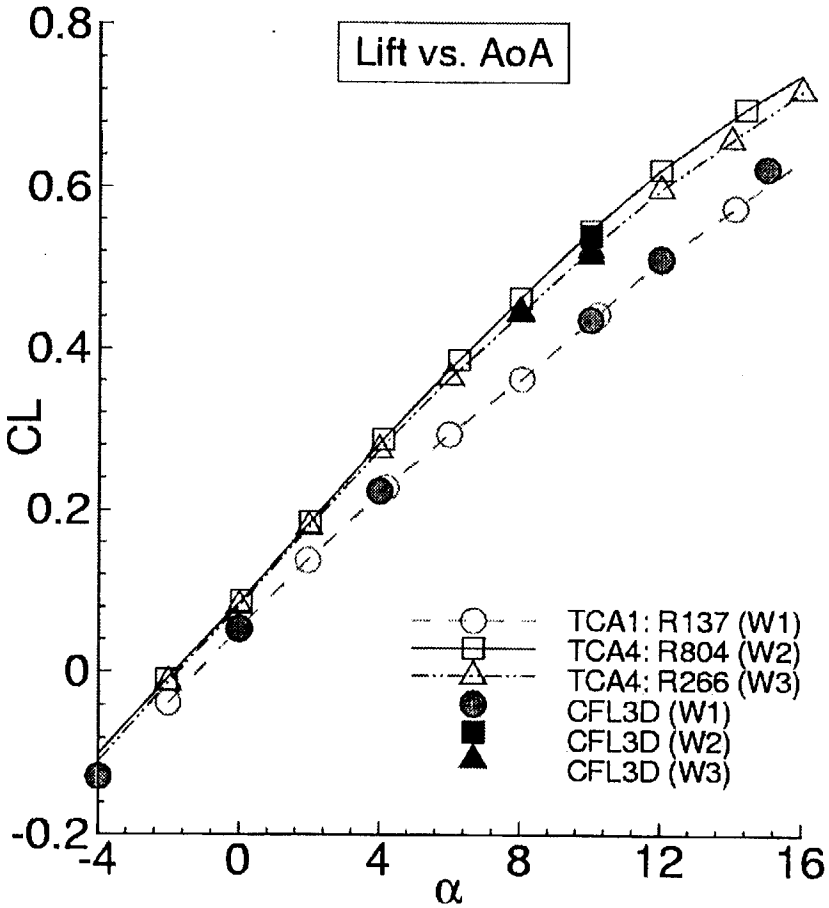

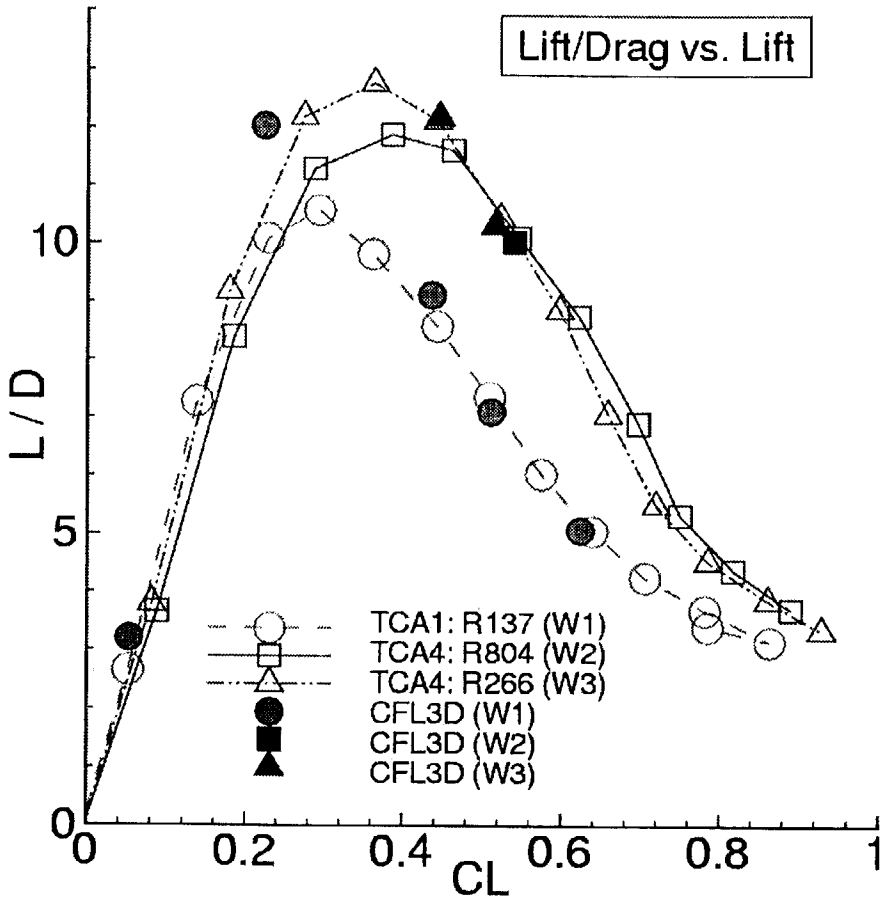

BOEING

Comparison of Computed and Measured Planform Effects

The drag polar and pitching moment comparisons with test data for all 3 wings are illustrated in this figure.

Favorable comparisons are observed between the numerical prediction and the test data for all 3 wings (W1, W2 and W3). It is noted that the drag is substantially higher for W1 as compared to W2 and W3 near the design point (CL~.5) due to the lower aspect ratio.

Comparison of Computed and Measured Planform Effects

HSCT Aerodynamics, Long Beach

Flaps (FS LE/TE)=30/10

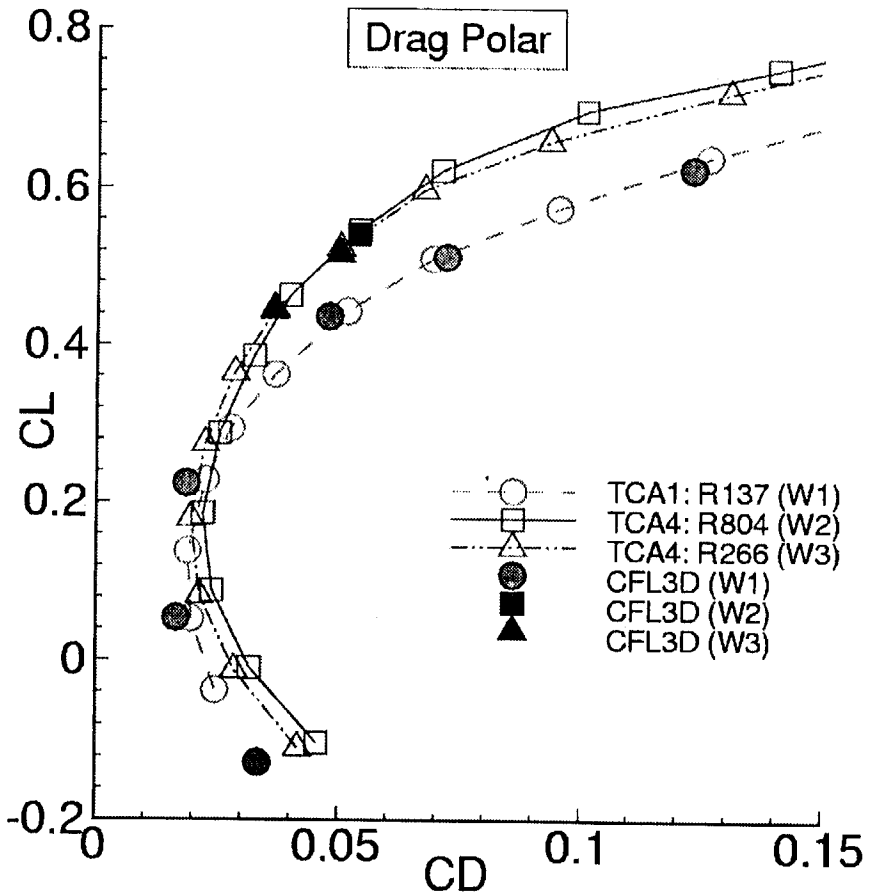

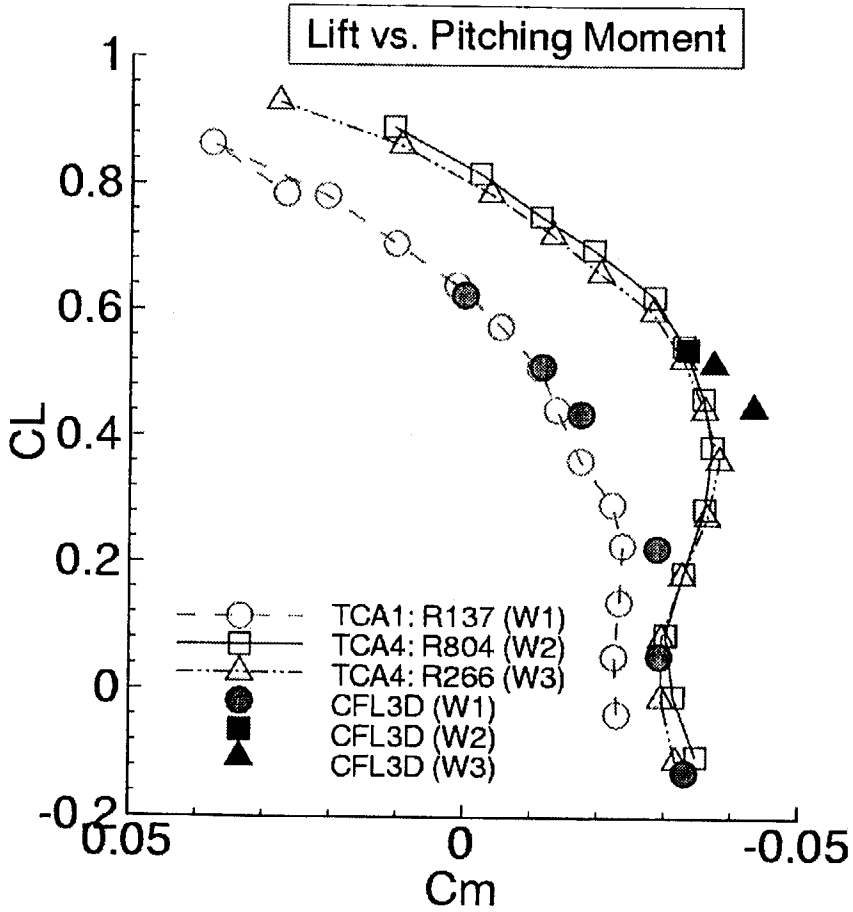

BOEING

CFD Analysis of Forebody Chine Effects

The effect of the forebody chine on the force and moment comparison has been evaluated since the chine is installed on most of the high-lift CFD configurations. The canard modeling procedure was used to model the forebody/chine while the flap procedure was utilized to model W/B with the LE and TE flap surfaces. The numerical solution was obtained using the CFL3D code through an overset-grid approach.

CFD Analysis of Forebody Chine Effects

HSCT Aerodynamics, Long Beach

- Assess the Effects on the Force & Moment Comparison
  - Use "Canard" Procedure + Flap Procedure
  - CFL3D Solution of Overset Grids

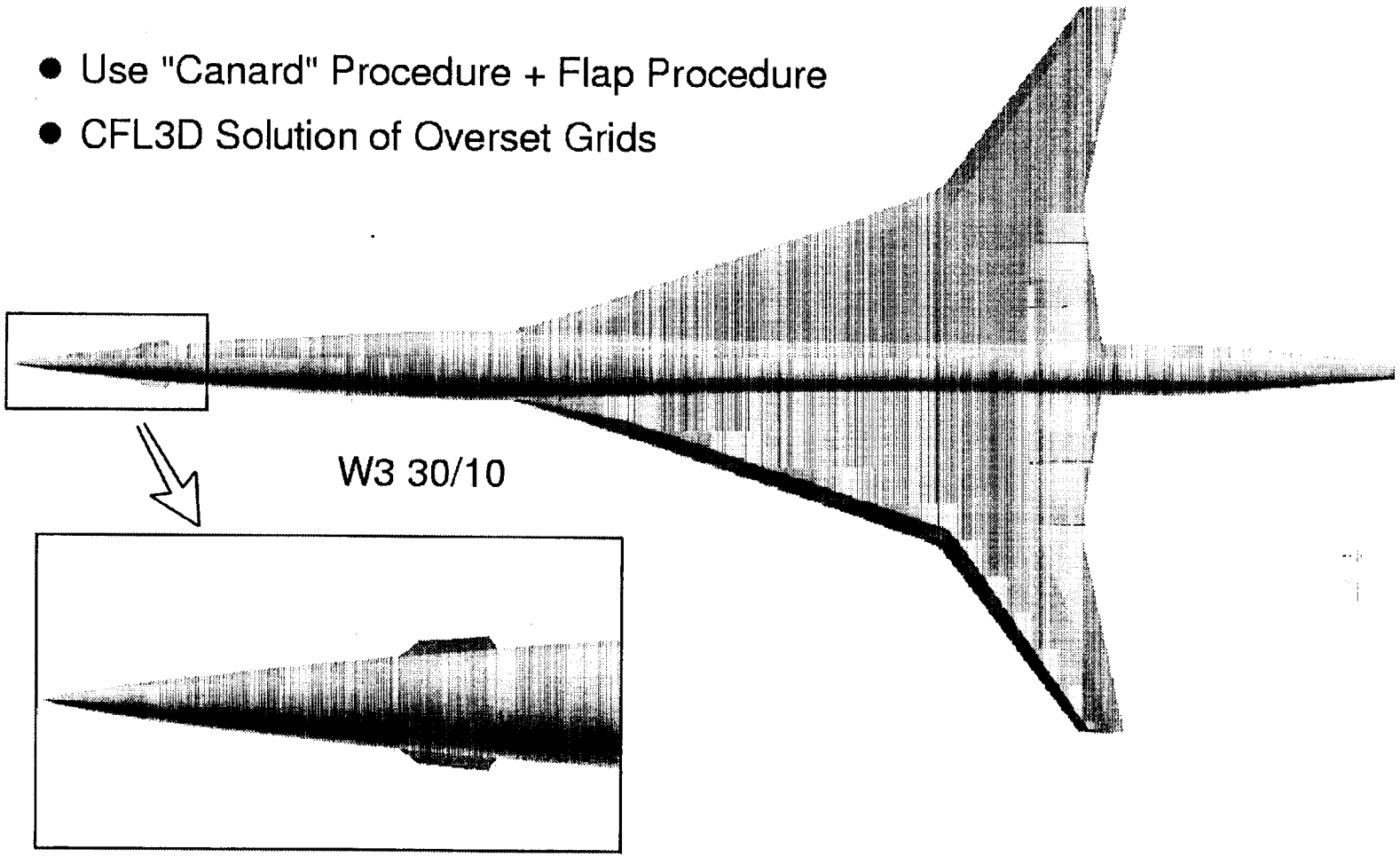

BOEING

Effect of Chines on W2 Forebody Vortex

The numerical prediction of the effects of forebody chines on the forebody flow field, forces and moment are illustrated in this figure. The half-body flow solutions were generated for W3 at alpha=10 degrees. For the case without the chines, the formation of the forebody vortex is seen close to the symmetry plan. For the case with the forebody chines, a vortex is shed from the chine surface which interacts with the upstream forebody vortex to form a well defined vortex. This vortex is further away from the symmetry plane as compared to the chine-off case. In terms of the force comparison, there is very little effect due to the chine. On the other hand, the forebody chines create a slightly higher nose-up pitching moment.

Effect of Chines on W2 Forebody Vortex

HSCT Aerodynamics, Long Beach

M=0.3, α=10°, Re=8 Million

Numerical results show:

CL, CD : about the same

Cm: Chines create a slightly higher noseup moment (~.001)

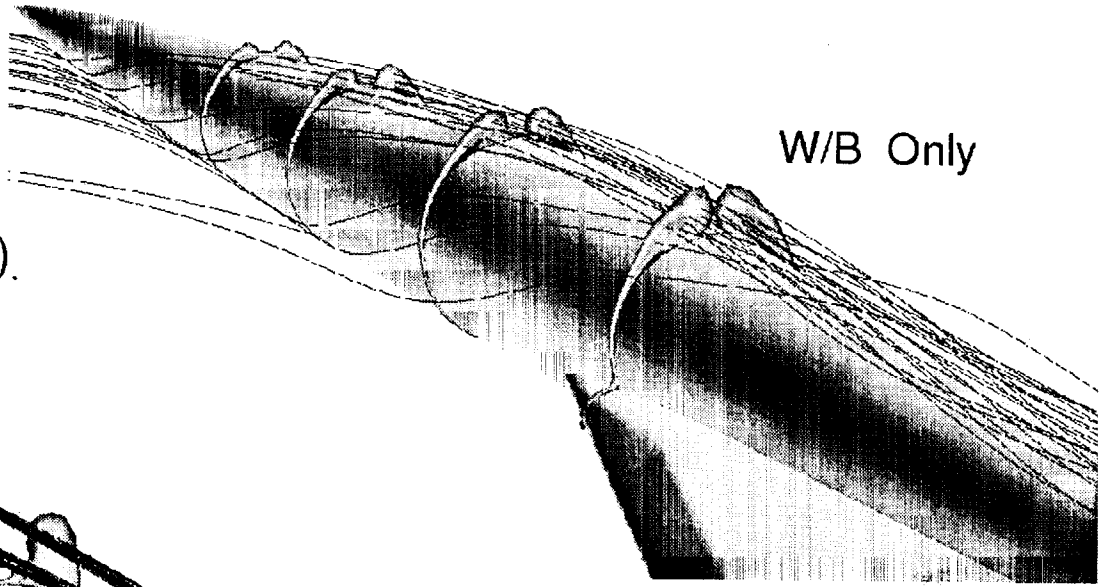

W/B Only

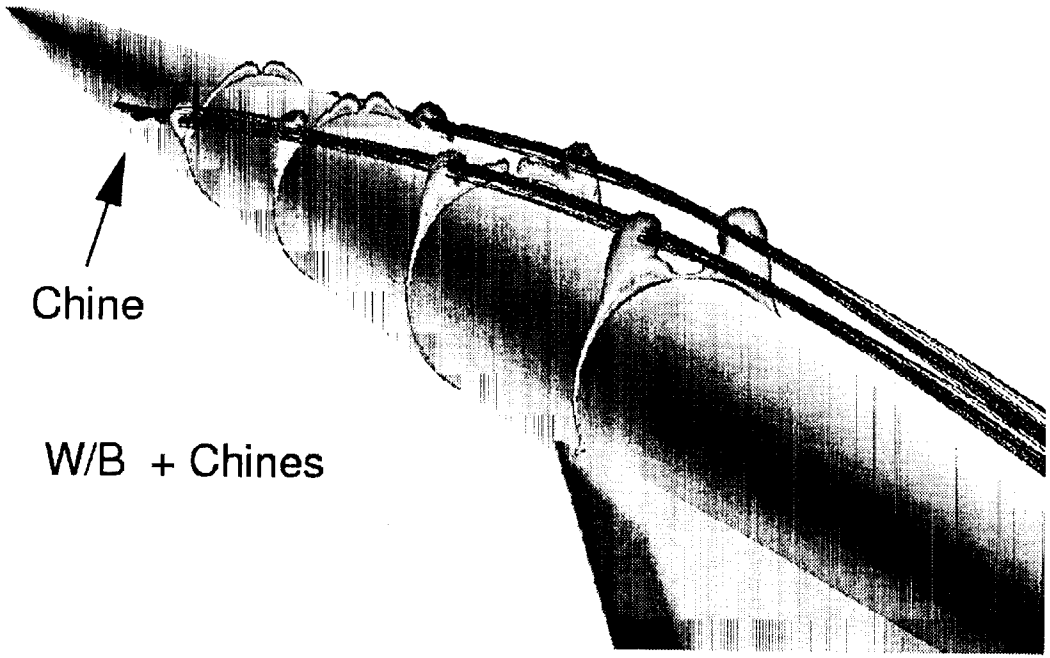

Chine

W/B + Chines

	CL	CD	Cm
w/o Chines	.516	.0500	–.0375
w/ Chines	.518	.0501	–.0365

BOEING

Forebody Flow Pattern Comparison for W3 30/10 at α=10

The forebody flow pattern in the presence of the chines is illustrated in this figure. A separation (converging) streamline pattern induced by the chine vortex is clearly captured in the figure and trails behind the chine surface. A similar flow pattern can be seen in the oil flow image from the TCA-4 test.

Forebody Flow Pattern Comparison for W3 30/10 at α=10

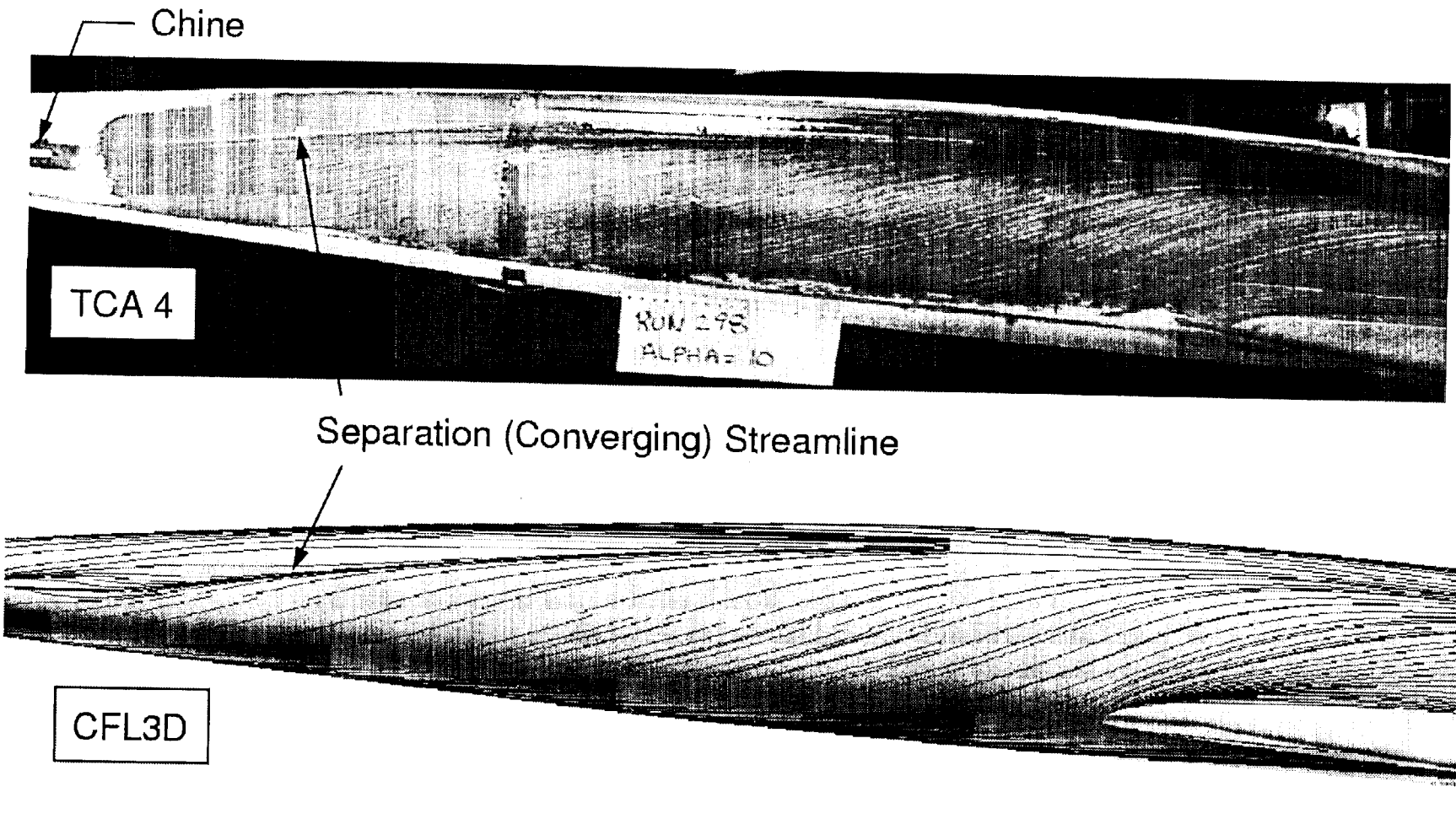

BOEING

Effect of Grids on W3 30/10 CFL3D Solutions

A grid sensitivity study with a different grid topology and surface distribution has been conducted using the CFL3D code. The study was conducted using the W3 30/10 configuration at alpha=10 degrees. One grid has a grid topology of H-H type that was generated at Seattle. The other grid is an C-O type of grid topology which was created using the Flap Deflection procedure at Long Beach. The predicted flow patterns for these two grids are shown to be very similar in terms of pressure contours, separation (converging) lines and reattachment (diverging) lines. The insensitivity of the flow solutions using different grids indicates the consistency of the numerical solutions as well as the similarity in quality of the computational models.

Effect of Grids on W3 30/10 CFL3D Solutions

HSCT Aerodynamics, Long Beach

M=0.3, α=10°, Re=8 million

H–H Grid

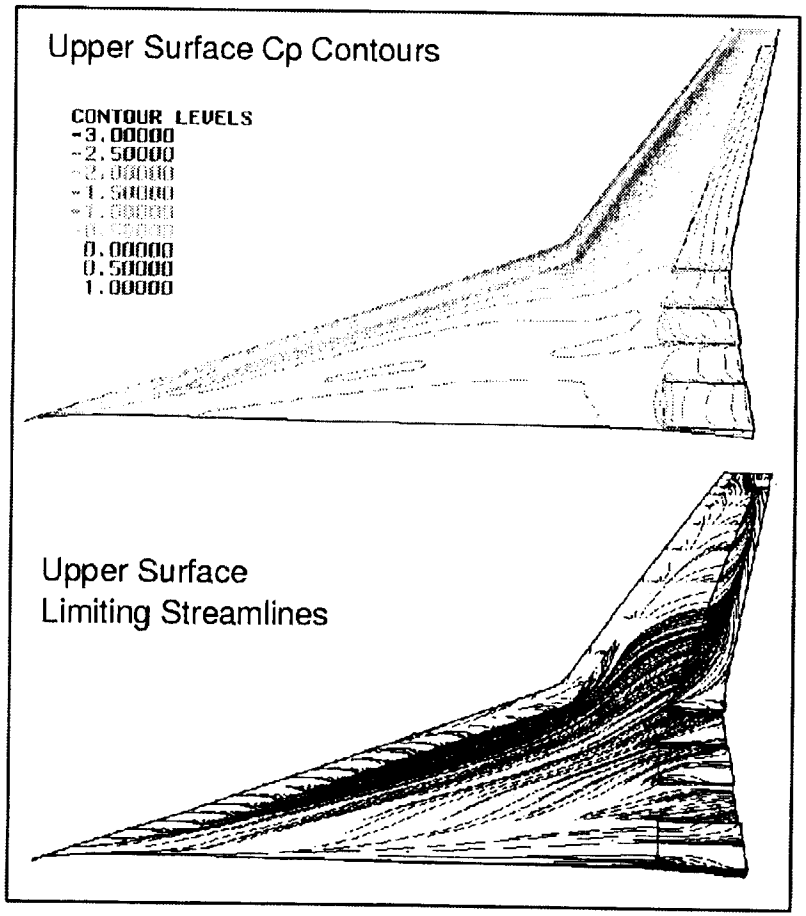

C–O Grid

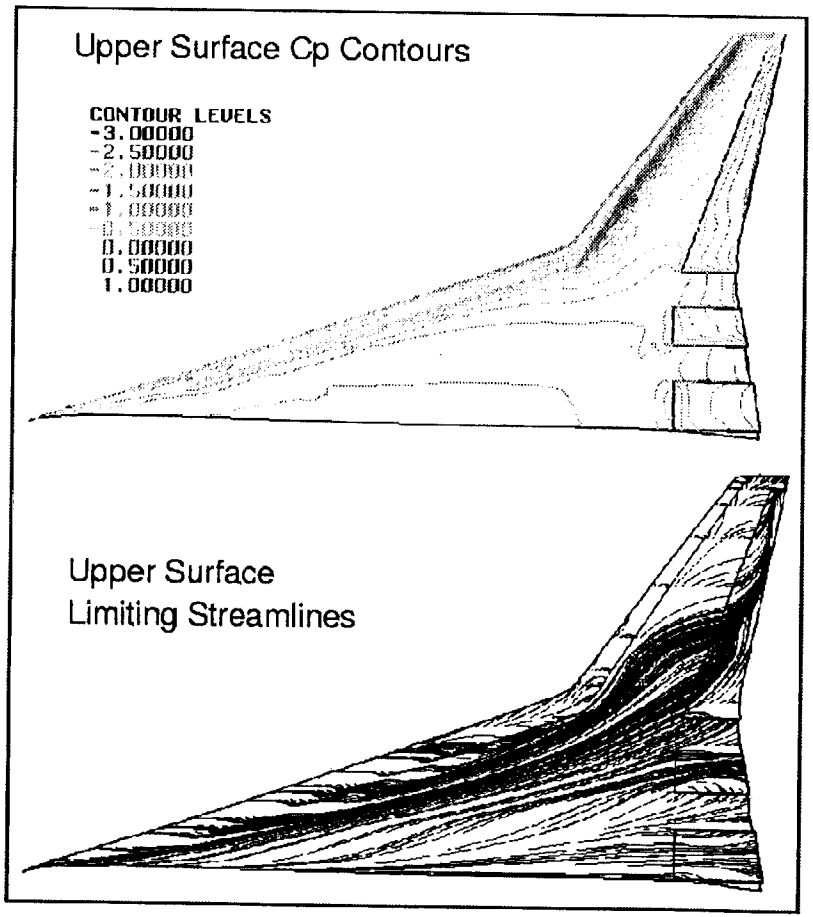

BOEING

Chordwise Pressure Comparison for W3 30/10 Configuration

A detailed pressure comparison of the the numerical solutions for the two different grids is illustrated in this figure along with the correlation with the wind-tunnel test data. The minor difference in the numerical solutions occurs primarily in the LE hingline region where the modeling techniques used to generate the deflected surface geometry may be different. Overall, the comparison of the numerical solutions and the test data is quite good.

Chordwise Pressure Comparison for W3 30/10 Configuration

HSCT Aerodynamics, Long Beach

M=0.3, AoA=10, Re=8 Million (MAC)

Solid	C-O Grid
Dashed	H-H Grid
Symbols	TCA-4, Run266

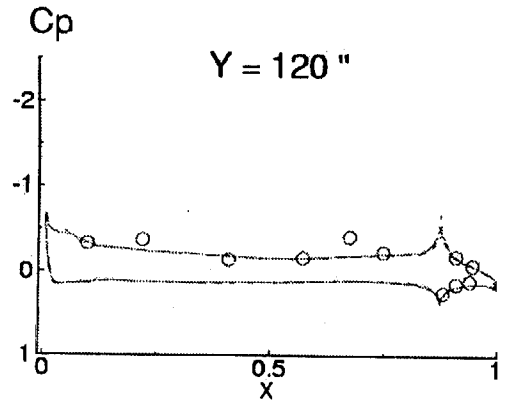

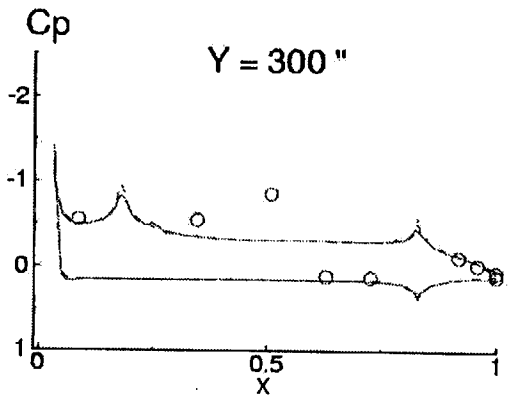

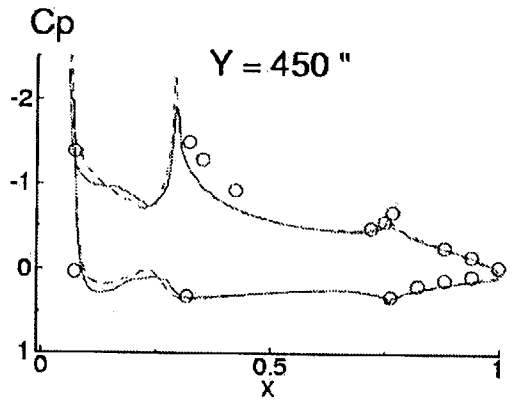

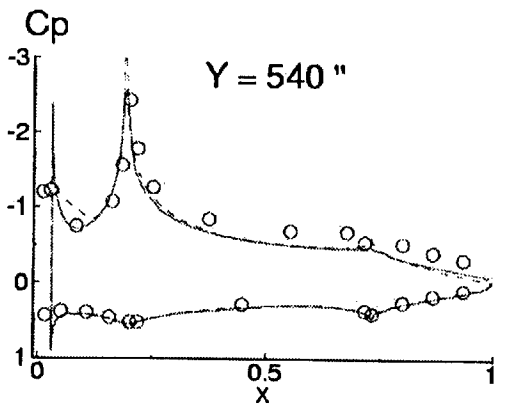

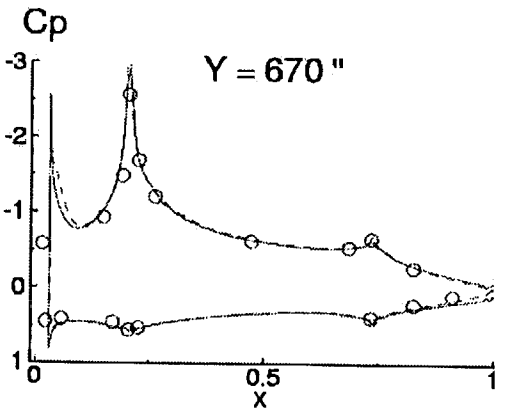

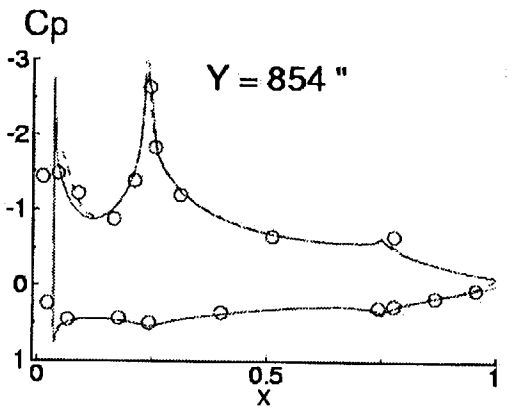

BOEING

TCA-4 Canard Study

Simulations of the TCA-4 canard configurations have been performed in parallel to the LaRC 14X22-foot test. The TCA-4 canard can be described as a mid-mount canard of PTC planform with an aft-elevator. The airfoil cross sections of the canard are made up of bi-convex surfaces with a sharp LE and TE.

The simulation objectives for the canard study will be focused on the canard flow characteristics at high lift conditions and its influence on the wing as a function of canard/elevator loading. Finally, the possibility of canard vortex ingestion by the inlets during ground roll will be investigated, and the use of a high-mount canard to alleviate this problem will be discussed.

TCA–4 Canard Study

HSCT Aerodynamics, Long Beach

Simulation Objectives:

- Canard Characteristics
- Influence on Various Planforms
- Effects of Canard Loading on the Wing
- Canard Vortex Ingestion by the Inlets

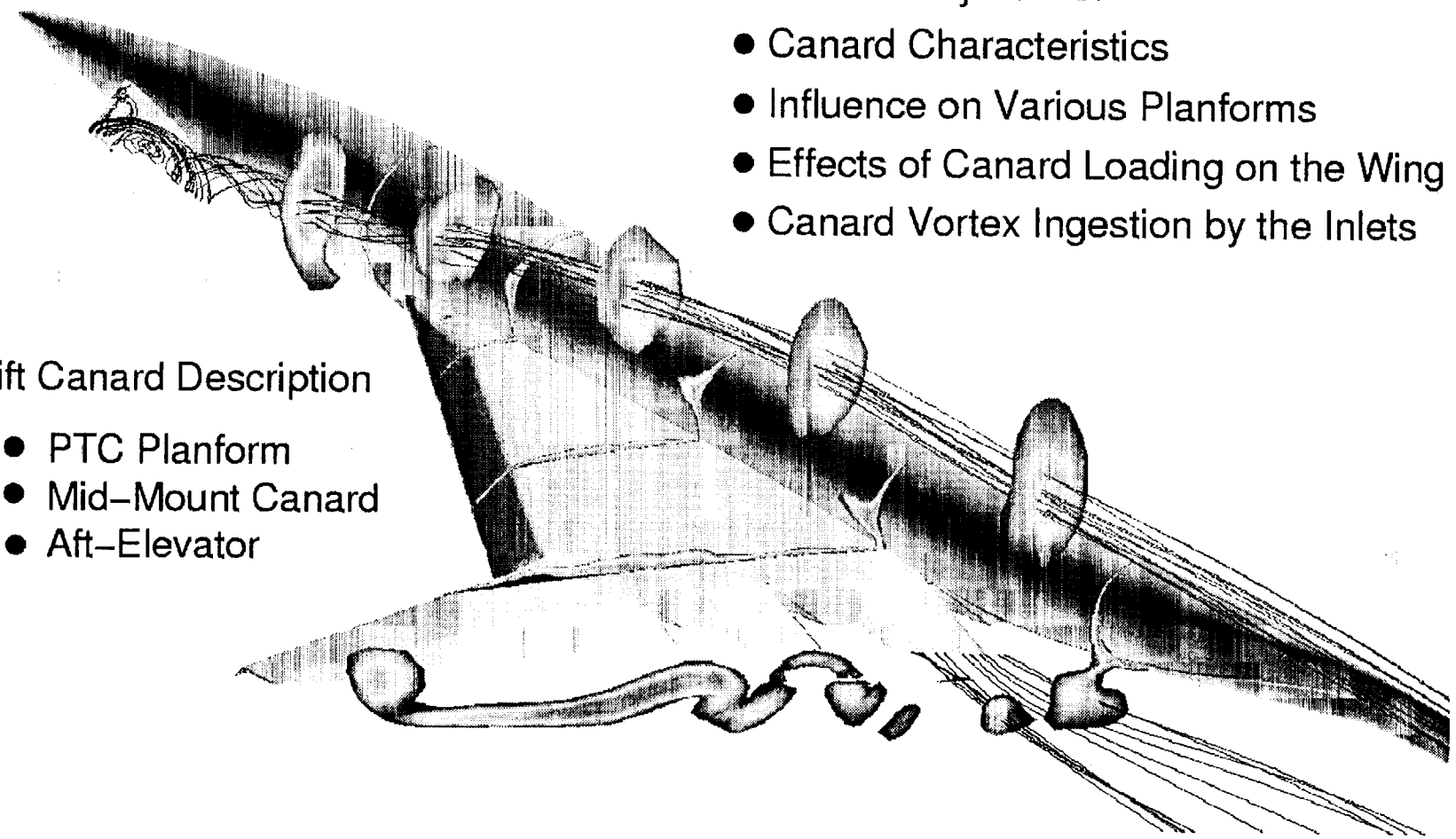

High–Lift Canard Description

- PTC Planform
- Mid–Mount Canard
- Aft–Elevator

BOEING

Automated Forebody Control Surface Modeling Capability

An automated canard modeling process has been developed to efficiently generate forebody/canard grids for CFD analysis. Canard configurations can be different in a variety of ways such as planform, position, deflection angles mounted on a forebody with or without a wiping surface. The use of the automated process will reduce the gridding time significantly for sensitivity studies of various canard configurations. This process has been further extended to model other types of forebody control surfaces applicable to forebody chines simulation and chin fin lateral control analysis.

Once the computational model of the forebody/canard is generated, the overset approach is utilized. The advantage of using the overset approach is that various canard configurations can be easily integrated into an existing CFD model or future models as the configuration evolves. This process has been successfully demonstrated for the ACC (Alternate Controls Concept) canard, PTC (Preliminary Technology Concept) canard with and without aft-elevator, and forebody chines. The process has also been used for modeling the chin fin to evaluate its lateral control effectiveness as well as other design alternatives. Details of the modeling procedure were presented in the 1998 HSR Annual Airframe Review.

Automated Forebody Control Surface Modeling Capability

HSCT Aerodynamics, Long Beach

Use Automated Process to:

- Modify mounting location & orientation
- Change angular deflection
- Model aft–elevator
- Create spanwise gap
- Generate volume grid
- Model various types of control surfaces

Use overset approach to integrate into existing CFD models

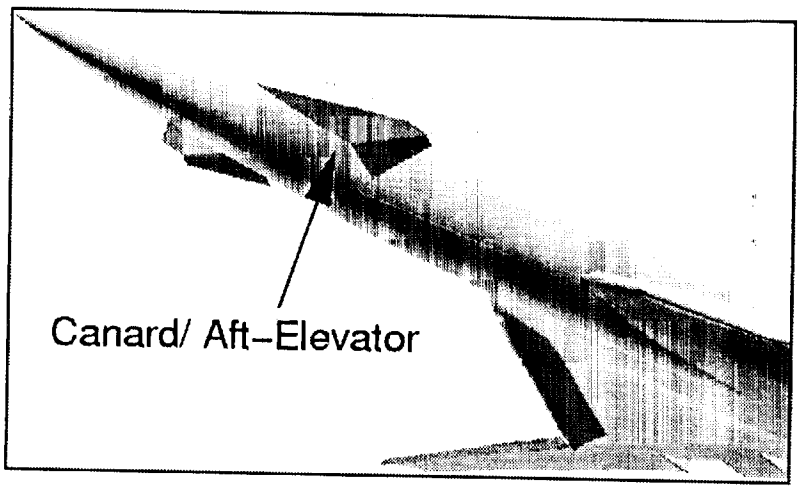

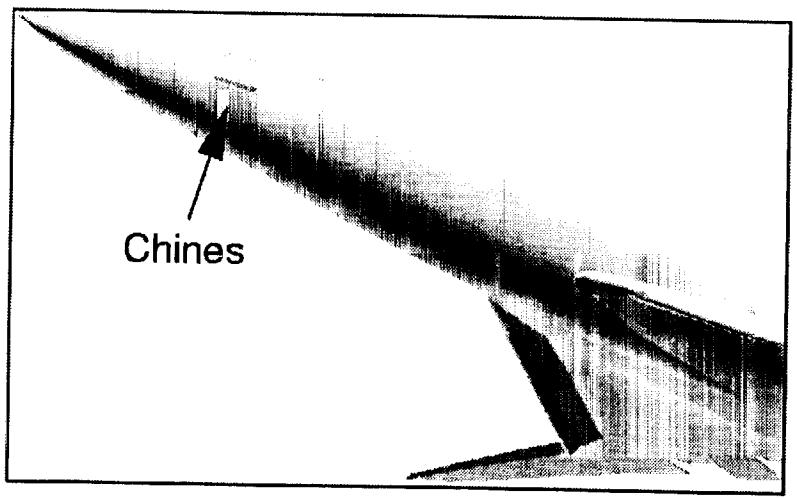

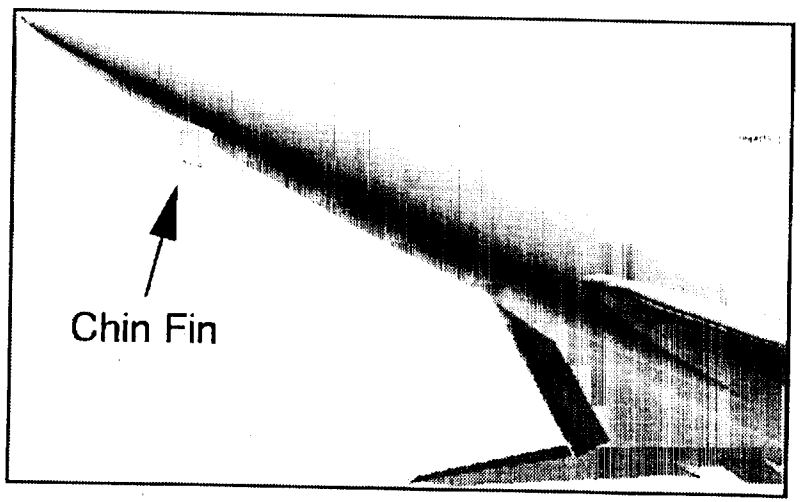

BOEING

PTC High-Lift Canard/Elevator Modeling

The presence of the spanwise gap between the deflected canard and the forebody without a wiping surface cannot be avoided. The gap modeling becomes important as the canard deflection increases in order to accurately predict the canard flow characteristics and its influence on the fuselage and the wing.

PTC High–Lift Canard/Elevator Modeling

- Gap Modeling becomes important as δ increases
  - Accurate modeling of the exposed area
  - 3D effect
  - Model the inboard vortex

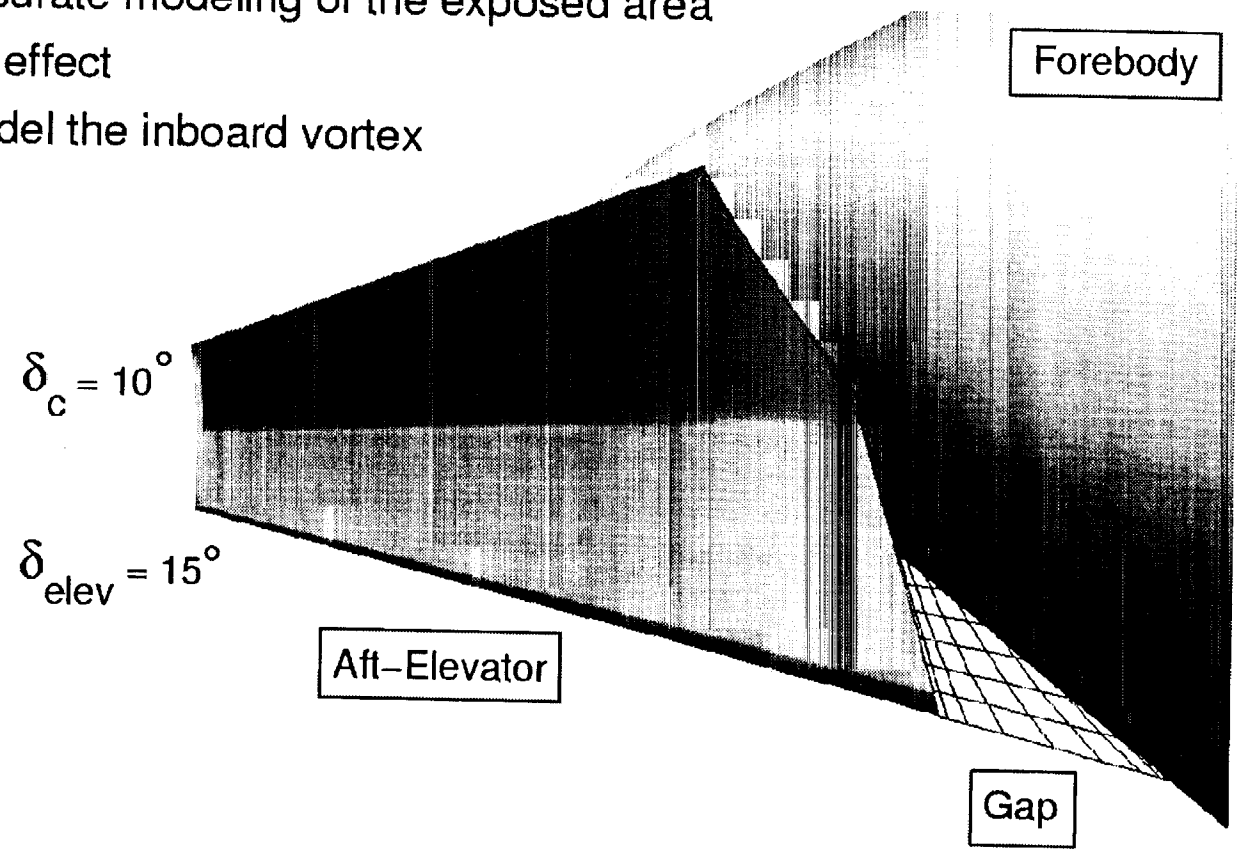

BOEING

Canard Upper Surface Flow Patterns at High-Lift Conditions

The figure shows the computed upper surface flow pattern at alpha=10 degrees with the canard/elevator deflection of -5/15 degrees. It clearly shows the familiar vortical flow pattern which indicates the canard is dominated by vortical flow. An attached flow is shown on the aft-elevator except in the tip region where there is a flow interaction between the leading-edge vortex and the tip vortex. A similar surface flow pattern is observed in the TCA-4 oil flow image shown here.

PTC Canard Flow Characteristics at High–Lift Condition

HSCT Aerodynamics, Long Beach

M=0.3, Re=8 million, α=10 deg, δ (CAN/ELEV)=–5/10 deg

TCA–4:
Run 940
Oil Flow

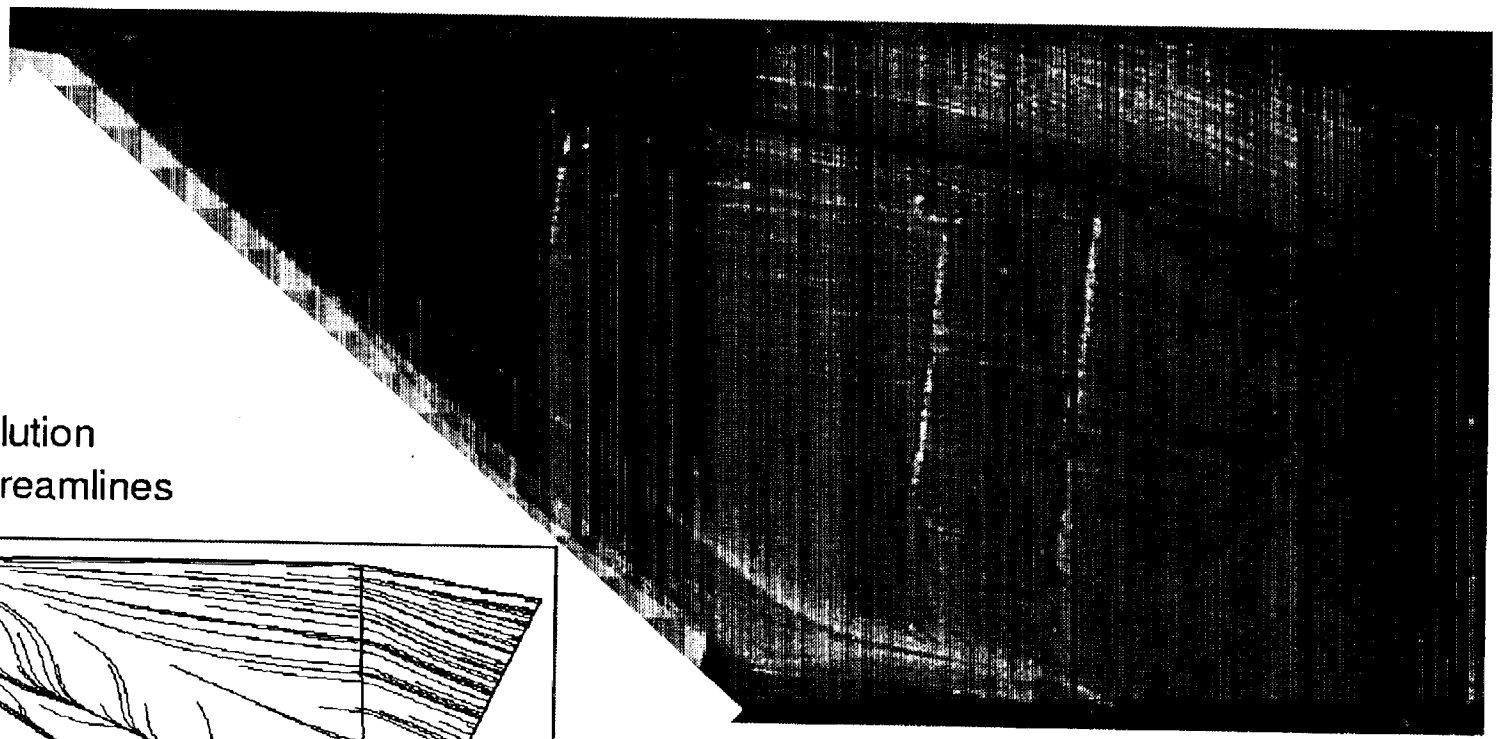

CFL3D Solution
Limiting Streamlines

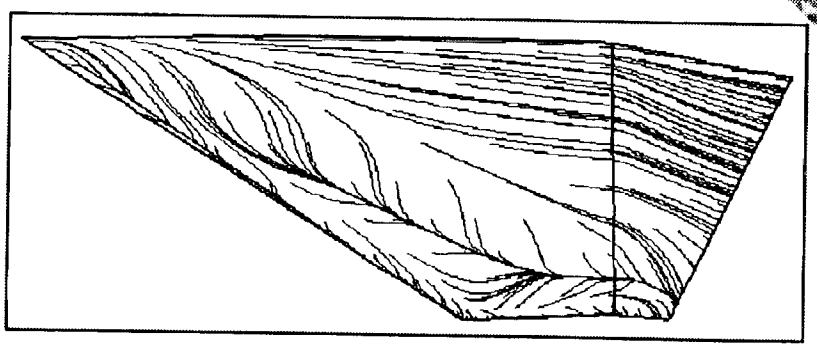

BOEING

Canard Flow Characteristics at High-Lift Conditions

This figure shows some canard upper surface flow patterns at high-lift conditions. It shows that the canard vortex induced suction increases as either the angle-of-attack or the canard deflection increases. It also illustrates that the elevator may be separated at off-design conditions as the canard/elevator incidence angle becomes large.

Canard Upper Surface Flow Patterns at High–Lift Conditions

HSCT Aerodynamics, Long Beach

Pressure Coefficient | Limiting Streamlines

$\alpha=10^{\circ}$
$\delta_{can/ele}=-5^{\circ}/15^{\circ}$

$\alpha=12^{\circ}$
$\delta_{can/ele}=-5^{\circ}/15^{\circ}$

$\alpha=10^{\circ}$
$\delta_{can/ele}=+5^{\circ}/30^{\circ}$

BOEING

Force and Moment Calculation Process for Overset Grids

The force and moment calculation process for the overset grids is different than that of a patched grid. In order to avoid double accounting of force and moment contribution in the overlap region, it is necessary to postprocess the solution. The FOMOCO utility codes developed at NASA Ames Research Center are capable of generating a "Zipper" grid between the computational surfaces with some user interaction. In order to automate this process with a minimal user interface, a patched surface grid concept has been developed. This process will generate the transition grid with patched boundaries between the surfaces on either side. The process is applicable to all cases for any canard/elevator setting.

Forces and Moment Calculation Process for Overset Grids

HSCT Aerodynamics, Long Beach

- Overset Surface Grids – Forces and moment counted twice

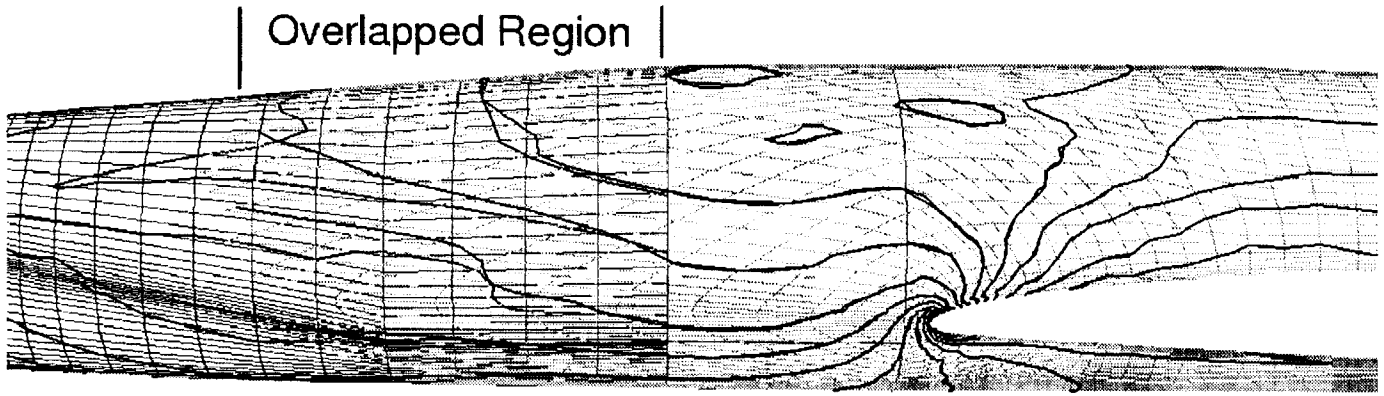

- Patched Surface Grids: Shared boundaries at both ends (No overlapping)

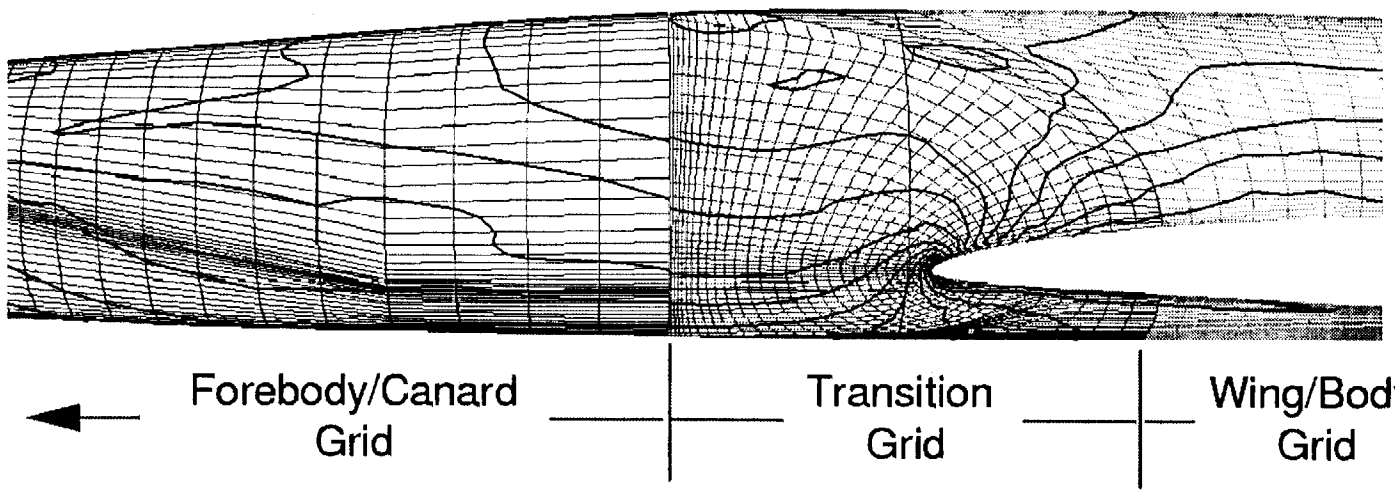

BOEING

Computed and Measured Canard Pitching Moment Effects

The effects of the canard on the pitching moment are illustrated in this figure for the W2 and W3 configurations with can/elev=-5/10 degrees. Both the absolute numbers and the relative trend for W2 compare well with test data. Due to the limited CFD runs in the TCA-4 test, the test data for the W3 W/B/C/N configuration (Run417) is used to assess the canard effect on pitching moment increment for W3. If the Nacelle effect (which creates a nose-down pitching moment of about .007 near CL~.5) is taken into account, the pitching moment increment comparison for W3 would also compare well with the test data.

The presence of the canard results an increment in nose-up pitching moment. Based on the CFD solutions, this increment is similar for all planforms at the same conditions indicating that the canard downwash does not greatly affect the outboard wing panel.

Computed and Measured Canard Pitching Moment Effects

HSCT Aerodynamics, Long Beach

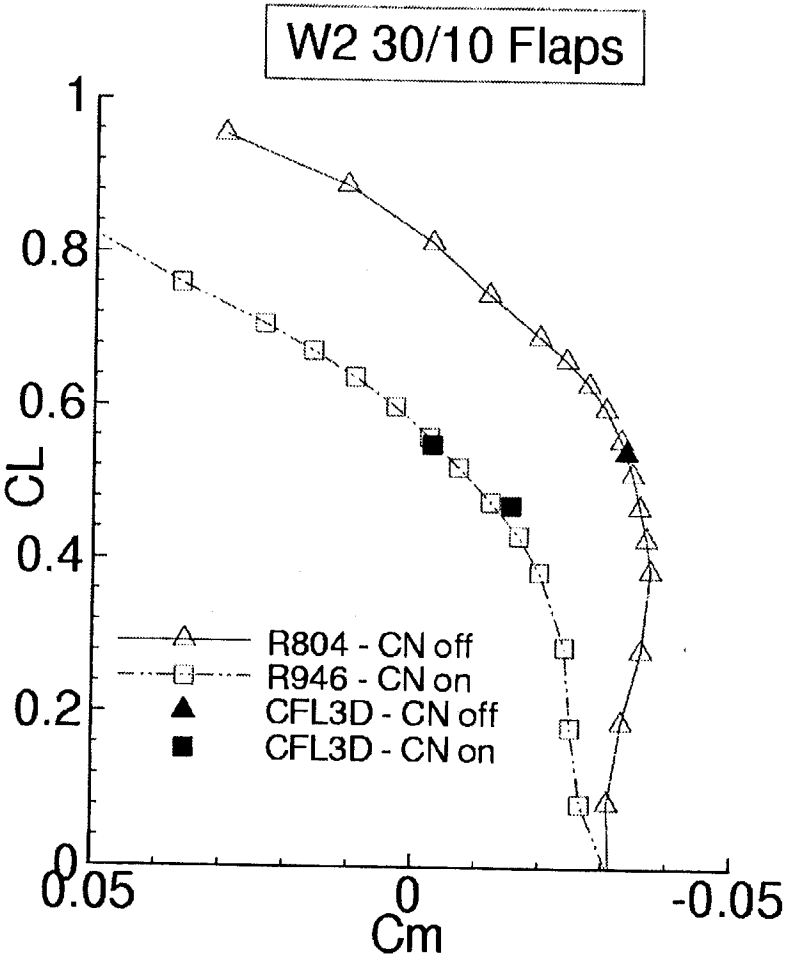

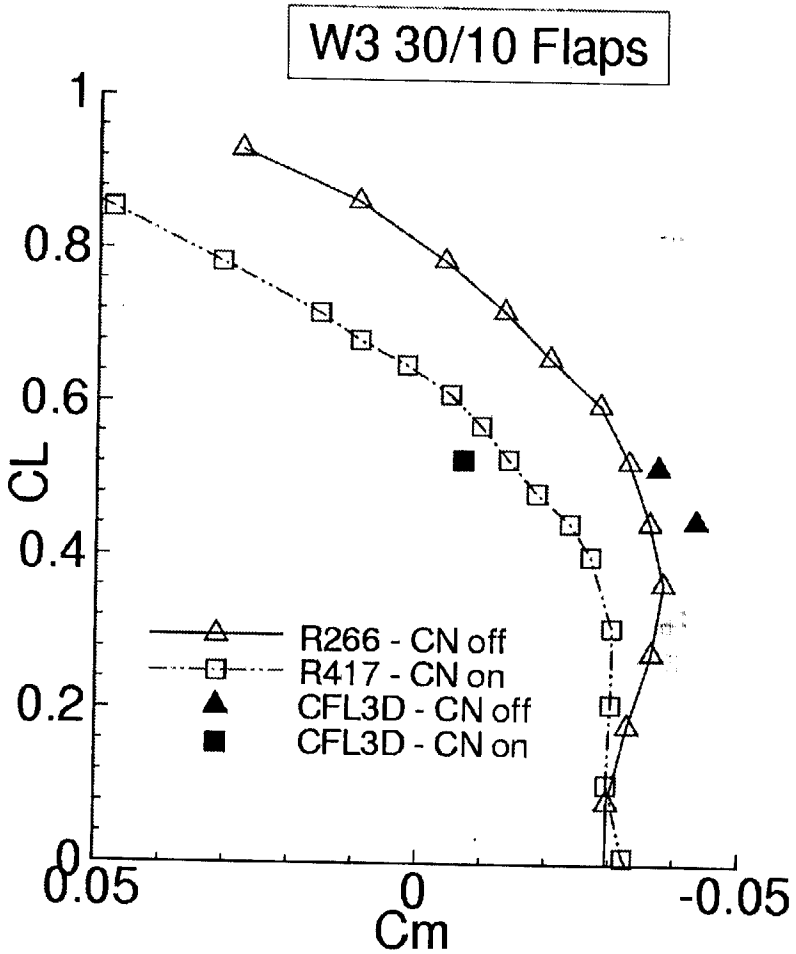

BOEING

Fuselage Flow Pattern for TCA W/B/C Configuration

The fuselage flow pattern for a TCA Wing-body-canard configuration is illustrated in this figure where a separation line (above the canard) is clearly visible due to the presence of the canard. A similar flow phenomenon is also illustrated from the oil flow pattern shown in the test image at the same flow condition.

Fuselage Flow Pattern for TCA W/B/C Configuration

HSCT Aerodynamics, Long Beach

TCA–4
Test

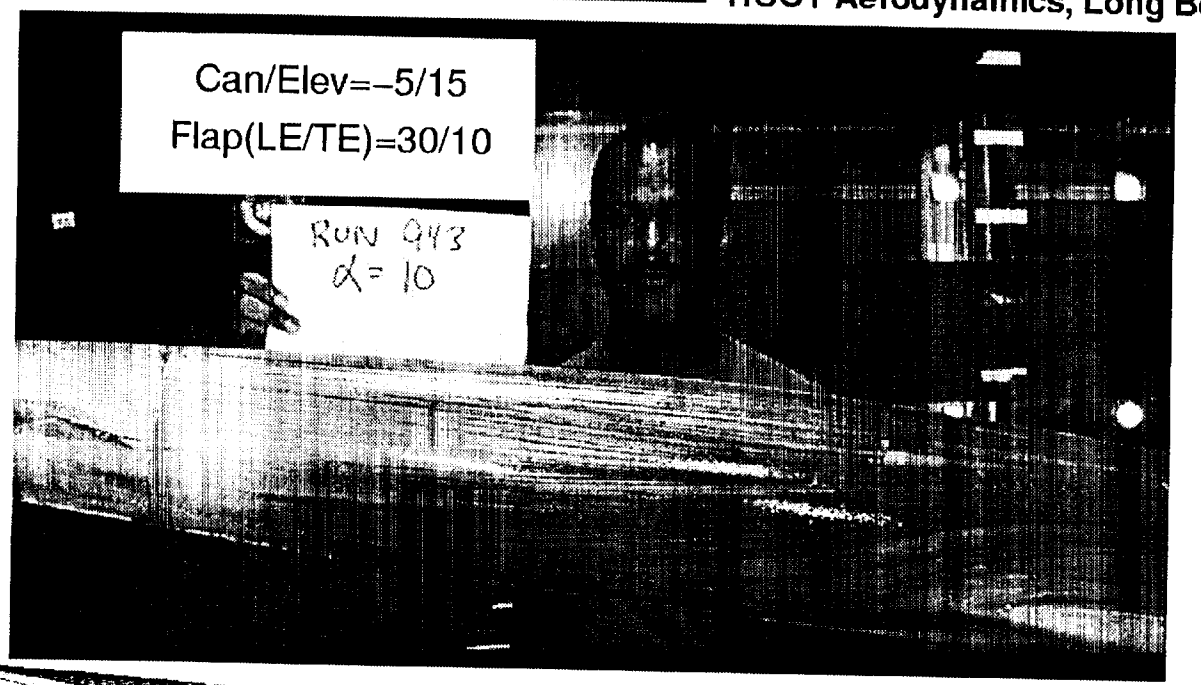

CFL3D
Prediction

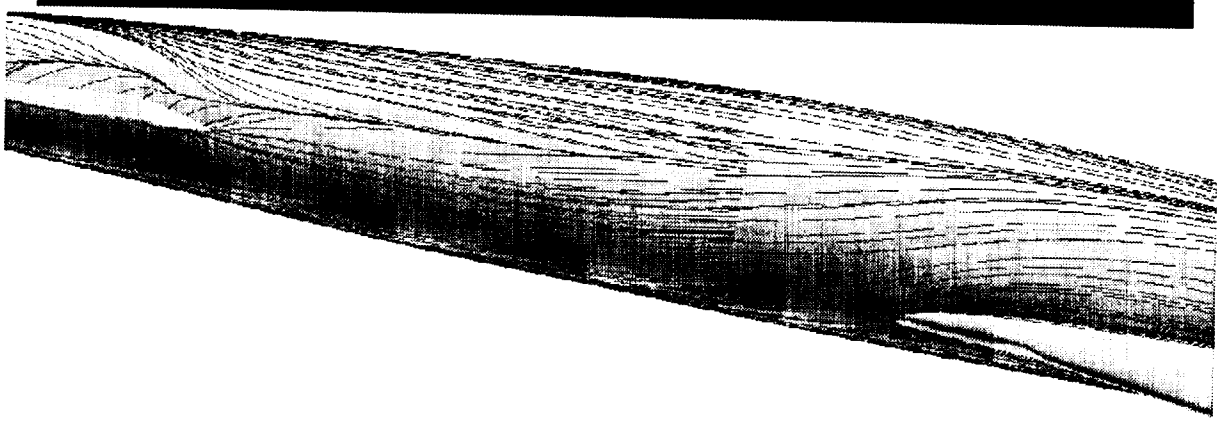

BOEING

Canard Influence on TCA Forebody Flow Patterns

The canard effect on the fuselage flow pattern is further illustrated by comparing the predicted flow patterns for the canard on and off cases. Without the canard, the formation of the forebody vortex is visible as indicated by the separation (converging) streamlines. For the case with the canard, the canard and its tip vortex is seen to induce downwash near the fuselage. The upwash created due to the angle-of-attack and the presence of the wing gradually turn the flow upward.

Canard Influence on TCA Forebody Flow Patterns

HSCT Aerodynamics, Long Beach

M=0.3, a=10, Can/Elev=–5/15, Flap(LE/TE)=30/10

W/B

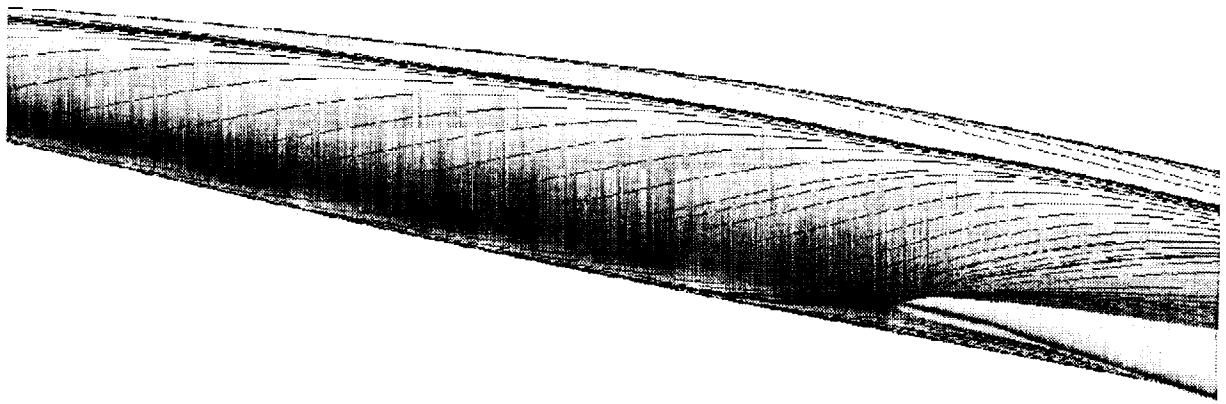

W/B/C

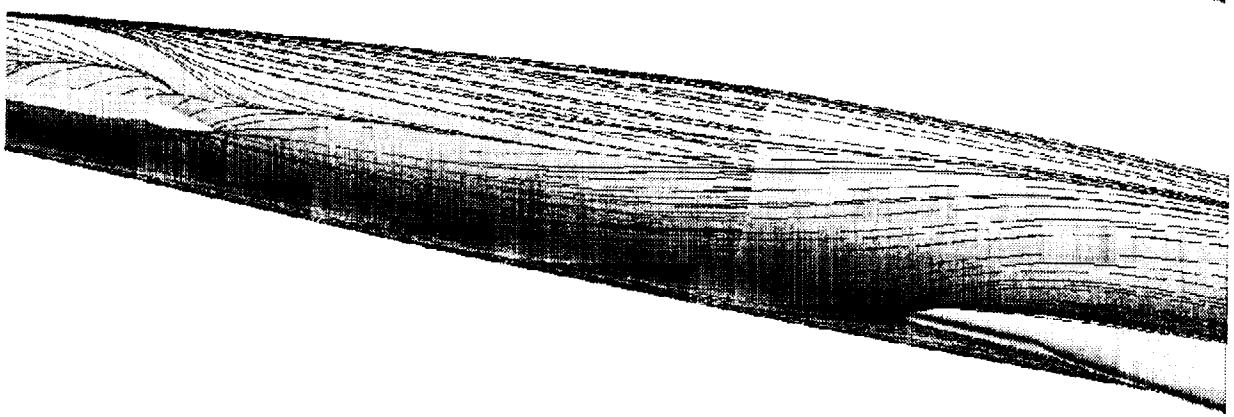

BOEING

Effect of Canard/Elevator Loadings on Wing Cp-Cp(no canard)

This figure shows the effect of canard loading on the wing pressure change. The contours are plotted for the difference of pressure coefficient between the configurations with and without canard. The contours with positive values denote higher pressures on the wing due to the canard effect. It can be seen that canard creates downwash in the inboard region resulting a lower suction (positive dcp) near the wing LE and the hingelines. In other words, the local angle-of-attack seen by the wing is reduced due to the canard downwash. It also shows that as the canard loading increases, the magnitude of the downwash also increases.

It is noted that the upwash generated by the canard tip vortex has very little influence on the wing as indicated by the absence of the negative Δcp's outboard of the canard tip.

Since the canard modifies the local flow in the inboard region, it directly affects the apex vortex characteristics altering the downstream flow field primarily in the inboard region.

Effect of Canard/Elevator Loadings on Wing Cp–Cp(no canards)

HSCT Aerodynamics, Long Beach

M=0.3, $\alpha=10^{\circ}$

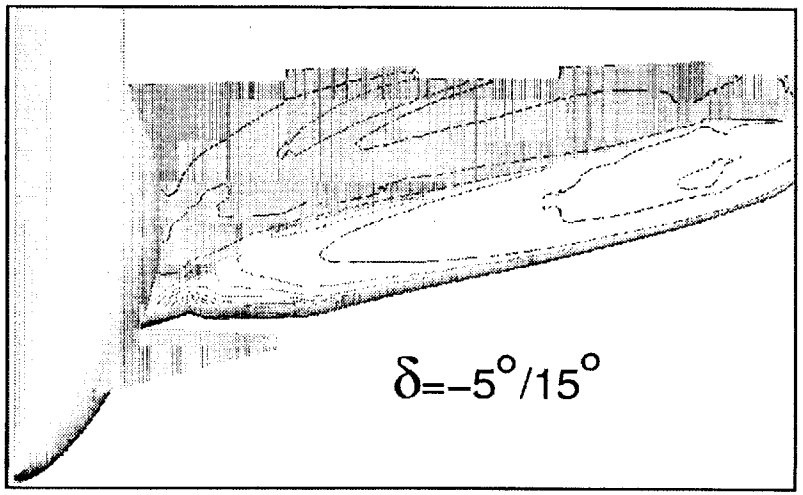

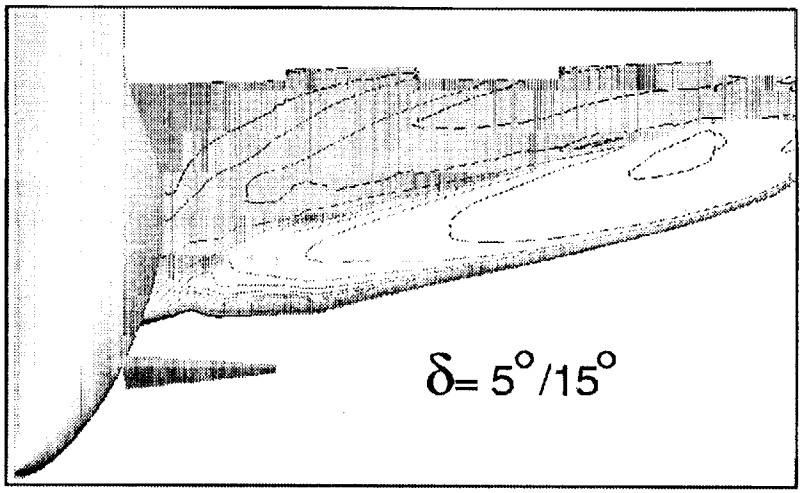

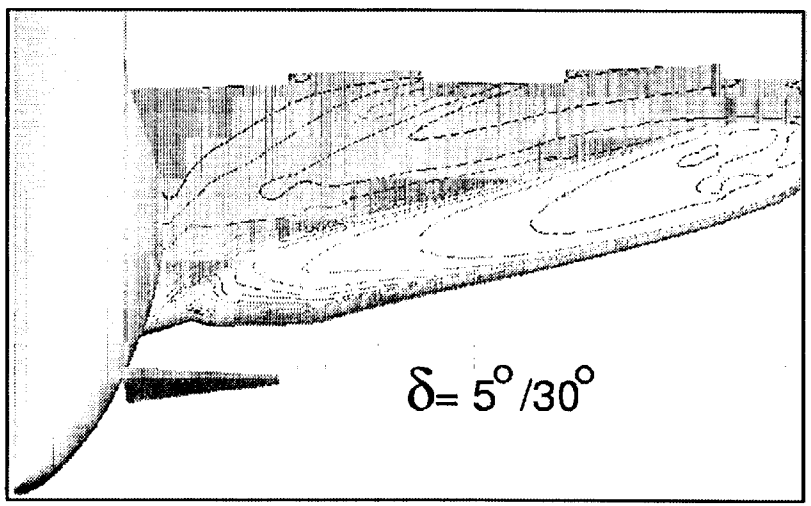

$\Delta Cp = Cp_{W/B/C} - Cp_{W/B}$

ΔCp > 0
Higher Pressure or
Lower Suction

BOEING

3-View Canard Vortex Traces for W1 30/10 Configuration

This figure shows the 3-view of the canard vortex traces for the TCA-4 canard and the low-mount ACC canard that was presented in the last year's HSR Workshop. It shows that the TCA-4 canard vortex is farther from the wing LE as compared to the ACC canard due to its size and location (disscussed in 1988). As a result, the influence of TCA-4 canard vortex should be less than the ACC canard vortex. Conversely, the wing influence on the TCA-4 canard vortex appears to be less as indicated by the reduced turning of the canard vortex above the wing.

It is interesting to note that the canard lift coefficients (based on the corresponding area) are about the same for these two canards, although the canard incidence (alpha+delta) are different. This implies that the use of aft-elevator increases the loading resulting in a lower canard incidence angle required to achieve the same lift. A better alignment with local flow at the same lift, usually results lower drag and better performance.

3–View Canard Vortex Traces for W1 30/10 Configuration

HSCT Aerodynamics, Long Beach

M=0.3, AoA=10 deg, Re=8 million

TCA–4 Canard

ACC Canard

- Front View

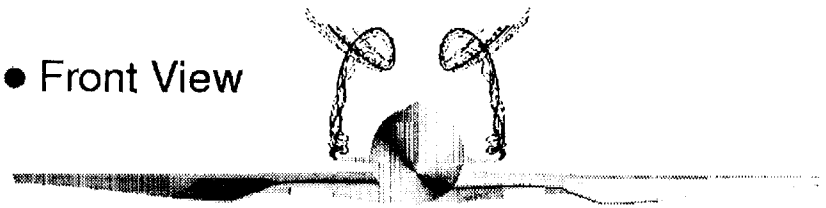

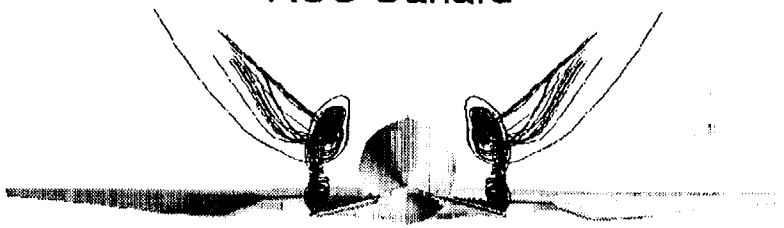

- Top View

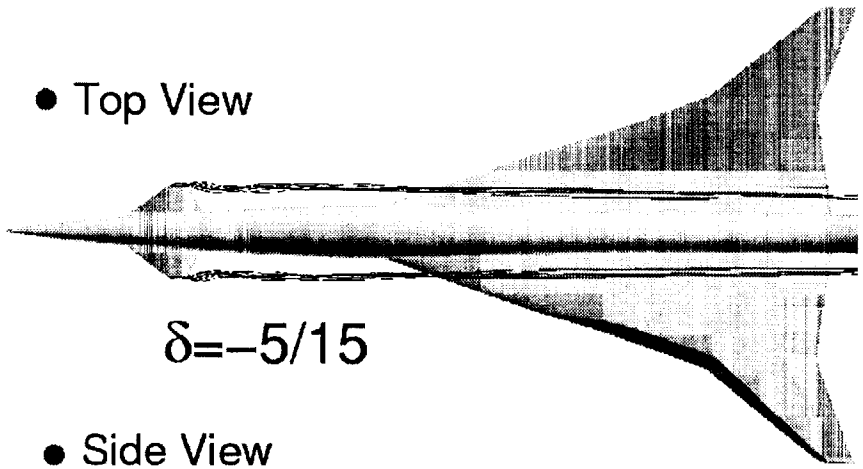

δ=–5/15

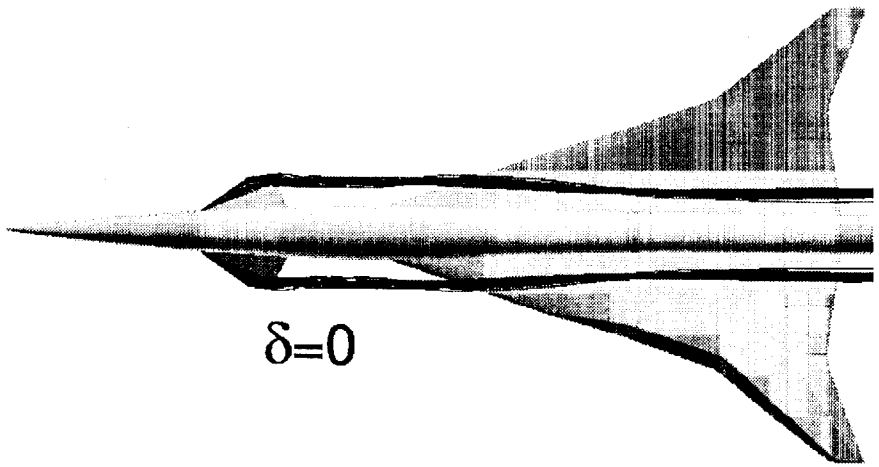

δ=0

- Side View

BOEING

Canard Vortex Path for W2 30/10 at AoA=0

The canard vortex entering the inlets during take-off may pose a potential problem to the flow quality near the inlet. A numerical simulation of TCA2.8-28 wing/body/canard high-lift configuration with flaps (LE/TE)=30/10, canard/elevator=10/15 degrees at alpha=0 degree (in free air) has been performed. The numerical solution shows the formation of the canard vortex off the canard tip. The vortex is shown to convect underneath of the wing. In order to clearly identify the vortex location relative to the inlet, the next chart shows the cross flow plane at a fuselage statation near the inlet face.

Canard Vortex Traces for W2 30/10 at α=0

HSCT Aerodynamics, Long Beach

M=0.3, Re=8 million, Flaps(LE/TE)=30/10, Can/Elev=10/15

PTC Canard
δ=10/15

- Investigate vortex entering the inlets

Full Span LE Flaps

Particle Traces and Total Pressure Loss

BOEING

Predicted Total Pressure Loss Near the Inlet Face

The total pressure loss near the inlet face station is plotted in this figure. It shows that the canard vortices are located near the inboard inlet while the inboard wing flap vortex is positioned close to the outboard inlet. A similar condition was tested in the TCA-4 test (can/elev=5/15) using a pink string, which has confirmed that the angle-of-attack at which the canard tip vortex passes from the lower surface to the upper surface is between 2 and 4 degrees alpha.

Total Pressure Loss Near the Inlet Face (X=2550)

HSCT Aerodynamics, Long Beach

TCA2.8–28 30/10 Configuration at $\alpha=0^{\circ}$,δ (can/elev) = $10^{\circ}/15^{\circ}$

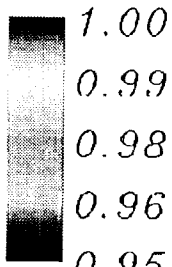

Free Stream : $P_T = 1$

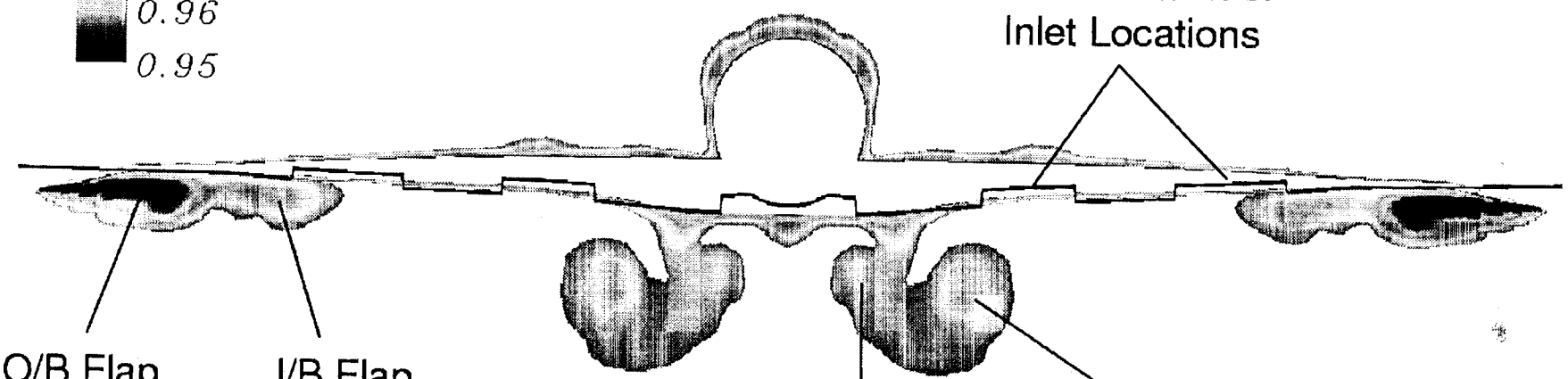

TE Lower Surface for Illustration of Inlet Locations

O/B Flap Vortex $P_T > 0.900$

I/B Flap Vortex $P_T > 0.970$

Canard I/B Gap Vortex $P_T > 0.985$

Canard LE and Tip Vortex $P_T > 0.980$

BOEING

Projected Canard Vortex Path at a High-Mount Location

In an effort to move the canard vortex above the wing at the same flow conditions, the canard is relocated 30 degree above the horizontal plane with 20 degrees dihedral angle. This figure shows the amount of geometric difference between the canard tips at the same canard/elevator deflection (10/15). It indicates that the canard displacement to the high-mount position should provide a sufficient clearance for the vortex to move over the wing at alpha of zero degree.

Projected Canard Vortex Path for A High–Mount Canard

HSCT Aerodynamics, Long Beach

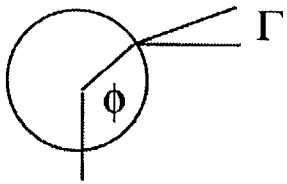

High mount (ϕ=120°, Γ=20°) , can/elev=10°/15°

Reference Lines at the Canard Tip

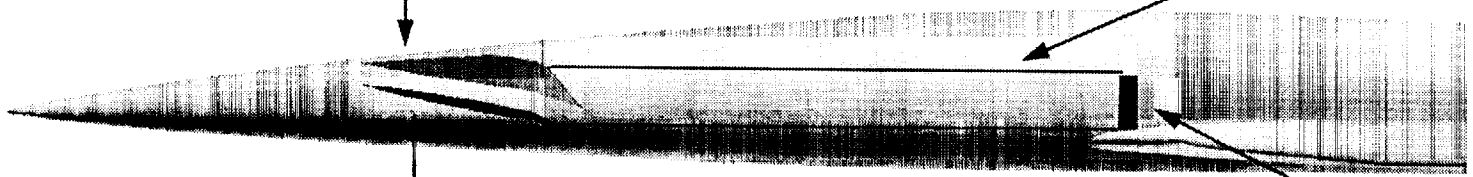

Baseline (ϕ=90°, Γ=0°), can/elev=10°/15°

Reference Length

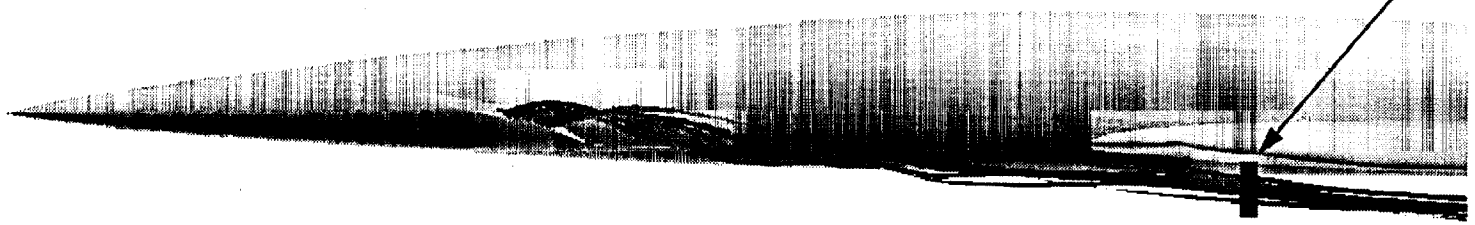

Baseline (Mid–mount) Solution at α=0°

BOEING

Summary (1/2)

In summary, the numerical modeling capability for the high-lift devices including multiple LE and TE flap surfaces and the forebody control surfaces has been demonstrated. The numerical results have shown the ability to capture the effects of planforms, inboard LE flaps and canard influence on the high-lift configurations. The pre-test analysis of ground roll inlet ingestion of the canard tip vortex was verified in the TCA-4 wind tunnel test. An alternative high-mount canard has been studied to move the canard vortex above the wing at alpha=0.

Additional study of the numerical issues is needed in the off-design conditions in order to accurately capture the viscous phenomena associated with flow separation, reattachment as well as vortex formation, convection and their interactions with the wing.

Summary (1/2)

- Demonstrated the capability to model high–lift configurations
  - * LE & TE flaps
  - * Canard/aft–elevator, chines
- CFL3D solutions, in general, have been shown to compare favorably with test data and associated flow physics
  - * LE spanwise extent
  - * Planform variation
  - * Canard Influence
- Study additional Numerical Issues at off–design Conditions
  - * Turbulence models
  - * Time steps
  - * Grid variation (has shown not sensitive)
    - – geometry fidelity, grid topology, orientation, distribution
- provideed input to alternative canard orientation to avoid possible ground roll inlet ingestion of the canard tip vortex

Summary (2/2)

The numerical results are summarized as follows:

Full span LE flaps have been shown to promote attached flow as compared to the part-span LE flaps resulting in a better lift-to-drag ratio and a more favorable pitch characteristics. In terms of the flow features for the different planforms, the numerical solutions have shown similar forebody and inboard wing flow patterns for the TCA-4 tested planforms. One of noticeable distinctions is the appearance of the outboard LE flap vortex on the baseline TCA near the design condition (CL=.5) while attached flow is observed in the outboard region for W2 and W3 wings. The forebody chine is predicted to have little influence on the lift and drag forces, but it creates a slightly higher nose-up pitching moment.

The effect of the TCA-4 canard is seen to create a downwash in the inboard region near the wing apex. The upwash influence associated with canard tip vortex appears to be insignificant. As a result, the influence of the planform change on the canard effect is expected to be small due to the local changes on the apex vortex that alters the downstream flow field primarily in the inboard region. The simulated canard tip vortex that enters the inlets at alpha=0 has been verified experimentally in the TCA-4 test. The TCA-5 high-mount canard tip vortex is predicted to pass above the wing at alpha=0.

Summary (2/2)

Numerical solutions have shown:

- Inboard LE Flaps promote attached flow for TCA planforms
- Planform Varition: Similar I/B flow patterns
  O/B LE flap vortex observed for W1
  O/B attached flow observed for W2 and W3
- Chine effect: Similar CL, CD, but creates higher nose–up moment
- TCA–4 Canard effect:
  * Creates downwash near I/B wing
  * Upwash influence appears to be insignificant
  * Effect on the planform change is expected to be small
  * Canard vortex entering inlets at α=0
- TCA–5 high–mount canard vortex at α=0 is predicted to pass above the wing

Future Plans for HSR High-Lift CFD Activities

The future plans for the high-lift CFD activities are summarized in this chart.

Additional pre-test analysis for TCA-5 will be conducted as necessary to assess the effects of high-mount canard and LE flaps on the high-lift performance. Code validation using different turbulence models will be performed to assess the numerical capability to simulate off-design conditions.

The numerical simulations of the TCA-3 conditions will be performed to provide a better understanding of the effects of Reynolds number and model deformation on the high-lift performance. The aeroelastic deformation data will be utilized to model the tunnel conditions at various dynamic pressures.

The flap optimization process has been successfully demonstrated in the transonic flight region within the Configuration Aerodynamics group with Euler simulations. This numerical capability will be utilized at high-lift conditions and demonstrated in a parallel computing environment.

Finally, pre-test analyses for the NTF 2.2% Ref-H configuration will be performed to support the CFD validation test at Ames 7-by-10 tunnel scheduled for June this year. The pre-test analysis results will be used for test planning as well as code validation as test data becomes available.

Future Plans for HSR High–Lift CFD Activities

HSCT Aerodynamics, Long Beach

- Perform pre–test analysis for TCA–5 wind tunnel test
  - * High–mount canard
  - * LE flap variation
- Code validation at off–design conditions
- Assess Re and aeroelastic effects
  - * Use model deformation data from TCA–3 test
  - * High Re simulation
- Initiate flap optimization demonstration at high–lift conditions
- Utilize parallel computing techniques – reduce wall clock time
- Support CFD validation test (Ames 7x10) – June 1999

BOEING

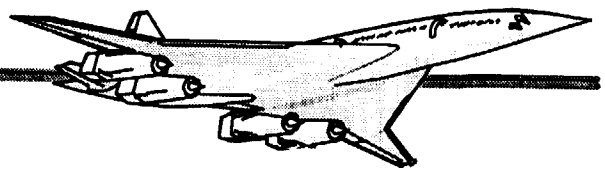

A Comparison of CFL3D and TLNS CFD Results on TCA and Ref-H High Lift Configurations

Tim Siebersma
Boeing Commercial Airplane Group

HSR Airframe Annual Review
February 10, 1999
Anaheim, California

Outline

This report begins with a list of the objectives for this study. Next, numerical results are presented for a TCA 2.8-38 high lift configuration. These include CFL3D results with two different grids, as well as comparisons between CFL3D, TLNS and wind tunnel data. Ref-H numerical results are then presented. These include both a flaps up CFL3D comparison with NTF wind tunnel data, and a leading edge flap span effect comparison between CFL3D, TLNS and 14x22 wind tunnel data. The report ends with a list of conclusions and recommendations.

Outline

- Study Objectives
- TCA 2.8-38 CFD Results
  - CFL3D Grid Sensitivity
  - CFL3D vs TLNS
- Ref-H CFD Results
  - Flaps Up
  - L.E. Flap Span Effect
- Conclusions & Recommendations

Study Objectives

HSCT High Lift Aerodynamics

One objective of this study was to apply the Boeing Phantom Works automated flap deflection gridding tools to several high lift configurations in order to increase their generality and robustness. These gridding tools can significantly reduce the cycle time required for Navier-Stokes analysis of HSCT high lift configurations. In this study, the gridding tools were applied to two different configurations; the TCA 2.8-38 and the Ref-H. These configurations have some differences in their high lift planforms that make for a good test of the gridding tools and an opportunity for enhancement.

Another objective of this study was to compare the numerical results of the two most popular Navier-Stokes codes available for the analysis of HSCT high lift configurations - CFL3D and TLNS. Along with the code-to-code comparison, comparison of numerical data with wind tunnel data was also an objective of this study. In the case of the TCA 2.8-38 configuration, wind tunnel data was available from the recent TCA-4 (NASA 473) test in the 14x22 wind tunnel at NASA Langley. For the Ref-H flaps up configuration, comparison data was available from several NTF wind tunnel tests. For the Ref-H leading edge flap span study, wind tunnel data was available from NASA429, also conducted in the 14x22 facility.

The final objective of this study was to use CFL3D to look at the leading edge flap span effect on the Ref-H configuration. Previous work looked at similar effects on the TCA configuration. The current Ref-H CFL3D results with full span and part span leading edge flaps are compared with both wind tunnel data and earlier TLNS results. A good comparison with test data on several configurations will give confidence in the code's ability to predict leading edge flap effects on future study configurations. In addition to the force and moment data, the numerical results can provide a physical understanding of the flow phenomena through visual presentation of flow field parameters.

Study Objectives

- Exercise CFL3D high lift gridding tools developed by Boeing Phantom Works
- Compare high lift N-S CFD results code-to-code (CFL3D and TLNS)
- Compare high lift CFD results with wind tunnel data
- Use CFL3D to look at the leading edge flap span effect on the Ref-H configuration

Study Objectives

CFL3D is a Reynolds-Averaged thin-layer Navier-Stokes flow solver for structured grids developed at NASA Langley Research Center. The spacial discretization involves a semi-discrete finite-volume approach. Upwind-biasing is used for the convective and pressure terms, while central differencing is used for the shear stress and heat transfer terms. In the current application, unless otherwise noted CFL3D is run with a C-O grid topology (C chordwise, O spanwise) and a Baldwin-Lomax turbulence model with the Degani-Schiff modification. The C-O grid consists of a single zone with approximately 3.4 million grid points.

TLNS solves the Reynolds averaged thin-layer N-S equations using a multi-stage local time-step iterative method. A central difference, finite volume discretization method with optional matrix dissipation is used to improve numerical accuracy. Mesh sequencing and multigrid are employed to accelerate convergence. Baldwin-Lomax, kw-sst, and Spalart-Allmaras turbulence models are available in the code. In the current application, TLNS is run with an H-H grid topology and a Spalart-Allmaras turbulence model. The H-H grid is divided into four blocks with a total of approximately 5.6 million points.

Study Objectives

N-S CFD Code Comparison

CFL3D

- Reynolds-Averaged thin-layer Navier Stokes flow solver for structured grids
- Semi-discrete finite volume approach for spacial discretization
- Upwind-biasing for convective and pressure terms / central differencing for shear stress and heat transfer terms
- For the current application, run with a Baldwin-Lomax turbulence model with the Degani-Schiff modification
- Unless noted, run with a C-O grid topology: single-zone with approx. 3.4 million grid points

TLNS (TLNS3DMB)

- Reynolds-Averaged thin-layer Navier Stokes flow solver for structured grids
- Finite volume discretization method
- Central differencing
- For the current application, run with a Spalart-Allmaras turbulence model
- For the current application, run with an H-H grid topology: four blocks with approx. 5.6 million grid points total

TCA 2.8-38 CFD Results

This figure the shows the TCA 2.8-38 wing planform. This configuration has a wing aspect ratio of 2.8 and an outboard wing sweep of 38 degrees. The CFD analysis of this configuration was made on the wing/body only, with no nacelles and no tail. The study was done with full span leading edge flaps deflected to 30 degrees and the trailing edge flaps deflected to 10 degrees. CFL3D was run at 10 degrees angle of attack, which is near the operating condition for this configuration, and at a Mach number of 0.3. Reynolds number was set to 8 million based on MAC, in order to match the available wind tunnel data. TLNS had previously been run on this configuration at several angles of attack from 4 to 22 degrees with a Mach number of 0.247. The effect of the Mach number difference between the two solutions is assumed to be negligible.

TCA 2.8-38 CFD Results

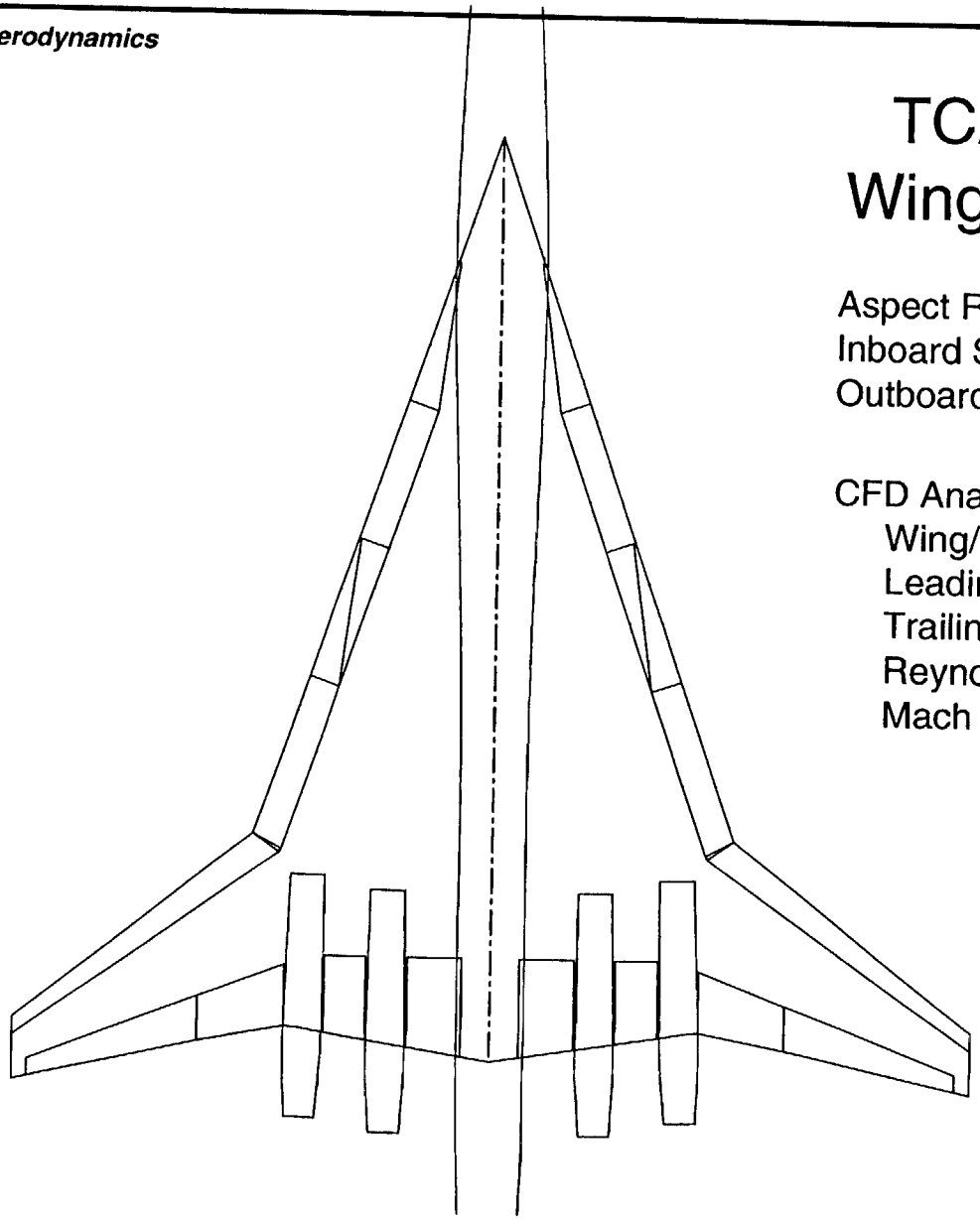

TCA 2.8-38 Wing Planform

Aspect Ratio = 2.8
Inboard Sweep = 71 deg
Outboard Sweep = 38 deg

CFD Analysis:
- Wing/Body Only
- Leading Edge Flaps = 30 deg
- Trailing Edge Flaps = 10 deg
- Reynolds Number = 8 m/mac
- Mach = .3 (CFL3D), .247 (TLNS)

TCA 2.8-38 CFD Results

This figure illustrates the difference between the H-H grid (henceforth H grid) and the C-O grid used in the CFD analysis of the TCA 2.8-38 configuration. For this study the H grid is standard for the TLNS runs, and the C-O grid is standard for the CFL3D runs, unless otherwise noted. The distorted cells on the forebody of the C-O grid may explain some of the differences seen in the flow over the body when comparing the two grids.

TCA 2.8-38 CFD Results

TCA 2.8-38 L30T10
Forebody Grid Comparison
(every other grid line shown for clarity)

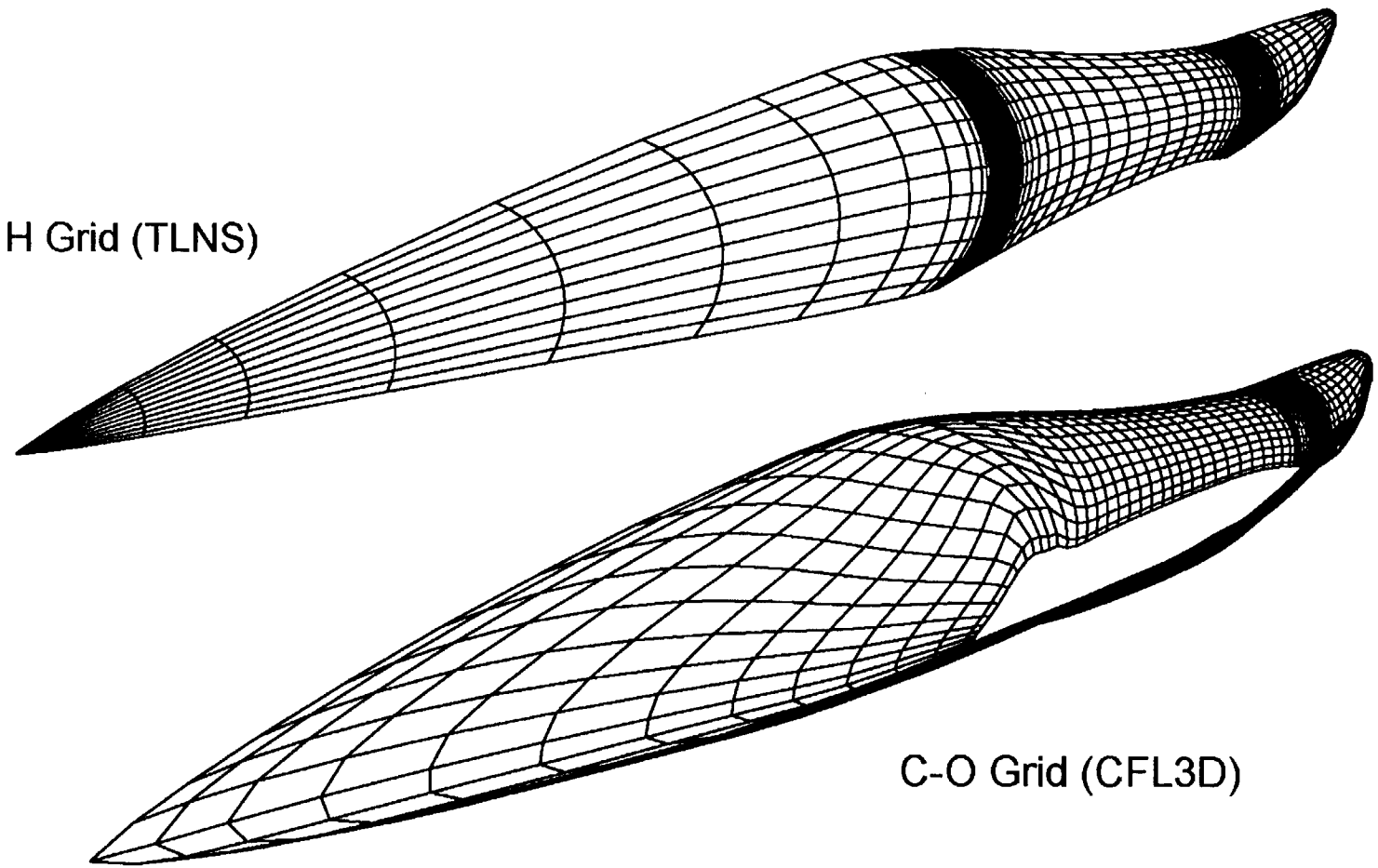

TCA 2.8-38 CFD Results

This figure the shows the lift comparison between CFL3D, TLNS and 14x22 wind tunnel data. The wind tunnel data is from TCA-4 (NASA473) with nacelles and tail off, and is fully corrected. The CFL3D data includes runs at 10 degrees angle of attack using both a C-O grid topology and an H grid topology. The TLNS data includes runs at several angles of attack, all using an H grid topology.

Both CFL3D results show good agreement with the test data, with a negligible effect on lift due to the grid topology. TLNS also matches the test data quite well, with just slightly lower lift at the operating condition (alpha = 10 deg.)

TCA 2.8-38 CFD Results

TCA 2.8-38 L30T10
CFL3D vs TLNS vs Test Data
Lift Curves

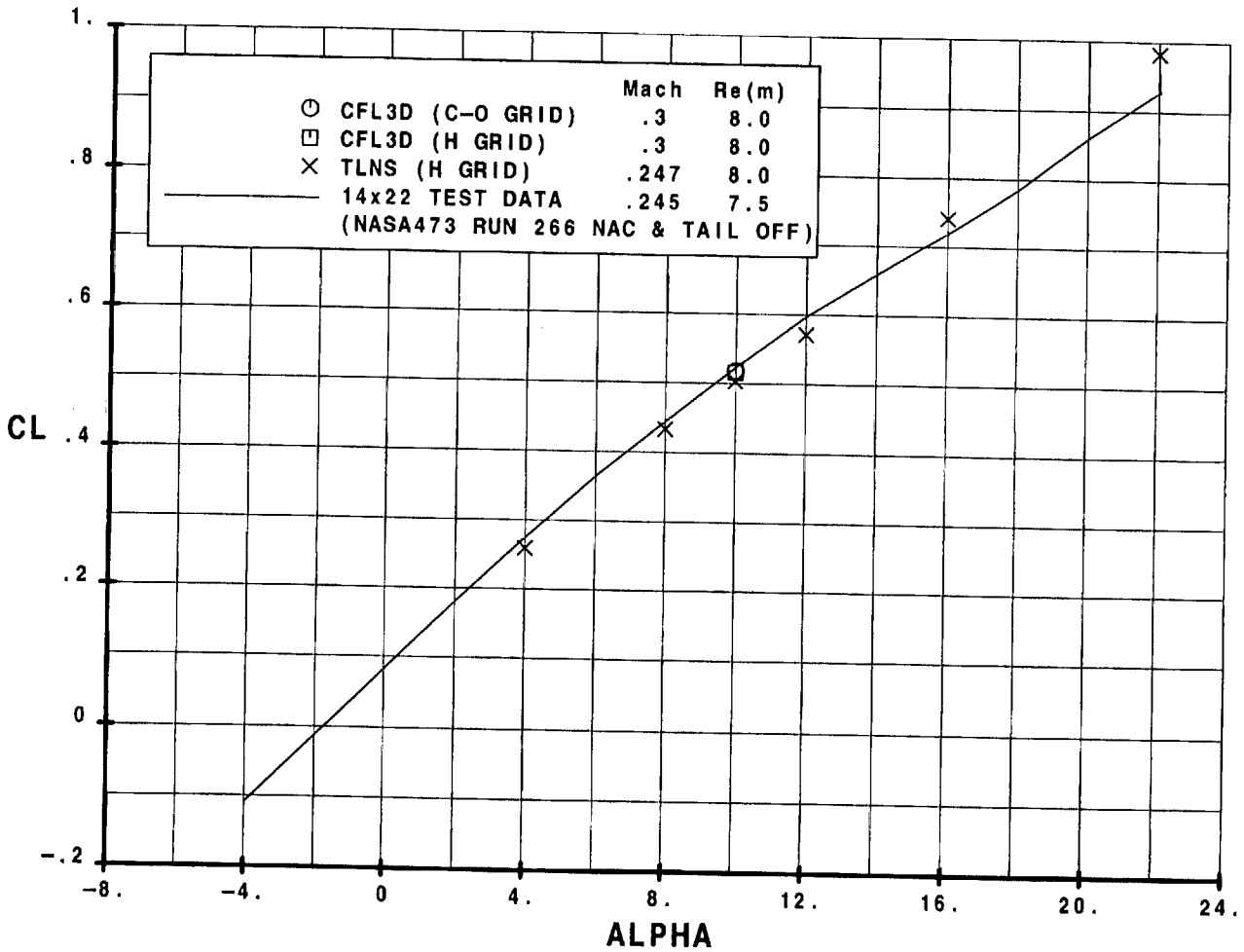

TCA 2.8-38 CFD Results

This figure the shows the drag comparison between CFL3D, TLNS and 14x22 wind tunnel data. The wind tunnel data is from TCA-4 (NASA473) with nacelles and tail off, and is fully corrected. The CFL3D data includes runs at 10 degrees angle of attack using both a C-O grid topology and an H grid topology. The TLNS data includes runs at several angles of attack, all using an H grid topology.

In the case of drag, both CFL3D runs show fairly good agreement with the test data, but they also show a significant difference due to the grid topology, with the C-O grid resulting in higher drag. The higher drag on the C-O grid is most likely due to the vortex formed on the body, emanating from the sharp forebody. The TLNS data shows significantly higher drag levels than the test data, with the delta drag increasing with increasing lift.

TCA 2.8-38 CFD Results

HSCT High Lift Aerodynamics

TCA 2.8-38 L30T10
CFL3D vs TLNS vs Test Data
Drag Polars

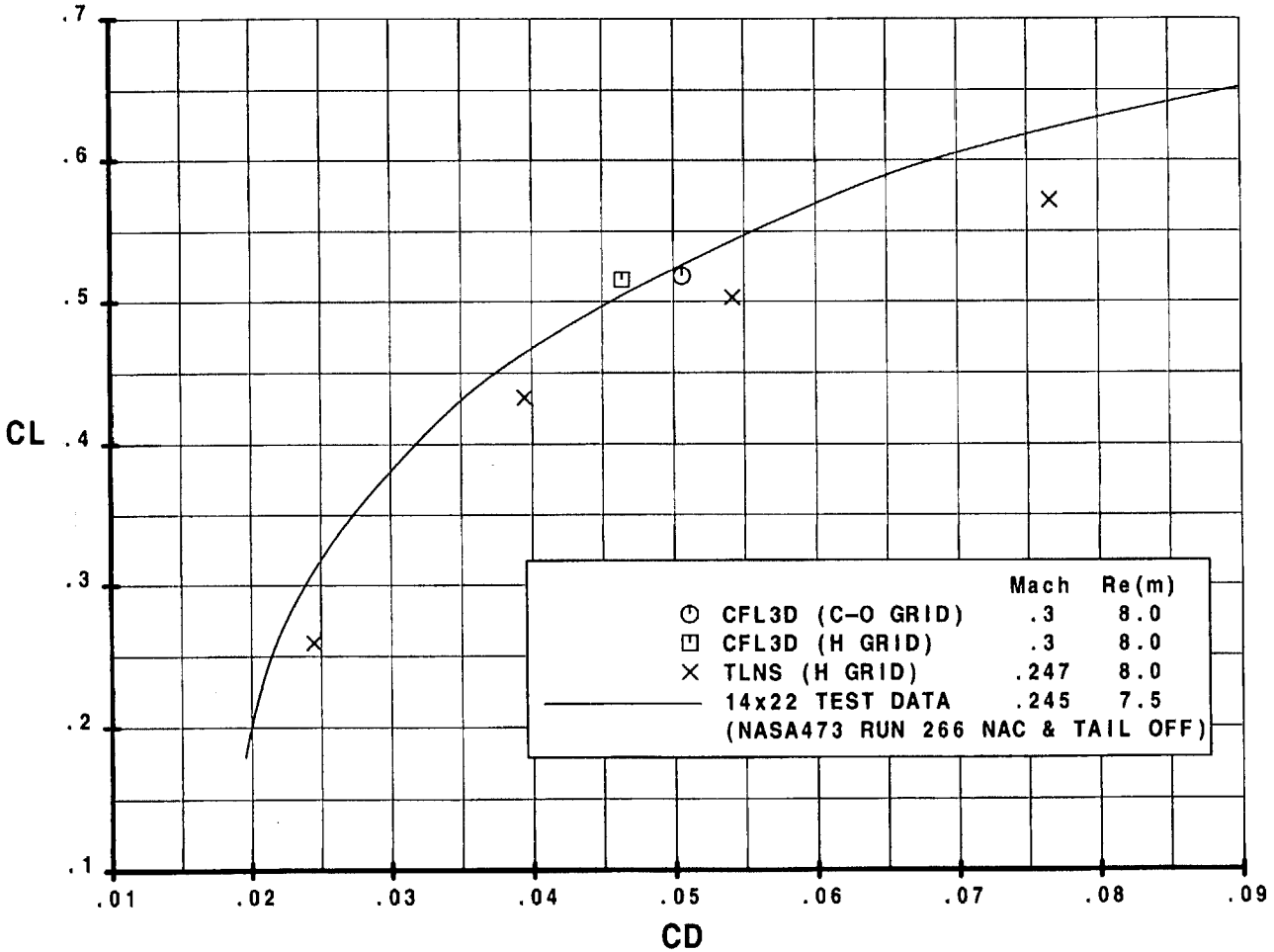

TCA 2.8-38 CFD Results

This figure the shows the lift-to-drag ratio comparison between CFL3D, TLNS and 14x22 wind tunnel data. The wind tunnel data is from TCA-4 (NASA473) with nacelles and tail off, and is fully corrected. The CFL3D data includes runs at 10 degrees angle of attack using both a C-O grid topology and an H grid topology. The TLNS data includes runs at several angles of attack, all using an H grid topology.

In the case of L/D, the CFL3D runs again bracket the test data, with the C-O grid having the lower L/D because of the higher drag. The TLNS data falls well below the test data at lower CLs, again due to the higher drag, but then matches the test data quite well at the highest CLs.

TCA 2.8-38 CFD Results

TCA 2.8-38 L30T10
CFL3D vs TLNS vs Test Data
Lift-to-Drag Ratio

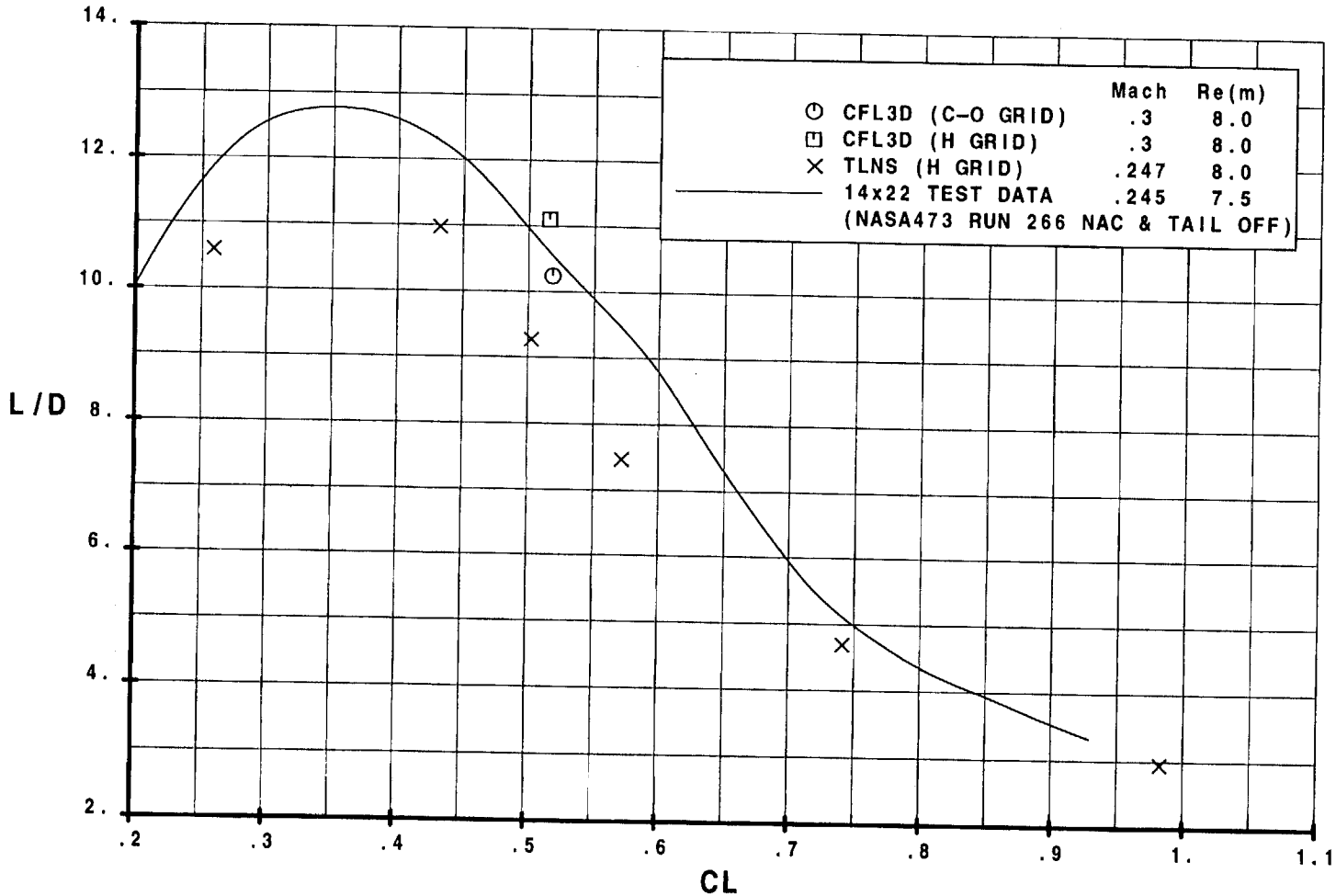

TCA 2.8-38 CFD Results

This figure the shows the pitching moment comparison between CFL3D, TLNS and 14x22 wind tunnel data. The wind tunnel data is from TCA-4 (NASA473) with nacelles and tail off, and is fully corrected. The CFL3D data includes runs at 10 degrees angle of attack using both a C-O grid topology and an H grid topology. The TLNS data includes runs at several angles of attack, all using an H grid topology.

In the case of pitching moment, both CFL3D runs show a larger nose-down moment than the test data, with the C-O grid being slightly more negative than the H grid. The TLNS data falls on the opposite (nose-up) side of the test curve, matching the test data quite well at low CLs, and then falling away at the higher CLs.

TCA 2.8-38 CFD Results

HSCT High Lift Aerodynamics

TCA 2.8-38 L30T10
CFL3D vs TLNS vs Test Data
Pitching Moment

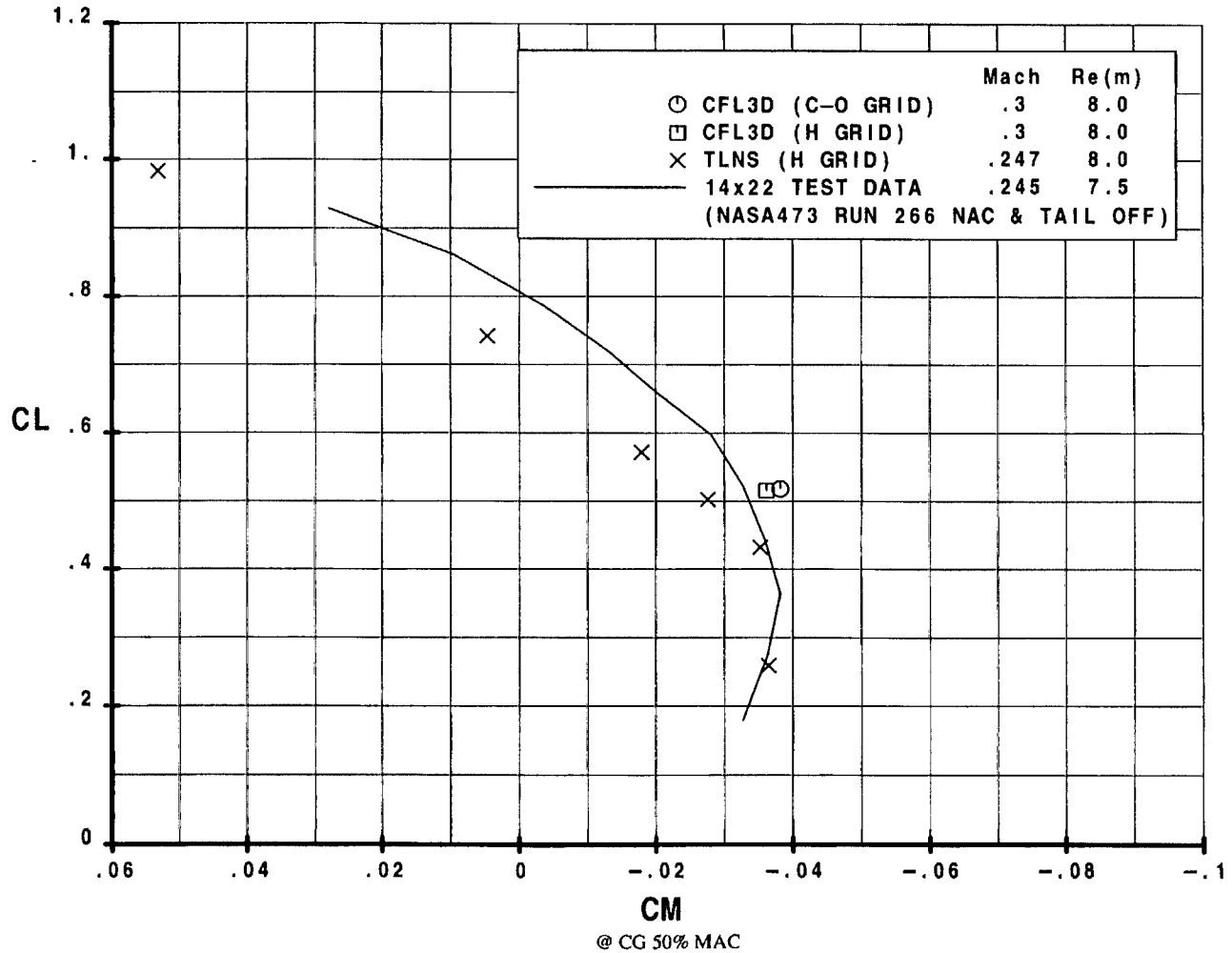

TCA 2.8-38 CFD Results

This figure the shows a spanwise pressure coefficient comparison between CFL3D, TLNS and 14x22 wind tunnel data at 10 degrees angle of attack. The wind tunnel data is from TCA-4 (NASA473) with nacelles and tail off, and has suspected bad pressures removed. The CFL3D data is from the C-O grid case, while the TLNS data again uses an H grid topology.

At this inboard station, TLNS seems to better capture the magnitude and location of the vortex induced pressure peak on the main wing.

TCA 2.8-38 CFD Results

TCA 2.8-38 L30T10
CFL3D vs TLNS vs Test Data
Spanwise Surface Pressure Distributions

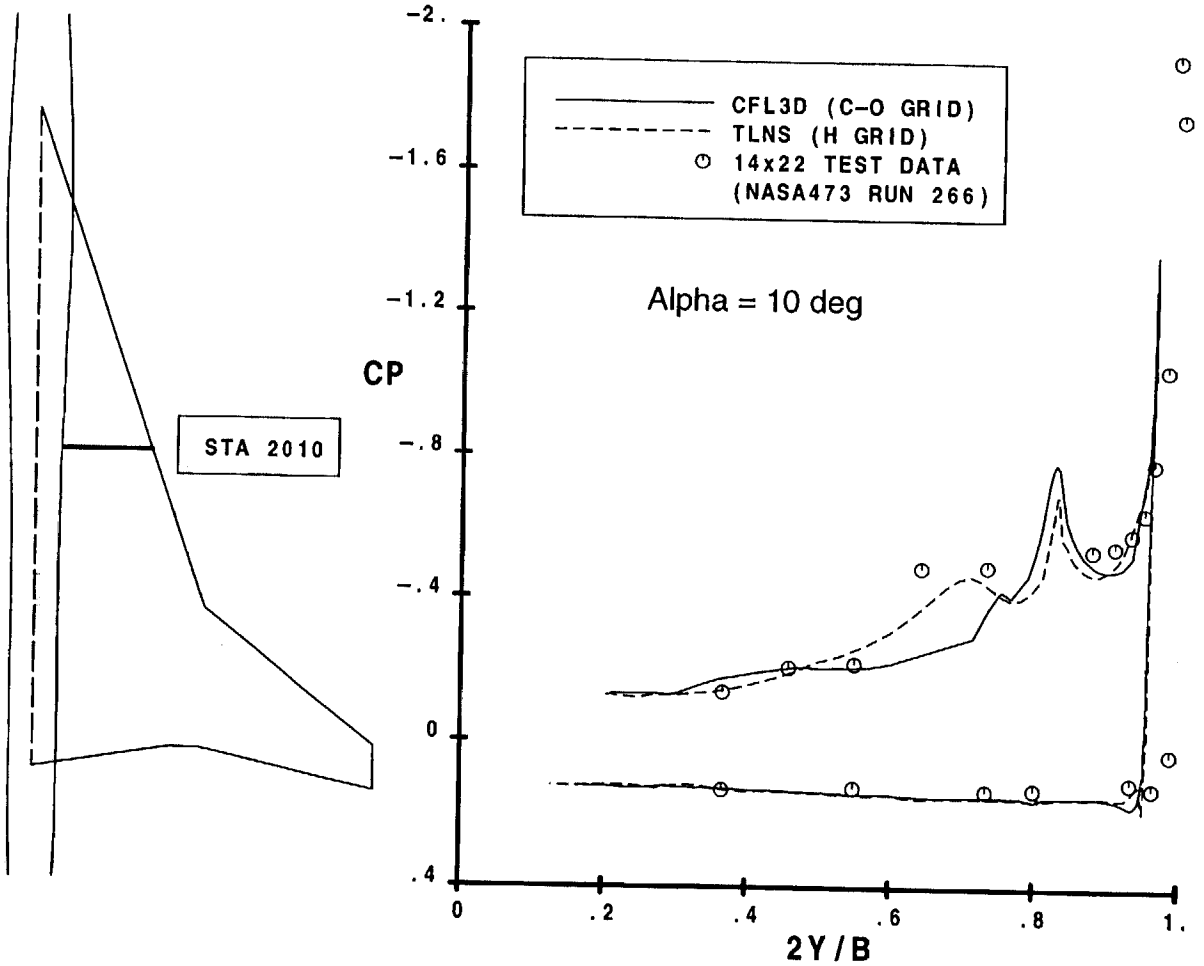

TCA 2.8-38 CFD Results

This figure the shows a chordwise pressure coefficient comparison between CFL3D, TLNS and 14x22 wind tunnel data at 10 degrees angle of attack. The wind tunnel data is from TCA-4 (NASA473) with nacelles and tail off, and has suspected bad pressures removed. The CFL3D data is from the C-O grid case, while the TLNS data again uses an H grid topology.

At this outboard buttline, CFL3D seems to better match the test data on the upper surface. At the trailing edge, a difference is seen between the two codes that may be due to the way in which they handle the boundary conditions.

TCA 2.8-38 CFD Results

TCA 2.8-38 L30T10
CFL3D vs TLNS vs Test Data
Chordwise Surface Pressure Distributions

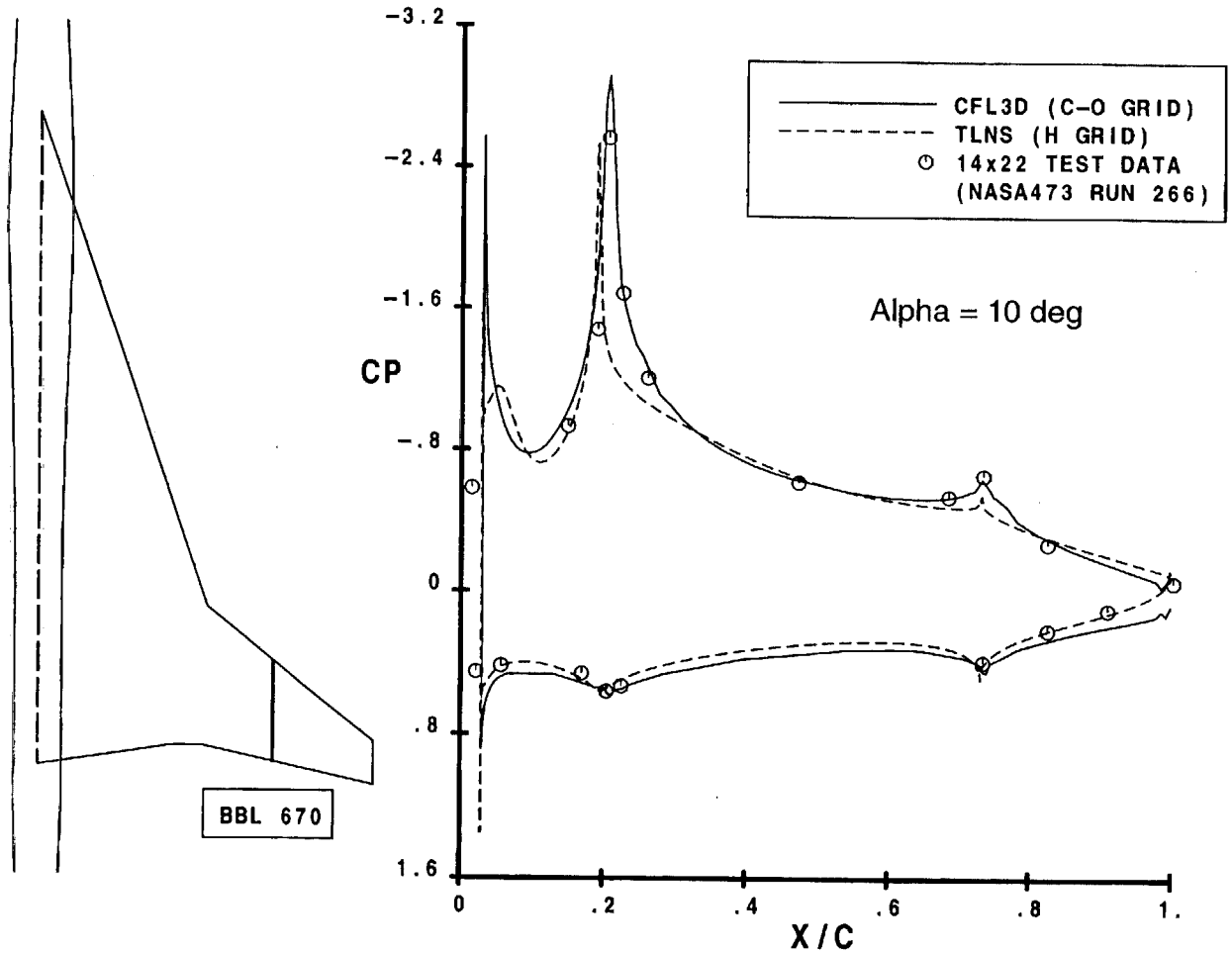

TCA 2.8-38 CFD Results

This figure the shows a total pressure ratio comparison between CFL3D run with a C-O grid topology and CFL3D run with an H grid topology, both at 10 degrees angle of attack. Total pressure is a convenient way to track vortical flow over the configuration.

The most obvious difference between the two grids is the vortex formed on the body with the C-O grid, which is not present with the H grid. This is possibly due to numerical error generated by the distorted shape of the grid cells on the sharp forebody of the TCA configuration when using a C-O grid topology. Other less significant differences can be seen in the size and location of the vortices emanating from the inboard leading edge, and in the strength of the tip vortex.

TCA 2.8-38 CFD Results

TCA 2.8-38 L30T10
CFL3D Grid Sensitivity - Total Pressure Ratio

Alpha = 10 deg Mach = .3 Re = 8 m/mac

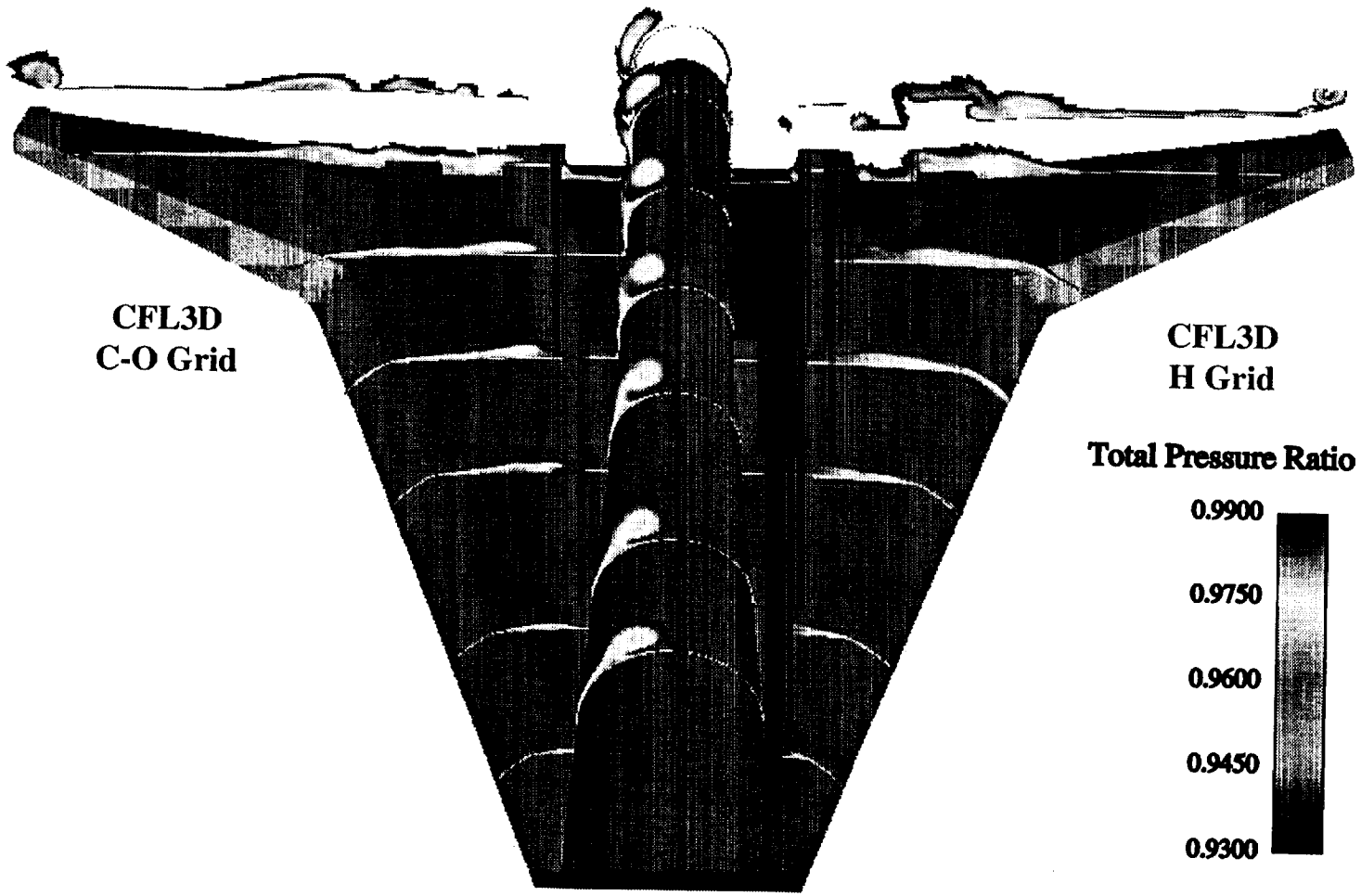

TCA 2.8-38 CFD Results

This figure the shows an upper surface pressure coefficient comparison between CFL3D run with a C-O grid topology and CFL3D run with an H grid topology, both at 10 degrees angle of attack.

Some differences in surface pressure can be seen, most notably near the outboard leading edge hingeline and near the trailing edge flap hingelines. These differences are probably due to the grid clustering and gap modeling details of each grid type.

TCA 2.8-38 CFD Results

TCA 2.8-38 L30T10
CFL3D Grid Sensitivity - Upper Surface Pressure

Alpha = 10 deg Mach = .3 Re = 8 m/mac

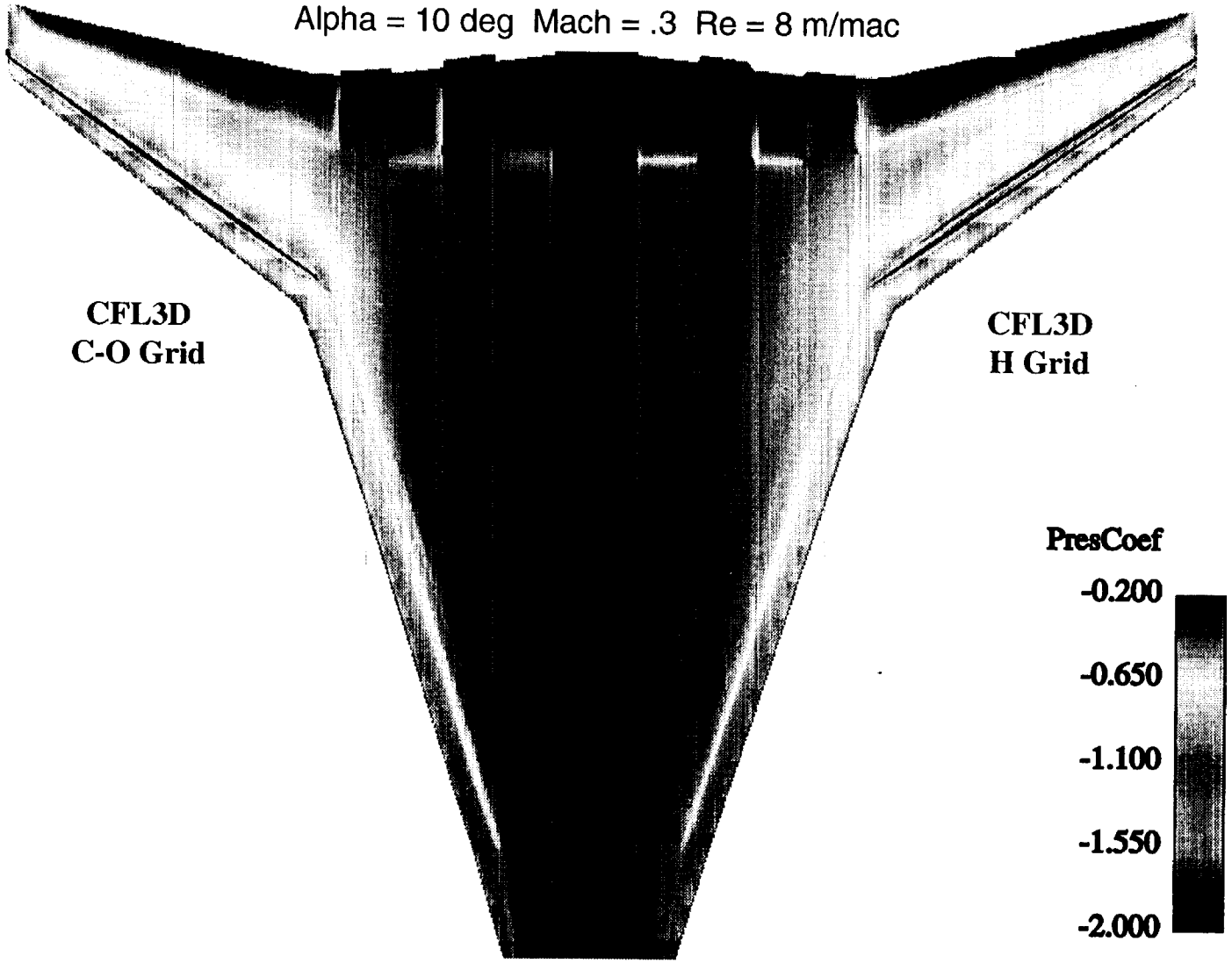

TCA 2.8-38 CFD Results

This figure the shows a total pressure ratio comparison between TLNS run with a H grid topology and CFL3D run with the same H grid topology, both at 10 degrees angle of attack. Total pressure is a convenient way to track vortical flow over the configuration.

With the two solvers running on essentially the same grid, differences can be seen in the size and location of the vortices emanating from the inboard leading edge and from the wing break, and in the strength of the tip vortex. The difference due to Mach number is assumed to be negligible, but this has not been verified.

TCA 2.8-38 CFD Results

TCA 2.8-38 L30T10
N.S. Solver Comparison - Total Pressure Ratio
Alpha = 10 deg Re = 8 m/mac

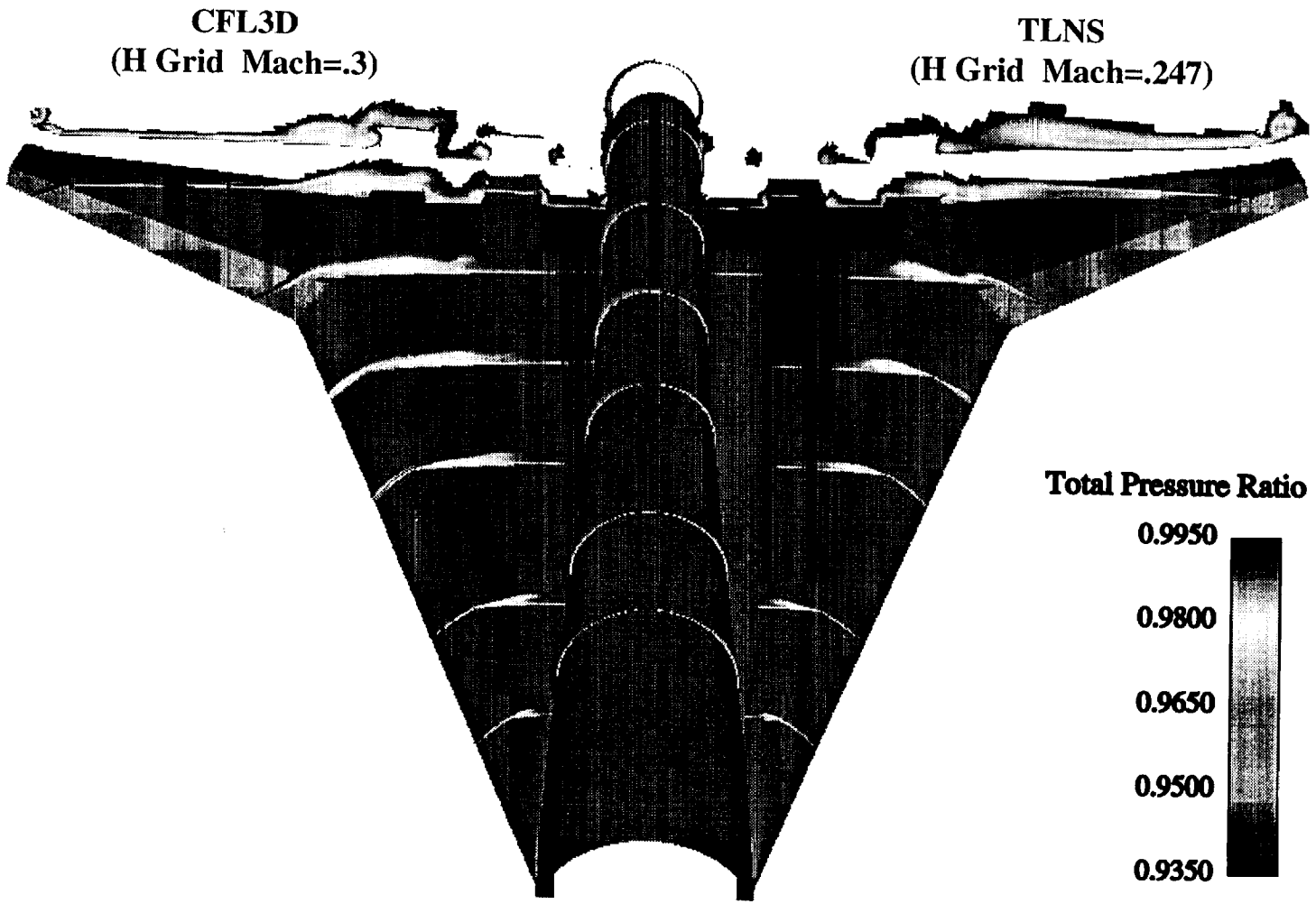

TCA 2.8-38 CFD Results

This figure the shows an upper surface pressure coefficient comparison between TLNS run with a H grid topology and CFL3D run with the same H grid topology, both at 10 degrees angle of attack.

The main differences are seen at the leading and trailing edge flap hingelines, where CFL3D shows stronger suction peaks. The difference due to Mach number is assumed to be negligible, but this has not been verified.

TCA 2.8-38 CFD Results

TCA 2.8-38 L30T10
N.S. Solver Comparison - Upper Surface Pressure

Alpha = 10 deg Re = 8 m/mac

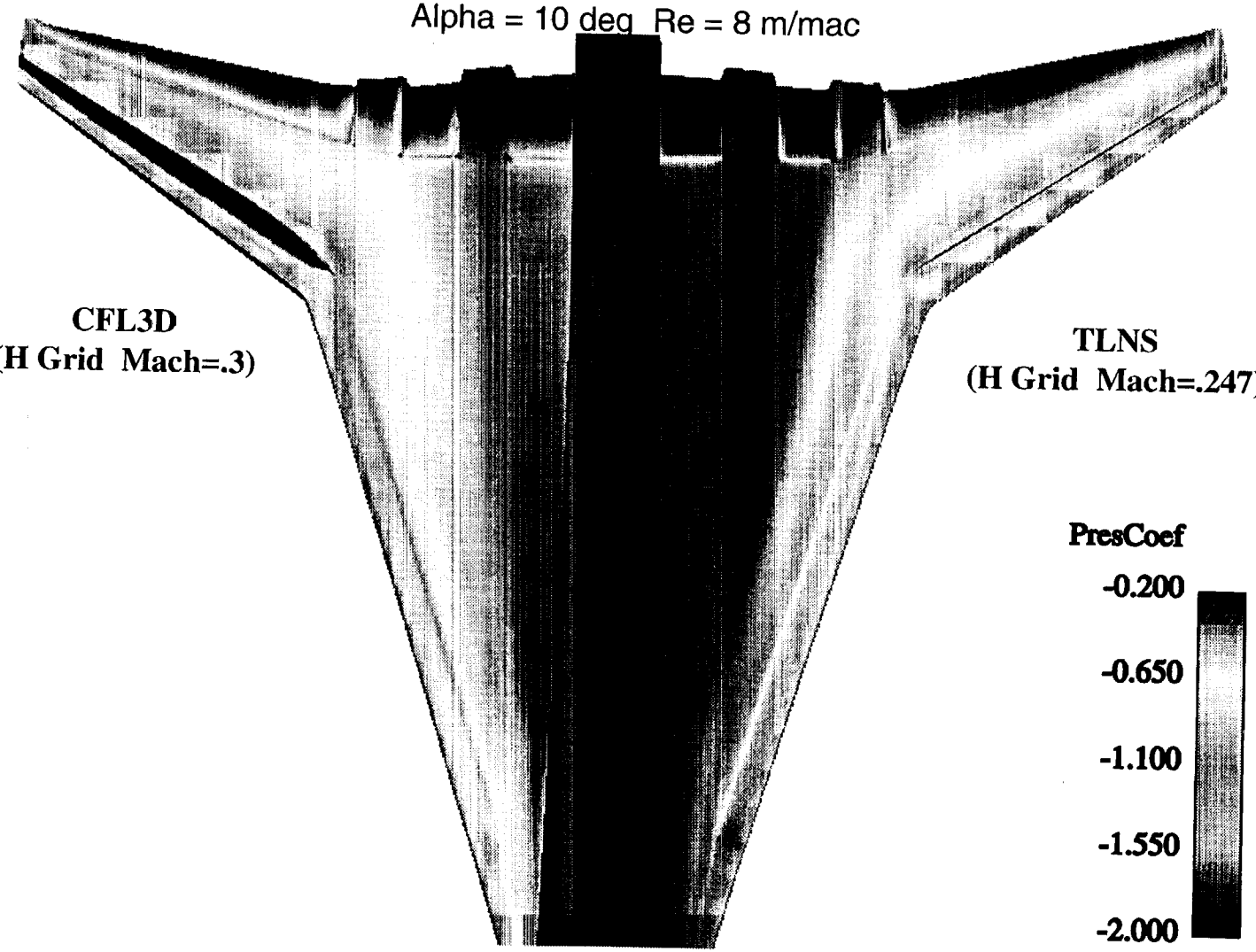

TCA 2.8-38 CFD Results

This figure the shows a total pressure ratio comparison between CFL3D run with a C-O grid and TLNS run with an H grid, both at 10 degrees angle of attack. For this study, these are the standard grids used for each of these two solvers. Total pressure is a convenient way to track vortical flow over the configuration.

Again the most visible difference is on the body, where CFL3D indicates a well formed vortex, while TLNS with an H grid does not. Another difference is the path of the vortex emanating from the wing apex. In CFL3D, this vortex stays further inboard, exiting the wing just outboard of the inboard nacelle. In TLNS, this vortex moves outboard more quickly, exiting the wing just outboard of the outboard nacelle. Another difference can be seen in the strength of the tip vortex, which shows more total pressure loss in CFL3D.

TCA 2.8-38 CFD Results

TCA 2.8-38 L30T10
CFL3D vs TLNS - Total Pressure Ratio

Alpha = 10 deg Re = 8 m/mac

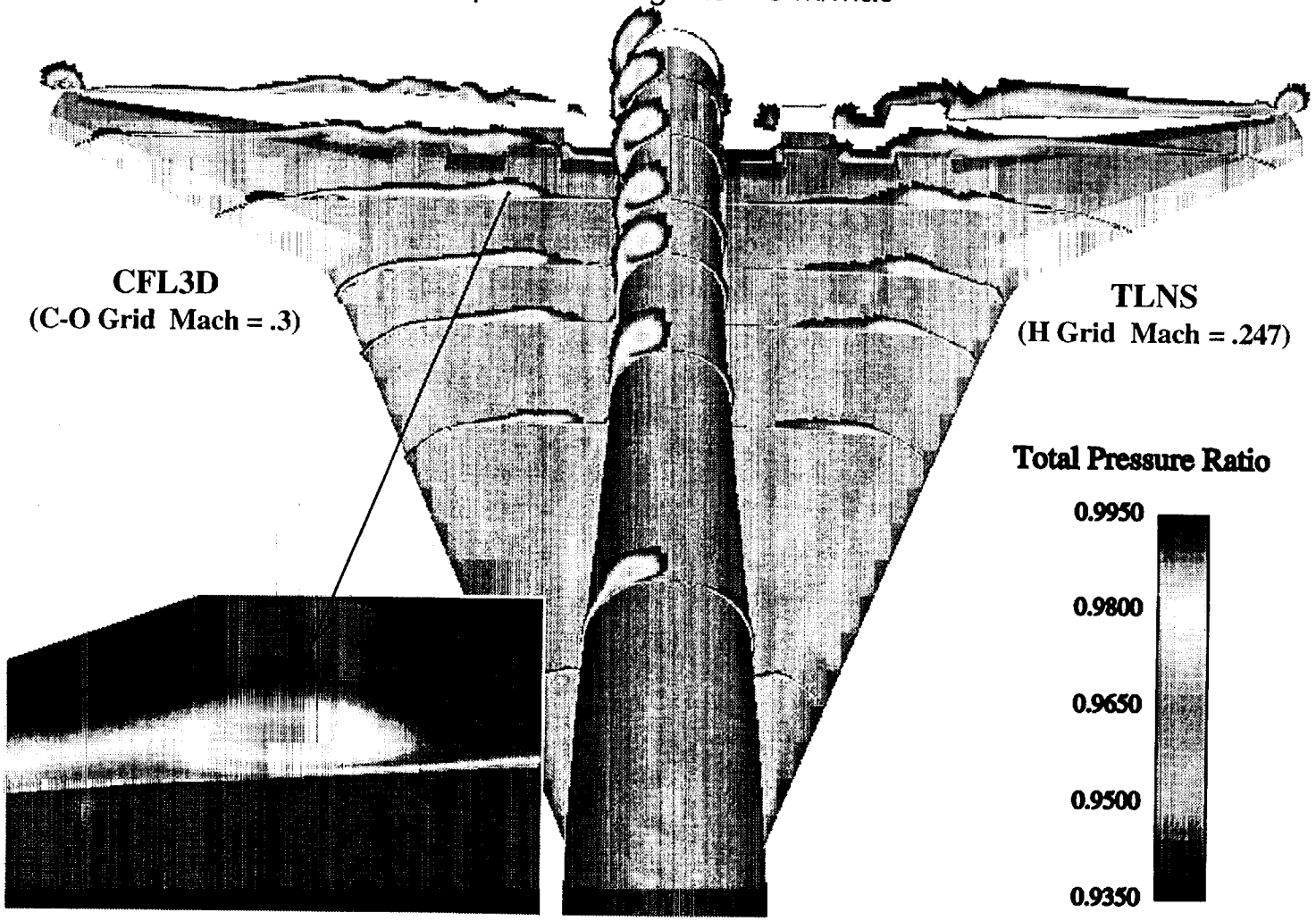

TCA 2.8-38 CFD Results

This figure the shows an upper surface-restricted streamline comparison between CFL3D run with a C-O grid and TLNS run with an H grid, both at 10 degrees angle of attack. For this plot, particle traces were released from and restricted to a layer two computational grid cells above the actual wing surface.

The major features of the flow are the same for the two solutions, but there are several differences in the details. One difference is in the attachment line location on the outboard leading edge flap. TLNS shows an attachment line that is further back on the flap, possibly indicating a larger leading edge vortex. Another difference is seen on the outboard trailing edge flap, where CFL3D shows more spanwise flow than does TLNS.

TCA 2.8-38 CFD Results

TCA 2.8-38 L30T10
CFL3D vs TLNS - Upper Surface Streamlines

Alpha = 10 deg Re = 8 m/mac

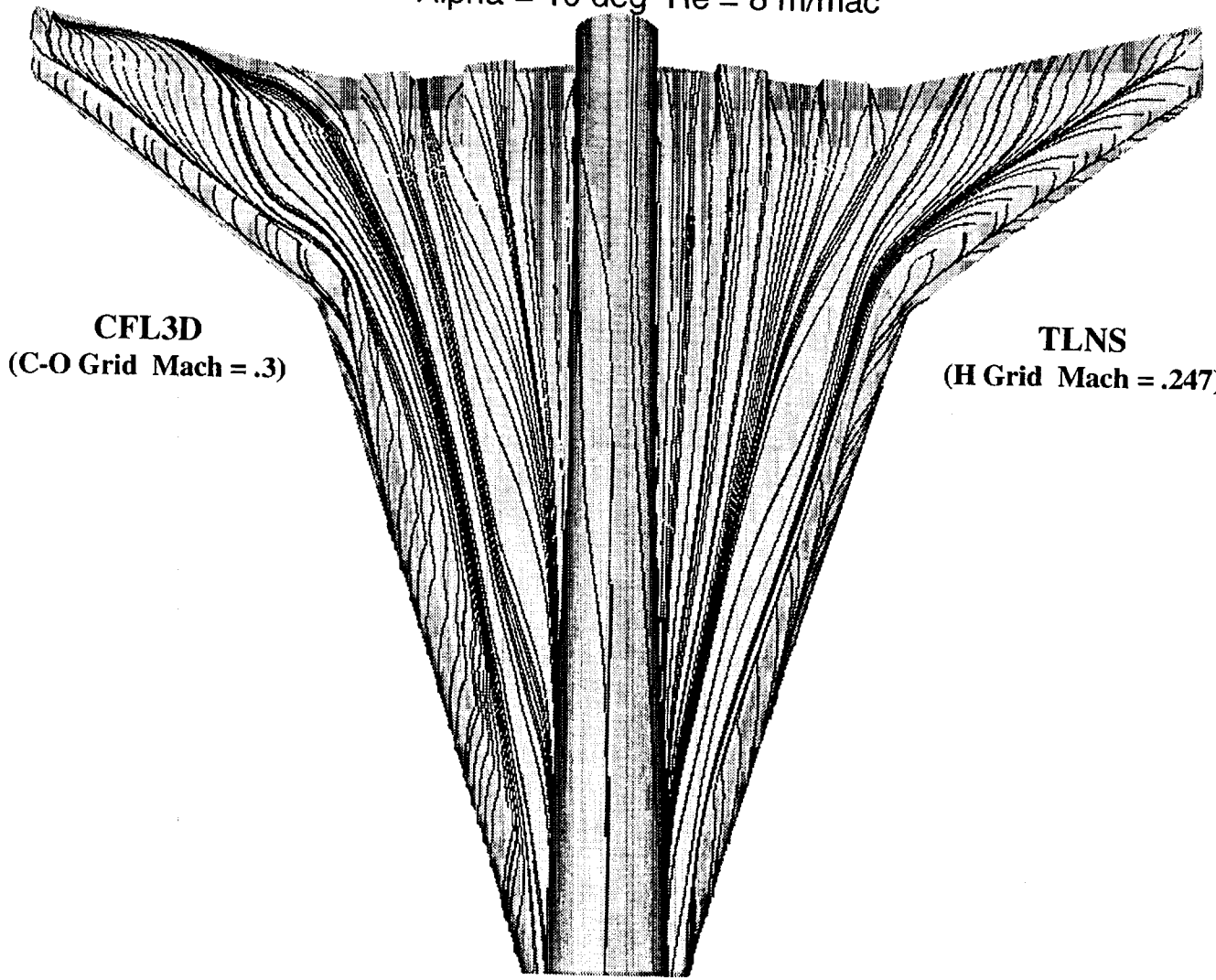

CFL3D
(C-O Grid Mach = .3)

TLNS
(H Grid Mach = .247)

Ref-H CFD Results

This figure the shows the Reference-H (henceforth Ref-H) wing planform. This configuration has a wing aspect ratio of 2.367 and an outboard wing sweep of 48 degrees. The CFD analysis of this configuration was made on the wing/body only, with no nacelles and no tail. The flap span study was done with full span and part span leading edge flaps deflected to 30 degrees and the trailing edge flaps deflected to 10 degrees. CFL3D was run at a Mach number of 0.3 and at angles of attack of 10 and 16 degrees. 10 degrees angle of attack is again near the operating condition for this configuration. Reynolds number was set to 8 million based on MAC, in order to match the available wind tunnel data. TLNS had previously been run on this configuration with both part span and full span leading edges and at angles of attack of 10, 14 and 22 degrees with a Mach number of 0.247. The effect of the difference in Mach number between the two solutions is again assumed to be negligible.

Ref-H CFD Results

Ref-H Wing Planform
Full-Span vs Part-Span LE Flaps

Aspect Ratio = 2.367
L.E. Sweep = 76.0/68.5/48.0 deg

CFD Analysis:
- Wing/Body Only
- Leading Edge Flaps = 30 deg
- Trailing Edge Flaps = 10 deg
- Reynolds Number = 8 m/mac
- Mach = .3 (CFL3D), .24 (TLNS)

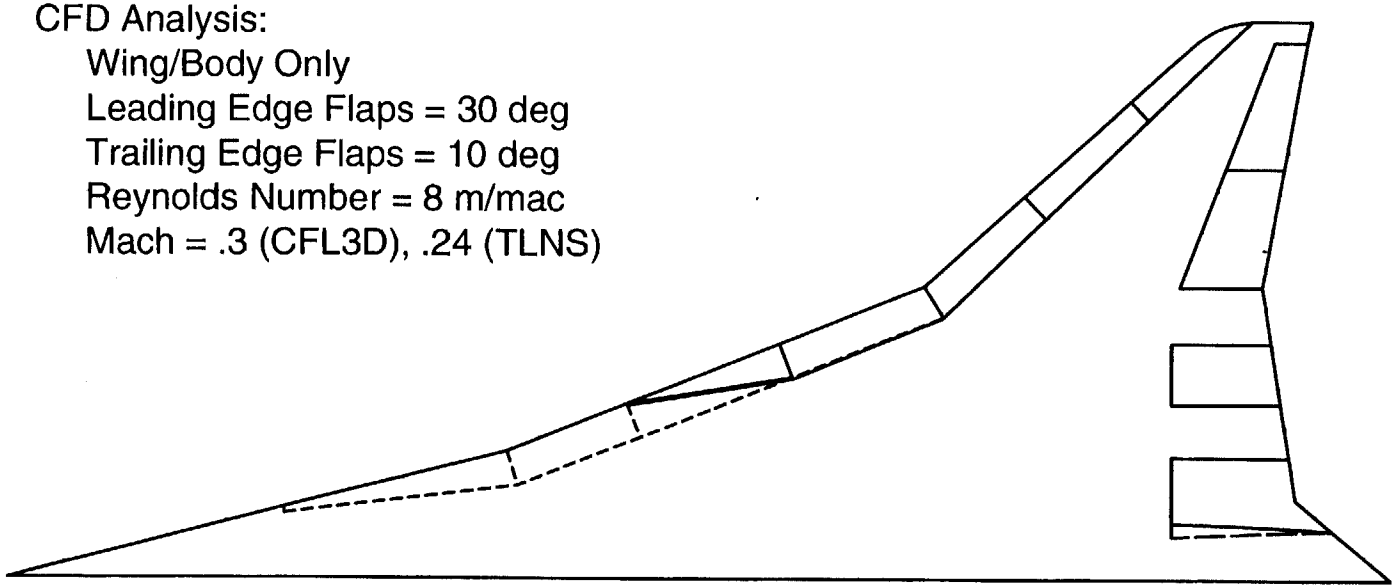

Ref-H CFD Results

This figure shows the upper surface grid used in the CFL3D analysis of the Ref-H configuration. After the clean wing grid is generated, the Boeing Phantom Works gridding tools are used to deflect the leading and trailing edge flaps and modify the volume grid. For this study, before the flaps down grid was generated, the clean wing case was run in CFL3D in order to compare with available NTF wind tunnel data.

Ref-H CFD Results

CFL3D Grid Generation
Upper Surface Grid For Wing/Body Flaps L30T10

(every other grid line shown for clarity)

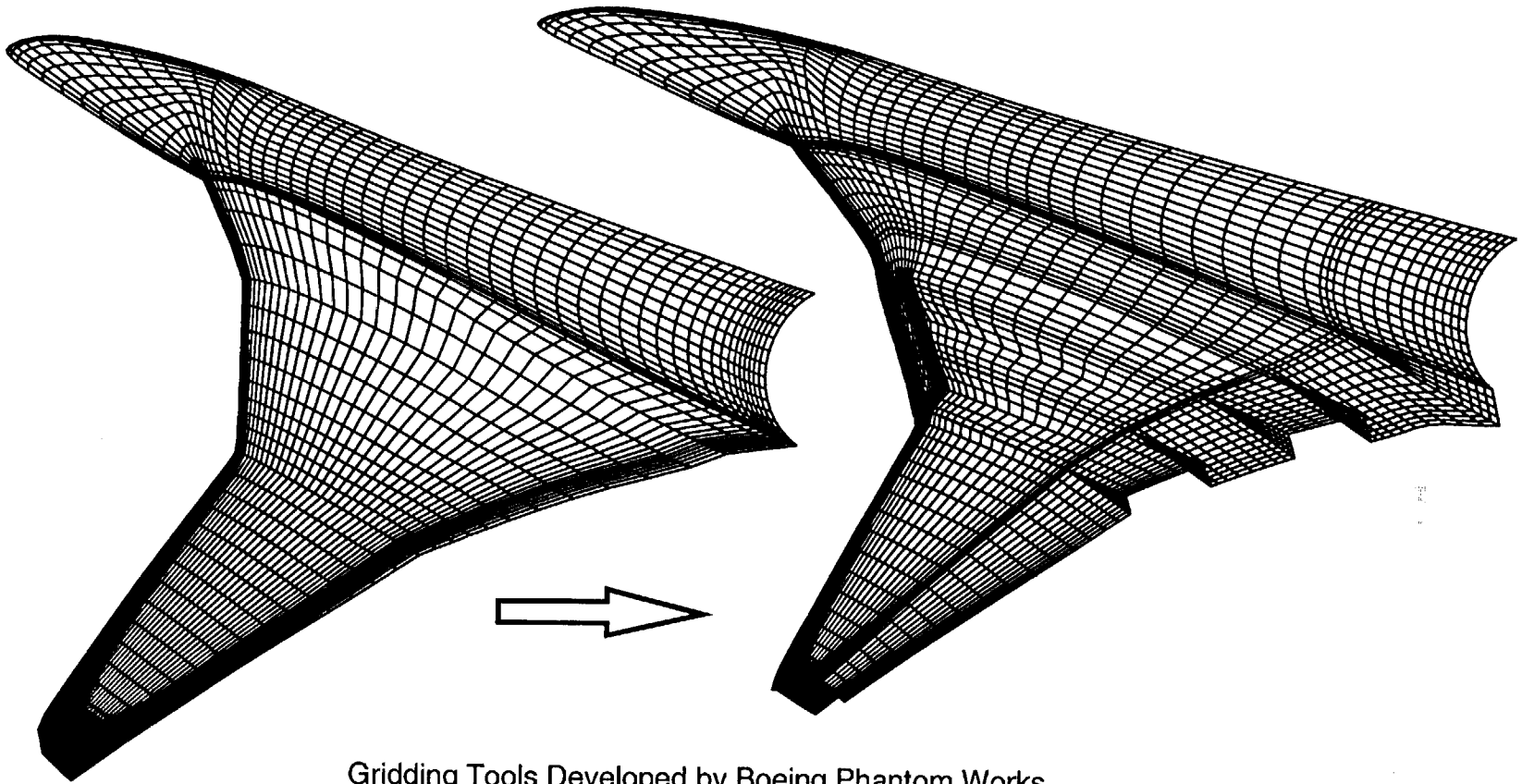

Gridding Tools Developed by Boeing Phantom Works

Ref-H CFD Results

This figure the shows the lift and drag comparison between CFL3D and NTF wind tunnel data for the Ref-H flaps up configuration. The wing/body only wind tunnel data is from NTF067 and is fully corrected. For this test, the model was mounted with a straight sting, so the biggest discrepancy between the wind tunnel model and the CFD model is the absence of the aft body in the tunnel. At 10 degrees angle of attack and a Mach number of 0.3, CFL3D shows excellent agreement with the test data in both lift and drag.

Ref-H CFD Results

Ref-H Flaps Up
CFL3D vs Test Data
Lift Curves and Drag Polars

DATA	TEST	RUN	MACH	Re(m)
———	NTF 067	197	.3	10.0
- - - - - - - -	NTF 067	199	.3	10.0
— — — — —	NTF 067	200	.3	10.0
⏲	CFL3D		.3	8.0

NOTE: NTF DATA IS WING/BODY ONLY WITH A STRAIGHT STING

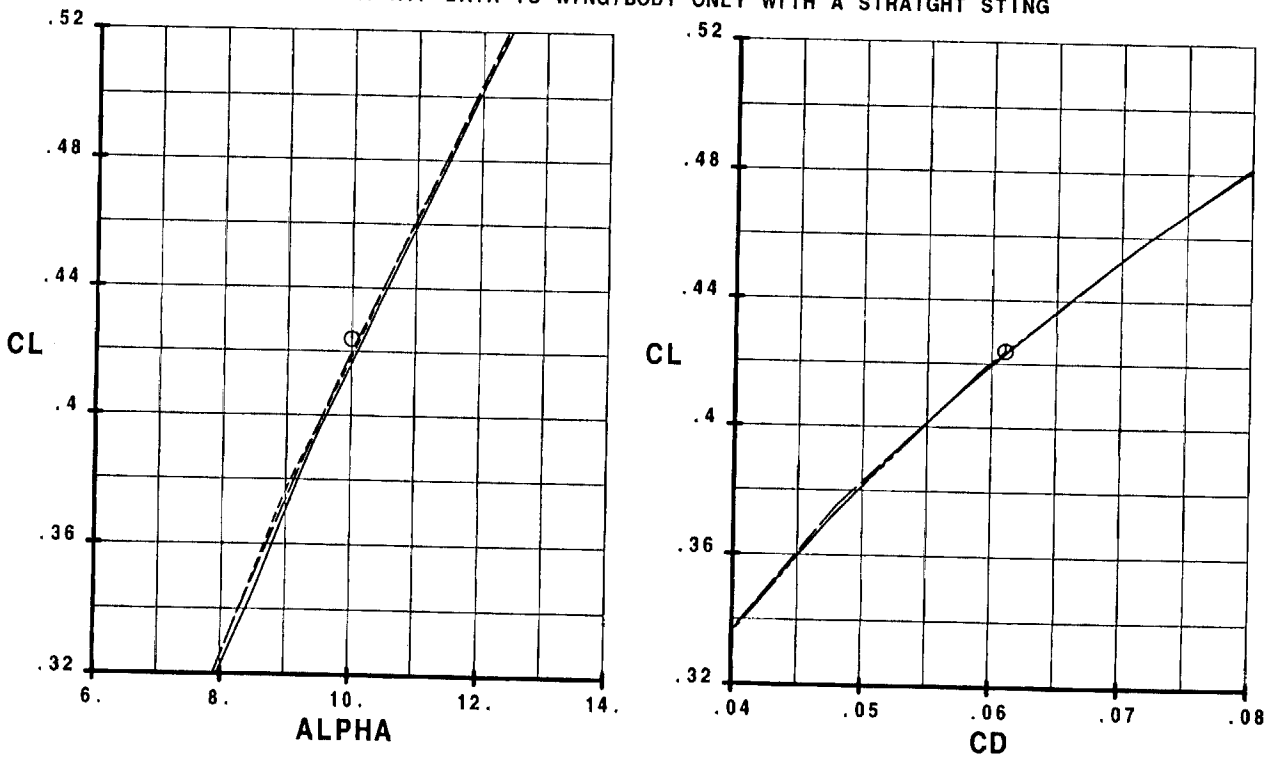

Ref-H CFD Results

This figure the shows the lift-to-drag ratio and pitching moment comparison between CFL3D and NTF wind tunnel data for the Ref-H flaps up configuration. At 10 degrees angle of attack, CFL3D shows excellent agreement with the test data in terms of L/D. The pitching moment does show some difference which may be due to the aforementioned tunnel mounting system.

Ref-H CFD Results

Ref-H Flaps Up
CFL3D vs Test Data
Lift-to-Drag Ratio and Pitching Moment

DATA	TEST	RUN	MACH	Re(m)
———	NTF 067	197	.3	10.0
- - - - - - - -	NTF 067	199	.3	10.0
— — — — —	NTF 067	200	.3	10.0
⏲	CFL3D		.3	8.0

NOTE: NTF DATA IS WING/BODY ONLY WITH A STRAIGHT STING

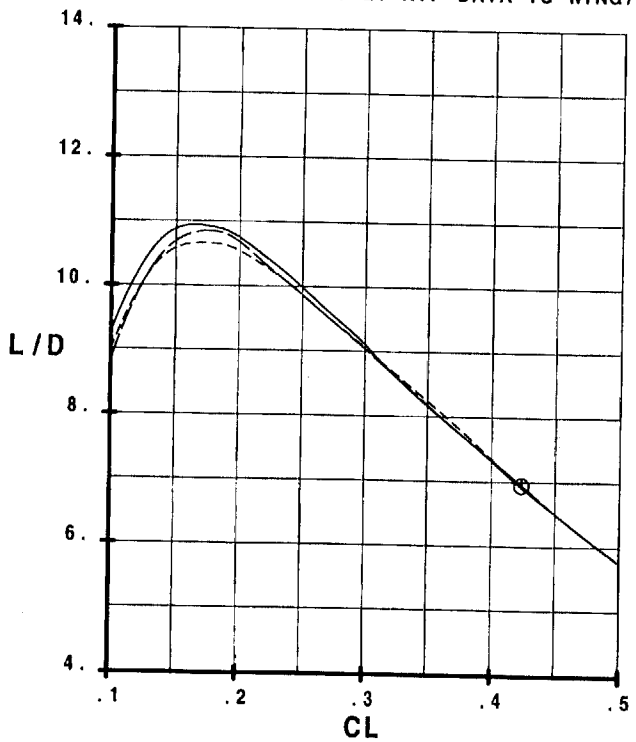

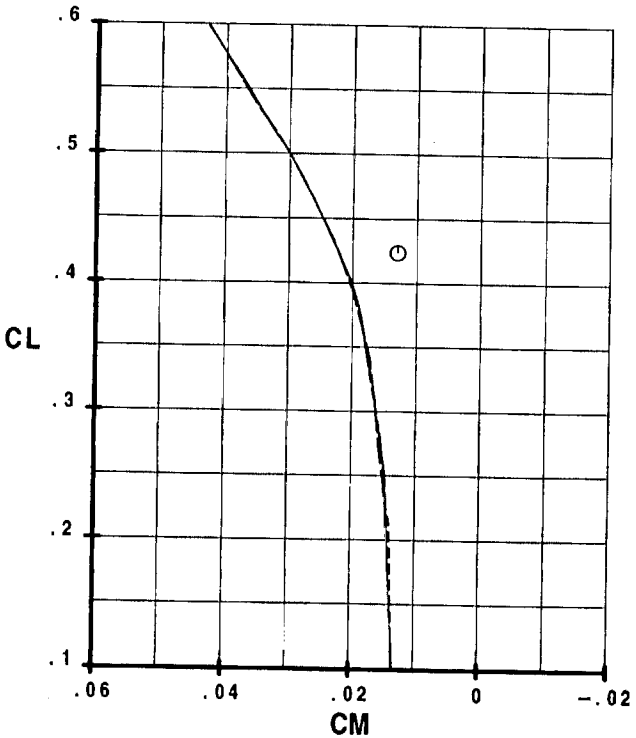

@ CG 50% MAC

Ref-H CFD Results

This figure the shows a shaded graphics picture of the CFL3D Ref-H upper surface grid with flaps deflected, and illustrates the difference between the full-span leading edge and the part-span leading edge, which is the focus of this part of the study.

Ref-H CFD Results

Ref-H L.E. Flap Span Study
CFL3D Upper Surface Grid

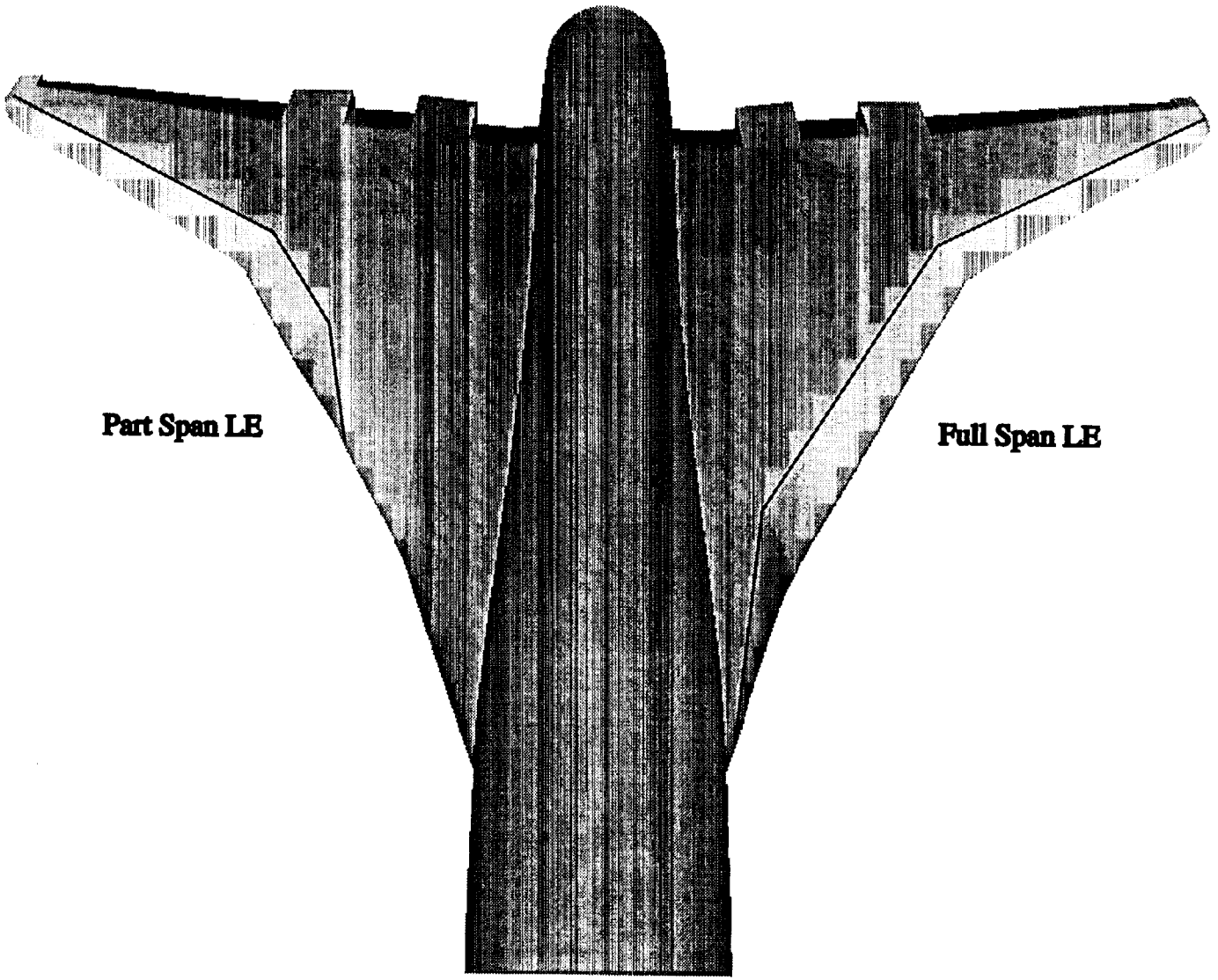

Ref-H CFD Results

This figure the shows the lift and drag convergence history for the Ref-H CFL3D case with the full-span leading edge and 10 degrees angle of attack. In this case convergence is very good, with drag changing by less than 5 counts over the last several hundred iterations.

Ref-H CFD Results

Ref-H L30T10
CFL3D Convergence
Full-Span L.E. Alpha = 10 Deg.

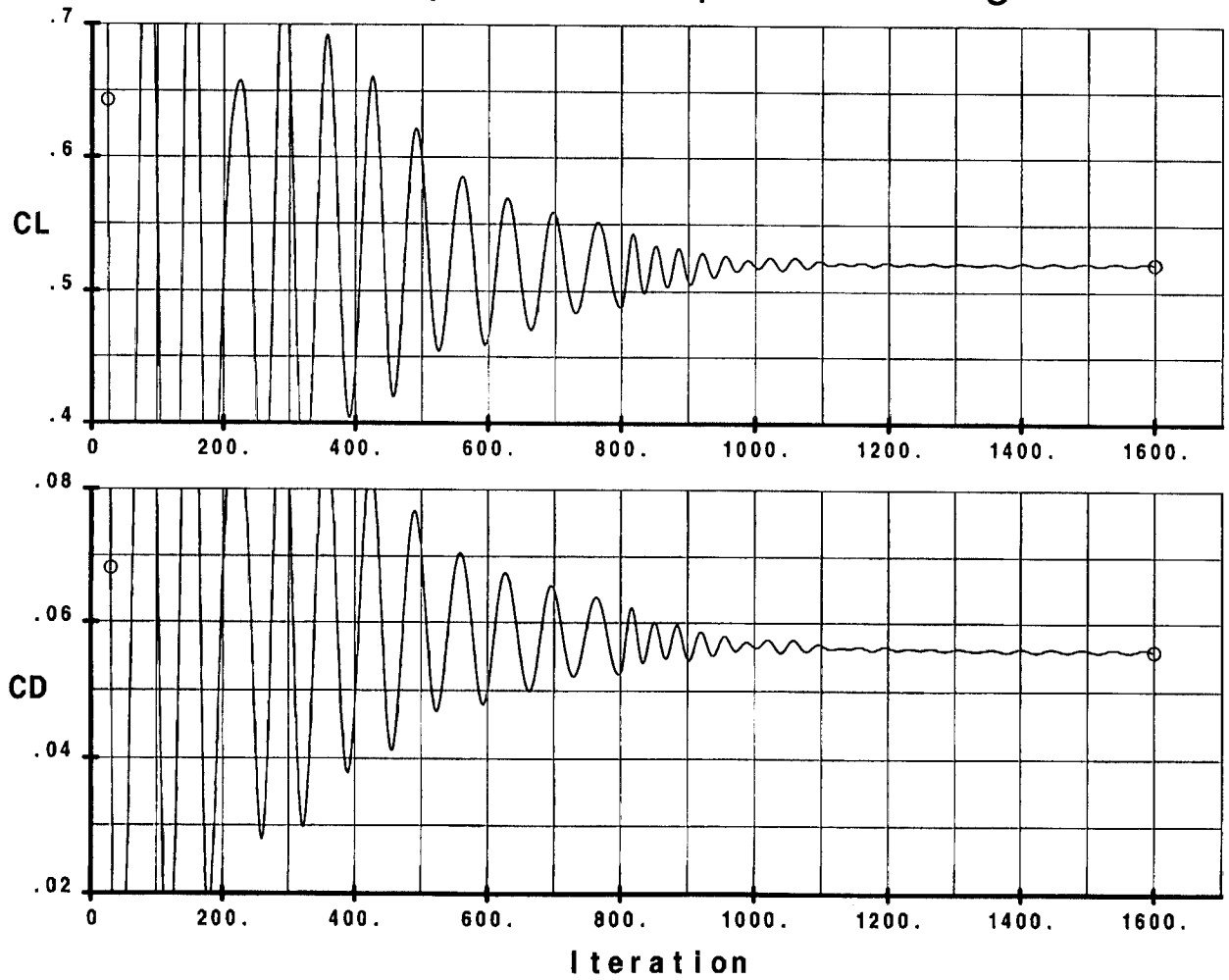

Ref-H CFD Results

This figure the shows the lift and drag convergence history for the Ref-H CFL3D case with the part-span leading edge and 10 degrees angle of attack. In this case convergence is again very good, with drag changing by less than 7 counts over the last several hundred iterations.

Ref-H CFD Results

Ref-H L30T10
CFL3D Convergence
Part-Span L.E. Alpha = 10 Deg.

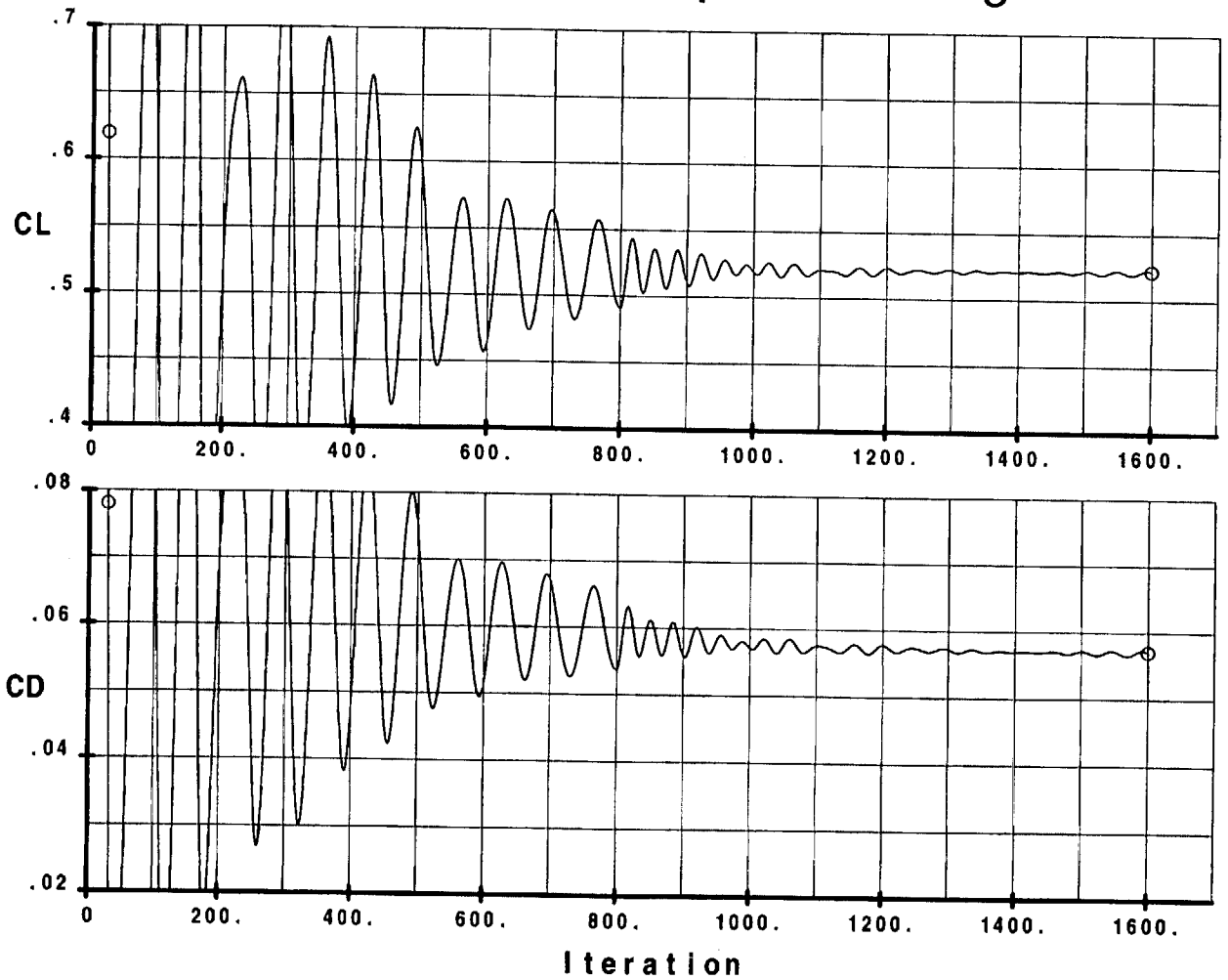

Ref-H CFD Results

This figure the shows the lift and drag convergence history for the Ref-H CFL3D case with the full-span leading edge and 16 degrees angle of attack. In this case convergence is not very good, with drag changing by more than 50 counts over the last two hundred iterations. The convergence difficulty is due to the highly vortical flow over the wing at this angle of attack.

Ref-H CFD Results

Ref-H L30T10
CFL3D Convergence
Full-Span L.E. Alpha = 16 Deg.

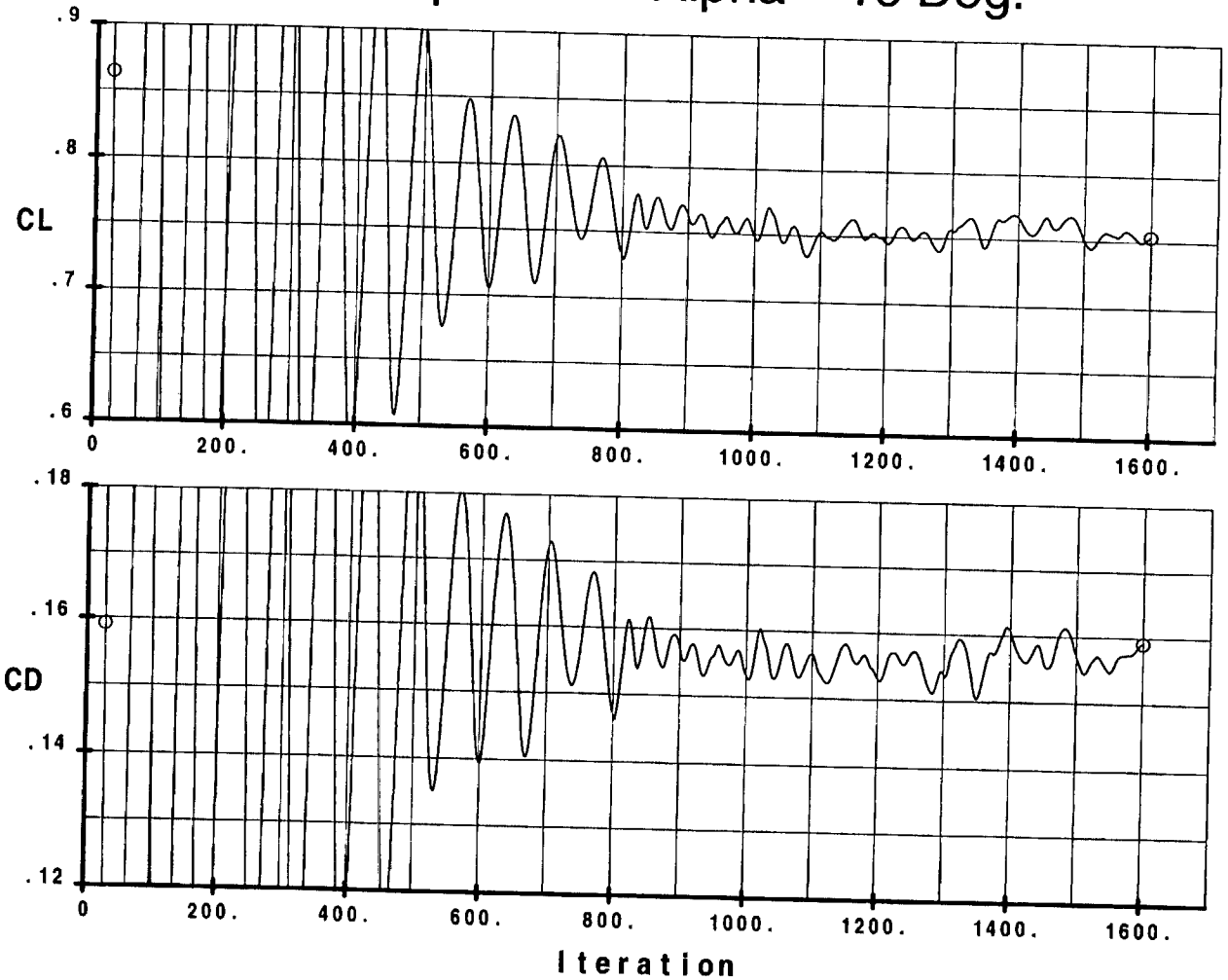

Ref-H CFD Results

This figure the shows the lift and drag convergence history for the Ref-H CFL3D case with the part-span leading edge and 16 degrees angle of attack. Convergence is again not very good, with drag changing by more than 100 counts over the last two hundred iterations. The convergence difficulty is due to the highly vortical flow over the wing at this angle of attack. As a result, the CFL3D results at this angle of attack should probably not be used in making high lift configuration decisions.

Ref-H CFD Results

Ref-H L30T10
CFL3D Convergence
Part-Span L.E. Alpha = 16 Deg.

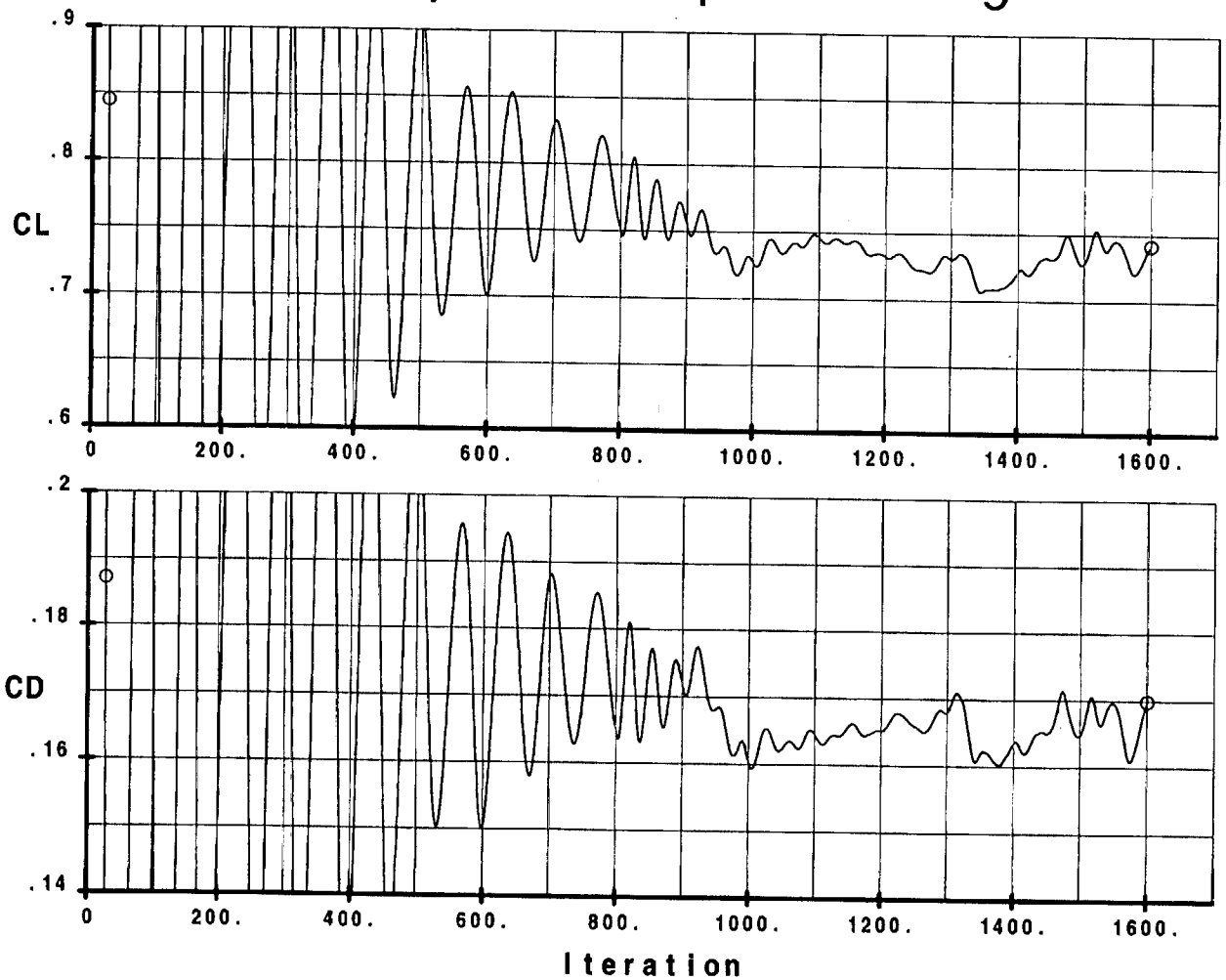

Ref-H CFD Results

This figure the shows the lift comparison between CFL3D, TLNS and 14x22 wind tunnel data for the Ref-H configuration with both full-span and part-span leading edge flaps. The wind tunnel data is from NASA429 with tail off but nacelles on, and does not include a T&I correction.

The main focus of the study is at 10 degrees angle of attack, where both codes match the test data in predicting a negligible leading edge flap span effect on lift. CFL3D does better match the lift level of the test data, although there are configuration differences as mentioned above. At higher angles of attack, both the test data and TLNS show increasing lift for the part-span case relative to the full-span case as a result of a strong vortex coming off the undeflected inboard leading edge. The non-converged CFL3D results do not show this effect.

Ref-H CFD Results

Ref-H L30T10
CFL3D vs TLNS vs Test Data
Lift Curves

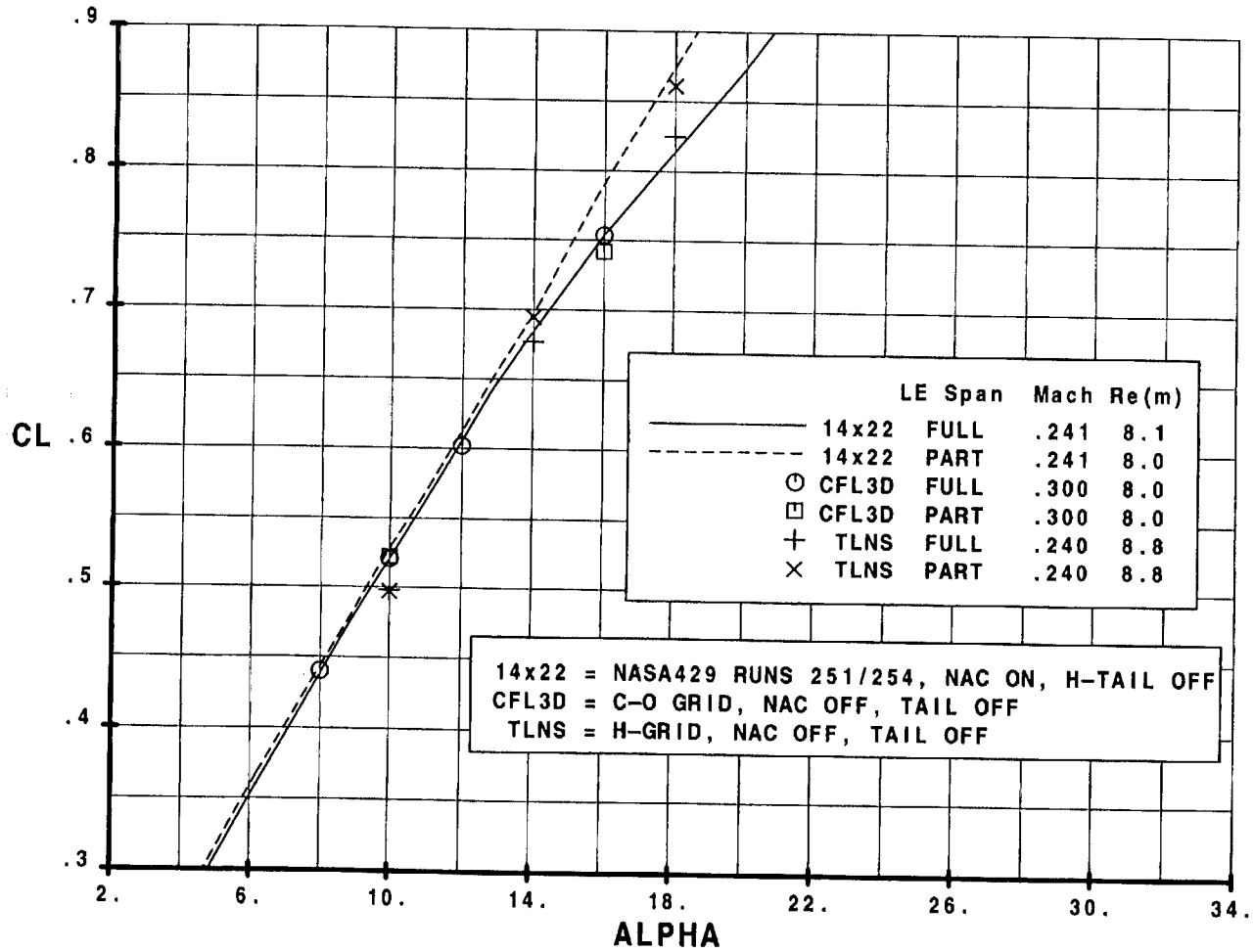

Ref-H CFD Results

This figure the shows the drag comparison between CFL3D, TLNS and 14x22 wind tunnel data for the Ref-H configuration with both full-span and part-span leading edge flaps. The wind tunnel data is from NASA429 with tail off but nacelles on, and does not include a T&I correction.

The main focus of the study is at a CL level near 0.5, where CFL3D matches the test data in showing negligible change in drag for the two flap spans. TLNS, on the other hand, does show a change due to leading edge span, with the part-span case having the higher drag. CFL3D also better matches the drag level of the test data, although there are configuration differences as mentioned above. At higher CLs, TLNS continues to show higher drag levels than the test data, especially with the part-span leading edge.

Ref-H CFD Results

Ref-H L30T10
CFL3D vs TLNS vs Test Data
Drag Polars

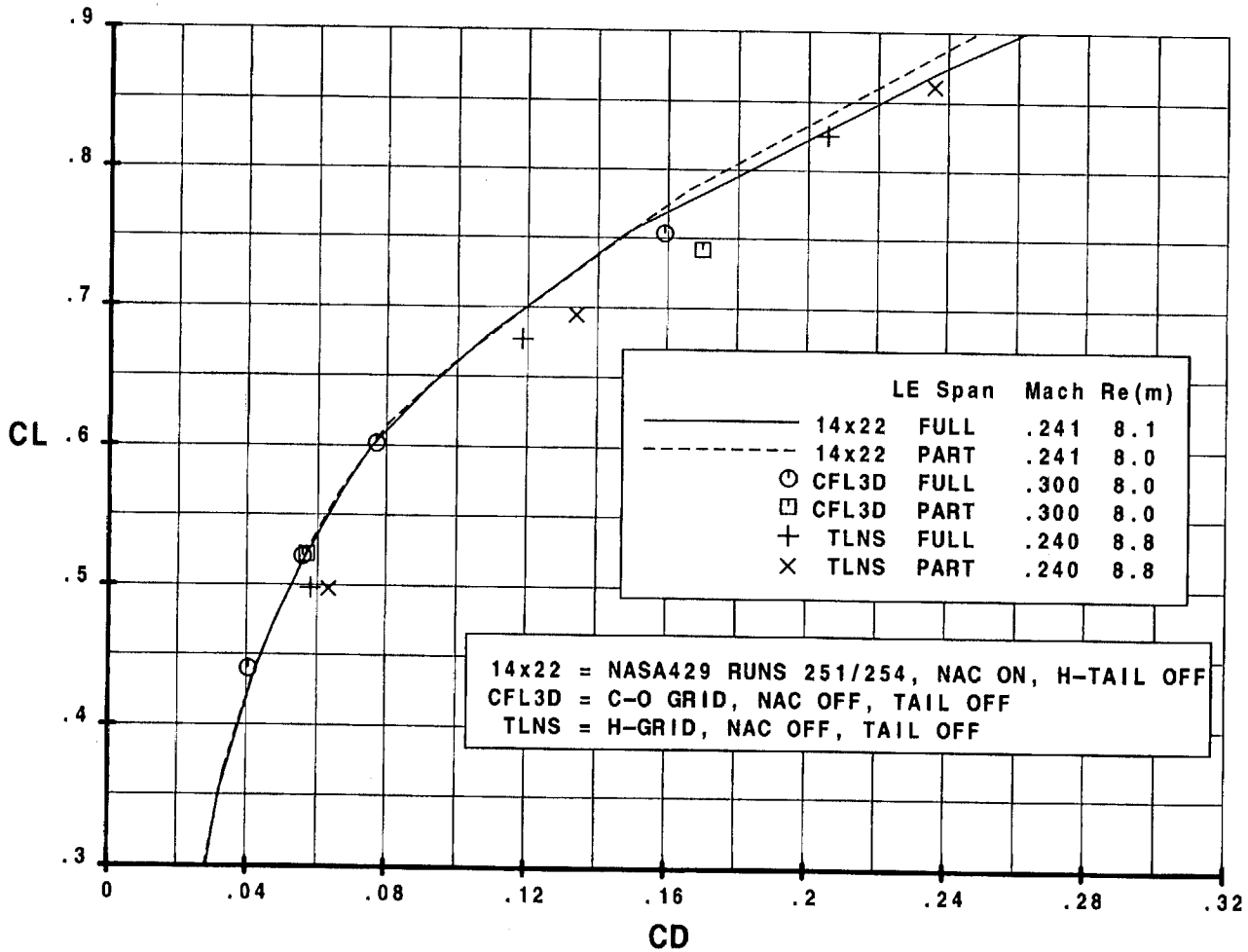

Ref-H CFD Results

This figure the shows the lift-to-drag ratio comparison between CFL3D, TLNS and 14x22 wind tunnel data for the Ref-H configuration with both full-span and part-span leading edge flaps. The wind tunnel data is from NASA429 with tail off, but nacelles on, and does not include a T&I correction.

The main focus of the study is again at a CL level near 0.5, where CFL3D matches the test data in showing very little change in L/D for the two flap spans. TLNS, on the other hand, does show a significant change in L/D due to leading edge span, with the part-span case having the lower value. CFL3D also better matches the L/D level of the test data, although there are configuration differences as mentioned above. At higher CLs, TLNS does a reasonable job of following the test data trends, especially with the full-span leading edge.

Ref-H CFD Results

Ref-H L30T10
CFL3D vs TLNS vs Test Data
Lift-to-Drag Ratio

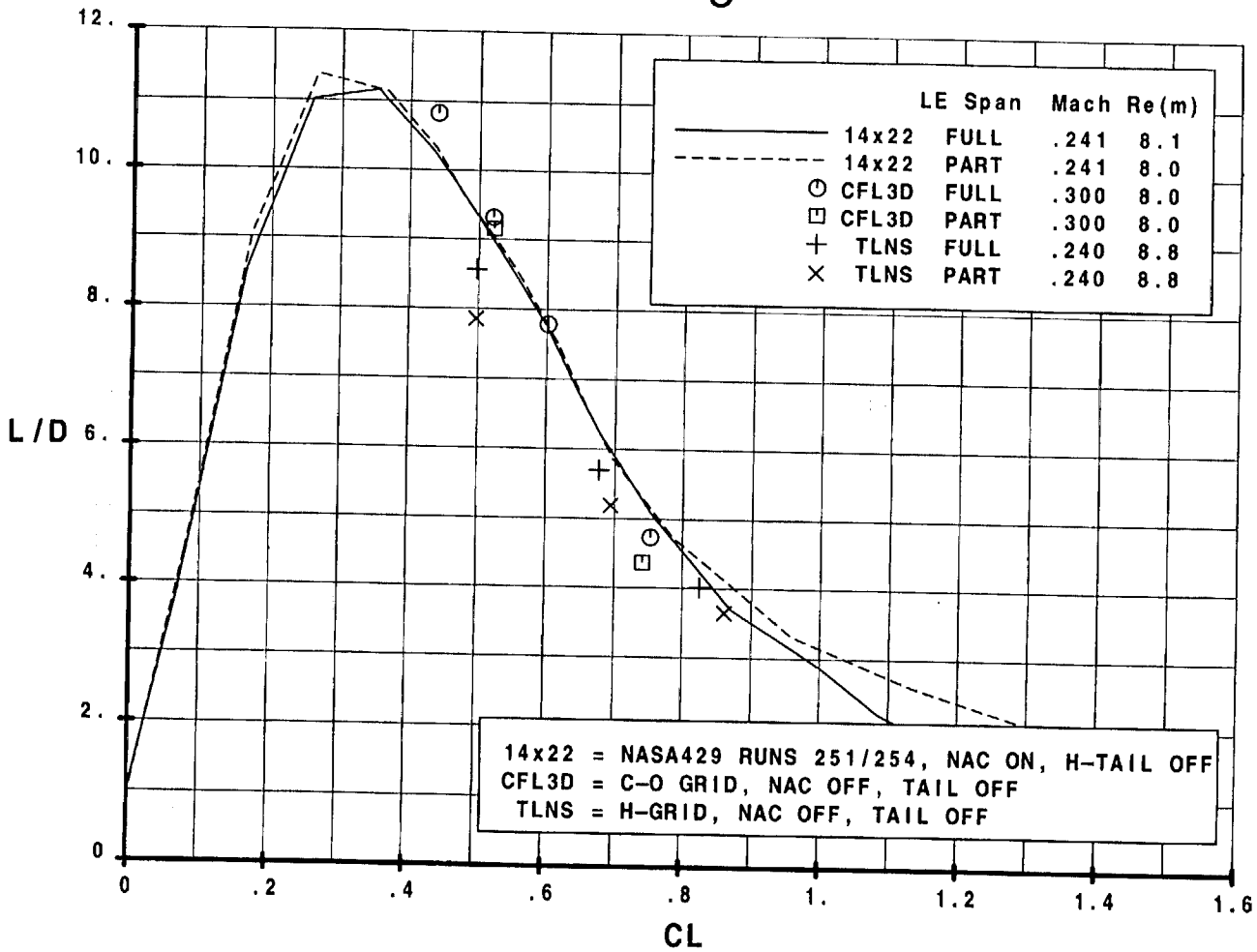

Ref-H CFD Results

This figure the shows the pitching moment comparison between CFL3D, TLNS and 14x22 wind tunnel data for the Ref-H configuration with both full-span and part-span leading edge flaps. The wind tunnel data is from NASA429 with tail off, but nacelles on, and does not include a T&I correction.

The main focus of the study is again at CL level near 0.5, where both codes predict the correct trend for the leading edge span effect, with the part-span case having a more nose-up pitching moment. CFL3D slightly underpredicts the magnitude of the effect, while TLNS predicts an effect nearly double that indicated by the test data. At higher and lower CLs, CFL3D follows the test data trend quite well in the case of the full-span leading edge. TLNS also follows the shape of the test curve, but at a consistently more positive pitching moment level.

Ref-H CFD Results

Ref-H L30T10
CFL3D vs TLNS vs Test Data
Pitching Moment

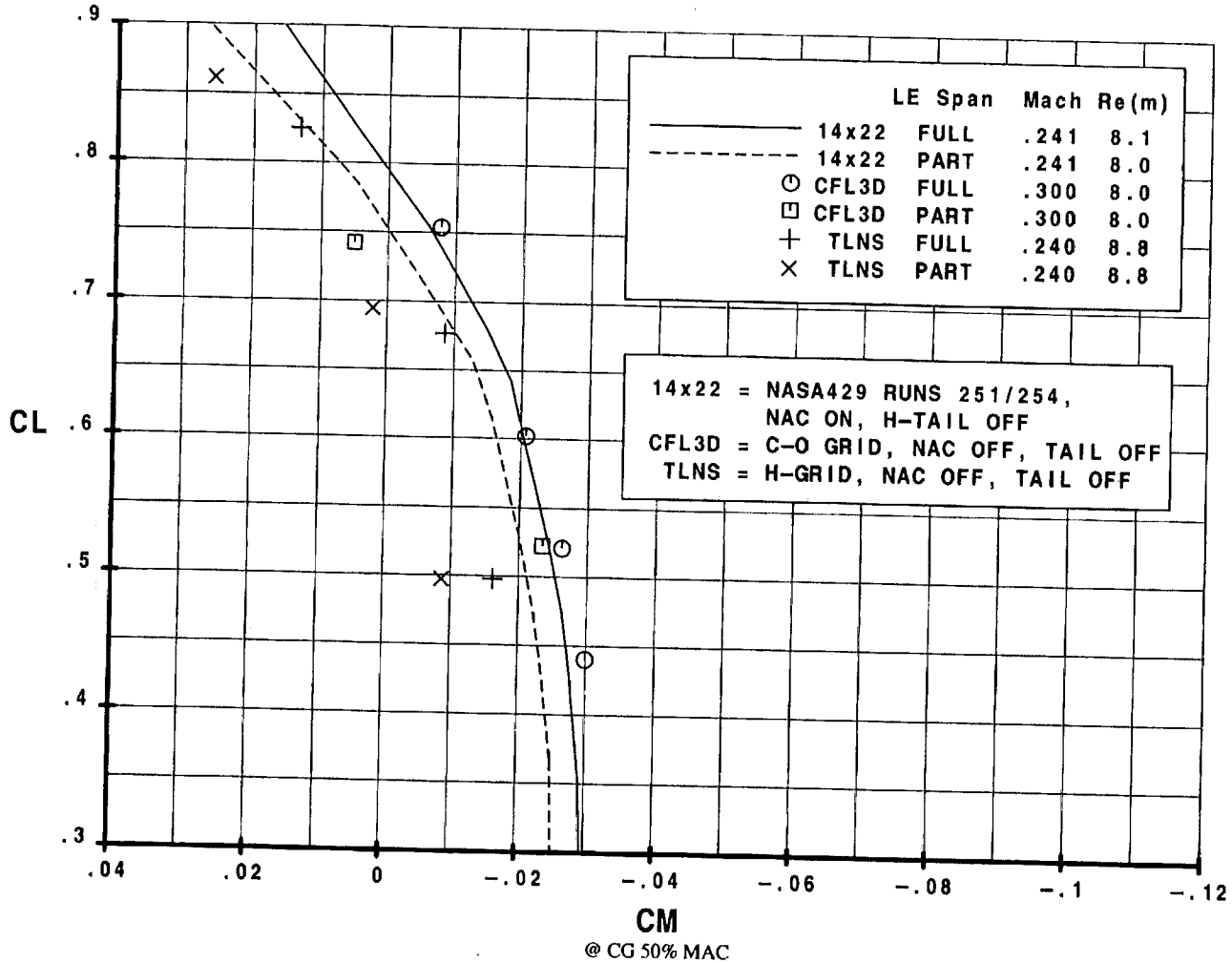

Ref-H CFD Results

This figure the shows a Ref-H CFL3D total pressure ratio comparison between the full-span leading edge case and the part-span leading edge case, both at 10 degrees angle of attack. Total pressure is a convenient way to track vortical flow over the configuration.

With the part-span leading edge, a second vortex can be seen coming from the separation just inboard of the deflected portion of the leading edge. The presence of this second vortex seems to reduce the size of the vortex emanating from the wing apex, resulting in a similar overall total pressure deficit over the wing.

Ref-H CFD Results

Ref-H L30T10

CFL3D L.E. Span Effect - Total Pressure Ratio

Alpha = 10 deg Mach = .3 Re = 8 m/mac

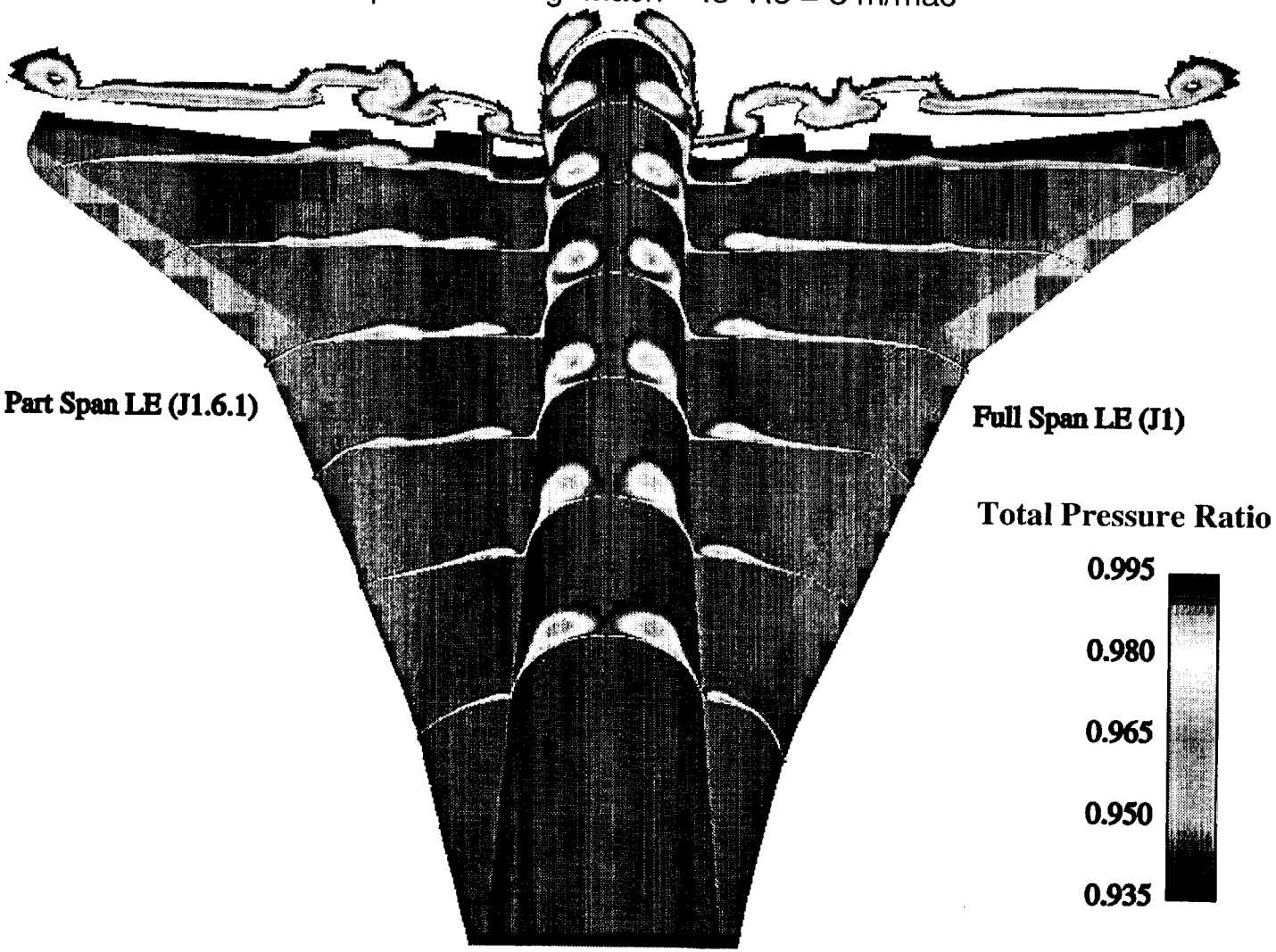

Ref-H CFD Results

This figure the shows a Ref-H CFL3D upper surface pressure coefficient comparison between the full-span leading edge case and the part-span leading edge case, both at 10 degrees angle of attack.

Other than movement of the pressure peak on the inboard leading edge, very little difference is seen between the two solutions over the rest of the wing.

Ref-H CFD Results

Ref-H L30T10

CFL3D L.E. Span Effect - Upper Surface Pressure

Alpha = 10 deg Mach = .3 Re = 8 m/mac

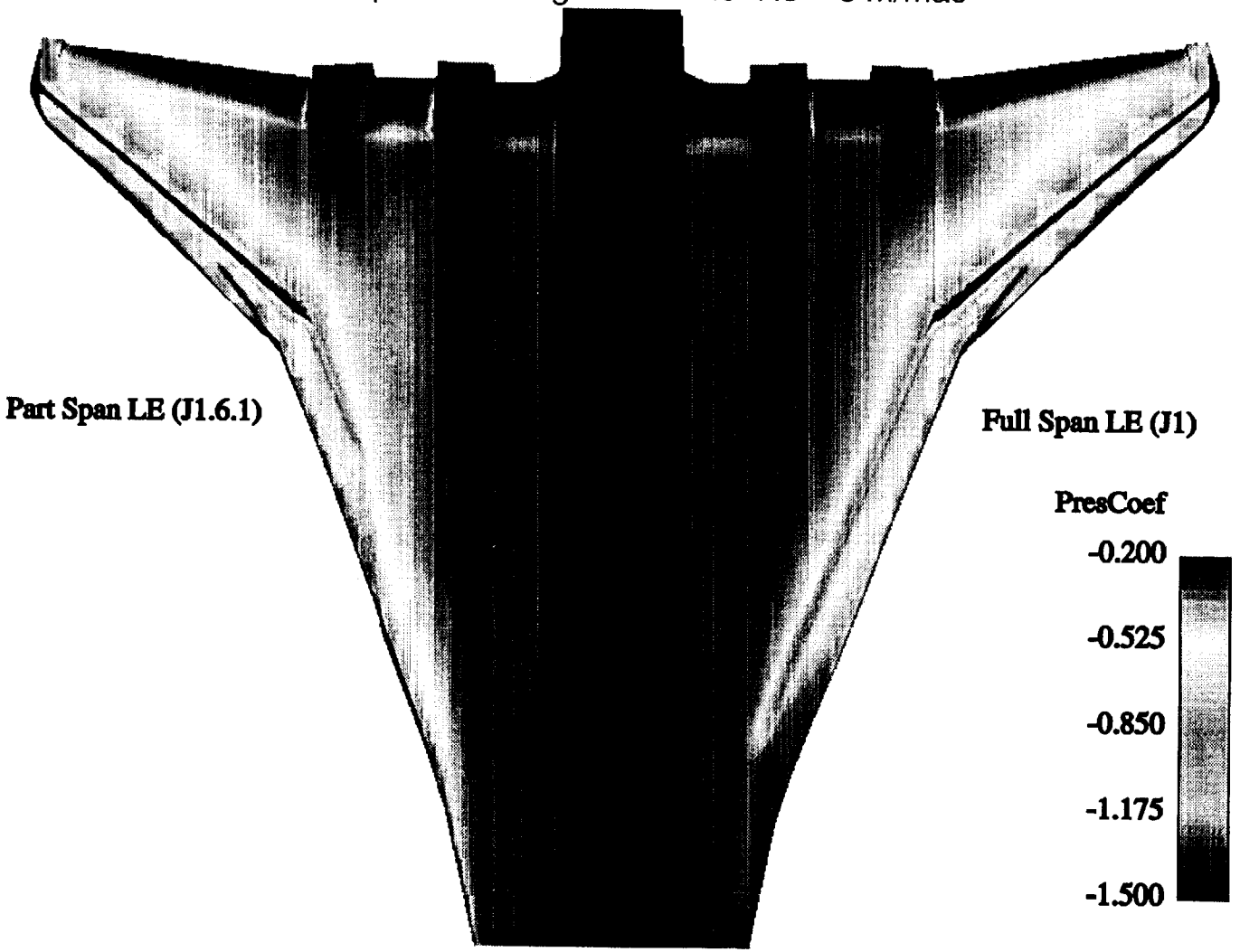

Ref-H CFD Results

This figure the shows a Ref-H TLNS total pressure ratio comparison between the full-span leading edge case and the part-span leading edge case, both at 10 degrees angle of attack. Total pressure is a convenient way to track vortical flow over the configuration.

In the case of TLNS, there is little vortical activity on the inboard wing with the full-span leading edge, while there is a significant vortex formed with the part-span leading edge. The result is a significant change in drag between the two cases, as seen in the force data.

Ref-H CFD Results

Ref-H L30T10

TLNS L.E. Span Effect - Total Pressure Ratio

Alpha = 10 deg Mach = .24 Re = 8.8 m/mac

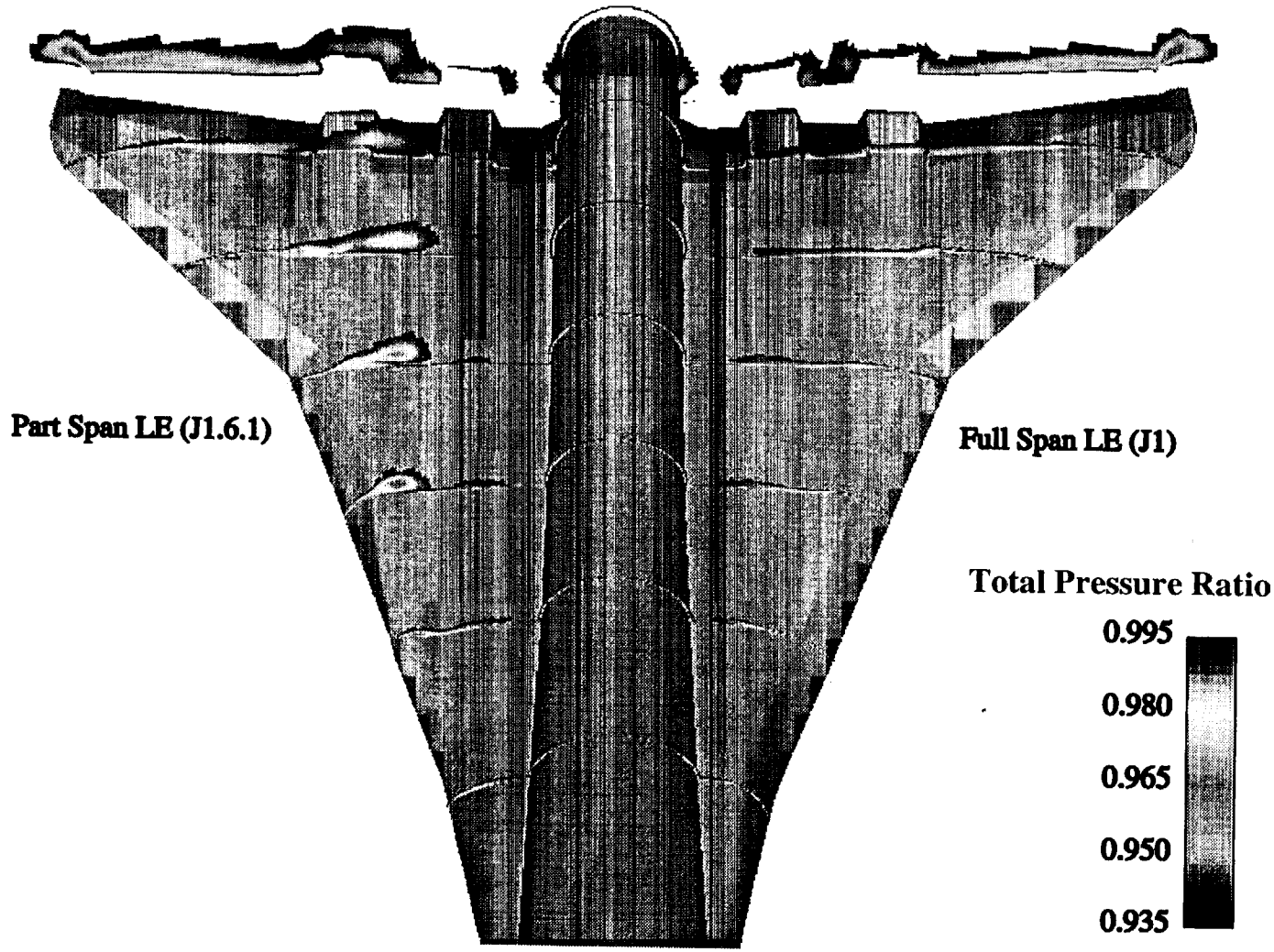

Ref-H CFD Results

This figure the shows a Ref-H TLNS upper surface pressure coefficient comparison between the full-span leading edge case and the part-span leading edge case, both at 10 degrees angle of attack.

With TLNS there is significantly more change in surface pressure due to the leading edge flap span than was seen with CFL3D. The effect of the vortex coming from the inboard end of the part-span leading edge is much more widespread.

Ref-H CFD Results

Ref-H L30T10

TLNS L.E. Span Effect - Upper Surface Pressure

Alpha = 10 deg Mach = .24 Re = 8.8 m/mac

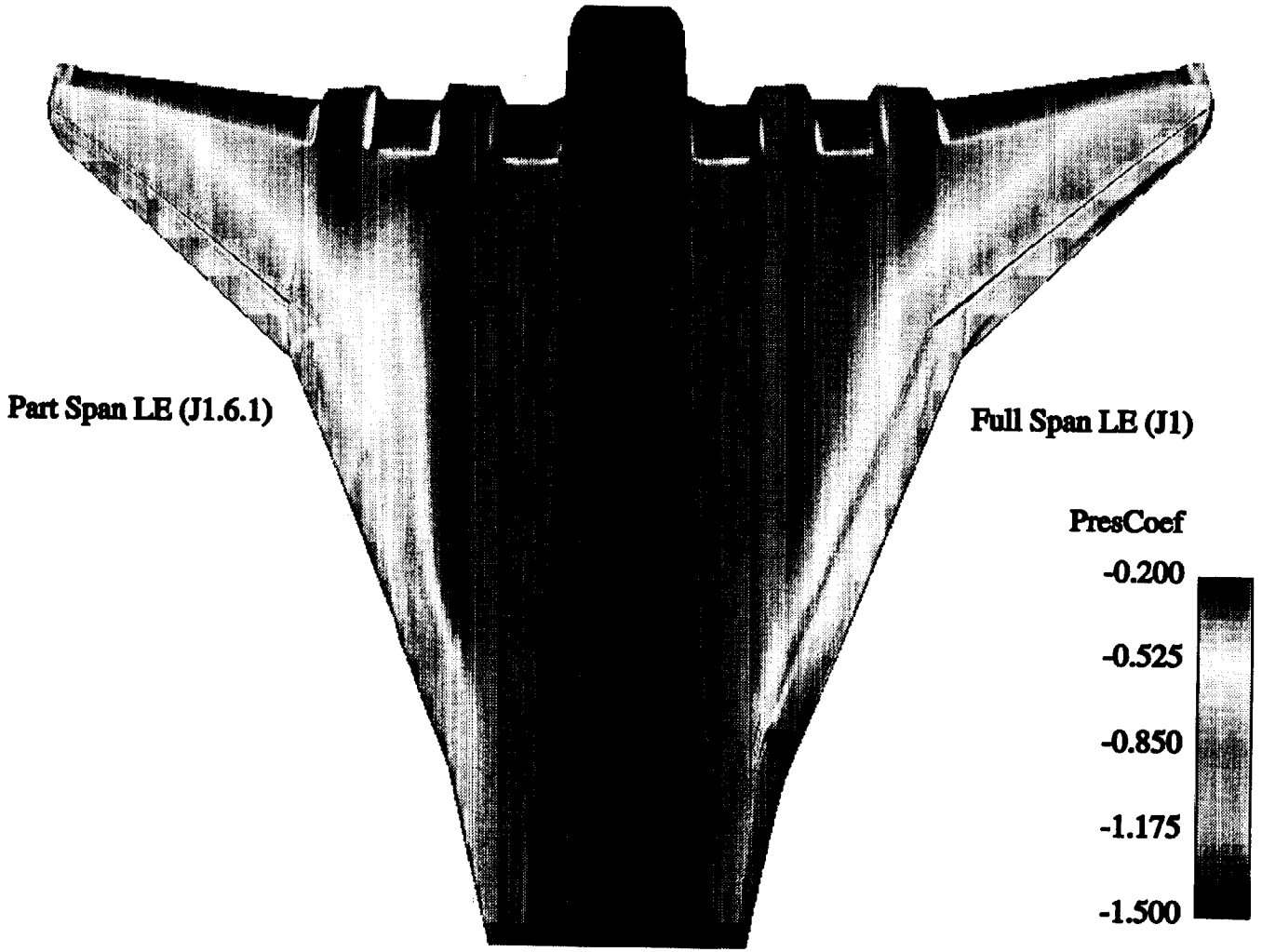

Ref-H CFD Results

This figure shows a total pressure ratio comparison between CFL3D and TLNS, both with full-span leading edge flaps and run at 10 degrees angle of attack. Total pressure is a convenient way to track vortical flow over the configuration.

This figure highlights the difference between the two codes. CFL3D indicates the presence of a well-formed vortex on the inboard wing originating from the wing apex, while TLNS shows a much less significant total pressure deficit over the inboard wing. The difference in the flow over the body is similar to that seen earlier on the TCA configuration, and is most likely due to the grid topology on the forebody.

Ref-H CFD Results

Ref-H L30T10 Full Span L.E.
CFL3D vs TLNS - Total Pressure Ratio

Alpha = 10 deg Re = 8 m/mac

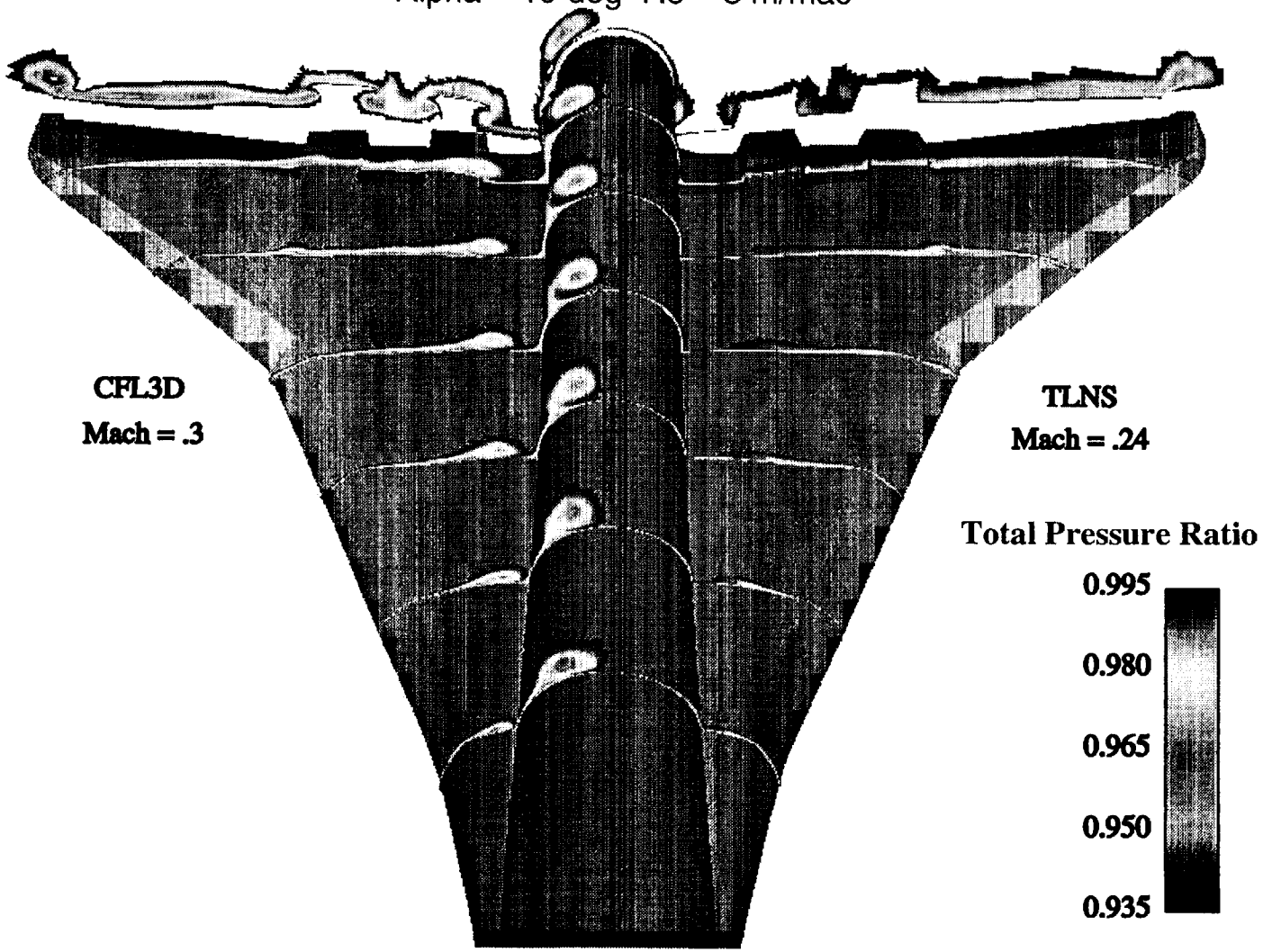

Ref-H CFD Results

This figure shows a total pressure ratio comparison between CFL3D and TLNS, both with part-span leading edge flaps and run at 10 degrees angle of attack. Total pressure is a convenient way to track vortical flow over the configuration.

This figure again highlights the difference between the two codes. CFL3D indicates the presence of a two similarly sized vortices on the inboard wing, while TLNS shows just a single relatively larger vortex coming from the inboard end of the deflected leading edge flaps. Other differences are seen in the flow over the body and in the strength of the wing tip vortex.

Ref-H CFD Results

Ref-H L30T10 Part Span L.E.
CFL3D vs TLNS - Total Pressure Ratio

Alpha = 10 deg Re = 8 m/mac

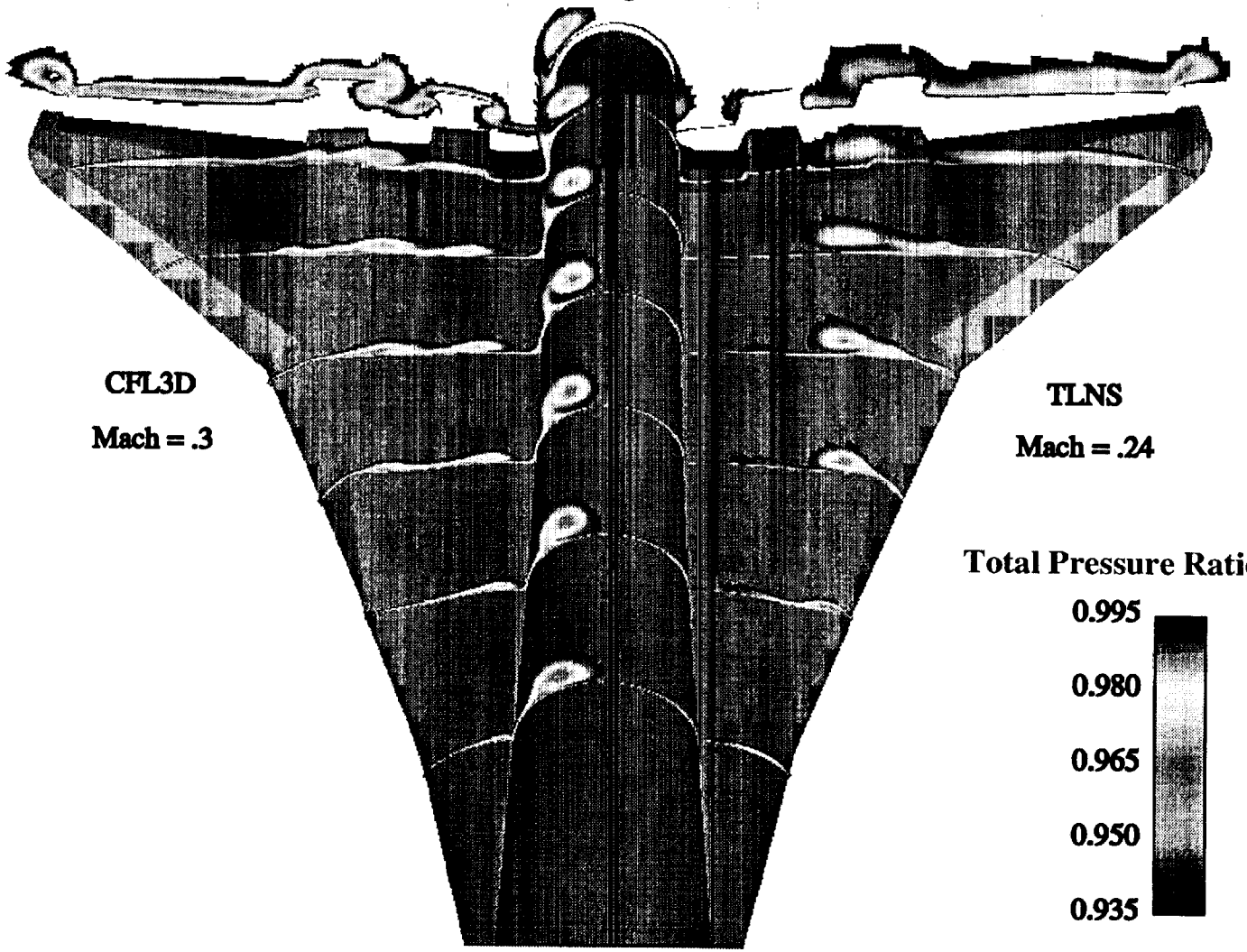

Conclusions & Recommendations

This study has shown that with the Boeing Phantom Works gridding tools, even an inexperienced CFD user can now successfully run 3D Navier-Stokes on a high lift HSCT configuration. These gridding tools simplify the creation of the flaps down grid, and significantly reduce the cycle time required for the numerical analysis. Running on several configurations has also created an opportunity to make the tools more general and more robust.

This study has also shown that the grid topology on the forebody of an HSCT configuration can affect the flow field over the body. This should not significantly influence the results of wing or flap studies, but may become important when looking at canard, chin fin, or other forebody studies. It remains to be verified which of the two body flow fields seen in these results is more realistic.

On the TCA 2.8-38 configuration, the CFD results have shown that CFL3D consistently shows better agreement with the wind tunnel force data than does TLNS. While both codes successfully capture the main flow features, several differences can be seen in the details of the flow field. Various aspects of each code's results are supported by the test data, and further comparison and analysis is warranted.

On the Ref-H configuration, CFL3D was shown to have better agreement with the test data in terms of the effect of leading edge flap span on lift and drag at the operating condition. Both CFL3D and 14x22 test data showed a negligible effect for changing the flap span, while TLNS showed a significant increase in drag for the part-span flaps relative to the full-span flaps. At angles of attack significantly higher than that for the operating condition, CFL3D did not converge well, especially with the part-span leading edge. Previous results with TLNS have shown good convergence and good results at these higher angles of attack.

This study has also left many questions unanswered and has shown a need for more comparisons between CFD results and test data. The upcoming CFD wind tunnel test in the Ames 7x10 tunnel and the upcoming TCA-5 test in the Ames 12' tunnel should provide a wealth of good data for further study of this kind. The CFD test will be using the Ref-H configuration, while TCA-5 will be using the TCA 2.8-38 configuration. Continued work in this area will pave the way for further optimization of high lift aerodynamic performance

Conclusions & Recommendations

- With Phantom Works tools, even a 2D panel code user can now run 3D High Lift Navier-Stokes
- Grid topology affects flow over the body and may become important for forebody studies
- On the TCA configuration, CFL3D consistently matches the wind tunnel force data better than TLNS
- On the Ref-H configuration, CFL3D does better than TLNS in capturing leading edge flap effects at the operating condition
- TLNS converges better than CFL3D at higher angles of attack for the configuration studied
- The upcoming 7x10 CFD test and TCA-5 test should give us good data for further N-S code comparisons

ASE Technologies, Inc.

Comparison of CFD Solutions with Test Data for TCA High Lift Configurations

Xuetong Fan
ASE Technologies, Inc.

High Speed Research Program
Airframe Technical Review
Anaheim Marriott, Anaheim, California
February 9–12, 1999

This report documents the comparison between CFL3D solutions and wind tunnel test data for TCA high lift wing/body and wing/body/nacelle configurations.This work is completed under the direction of Roger Clark of Boeing Long Beach. I hereby acknowledge the support and help from Roger Clark, David Yeh, and Ryan Polito of Boeing Long Beach.

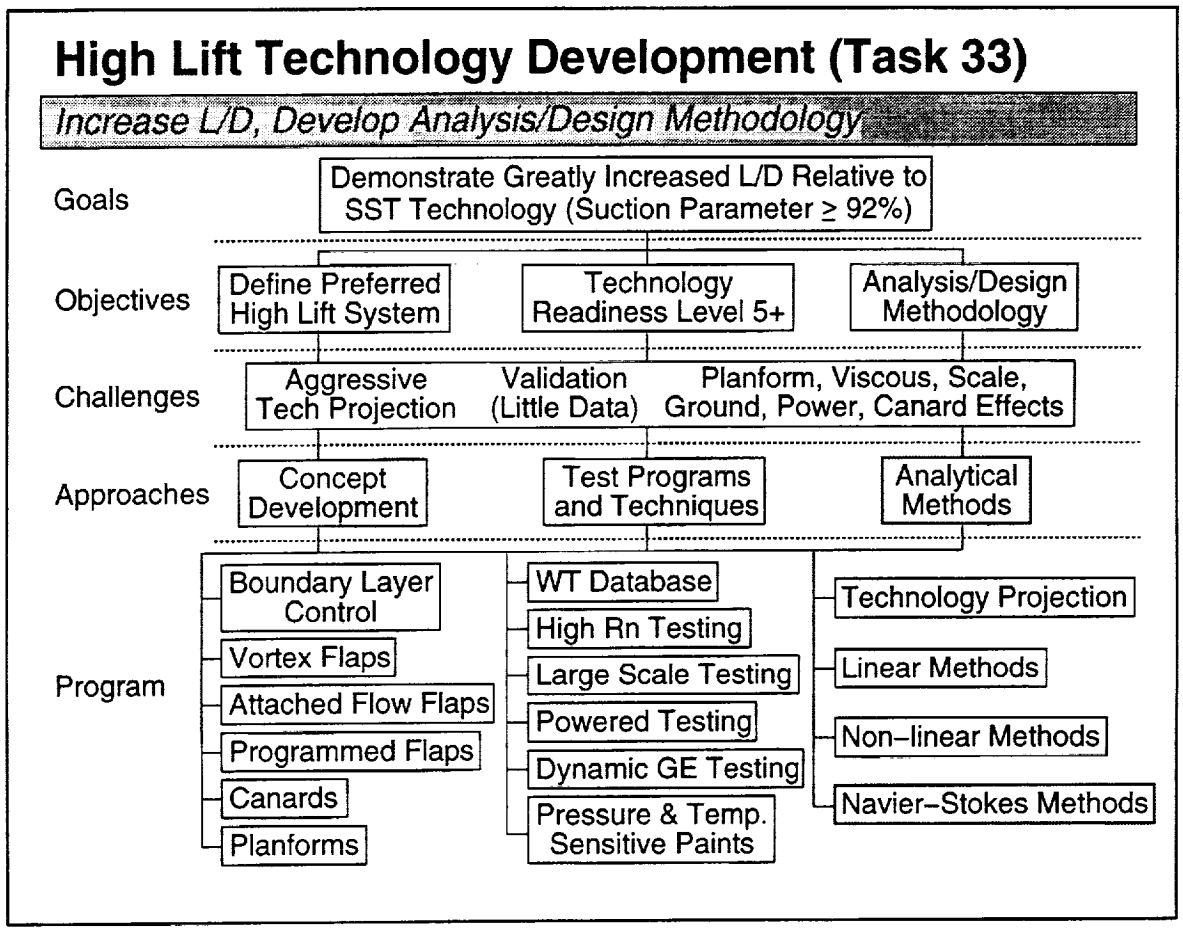

In the High Lift Technology Development program (Task 33), this work falls in the category of Navier–Stokes Methods under Analytical Methods.

Objectives and Scope

- To better understand the aerodynamics of TCA high lift configurations
- To evaluate and document the results of comparison between CFL3D solutions and wind tunnel test data
- To assess the capability of CFD methods in high lift applications
- Configurations:
  - TCA High Lift W/B and W/B/N (partial span)
  - Flap Settings: 0/0 and 30/10
- Test Data:
  - Integrated Forces: TCA 3 Test
  - Pressure Data: TCA 1 Test
- CFL3D Solutions:
  - W/B Solutions: AOA=10 and 12 degrees completed by Boeing
  - W/B/N Solutions: AOA=10 and 12 degrees completed by ASE

The main objective of this work is to evaluate and document the comparison between CFL3D solutions and wind tunnel test data for TCA high lift configurations. Through this effort, we hope to obtain a better understanding of the aerodynamics of TCA high lift configurations and a more accurate assessment of the CFD capabilities.

The configurations we studied in this work include the baseline TCA wing/body and wing/body/nacelle with partial-span leading edge flaps and flap settings of 0/0 and 30/10. The CFL3D solutions were obtained at AOA=10 and 12 degrees. The integrated force data were from the TCA-3 test and the pressure data were from TCA-1 test.

Outline

Part I: Comparison of Integrated Forces

- To compare values of C_L and C_D between CFL3D and Test Data
- To evaluate lift and drag increments due to nacelles

Part II: Comparison of Pressure Distribution on Wing Surfaces

- To compare strength and locations of LE vortices between CFL3D and test data
- To identify bad data points or pressure taps in test data

Part III: Comparison of Change in Pressure Distribution from Wing/Body to Wing/Body/Nacelle

- To evaluate the effect of nacelles on pressure distribution
- To compare changes in LE vortex locations between W/B and W/B/N

This report includes three parts. Part I compares the lift and drag coefficients between CFL3D and test data with emphasis on the predicted and measured lift and drag increments due to nacelles. Part II compares the pressure distribution on wing upper and lower surfaces between CFL3D and test data to show the strength and locations of LE vortices. Part III compares the change in pressure distribution from wing/body to wing/body/nacelle on wing upper surface. This comparison will reveal the effect of nacelles on the LE vortices.

Part I
Comparison of Integrated Forces

Part I includes the comparison of integrated lift and drag forces.

Lift and Drag Coefficients: TCA 0/0

C_L	AOA=10 Degrees		AOA=12 Degrees	
	CFL3D	Experiment	CFL3D	Experiment
W/B	0.3819	0.3749	0.4735	0.4560
W/B/N	0.4111	0.3711	0.4852	0.4500
W/B/N–W/B	0.0292	–0.0038	0.0117	–0.0060

C_D	AOA=10 Degrees		AOA=12 Degrees	
	CFL3D	Experiment	CFL3D	Experiment
W/B	0.0581	0.0606	0.0890	0.0883
W/B/N	0.0645	0.0616	0.0935	0.0891
W/B/N–W/B	0.0064	0.0010	0.0045	0.0008

These two tables show the predicted and measured lift and drag coefficients for TCA 0/0 W/B and W/B/N configurations at AOA=10 and 12 degrees. Considerable differences in C_L and C_D are found between the CFL3D prediction and the wind tunnel measurements. In particular, the test data shows that C_L decreases due to nacelles whereas CFL3D predicts the opposite.

Lift and Drag Coefficients: TCA 30/10

C_L	AOA=10 Degrees		AOA=12 Degrees	
	CFL3D	Experiment	CFL3D	Experiment
W/B	0.4424	0.4260	0.5283	0.4981
W/B/N	0.4635	0.4697	0.5486	0.5440
W/B/N-W/B	0.0211	0.0437	0.0203	0.0459

C_D	AOA=10 Degrees		AOA=12 Degrees	
	CFL3D	Experiment	CFL3D	Experiment
W/B	0.0500	0.0505	0.0837	0.0686
W/B/N	0.0581	0.0602	0.0917	0.0867
W/B/N-W/B	0.0081	0.0097	0.0080	0.0181

These two tables show the predicted and measured lift and drag coefficients for TCA 30/10 W/B and W/B/N configurations at AOA=10 and 12 degrees. Again, considerable differences in C_L and C_D are found between the CFL3D predictions and the wind tunnel measurements. In terms of nacelle effect, both test data and CFL3D show an increase in C_L due to nacelles.

Integrated Force Comparison for TCA 0/0: C_L vs. AOA

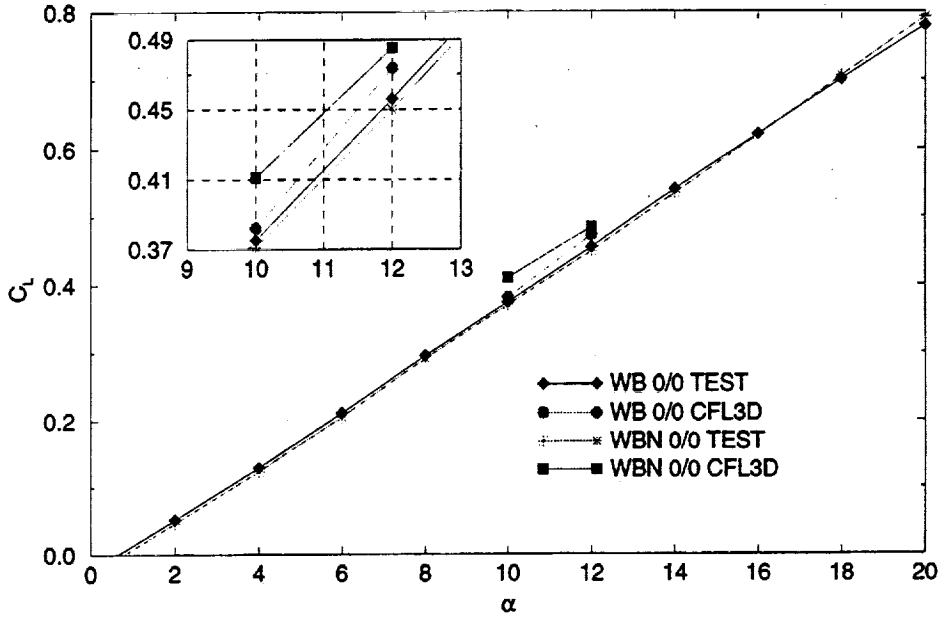

This figure shows the CFL3D data points on the lift curve from test data for TCA 0/0 configurations.

Integrated Force Comparison for TCA 0/0: C_L vs. C_D

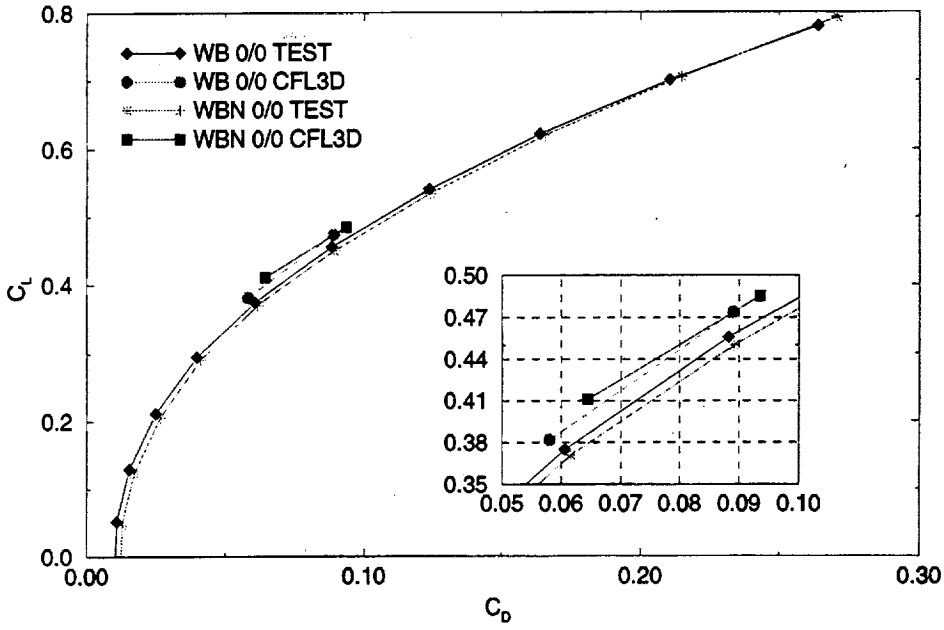

This figure shows the CFL3D data points on the drag polar plot from test data for TCA 0/0 configurations.

Integrated Force Comparison for TCA 0/0: L/D vs. C_L

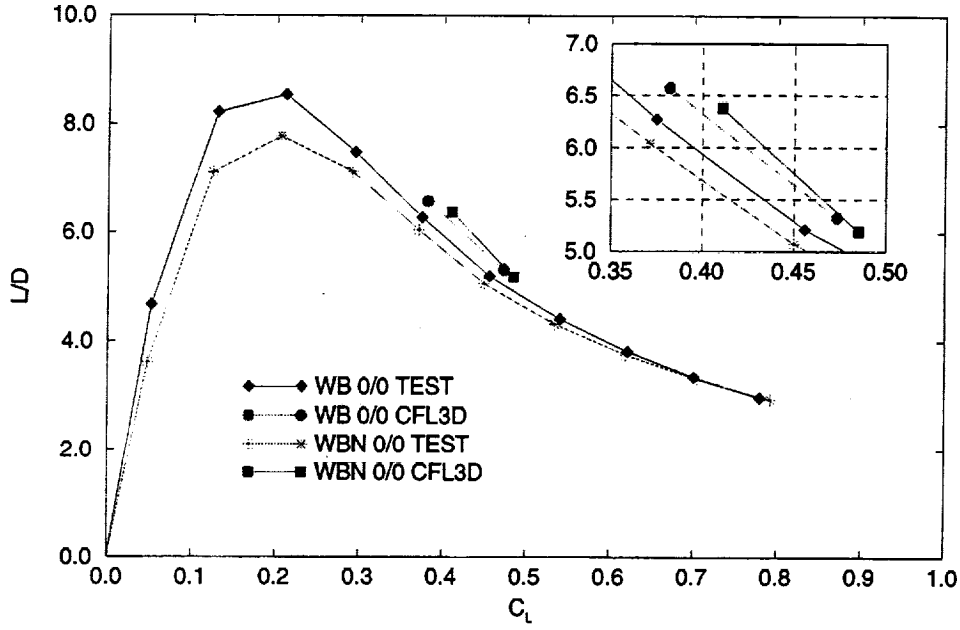

This figure shows the CFL3D data points on the L/D vs. C_L curve from test data for TCA 0/0 configurations.

Integrated Force Comparison for TCA 30/10: C_L vs. AOA

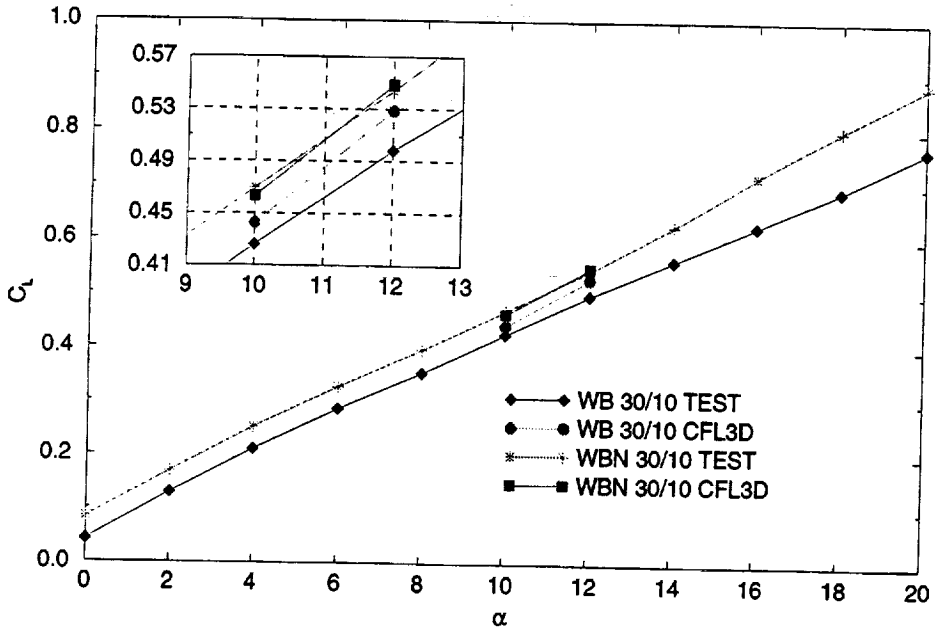

This figure shows the CFL3D data points on the lift curve from test data for TCA 30/10 configurations.

Integrated Force Comparison for TCA 30/10: C_L vs. C_D

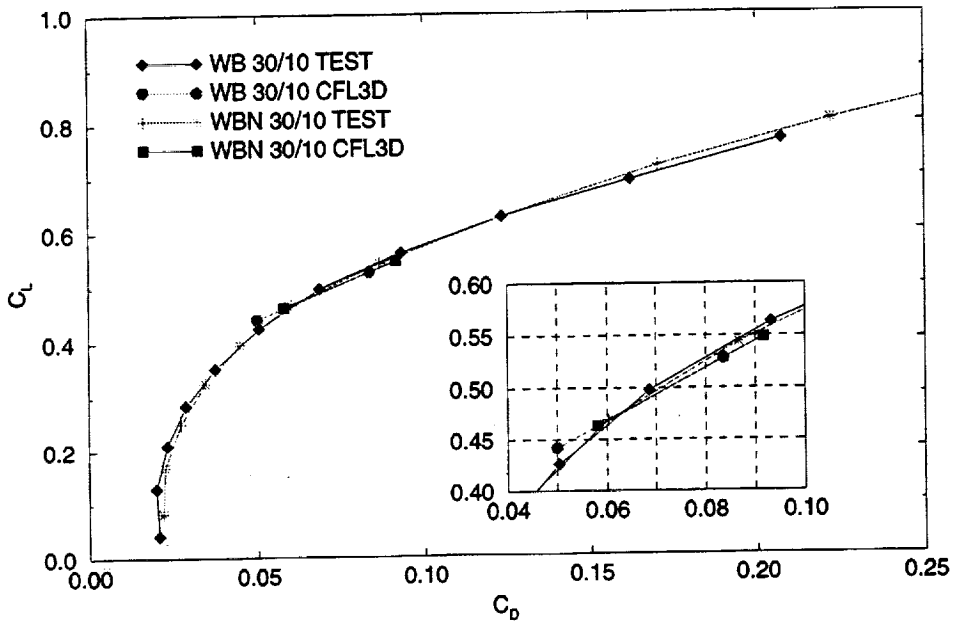

This figure shows the CFL3D data points on the drag polar plot from test data for TCA 30/10 configurations.

Integrated Force Comparison for TCA 30/10: L/D vs. C_L

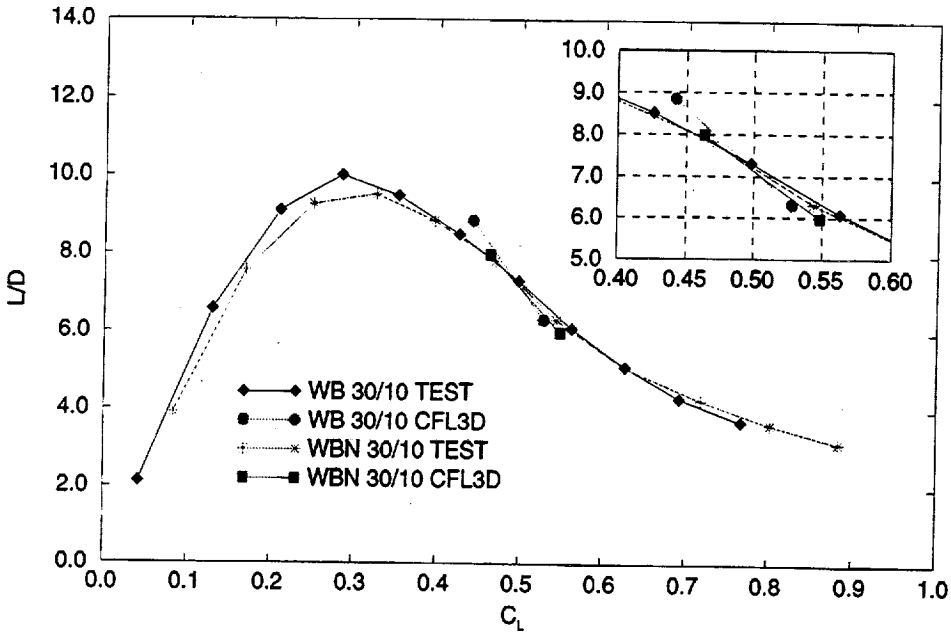

This figure shows the CFL3D data points on the L/D vs. C_L curve from test data for TCA 30/10 configurations.

Summary: Comparison of Integrated Forces

- C_L and C_D values predicted by CFL3D are close to test data, but discrepancies exist
- CFL3D solutions and test data show inconsistent trend in lift and drag increment due to nacelles
- Suggestions for future effort::
  - Make more CFL3D runs to expand data base
  - Investigate further into test data correction

In summary, The predicted lift and drag coefficients are close to test data at certain points but discrepancies exist. In particular, CFL3D and test data show a different trend in lift increment due to nacelles for TCA 0/0 configurations.

For future effort, more CFL3D runs should be performed to expand the CFD data base. In addition, the detailed corrections to the test data should be documented to ensure consistent data comparison.

Part II
Comparison of Pressure Distribution on Wing Surfaces

Part II includes the comparison of pressure disribution on wing upper and lower surfaces. The comparison will be performed for the spanwise pressure distribution on wing upper and lower surfaces between CFL3D solutions and wind tunnel test data for TCA high lift configurations.

Wing Surface Pressure Distribution

TCA 0/0 W/B AOA=10 Degrees

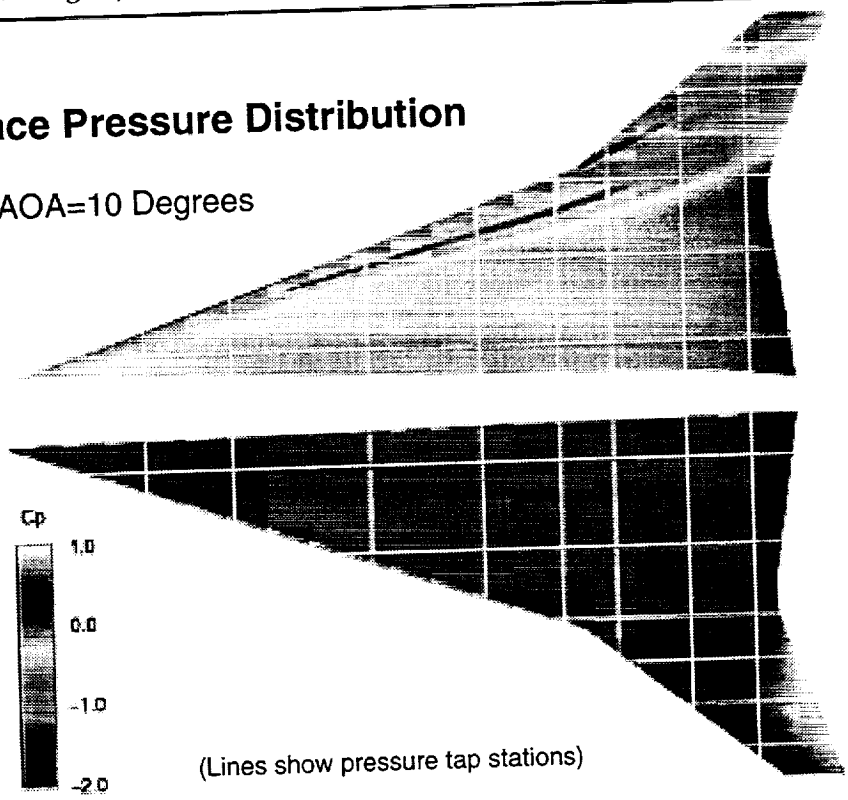

This figure shows the predicted pressure distribution on wing upper and lower surfaces for TCA 0/0 wing/body configuration at AOA=10 degrees. The lines show the streamwise and spanwise stations where the pressure taps are located. The comparison of spanwise pressure distribution will be performed at eight streamwise stations as shown.

Spanwise Pressure Distribution: CFL3D vs. Test Data

TCA 0/0 W/B AOA=10 Degrees

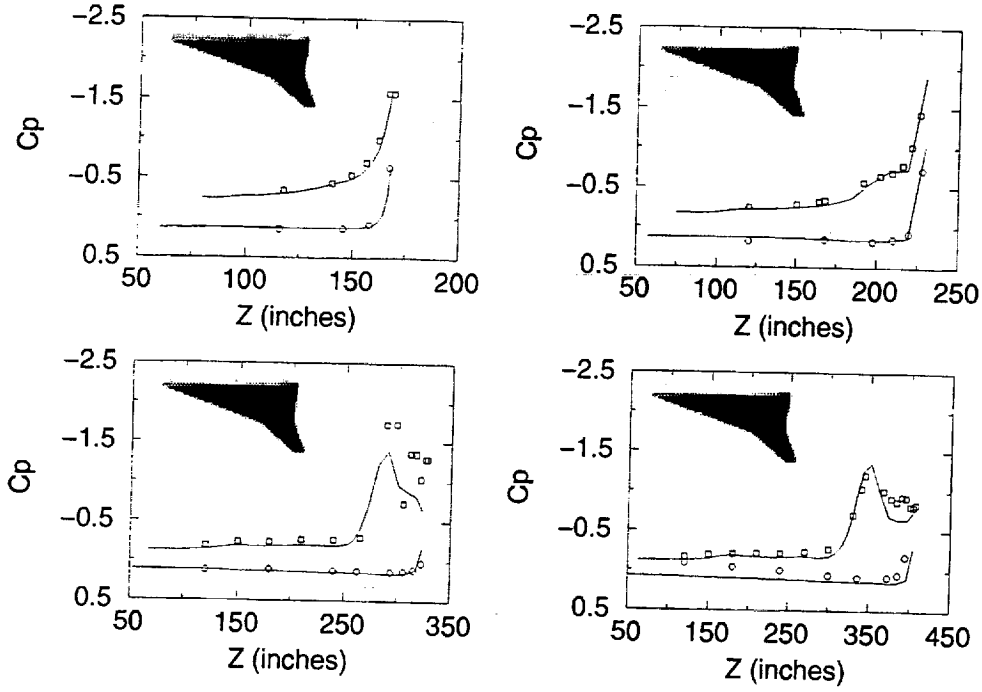

These figures show the spanwise pressure distribution at the four upstream stations for TCA 0/0 wing/body configuration at AOA=10 degrees. Good agreement is found between the CFL3D solution (shown in lines) and the test data (shown in legends).

Spanwise Pressure Distribution: CFL3D vs. Test Data

TCA 0/0 W/B AOA=10 Degrees

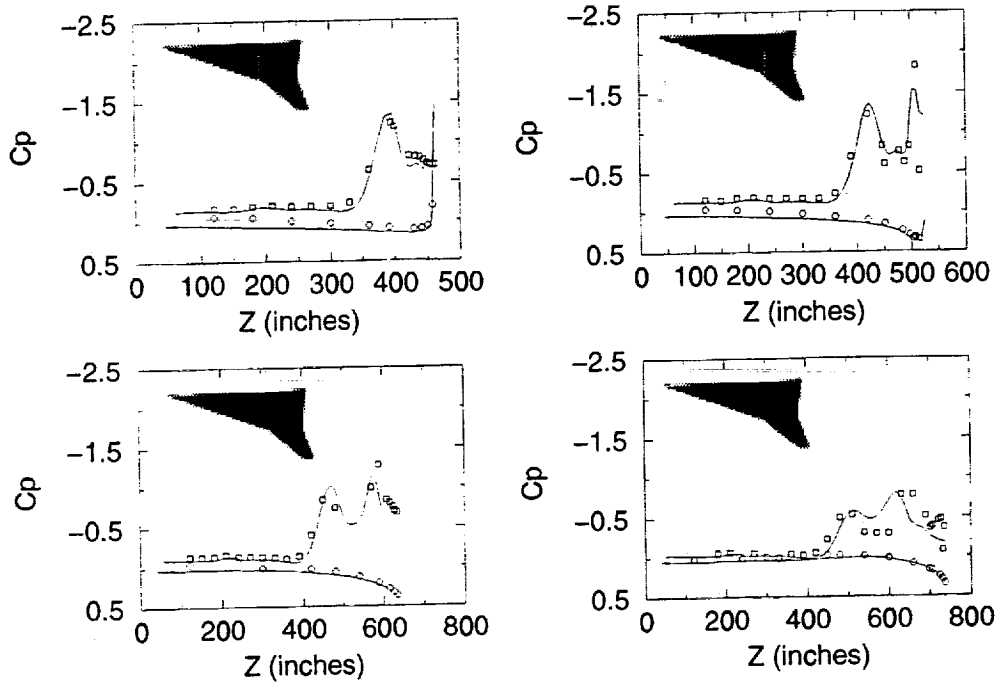

These figures show the spanwise pressure distribution at the four downstream stations for TCA 0/0 wing/body configuration at AOA=10 degrees. Again, good agreement is found between the CFL3D solution and the test data. In particular, Both CFL3D and test data show two pressure peaks which represent two separate LE vortices.

Wing Surface Pressure Distribution

TCA 0/0 W/B AOA=12 Degrees

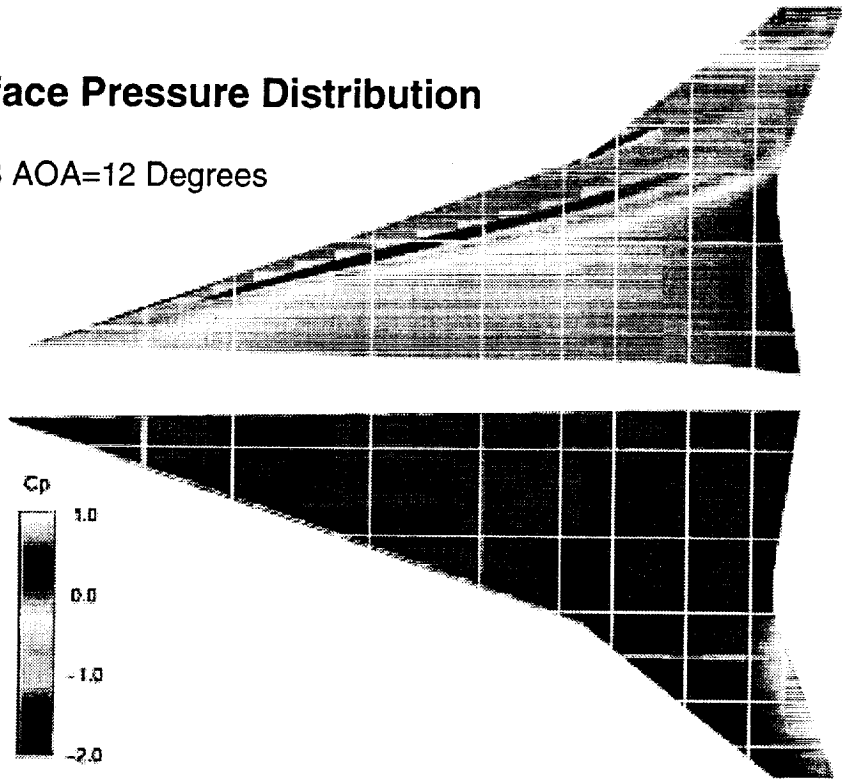

This figure shows the predicted pressure distribution on wing upper and lower surfaces for TCA 0/0 wing/body configuration at AOA=12 degrees.

Spanwise Pressure Distribution: CFL3D vs. Test Data

TCA 0/0 W/B AOA=12 Degrees

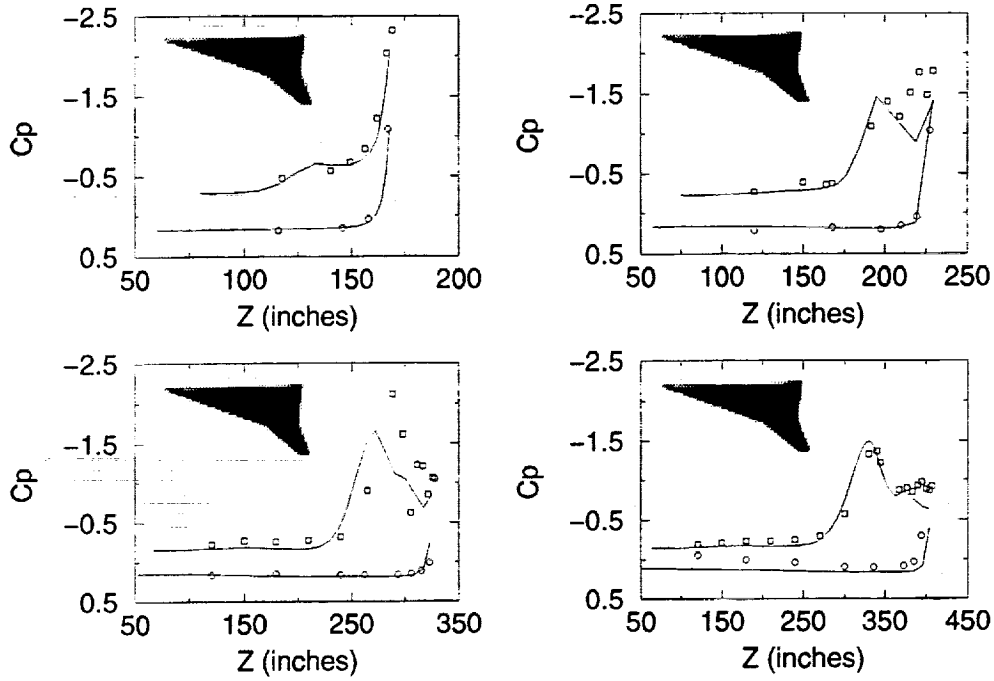

These figures show the spanwise pressure distribution at the four upstream stations for TCA 0/0 wing/body configuration at AOA=12 degrees. Good agreement is found between the CFL3D solution and the test data.

Spanwise Pressure Distribution: CFL3D vs. Test Data

TCA 0/0 W/B AOA=12 Degrees

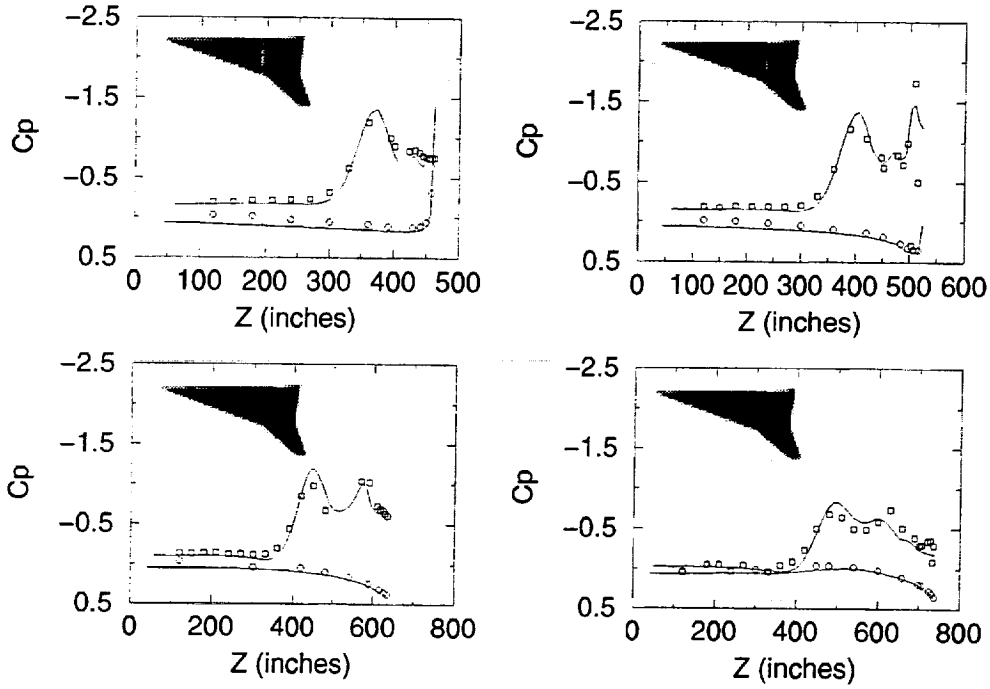

These figures show the spanwise pressure distribution at the four downstream stations for TCA 0/0 wing/body configuration at AOA=12 degrees. Good agreement is found between the CFL3D solution and the test data. Again, two pressure peaks represent the two separate vortices.

Wing Surface Pressure Distribution

TCA 30/10 W/B AOA=10 Degrees

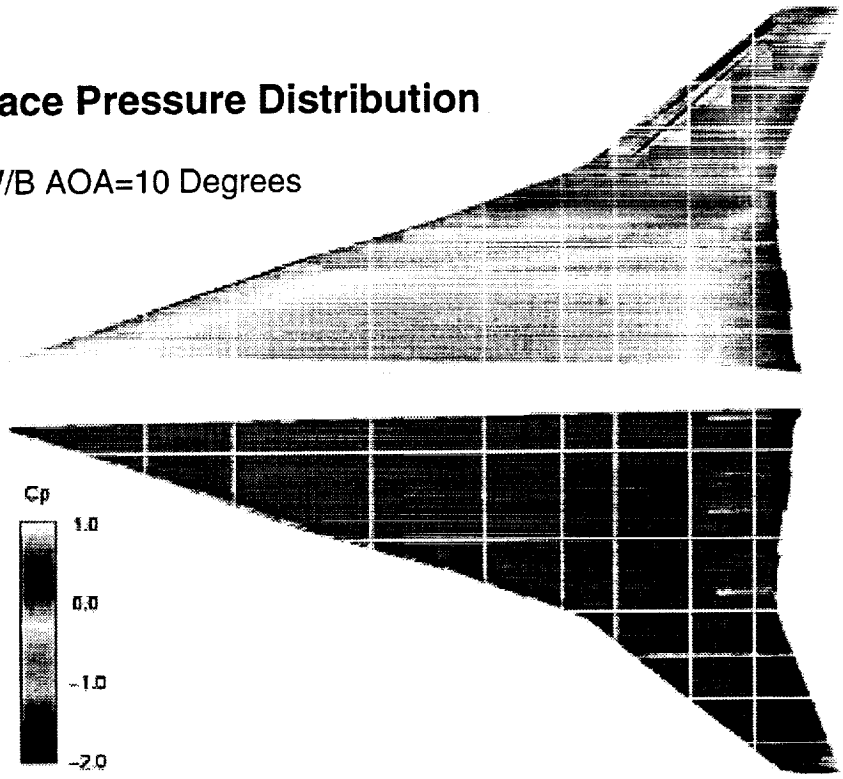

This figure shows the predicted pressure distribution on wing upper and lower surfaces for TCA 30/10 wing/body configuration at AOA=10 degrees.

Spanwise Pressure Distribution: CFL3D vs. Test Data

TCA 30/10 W/B AOA=10 Degrees

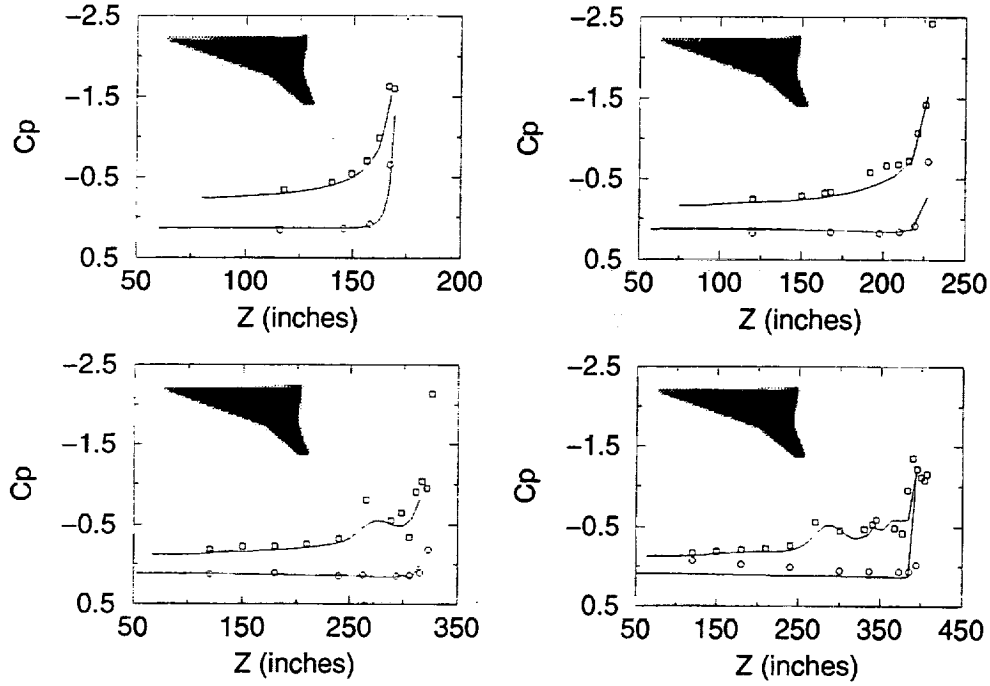

These figures show the spanwise pressure distribution at the four upstream stations for TCA 30/10 wing/body configuration at AOA=10 degrees. Good agreement is found between the CFL3D solution and the test data. At these upstream stations, there is no apparent LE vortex.

Spanwise Pressure Distribution: CFL3D vs. Test Data

TCA 30/10 W/B AOA=10 Degrees

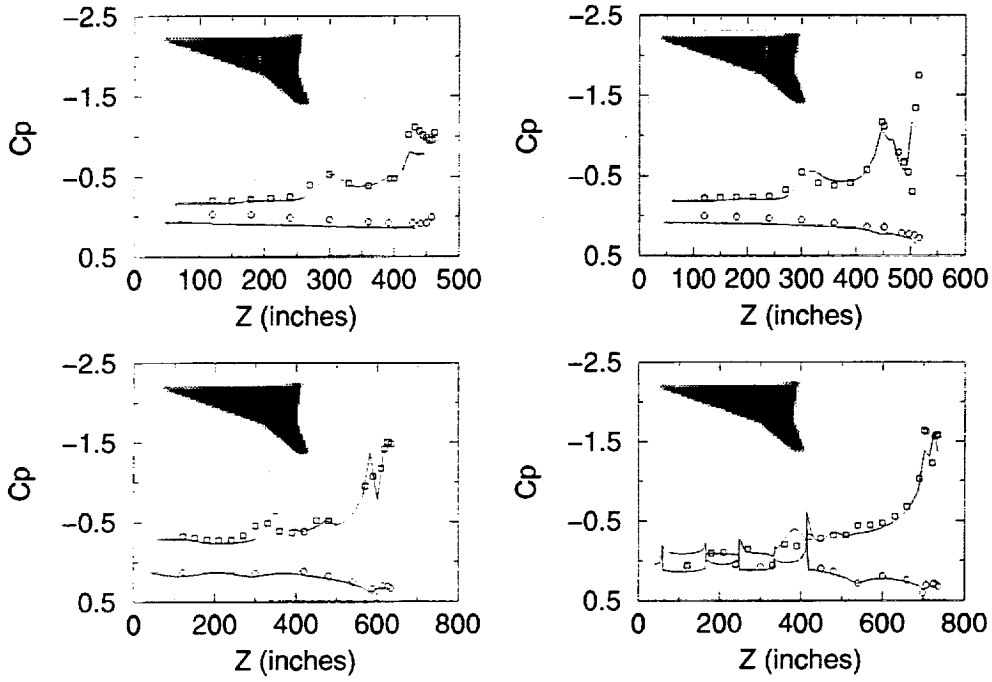

These figures show the spanwise pressure distribution at the four downstream stations for TCA 30/10 wing/body configuration at AOA=10 degrees. Good agreement is found between the CFL3D solution and the test data. In particular, the CFL3D solution and the test data picked up the same pressure peak in the outboard wing section.

Wing Surface Pressure Distribution

TCA 30/10 W/B AOA=12 Degrees

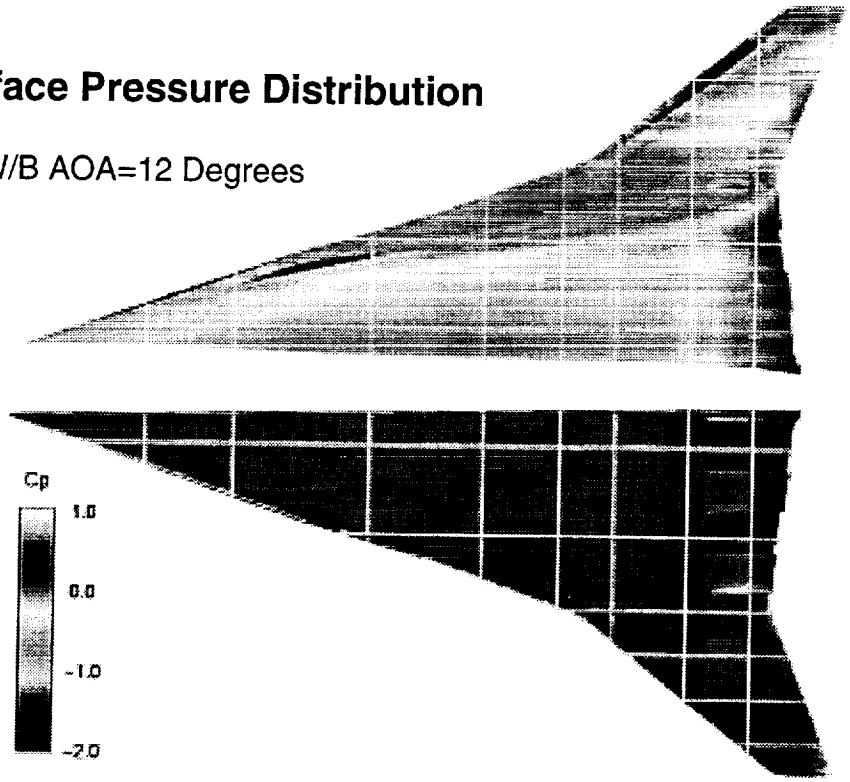

This figure shows the predicted pressure distribution on wing upper and lower surfaces for TCA 30/10 wing/body configuration at AOA=12 degrees.

Spanwise Pressure Distribution: CFL3D vs. Test Data

TCA 30/10 W/B AOA=12 Degrees

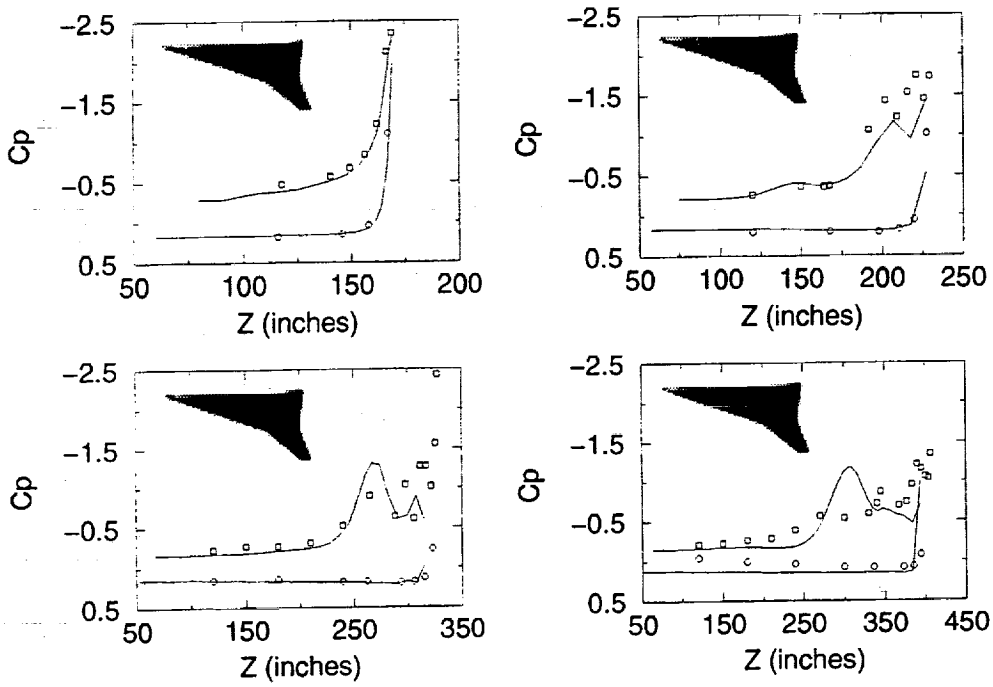

These figures show the spanwise pressure distribution at the four upstream stations for TCA 30/10 wing/body configuration at AOA=12 degrees. Good agreement is found between the CFL3D solution and the test data. There appears to be a vortex formation off the leading edge.

Spanwise Pressure Distribution: CFL3D vs. Test Data

TCA 30/10 W/B AOA=12 Degrees

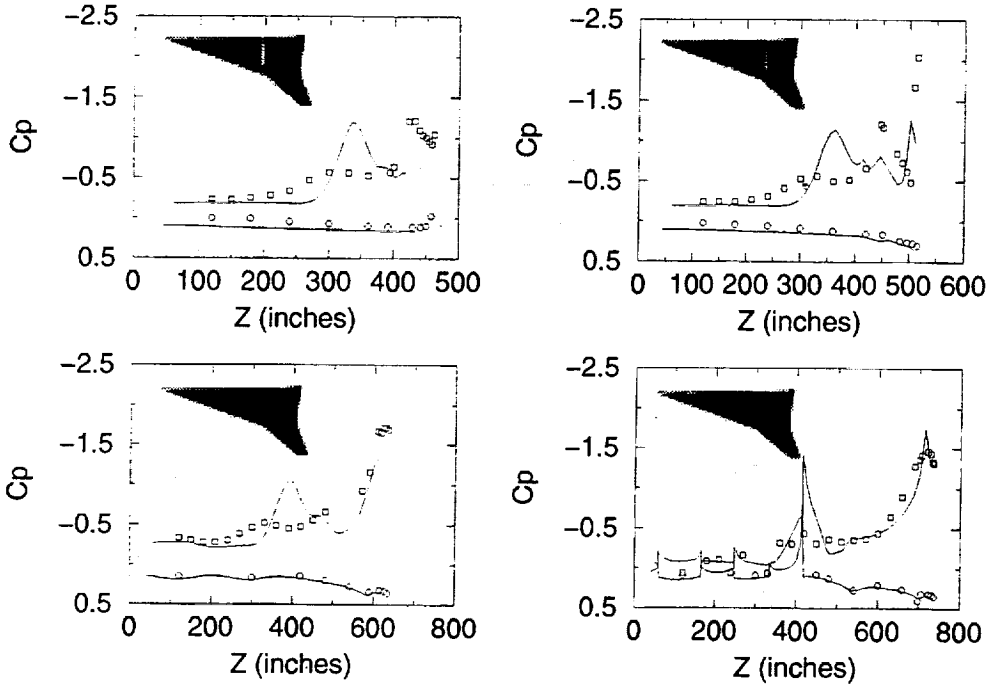

These figures show the spanwise pressure distribution at the four downstream stations for TCA 30/10 wing/body configuration at AOA=12 degrees. The CFL3D solution indicates that the LE vortex remains attached to the wing upper surface whereas the test data does not contain the pressure peak. Otherwise, good agreement is found between the CFL3D solution and the test data.

Wing Surface Pressure Distribution

TCA 0/0 W/B/N AOA=10 Degrees

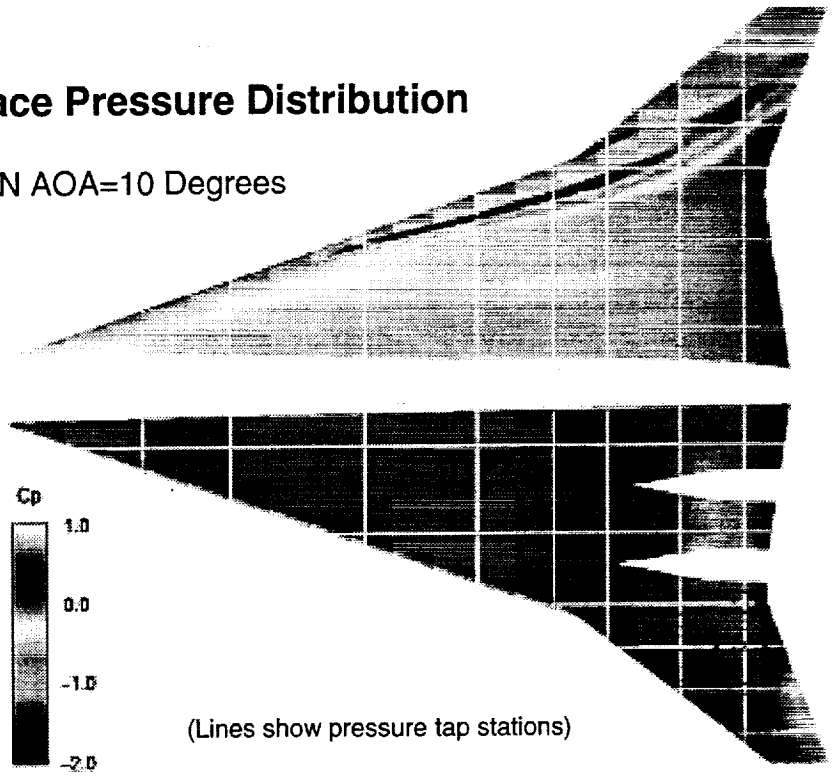

This figure shows the predicted pressure distribution on wing upper and lower surfaces for TCA 0/0 wing/body/nacelle configuration at AOA=10 degrees. It appears that the two vortices off the leading edge merged into one in the outboard region.

Spanwise Pressure Distribution: CFL3D vs. Test Data

TCA 0/0 W/B/N AOA=10 Degrees

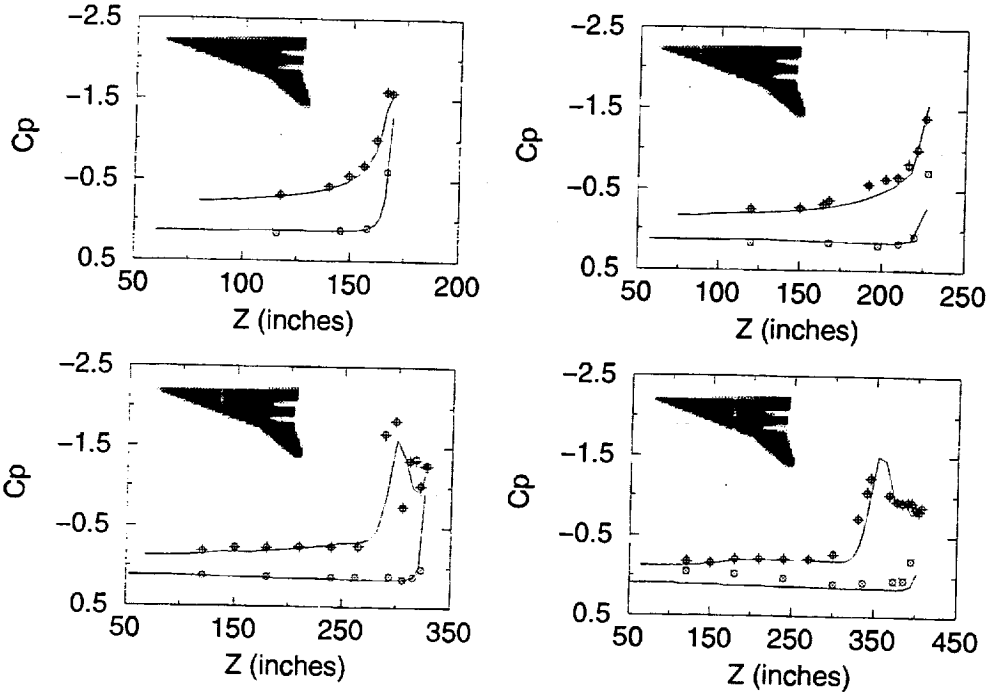

These figures show the spanwise pressure distribution at the four upstream stations for TCA 0/0 wing/body/nacelle configuration at AOA=10 degrees. Good agreement is found between the CFL3D solution and the test data.

Spanwise Pressure Distribution: CFL3D vs. Test Data

TCA 0/0 W/B/N AOA=10 Degrees

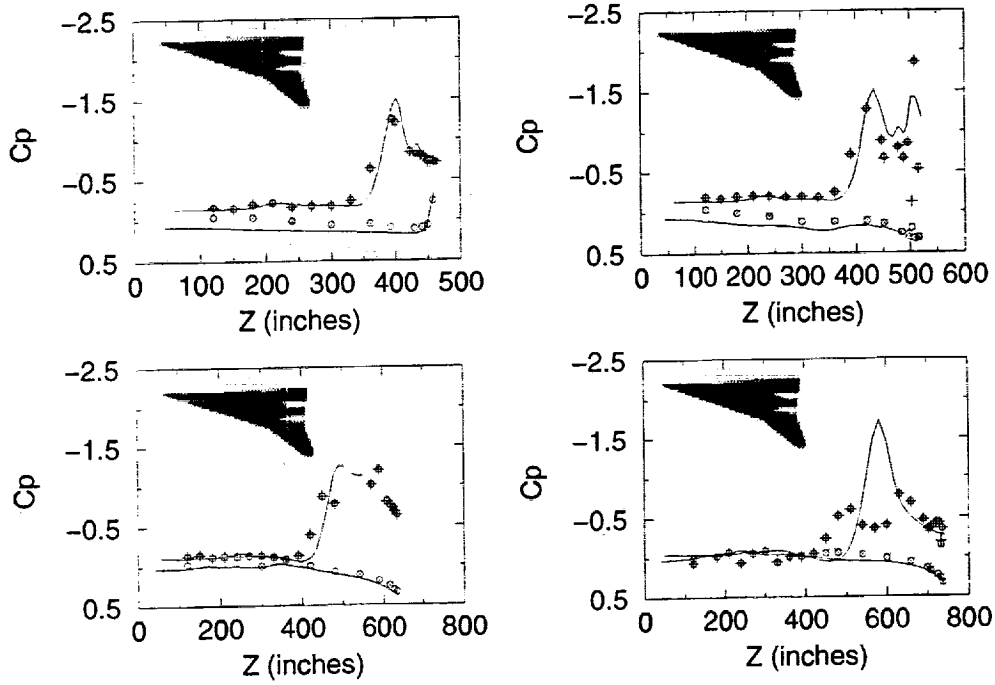

These figures show the spanwise pressure distribution at the four downstream stations for TCA 0/0 wing/body/nacelle configuration at AOA=10 degrees. The two distinct pressure peaks in the test data show that the two LE vortices remain separate. However, there is only one peak in the CFL3D solution which indicate the merging of the two LE vortices

Wing Surface Pressure Distribution

TCA 0/0 W/B/N AOA=12 Degrees

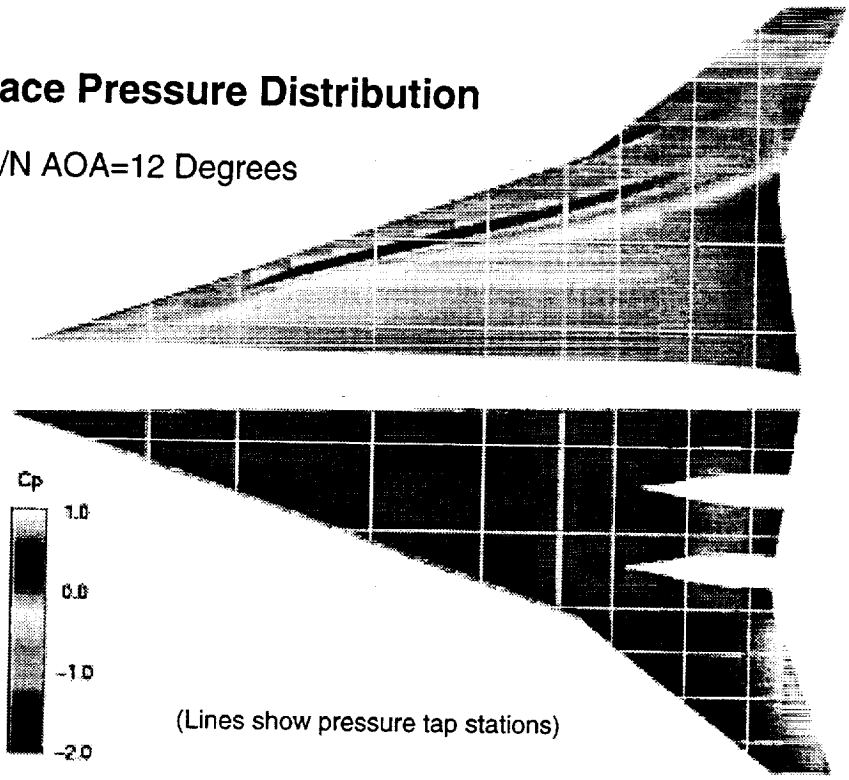

This figure shows the predicted pressure distribution on wing upper and lower surfaces for TCA 0/0 wing/body/nacelle configuration at AOA=12 degrees. Unlike the case at AOA=10 degrees, It is clear from the pressure distribution that the two LE vortices remain separate in the CFL3D solution.

Spanwise Pressure Distribution: CFL3D vs. Test Data

TCA 0/0 W/B/N AOA=12 Degrees

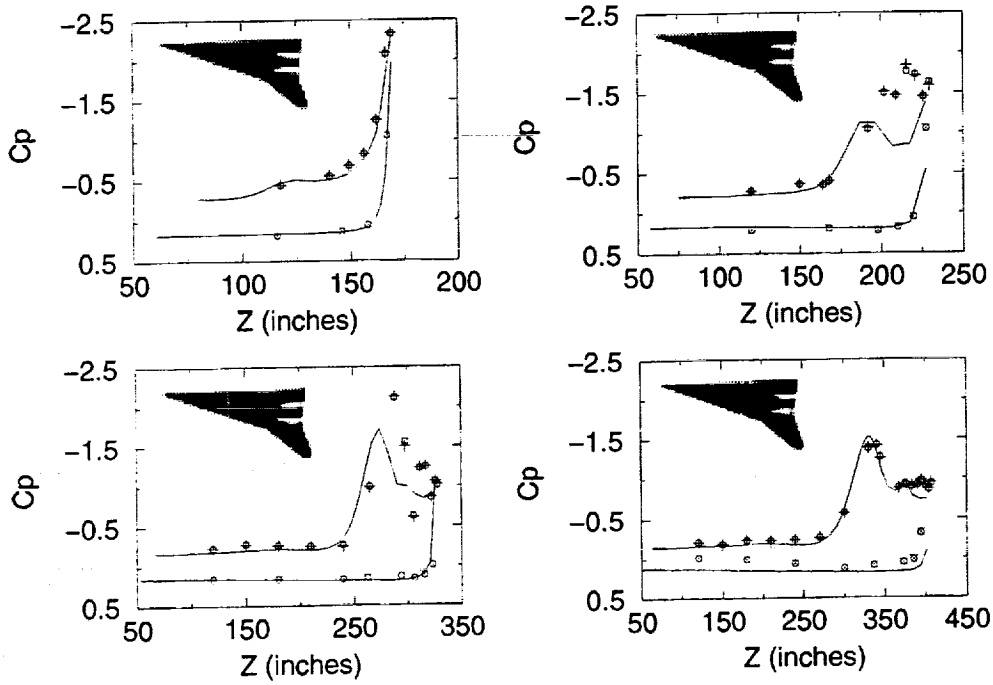

These figures show the spanwise pressure distribution at the four upstream stations for TCA 0/0 wing/body/nacelle configuration at AOA=12 degrees. Good agreement is found between the CFL3D solution and the test data.

Spanwise Pressure Distribution: CFL3D vs. Test Data

TCA 0/0 W/B/N AOA=12 Degrees

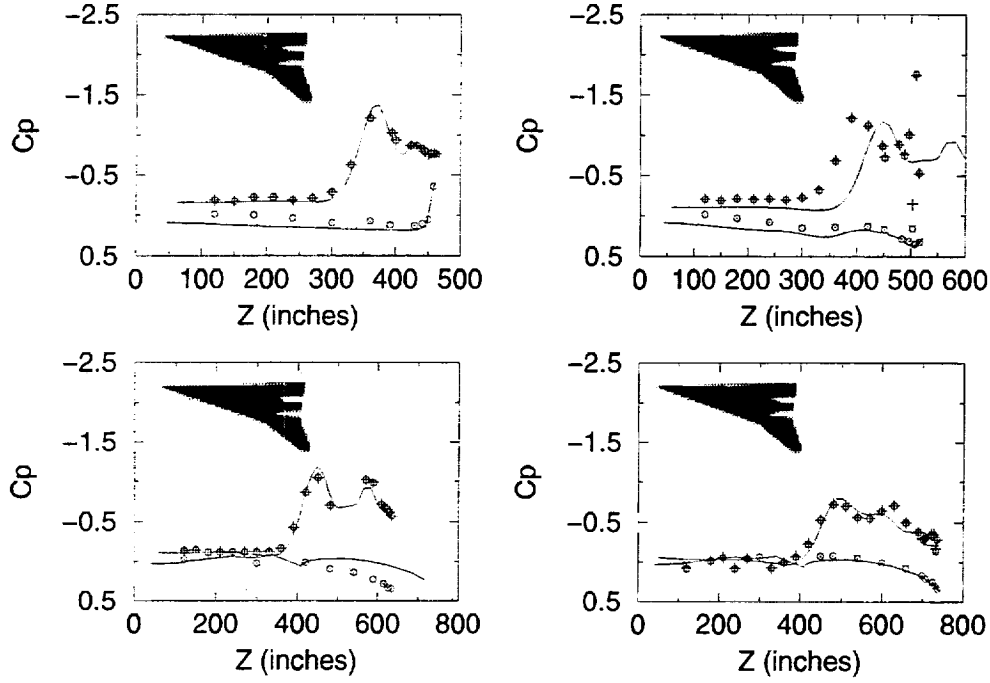

These figures show the spanwise pressure distribution at the four downstream stations for TCA 0/0 wing/body/nacelle configuration at AOA=12 degrees. As in the test data, two pressure peaks are found in the CFL3D solution which indicate the separate LE vortices in the flow.

Wing Surface Pressure Distribution

TCA 30/10 W/B/N AOA=10 Degrees

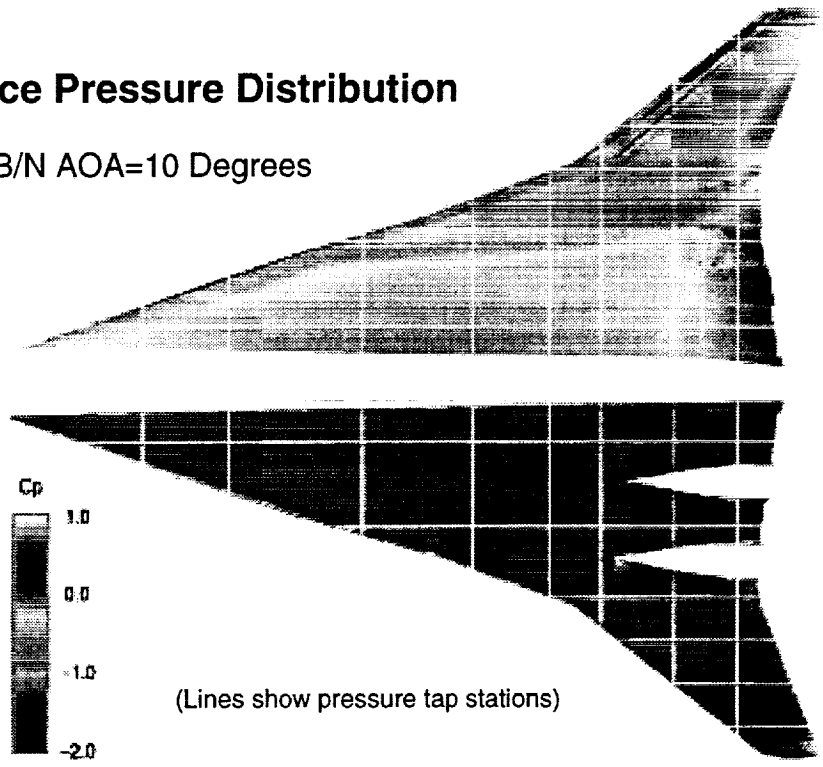

This figure shows the predicted pressure distribution on wing upper and lower surfaces for TCA 30/10 wing/body/nacelle configuration at AOA=10 degrees.

Spanwise Pressure Distribution: CFL3D vs. Test Data

TCA 30/10 W/B/N AOA=10 Degrees

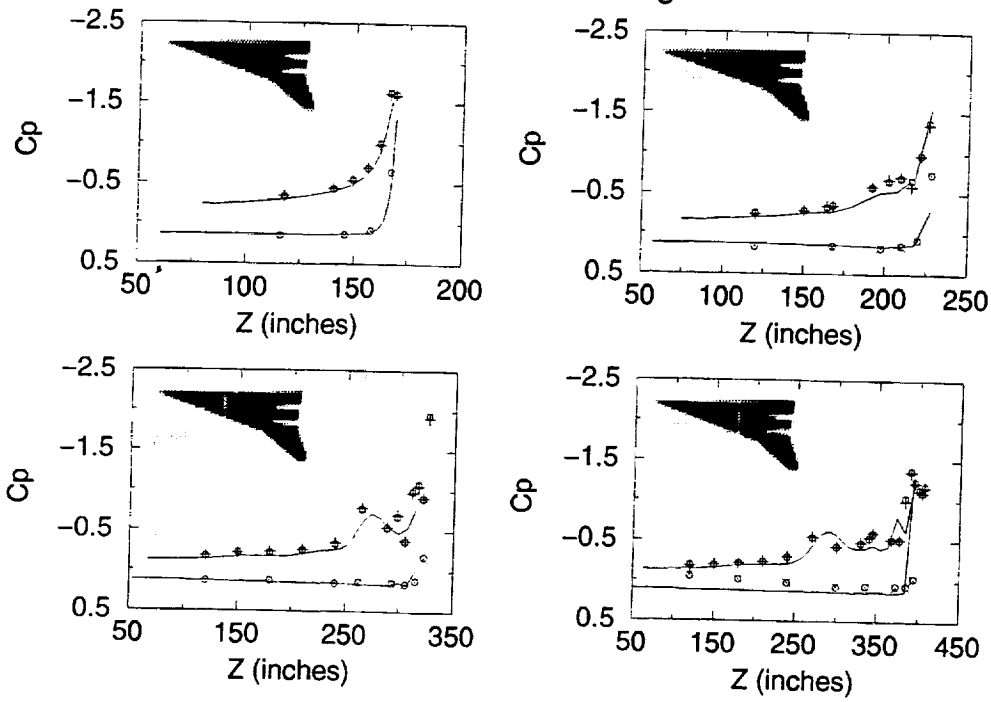

These figures show the spanwise pressure distribution at the four upstream stations for TCA 30/10 wing/body/nacelle configuration at AOA=10 degrees. Good agreement is found between the CFL3D solution and the test data. At these upstream stations, there is no apparent formation of a strong LE vortex.

Spanwise Pressure Distribution: CFL3D vs. Test Data

TCA 30/10 W/B/N AOA=10 Degrees

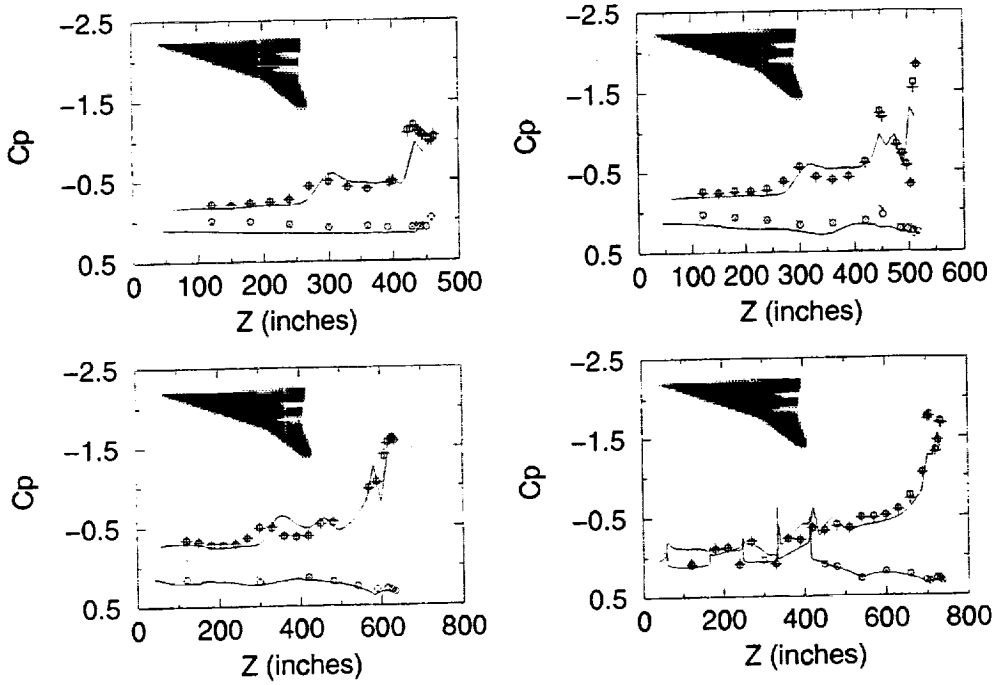

These figures show the spanwise pressure distribution at the four downstream stations for TCA 30/10 wing/body/nacelle configuration at AOA=10 degrees. Good agreement is found between the CFL3D solution and the test data.

Wing Surface Pressure Distribution

TCA 30/10 W/B/N AOA=12 Degrees

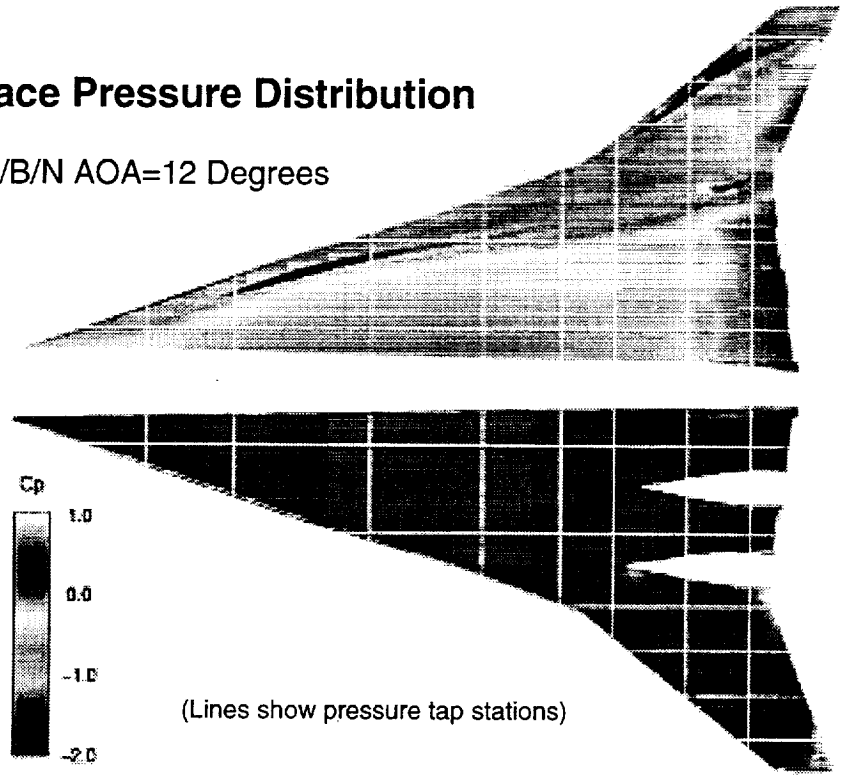

This figure shows the predicted pressure distribution on wing upper and lower surfaces for TCA 30/10 wing/body/nacelle configuration at AOA=12 degrees.

Spanwise Pressure Distribution: CFL3D vs. Test Data

TCA 30/10 W/B/N AOA=12 Degrees

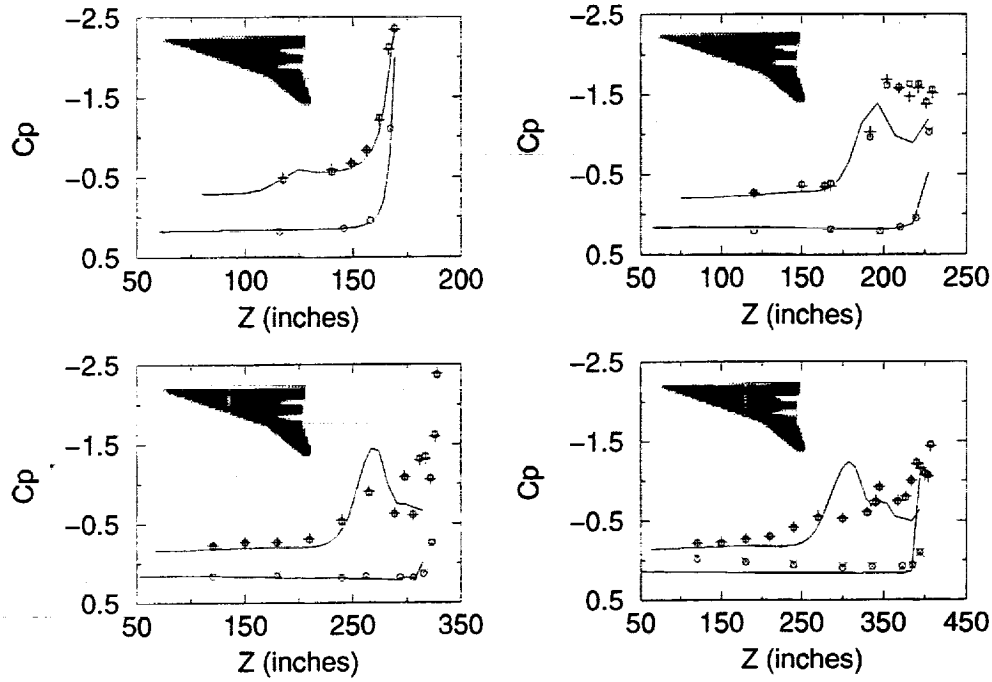

These figures show the spanwise pressure distribution at the four upstream stations for TCA 30/10 wing/body/nacelle configuration at AOA=12 degrees. Good agreement is found between the CFL3D solution and the test data. There appears to be a vortex formation off the leading edge.

Spanwise Pressure Distribution: CFL3D vs. Test Data

TCA 30/10 W/B/N AOA=12 Degrees

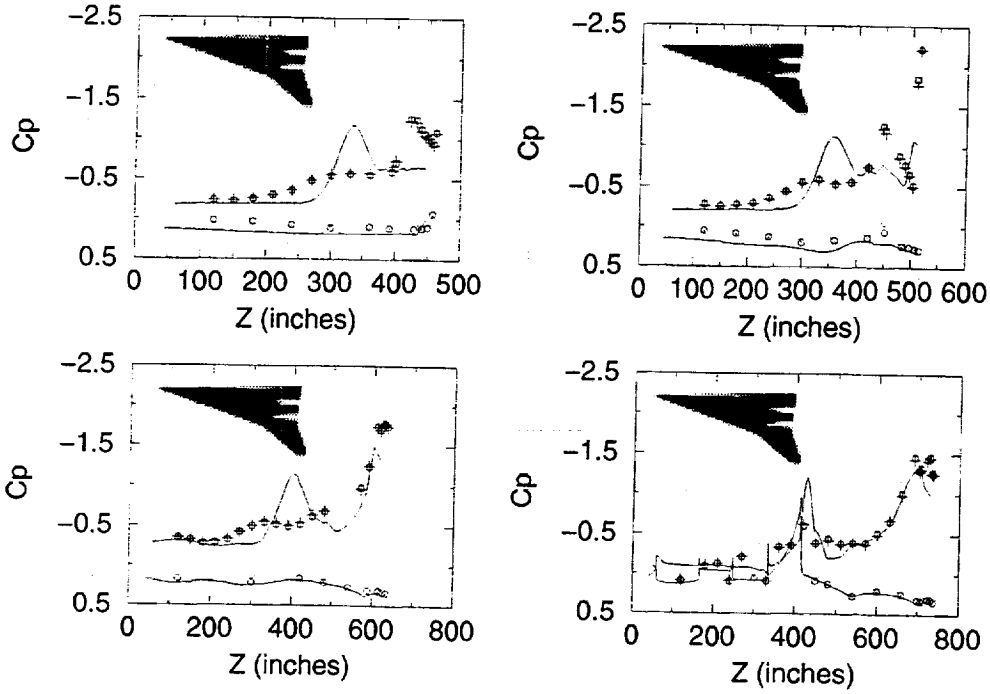

These figures show the spanwise pressure distribution at the four downstream stations for TCA 30/10 wing/body/nacelle configuration at AOA=12 degrees. The CFL3D solution indicates that the LE vortex remains attached to the wing upper surface whereas the test data does not contain an apparent pressure peak. Otherwise, good agreement is found between the CFL3D solution and the test data.

Summary: Comparison of Pressure Distribution

- CFL3D solutions and test data show similar overall trend in pressure distribution on wing upper and lower surfaces
- Discrepancies exist in the location and strength of leading edge vortices between CFL3D solutions and test data
- Tested configurations are slightly different from CFD models which may explain some of the discrepancies
  - Chines and vertical tails in tested configurations
  - Effect of post and walls in wind tunnel on pressure data

In summary, CFL3D solutions and the test data for TCA W/B and W/B/N configurations agree fairly well in the pressure distributions on wing upper and lower surfaces. In a few cases, e.g., TCA 0/0 W/B/N at AOA=10 degrees and TCA 30/10 W/B and W/B/N at AOA=12 degrees, some discrepancies exist in following the LE vortices.

Part III
Comparison of Change in Pressure Distribution from Wing/Body to Wing/Body/Nacelle

To better understand the findings in the pressure distribution comparison, we computed the difference in pressure coefficient between wing/body and wing/body/nacelle configurations and present the delta–Cp comparison in this section. The focus is on the vortex behavior off wing upper surface

Difference in Pressure Distribution on Wing Surface (WBN–WB)

TCA 0/0 AOA=10 Degrees

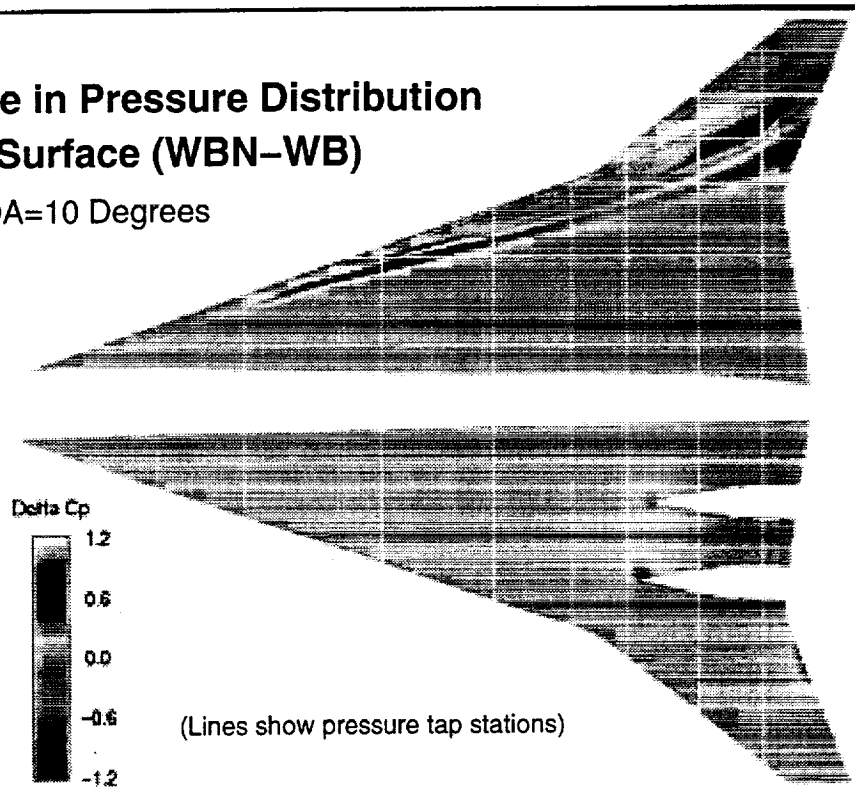

This figure shows the contours of Delta–Cp between TCA 0/0 W/B and W/B/N configurations on wing upper and lower surfaces, as predicted by CFL3D solutions at AOA=10 degrees. The behavior on the wing lower surface is very much as expected. On the wing upper surface, the positive and negative peaks indicate an outboard shift in vortex location due to nacelles.

Difference in Spanwise Pressure Distribution (WBN–WB)

CFL3D vs. Test Data; TCA 0/0 AOA=10 Degrees

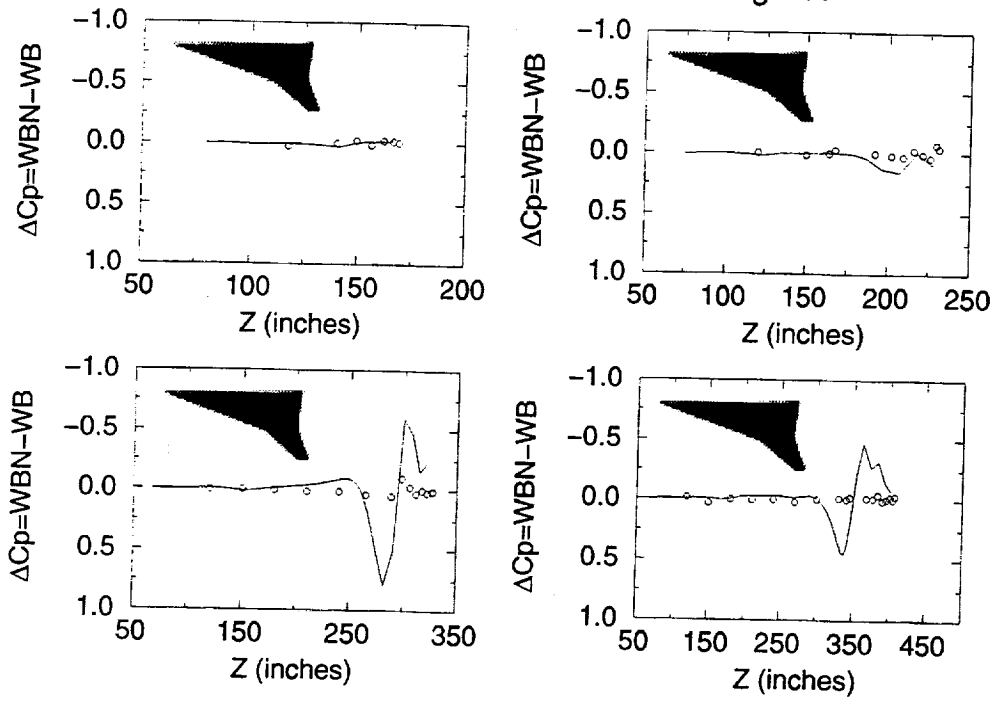

However, the test data show little change in pressure distribution from W/B to W/B/N on wing upper surface. The above figures show the Delta–Cp plots for the four upstream stations.

Difference in Spanwise Pressure Distribution (WBN–WB)

CFL3D vs. Test Data; TCA 0/0 AOA=10 Degrees

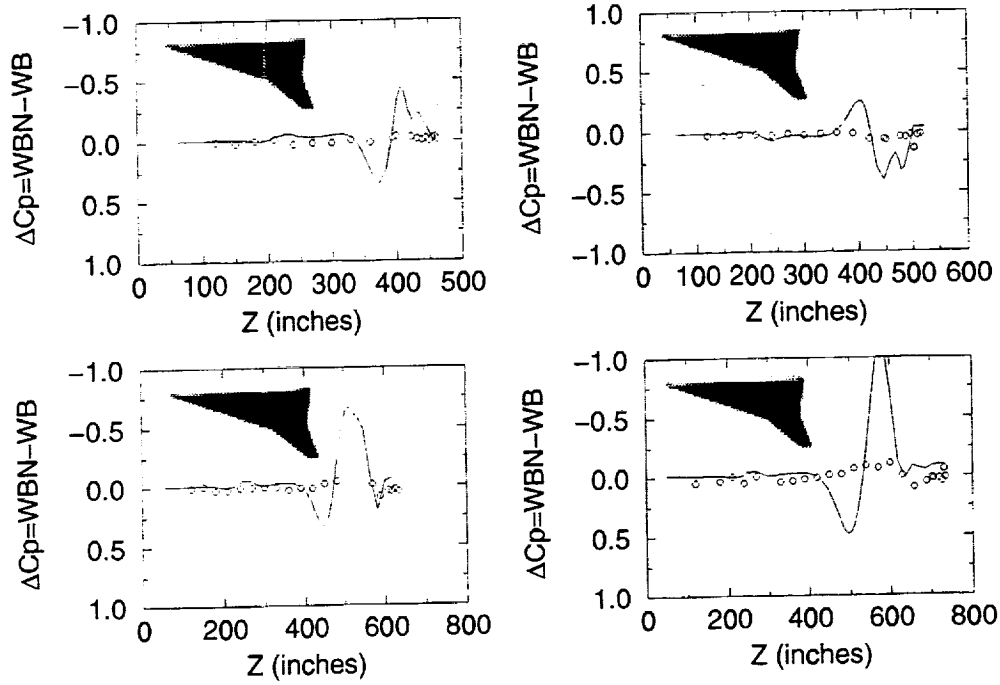

Similar discrepancies in the Delta–Cp comparison between CFL3D and test data in the Delta–Cp plots for the four downstream stations. It is noted that this is the only case (TCA 0/0 AOA=10 degrees) that such major discrepancies exist. Good agreement is found for all other cases as will be seen in the remainder of this section. Based on the discussion with high lift team members, for the case of TCA 0/0 AOA=10 degrees, it is difficult to capture the leading edge vortices using CFL3D without tuning the Baldwin–Lomax turbulence models.

Difference in Pressure Distribution on Wing Surface (WBN–WB)

TCA 0/0 AOA=12 Degrees

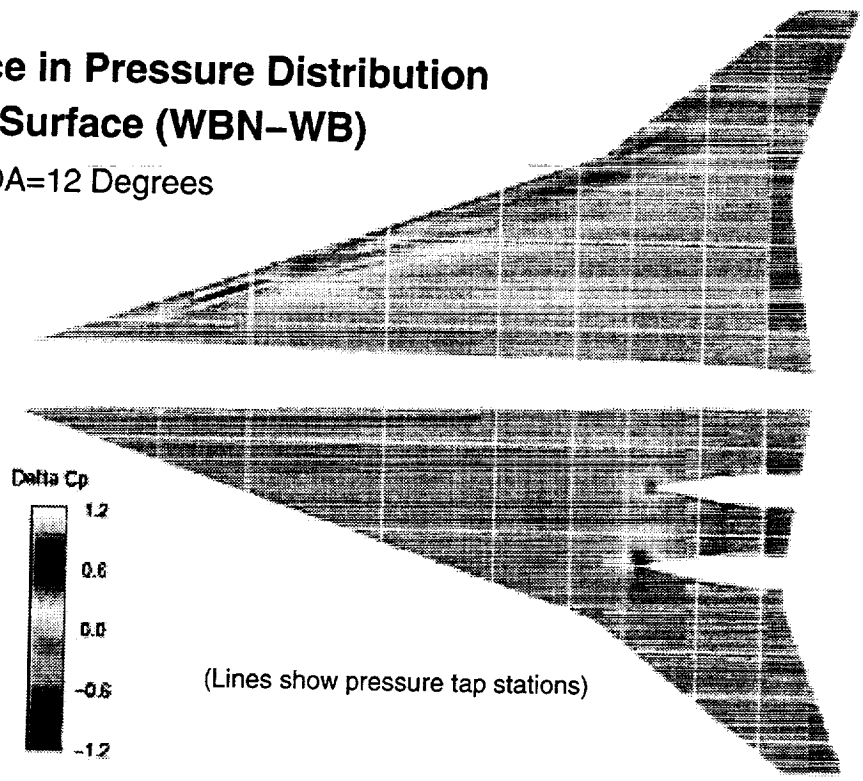

This figure shows the contours of Delta–Cp between TCA 0/0 W/B and W/B/N configurations on wing upper and lower surfaces, as predicted by CFL3D solutions at AOA=12 degrees. There is very little change from W/B to W/B/N in the pressure distribution on wing upper surface.

Difference in Spanwise Pressure Distribution (WBN–WB)

CFL3D vs. Test Data; TCA 0/0 AOA=12 Degrees

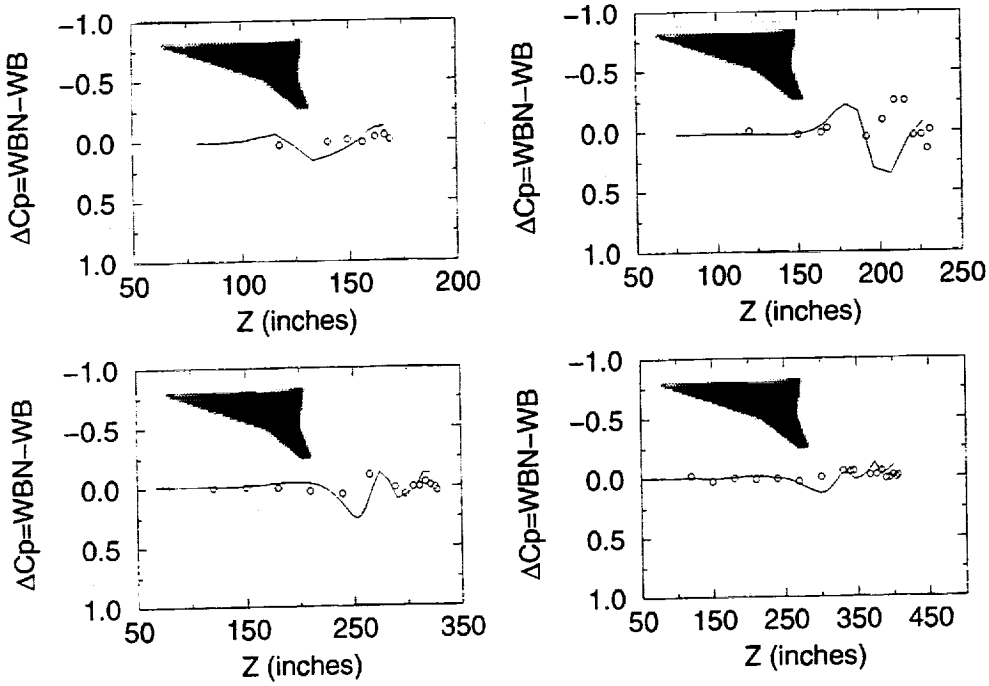

At the four upstream stations, CFL3D solution agrees well with the test data in the Delta–Cp comparison on wing upper surface.

Difference in Spanwise Pressure Distribution (WBN–WB)

CFL3D vs. Test Data; TCA 0/0 AOA=12 Degrees

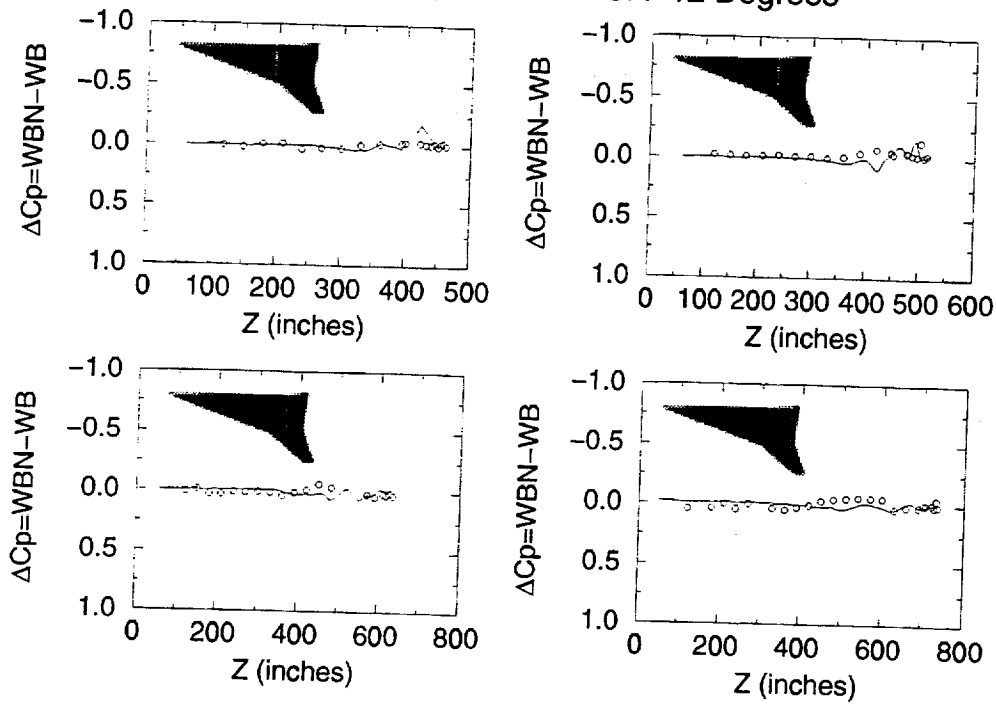

Similar agreement is found in the Delta–Cp comparison at the four downstream stations on wing upper surface between CFL3D solution and test data.

Difference in Pressure Distribution on Wing Surface (WBN–WB)

TCA 30/10 AOA=10 Degrees

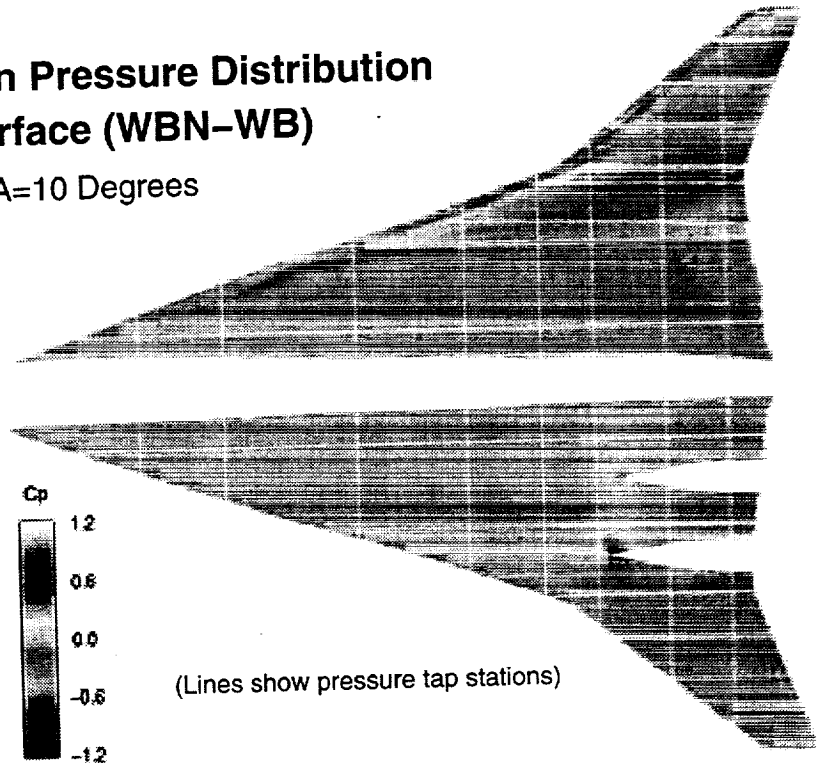

This figure shows the contours of Delta–Cp between TCA 30/10 W/B and W/B/N configurations on wing upper and lower surfaces, as predicted by CFL3D solutions at AOA=10 degrees. There is very little change from W/B to W/B/N in the pressure distribution on wing upper surface.

Difference in Spanwise Pressure Distribution (WBN–WB)

CFL3D vs. Test Data; TCA 30/10 AOA=10 Degrees

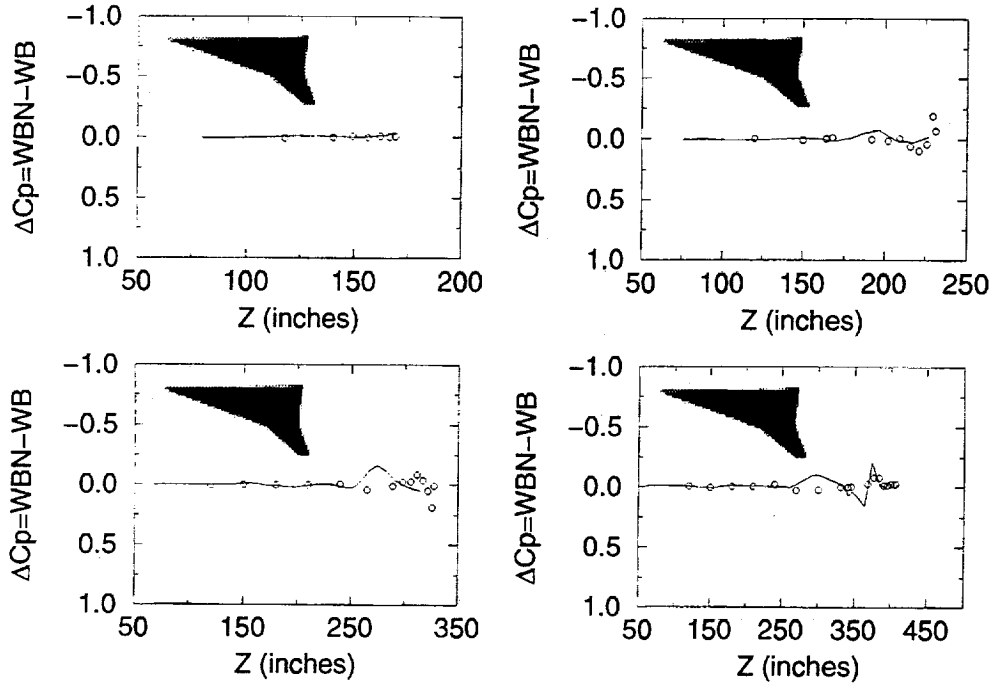

At the four upstream stations, CFL3D solution agrees well with the test data in the Delta–Cp comparison on wing upper surface.

Difference in Spanwise Pressure Distribution (WBN–WB)

CFL3D vs. Test Data; TCA 30/10 AOA=10 Degrees

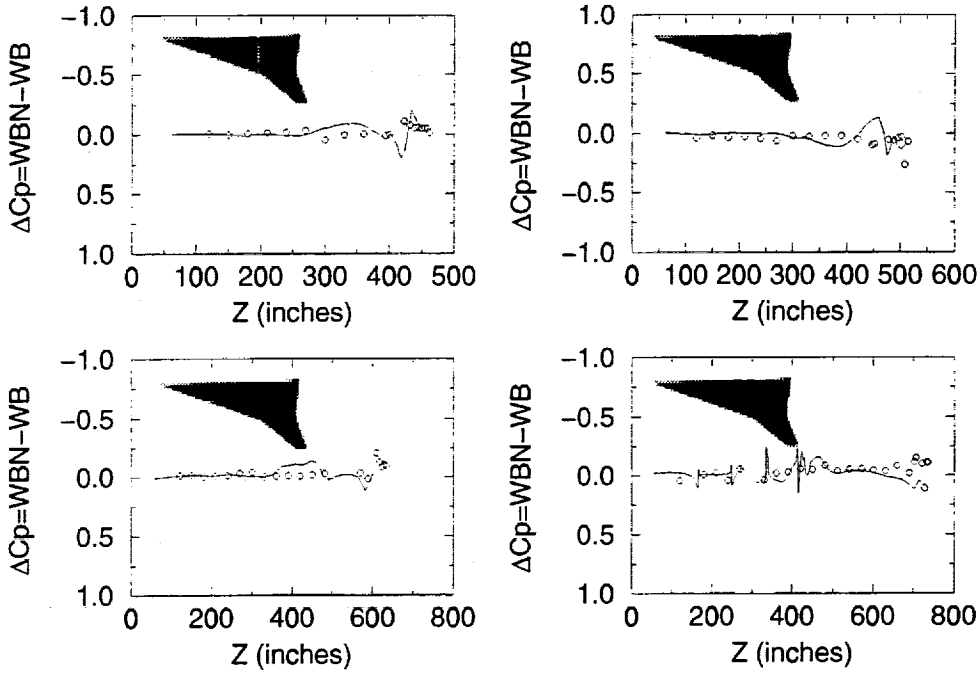

Similar agreement is found in the Delta–Cp comparison at the four downstream stations on wing upper surface between CFL3D solution and test data.

Difference in Pressure Distribution on Wing Surface (WBN–WB)

TCA 30/10 AOA=12 Degrees

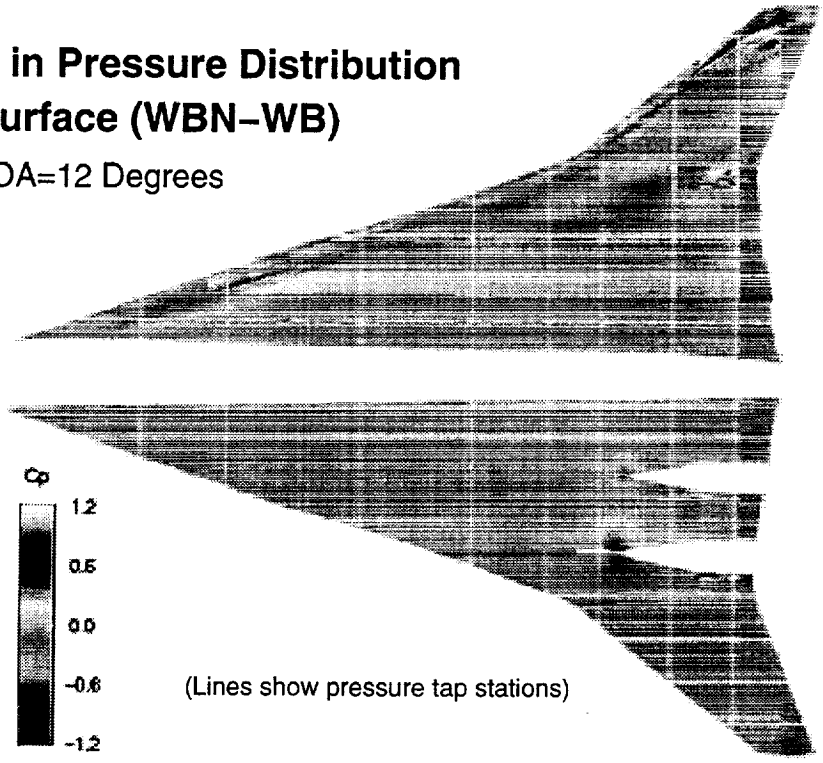

This figure shows the contours of Delta–Cp between TCA 30/10 W/B and W/B/N configurations on wing upper and lower surfaces, as predicted by CFL3D solutions at AOA=12 degrees. There is very little change from W/B to W/B/N in the pressure distribution on wing upper surface.

Difference in Spanwise Pressure Distribution (WBN–WB)

CFL3D vs. Test Data; TCA 30/10 AOA=12 Degrees

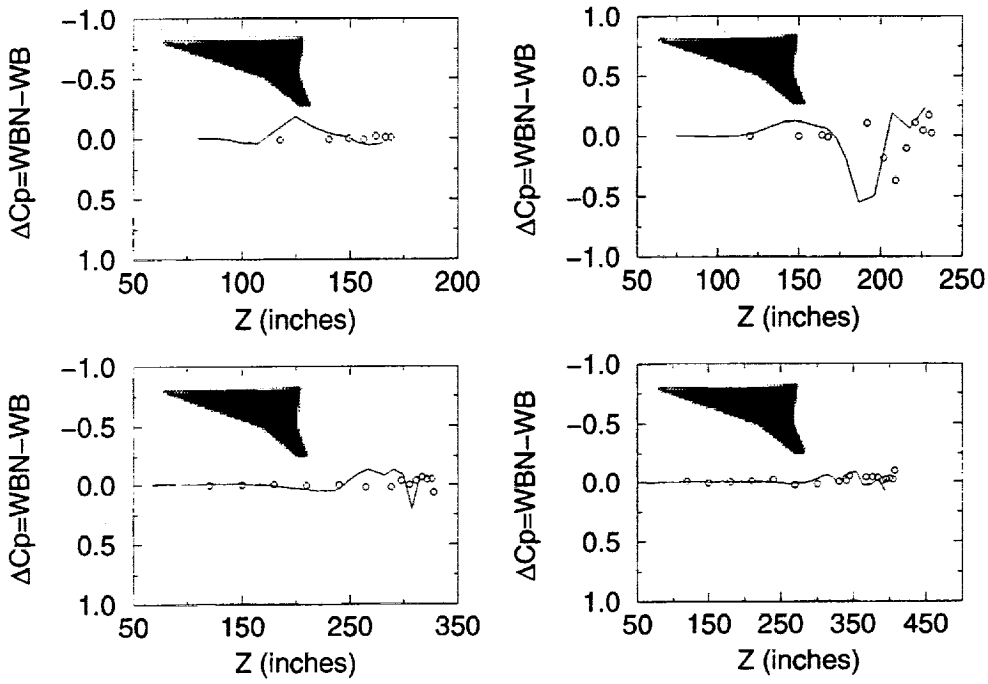

At the four upstream stations, CFL3D solution agrees well with the test data in the Delta–Cp comparison on wing upper surface.

Difference in Spanwise Pressure Distribution (WBN–WB)

CFL3D vs. Test Data; TCA 30/10 AOA=12 Degrees

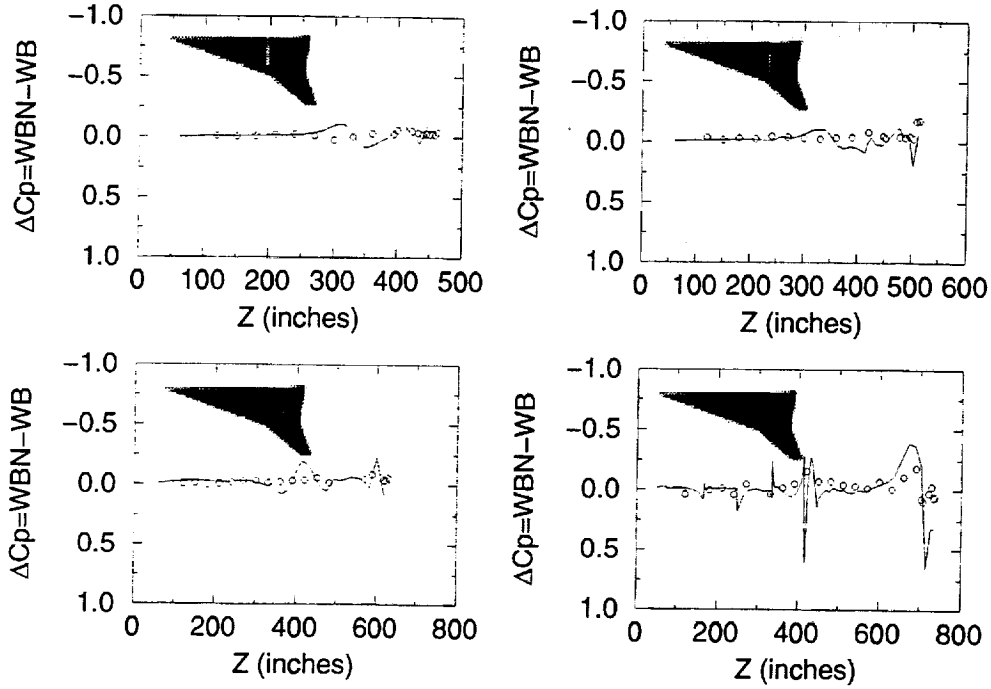

Similar agreement is found in the Delta–Cp comparison at the four downstream stations on wing upper surface between CFL3D solution and test data.

Summary: Comparison of Change in Pressure Distribution from Wing/Body to Wing/Body/Nacelle

- Test data show little or no change in the strength and location of leading edge vortices between W/B and W/B/N
- For TCA 30/10 W/B and W/B/N configurations, CFL3D solutions agree well with test data in this comparison
- For TCA 0/0 W/B and W/B/N configurations:
  - At AOA=12 degrees, CFL3D results agree with test data
  - At AOA=10 degrees, CFL3D shows an outboard shift in vortex location from W/B to W/B/N.
- CFL3D solutions for TCA 0/0 W/B and W/B/N at AOA=10 degrees were updated and similar results were obtained from the comparison

In summary, we completed the comparison of change in pressure distribution from wing/body to wing/body/nacelle configurations on wing upper surface between CFL3D solutions and the test data. The test data show very little change in the pressure distribution on the wing upper surface due to nacelles. And the CFL3D solutions agree well with the test data except in the case of TCA 0/0 at AOA=10 degrees. Further investigation into the CFL3D solution for TCA 0/0 wing/body/nacelle configurations at AOA=10 degrees is warranted

Numerical Analysis of Lateral Control Characteristics of HSCT Forebody Control Surfaces

David T. Yeh and Roger W. Clark
Boeing, Long Beach

HSR Airframe Technical Review
High Lift Aerodynamics
at
Anaheim, CA
February 9–11, 1999

BOEING

This slide shows an outline of the High-Lift Technology program.

High Lift Technology Development (Task 33)

Increase L/D, Develop Analysis/Design Methodology

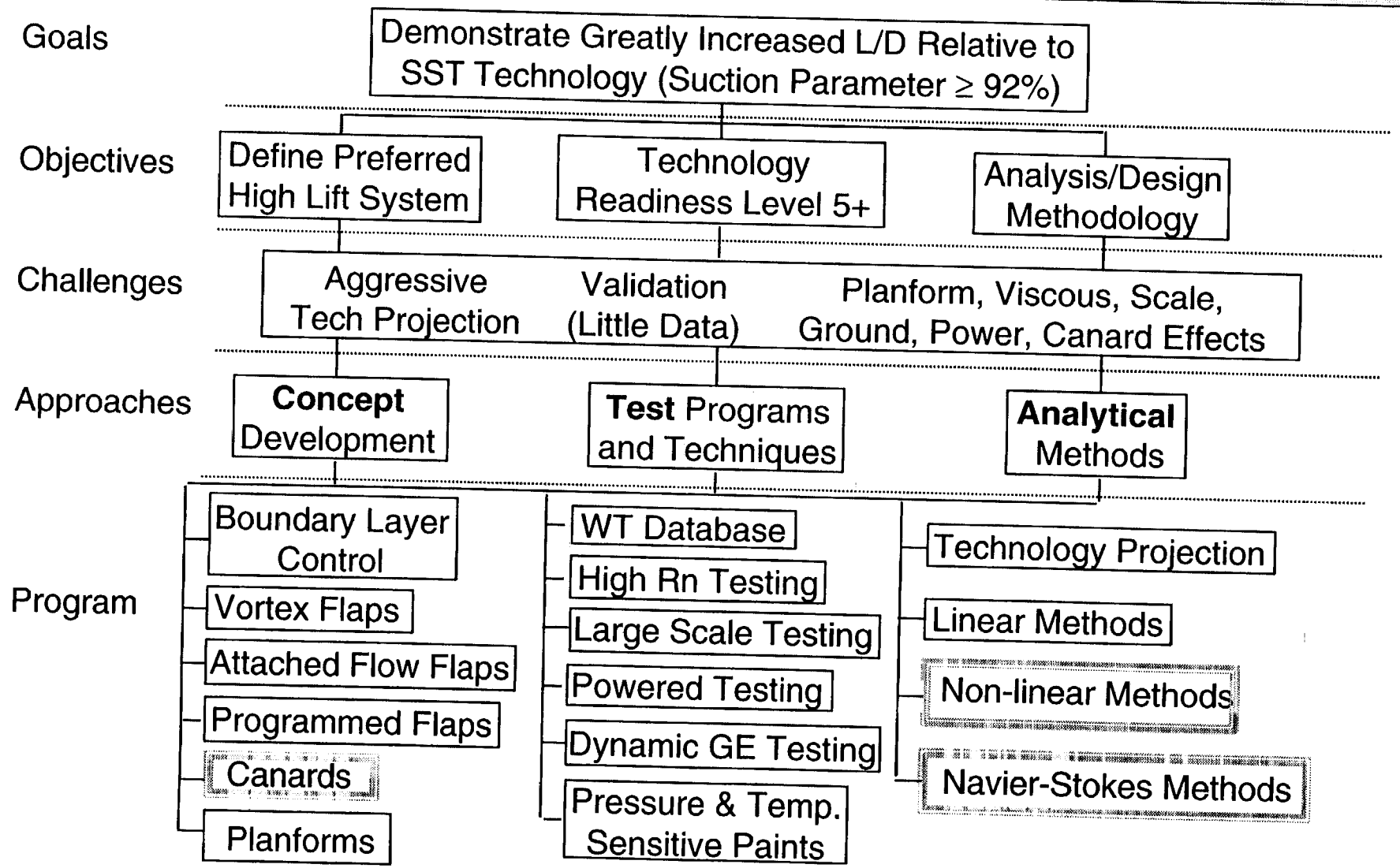

Outline

This report starts with the description of the objective and the focus of current study, followed by the approach. The numerical results will be presented for the chin fin lateral control effectiveness at various angle-of-attack and an alternative control concept using the high-mount canards with asymmetric elevator deflection. The numerical results for the chin fin study will be compared with TCA 4 test results for data correlation. The numerical results for the high-mount canards will be used to define some of the CFD runs in TCA-5 test.

Outline

- Objective & Current Study Focus
- Approach
- Numerical Results and Code Validation
  - Chin Fin Characteristics
  - High–Mount Canards with Asymmetric Elevator Deflection
- Summary

BOEING

Objective

The objective of this study was initially motivated by the TCA-4 data that shows the diminishing chin fin lateral control effectiveness as alpha approaches 10 degrees. Numerical simulation of the chin fin was conducted in an effort to simulate the flow phenomena and to provide the understanding of the flow physics. The numerical simulation was performed for the portion of the fuselage ahead of the wing apex, since the objective was to evaluate the local influence of the chin fin vortex on the fuselage. The numerical results are compared with the test data to assess whether the first order effect is adequately captured.

An alternative lateral control concept using high-mount canards is also evaluated as a pre-test analysis for the TCA-5 wind tunnel test.

Objective

- Understand TCA 4 data – Chin Fin Lateral Control Effectiveness diminishes as α –> 10°
  - Numerical Simulation of the Chin Fin Lateral Control Characteristics
  - Correlate data with isolated forebody CFD solutions – Capture O(1) effects ?
- Evaluate Alternative Lateral Control Devices

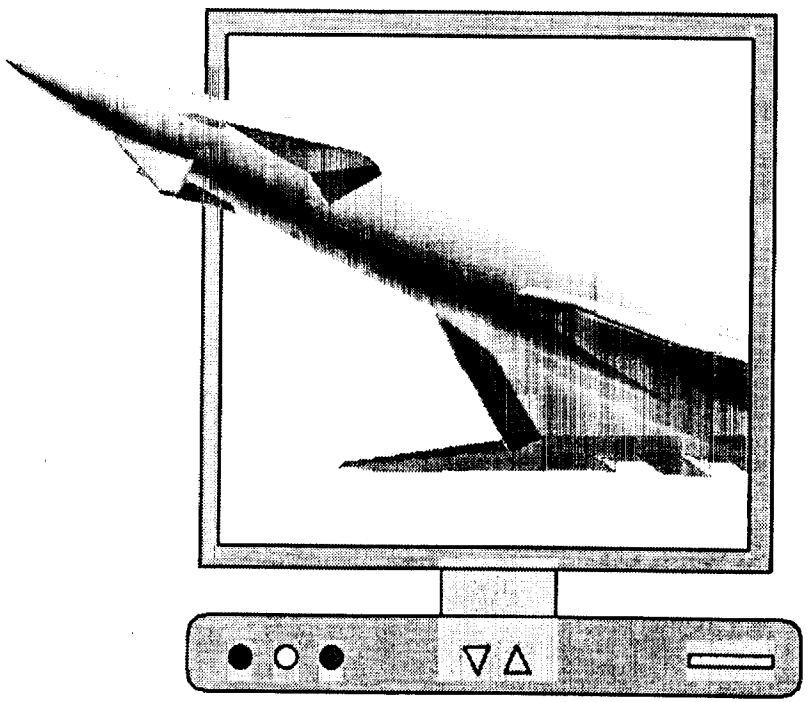

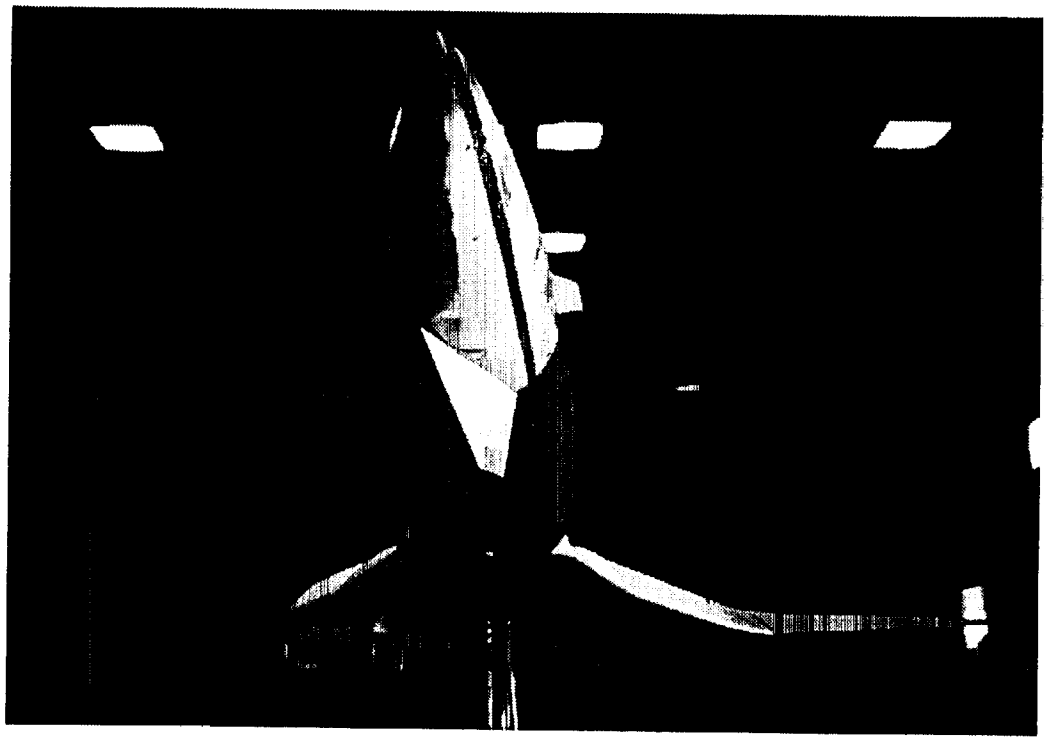

BOEING

Current Study Focuses

The current study is focused on the evaluation of the lateral control effectiveness for the forebody control surfaces including the loading distribution as well as the trailing vortex influence on the forebody. Specifically, the emphases will be focused in the following 3 areas:

1. TCA-4 Chin Fin Simulation

The TCA forebody with 20-degree chin fin deflection is simulated for alphas of 0 and 10 degrees. The numerical solutions will be compared with the TCA-4 test results for data correlation. The behavior of the trailing vortex will be analyzed to assess its influence on the forebody.

2. Chin Fin at alpha -10 degrees

This condition would be similar to the case of the control surface mounted on the top at alpha 10 degrees. The lateral control characteristics and vortex interaction will be evaluated.

3. High-mount canards with asymmetric elevator deflections

Simulation of the lateral control characteristics of the high-mount canards will be conducted as a pre-test analysis for the TCA-5 test.

Current Study Focuses

- Lateral Control Effectiveness – Cy and Cmz
- Loading Distribution and Vortex Influence

1. TCA–4 Chin Fin Simulation

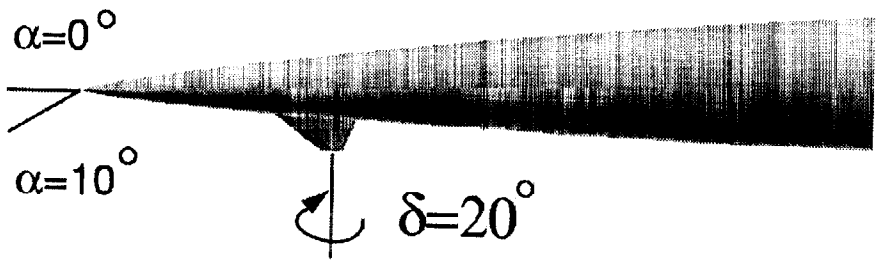

2. Chin Fin @ α=–10° (~Mounted on the top)

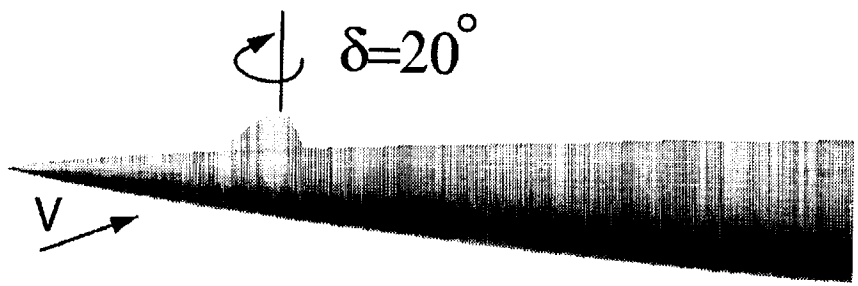

3. High–mount canards with asymmetric elevator deflections (TCA–5 Test)

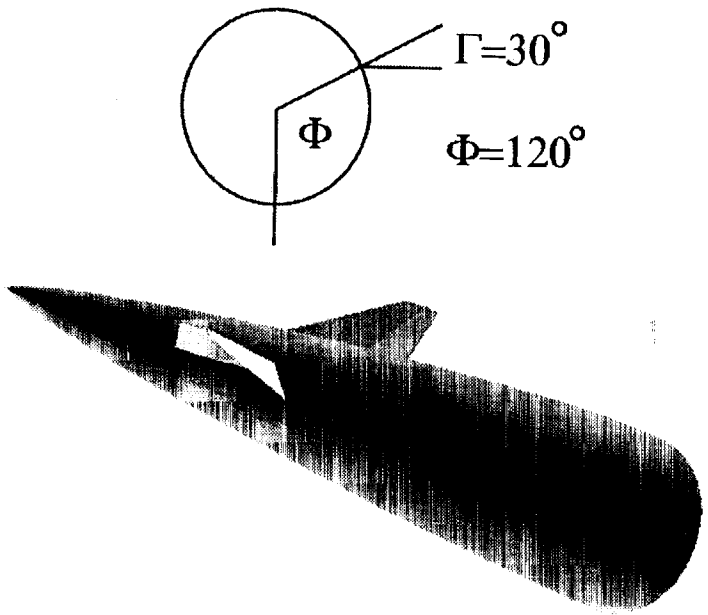

BOEING

Approach

The approach is to modify the canard procedure for modeling the chin fin and high-mount canards including the aft-elevators with correct modeling of the spanwise gap between the canard and the fuselage. The details of the modeling procedure can be found in the last year's HSR Workshop Proceedings. The numerical simulation is performed using the Navier-Stokes option of the CFL3D code to simulate an isolated forebody and the control surfaces. The numerical results will be utilized for flow visualization as well as correlation with the test data. This process is repeated for the analysis and evaluation of design alternatives such as high-mount canards.

Approach

- Modify Canard Procedure for Chin Fin / High–Mount Canards

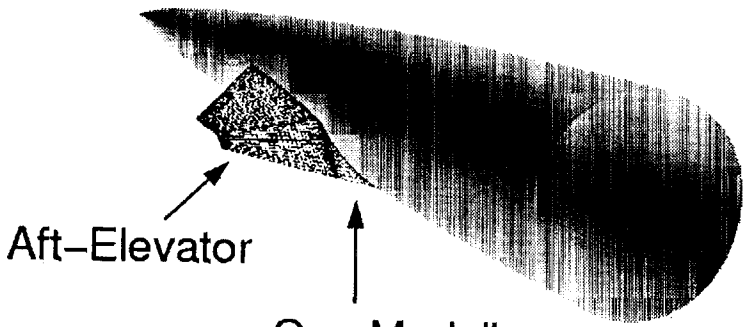

- Numerical Simulation – CFL3D

Isolated Forebody

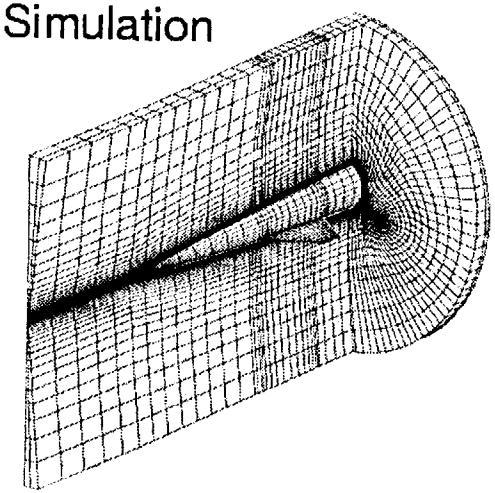

- Evaluate Lateral Control Concepts

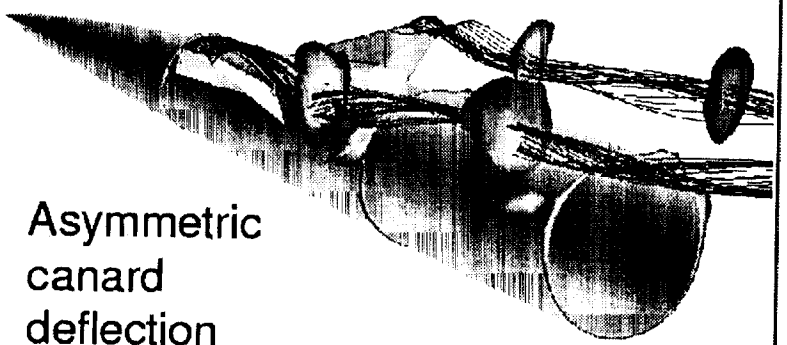

- Data Correlation / Flow Visualization

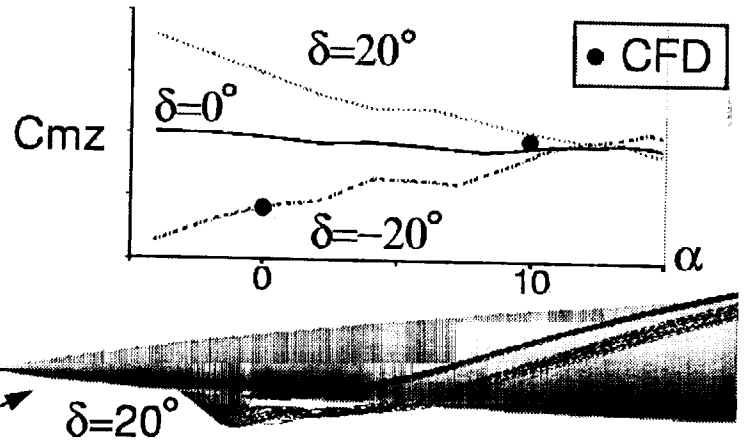

BOEING

Computational Model for Chin Fin Simulation

This figure shows the surface geometry of the CFD model for the chin fin simulation as well as the centerline grid. Since the deflected chin fin results in a non-symmetric configuration, both left and right parts of the geometry were modeled, rather than using a reflection plane. The gap between the chin fin and the forebody is modeled for a chin fin deflection of 20 degrees. A constant cross section downstream of the actual forebody geometry is also numerically modeled to minimize the potential downstream gradient that would propagate upstream.

Computational Model for Chin Fin Simulation

HSCT Aerodynamics, Long Beach

- Model Isolated Forebody/Chin Fin Configuration
- Model Full Body – Account for Asymmetry
- Model Spanwise Gap for Large Deflections
- Model Downstream Extension – Minimize Downstream Gradient

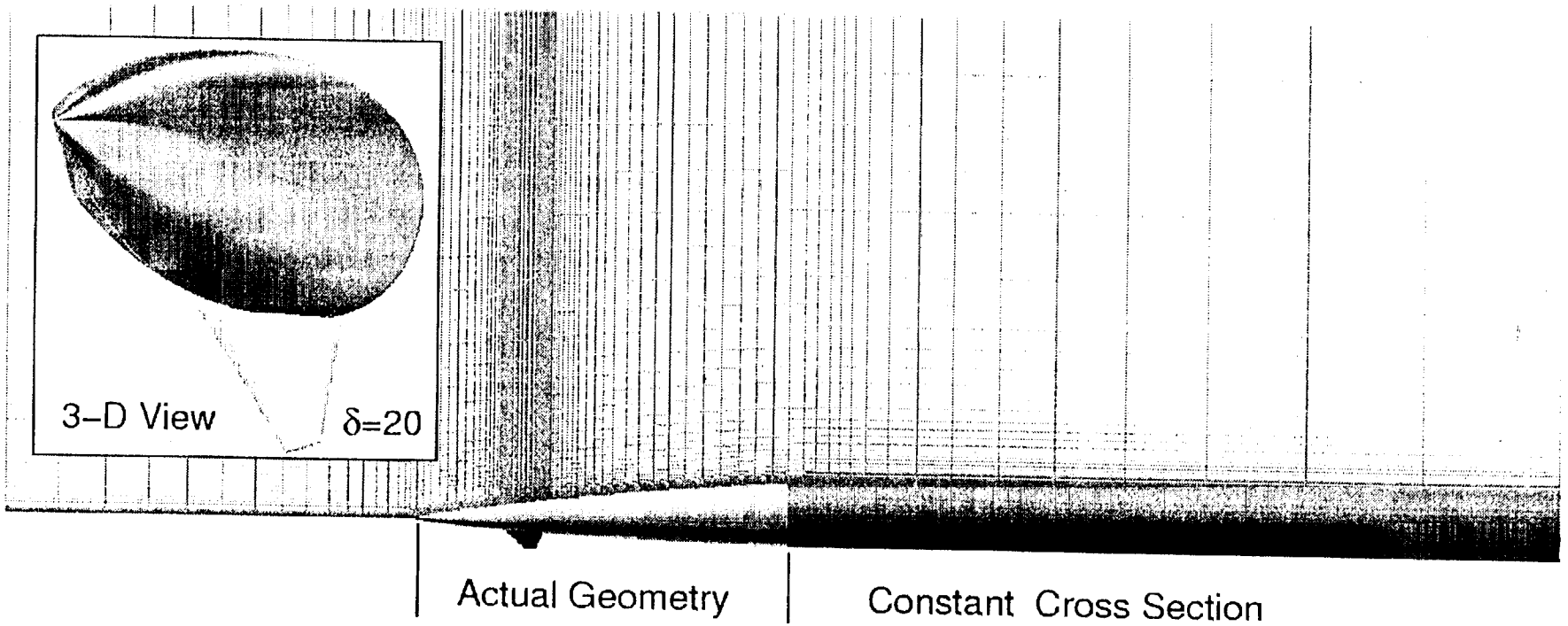

BOEING

Chin Fin Flow Characteristics at δ=20, α=0

This figure shows the chin fin flow characteristics at 20 degrees deflection and alpha of 0 degree. The airfoil sections of the chin fin are bi-convex airfoils with a sharp LE and TE. At 20-degree deflection, high pressure is seen on the windward side with the attachment (diverging) streamline formed right behind the LE. On the leeward side, a familiar vortical flow pattern and the vortex induced suction (low pressure) region are visible. The pressure difference between the chin fin surfaces results in a side force acting on the chin fin.

Chin Fin Flow Characteristics at $\delta=20^{\circ}$, $\alpha=0^{\circ}$

HSCT Aerodynamics, Long Beach

- Chord Sections: Bi–Convex Surfaces

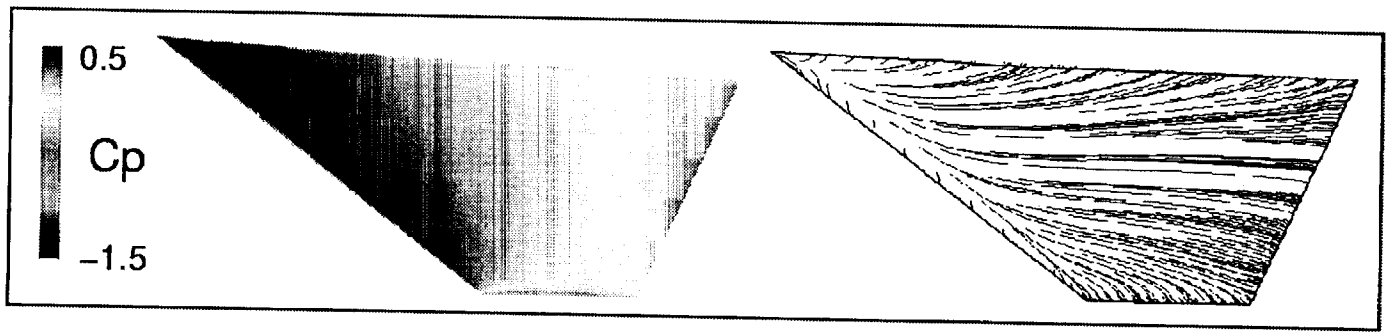

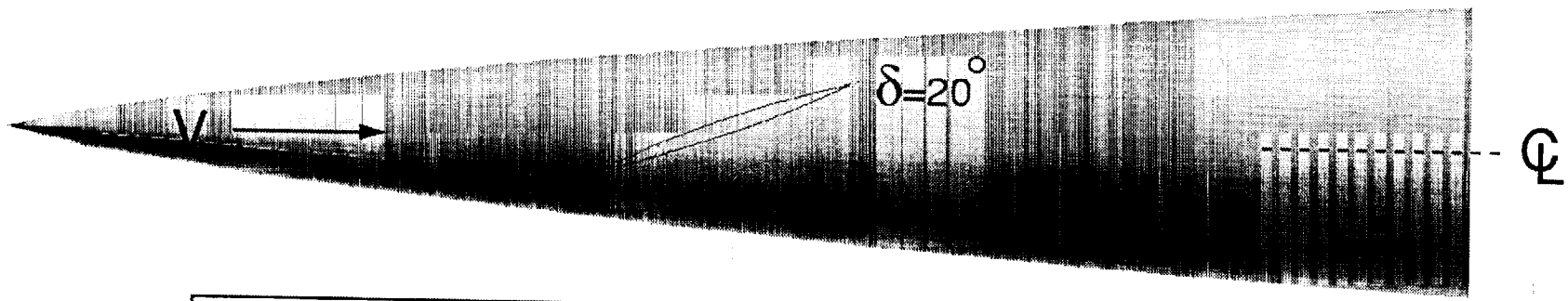

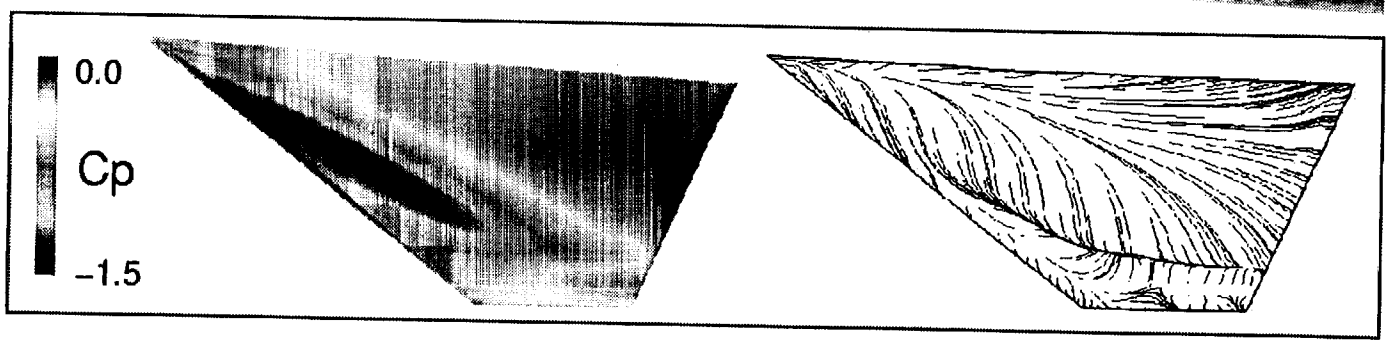

BOEING

Chin Fin Vortex Traces at α=0, δ=20

This figure shows the chin fin vortex traces at alpha=0 with the deflection angle of 20 degrees. The formation of the chin fin vortex is seen and trails behind from the TE tip region. Since the free vortex can not sustain any force, the chin fin vortex is convected in the direction of the local flow. This local flow is influenced by the angle-of-attack, forebody geometry and the bound vortex (chin fin) induced velocity. The vortex is seen to convect downstream as well as laterally away from the body centerline.

Chin Fin Vortex Traces at $\alpha=0^{\circ},\delta=20^{\circ}$

HSCT Aerodynamics, Long Beach

M=0.3, Re=8 Million

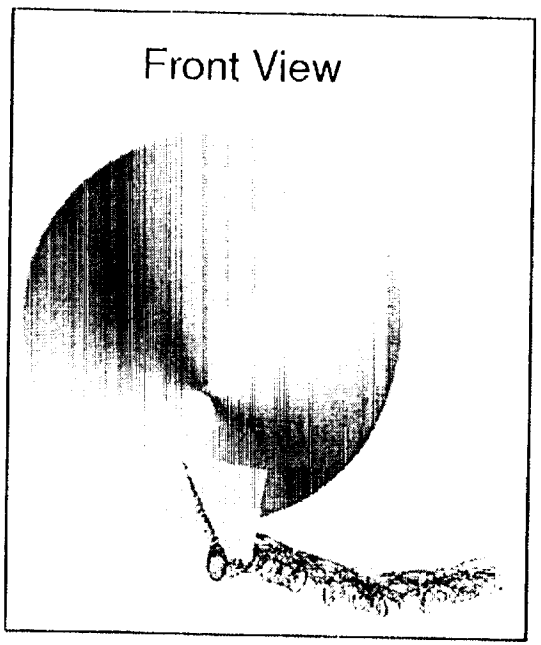

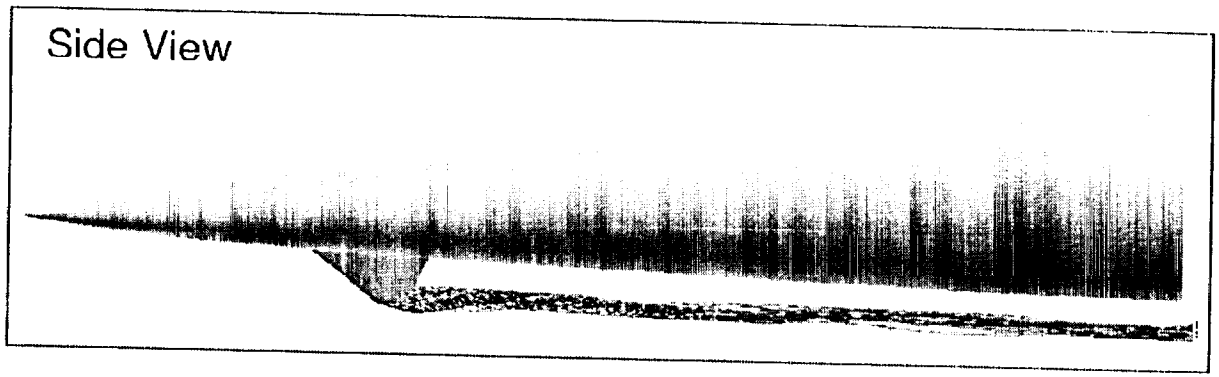

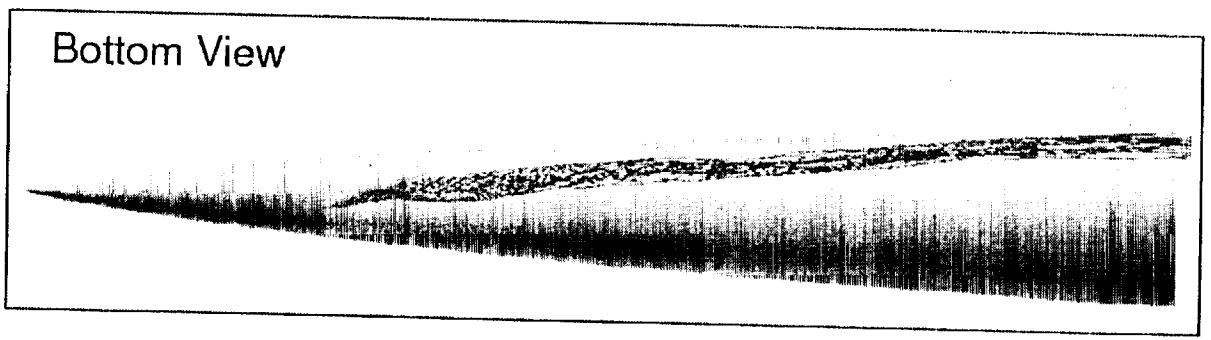

BOEING

Chin Fin Vortex Traces at α=10, δ=20

With the same chin fin deflection angle at alpha=10 degrees, the chin fin vortex is seen to wrap around the fuselage before moving away from the fuselage. As a result, the chin fin vortex is expected to generate the suction force on the fuselage that is opposite to that acting on the chin fin.

Chin Fin Vortex Traces at $\alpha=10^{\circ}$, $\delta=20^{\circ}$

M=0.3, Re=8 Million

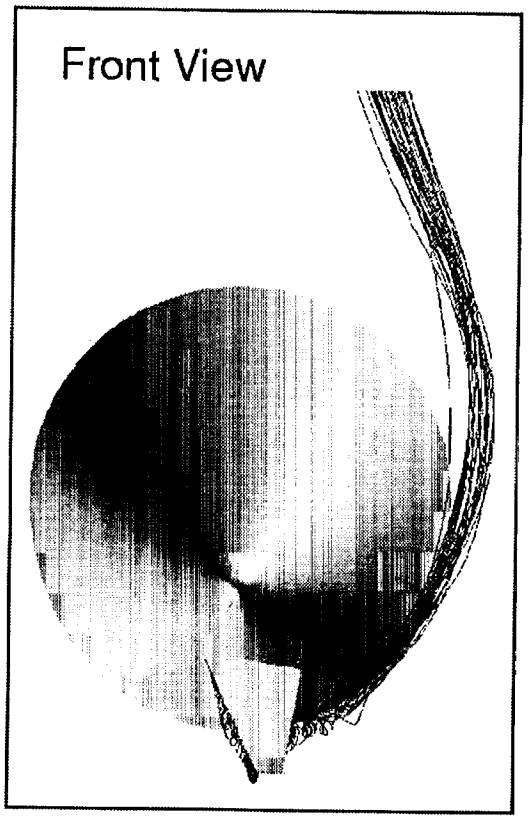

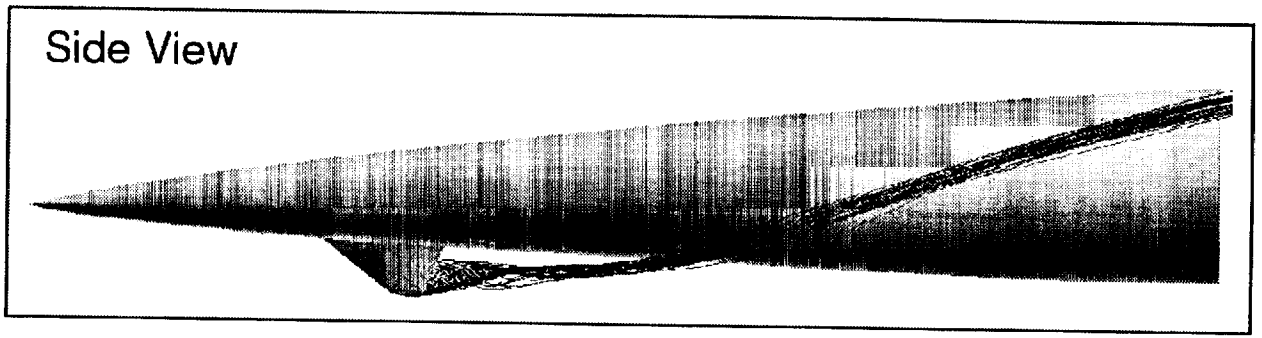

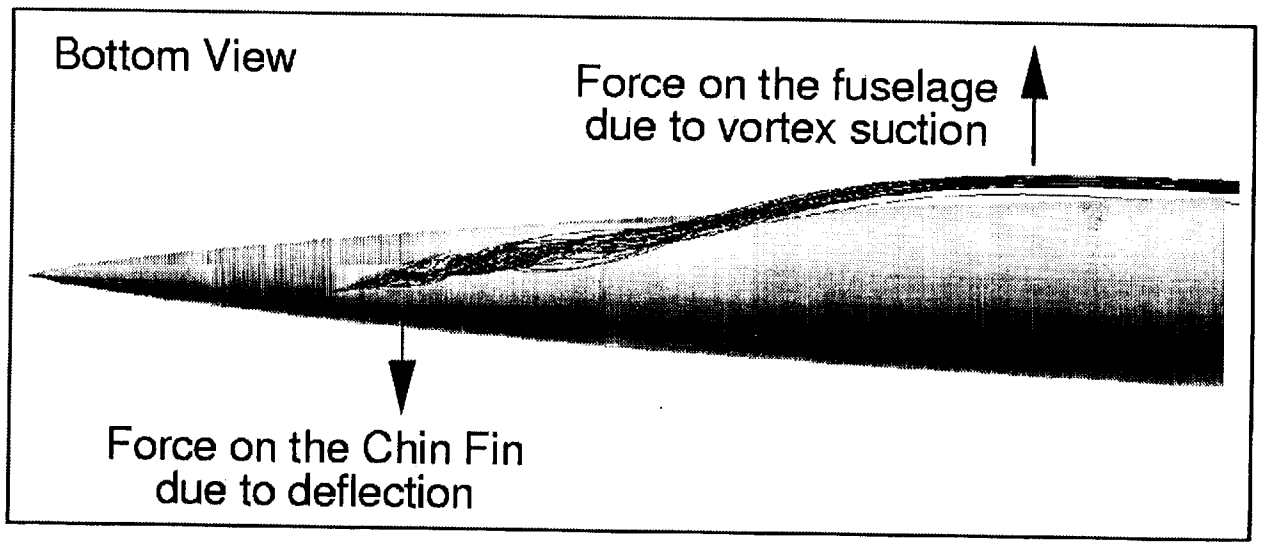

BOEING

Chin Fin Vortex Influence on the Forebody Pressure
(α=10, δ=20)

This figure shows the surface pressure contours in the presence of the chin fin vortex. As expected, the chin fin vortex is seen to induce a low pressure region as it wraps around the fuselage. This suction force translates into a side force which counteracts the force generated by the chin fin.

Chin Fin Vortex Influence on the Forebody Pressure (α=10°, δ=20°)

HSCT Aerodynamics, Long Beach

M=0.3, Re=8 Million

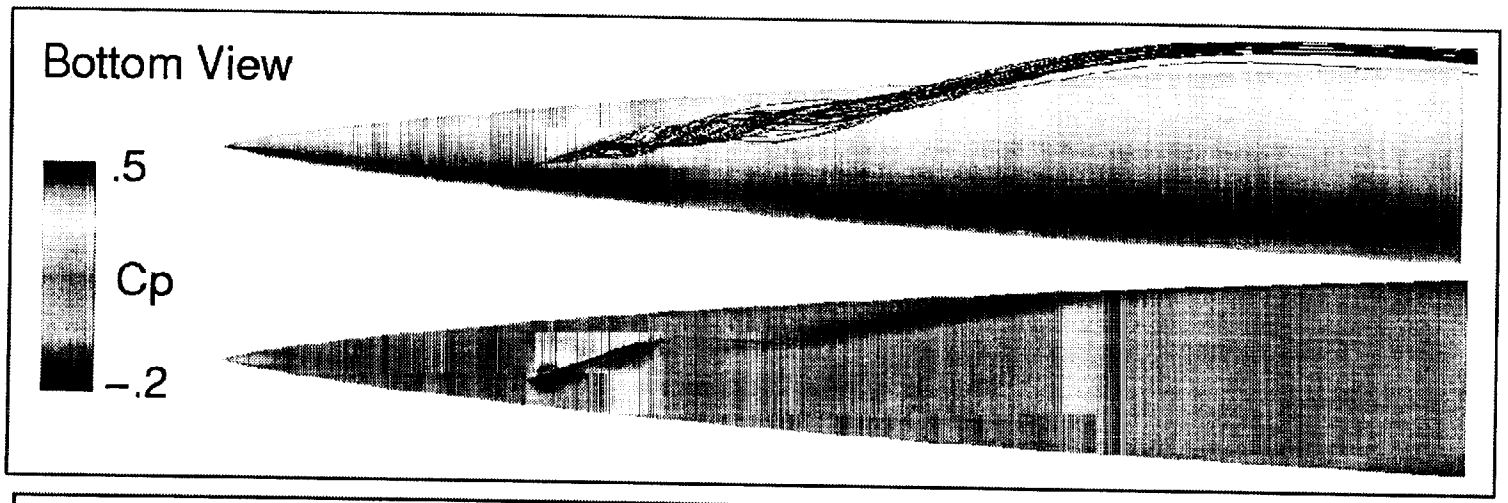

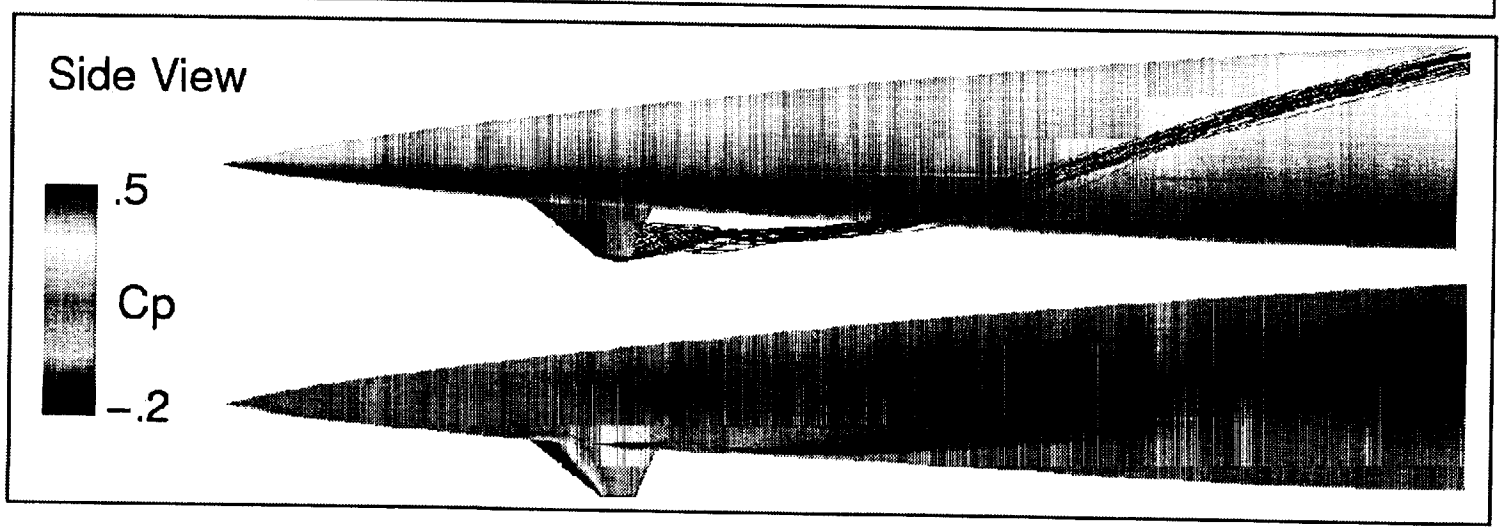

BOEING

Effect of AoA on Chin Fin Force and Moment Build-Up

To provide some insight into the force distribution over the fuselage, this figure shows the total integrated side force and yawing moment as a function of axial distance for the alpha of 0-deg and 10-deg cases. For both cases, the integrated force and moment stay nearly zero from the nose up to the region close to the chin fin apex. The local lateral control effectiveness for both cases can be seen through the indication of sudden increase of the integrated force and moment. However, the lateral control effectiveness for the alpha=10 case gradually diminishes downstream of the chin fin TE. This is a result of the counteracing force generated by the vortex induced suction on the forebody.

Based on this phenomenon, It is expected that a variation in axial location of the chin fin would not have any significant effect on improving the overall chin fin effectiveness.

It is noted that the force acting on the chin fin at alpha=10 is less than that at alpha=0. This is, in part, due to the presence of the body that influences the flow over the chin fin itself. It is also interesting to note that the rate change of the yawing moment in the downstream region is less than that of the side force. This is due to the fact that the moment arm decreases as the axial distance from the nose increases.

Effects of AoA on Chin Fin Force and Moment Build–Up

HSCT Aerodynamics, Long Beach

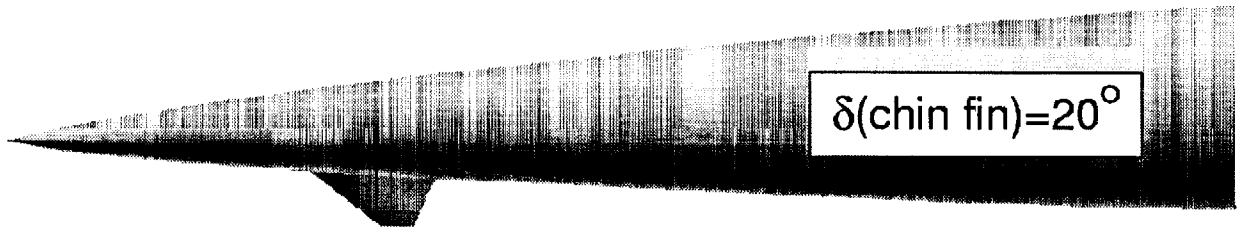

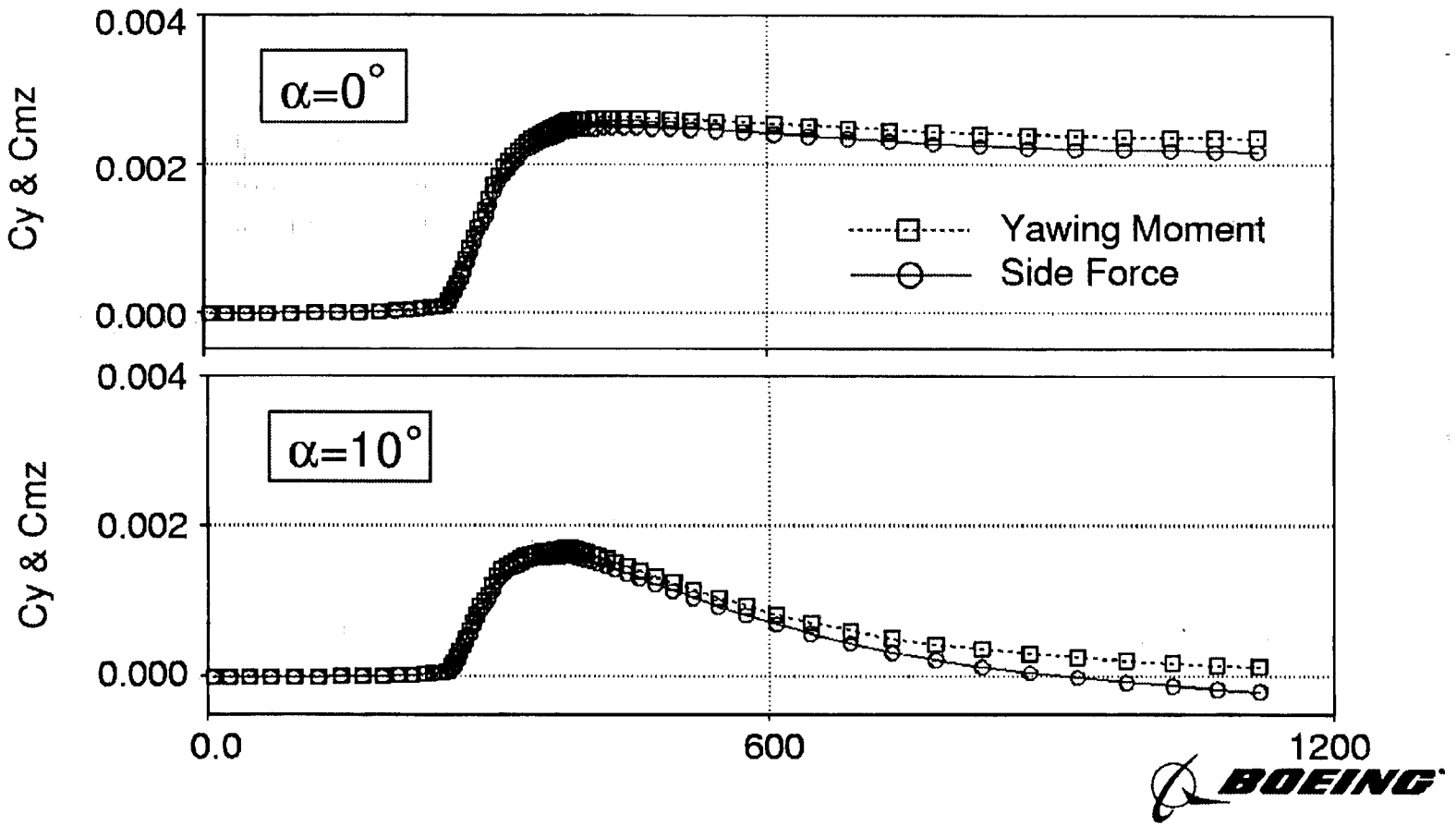

BOEING

Effects of Chin Fin Angle on TCA 4 Side Force & Yawing Moment

This chart shows the effects of chin fin angle on the TCA-4 side force and yawing moment. The test data clearly shows the diminishing of the chin fin lateral control effectiveness around alpha of 10 degrees. This phenomenon is clearly captured by the computational results with a surprisingly good agreement. The intent of the data correlation is to compare the trend rather than the absolute level, since the computational model only consists of a simplified model.

It is also noted that there is some asymmetry in the experimental data for the side force. The comparison agreement for the side force would be sensitive to the sign of the deflection angle. On the other hand, the pitching moment data appears to be less sensitive.

Effects of Chin Fin Angle on TCA 4 Side Force & Yawing Moment

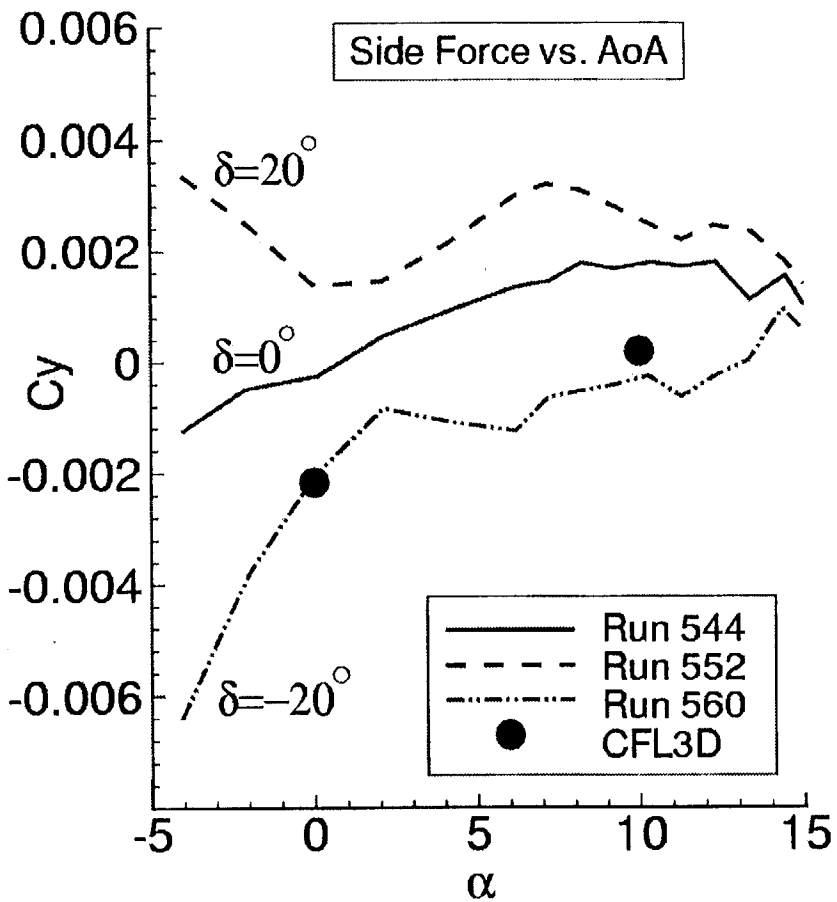

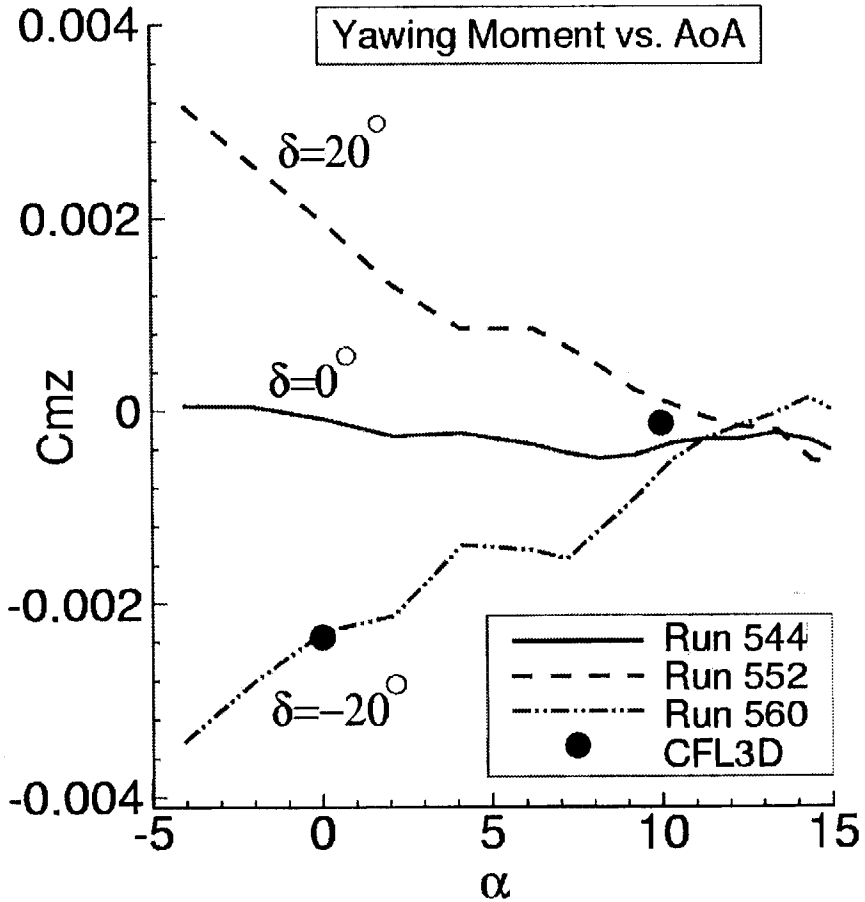

BOEING

Chin Fin Vortex Traces at α=–10, δ=20

A further study of the chin fin lateral control effectiveness at alpha=-10 degrees has been performed. This configuration is equivalent to a control surface mounted on the top of the fuselage at positive angle of attack. The objective of this study is to provide some physical insight on the influence of the forebody vortex as well as the effect of "top-mounted" control surface vortex on the lateral control characteristics.

This chart shows the chin fin vortex traces at alpha=-10 degrees with a deflection of 20 degrees. The chin fin vortex is seen to convect laterally in a manner similar to the alpha=0 case, with a downward slope due to the negative angle-of-attack.

Chin Fin Vortex Traces at $\alpha=-10^{\circ}$, $\delta=20^{\circ}$

HSCT Aerodynamics, Long Beach

M=0.3, Re=8 Million

Front View

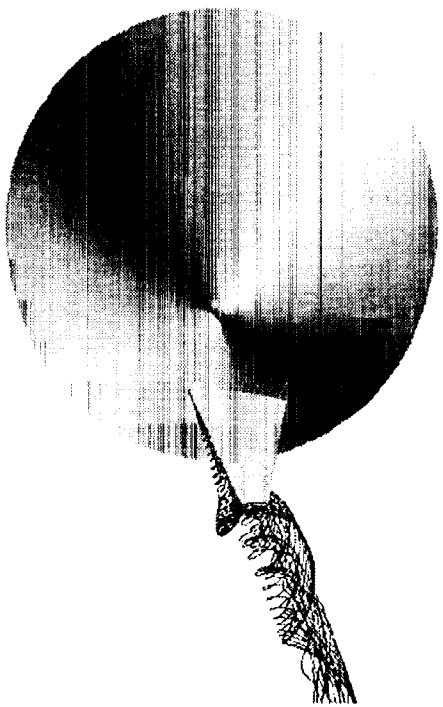

Side View

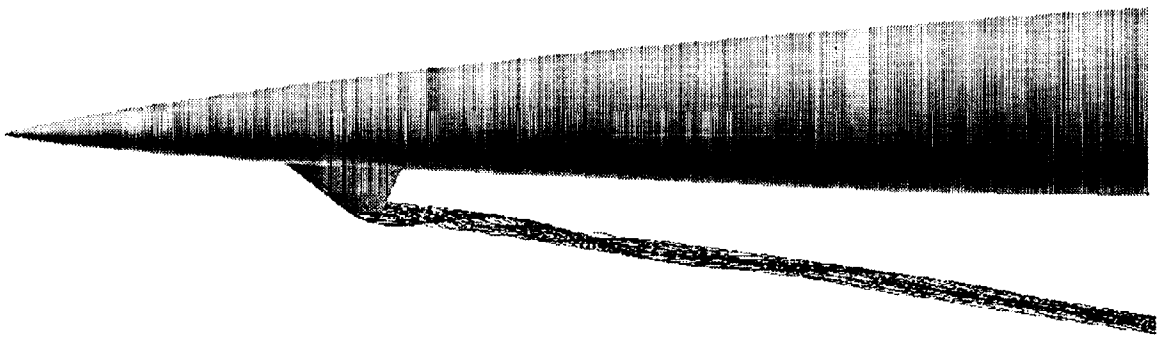

Bottom View

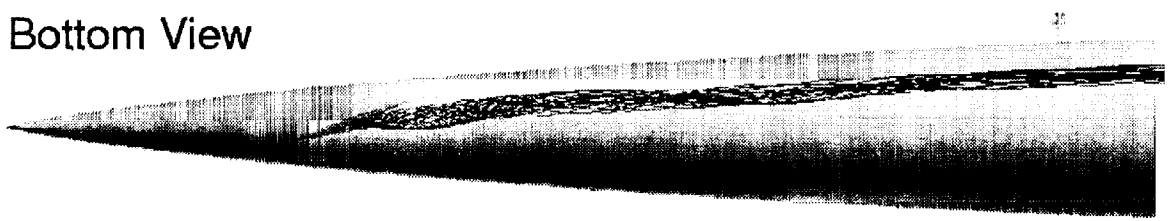

BOEING

Forebody Chin Fin Flow Characteristics at α=–10, δ=20

This chart shows some of the flow features for the forebody chin fin configuration at alpha=-10 degrees with deflection of 20 degrees. Both inboard and outboard chin fin vortices are illustrated through the releasing the particle traces and total pressure loss contours. The cross flow forebody vortices are also visible from the total pressure loss contours.

This figure illustrates the asymmetric flow phenomenon, the convection of the tip vortex as well as the vortex interactions between the inboard vortex and the cross flow forebody vortex.

Forebody Chin Fin Flow Characteristics, $\alpha=-10^{\circ}$, $\delta=20^{\circ}$

HSCT Aerodynamics, Long Beach

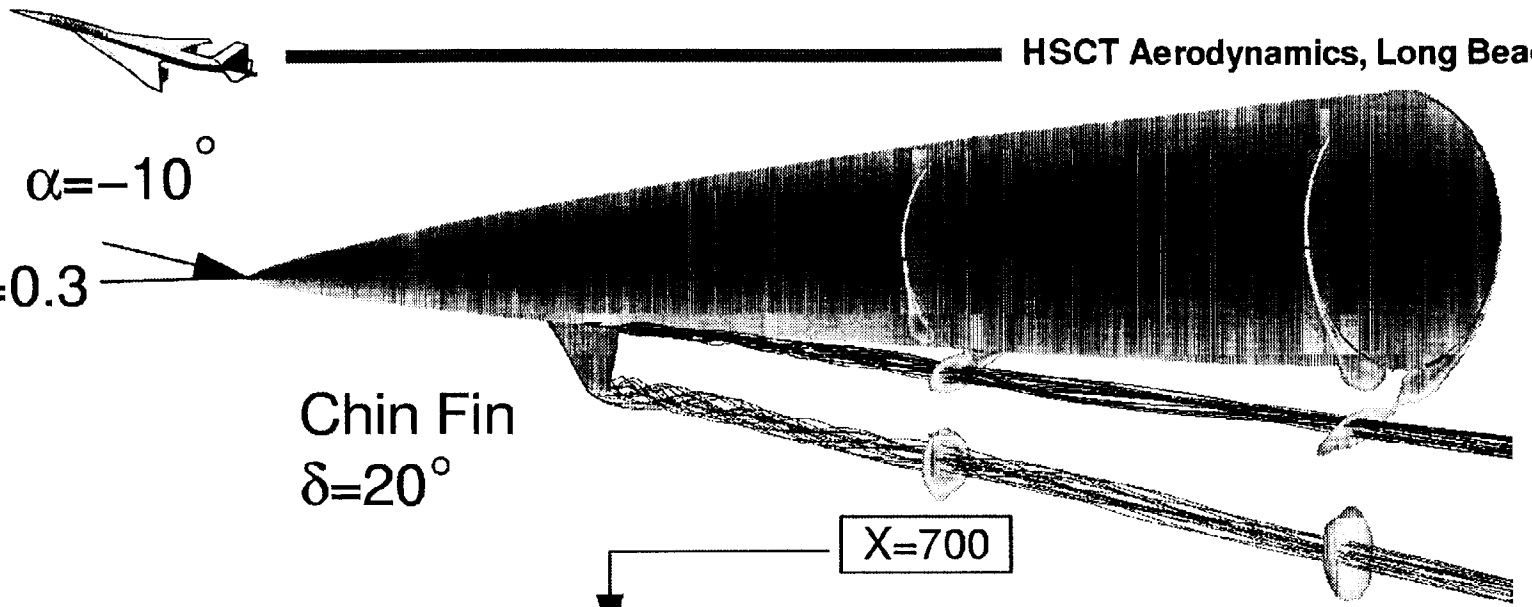

Normalized Total Pressure Loss

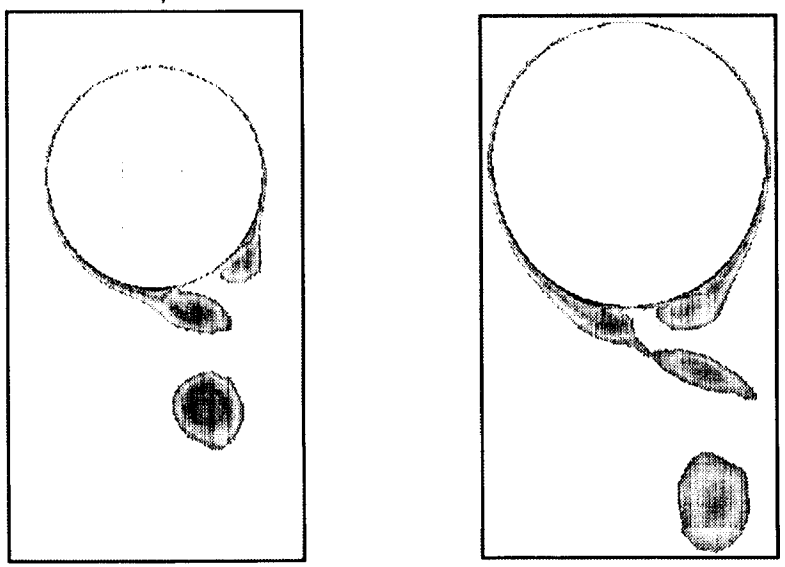

BOEING

Chin Fin Force and Moment Build-Up at α=–10, δ=20

This chart shows the force and moment build-up at alpha=-10 degrees with the deflection of 20 degrees. It clearly illustrates the augmentation of the side force and yawing moment behind the chin fin region. The numerical result shows the amount of the lateral control augmentation behind the control surface can be of the same order of magnitude as the contribution from the chin fin itself.

Chin Fin Force and Moment Build–Up at α=–10, δ=20

HSCT Aerodynamics, Long Beach

M=0.3, δ=20°

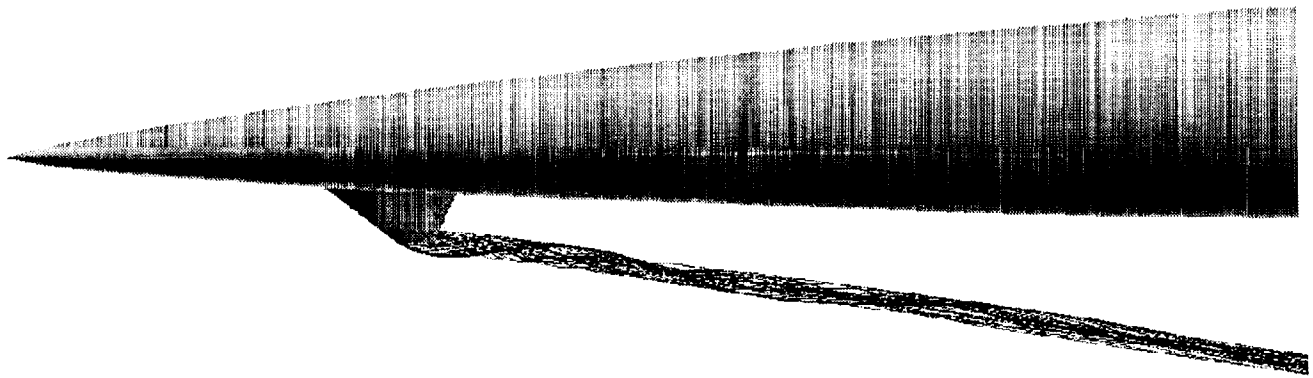

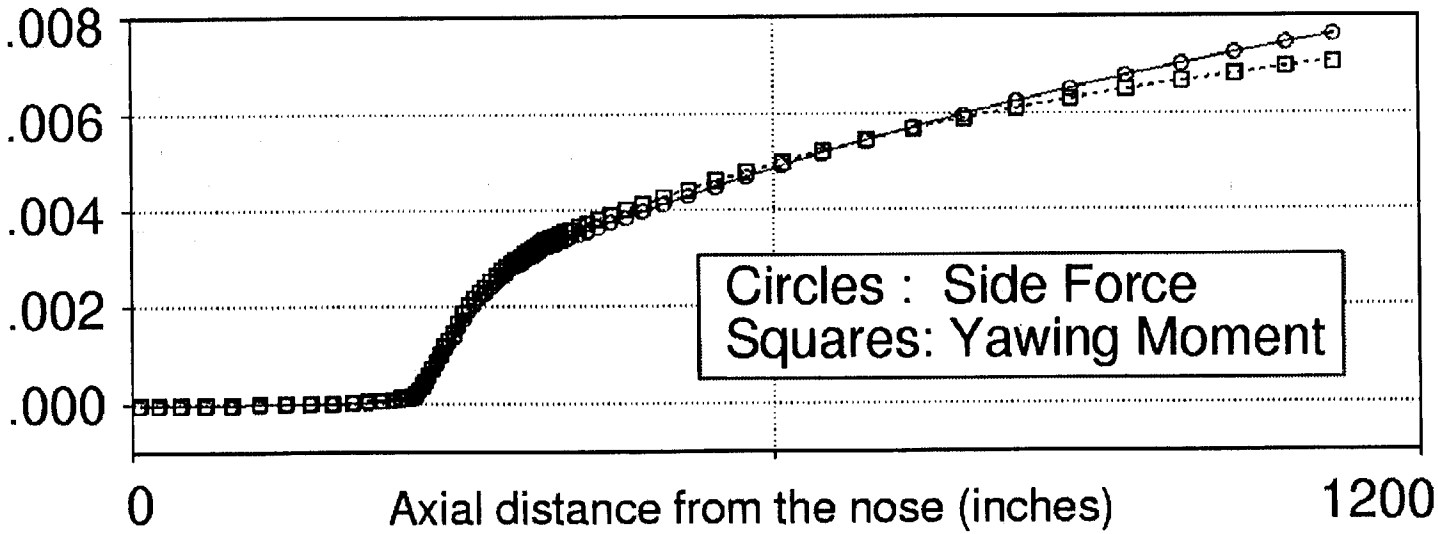

BOEING

Chin Fin Vortex Influence on the Cross Flow at α=–10

This figure shows the chin fin vortex influence on the cross flow at alpha=-10 with the deflection angle of 20 degrees. The cross flow velocity vector plot shows the velocity profiles around the fuselage at x=533.5. It illustrates the vortex positions and the surface separation locations. It appears that the flow separates earlier from the forebody on the right-hand side of the chart than the left-hand side. In addition, the trailing vortex from the tip of the chin fin induces a circulation about the fuselage which in turn generates an additional side force acting on the fuselage.

Chin Fin Vortex Influence on the Cross Flow at α=–10°

M=0.3, δ=20°

3–D Front View

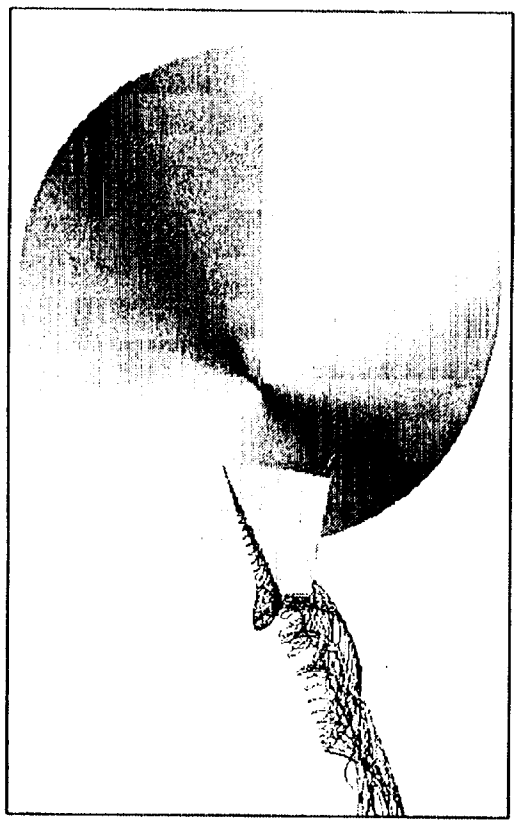

Cross Flow Velocity Vectors

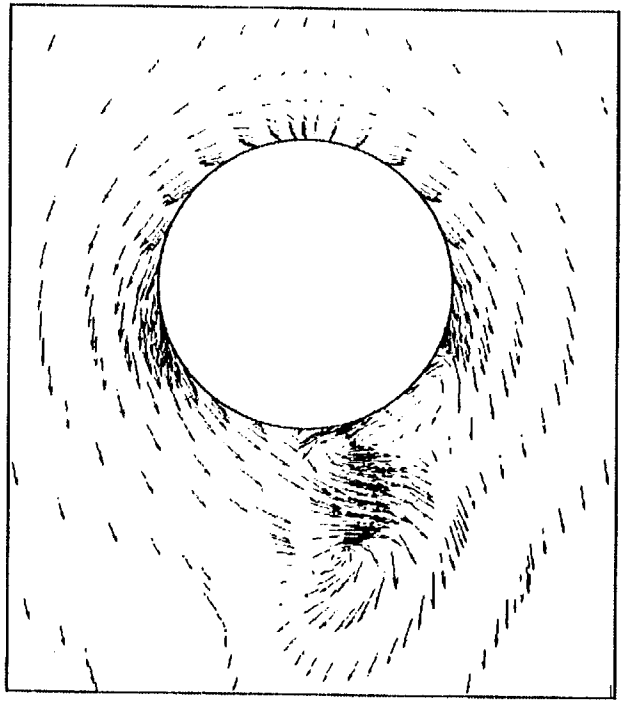

x=533.5

Pressure Field

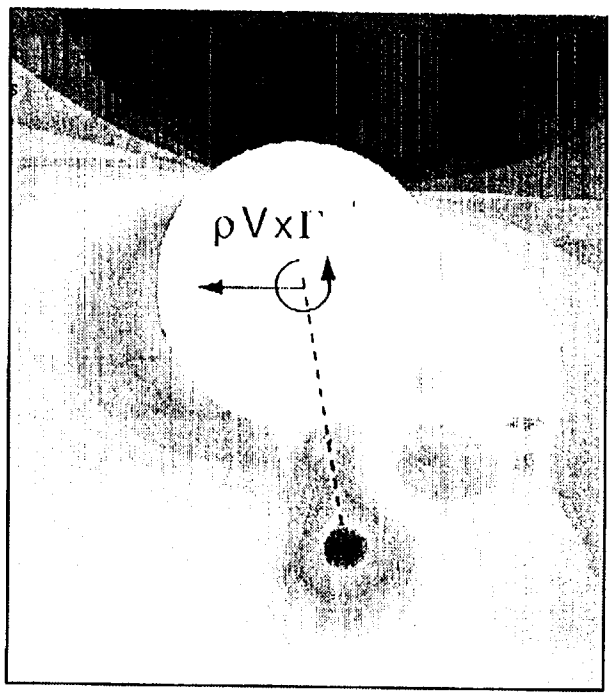

BOEING

Lateral Control Using Asymmetric High-Mount Canards

As a further investigation of the lateral control effectiveness, numerical simulations of a forebody and high-mount canards with asymmetric deflection of the elevators have been performed. The high-mount canards have the same geometries as that of the planned TCA-5 canards which will be tested in August1999. The canard is positioned 30 degrees above the horizontal plane with 30 degrees dihedral angle.

The objective of this study is to evaluate the lateral control characteristics, specifically, the side force and yawing moment. This study will be also used to provide the physical insight into the flow phenomenon and vortex influence on the fuselage.

Lateral Control Using Asymmetric High–Mount Canards

- Evaluate Lateral Control Characteristics, Cy and Cmz
- Assess Canard Vortex Influence and Interactions

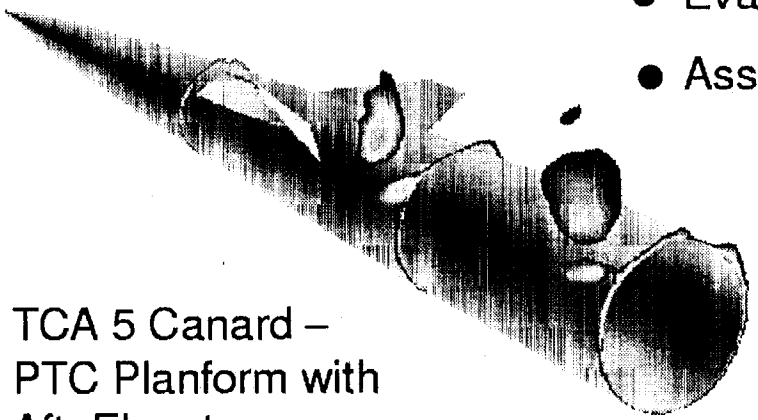

TCA 5 Canard –
PTC Planform with
Aft–Elevator

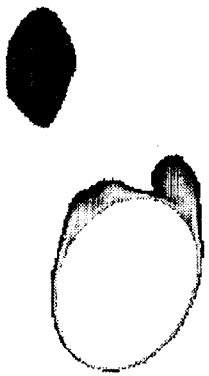

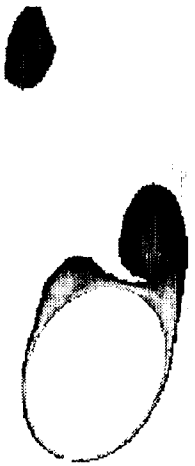

High–Mount Canard Position

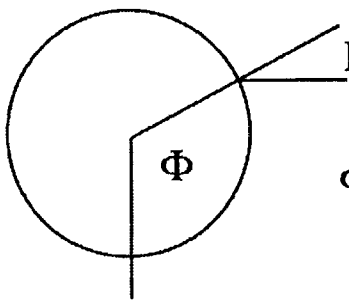

BOEING

Computational Run Matrix for High-Mount Canards

This figure shows the computational run matrix for the high-mount canard study. There are a total of 3 cases to be analyzed at M=0.3, alpha=10, with the canard deflection of -5 degrees on both side.

The baseline configuration is considered to be the symmetrical case where the elevators on both sides are deflected 15 degrees. The first two cases will address elevator deflection changes of +15 and -15 degrees. The first case is to undeflect one side of the elevator by 15 degrees from the baseline, while the second case deflects the elevator by an additional 15 degrees. The third case will be focused on the elevator deflection change of 30 degrees.

The numerical results of these cases will be used to evaluate the lateral control effectiveness as well as to assess the linearity of the forces and moment at large elevator deflections.

Computational Run Matrix for High–Mount Canards

HSCT Aerodynamics, Long Beach

- 3 Cases at M=0.3, $\alpha=10^{\circ}$, $\delta_{can}=-5^{\circ}$

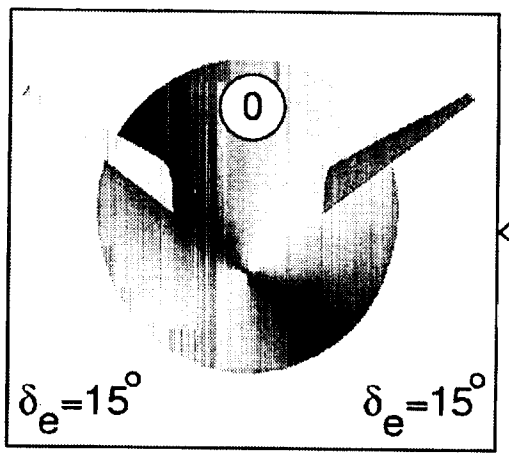

$\Delta\delta_e=15^{\circ}$

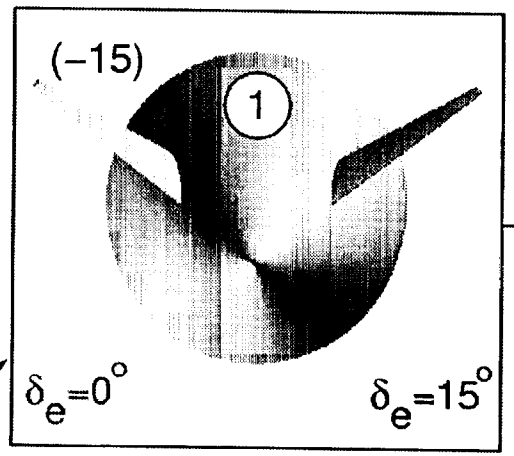

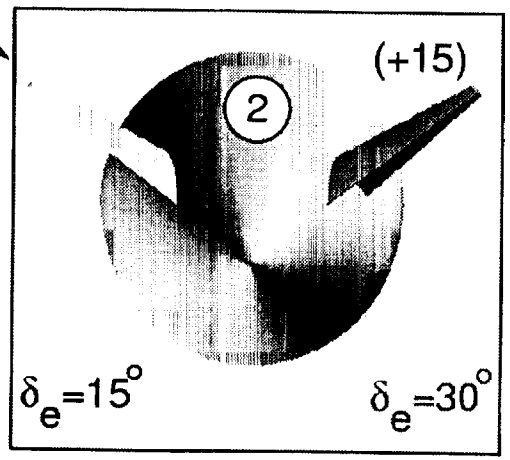

$\Delta\delta_e=30^{\circ}$

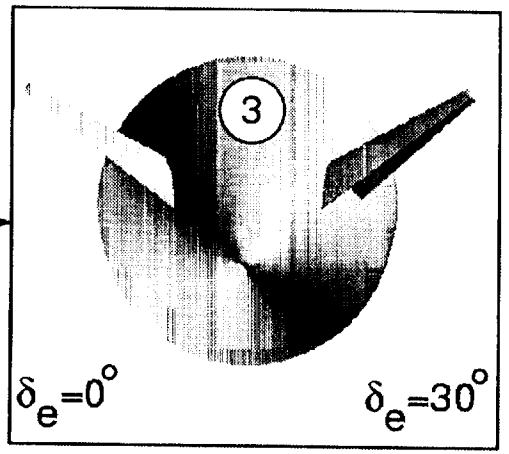

Compare Cy & Cmz:

- 1 & 2 – Effectiveness
- 1 & 3 – Linear ?

BOEING

Flow Solutions for High-Mount Canards with $\Delta\delta_e$=15

This figure shows the comparison of the flow solutions for cases 1 and 2, that both have delta elevator deflection of 15 degrees. For case 1, the elevator is unloaded on one side resulting in a weak trailing vortex. On the other hand, the elevator is further deflected in case 2 resulting in a stronger vortex on one side as well as a stronger vortex interaction between the gap vortex and the forebody flow field.

Flow Solutions for High–Mount Canards with $\Delta\delta_e$=15 deg

M=0.3, α=10 degrees (Total Pressure Contours)

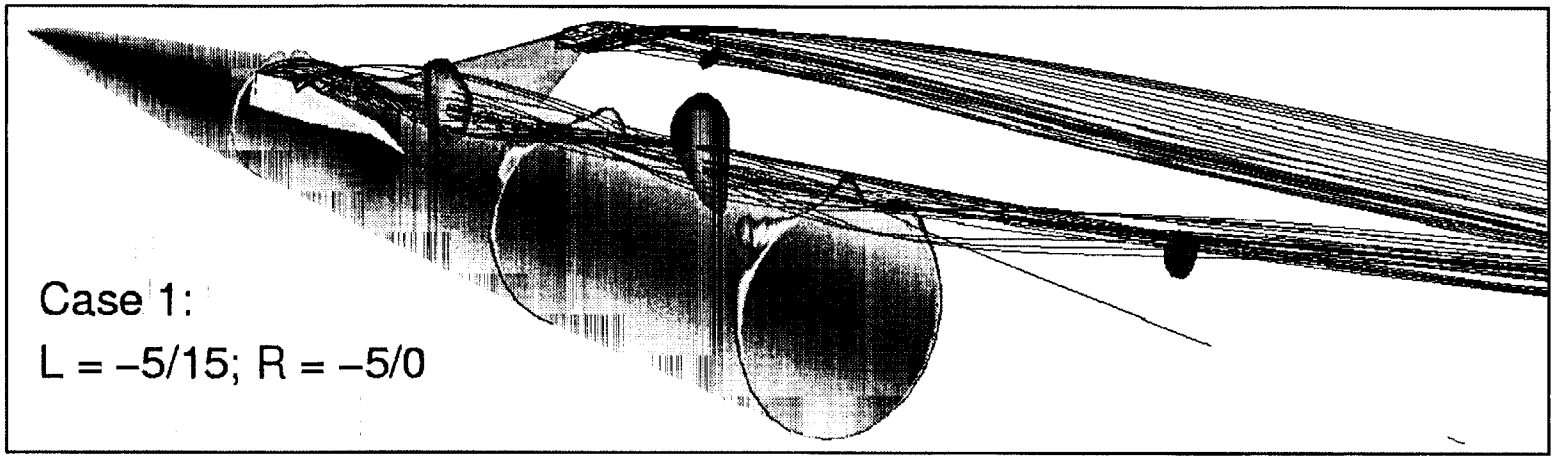

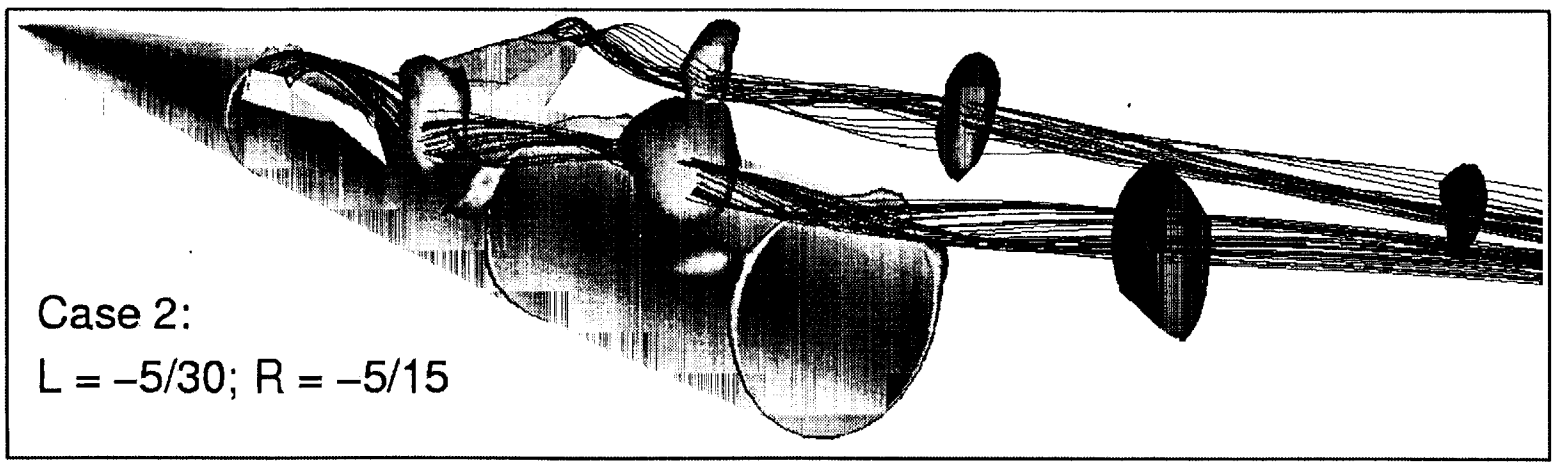

BOEING

High-Mount Canard Force and Moment Build-Up for $\Delta\delta e=15$

The chart shows the force and moment build-up for the cases 1 and 2. For case 1, the side force and yawing moment created by the asymmetric elevator deflections can be seen in the canard region. It is also observed that the lateral control is further augmented by the favorable vortex influence on the body behind the canard trailing edge. The generation of the lateral control in the canard region for case 2 can also be seen, although the magnitude is less compared to that in case 1. The noticeable difference between case 1 and 2 is that there is no additional augmentation of the lateral control behind the canards in case 2.

The effects of the canards and vortex influence have been analyzed and will be presented in the next few charts.

High-Mount Canard Force and Moment Build-up for $\Delta\delta_e$=15 Cases

HSCT Aerodynamics, Long Beach

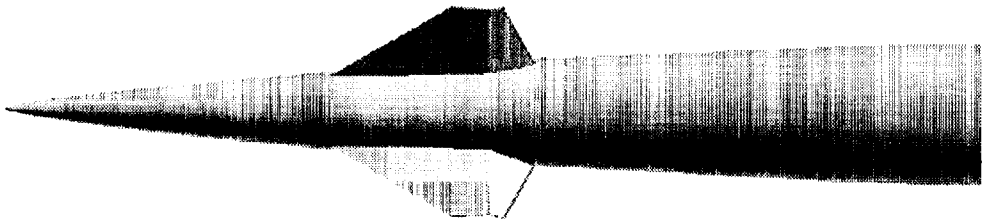

-5/0 -5/15

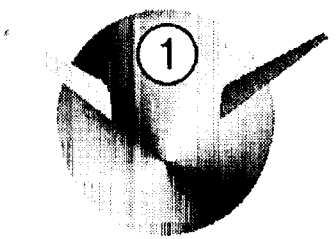

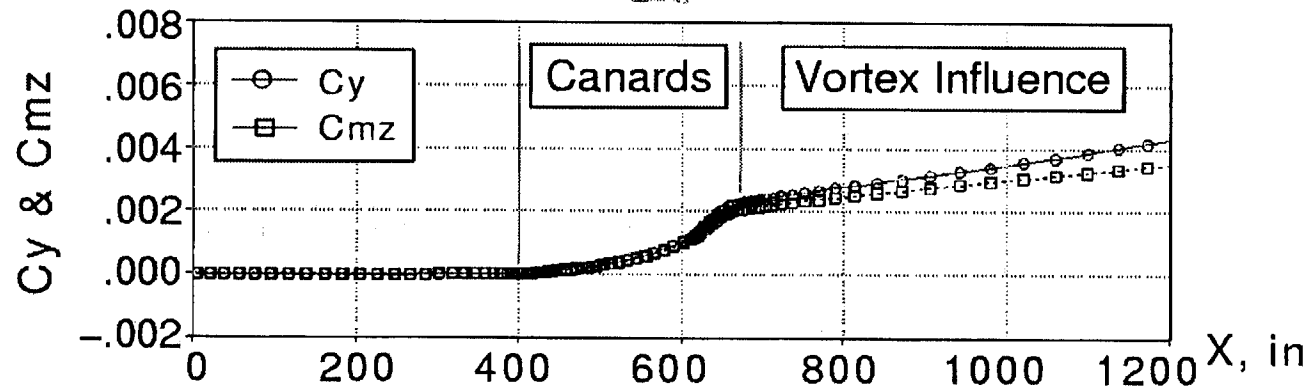

-5/15 -5/30

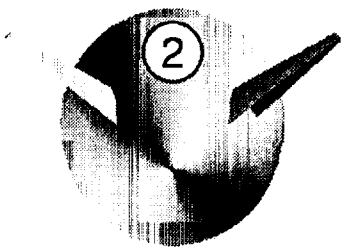

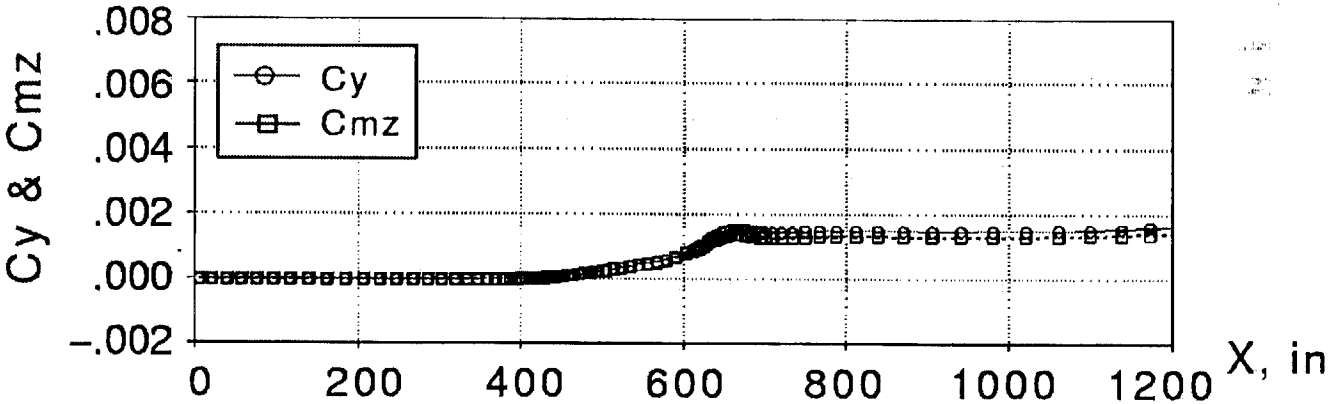

BOEING

Comparison of Surface Streamlines for $\Delta\delta e$=15 Cases

The comparison of the computed surface streamlines for asymmetric elevator deflection of 15 degrees is illustrated in this figure.

For case 1, the flow remains attached on the elevator when the elevator has zero deflection angle. On the other hand, the flow is seen to be separated along the hingeline as the elevator is set at 15-degree deflection. It is expected that the elevator effectiveness will decrease beyond 15 degrees deflection due to this elevator separation (stalled) phenomenon.

For case 2, the TE hingeline separation is observed on both sides of the elevator surfaces for the elevator deflections of 15 and 30 degrees. The flow appears to be more symmetric in this case. As a result, the lateral control power is reduced as compared to case 1.

Comparison of Surface Streamlines for $\Delta\delta_e$=15 Cases

$M=0.3, \alpha=10^\circ, \delta_{canard}=-5^\circ$

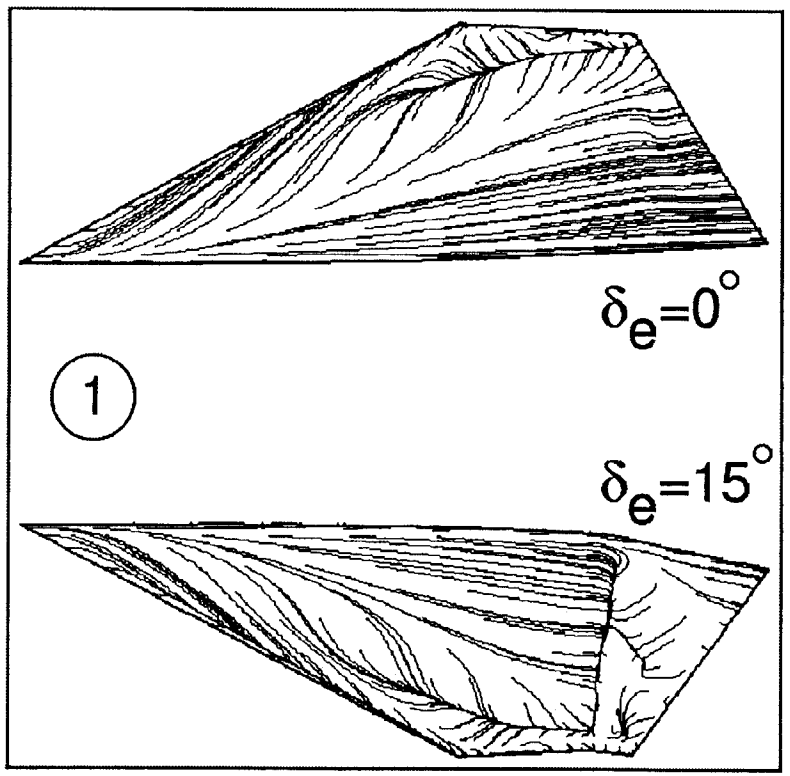

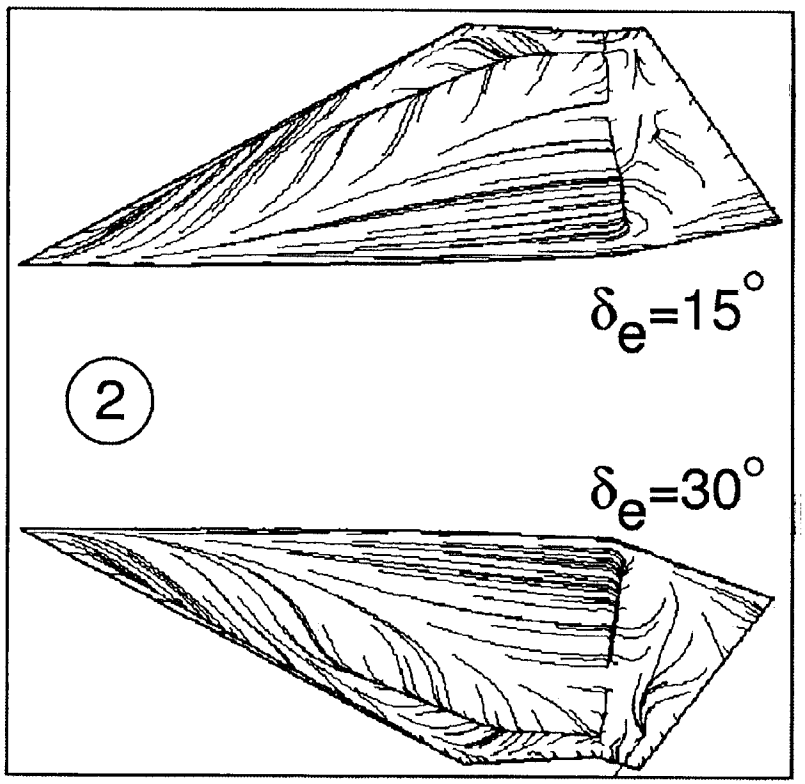

BOEING

High-Mount Canard Cross Flow for $\Delta\delta e=15$ Cases

This chart shows the cross flow fields for cases 1 and 2. For the first case, the asymmetric vortical flow appears to induce a circulation around the body resulting in augmentation of the lateral control effectiveness.

High Mount Canard Cross Flow for $\Delta\delta_e$=15 Cases

HSCT Aerodynamics, Long Beach

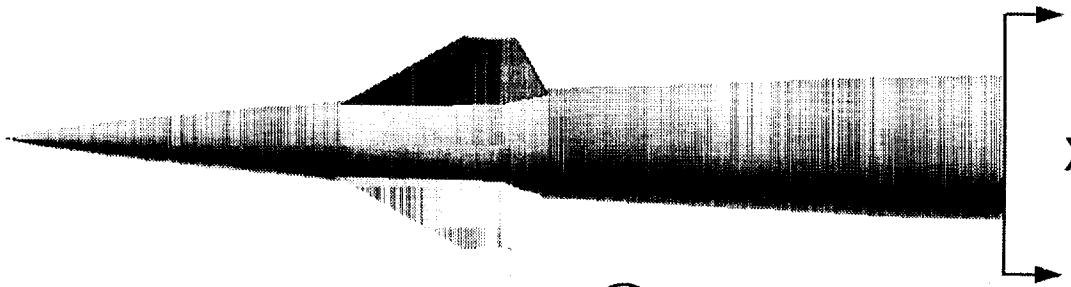

① δ_e=0 δ_e=15

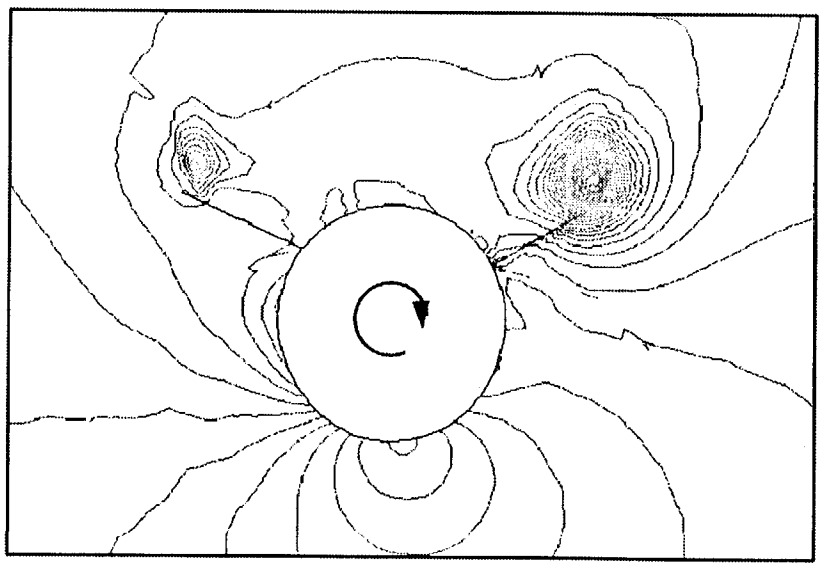

② δ_e=15 δ_e=30

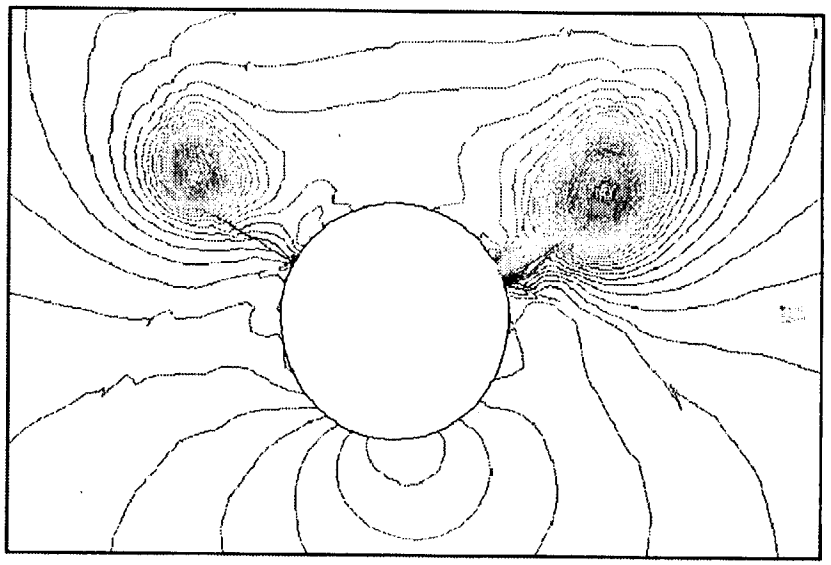

BOEING

Flow Solutions for High-Mount Canards (Cases 1 & 3)

This chart shows the comparison of the flow solutions for cases 1 and 3. For both of the cases, the canard has been unloaded on one side. The canard vortex is seen to be stronger for the third case where the elevator has been deflected twice as much as compared to the second case. The focus of this study is to assess the lateral control effectiveness at large elevator deflections.

Flow Solutions for High–Mount Canards with $\Delta\delta_e$=15 deg and $\Delta\delta_e$=30 deg

M=0.3, α=10 degrees (Total Pressure Contours)

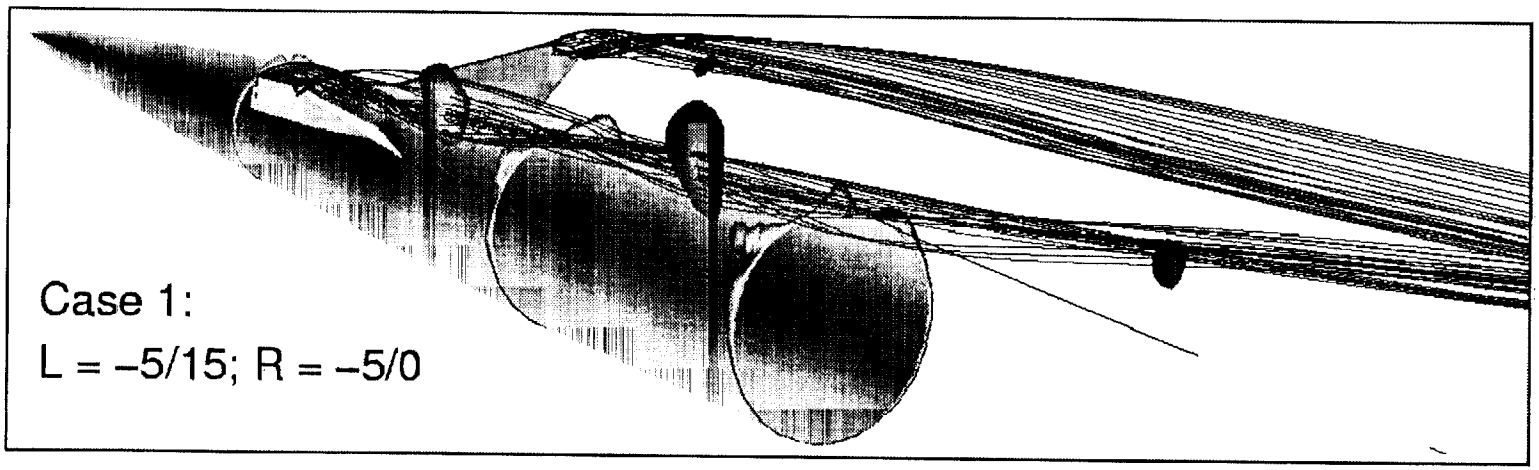

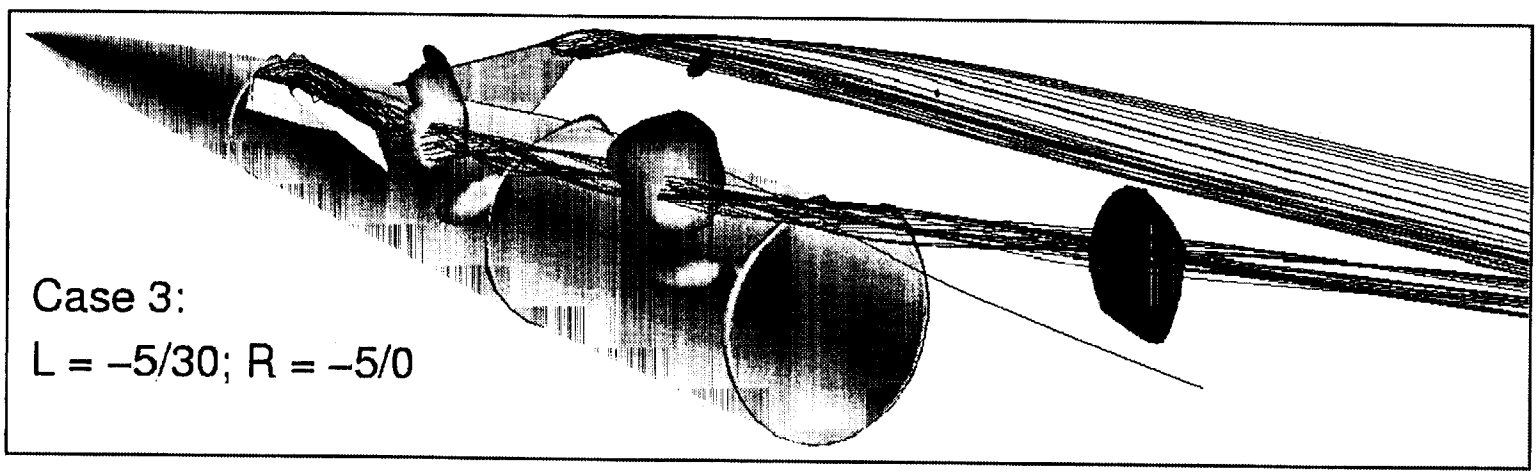

BOEING

Force and Moment Build-Up for $\Delta\delta e=15, \Delta\delta e=30$ Cases

This chart shows the comparison of the force and moment build-up for cases 1 and 3. For both of the cases, the side force and yawing moment are generated by the high-mount canards. The augmentation of the lateral control is also observed for both cases due to the favorable influence of the symmetric vortices. It is also noted that the lateral control effectiveness increases as the elevator deflection increases. This phenomenon is seen both in the canard region as well as behind the canard.

Force & Moment Build-Up for $\Delta\delta_e$=15 and $\Delta\delta_e$=30 Cases

HSCT Aerodynamics, Long Beach

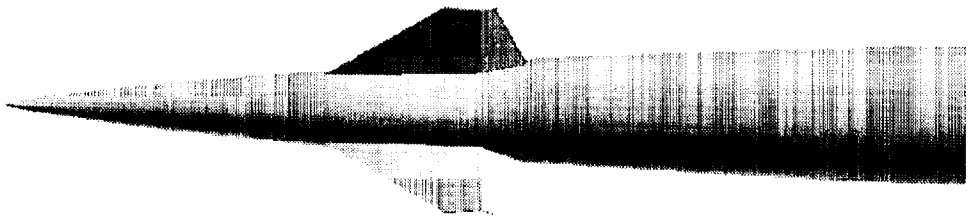

-5/0 -5/15

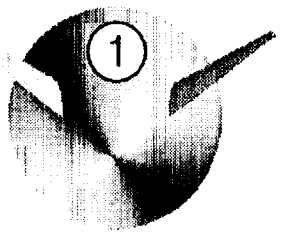

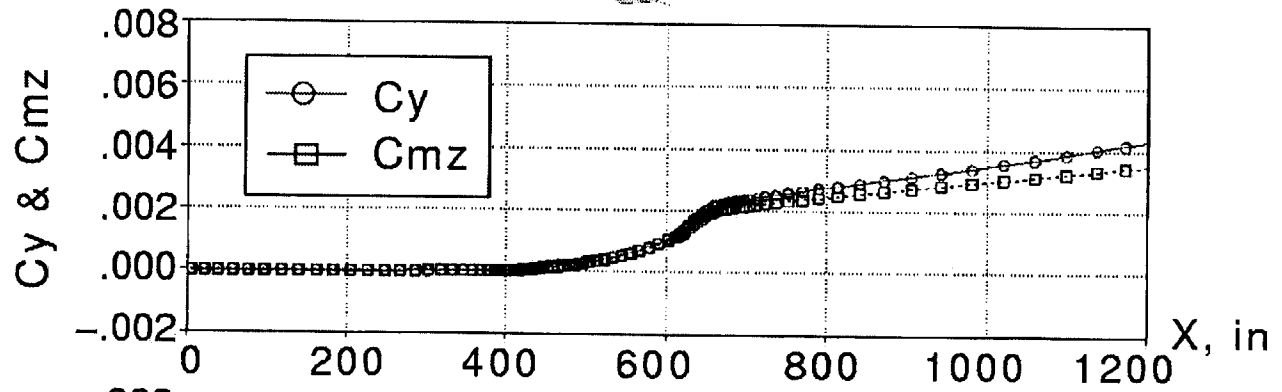

-5/0 -5/30

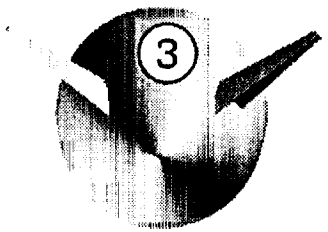

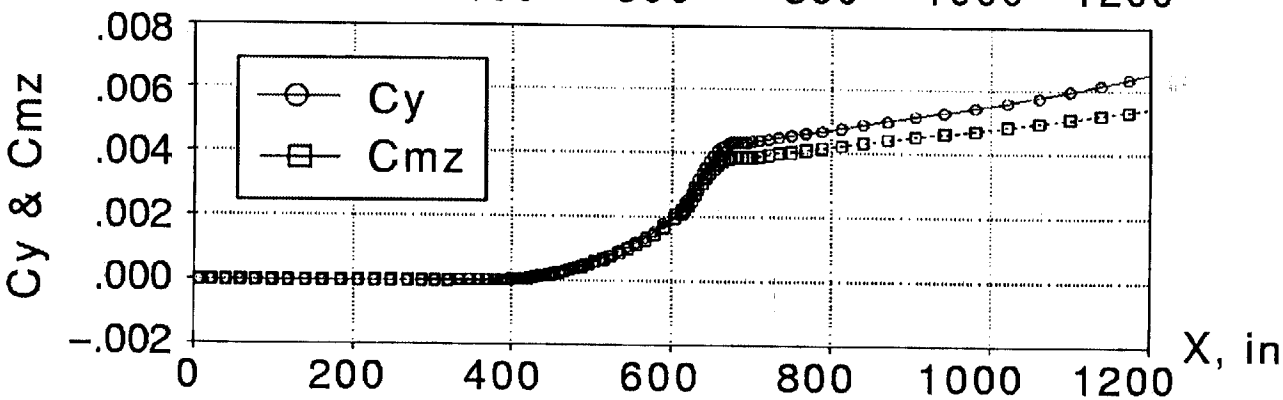

BOEING

Comparison of Surface Streamlines for $\Delta\delta e=15$, $\Delta\delta e=30$ Cases

This chart shows the upper surface flow patterns for the cases 1 and 3. It can be seen that as the elevator deflection is increased to 30 degreees in the third case, its influence on the opposite side of the canard becomes greater as indicated by the partly separated flow on the elevator surface.

The side force and yawing moment generated by each configuration is also tabulated in the chart. It is shown that the increment in lateral control power is not linear due to the stalled flow on the aft-elevator.

Comparison of Surface Streamlines for $\Delta\delta_e$=15 and $\Delta\delta_e$=30 Cases

HSCT Aerodynamics, Long Beach

$M=0.3, \alpha=10^\circ, \delta_{canard}=-5^\circ$

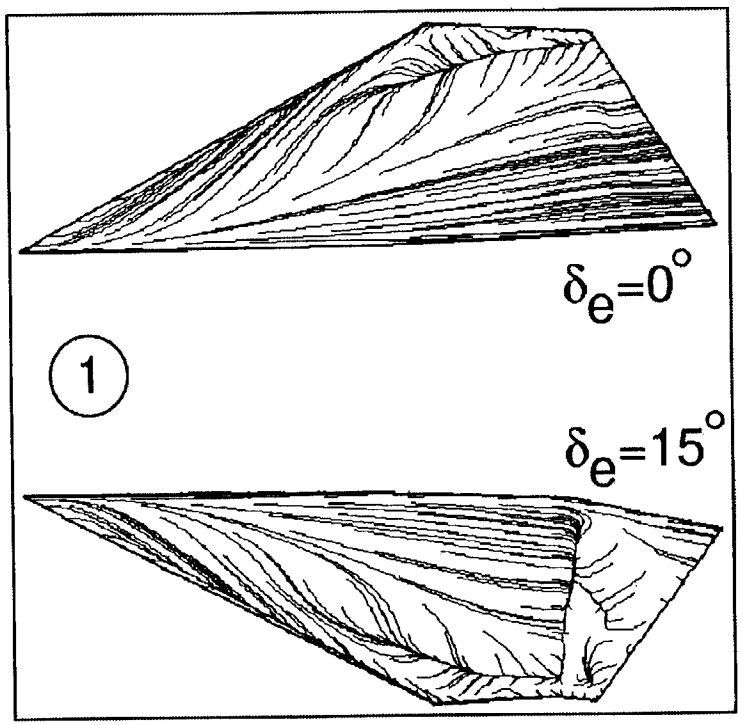

Cy =.0043
Cmz=.0035

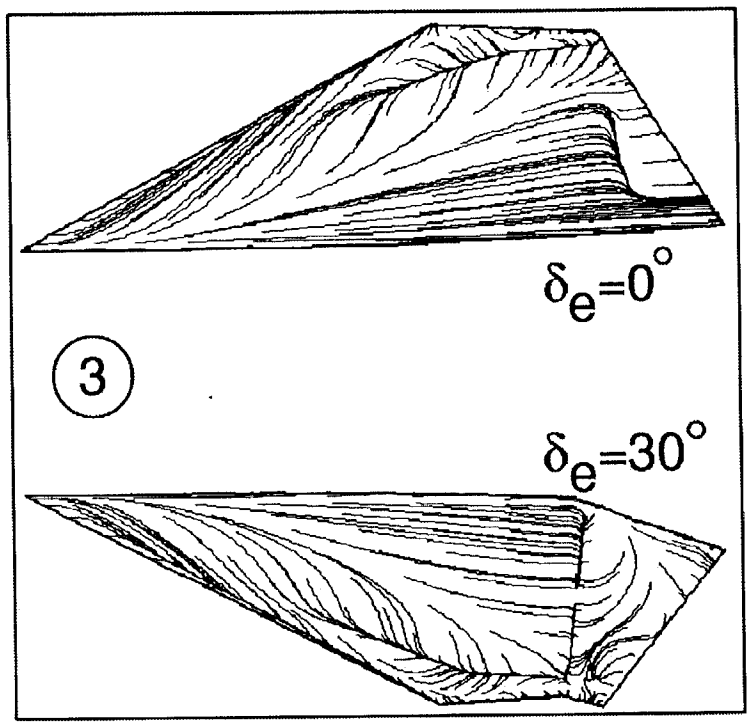

Cy =.0066
Cmz=.0054

BOEING

High-Mount Canard Cross Flow for $\Delta\delta e=15$ & $\Delta\delta e=30$ Cases

The cross flow pressure fields for cases 1 and 3 are illustrated in this chart. Similar flow phenomenon is seen for both cases where a low pressure is induced on the side of body which further enhances the control power downstream of the canard region.

High Mount Canard Cross Flow for $\Delta\delta_e$=15 and $\Delta\delta_e$=30 Cases

HSCT Aerodynamics, Long Beach

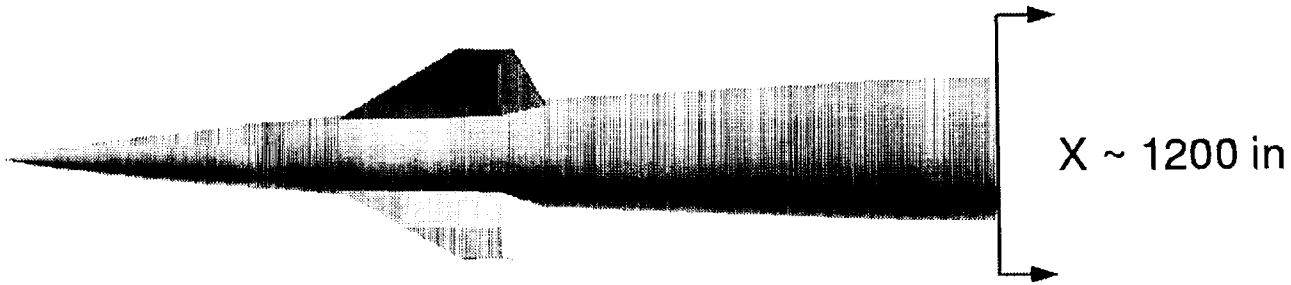

① δ_e=0 δ_e=15

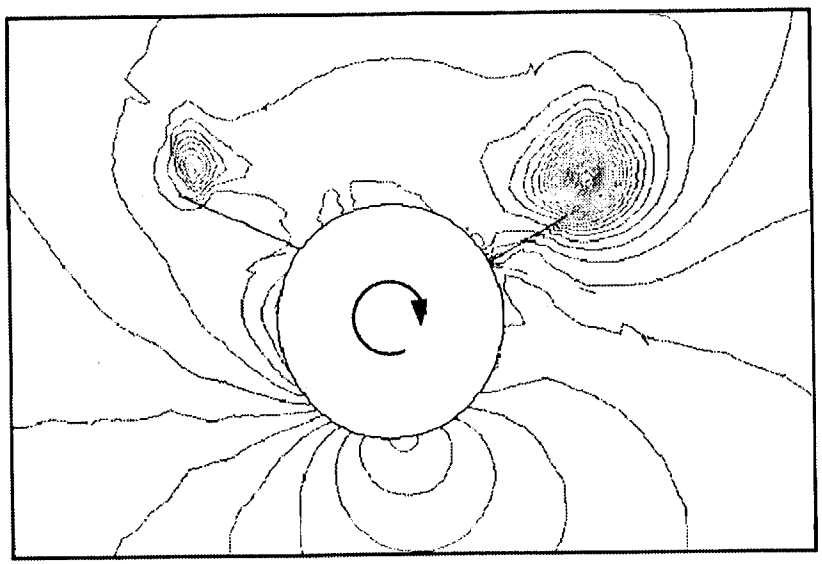

③ δ_e=0 δ_e=30

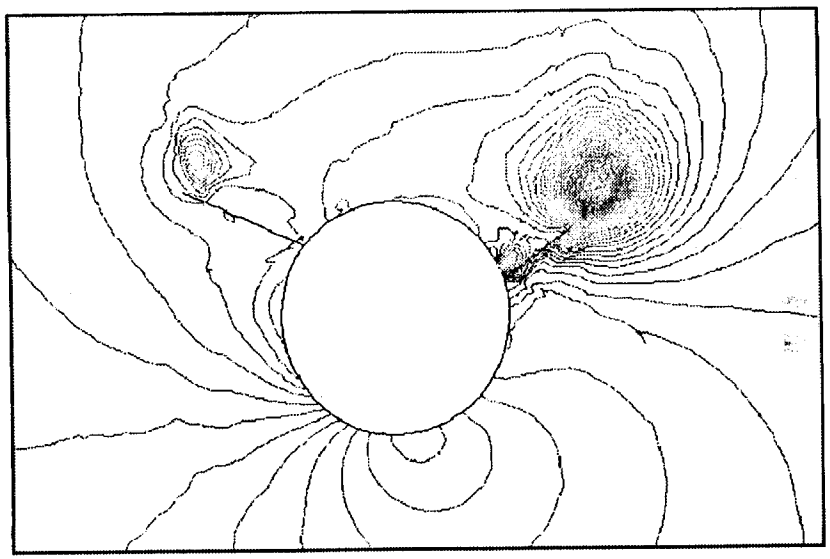

BOEING

Summary

The numerical capability to model forebody control surfaces has been demonstrated for the chin fin and asymmetric canard deflections. Favorable comparisons of the trends for the side force and yawing moment are observed between the numerical prediction and the TCA-4 chin fin test results.

The numerical results have shown that the chin fin provides the lateral control at alpha zero, but the effectiveness vanishes at alpha 10 degrees due to the counteracting vortex influence on the side of forebody. On the other hand, the lateral control is enhanced at alpha=-10, which is equivalent to a top-mount control surface at alpha=10, due to the favorable vortex interaction in the cross flow.

The numerical solutions have also shown that the high-mount canard with asymmetric elevator deflections provides the lateral control effectiveness. Based on the simulated cases, it is observed that the lateral control would be enhanced when one side of the canard/elevator is unloaded. By unloading one side, the potential stalling phenomenon can be avoided which would provide a greater asymmetry in the canard region. The asymmetrical influence by the favorable vortex interaction in cross flow further enhances the lateral control authority.

Summary

- Demonstrated the capability to model forebody control surfaces
- Forebody/chin fin solutions and TCA–4 data show good correlation
- Numerical solutions have shown:
  - The Chin Fin
    - * Provides Cy and Cmz at α=0
    - * Lateral control is diminished at α=+10
      - –due to counteracting vortex influence on the forebody
    - * Lateral control is enhanced at α=–10 (~top mount)
      - –due to favorable vortex interaction in the cross flow
  - The High–mount canards with asymmetric elevator deflection
    - * Provides Cy and Cmz
    - * Lateral control is enhanced when one side is unloaded
      - – avoid stalling
      - – provides greater asymmetry in the canard region
      - – influenced by favorable vortex interaction in the cross flow

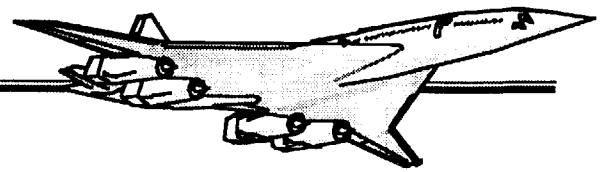

High-Lift CFD Validation

Wendy B. Lessard

Airframe Annual Review
February 10, 1999

High Lift Technology Development (Task 33)

Increase L/D, Develop Analysis/Design Methodology

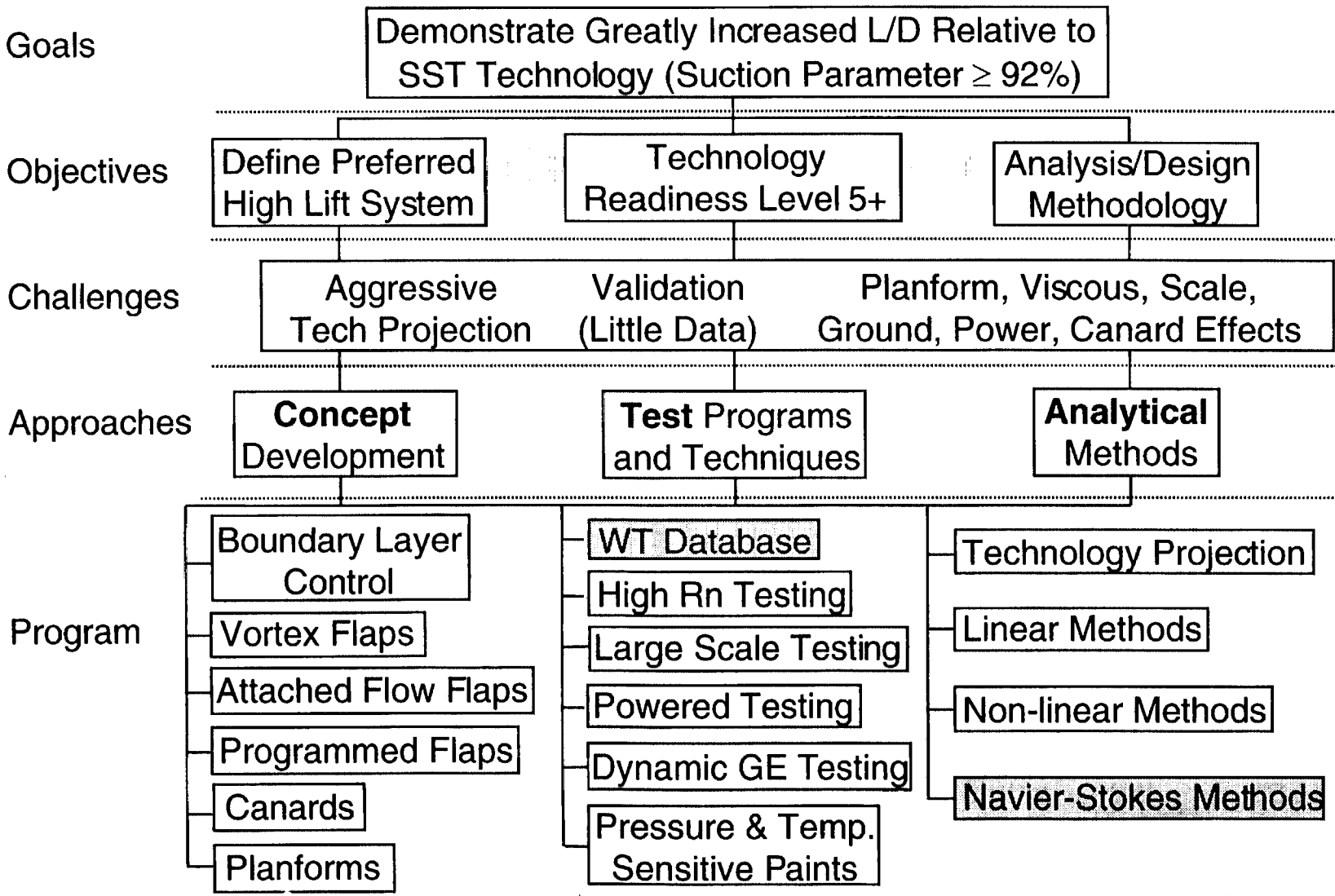

The outline for this talk is listed here. This presentation will basically cover the objectives, background material, proposed plans for a 7x10 validation test, and some pre-test CFD predictions.

Outline

- Objectives
- Introduction
- Database (1994-1998)
- Team Participants
- CFD Validation Test in Ames' 7x10
- Pre-test CFD calculations
- Conclusions

The main objective of the Ames' 7x10 wind-tunnel test is to measure the off-body and surface flow field of the 2.2% Reference H high-lift (30/10) configuration. The measurements obtained will be detailed and accurate for CFD validation.

Objectives

- To acquire a set of accurate surface and off-surface flow field data for code validation. These data will be unique in that all flow field measurements obtained will be performed using state-of-the-art experimental techniques, which will complement each other. All this done in one test.
- The objective can be accomplished with a well planned test entry in the Ames 7x10 wind tunnel with shared responsibility between Ames, Langley, and Boeing.

It is not unusual when comparing CFD data to experimental data to find discrepancies between the results. Sometimes forces and moments compare well, while surface pressures do not, and vice versa. It is commonplace for the researcher to believe that the flow field has been accurately simulated when these types of measurements compare well. However, being able to routinely predict boundary layer transition and separated flows are not guaranteed. In fact accurate simulation of these types of flow physics has been a challenge to the CFD community. In order to improve Navier-Stokes predictions for complex vortical flow fields, more detailed information about the flow physics is necessary. Unfortunately, the many wind-tunnel tests performed in Langley's NTF and 14x22 facilities as well as in the Ames' 12 ft Tunnel provided little information about the detailed flow physics, and no priority was given to obtaining any CFD measurements. Using the latest experimental techniques, this information can and should be obtained for present and future use.

Introduction

- Existing HSR high-lift databases include mainly force and moment data. Obtaining detail flow measurement for CFD validation was not a priority for any HSR H-L test.
- Using existing databases it appears that the N-S flow solvers have reached their plateau in terms of applicability to complex flows.
  - NTF Tests: 057, 060, 067, 070, 073, 078, 080, 084, 089.
  - 14x22 Test: 404, 421, 428, 429, 437, 442, 449, 473.
  - Ames 12-Ft Tests: 019, 037.
- Need for a detailed set of quantitative measurements, which will complement the existing data obtained.

The 7x10 CFD validation test is a joint effort between NASA and Industry. The team members from each organization are listed.

Team Participants

- Ames: Bruce Storms, J.T. Heineck, Dave Driver, James Bell, Julie Pollitt, Ching-Mao Hung.
- Langley: Wendy Lessard, Steve Yaros, John Carlson
- Boeing Seattle: Allen Chen, Tim Siebersma.
- Boeing Long Beach: David Yeh.

The acquisition of force and moment data and surface pressures do not provide enough information about the flow physics to adequately validate/calibrate the Navier-Stokes codes for these highly 3D vortical flow fields. In order to eventually use these codes for design and rely less on wind-tunnel testing, the researcher must have confidence in the predicted results. The codes should be able to predict flow features such as boundary-layer transition, 3D vortical flow fields, surface flow quantities, and total pressures in the wake.

CFD Validation Test
Measurement Requirements

- CFD team has identified elements missing from the HSR H-L CFD database.
- Important items would include measuring:
  - Boundary-layer transition.
  - Off-body flow, highly 3D vortical flow field.
  - Surface flow quantities.
  - Total pressure in the wake region.

A CFD validation test is planned in Ames' 7x10. Detailed flow measurements will be obtained on an already existing model, the 2.2% Reference H model, which was tested in NTF. The plan of test will cover only two angle of attack conditions: 8° and 12° at M = 0.3 and a Reynolds number, which is based on the mean aerodynamic chord, of 4 million. The 8° and 12° angle of attack cases were chosen since they are representative of an attached and separated flow field. The idea here is to correlate the measurements of the attached, well-behaved vortical flow field to the separated flow field. Since the complex flow features for the separated case will be more difficult to measure accurately, the attached flow case may provide insight into the flow physics of the separated flow field. The instrumentation that will be used in the 7x10 tunnel test are listed.

CFD Validation Test
Approach

- 2.2% NTF high-lift (30/10) model in Ames 7x10.
- M = 0.3, Re = 4 million, based on MAC.
- Two angles of attack - 8° (attached) & 12° (separated).
- Instrumentation:
  - PIV - instantaneous and mean flow velocities.
  - PSP - global picture of surface pressure.
  - ESP - surface pressure measurements.
  - Oil Interferometry - skin friction and transition.
  - Oil flow - separation and vortex core flow path.
  - Pitot rakes - measure total pressure in the wake.
  - Balance - Total forces and moments.

The Reference H has been tested before, and there are existing 6.0% and 2.2% scale CFD solutions for this particular configuration, which is the wing/body with all leading edge flaps deflected at 30 degrees and all trailing edge flaps deflected at 10 degrees. Since this is the first time this model will be tested in the 7x10, the effect of the post-mount on the flow aerodynamics was assessed using A502. Getting accurate total pressure measurements using either a pitot tube rake or Kiel tube in the wake was another concern, and the flow angularities were investigated.

Pre-test CFD Results

- Effect of mounting post using A502.
- N-S solutions - flow field characteristics to aid in guiding the experiment.
- Flow angularities in the near wake - aid in selection of appropriate instrumentation for total pressures.

The 2.2% Reference H model is shown mounted sideways, which is necessary to perform PIV. An existing post and box beam are also shown. The model is mounted to the post via a sting, which is being designed and fabricated at Ames.

2.2% Reference H Model Test Set-Up
In the 7x10 Tunnel at Ames

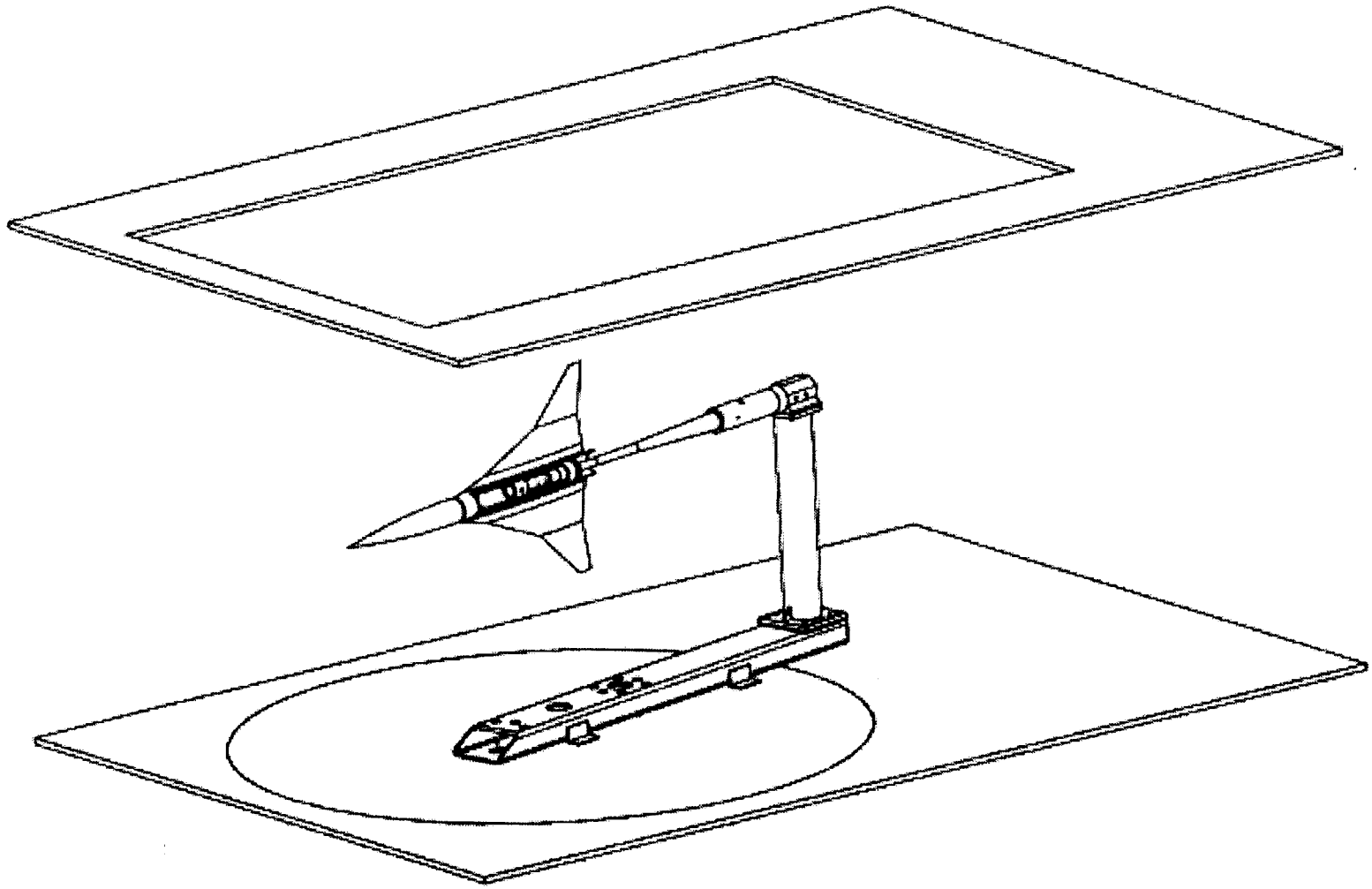

The A502 solution is shown for the model and post, which are inside the 7x10. Note the sting and box beam were not modeled. This figure depicts surface pressure coefficients, and shows that the post has little effect on the model; however, there is some pressure variation seen on the tunnel walls due to the post and model.

Ref. H W/B, Flaps LE 30/TE 10 in '7x10' With Half Post A502 Solution for Mach 0.3, Model Alpha 12 Degrees

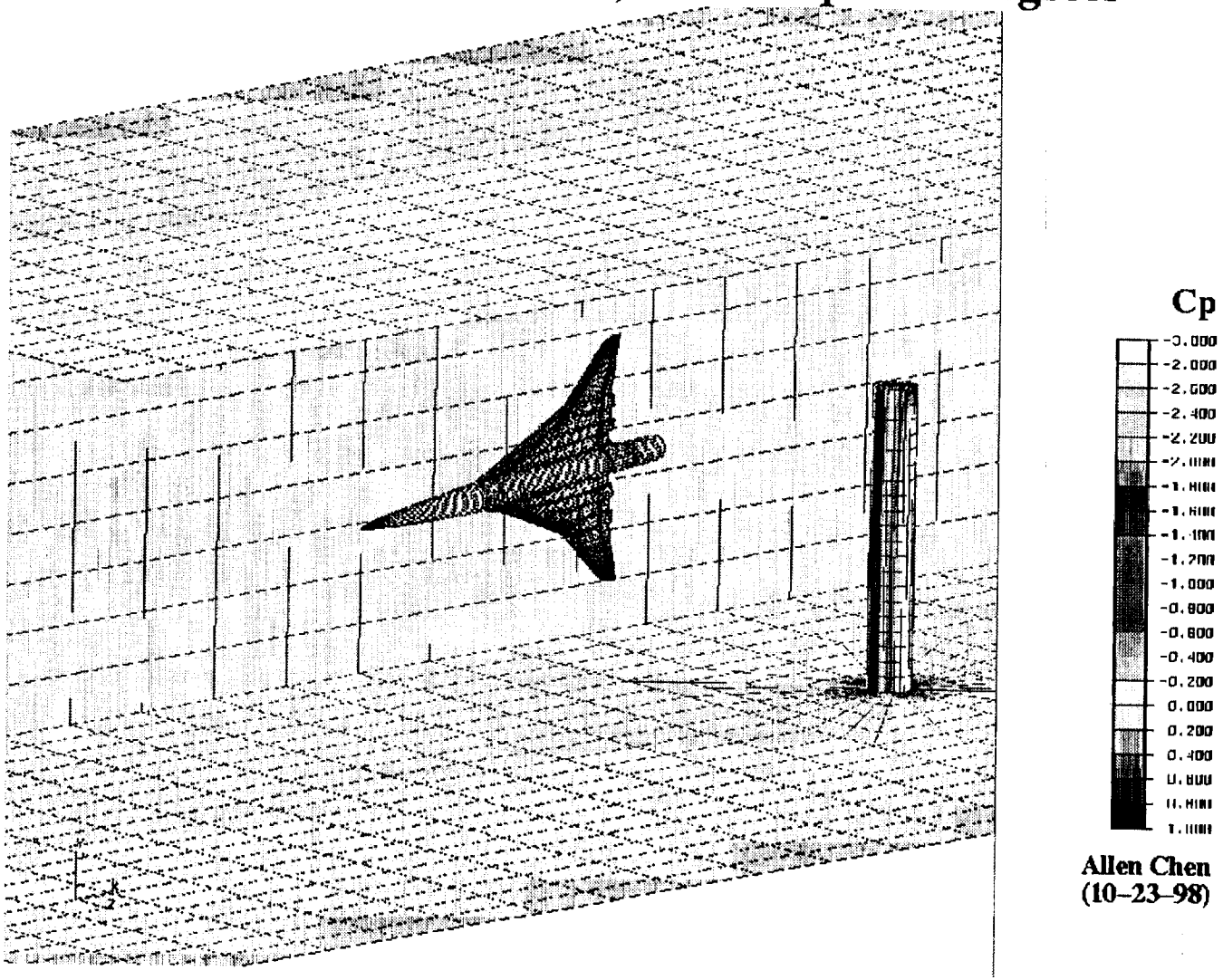

This figure shows that the extracted surface pressures on the right and left wing of the model are the same with the post mounted in the tunnel; the surface pressure distribution curves lie on top of each other. As shown in the figure, an inboard and outboard location was chosen for this comparison.

Ref. H W/B in Ames '7x10' with Half Post 48" From Tip TE, Flaps 30/10
A502 Wing Surface Pressures for Mach 0.3, Alpha 12 Degrees

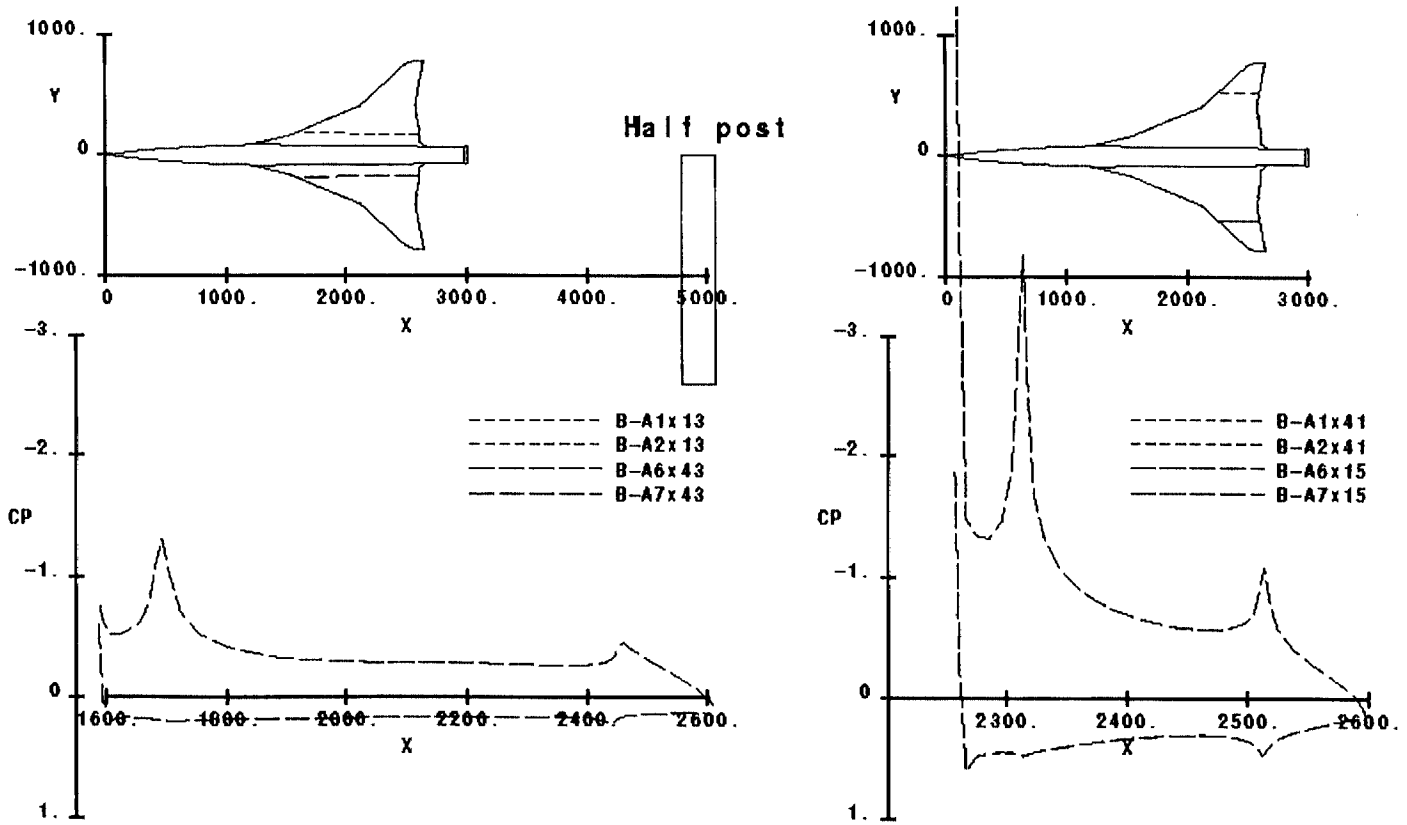

Note: Pressures on the port side wing are practically identical to the ones on the starboard side

This figure shows the effect of the model and post on the near and far walls of the wind-tunnel. A $\pm$ 0.02 range in total pressure coefficient is seen for all streamwise locations. The largest variation in pressures are seen near the post-mount. It would probably be prudent to model the tunnel walls for the CFD calculations.

Ref. H W/B in Ames '7x10' with Half Post, Flaps 30/10
A502 Wall Pressures for Mach 0.3, Alpha 12 Degrees

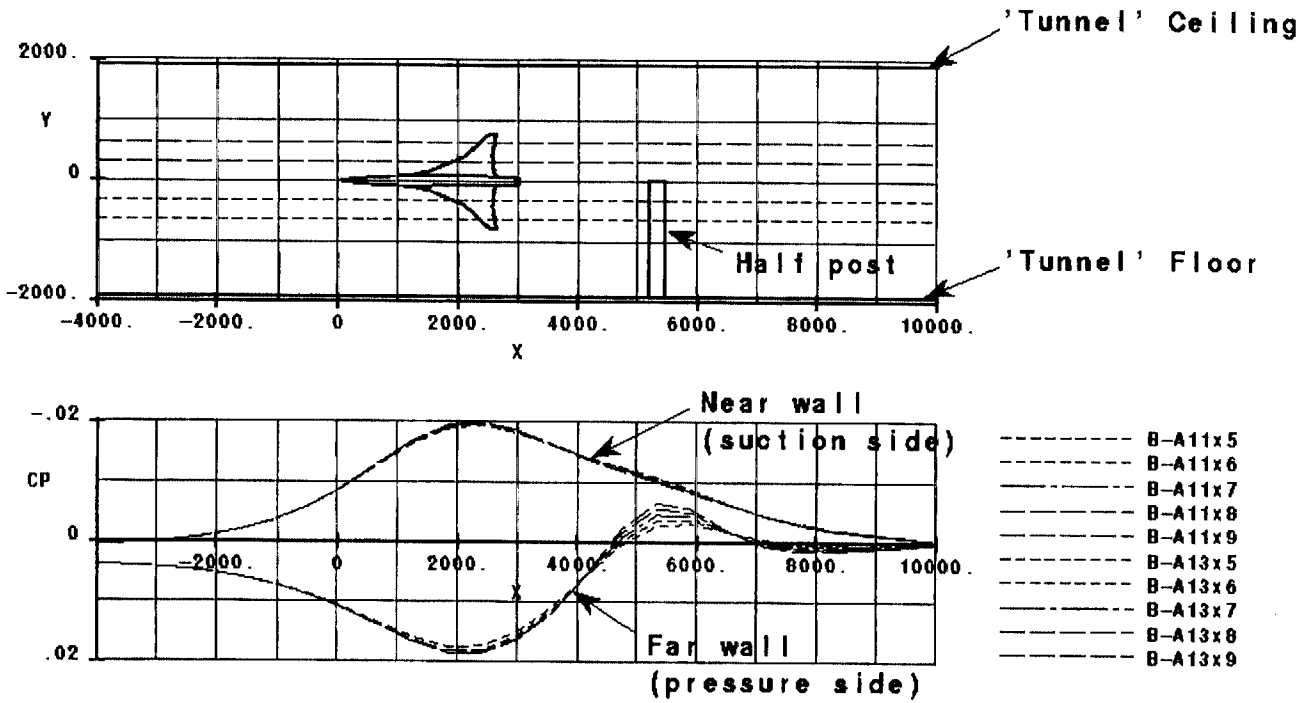

The Navier-Stokes solutions using CFL3D are shown for the 8° and 12° angle of attack conditions. The wind tunnel Reynolds number is 8 million, or 4 million based on MAC. The 8° case reveals that the flow over the Reference H is mostly attached, although there is a small inboard vortex. Unlike the 8° case, which shows attached flow over the outboard portion of the wing, the 12° case shows a highly 3D vortical spanwise flow, which results in extensive separation on the outboard wing region. Of particular interest is the vortical flow field features in the wake region.

CFL3D Flow Solutions for Reference H 30/10 Configuration

M = 0.3, Re = 8 million

Total Pressure Contours and Ribbon Traces

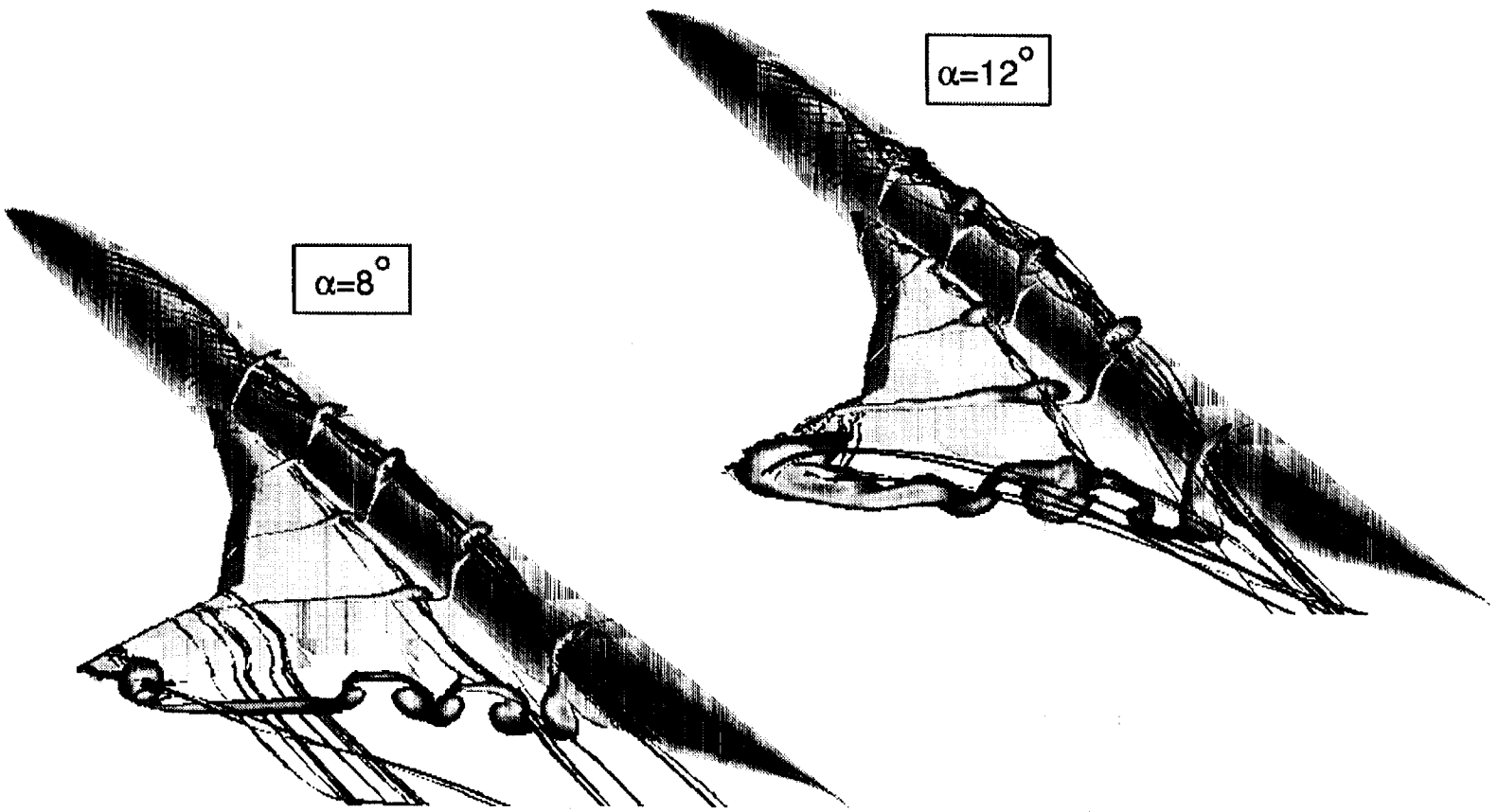

In order to determine the correct type of instrumentation needed to accurately measure the total pressures in the wake region, the flow angularities had to be determined. A pitot rake can accurately measure total pressures at flow angles of $\pm$ 10°, while a kiel tube can accurately measure pressure at flow angularities of $\pm$ 30°. Three planes were extracted from the Navier-Stokes solution, at 1, 5, and 10 tip chords from the trailing edge. The v and w angular velocities are plotted at each station, and are useful in determining what type of instrumentation to use to measure total pressures.

Wake Survey Locations for Reference H 30/10 Configuration

α = 12 deg

Model is pivoted 46.33 in. from the nose

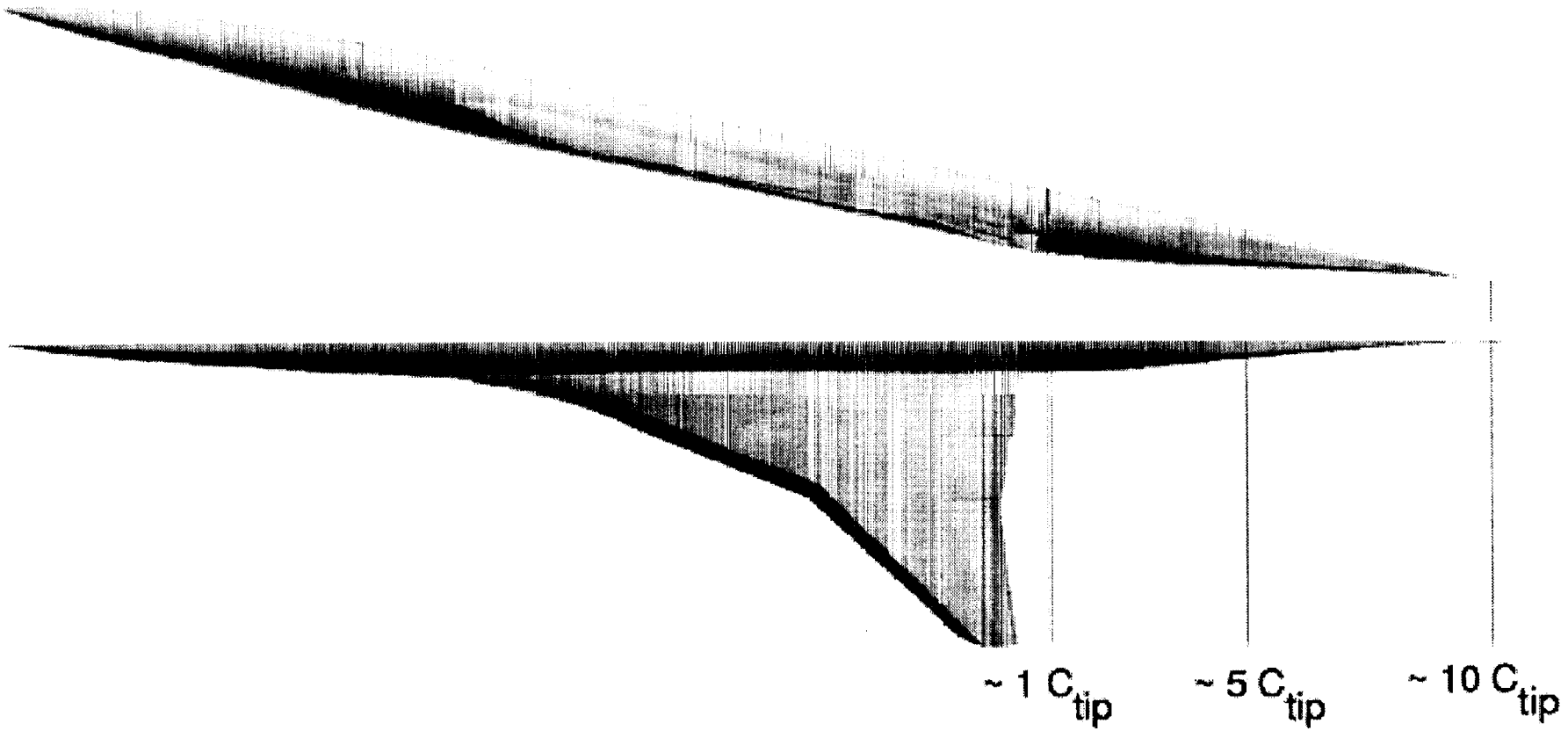

At 1 tip chord downstream of the trailing edge,the solution is plotted in terms of v and w angular velocities in the cross flow plane. The predicted flow angles exceed the measuring capabilities of both the pitot rake and the Kiel tube.

Wake Flow Predictions for Reference H 30/10 Configuration

M = 0.30, Re = 8 million, α = 12 deg.

Solution at 1 tip-chord downstream of the trailing edge

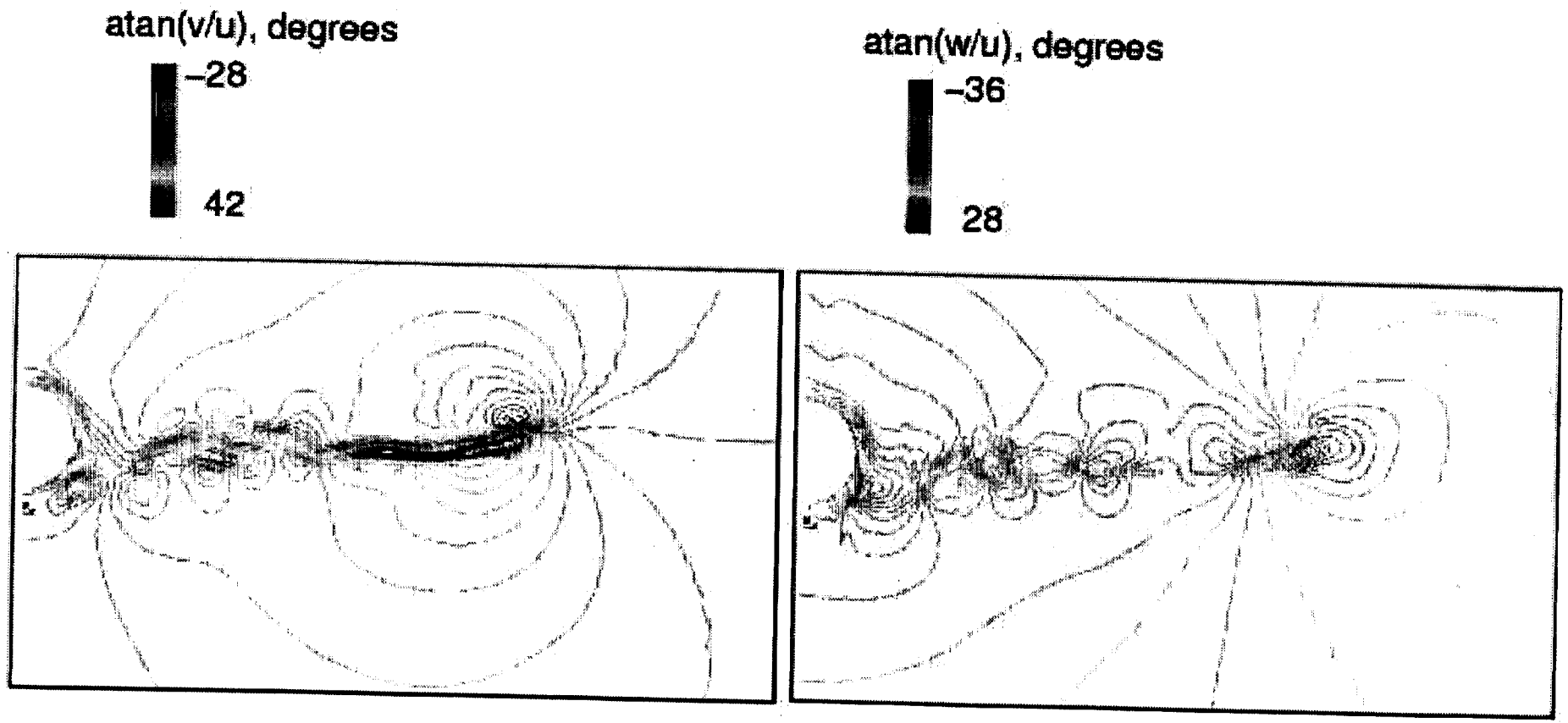

At 5 tip chords downstream of the trailing edge, the angular velocities have decreased, and a Kiel tube may be sufficient to measure total pressures at this station.

Wake Flow Prediction for Reference H 30/10 Configuration

M = 0.30, Re = 8 million, α = 12 deg.

Solution at 5 tip-chords downstream of the trailing edge

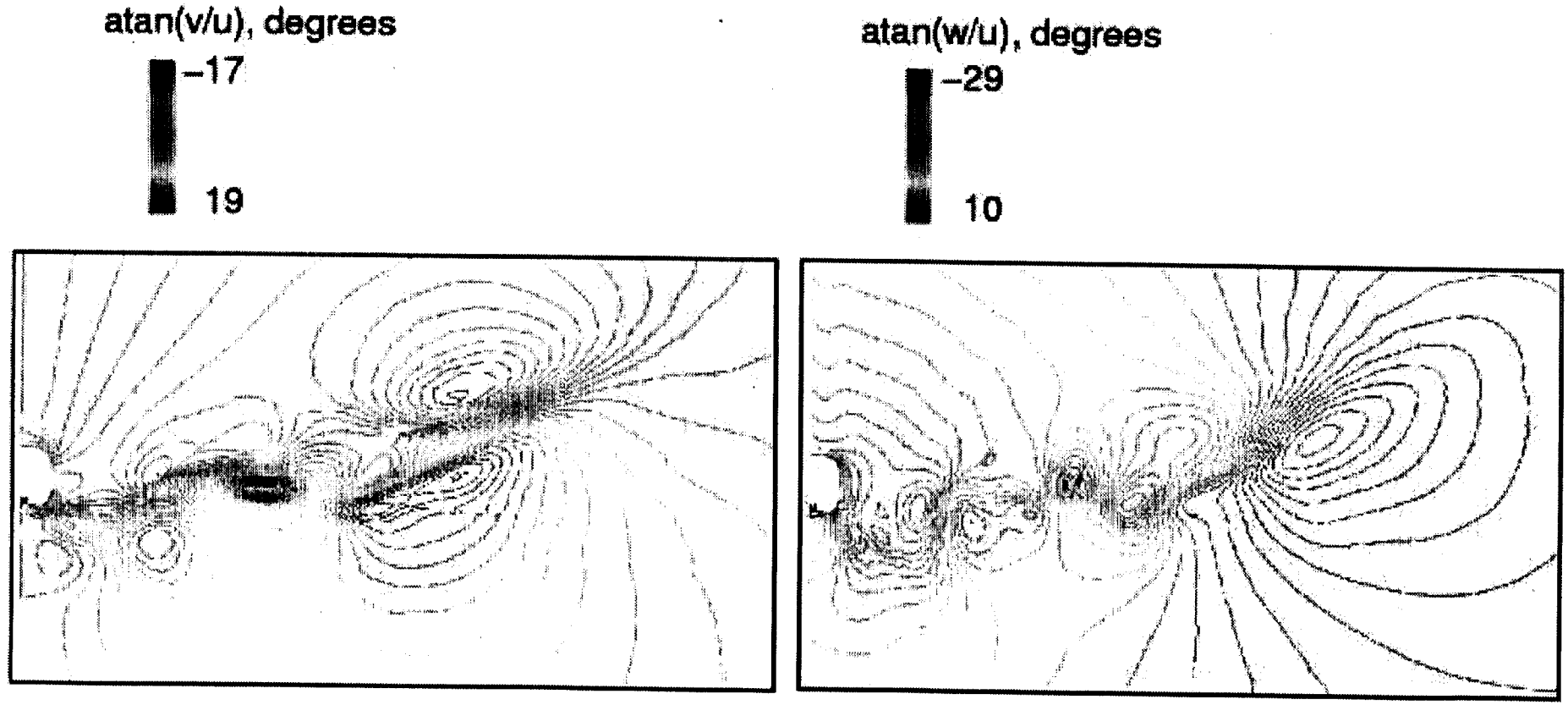

At 10 tip chords downstream of the trailing edge, the v and w angular velocities are reduced further, but still not enough to confidently use a pitot rake for measuring total pressures.

Wake Flow Predictions for Reference H 30/10 Configuration

M = 0.30, Re = 8 million, α = 12 deg.

Solution at 10 tip-chords downstream of the trailing edge

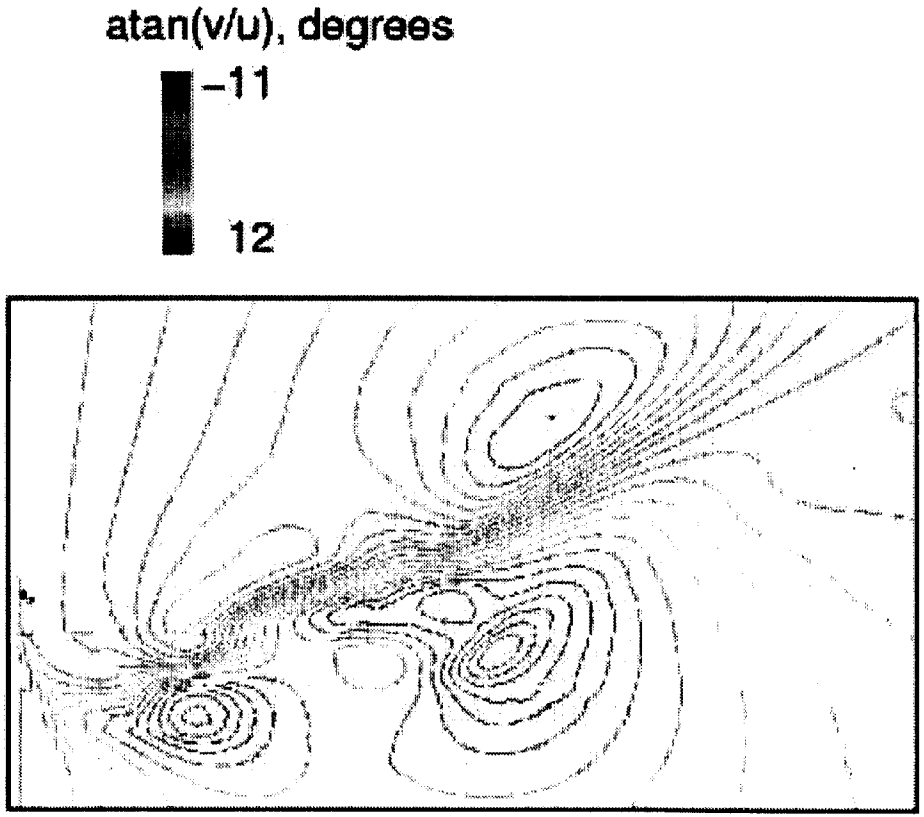

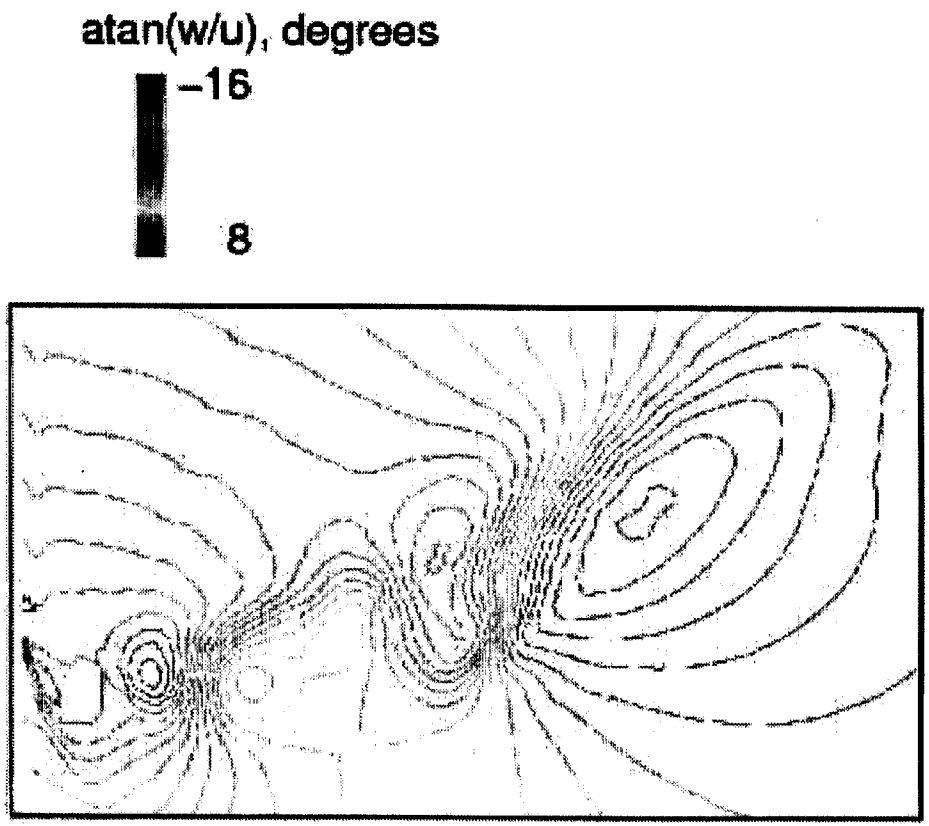

In conclusion, the Ames' 7x10 wind-tunnel test presents a great opportunity to acquire some detailed quantitative and qualitative flow measurements. This data will complement already existing wind-tunnel data as well as provide much needed flow field information for future code development and validation.

Conclusions

- Dedicated test for CFD validation.
- Measurement of detailed flow physics will be a priority.
- This test will use different techniques to measure the same regions of the flow field - redundant measurements will increase the confidence in data set.
- Opportunity to acquire a complementary set of detailed flow data using state-of-the-art measuring techniques. Value added to existing databases.
- Provide additional insight into the flow physics as well as provide information to the CFD community.

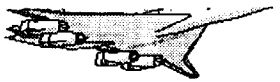

Panel Method Analysis of Wind Tunnel Model Support Effects in the Langley 14x22-ft and Ames 12-ft Wind Tunnels

Ryan Polito

HSR Airframe Annual Review
Anaheim, CA Feb 9-12, 1999

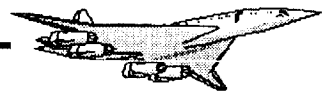

This slide shows an outline of the High-Lift Technology program.

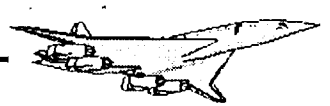

High Lift Technology Development (Task 33)

Increase L/D, Develop Analysis/Design Methodology

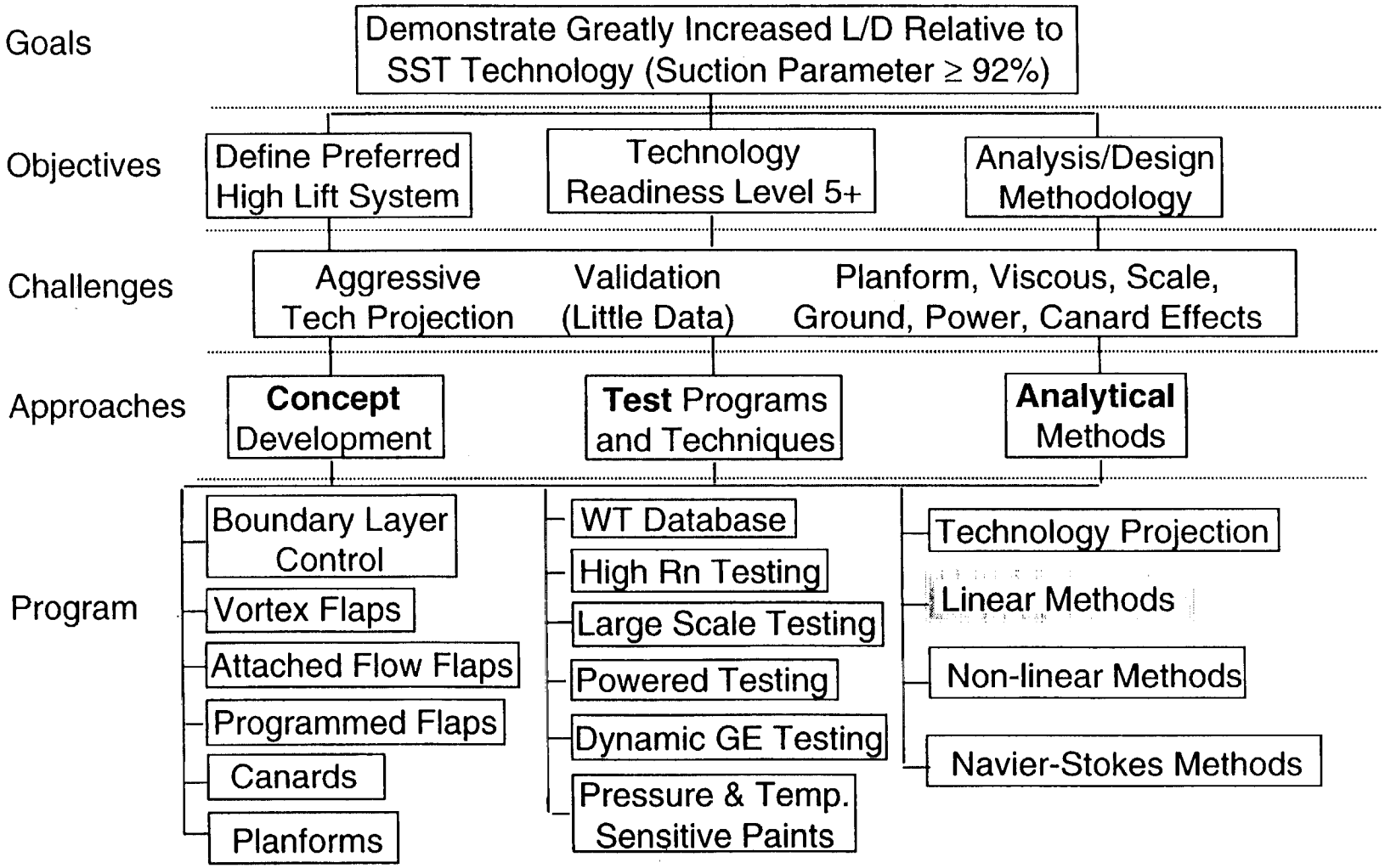

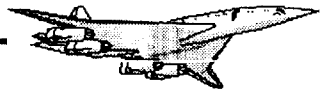

This paper is separated into two sections.

Section 1 is a continuation of an earlier paper presented at the 1997 HSR Workshop and centers around LaRC 442 Ref H U&I test conducted in November, 1996.

Section 2 is an attempt to apply what was learned from the U&I test to the TCA configuration in the LaRC 14x22-ft and Ames 12-ft tunnels.

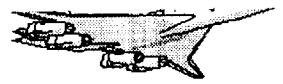

Part I: LaRC 14x22-ft Tunnel

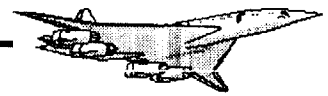

This paper is a continuation of the study started in 1996 after the Ref H U&I test (LaRC 442) and reported on during the 1997 HSR Workshop. In that study, methods were developed using the DACVINE panel code to predict support post interference on the 6% Ref H model in Langley's 14x22-ft Low Speed Wind Tunnel.

In addition, this paper will attempt to apply what was learned from the Ref H exercise to the 5% TCA tests in the 14x22-ft tunnel and the Ames 12-ft tunnel. In addition, alternate methods of simulating the support post and wake in the Ames 12-ft tunnel will be presented.

Objectives

- The report presented during the 1997 HSR Workshop was a "work-in-progress". A complete correlation had not yet been made with the data taken during the Ref H U&I test (LaRC442).
- Compute and compare Ref H & TCA post effects in 14x22-ft tunnel
- Compute and compare 14x22-ft and 12-ft TCA post effects

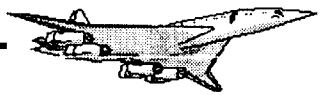

The 3-D higher-order panel method is used to model the effects of the model support system on the computed model forces and moments. Since the support posts used in the Ames 12-ft and the LaRC 14x22-ft tunnels are circular in cross-section, a thick viscous wake will form behind the post. In order to accurately model the effects of the post using an inviscid panel method, it is necessary to model this wake explicitly.

For the 14x22-ft tunnel, the data from the Ref H Upflow & Interference test (LaRC442) is used to calibrate the wake model. For the 12-ft tunnel, the wall pressure data is used to calibrate the wake model.

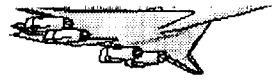

Approaches

- Use inviscid 3-D panel method (DACVINE) to model effects of the posts
- Must also include modeling of wake to get correct post blockage effects
- Apply post wake model to TCA configuration
- Use wall pressures to match DACVINE post wake modeling in Ames 12-ft tunnel

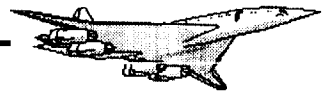

By using a 2-D Navier-Stokes model, it initially looked as though a wake model that was about 3 times as long as it was wide wold be a match. While it came much closer to the test data than the post alone, it was still under-predicting the interference increments. The next step was to go to a slightly larger wake. This second try was four times as long as it was wide.

Continuation of Ref H Work

- Previous work included modeling the support post with a solid body wake
- First effort included a post wake body that was 3x the diameter of the post alone
- 3d wake was on the right track, but wasn't enough
- 4d wake was modeled

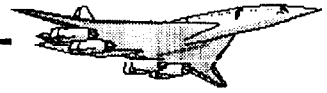

The way the DACVINE grids are constructed requires the post wake and the fuselage grids to be intersected and a large portion of the fuselage removed. With this section removed, the forces that would normally be acting on it are not included in the final calculation. These forces need to be recovered. To do this, the pressures along the top edge of the post wake are integrated which gives the C_N contribution. The pitching moment contribution is then calculated based on the distance from the nose. From these two numbers ΔC_L, ΔC_D and ΔC_m can be determined.

Modeling of Post/Fuselage Intersection

$$\Delta C_N = \frac{\int C_p y dx}{S_{ref}}$$

$$X_{C_p} = \frac{\int C_p y x dx}{\int C_p y dx}$$

$$\Delta C_m = \frac{\Delta C_N (X_{C_p} - X_{MAC})}{c_{ref}}$$

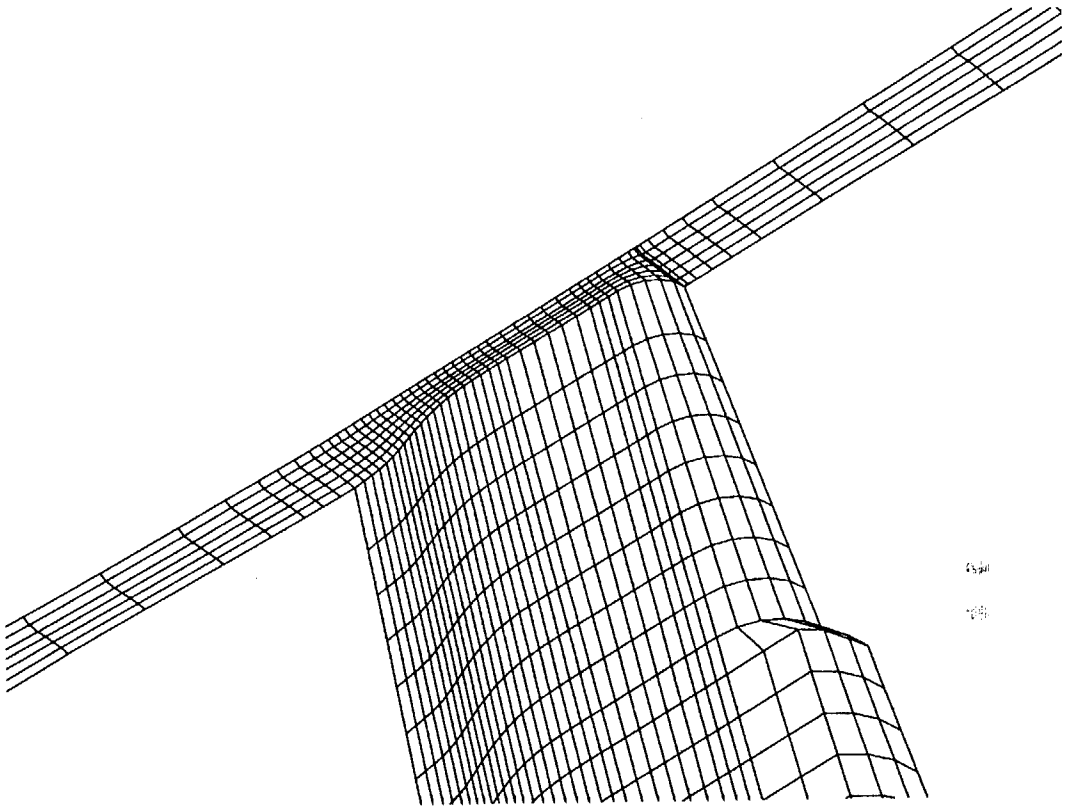

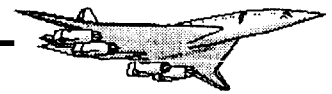

This first plot compares the DACVINE predictions for the lift increments of the various post wake models to the Ref H test data from LaRC442 in the 14x22-ft tunnel. It would appear that a wake model sized somewhere between 3x and 4x the diameter of the post would capture the level and trend of the interference for the 00°/00° flaps case, but only captures the level correctly for the 30°/10° configuration.

Note: The data shown here for LaRC 442 is flap specific. In the second half of this paper the analytical data is compared to an average of the clean wing and high lift flaps because it was determined that the interference increments are essentially flap independent.

Effects of Post/Wake Models on Ref H Lift

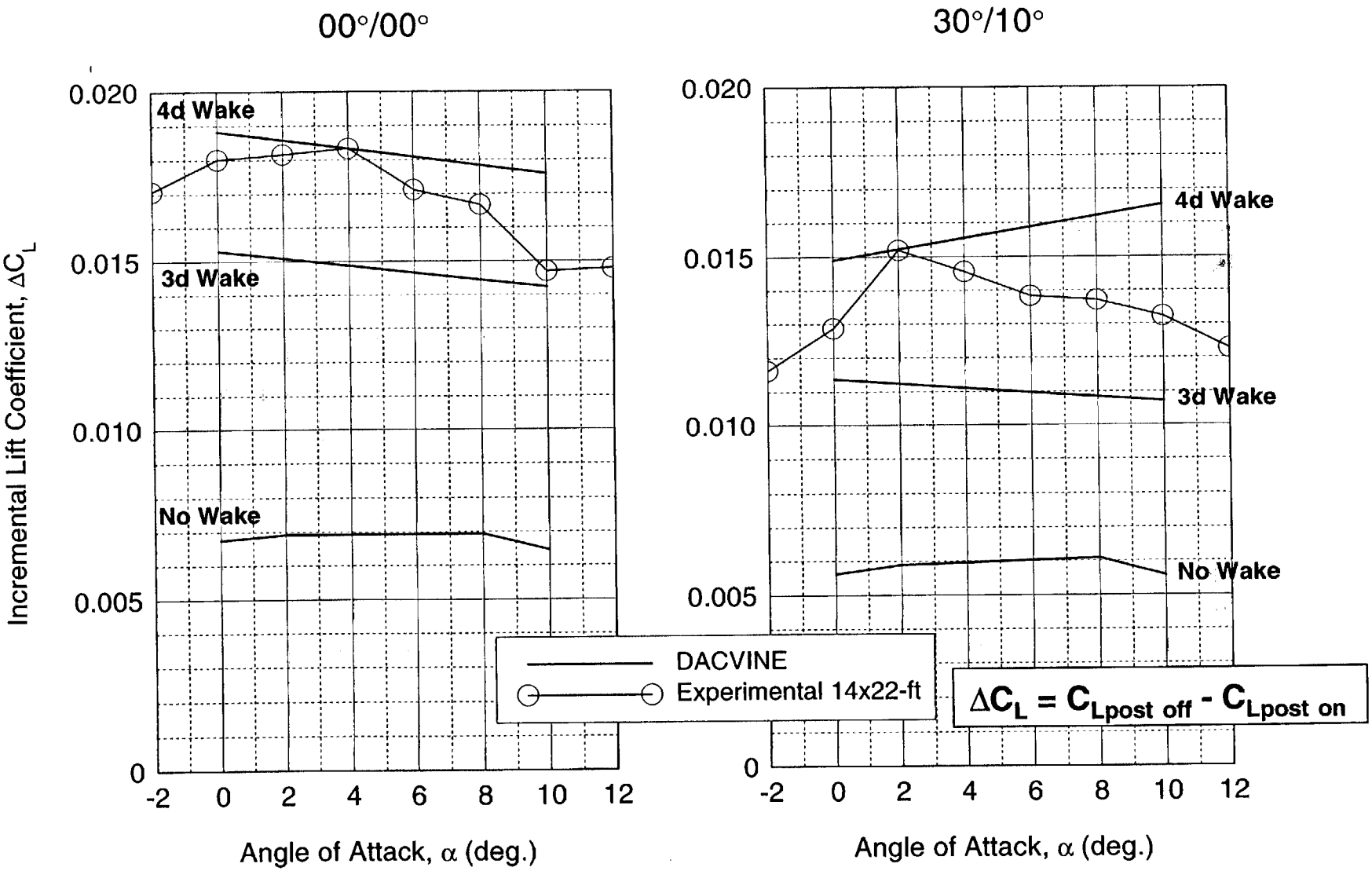

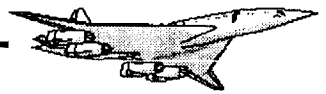

The trends of the drag plots seem to contradict those of the lift plots. These increments suggest that a wake model longer than the 4d would agree better with the test data for both flap settings at a significant number of angles where the lift suggested a slightly shorter one would be optimal.

Note: The data shown here for LaRC 442 is flap specific. In the second half of this paper the analytical data is compared to an average of the clean wing and high lift flaps because it was determined that the interference increments are essentially flap independent.

Effects of Post/Wake Models on Ref H Drag

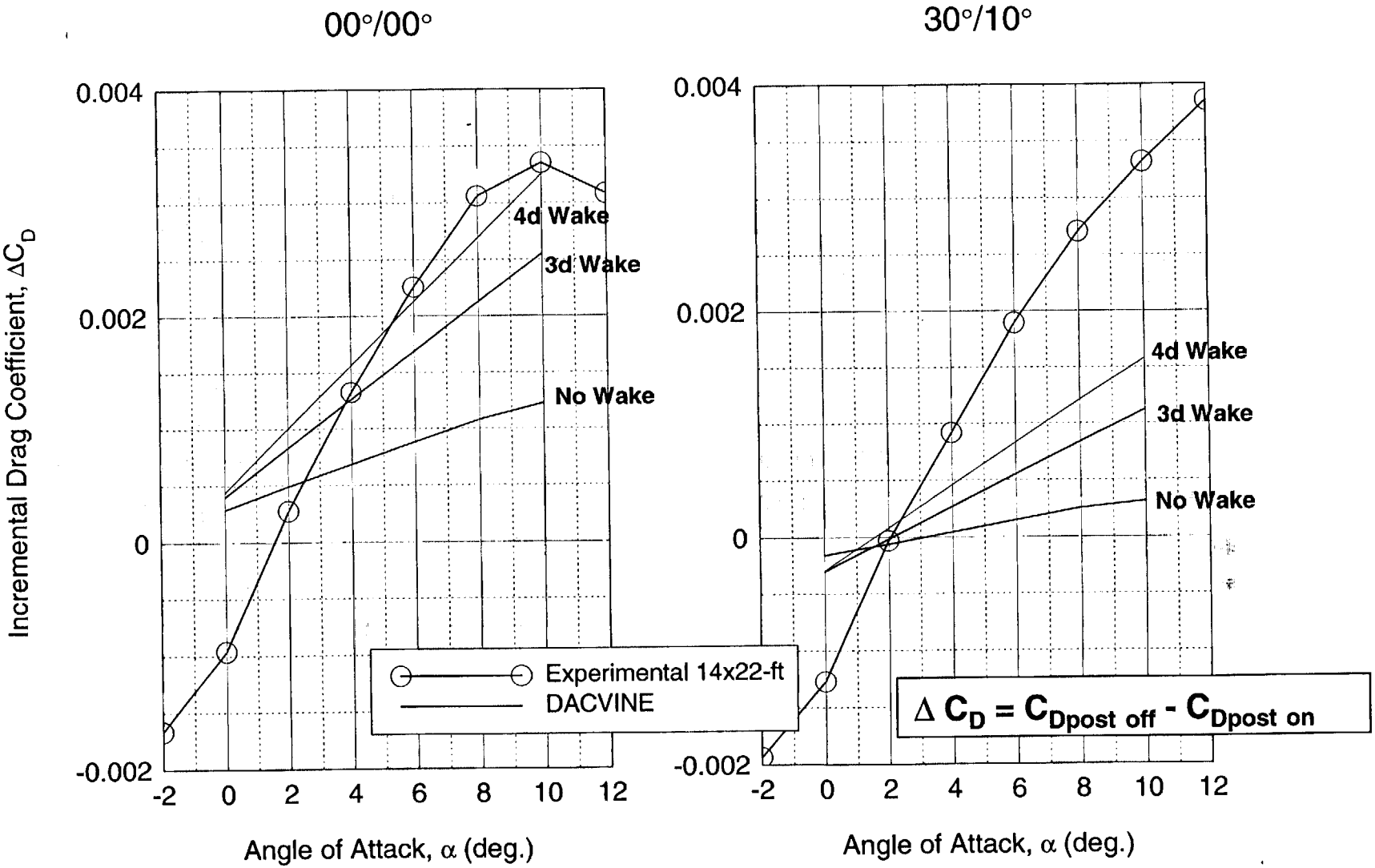

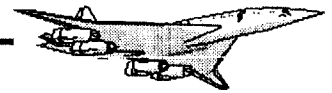

DACVINE does not do a good job of predicting pitching moment on highly swept wings because it doesn't model leading-edge vortices. Leading-edge vortices shift the center of pressure forward on the wing and therefore completely alter the pitching moment polar. DACVINE also does not model trailing-edge separation. DACVINE's inability to properly model the aerodynamics of the leading-edge vortices prevents it from being used as a reliable pitching moment tool.

Note: The data shown here for LaRC 442 is flap specific. In the second half of this paper the analytical data is compared to an average of the clean wing and high lift flaps because it was determined that the interference increments are essentially flap independent.

Effects of Post/Wake Models on Ref H C_m

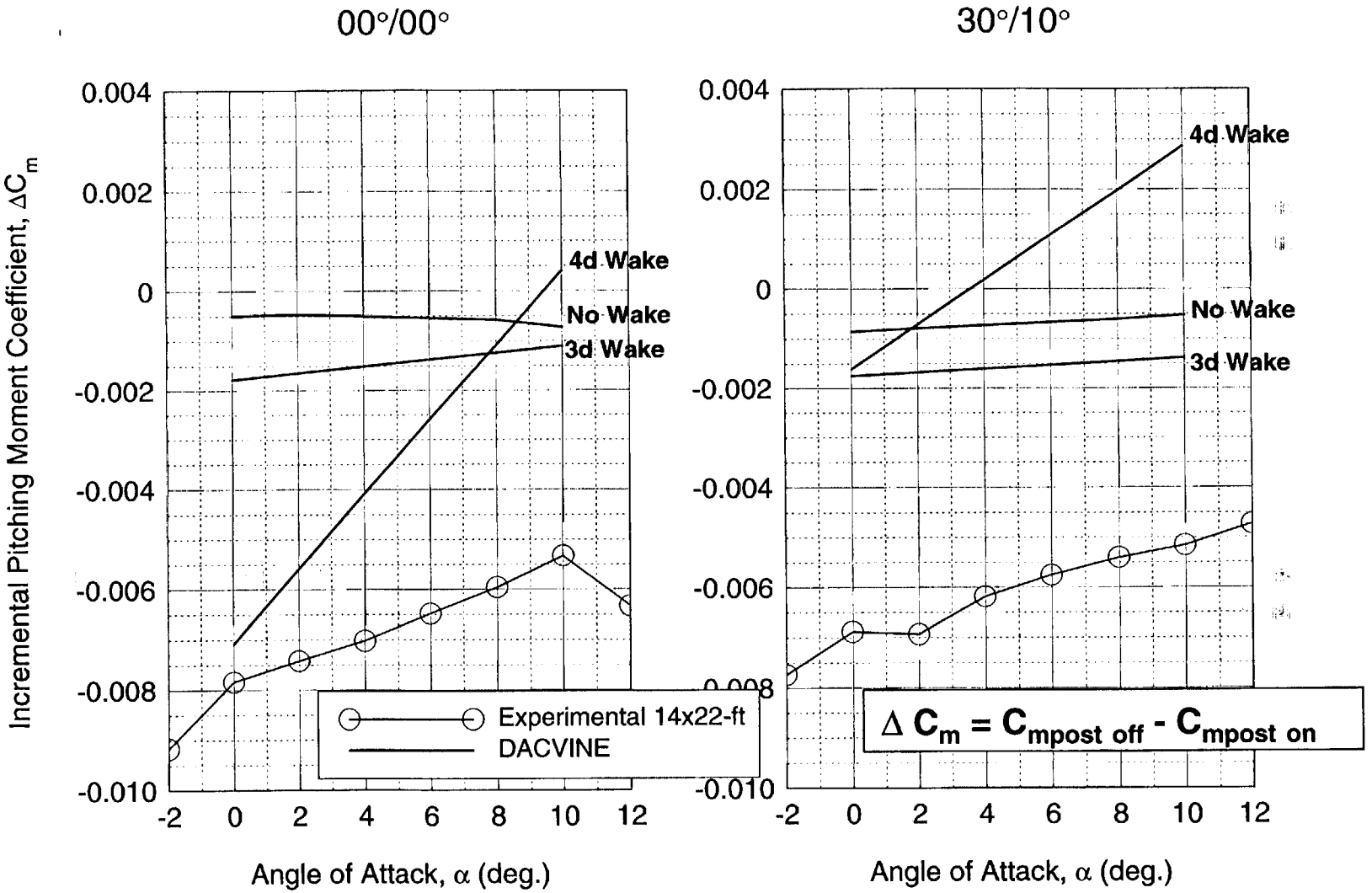

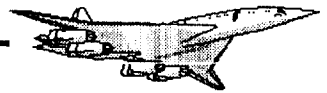

The next step is to replace the 6% Ref H model with the 5% TCA model. The only other changes made were to the top of the post wake geometry. The grid of the post was modified to have a seamless fit with the bottom of the TCA fuselage.

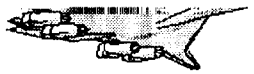

Application to TCA Configuration

- The 4d post wake model was mated with the 5% TCA configuration in the 14x22-ft tunnel
- The following plots show how these increments compare

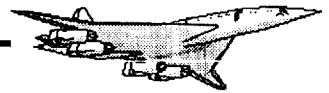

This next chart shows just how much larger the 6% Ref H model is compared to the 5% TCA model. It's important to notice the relative size and location of the 14x22-ft tunnel's support post. The trailing-edge flaps of the TCA model are much closer to the post than the Ref H model.

Comparison of Planforms & Installations

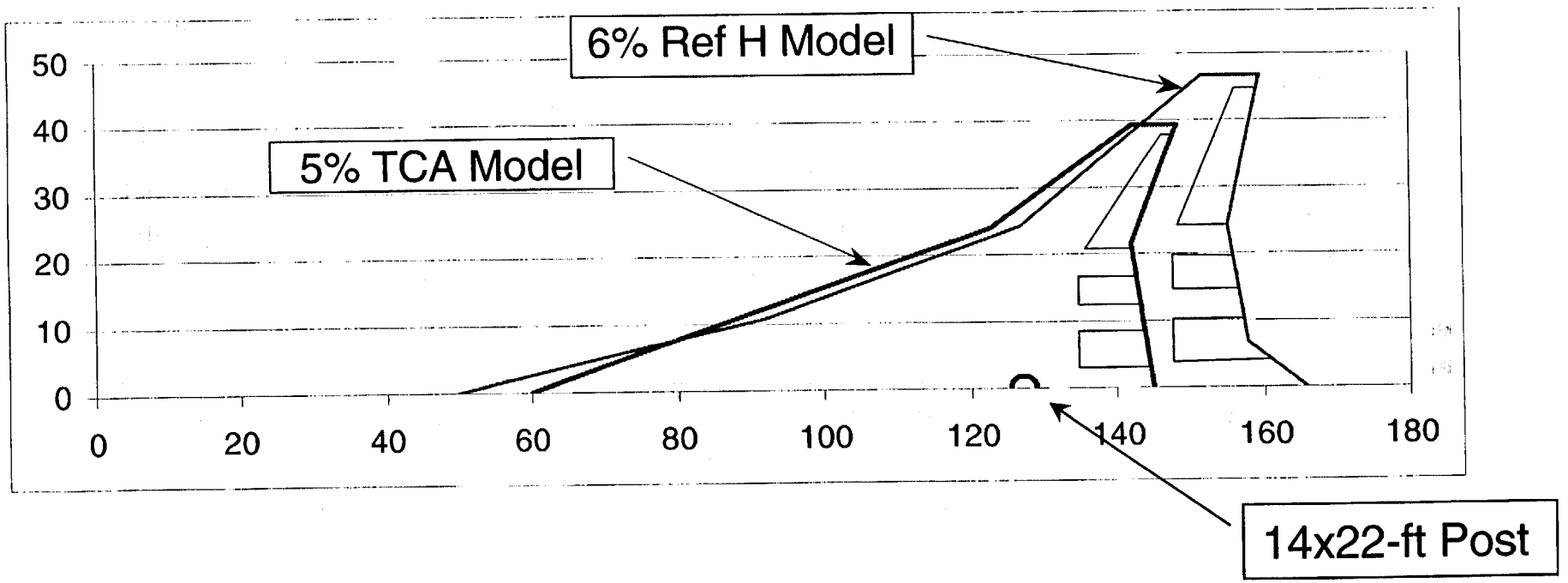

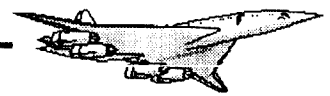

DACVINE managed to capture the trend of the lift curve. Only a small 1st order correction is necessary to adjust the increments for the TCA model.

The higher levels of the TCA are due to the relative size of the models with respect to the support post. Full scale, the two configurations are similar, but the Ref H model is a 6% scale and the TCA is only a 5% scale.

Note: Current experimental data corrections for TCA 5% 14x22-ft test *does not* account for this increase in relative post size and corresponding larger interference increments.

Comparison of Increments - TCA vs Ref H

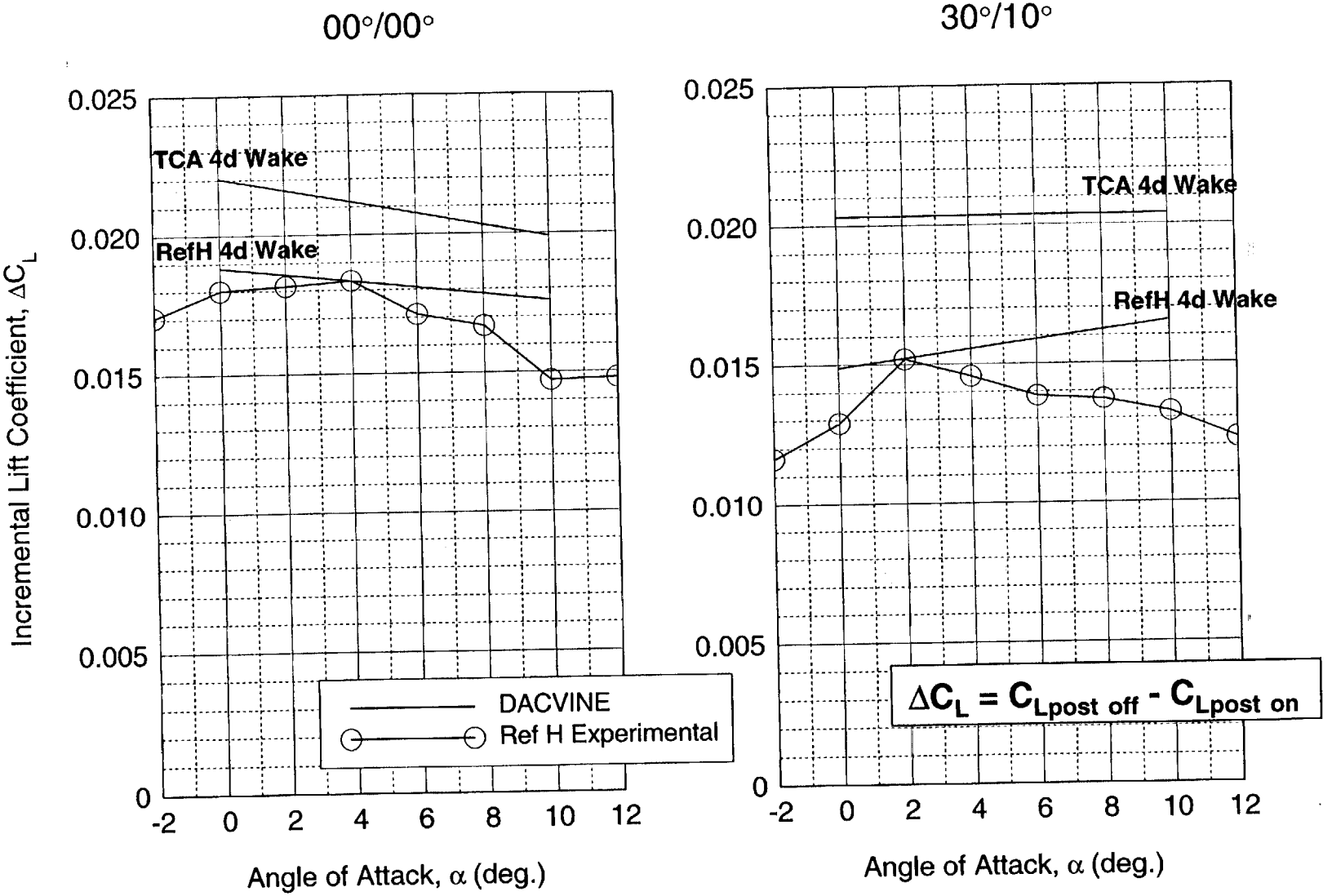

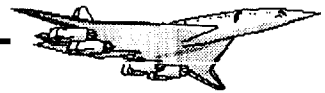

Like the lift increments, the drag interference increments are a little under-predicted. This is due to the relative size of the 5% TCA model with respect to the support post. The 6% Ref H model is larger and therefore the post has a smaller interference figure.

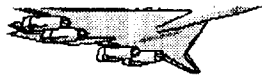

Comparison of Increments - TCA vs Ref H

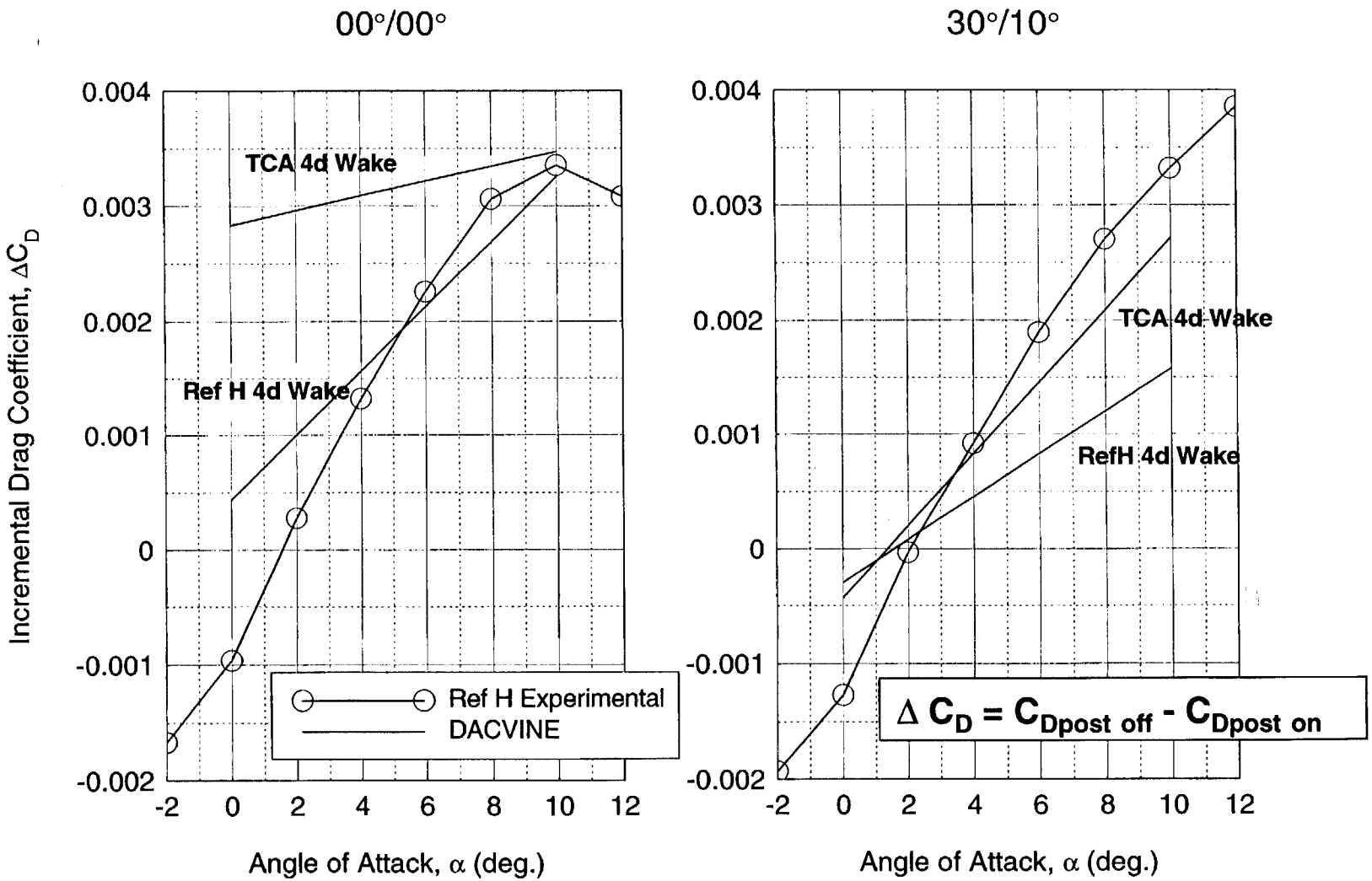

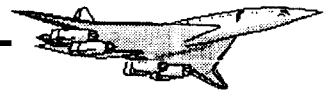

DACVINE is still not able to predict pitching moments very well.

Comparison of Increments - TCA vs Ref H

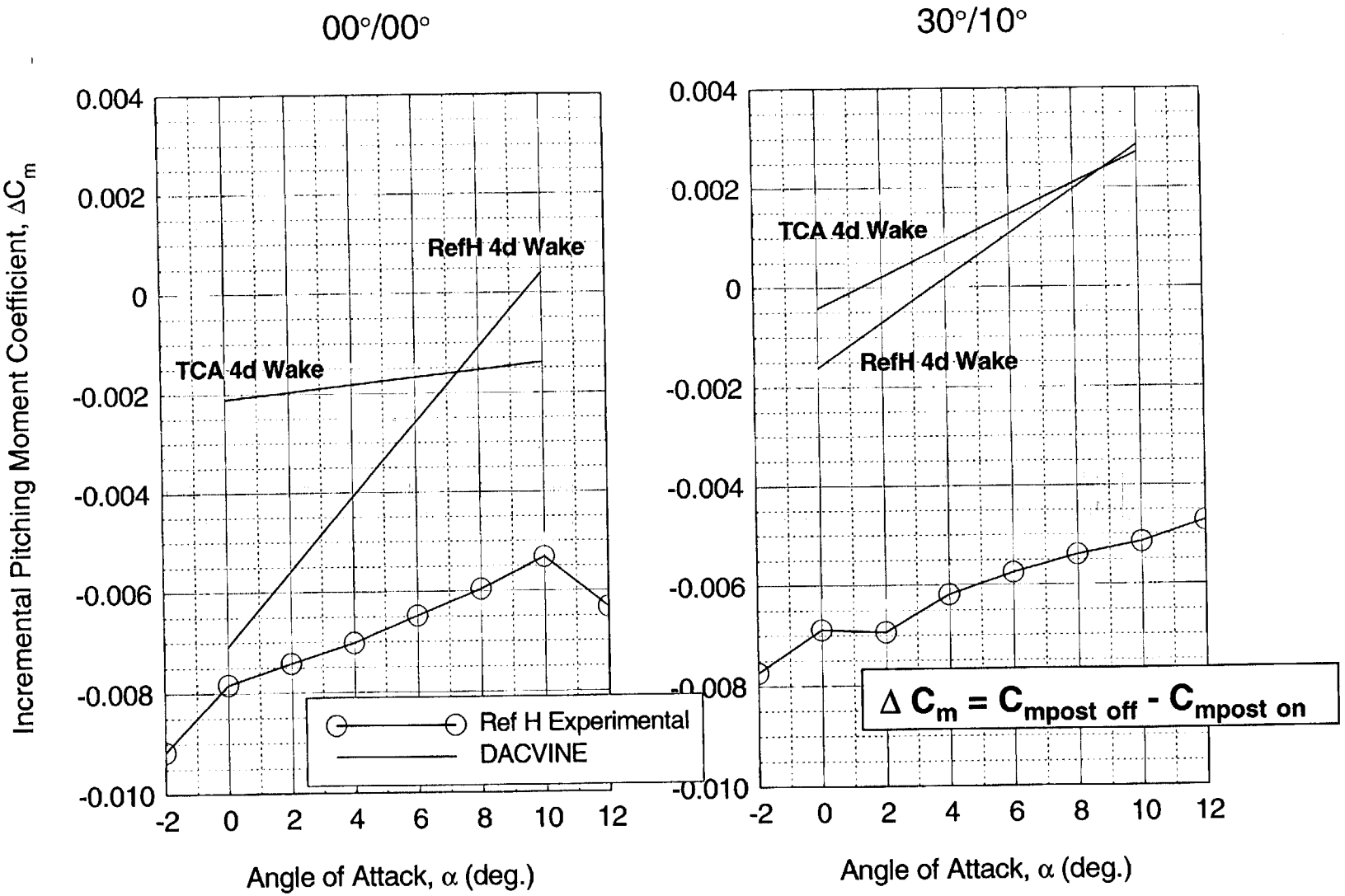

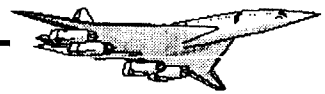

Part II: Ames 12-ft Tunnel

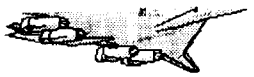

While there is no actual interference test data for the TCA configuration in the 12-ft tunnel, wall pressure data does exist for the bi-pod support posts. Several different post wake models were run in DACVINE to try to reproduce the effects of the post on the wall pressures. The theory being, if the wall pressures could be recreated, then the resulting pressure field should have an equivalent effect on other objects in the tunnel that the real wake would.

A solid post wake was constructed for the 12-ft's bi-pod mounting system. This model was considerably longer than the model for the 14x22-ft tunnel because it was felt that the wake should incorporate both posts.

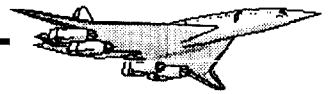

Ames 12-ft Interference Increments

- Interference test data is not available for any HSCT model in the 12-ft tunnel
- Wall pressure data of the bi-pod mount in the tunnel is available from the WICS calibration tests
- A solid-body post wake model was tried using the same method as with the 14x22-ft model

This chart shows the relative size of the 4d and 5d post wake models. These are models of two different posts from two different tunnels.

- The 4d is from the 14x22-ft at Langley
- The 5d is from the 12-ft at Ames

The 5d wake is actually about 7x the diameter of the post. This length was used to incorporate the aft pitch post that is present in the 12-ft bipod mount system which would extend the overall length of the wake to about the length of the 5d post wake model.

Note: The 4d/5d names are for identification and not intended to be accurate descriptions.

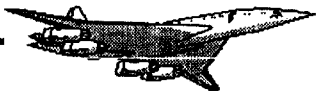

4d/5d Post Wake Geometry

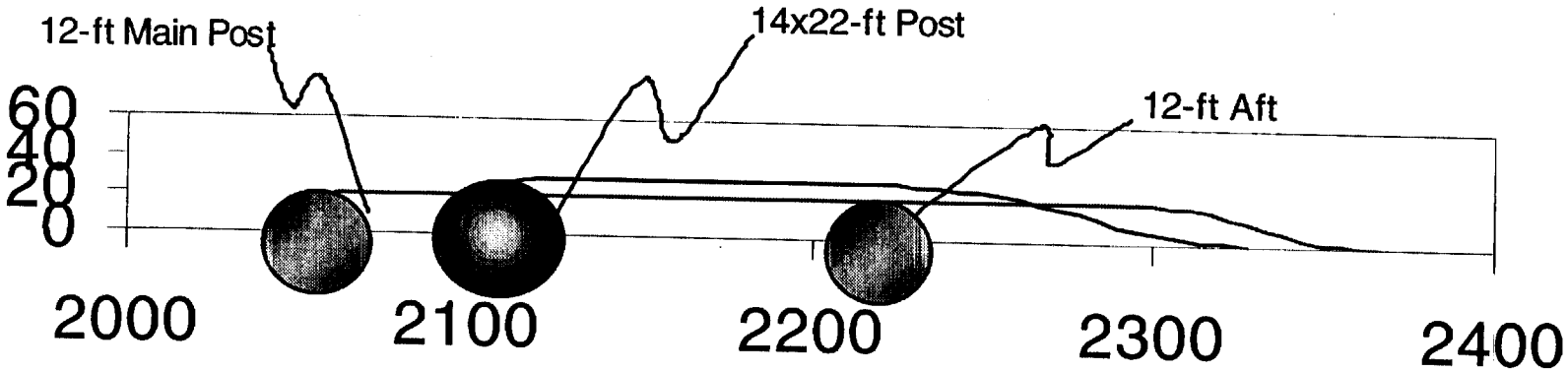

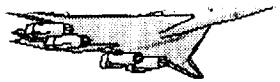

The only test data available is from the Wall Interference Correction System (WICS) calibration test performed in the 12-ft. The data consists of tunnel wall pressures obtained from 8 longitudinal pressure tap rows spanning the length of the test section for the bi-pod system installed without a model.

The average of the 4 lower rows (below tunnel centerline) was plotted against the wall pressures of several different interference models run in DACVINE.

The wall pressure increments from the tunnel (tunnel w/posts - empty tunnel) are compared to the DACVINE 5d post increments on this slide. The 5d post increments match the magnitude of the test data at the post location very well, but do not match quite as well downstream. This is due, in part to an aft strut that was installed near the downstream end of the test section causing some additional blockage. The strut was not installed during the TCA test and was not included in this DACVINE model.

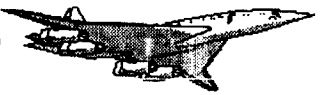

Effects of Post Presence on Wall Pressure Increments

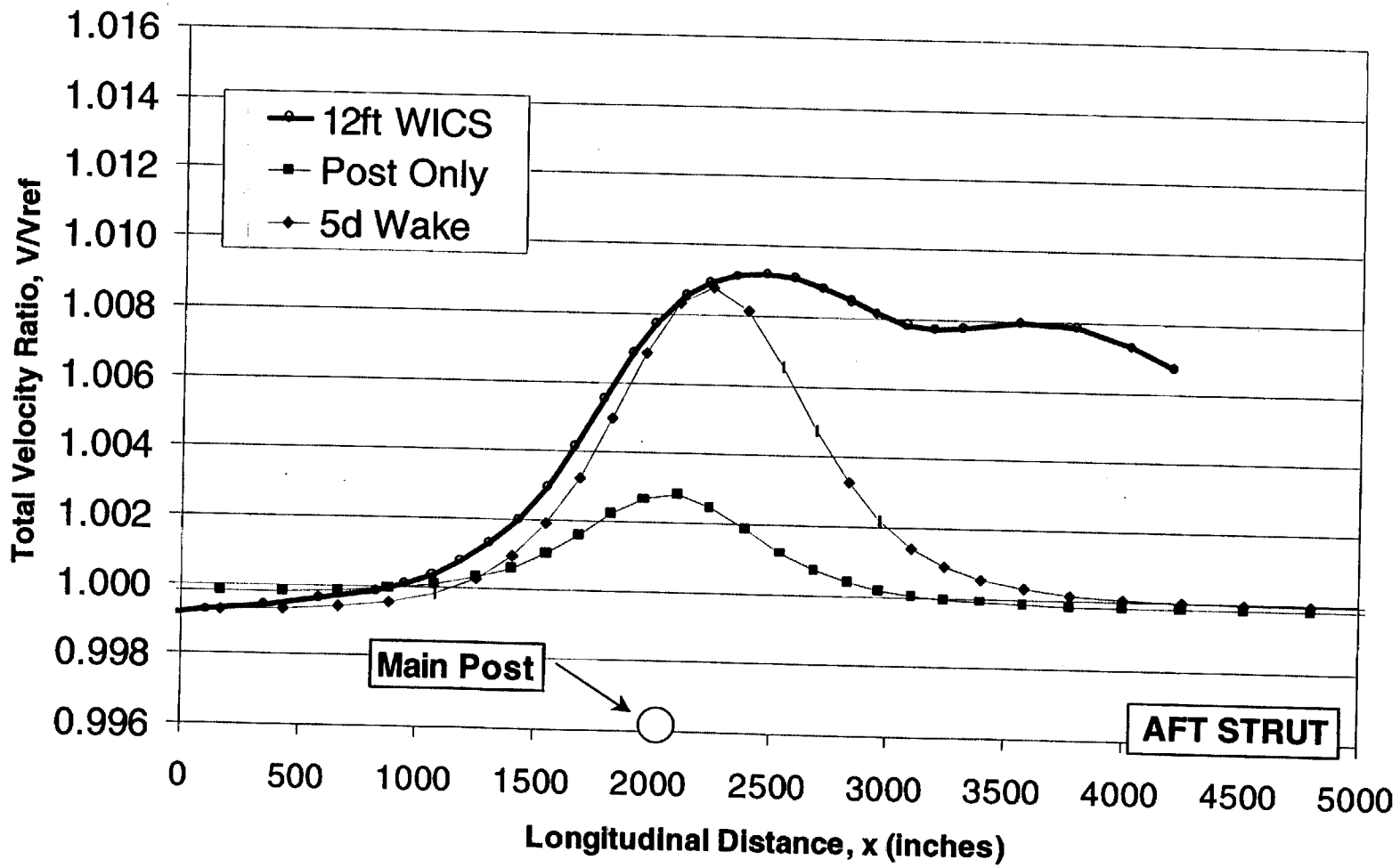

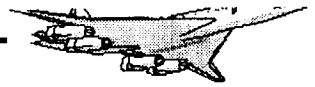

While using the lift increments from Ref H for the TCA model in the 14x22-ft tunnel may have been a little conservative, using these same increments for the TCA in the 12-ft yields a reasonable comparison. The narrower posts of the 12-ft coincidentally produce interference increments that match DACVINE's predictions very well.

Note: The data shown here for the 14x22-ft increments is averaged data from several repeat runs of both clean wing and high lift flap configurations. It was determined from LaRC 442 test data that the interference increments had little dependence on flap settings.

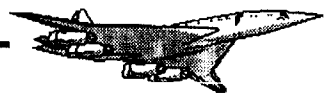

Effects of Wake Models on Lift

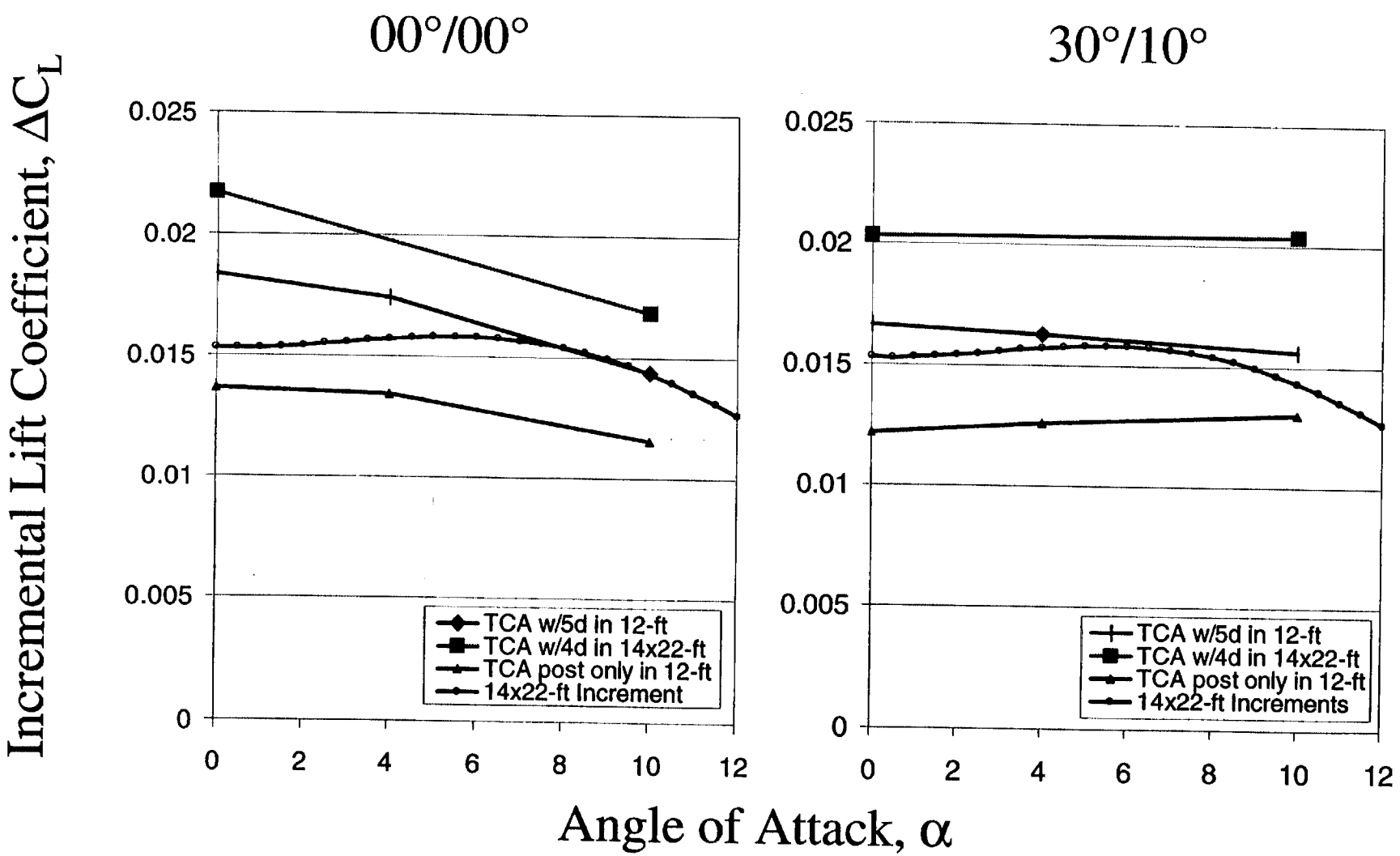

Like the lift increments, the 14x22-ft Ref H drag increments agree well with the DACVINE predictions. Again, the test increments shown are averaged from several repeat runs and both clean wing and high lift flap configurations.

Effects of Wake Models on Drag

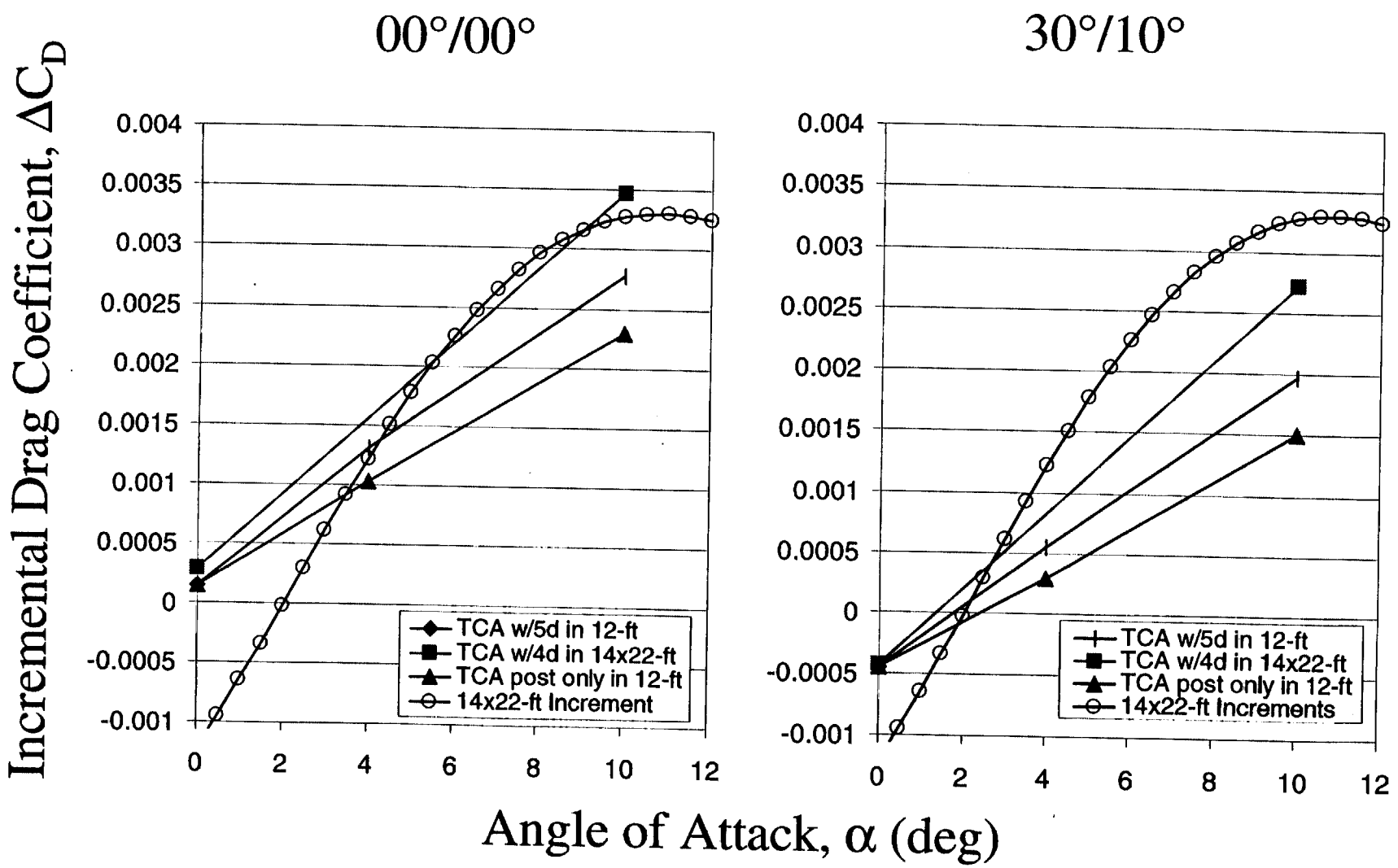

Summary

- Post effects in 14x22-ft computed for TCA & Ref H
  - TCA post increments for lift & drag slightly larger than Ref H
  - Moments not well predicted
- Post effects in 12-ft computed for TCA
  - Transferred solid post wake method to 12-ft tunnel
  - WICS wall pressures used to calibrate DACVINE model
  - Predicted lift & drag increments close to Ref H test data

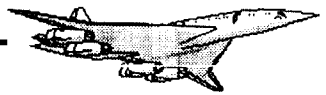

The interference increments currently being used are conservative and based on the relative size of the two model geometries suggests that the 5% TCA interference increments should be larger than the 6% Ref H increments. DACVINE can be used to estimate the levels one would expect to see for the TCA model. By using the DACVINE results for the Ref H one could estimate a set of interference increments for the TCA based on the Ref H test data.

The DACVINE increments for the TCA model in the 12-ft tunnel match reasonably well with the Ref H test increments from the 14x22-ft. In order to have more accurately corrected data, the interference increments should be applied to the 12-ft data.

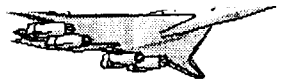

Recommendations

- Using Ref H increments is too conservative for 14x22-ft tunnel
- Some effort should be made to fine-tune increments for use with TCA test data
  - Using test data from a similar planform to calibrate DACVINE's solid wake model then swapping with desired airplane geometry yields acceptable results
  - Applying Ref H increments to 12-ft is a reasonable assumption based on DACVINE predictions

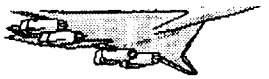

Evaluation of the Linear Prediction of the Effects of Planform Variation and Flap Deflection

Roger Clark and Ryan Polito

The Boeing Company
Phantom Works, Long Beach

Presented at
HSR Airframe Annual Review
February 9-12, 1999
Anaheim, CA

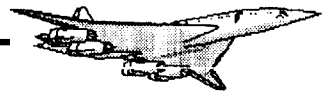

This slide shows an outline of the High-Lift Technology program.

High-Lift Technology Program

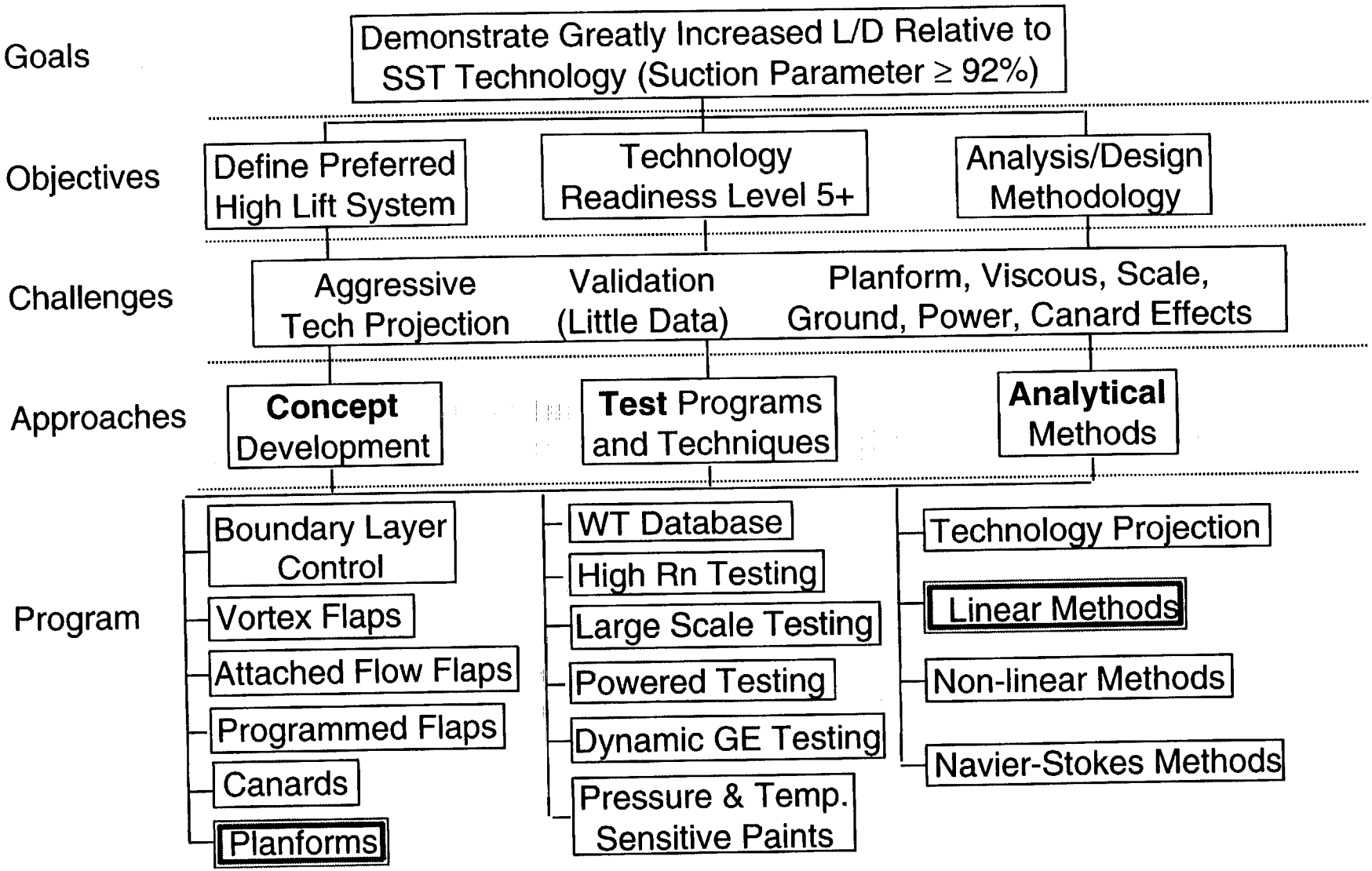

This paper presents a documentation of the capabilities of the linear performance prediction code, Aero2s/Aero3s, which is widely used to provide aerodynamic performance build up required for aircraft sizing studies. The code predictions are evaluated against the database obtained for the TCA 5% high-lift model tested in the Langley 14x22-foot Wind Tunnel in tests TCA 1 (LaRC 449) and TCA 4 (LaRC 473).

These tests provide data for the baseline TCA configuration, as well as for two alternate planform configurations.

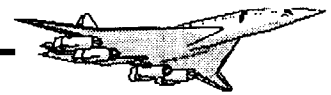

Outline

- Linear Method Capabilities
- Comparison data
- Planform Effects
- Leading-edge Flap Extent
- Leading-edge Flap Deflection
- Trailing-Edge Flap Deflection

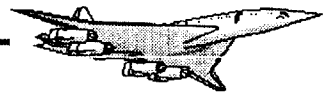

Aero2s, (and the more recently released version Aero3s) is a vortex lattice code, in which the wing thickness and camber distribution are represented by a network of bound vortices over the wing planform, together with a source distribution to represent the local wing thickness. An empirical leading-edge suction model is used to evaluate the attainable leading-edge thrust which a given configuration can sustain. The attainable thrust calculation is based on an empirical database, which takes in to account the wing leading-edge radius and sweep, the Reynolds number, and the Mach Number.

The code has the capability to model both leading- and trailing-edge flap deflections, as well as modeling canard and tail surfaces.

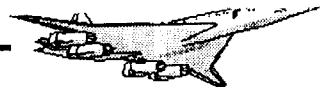

Linear Methodology

- Aero2s/Aero3s
  - empirical attainable thrust evaluation
  - leading- and trailing-edge flap modeling
  - two- and three-surface modeling
  - relied on heavily to provide performance build up (Common Process)

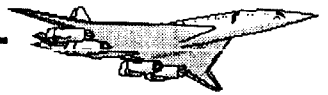

The high-lift Common Process team has reached a consensus on most of the major steps in the assessment of candidate configurations. The flow chart summarizes the steps used to build up from wind tunnel data the trimmed lift curves and drag polars of new configurations.

The steps to the left of the dashed line are not routinely performed. These steps are only required when a new wind tunnel database is obtained.

The steps to the right of the dashed line are performed for each flap setting with the exception of calculation of ΔC_{Do} in A389, which is a supersonic linear preliminary design (PD) code which computes an estimate for turbulent boundary-layer skin-friction.

Depending on what baseline data are available, *AERO3S* may be used to predict not only the effects of the planform changes from the baseline configuration to the new configuration, but also the effects of flap deflection changes.

Process Summary

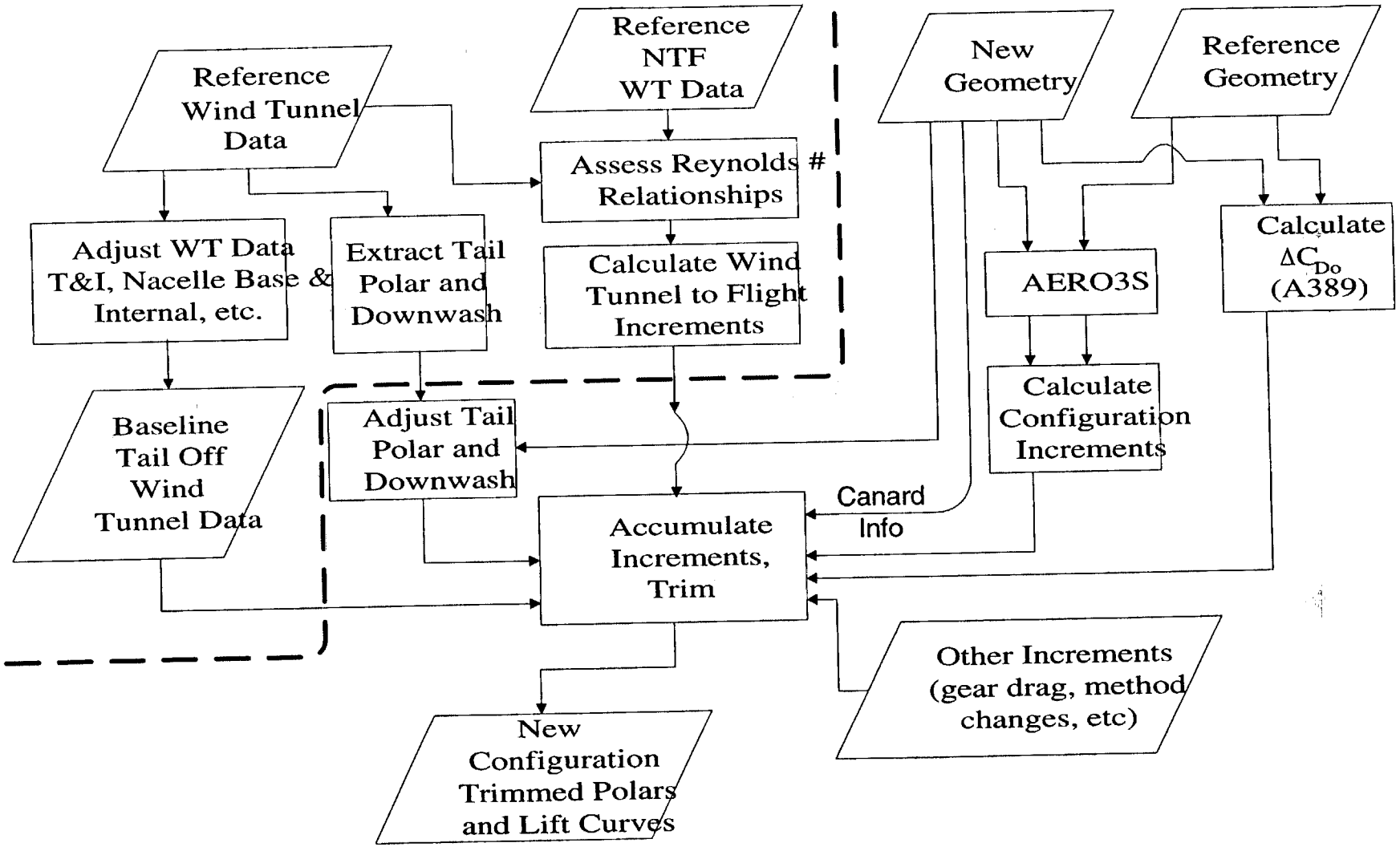

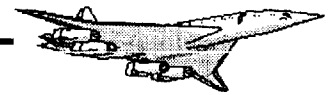

In order to provide an assessment of the preliminary design capability of Aero2s, the code has been compared with data obtained from the recent TCA 4 high-lift test of the 5% TCA wind-tunnel model in the LaRC 14x22-foot wind tunnel. In the common process outlined above, Aero2s is used to provide incremental effects due to geometry variations, rather than to provide absolute data. To assess the validity of this approach, the code is compared with the experimental data in order to evaluate its consistency in predicting the aerodynamic effects of planform and flap changes.

The test provided a database for the baseline TCA configuration (W1) as well as for two alternate planforms, W2 and W3. The aspect ratio for each of these configurations is 2.0 for the baseline, and 2.8 for the alternates, while the outboard wing panel leading-edge sweep is 52° for W1, 28° for W2 and 38° for W3. The three planforms are shown in this figure.

Due to test time limitations, a full set of data on the baseline configuration was not obtained in TCA 4, so that some of the data presented here for W1 will make use of data from the first test entry of this model in the 14x22-foot tunnel, TCA 1. While there were some concerns over the data quality obtained in TCA 1, it is believed that the data used here is consistent with that obtained from TCA 4. A more detailed discussion of the wind tunnel data available for the TCA configuration was provided in the recent "TCA Final Assessment Report" delivered on 9/15/98.

Comparison of Wing Planforms Tested in TCA 4

W1 2.0-52°

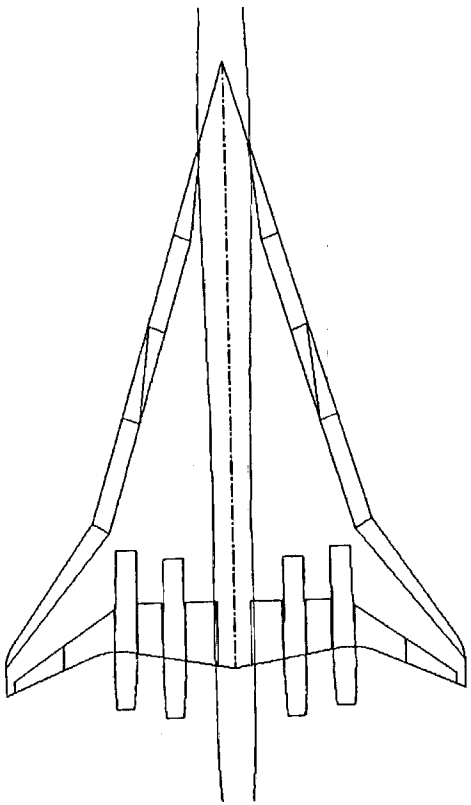

W2 2.8-28°

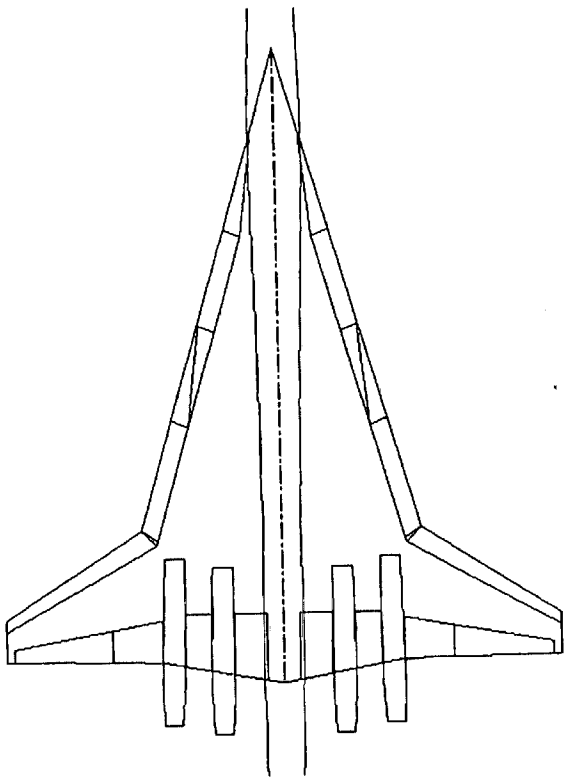

W3 2.8-38°

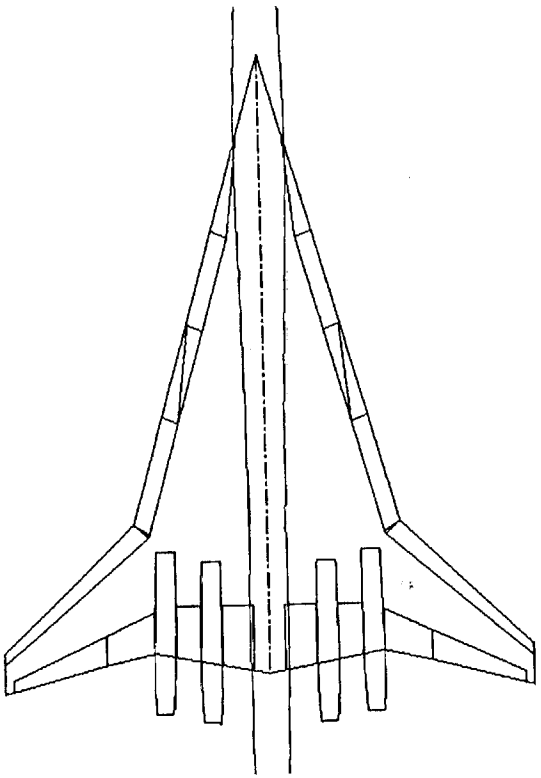

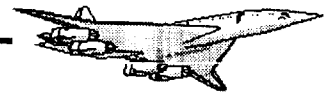

The following two figures show the effect of the planform variation for all three configurations with undeflected flaps.

This figure compares the Aero2s computed and measured lift for the three planforms. For each configuration, the linear code predicts an increase in the lift curve slope at about 8°-10° angle-of-attack as the code predicts the onset of leading-edge separation. In the experimental data, however, there is no such increase observed, and in fact, for the baseline W1 configuration, the lift curve slope decreases.

The linear curve models the change in lift curve slope close to zero angle-of-attack (which is a simply an aspect ratio effect) while the more complex viscous effects associated with thee onset of leading-edge separation are not well predicted.

Aero2s - Effects of Planform Variation
Undeflected Flaps

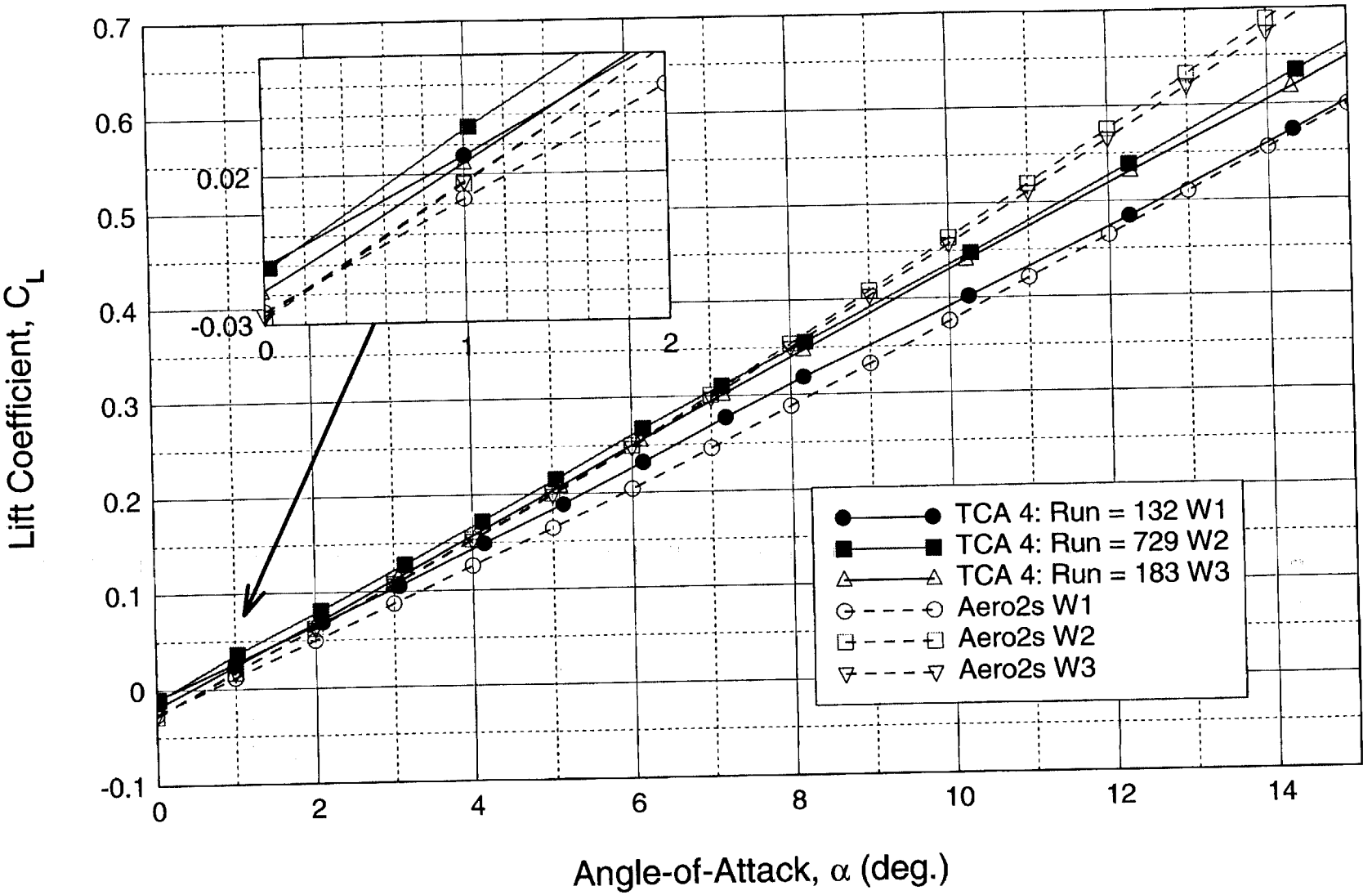

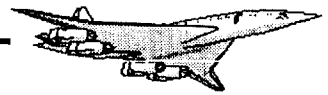

This figure compares the Aero2s computed and measured Lift-to-Drag ratio for the three planforms with undeflected flaps. In each of the theoretical curves, an adjustment to the drag has been added based on the experimentally measured minimum drag.

It can be seen that, while the L/D for W1 is reasonably well predicted, Aero2s greatly over-estimates the performance for the alternate planforms, W2 and W3.

Aero2s - Effects of Planform Variation
Undeflected Flaps

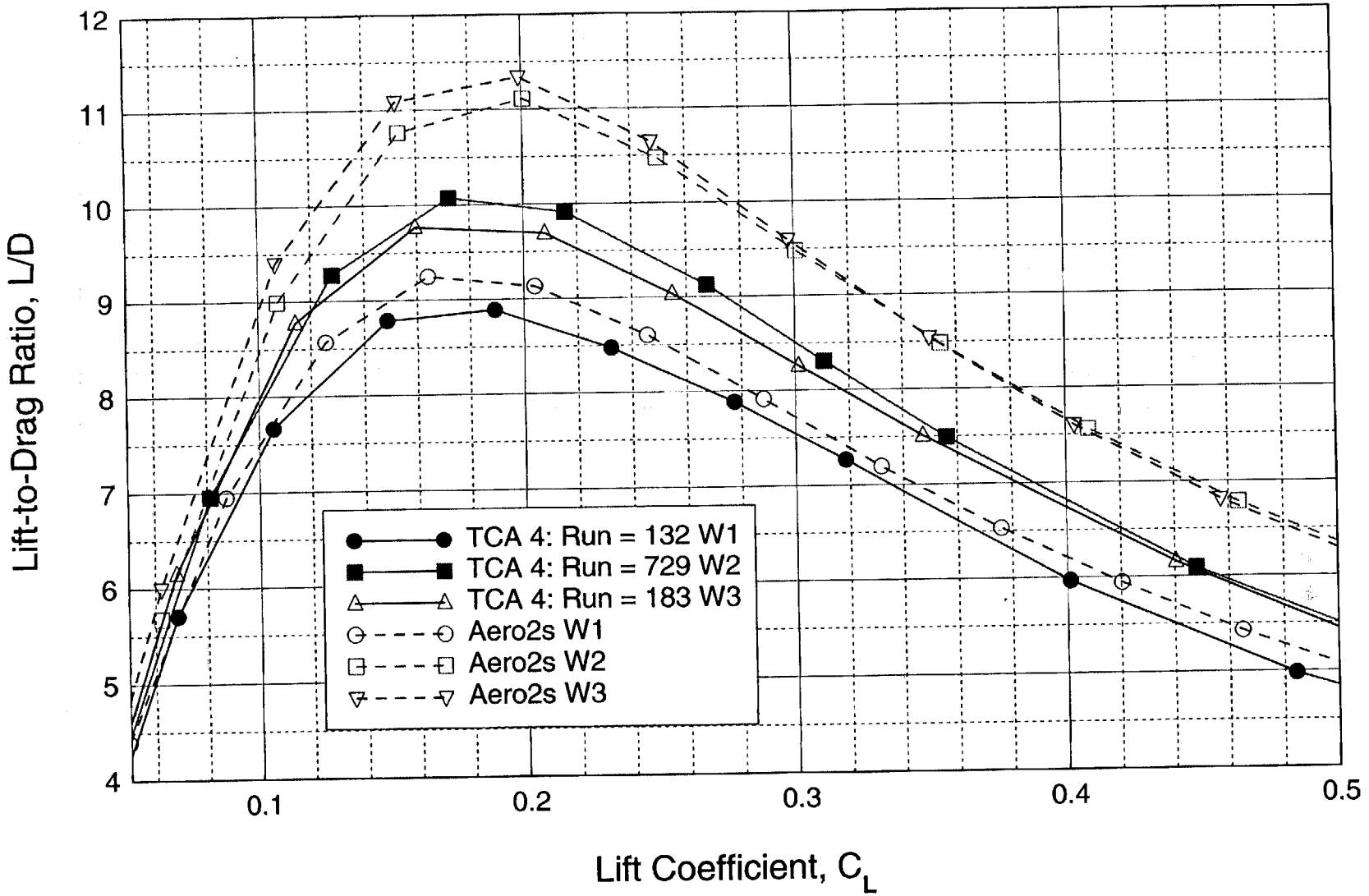

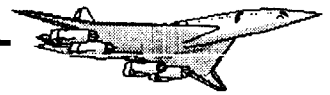

The following four figures show a comparison between the computed and the measured aerodynamic performance and pitching moment for the high-lift configurations with full-span leading-edge flaps deflected 30°, and the trailing-edge flaps deflected 10°.

This figure compares the Aero2s computed and measured lift for the three planforms. It can be seen that at lower angles-of-attack, the lift is very well predicted, although at higher angles-of-attack, Aero2s over-predicts the lift. In the experimental data, increased vortex lift is achieved as the flow separates and forms a strong vortex originating at the leading edge. This lift is offset by the effects of flow separation on the outboard wing panel. For the lower outboard wing sweeps of W2 and W3, there is a stronger rounding over in the lift curve due to this separation, since the reduced leading-edge sweep can not maintain a coherent leading-edge vortex.

Since this is primarily a viscous flow phenomenon, it is not surprising that the linear code is unable to accurately predict this behavior.

Aero2s - Effects of Planform Variation
LE/TE Flaps 30°/10° (Full-Span)

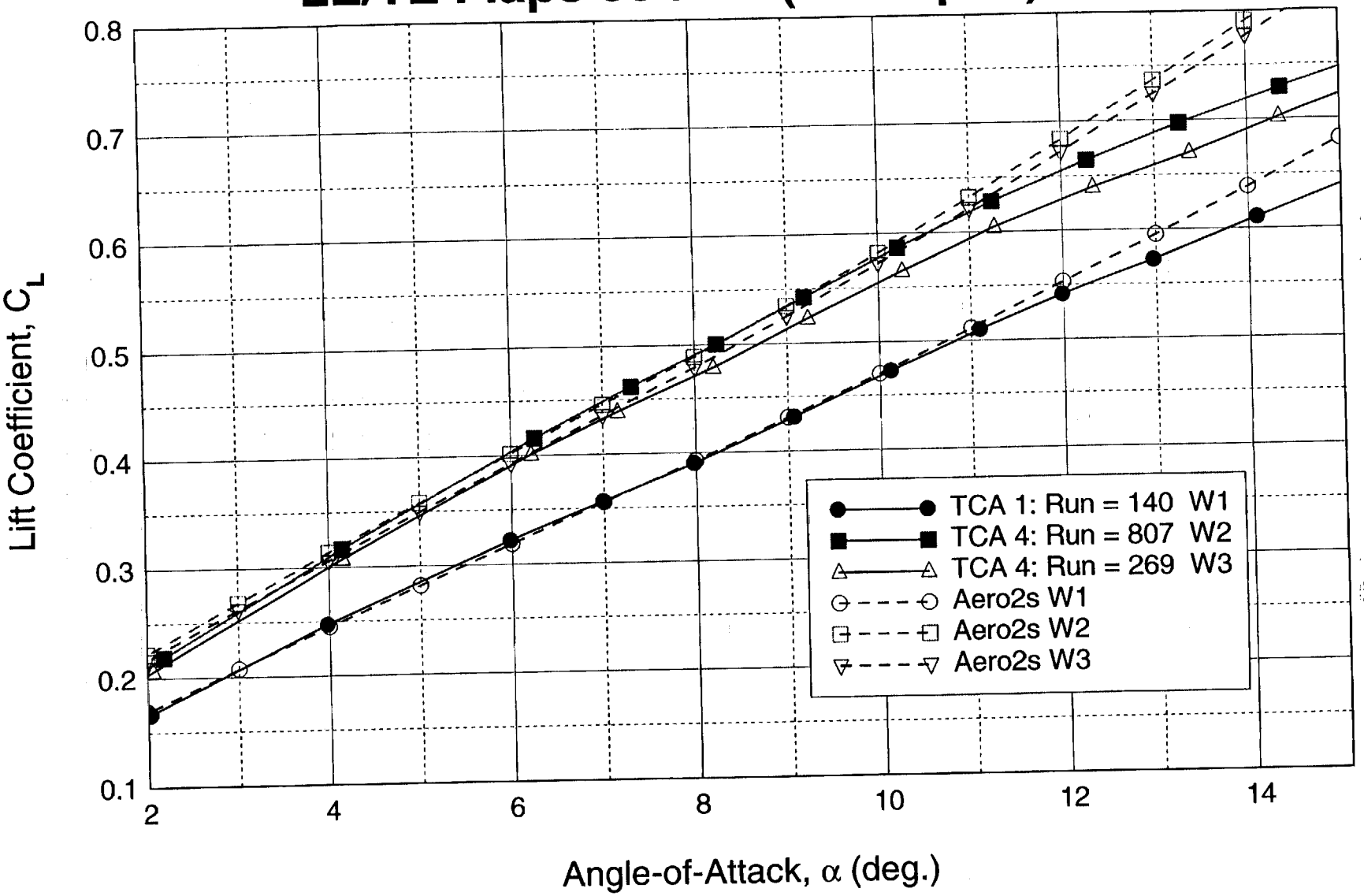

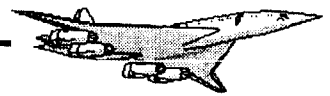

This figure compares the measured and predicted drag polars for the three high-lift configurations. The predicted results include an estimate for the skin-friction drag based on the experimental minimum drag data for the flaps up configuration. For W2 and W3, the estimates close to the nominal design point (C_L = 0.5) are reasonable, and the code provides a reasonable relationship between the two configurations. The values for the baseline configuration are considerably overestimated, primarily because the code predicts a significantly lower minimum induced drag for this configuration as compared to W2 and W3. The data presented here for wings W2and W3 is taken from the TCA 4 test, while the data for W1 is taken from TCA 1 (in order to use data for a consistent set of flap deflections. The reason for the variation in the predicted minimum drag from Aero2s is not clear at this time.

Aero2s - Effects of Planform Variation
LE/TE Flaps 30°/10° (Full-Span)

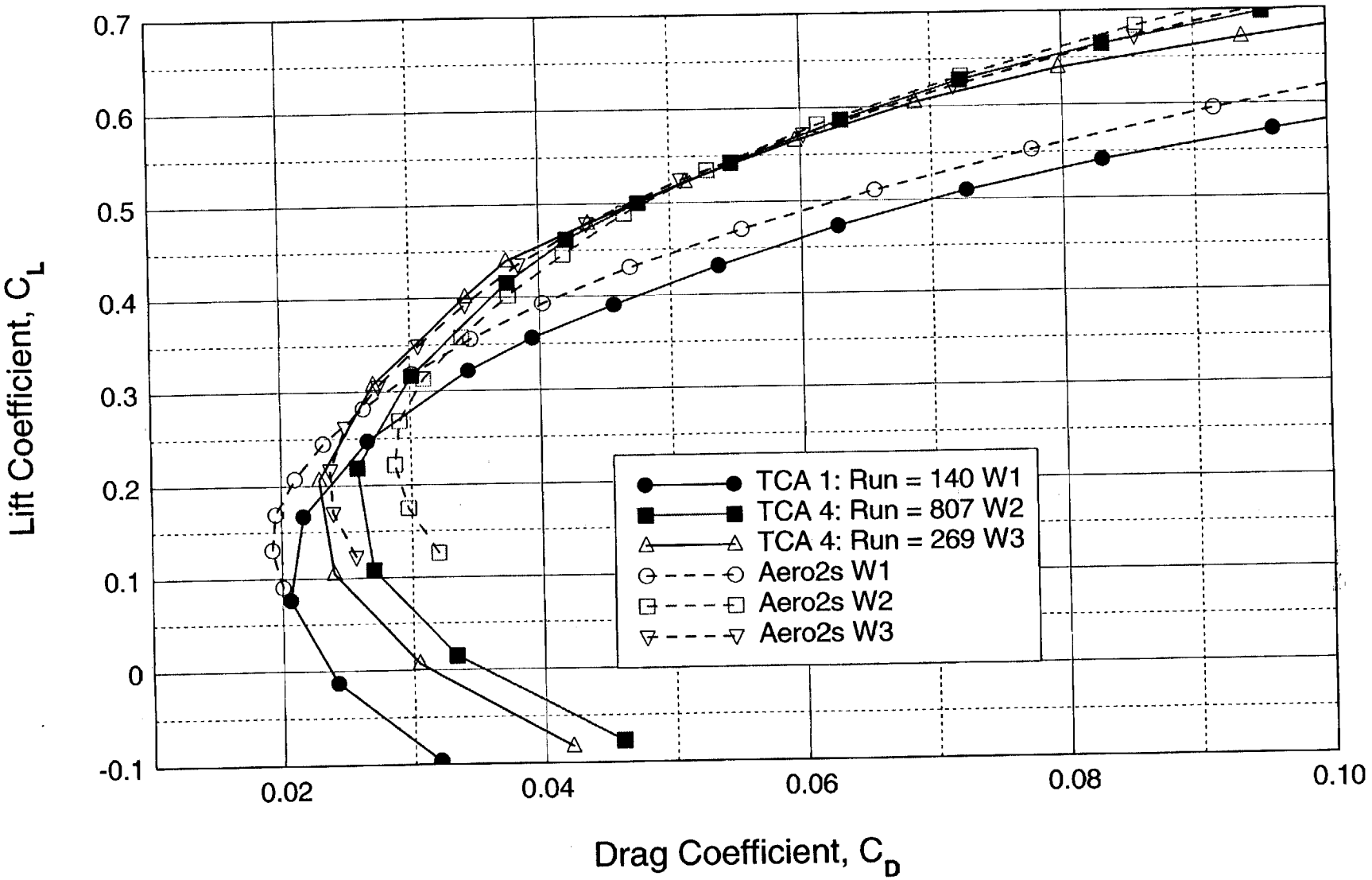

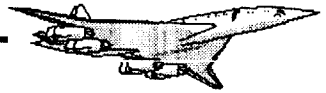

This figure compares the measured and predicted L/D for the three high-lift configurations. The predicted results include an estimate for the skin-friction drag based on the experimental minimum drag data for the flaps up configuration. For W2 and W3, the estimates close to the nominal design point (C_L = 0.5) are reasonable, and the code provides a reasonable relationship between the two configurations. Due to the differences in the drag noted in the previous figure, the L/D values for the baseline configuration are considerably over-estimated.

Aero2s - Effects of Planform Variation
LE/TE Flaps 30°/10° (Full-Span)

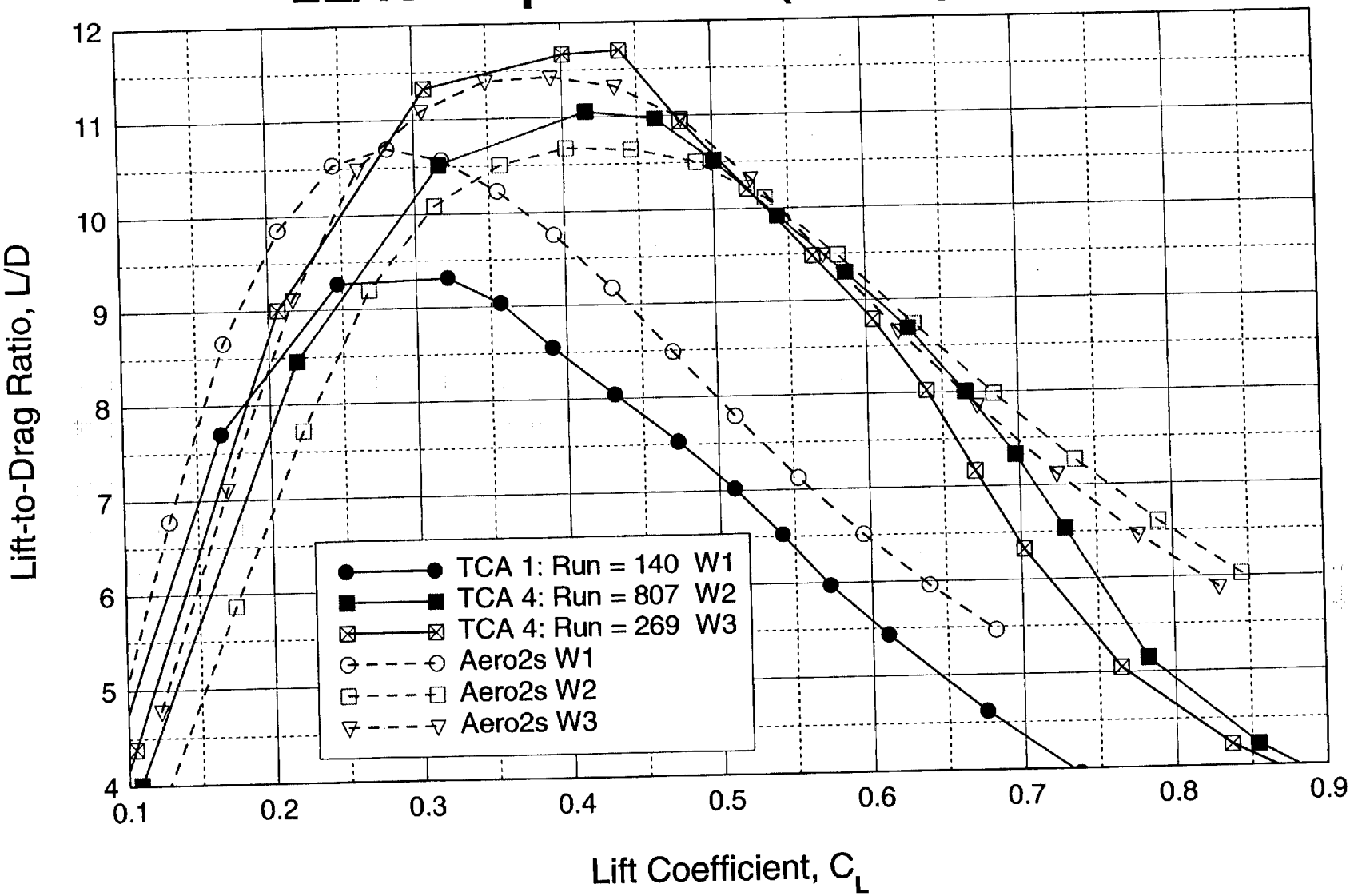

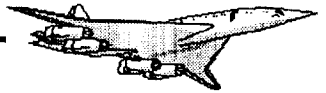

This figure compares the measured and predicted pitching moments for the the three high-lift configurations. The Aero2s results do not capture the pitch break which occurs in the experimental data as the leading-edge vortex begins to form. The linear code accounts empirically for the lift and drag effects of the leading-edge separation, but it does not attempt to model the change in load distribution which results from the presence of the leading-edge vortex.

Near the design point, the pitching moment increments due to the planform variation are captured reasonably well, although the absolute levels differ from the tunnel data. The code does however predict a difference between W2 and W3 for lift coefficients greater than about 0.4, while the experimental data indicates little difference between the two wings. The stronger viscous effects on these wings which cause the round over in the lift curves which was seen earlier could account for this difference.

Aero2s - Effects of Planform Variation
LE/TE Flaps 30°/10° (Full-Span)

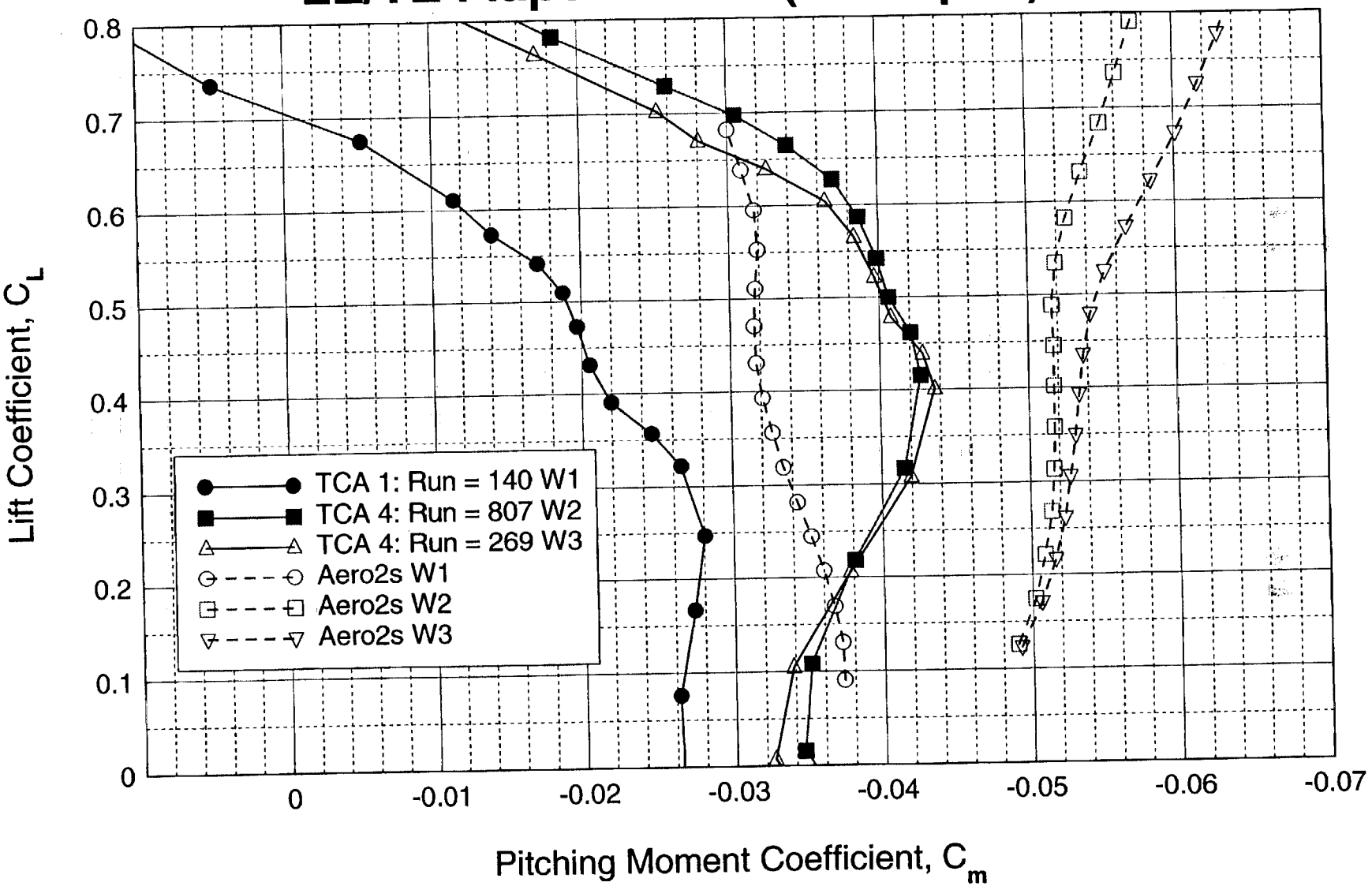

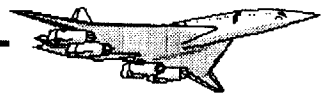

This figure compares the effects on the lift curves due to a variation in spanwise leading-edge flap extent between the predicted and the experimental data. In particular, results are presented for the full-span leading-edge flap which extends to the side of the fuselage, and the part-span flap which tapers to zero chord length at about 30% semi-span location (as shown in the earlier planform figure).

For W2 and W3, the experimental data shows that the part-span flap has little effect on lift up to about 12° angle-of-attack, after which the effects of a stronger leading-edge vortex forming over the undeflected portion of the wing leading-edge result in a significant increase in lift curve slope. The data for W1 also shows an increase in lift for the part-span flap at lower angles-of-attack, although, in light of the data for the other planforms, part of this is most likely to be due to experimental error. It should be noted that this data was obtained in TCA 1.

The Aero2s results also show an increase in predicted lift for the part-span flap, although the strong effects of the increased vortex lift at higher angles-of-attack are not captured well. Also, as noted earlier, the absolute lift levels at these conditions are not well predicted.

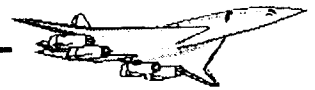

Aero2s - Effects of Leading-Edge Flap Extent (LE/TE 30°/10°)

Aero2s results

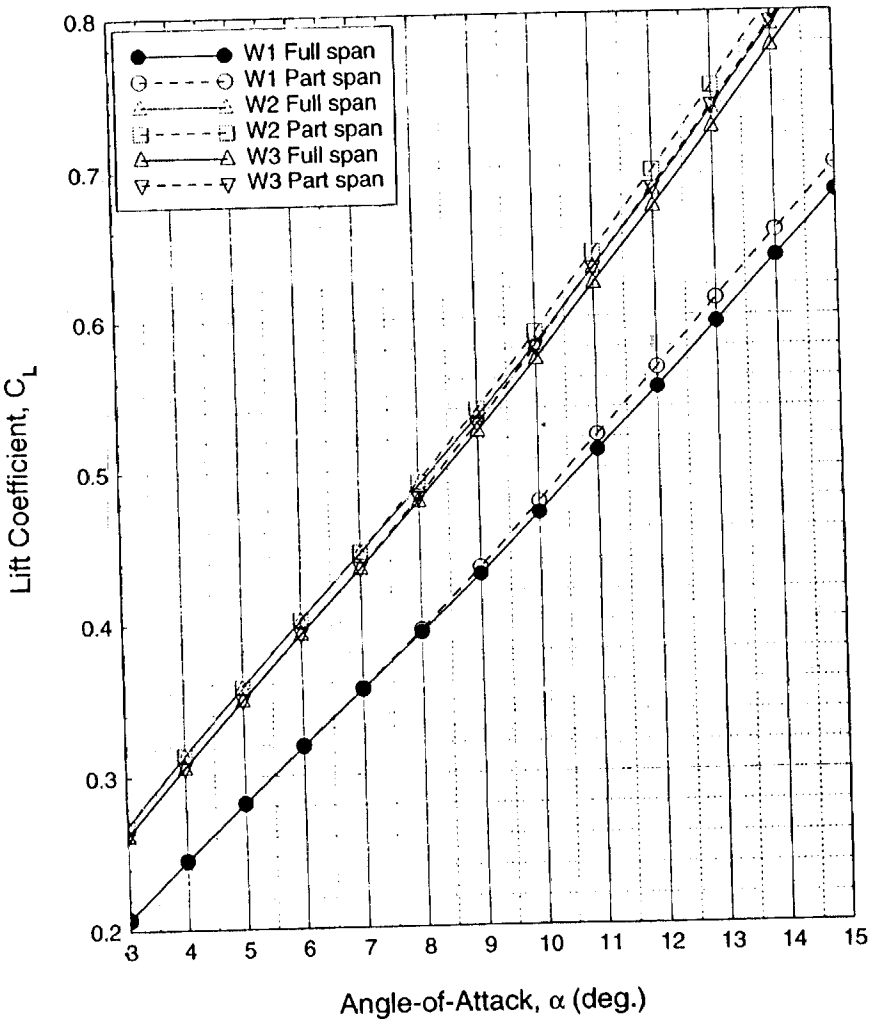

Experimental data (TCA 1, TCA 4)

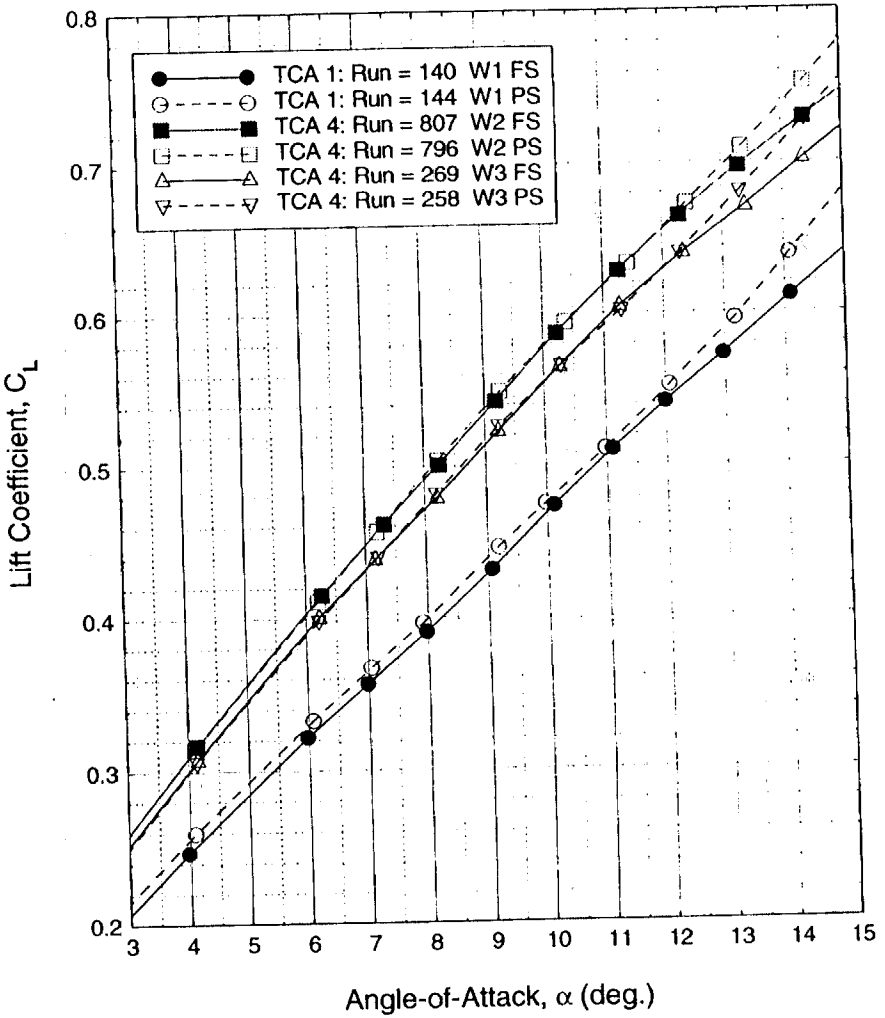

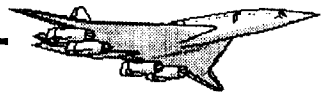

This figure compares the effects on the L/D due to a variation in spanwise flap extent between the predicted and the experimental data. In particular, results are presented for the full-span leading-edge flap which extends to the side of the fuselage, and the part-span flap which tapers to zero chord length at about 30% semi-span location (as shown in the earlier planform figure).

As in the previous slide, trends near the design point are predicted reasonably well for W2 and W3 with the code predicting little reduction in L/D between the full- and part-span configurations, although the loss in L/D at higher angles-of-attack due to the stronger vortex is underestimated. Also, the experimental data shows a reduction in L/D at low lift conditions for the part-span flap which is not captured computationally. This reduction could be due to flow separation induced close to the region in which the flap tapers to zero length.

As noted earlier, the absolute levels for the W1 configuration are not well predicted.

Aero2s - Effects of Leading-Edge Flap Extent (LE/TE 30°/10°)

Aero2s results

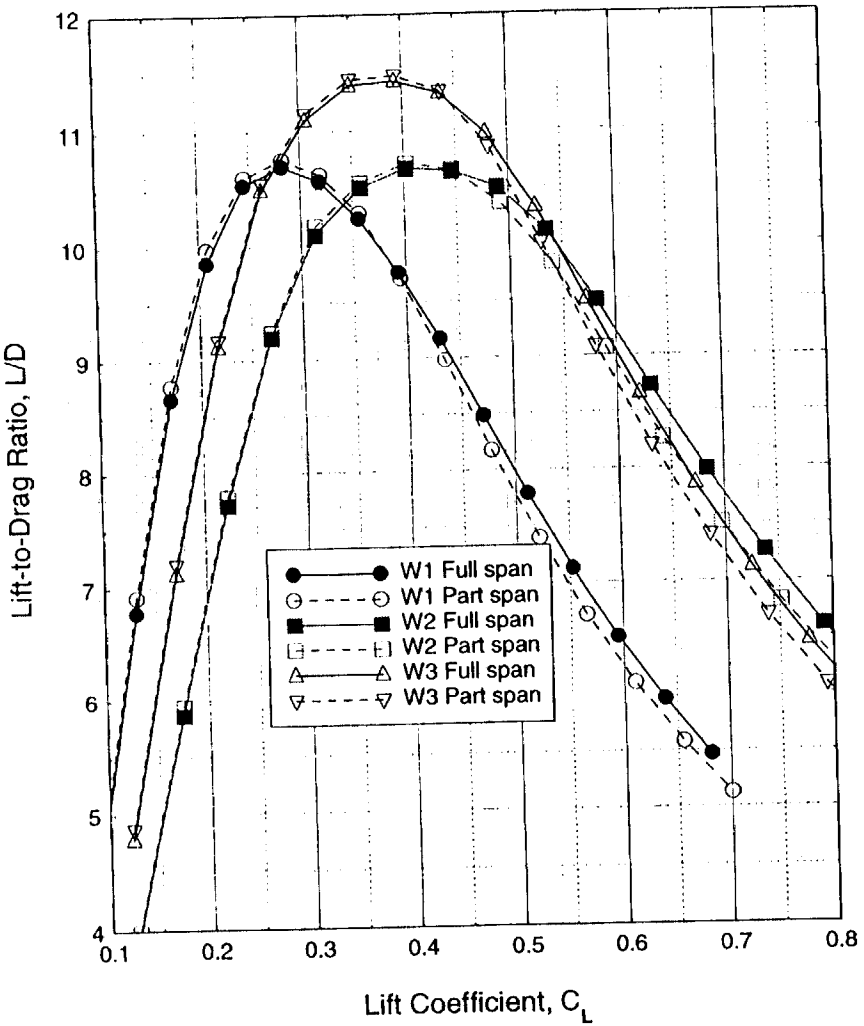

Experimental data (TCA 1, TCA 4)

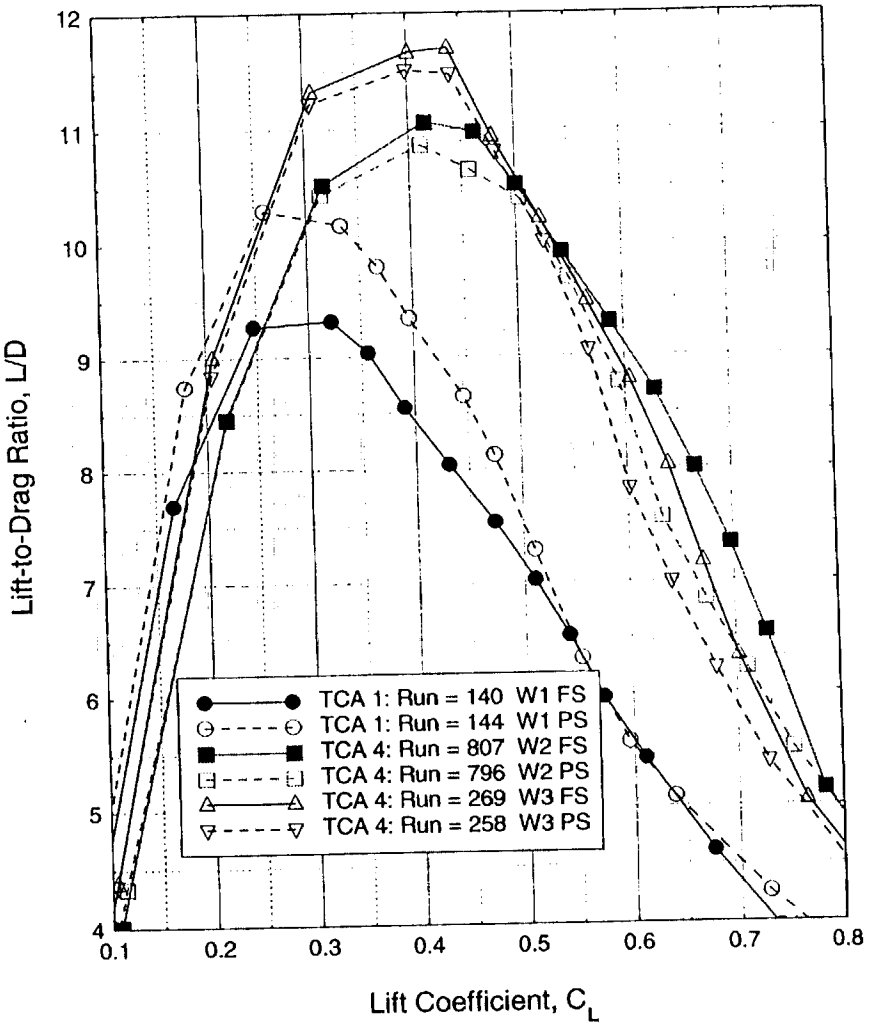

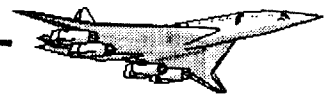

This figure compares the effects of the outboard leading-edge flap deflection predicted by Aero2s against the data measured in TCA 4 for the higher aspect ratio wings, W2 and W3. This figure shows the computed and experimental lift curves for the two wings with leading-edge flaps deflected to 30° inboard, and 30° and 25° outboard, both with 10° trailing-edge flaps. The configurations are denoted 30/10 and 30(25)/10 respectively. It can be seen that the measured data for W3 shows very little sensitivity to the change in outboard flap deflection at all angles of attack, while W2 shows an increase in lift as the flap deflection is reduced up to an angle of attack of about 13°. The reason for this difference is not clearly understood. However, the lift increment for W2 is captured by Aero2s.

Aero2s - Effects of Outboard Flap Deflection

Aero2s results

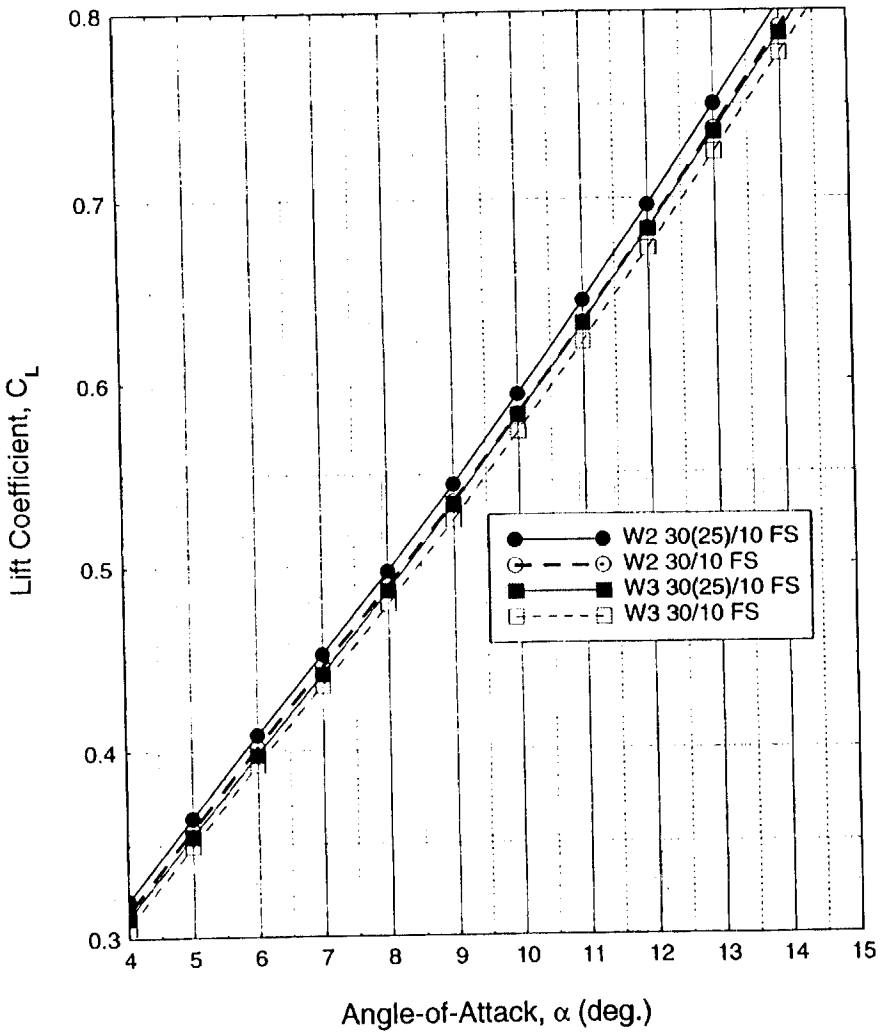

Experimental data (TCA 4)

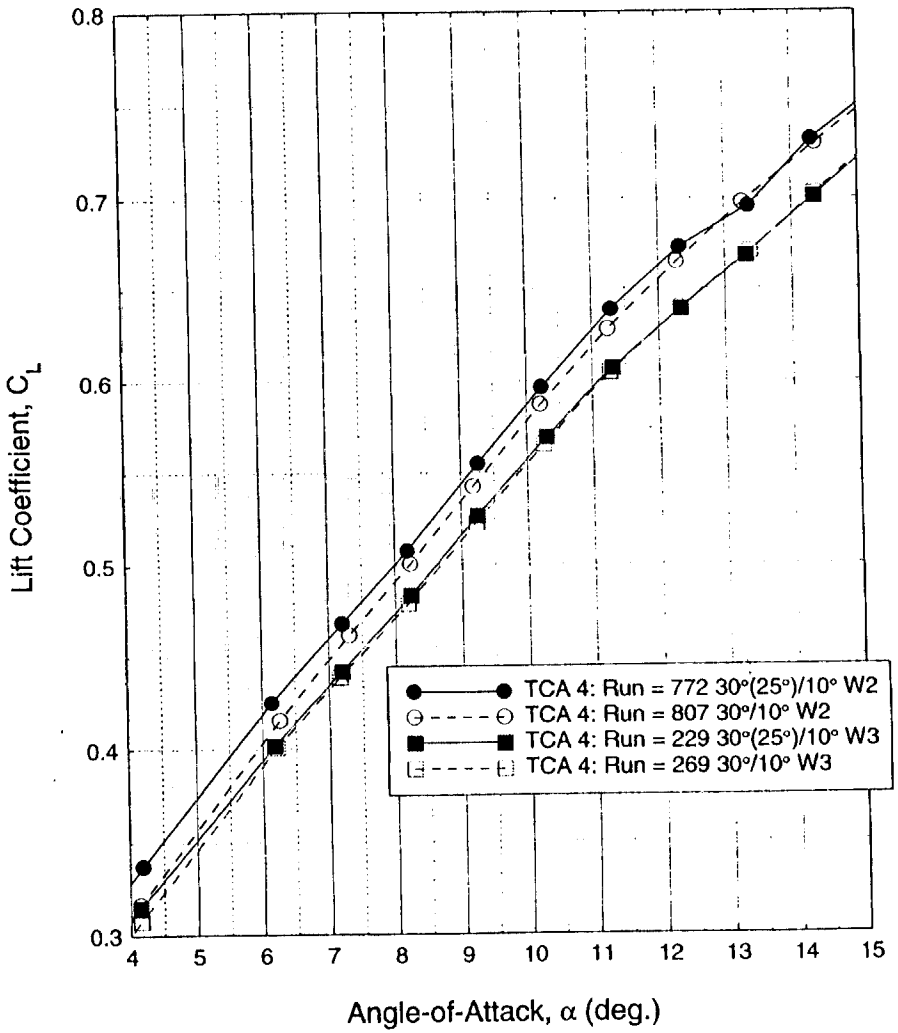

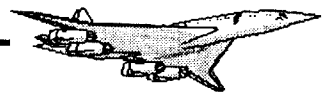

This figure compares the effects of the outboard leading-edge flap deflection on the Lift-to-Drag ratio predicted by Aero2s against the data measured in TCA 4 for the higher aspect ratio wings, W2 and W3.

At low lift conditions, the L/D is reduced with increasing outboard flap deflection as would be expected since the outboard leading-edge flap is now over deflected for the lower angle of attack. While Aero2s predicts about the same reduction in maximum L/D for both planforms, the experimental data indicates that there is a greater reduction for the lower outboard wing sweep (W2).

Close to the nominal design lift coefficient, there was little increase in L/D associated with the reduced outboard flap deflection for W3, which is captured well by Aero2s, while for W2 there was some benefit to be gained from the 25° outboard flap, which was again captured reasonably well by the Aero2s results.

Aero2s - Effects of Outboard Flap Deflection

Aero2s results

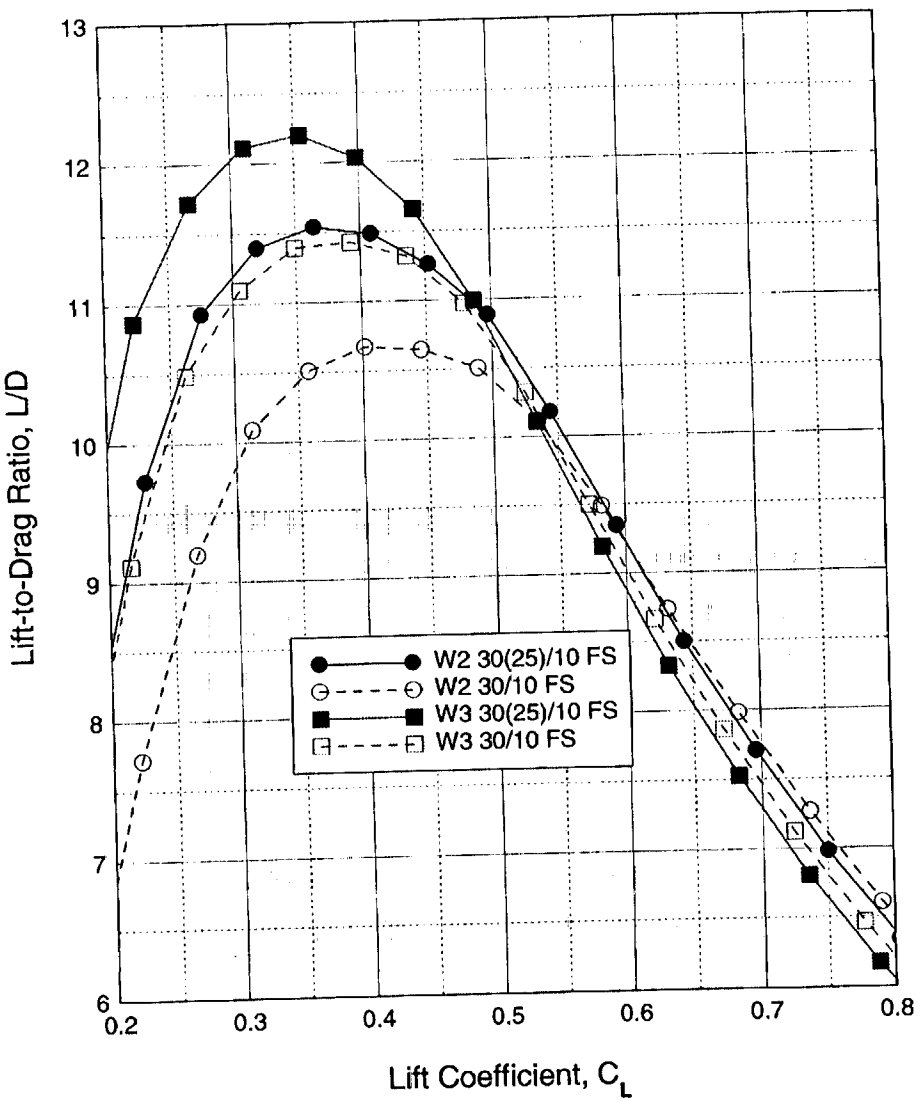

Experimental data (TCA 4)

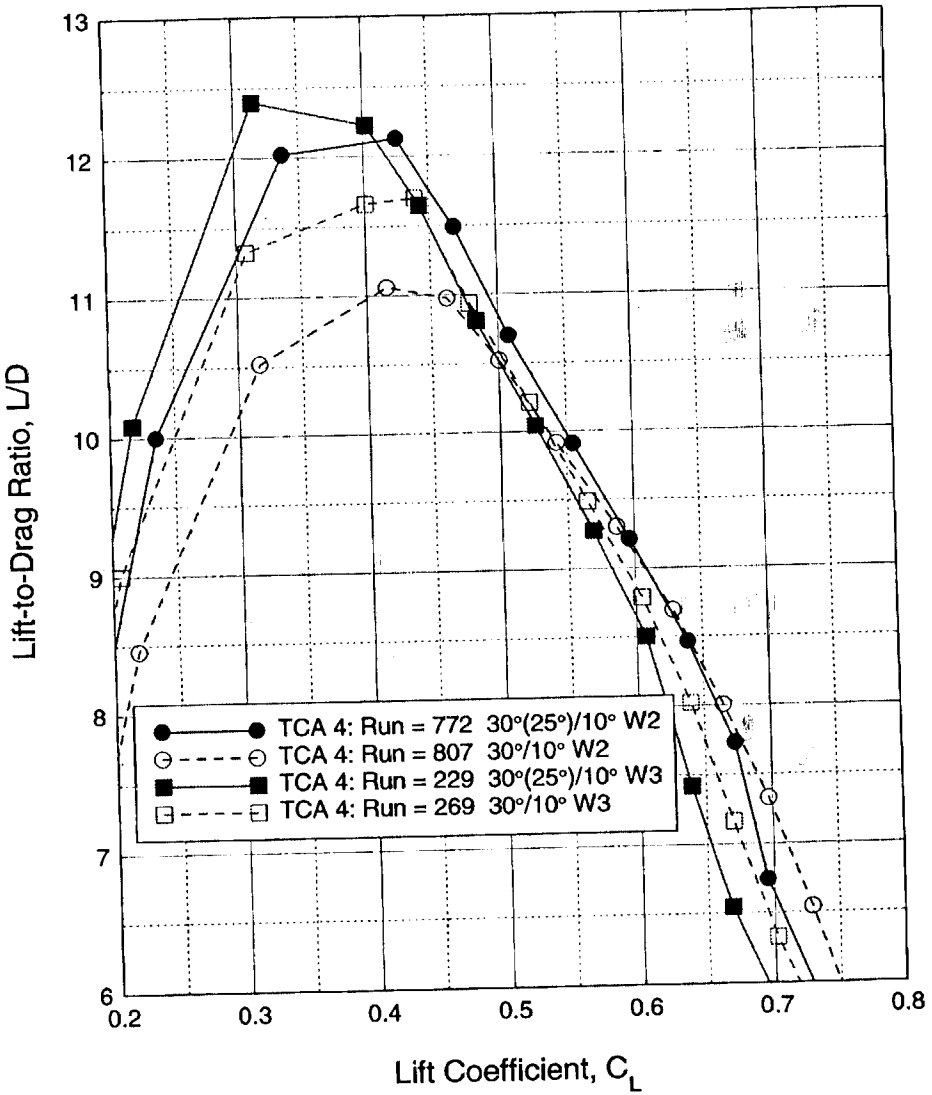

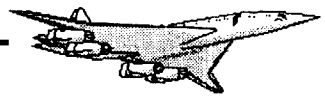

This figure compares the effects of the trailing-edge flap deflection on the computed and experimental lift curves. It can be seen that Aero2s does a reasonable job of predicting the lift increment resulting from the increased flap deflection for the lower flap-deflection angles for angles-of-attack up to about 10° for the 100° and 20° trailing-edge flap deflection. The lift for the 30° trailing-edge flap deflection is over predicted by Aero2s, indicating that the boundary-layer separation is becoming more significant for this flap deflection leading to a reduction in the trailing-edge flap effectiveness seen in the experimental data.

Aero2s - Effects of Trailing-Edge Flap Deflection
Lift vs. Angle-of-Attack

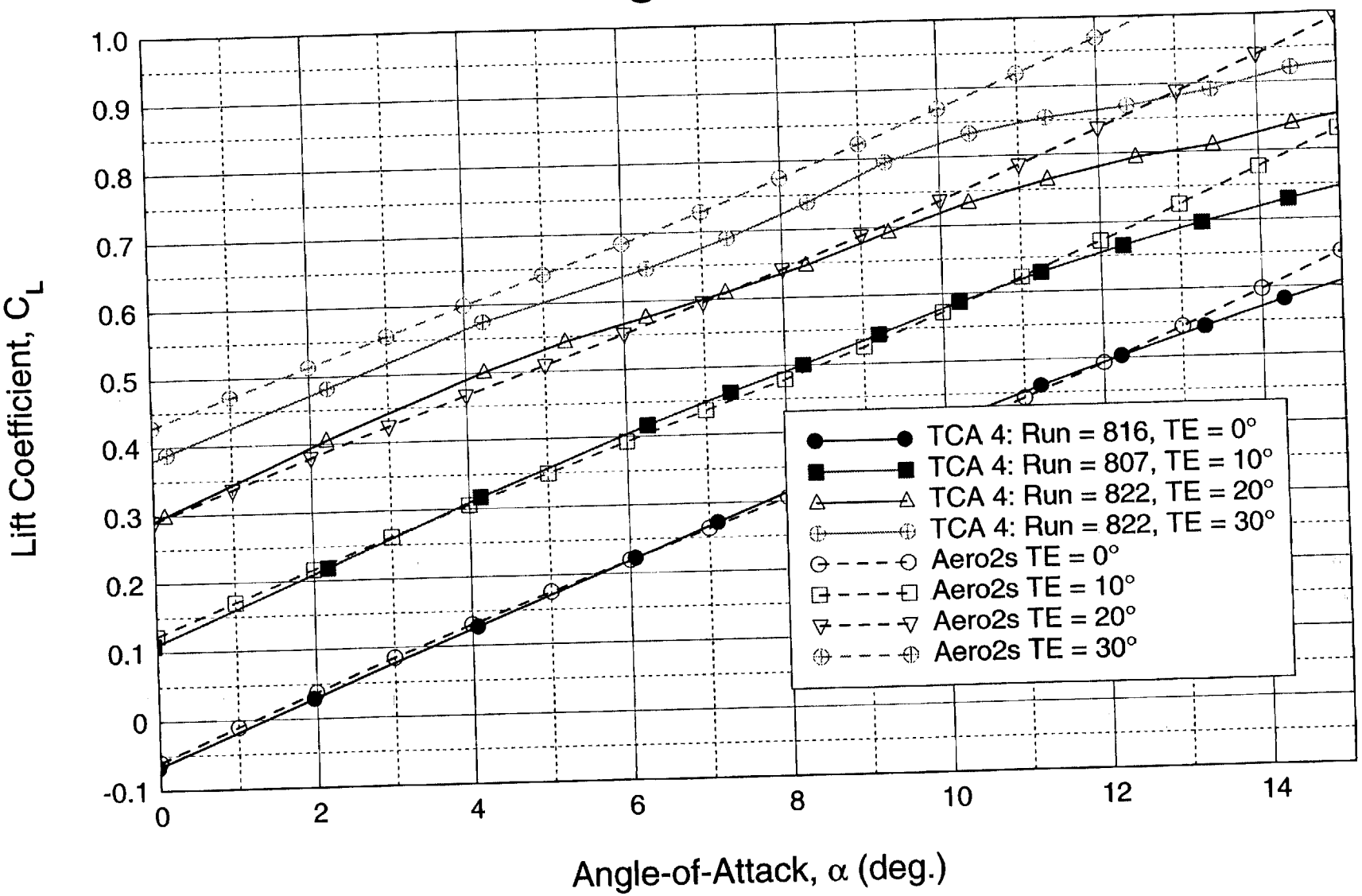

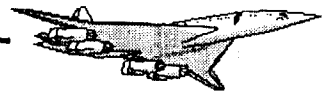

This figure compares the effects of the trailing-edge flap deflection on the computed and experimental drag. As seen in the previous slide, the results for the lower flap deflections are reasonable up to about 10° angle-of-attack. Again, the effects of the separation on the trailing-edge flaps will not be captured by the linear code.

Aero2s - Effects of Trailing-Edge Flap Deflection
Drag vs. Angle-of-Attack

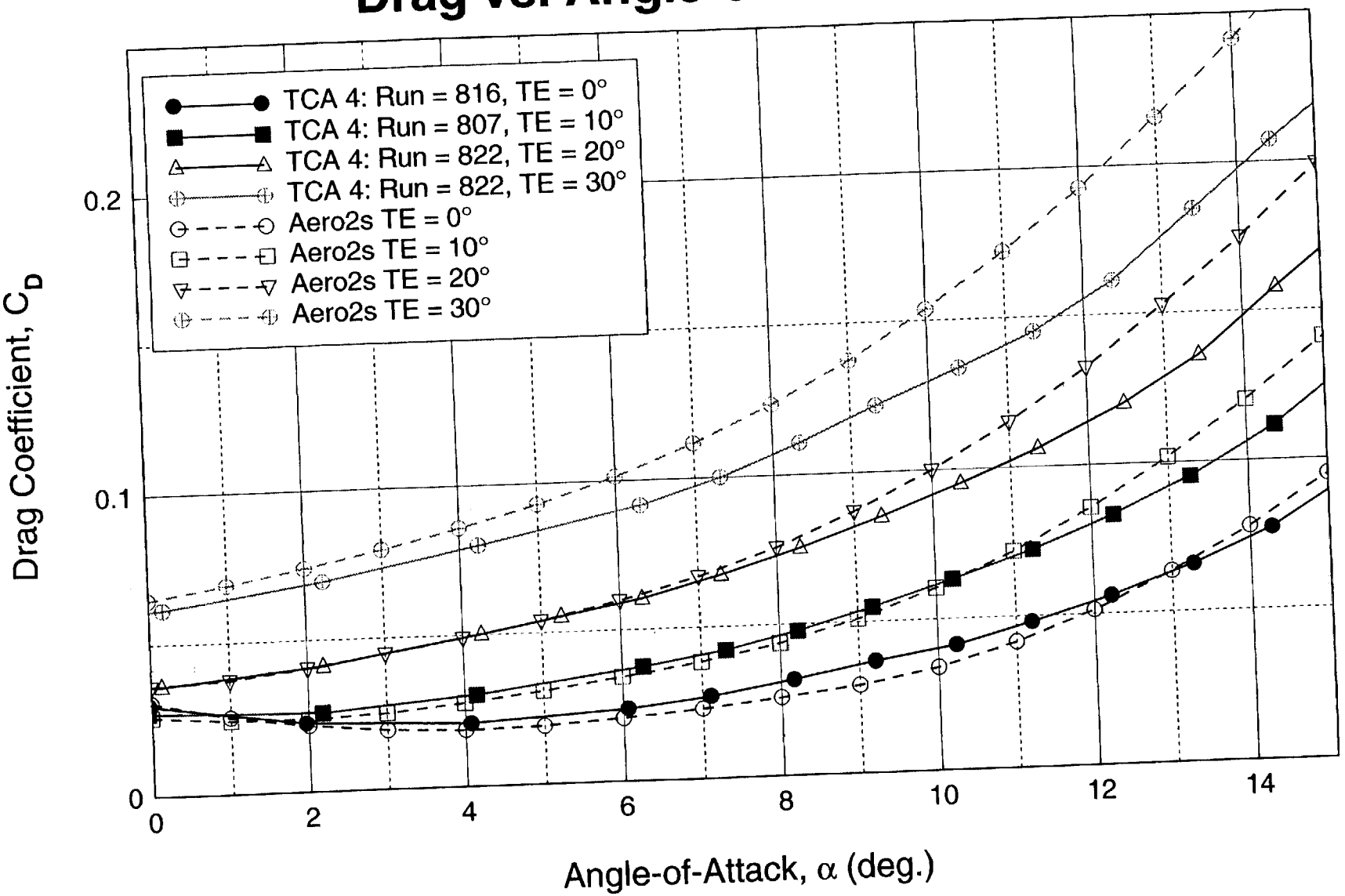

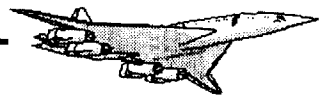

This figure compares the effects of the trailing-edge flap deflection on the computed and experimental Lift-to-Drag ratio. As seen in the previous slide, the results for the lower flap deflections are reasonable up to about 10° angle-of-attack. Again, the effects of the separation on the trailing-edge flaps will not be captured by the linear code.

Aero2s - Effects of Trailing-Edge Flap Deflection
Drag vs. Angle-of-Attack

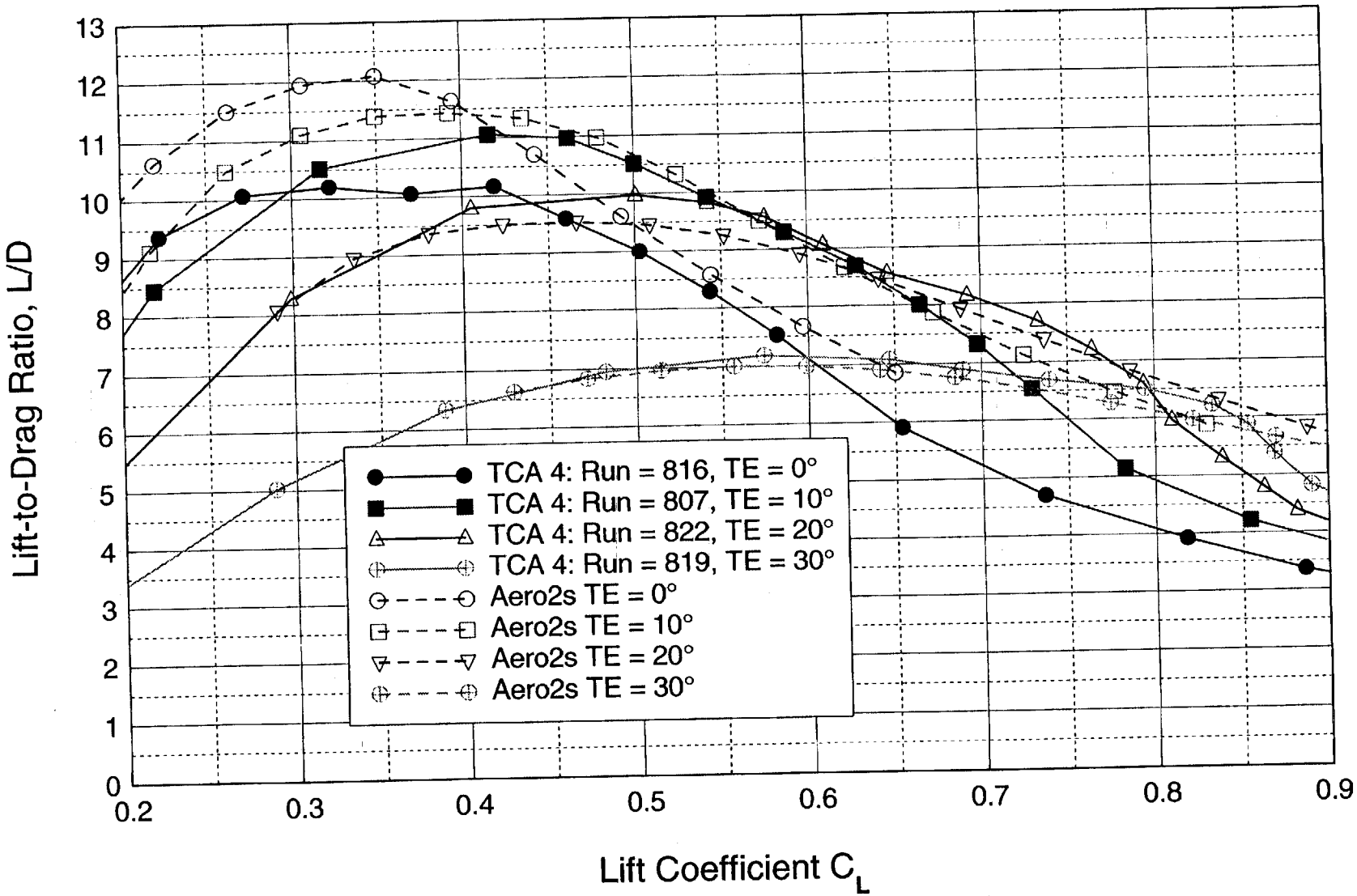

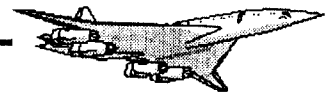

The conclusions from this study are outlined here.

While the code does a reasonable job of predicting the forces for predominantly attached flow, it becomes unreliable as the effects of viscous separation become larger. For the baseline TCA wing, W1, where there is significant flow separation on the outboard wing panel at the nominal design point, Aero2s significantly under-predicts the drag. On the other hand, for the higher aspect ratio wings, W2 and W3, the absolute levels of lift and drag are predicted reasonably well. This means that the performance increments resulting from the change in aspect ratio and outboard wing sweep are not well captured by the code.

The use of Navier-Stokes methods can give a much more accurate indication of high-lift performance, but the complexity and computational cost of such methods does not yet permit extensive use in the preliminary design process.

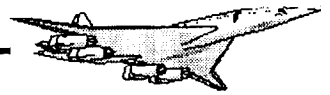

Conclusions

- Lift and drag variations with planform predicted reasonably well for predominantly attached flow
- For significantly separated flows, there can be significant errors in both lift and drag
- Trailing-Edge Flap Deflection effects predicted reasonably well
- Need improved fast methods to reliably support design trade studies

REPORT DOCUMENTATION PAGE

Form Approved
OMB No. 07704-0188

1. AGENCY USE ONLY *(Leave blank)*	2. REPORT DATE	3. REPORT TYPE AND DATES COVERED
	December 1999	Conference Publication

4. TITLE AND SUBTITLE
1999 NASA High-Speed Research Program Aerodynamic Performance Workshop
Volume II—High Lift

5. FUNDING NUMBERS
537-07-51-10

6. AUTHOR(S)
Edited by David E. Hahne

7. PERFORMING ORGANIZATION NAME(S) AND ADDRESS(ES)
NASA Langley Research Center
Hampton, VA 23681-2199

8. PERFORMING ORGANIZATION REPORT NUMBER
L-17911D

9. SPONSORING/MONITORING AGENCY NAME(S) AND ADDRESS(ES)
National Aeronautics and Space Administration
Washington, DC 20546-0001

10. SPONSORING/MONITORING AGENCY REPORT NUMBER
NASA/CP-1999-209704/
VOL2/PT2

11. SUPPLEMENTARY NOTES

12a. DISTRIBUTION/AVAILABILITY STATEMENT
Unclassified–Unlimited
Subject Category 02 Distribution: Nonstandard
Availability: NASA CASI (301) 621-0390

12b. DISTRIBUTION CODE

13. ABSTRACT *(Maximum 200 words)*

NASA's High-Speed Research Program sponsored the 1999 Aerodynamic Performance Technical Review on February 8-12, 1999 in Anaheim, California. The review was designed to bring together NASA and industry High-Speed Civil Transport (HSCT) Aerodynamic Performance technology development participants in the areas of Configuration Aerodynamics (transonic and supersonic cruise drag prediction and minimization), High Lift, and Flight Controls. The review objectives were to (1) report the progress and status of HSCT aerodynamic performance technology development; (2) disseminate this technology within the appropriate technical communities; and (3) promote synergy among the scientists and engineers working on HSCT aerodynamics. In particular, single and midpoint optimized HSCT configurations, HSCT high-lift system performance predictions, and HSCT simulation results were presented, along with executive summaries for all the Aerodynamic Performance technology areas. The HSR Aerodynamic Performance Technical Review was held simultaneously with the annual review of the following airframe technology areas: Materials and Structures, Environmental Impact, Flight Deck, and Technology Integration. Thus, a fourth objective of the Review was to promote synergy between the Aerodynamic Performance technology area and the other technology areas of the HSR Program.

14. SUBJECT TERMS
High-speed research; High-Speed Civil Transport

15. NUMBER OF PAGES
485

16. PRICE CODE
A21

17. SECURITY CLASSIFICATION OF REPORT	18. SECURITY CLASSIFICATION OF THIS PAGE	19. SECURITY CLASSIFICATION OF ABSTRACT	20. LIMITATION OF ABSTRACT
Unclassified	Unclassified	Unclassified	UL

NSN 7540-01-280-5500

Standard Form 298 (Rev. 2-89)
Prescribed by ANSI Std. Z39-18
298-102